Transactions of the ASME

Journal of Fluids Engineering

Published Quarterly by The American Society of Mechanical Engineers

VOLUME 113 • NUMBER 4 • DECEMBER 1991

(Contents continued on page 590)

Transactions of the ASME, Journal of Fluids Engineering (ISSN 0098-2202) is published quarterly (Mar., June, Sept., Dec.) for $110.00 per year by The American Society of Mechanical Engineers, 345 East 47th Street, New York, NY 10017. Second class postage paid at New York, NY and additional mailing offices. POSTMASTER: Send address changes to Transactions of the ASME, Journal of Fluids Engineering, c/o THE AMERICAN SOCIETY OF MECHANICAL ENGINEERS, 22 Law Drive, Box 2300, Fairfield, NJ 07007-2300.
CHANGES OF ADDRESS must be received at Society headquarters seven weeks before they are to be effective. Please send old label and new address.
PRICES: To members, $36.00, annually; to nonmembers, $110.00. Add $20.00 for postage to countries outside the United States and Canada.
STATEMENT from By-Laws. The Society shall not be responsible for statements or opinions advanced in papers or . . . printed in its publications (B7.1, Par. 3).

INDEXED by Applied Mechanics Reviews and Engineering Information, Inc.
Canadian Goods & Services Tax Registration #126148048

(Contents continued)

Report of the Executive Committee on the Reorganization of the ASME Fluids Engineering Division

R. A. Bajura
Program Representative

The *Journal of Fluids Engineering* is the archival publication sponsored by the Fluids Engineering Division of ASME. In addition to advertising our technical meetings and programs, the Editor also invites news articles about the Division which are of special interest to our readers. This editorial contribution describes a part of our coordinated activity as a Division to review our present status and redefine future goals.

At the 1989 Winter Annual Meeting, the Executive Committee (EC) of the Fluids Engineering Division (FED) proposed a review of the organizational structure of the Division to ensure better coordination and to increase participation by industrial members of the Division in our technical programs.

The Committee solicited input from the technical committee and coordinating group chairs and reviewed this advice at the Technology Executives Conference in March, 1990. We then circulated a proposal to the membership in advance of the 1990 Fluids Engineering Division Spring Meeting in Toronto in June.

Paul Cooper and Sam Martin chaired an open meeting of the Division in Toronto during which the membership authorized a new committee structure. The major change resulted in the formation of two technical committees to replace three existing technical committees: Fluid Mechanics, Fluid Machinery, and Fluid Transients. One of the new committees would emphasize fundamental fluid mechanics and the other new committee would emphasize engineering applications of fluid mechanics.

Task Force Report Summary

Members of the Executive Committee, together with the technical committee chairs, met in Newark, NJ as a Task Force in October, 1990 to formulate procedures to implement the recommended changes. Figure 1 illustrates the organizational structure of the Fluids Engineering Division resulting from these discussions. Highlights of the Task Force Report are summarized below.

1. The Fluid Mechanics Committee, the Fluid Transients Committee, and the Fluid Machinery Committee are combined into two technical committees named, respectively:
   (*a*) Fluid Applications and Systems Technical Committee (FASTC), and
   (*b*) Fluid Mechanics Technical Committee (FMTC)
   The new Fluid Mechanics Technical Committee is contracted in scope compared to the former committee. The Fluid Applications and Systems Technical Committee is an expansion of the remaining elements of the Fluid Mechanics Committee and the former Fluid Transients and Fluid Machinery Committees. Tables 1 and 2 outline the program areas and subcommittee structure proposed for these two newly-formed committees.
2. The Multiphase Flow Technical Committee (MFTC) remains essentially unchanged. Program areas and the subcommittee structure for the MFTC are listed on Table 3. Topics covered by this committee include all areas and applications treated by the Fluid Applications and Systems and Fluid Mechanics Technical Committees, but as applied to multiphase flows.
3. The Coordinating Group for Fluid Measurements (CGFM) and the Coordinating Group for Computational Fluid Dynamics (CGCFD) were not affected by the proposed reorganization.
4. An Advisory Board is instituted to provide input to the FED Executive Committee and to oversee other division-wide programs.
5. Elections of officers for the two new committees were held at the 1990 WAM. Current officers for the various committees are:
   FASTC - Steve Zakem
   FMTC - Hugh Coleman
   MFTC - Jong Kim
   CGFM - Ed Rood
   CGCFD - Ismail Celik
   Their terms expire in June, 1992.
6. All committees and coordinating groups will undergo a

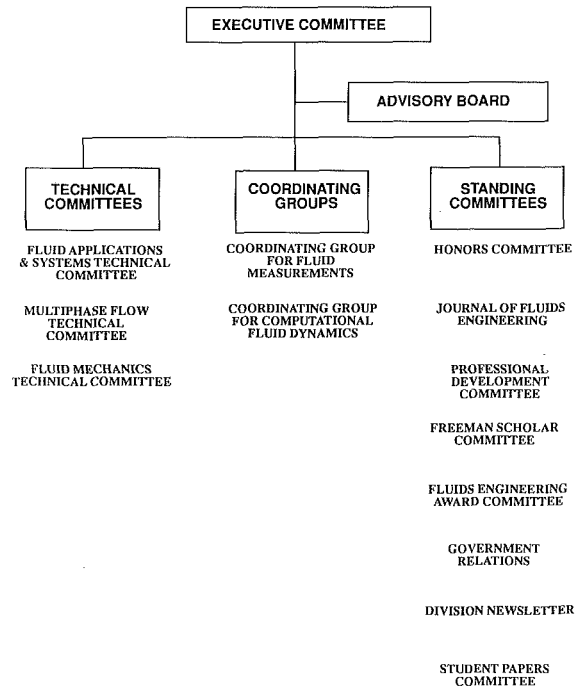

Fig. 1 Organization chart, ASME Fluids Engineering Division, November 1991

Table 1 Fluid Applications and Systems Technical Committee

Program areas and subcommittee structure

1. Fluid Machinery and Components:
   -Turbomachinery (compressors, pumps and turbines)
   -Hydropower
   -Hydropropulsion (propellers, jet pumps, torpedoes, submarines, hydrofoils, flow noise)
   -Valves, Flow Controllers, and Dividers
   -Performance of Machines and Components
   -Other Fluid Machines
2. Fluid Transients and Structural Interactions:
   -Piping System Transients
   -Power Plant Transients
   -System Transients
   -Fluid Transmission Lines
   -Waterhammer
   -Flow Induced Vibrations
3. Industrial and Environmental Applications:
   -Positive Displacement Compressors, Pumps, and Motors
   -Internal Combustion Systems
   -Fluid Mechanics in Manufacturing Processes
   -Spray Systems
   -Energy Conversion
   -Fluidics
   -Vehicle Aerodynamics and Hydrodynamics
   -Industrial Aerodynamics and Hydrodynamics
   -Municipal, Industrial, and Medical Waste Treatment and Disposal
   -Mixing Processes and Atmospheric Transport
   -Spills
   -Porous Media Flows
   -Space Systems

Table 2 Fluid Mechanics Technical Committee

Program areas and subcommittee structure

1. Turbulence and Shear Flows:
   -Boundary Layers
   -Separated Flows, Jets, Wakes, and Cavity Flows
   -Bluff Bodies
   -Turbulence
   -Transition
   -Mixing, Dispersion, Plumes, Diffusion
2. Unsteady Flows:
   -Waves
   -Periodic Flows
   -Unsteady Boundary Layers, Transition, and Separated Flows
   -Biological Flows
   -Vortex Dynamics
   -Instabilities
3. Aero-Dynamics and Hydro-Dynamics:
   -External Flows
   -Lubrication
   -Potential Flows
   -Shock Waves
   -Inviscid Flows
   -Free Surface Phenomena
4. Unconventional and Emerging Topics:
   -Chaos and Non-Linear Dynamics
   -Liquid Metals
   -Microgravity
   -Micro Fluid Mechanics (creeping flows, vapor deposition, crystal growth)
   -Non-Newtonian Flows
   -Reacting Flows

Table 3 Multiphase Flow Technical Committee

Program areas and subcommittee structure

1. Gas-Solid Flows:
   -Particulate Flows and Aerosols
   -Fluidized Beds
   -Combustion Products
   -Air Pollutants
   -Dusty Flow
   -Snow Motion
   -Particulate Plumes
2. Gas-Liquid Flows:
   -Cavitation and Related Areas (noise inception, performance of propellers, hydrofoils, underwater vehicles, pumps, turbines, valves, and orifices)
   -Flow Regimes (bubbly, slug, annular, misty, frothy, and film)
   -Sprays, Droplets, and Atomization
   -Aeration
   -Entrainment
3. Liquid-Solid Flows:
   -Slurry Flows
   -Sewage Flows and Waste Treatment
   -Muds and Solid Suspensions
   -Mixing of Powders
   -Segregation of Solids
   -Materials Processing
4. Multicomponent Flows
   -Three Phase Flows
   -Stratified Flows
   -Immiscible Liquids and Gas Mixtures
   -Related Areas

reevaluation of goals and membership. For those persons wishing to participate in the programs of the FED, please return the member interest form reproduced as Fig. 2 to R. Bajura.

We invite participation in the work of the Fluids Engineering Division by both members and nonmembers. The committees and coordinating groups regularly meet at the Winter Annual Meetings (WAM) and the Summer Meeting of the FED.

Coordinating Groups

The coordinating groups were organized to focus on special areas of fluids engineering which are common to the interests of the technical committees and the Division as a whole. The technical committees and the cooordinating groups will work in a matrix-like mode of operation. The coordinating groups communicate with the technical committees through a strong liaison representative structure.

TO: R. A. Bajura Phone: 304/293-3449
105 Stewart Hall Fax: 304/293-7554
West Virginia University
Morgantown, WV 26506-6001

FROM: Name_____
Org._____
Street_____
City/St/Zip_____
Phone_____Fax_____

____ Add me to the mail list for the FED Newsletter

INTEREST AREAS

____ Fluid Applications and Systems Technical Committee
____ Fluid Mechanics Technical Committee
____ Multiphase Flow Technical Committee
____ Coordinating Group on Fluid Measurements
____ Coordinating Group on Computational Fluid Dynamics
____ Journal of Fluids Engineering Editorial Board (Ass. Ed.)
____ Advisory Committee
____ FED Student Papers Contest
____ Special Programs (Education, Research, Industry, etc.)
(Specify _____)
____ FED Executive Committee
____ Honors Committee
____ Professional Development Committee
____ Committee/Group Officer (specify office and committee/group of interest):_____

Comments:

Fig. 2 Member interest form

A. Coordinating Group for Fluid Measurements

The CGFM will continue its present programs in areas such as fluid meters, laser doppler anemometry and other optical flow measurement and visualization applications, pressure and temperature measurements, and experimental uncertainty.

The purpose of this Group is to coordinate with the technical committees to advance the science and application of fluid measurement techniques in fluids engineering. Membership is open to all interested persons. To ensure coordination of programs, the three technical committees will each appoint two liaison representatives to serve on the CGFM.

B. Coordinating Group for Computational Fluid Dynamics

The CGCFD will continue its present programs in applying computational fluid dynamics techniques to the solution of fluids engineering problems. Program areas include numerical uncertainty, the identification of benchmark cases, and cooperation with similar groups from other technical societies.

The purpose of this Group is to coordinate with the technical committees to provide a forum for discussing the generic area of computational fluid dynamics among the members of the division and to interact with similar committees/groups of the other technical societies. Membership is open to all interested persons. To ensure coordination of programs, the three technical committees will each appoint two liaison representatives to the CGCFD.

Advisory Board

The FED is instituting a new organizational unit called the Advisory Board (AB). The Advisory Board will have three major activities:

1. Serve in an advisory capacity to the FED Executive Committee in areas such as:
   -future directions for technical programs
   -ways to enhance industry, government, and university cooperation and information exchange
   -involvement in government liaison and input into ASME's national agenda
   -ways to increase participation by industrial members in activities of the FED
   -other related activities
2. Work with the Executive Committee on the FED Student Papers Contest and review the program on a periodic basis
3. Recommend agendas for special programs such as Education, Industry/Government/University Cooperative Programs, Research Funding, Industry Programs, and other division-wide activities on timely topics.

Membership on the Advisory Board is open to resource persons such as past Executive Committee members, past Technical Committee and Coordinating Group chairs, senior members of the Division, and others familiar with the broad programs of the FED and Fluids Engineering.

The main function of the Advisory Board will be to conduct brainstorming meetings, review the structure of the FED on a periodic basis, suggest future directions for the FED, and provide advice to the Executive Committee on matters pertaining to the operation of the Division. Advisory Board meetings will be informal. Normal duties of the Advisory Board members will be to attend the meetings and express their opinions for the benefit of the Division. Projects and special assignments will be (gladly) made available to those AB members interested in assuming responsibility for implementing ideas developed by the Advisory Board.

The Senior Member of the FED Executive Committee will be an ex officio member of the Advisory Board and serve as secretary to the Board to ensure continuity of information to the Executive Committee. The Executive Committee may recommend agenda items to the Advisory Board, which will be free to determine its own agenda items and organizational structure in the course of its work.

Warren Wade, Chairman
Richard Bajura, Program Representative
Donald Webb, Secretary
Michael Billet, Membership Representative
Clayton Crowe, Senior Member
Members of the Executive Committee for 1991–1992

Review—Vortex Shedding Lock-on and Flow Control in Bluff Body Wakes

O. M. Griffin
Naval Research Laboratory,
Washington, DC 20375-5000.
Fellow ASME

M. S. Hall
Science Applications International Corporation,
McLean, VA 22102

The results of recent experiments demonstrate that the phenomenon of vortex shedding resonance or lock-on is observed also when a bluff body is placed in an incident mean flow with a periodic component superimposed upon it. This form of vortex shedding and lock-on exhibits a particularly strong resonance between the flow perturbations and the vortices, and provides one of several promising means for modification and control of the basic formation and stability mechanisms in the near-wake of a bluff body. Examples are given of recent direct numerical simulations of the vortex lock-on in the periodic flow. These agree well with the results of experiments. A discussion also is given of vortex lock-on due to body oscillations both normal to and in-line with the incident mean flow, rotational oscillations of the body, and of the effect of sound on lock-on. The lock-on phenomenon is discussed in the overall context of active and passive wake control, on the basis of these and other recent and related results, with particular emphasis placed on active control of the circular cylinder wake.

Introduction

Vortex streets are formed in the wakes of bluff, or unstreamlined, bodies over a wide range of Reynolds numbers, from approximately 50 to 10^6 and even higher. The physics of vortex street formation and the near-wake flow have been the focal point for many past experimental studies, e.g., Roshko (1954, 1955), Gerrard (1966), Bearman (1965, 1967), Griffin and Ramberg (1974) and, most recently, Unal and Rockwell (1988a, b), Ongoren and Rockwell (1988a, b), and Williamson and Roshko (1988). One reason for this interest has been the importance of knowing how the mean and fluctuating fluid forces are generated on the body due to vortex shedding. Another reason is the perceived connection of the near-wake flow to the eventual evolution of the overall middle and far-wake vortex patterns (Cimbala et al., 1988; Browne et al., 1989). One of the most cogent descriptions of the physics of vortex streets and bluff body wakes was given by Morkovin (1964) as "a kaleidoscope of challenging fluid phenomena." This description is in many ways still true today. Modern high-speed computers and direct and large-eddy numerical simulation techniques now allow and, in the future, will further allow the vortex formation and wake modification and control processes to be studied computationally at high resolution (Karniadakis and Triantafyllou, 1989, 1990; Grinstein et al., 1990, 1991).

If a bluff cylinder is flexible and lightly damped, or rigid and flexibly mounted, then resonant oscillations can be excited by the incident flow. As a consequence of this flow-induced resonance, the body and wake oscillations have the same frequency which is near one of the characteristic frequencies of the structures (Bishop and Hassan, 1964; Koopmann, 1967). Extensive recent reviews of vortex shedding from bluff bodies and vortex-induced oscillations have been given by Sarpkaya (1979) and Bearman (1984). This coincidence or resonance of the vortex and vibration frequencies is commonly termed lock-on. The term phase-locking also has been used in the literature (Rockwell, 1990). Lock-on or resonance occurs when the body is oscillated in-line with the incident flow (Griffin and Ramberg, 1976; Ongoren and Rockwell, 1988b), and the lock-on resonance also is induced when a cylinder is forced to oscillate normal to the flow over the appropriate range of imposed frequencies and amplitudes. Two recent studies (Tokomaru and Dimotakis, 1991; Filler et al., 1991) have shown that rotational oscillations of a circular cylinder can cause lock-on. The recent computations of Karniadakis and Triantafyllou show that a lock-on state can be reached when a small spatially and temporally varying periodic disturbance is introduced into the near-wake of the cylinder. The disturbance is analogous to a vibrating wire with the appropriate frequency and amplitude.

Vortex resonance, or lock-on, has been observed also when the incident mean flow has a sufficiently large periodic component superimposed upon it (Barbi et al., 1986; Armstrong et al., 1986, 1987). In this case the cylinder remains stationary, but the vortex lock-on resulting from the inflow perturbation modifies the character of the near-wake flow. There is a complete equivalence between this case and in-line oscillations of the cylinder when the acoustic wavelength is long compared to the cylinder's diameter. The introduction of an appropriate sound field also can cause lock-on to occur (Blevins, 1985). All of these external disturbances represent potential means

Contributed by the Fluids Engineering Division for publication in the JOURNAL OF FLUIDS ENGINEERING. Manuscript received by the Fluids Engineering Division March 19, 1991.

for active control of the bluff body near-wake flow (Rockwell, 1987, 1990). Active control of the vortex shedding in the wake of a stationary circular cylinder by means of acoustic feedback was demonstrated in the recent experiments of Ffowcs Williams and Zhao (1989). Passive control of the shedding process can be accomplished by geometric alterations such as a wake splitter plate (Bearman, 1965; Roshko, 1954, 1955; Mansingh, 1986). Recent discussions of the stability and control of separated flows in general are given by Oertel (1990) and Rockwell (1990).

Vortex lock-on and resonance phenomena have numerous practical engineering applications. These applications abound in offshore exploration and drilling, Naval and marine hydrodynamics, and underwater acoustics. Other areas of engineering practice impacted by these phenomena are civil and wind engineering, nuclear and conventional power generation, and electric power transmission. Modification and control of the flow can be employed to reduce the intensity of the wake in order to reduce the drag, for example. These same processes also can be used to intensify the wake flow in order to enhance heat transfer, mixing and combustion.

The emphasis of this review paper is on vortex shedding resonance and lock-on in the near-wakes of bluff bodies. Vortex shedding in a flow with a periodic component superimposed on the basic mean flow is introduced here as the first case for study. This is an interesting bluff body flow which has not been studied previously in detail. The more widely studied cases of vortex shedding resonance and lock-on due to body oscillations both normal to, in-line with the incident mean flow, and rotational are also discussed in some detail. The introduction of sound also is discussed for the relatively few contributions which are available. The discussion here is directed principally toward the circular cylinder, but limited discussion of other body configurations is introduced at places where it seems appropriate to do so.

Near-Wake Flow Scaling

Roshko (1954, 1955) and Bearman (1967) originally showed that a characteristic group of nondimensional parameters for scaling of the wakes of bluff bodies could be derived by applying relatively simple physical arguments. The most recent formulation (Griffin, 1978, 1981, 1989) is a universal wake Strouhal number St* for vortex shedding based upon measured parameters of the bluff body near-wake flow.

If one considers two shear layers a distance d' apart, with the velocity just outside the layers equal to U_b, the mean velocity at separation, then a wake Strouhal number can be defined as

$$\mathrm{St}^* = \frac{f_{so} d'}{U_b} = \mathrm{St}\left(\frac{U}{U_b}\right)\left(\frac{d'}{d}\right). \tag{1}$$

The characteristic frequency f_{so} associated with the flow is assumed to be proportional to the ratio U_b/d'. Here the classical Strouhal number of the vortex wake is

$$\mathrm{St} = \frac{f_{so} d}{U}, \tag{2}$$

where d is the cylinder diameter and U is the incident flow velocity. When Bernoulli's equation is applied to the flow just outside the boundary layer at separation, the base pressure coefficient is

$$C_{pb} = \frac{2(p_b - p_\infty)}{\rho U^2} = 1 - \left(\frac{U_b}{U}\right)^2. \tag{3}$$

If the base pressure parameter or velocity ratio $K = U_b/U$ is introduced, then

$$K^2 = 1 - C_{pb} \tag{4}$$

and

$$\mathrm{St}^* = \frac{\mathrm{St}}{K}\left(\frac{d'}{d}\right). \tag{4a}$$

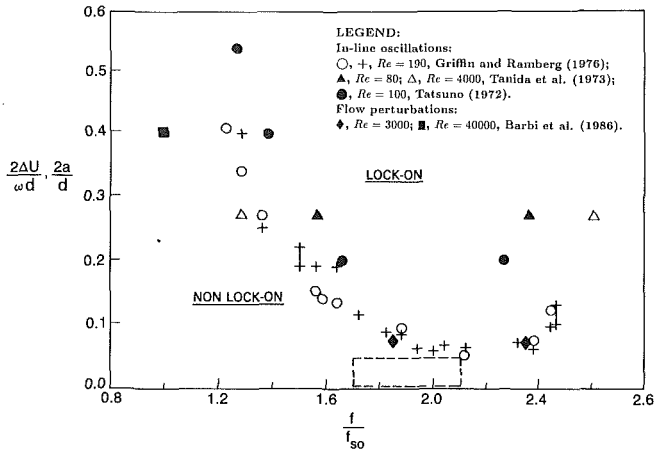

Fig. 1 Limits of the lock-on regime as a function of amplitude and frequency for in-line oscillations and flow perturbations. For the region enclosed by the dashed lines, see Fig. 2.

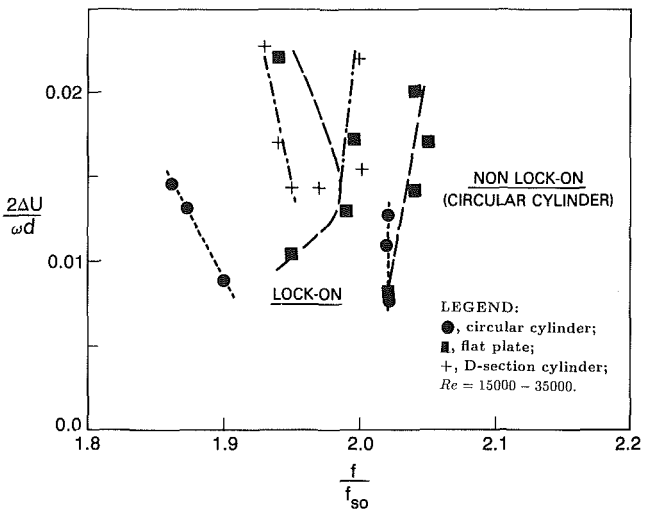

Fig. 2 Limits of the lock-on regime as a function of amplitude and frequency for in-line flow perturbations; data from Armstrong et al. (1986)

A wake Reynolds number Re* is defined in a corresponding way as

$$\mathrm{Re}^* = \frac{U_b d'}{\nu} = \mathrm{Re} K\left(\frac{d'}{d}\right), \tag{5}$$

where $\mathrm{Re} = Ud/\nu$ is the usual free-stream Reynolds number. These scaling relations are employed later in the paper to correlate the near-wake flow properties with one another.

Flow Perturbations and In-Line Oscillations

The recent experiments of Armstrong et al. (1986, 1987) and of Barbi et al. (1986) were conducted to examine the problem of vortex lock-on for a cylinder in a stream consisting of a steady flow with a periodic component superimposed upon it. In earlier experiments, Hatfield and Morkovin (1973) attempted to study the same problem, but the results were inconclusive because the flow perturbation amplitude and frequency were too low to cause lock-on. The results obtained by Barbi et al. and Armstrong et al. show some very basic similarities with the earlier experiments of Griffin and Ramberg (1976), which were conducted to examine vortex shedding lock-on for a cylinder oscillating in-line in a steady incident flow.

The vortex lock-on regime measurements by Barbi et al. are compared with those of Griffin and Ramberg in Fig. 1. The vertical axis represents two different measures of the perturbation amplitude. For the experiments of Griffin and Ram-

berg, the amplitude parameter is defined by the ratio of the peak-to-peak amplitude of cylinder displacement $2a$ and the cylinder diameter d. And for the experiments of Barbi et al., the normalized "peak-to-peak" incident velocity perturbation is given by $2\Delta U/\omega d$. The horizontal axis is the ratio of the vibration frequency f and the Strouhal frequency f_{so} of a stationary cylinder. Also shown are the cylinder vibration results of Tanida et al. (1973) and of Tatsuno (1972), reproduced from the paper by Griffin and Ramberg. The dashed lines enclose the region occupied by the results of Armstrong et al. (1986, 1987) which are shown on an expanded scale in Fig. 2. Vortex lock-on and cross-flow oscillations usually occur near the Strouhal shedding frequency f_{so}. For in-line oscillations and flow perturbations, the lock-on is caused by frequencies which occur near twice the Strouhal frequency, $f=2f_{so}$, since the fluctuating drag force is in the flow direction. However, in many cases the actual lock-on frequency is near the Strouhal frequency, or half the oscillation or perturbation frequency.

There is generally good agreement between the bounds of the lock-on regime for the two different types of external disturbance or flow control, though there is some scatter at the highest amplitudes. This is most likely due to Reynolds number effects, as noted by Barbi et al. The latter experiments were conducted at Re between 3,000 and 40,000, whereas the results of Tanida et al., Tatsuno, and of Griffin and Ramberg were conducted at Re between 80 and 4,000. The overall differences are relatively small in any case.

In Fig. 2 the vertical and horizontal axes have been scaled in the same way as in the previous figure. The original results of Armstrong et al. had been plotted in terms of the rms velocity u' and the reduced velocity $U/f_{so}d$. Three body shapes were investigated, i.e., a circular cylinder, a D-section cylinder, and a vertical flat plate. It is clear that the circular cylinder, with free separation points, has a lock-on range of about twice the breadth of the two bodies with fixed separation points. This basic difference in the lock-on behavior for these types of bluff bodies was previously discussed by Bearman and Davies (1975) and by Bearman (1984) for the case of body oscillations only. As shown by the former, the afterbody shape plays an important role in the character of the lock-on or resonance, e.g., in terms of the response of the base pressure and near wake flow to the forcing.

The base pressure coefficient C_{pb} is influenced by the flow perturbations in much the same manner as in the case of cylinder oscillations. For the stationary cylinder the base pressure coefficient is near $C_{pb}=-1.44$; this value, though somewhat low for a circular cylinder, is in reasonable agreement with the results of West and Apelt (1982) for a comparable wind tunnel blockage ratio of nine percent. When the flow perturbation was largest, the base pressure was decreased to $C_{pb}=-1.85$ at the point of maximum resonance, a reduced velocity of $U/f_{so}d=2.5$ (half the Strouhal value). The measured vortex formation region length l_f was reduced by this level of perturbation to $0.9d$ from $1.2d$, the value measured for the unperturbed flow (Armstrong et al. 1987).

Lesser decreases in C_{pb} were measured for smaller levels of the flow perturbation, with an overall dependence upon reduced velocity $U/f_{so}d$. The mean drag coefficient C_D increased from 1.28 to 1.52 for the perturbed flow as compared to the unperturbed flow. The base pressures of the flat plate and D-section bodies also were decreased by the introduction of the incident flow perturbations. But the decrease was only half of that measured for the circular cylinder at the same perturbation amplitude, which further shows the effect of free versus fixed separation points on the vortex resonance. These experiments were conducted at Reynolds numbers between 15,000 and 35,000, and the base pressure coefficients of all three stationary bodies in the unperturbed flow were effectively constant over this range.

A recent experimental study of vortex resonance and lock-on due to in-line oscillations of a circular cylinder was conducted by Ongoren and Rockwell (1988b). These experiments also included oscillations of the cylinder at inclination angles to the flow between $\alpha=0$ degrees (in-line) and $\alpha=90$ degrees (cross-flow), but the emphasis of the discussion here is on the in-line oscillations. The cross-flow oscillations (Ongoren and Rockwell, 1988a) are discussed in the next section. A wide range of vortex patterns was visualized by introducing pulsed hydrogen bubbles into the incident flow about a circular cylinder mounted vertically in a free-surface water channel.

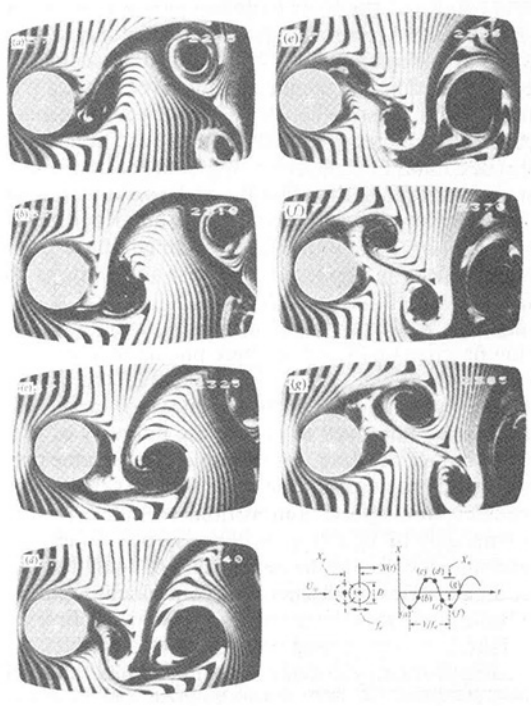

Fig. 3 Time sequence of locked-on vortex shedding produced by cylinder oscillations in-line with the flow at an oscillation frequency of $f=2f_{so}$; from Ongoren and Rockwell (1988b)

Both symmetric and asymmetric vortex patterns were observed over a wide range of oscillation conditions. For the in-line oscillations, vortex lock-on was observed at $f=2$, 3, and 4 f_{so}, with an asymmetric street formed at twice the basic Strouhal frequency and a symmetric street formed at three times the Strouhal frequency. The asymmetric pattern was complex in that one row consisted of a line of single vortices, whereas the other row consisted of a line of oppositely rotating vortex pairs. The vortex lock-on at three times the Strouhal frequency resulted in the formation of a symmetric street of vortices. In these cases the basic patterns persist downstream over a large number of oscillation cycles. When the oscillation frequency is four times the Strouhal frequency, a symmetric pattern is formed but rapidly loses its coherence in the early wake.

A time sequence over a full in-line oscillation cycle is shown in Fig. 3 for the condition $f=2f_{so}$. Figure 3(a) was taken with the cylinder in its forwardmost position and shows a vortex shedding from one side of the cylinder as in Figs. 3(c) and (d). As the cylinder moves through its maximum downstream position and changes direction, a second vortex is formed and shed from the same side of the cylinder as in Figs. 3(e) and (f). Then a single vortex is formed from the other side of the cylinder as the motion cycle continues as shown in Fig. 3(g). Ongoren and Rockwell observed that the pattern persisted over 50 or more cycles of the oscillation, but often, if the flow was stopped and restarted, a mirror image of the pattern was formed. This is but one example of the complexity of the flow patterns which accompany the oscillations. In this case the

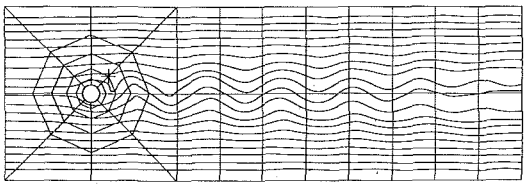

Fig. 4 Instantaneous streamlines, at Re = 200, of the forced wake response at $f = 2.2 f_{so}$ for vortex shedding from a cylinder in a perturbed flow. The wavelength λ of the vortex street is 4.66 cylinder diameters. The spectral element computational grid is superimposed on the streamline pattern.

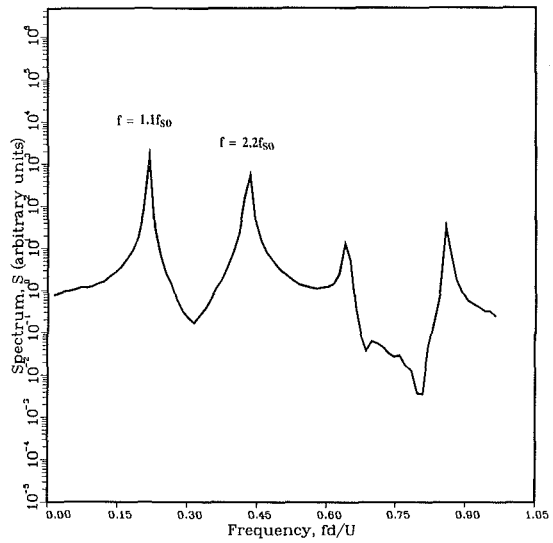

Fig. 5 A typical power spectrum of the flow velocity, at Re = 200, for the location ($x = 2d$, $y = 2d$) and the forcing conditions given in Fig. 4. Only the locked-on shedding frequency, $f = 1.1 f_{so}$, the perturbation frequency, $f = 2.2 f_{so}$, and their harmonics are dominant in the spectrum.

oscillation and vortex frequencies are phase-locked, but under other nonresonant conditions there was competition between the symmetric and asymmetric modes. Under these conditions, the lock-on persists in one mode over a specified number of cycles and then switches to the other mode. The mode competition also is influenced by the upstream feedback of disturbances from the near-wake of the cylinder. Complex patterns of three vortices such as these also were photographed by Griffin and Ramberg (1976) at similar frequencies during their wind tunnel experiments.

Numerical simulation provides yet another method of examining the effects of inflow perturbations and cylinder oscillations on the wake. This consists of superimposing an oscillatory component on the inflow boundary condition for a domain such as that shown by the spectral element grid in Fig. 4. The example given here was computed at NRL using a computer code similar to one employed extensively by Karniadakis and Triantafyllou (1989, 1990). The grid consists of 56 spectral elements, each of order $N = 6$. Results of the computation are shown in Figs. 4, 5, and 6, in which the lowest dominant frequency of the resulting vortex wake is near half the perturbation frequency when a boundary condition of the form

$$u = 1.0 + (0.8)\sin(4.4\pi f_{so}\, t)$$

$$v = 0.$$

is enforced at the inflow. This also represents an in-line oscillation, and is thus expected to result in a shedding frequency near $f = 1.1 f_{so}$ if lock-on occurs at one-half the perturbation frequency. The amplitude of the oscillatory component can be expressed as

$$a = 0.8 = 7.03\pi f_{so},$$

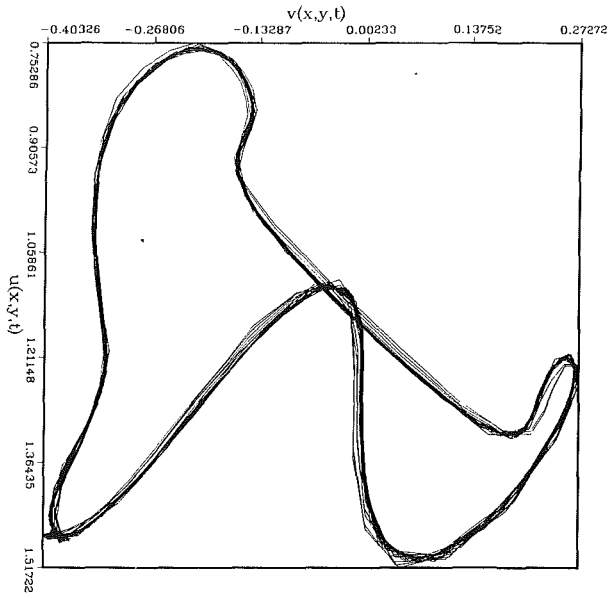

Fig. 6 Phase plane plot of the fluctuating velocity components, at Re = 200, for the location and forcing conditions given in Figs. 4 and 5. The regularity of the plot is demonstrative of the locked-on state of the vortex shedding.

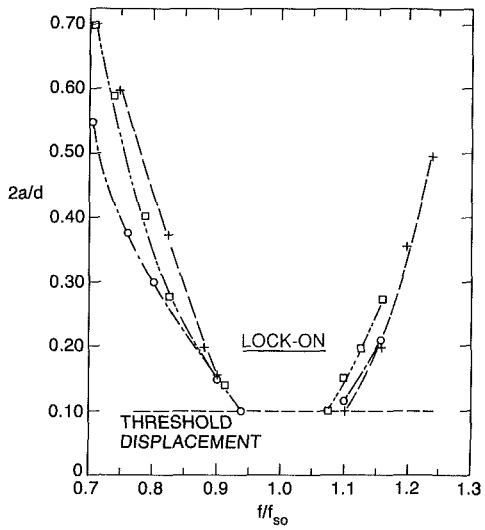

Fig. 7 Limits of the lock-on regime as a function of amplitude and frequency for cross-flow oscillations; from Koopmann (1967)

so that lock-on does occur and the results are in keeping with those shown in Fig. 1.

After an initial period of time corresponding to the quasi-steady stage in the forced perturbed flow calculation, the resulting streamwise velocity history at a point in the near wake is periodic. The corresponding power spectrum in Fig. 5 contains primary peaks at $f = 1.1$ and $2.2\ f_{so}$ as expected, and secondary peaks at superharmonics of these values. No additional peaks appear in the spectrum. The phase plane plot corresponding to this case is shown in Fig. 6, and with the power spectrum gives evidence of lock-on in the fully developed flow. Streamlines corresponding to this case are also shown in Fig. 4. The vortex spacing here is approximately $\lambda = 4.66d$, representing a decrease of seven percent over the unforced value of $\lambda = 5d$. The normalized frequency $\lambda/d(f/nf_{so}) = 5.13$ for this case. These values compare well with the results of experiments which are discussed later in the paper. A more extensive discussion of the spectral element computations of the perturbed flow cylinder lock-on is given by Hall and Griffin (1991).

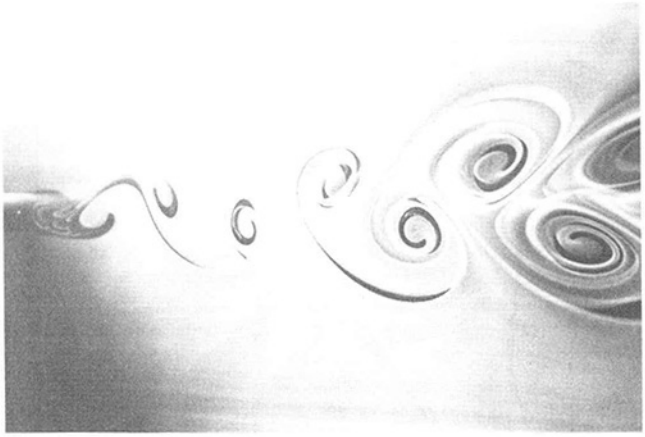

Fig. 8(a)

Fig. 8(b)

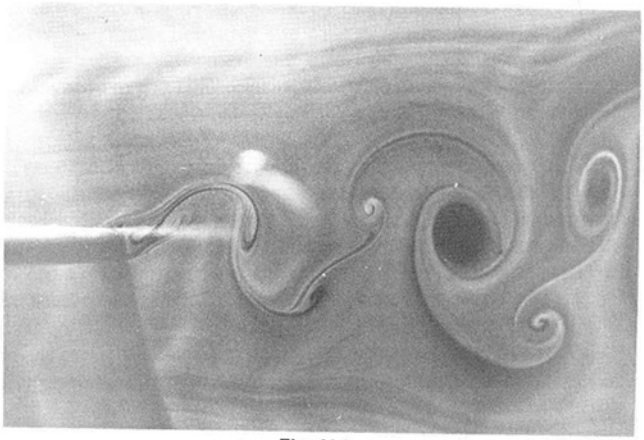

Fig. 8(c)

Fig. 8 Flow visualization of the vortex shedding from a circular cylinder oscillating in cross-flow at a Reynolds number of Re = 190. (*a*) stationary cylinder, unforced wake; (*b*) $2y/d = 0.5$, $f/f_{so} = 0.9$; (*c*) $2y/d = 1.1$, $f/f_{so} = 0.9$.

Cross-Flow Oscillations

The excellent reviews by Sarpkaya (1979) and by Bearman (1984) dealt with cross-flow oscillations of flexibly-mounted bluff bodies, bodies which were free to oscillate, and those which were forced. The purpose of the present paper is to complement these works, to compare with some pertinent past results, and to highlight more recent developments in the context of flow control and modification. The basic character of cross-flow lock-on due to forced oscillations can be represented by the measurements of Koopmann (1967) which are shown in Fig. 7. The appearance of the lock-on range is very similar overall to the corresponding cases of in-line oscillations and

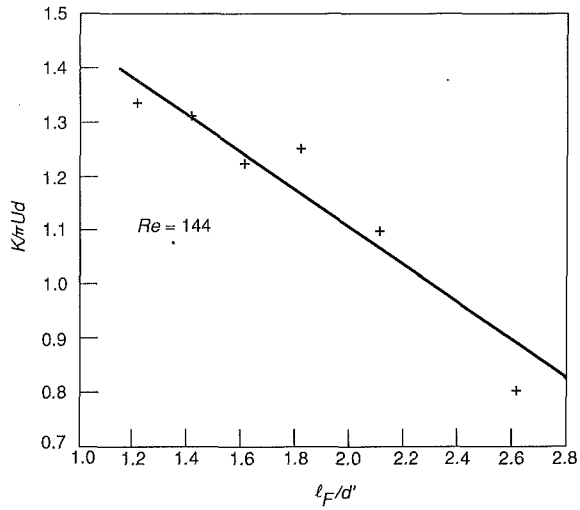

Fig. 9 The measured dependence between the initial circulation K of the vortices and the ratio of the formation region length l_f and the wake width d' at formation. The Reynolds number is Re = 144; from Griffin and Ramberg (1974).

flow perturbations shown in Figs. 1 and 2. However, the imposed oscillations are near the Strouhal frequency f_{so} rather than twice its value.

Many other effects of the cross-flow oscillations are also similar. For example, the longitudinal spacing of the vortex street adjusts in a similar manner to the example shown earlier; oscillation frequencies less than f_{so} expand the vortex street while frequencies greater than f_{so} contract the pattern. Increasing the amplitude of oscillation reduces the lateral spacing of vortices to the point of zero spacing, after which there is a drastic change in the appearance of the pattern as the flow adjusts to preclude the transition to a thrust-type vortex street. Three previously unpublished examples from experiments at NRL which demonstrate this effect are shown in Fig. 8. The street behind a stationary cylinder appears in Fig. 8(*a*) and shows the well-known geometry which has been visualized by numerous investigators. When the amplitude of oscillation is increased as shown in Fig. 8(*b*), the lateral spacing is much reduced. For still higher amplitudes of oscillation, beyond the limit of zero lateral spacing, a complex asymmetric pattern such as that shown in Fig. 8(*c*) emerges. These photographs were taken in a wind tunnel using an aerosol as the indicator. This emergence of the asymmetric pattern also has been observed by Ongoren and Rockwell (1988a) in water, using hydrogen bubbles as the flow indicator.

The formation region of the vortices as defined by the model of Gerrard (1966) also varies inversely with frequency in the resonance or lock-on regime (Griffin and Ramberg, 1974; Ongoren and Rockwell, 1988a), and is reduced in length by increasing amplitude of oscillation at any given constant frequency. These changes in the near wake vortex formation cause corresponding changes in the strength or circulation of the vortices. Reductions in the vortex formation length result in increasing the vortex strength by as much as 75 percent at a Reynolds number of 144. An example is shown in Fig. 9 where the nondimensional initial circulation of the vortices is plotted against the ratio of the formation length to the wake width at formation. The basic importance of the length scales to the near wake flow physics is discussed later in the paper. This increase in the vortex strength is accompanied by a corresponding increase in the rate of vorticity generation with amplitude of oscillation.

The base pressure coefficient C_{pb} also is reduced significantly by the oscillations in the lock-on or resonance regime (Stansby, 1976). As an example, the minimum base pressure on a circular cylinder at resonance was decreased by 33 percent as the am-

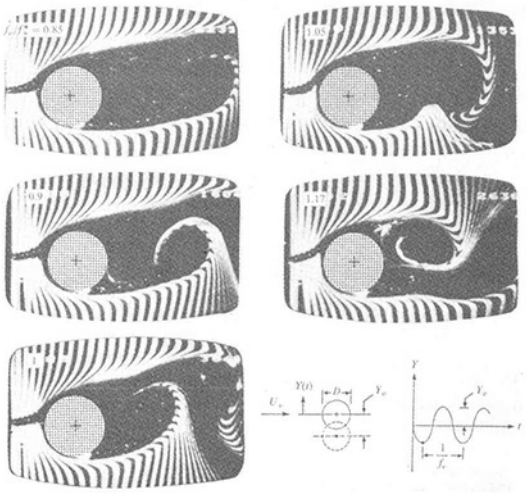

Fig. 10 Effect of the ratio of oscillation frequency f to the natural shedding or Strouhal frequency f_{so} on the vortex formation region of a circular cylinder; from Ongoren and Rockwell (1988a). All of the photographs were taken with the cylinder at its maximum negative position.

plitude of oscillation (measured in diameters from equilibrium) increased from $0.1d$ to $0.3d$. The Reynolds number of the experiment was Re = 8600. As mentioned earlier herein, Armstrong et al. (1987) measured comparable decreases in the base pressure. However, the level of inflow perturbations was much less than the oscillation levels required to achieve the same level of base pressure modification. As noted earlier, the latter reduction in base pressure was accompanied by a reduction in the length of the vortex formation region from $1.2d$ to $0.9d$.

The most comprehensive recent study of cross-flow oscillations is that of Ongoren and Rockwell (1988a). The Reynolds number range of the experiments was Re = 580 to 1300. They found that two fundamental types of lock-on take place; at a frequency of one-half of the Stouhal frequency, a subharmonic form of lock-on takes place whereby the shed vortex is always from one side of the body, whereas at frequencies near the Strouhal frequency the classical form of lock-on described above takes place as vortices are shed alternately from the body to form an altered Karman vortex street pattern.

It has been known for some time (Bearman and Currie, 1979; Zdravkovich, 1982) that a drastic change in the phase of the vortex shedding, relative to the body oscillations, occurs in the vicinity of the natural shedding frequency. However, Ongoren and Rockwell and, earlier, Bearman and Davies (1975) showed that the afterbody shape plays an important role in the phase shifting in that bodies with a short or nonexistent afterbody, i.e., a circular or triangular cylinder, experience a large phase shift, while a body such as a square or rectangular cylinder with a relatively large afterbody experiences little or no phase shift. This phase shift results in the switch of the initially shed vortex from the upper to the lower side of the cylinder or vice versa. The presence of the afterbody appears to induce reattachment of the initially shed vortex and to reduce the likelihood of the phase shifting. This is yet another indication of the importance of the vortex formation region and near-wake flow to the shedding process.

The changes in the vortex formation region with the frequency of the oscillations are shown by the photographs in Fig. 10 from Ongoren and Rockwell (1988a). The flow was visualized in water in the manner described in the previous section of the paper, and again the results are remarkably similar to the earlier wind tunnel photographs of Griffin and Ramberg (1974). All of the photographs were taken with the cylinder at its lowest position in the oscillation cycle, and the shift in phase of the shedding relative to the cylinder can be seen by comparing the wakes at $f = 0.9\,f_{so}$ and $f = 1.05\,f_{so}$. The

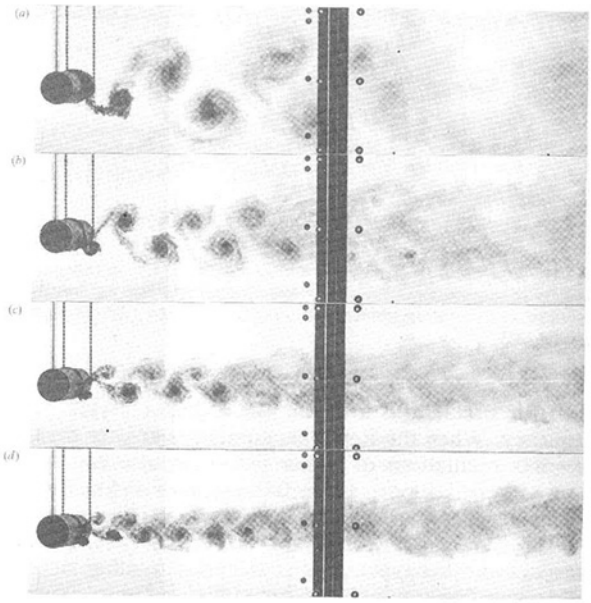

Fig. 11 Flow visualization of synchronized vortex shedding due to rotational oscillation of a circular cylinder. Legend for data points: $\Omega_1 = 8$; Re = 15,000; (*a*) $St_f = 0.3$, (*b*) $St_f = 0.5$, (*c*) $St = 0.7$, (*d*) $St_f = 0.9$; from Tokumaru and Dimotakis (1991).

substantial decrease in the length of the vortex formation region with frequency of oscillation also is evident from the photographs.

Other effects of the cross-flow oscillations observed by Ongoren and Rockwell included a large swinging motion of the circular cylinder wake about the body at frequencies less than the Strouhal frequency. This swinging motion is largest near the Strouhal frequency and then it abruptly disappears. There is evidence of some correlation between the phase shift in the shedding and the abrupt disappearance of the swinging motion. The swinging motion does not appear in the case of bodies with fixed separation points. There were numerous complex wake patterns observed at other frequencies. For instance, small-scale vortices were shed at superharmonic frequencies of $n = 2$, 3, 4, and higher nonharmonic frequencies, and the downstream wake eventually recovered to a lock-on and altered asymmetric pattern similar in form to the classical Karman vortex pattern. However, the altered pattern departed substantially from the classical Karman street, with the frequency taking the values $f_a = f/n$. An interesting aspect of the paper by Ongoren and Rockwell is the number of historical references, e.g., Meier-Windhorst (1939).

Rotational Oscillations

Vortex lock-on and control of the near-wake flow also can be realized with small rotational oscillations of a circular cylinder. There are very few studies of this aspect of the problem, the most recent being those of Tokumaru and Dimotakis (1991) and of Filler et al. (1991). An important distinction between the two studies is that in the experiments of Tokumaru and Dimotakis the maximum rotational velocity of the cylinder was on the order of the velocity outside the boundary layer at separation (approximately $1.4U$), whereas in the experiments of Filler et al. the maximum rotational velocity of the cylinder was only $0.03U$. These studies seem to show, however, that the range of lock-on frequencies, though still probably amplitude-dependent, is much reduced from what has been observed for imposed oscillations and flow perturbations as discussed earlier. There are essentially two types of forcing which can be introduced by rotational oscillations. The first is the classical form of lock-on or resonance which takes place

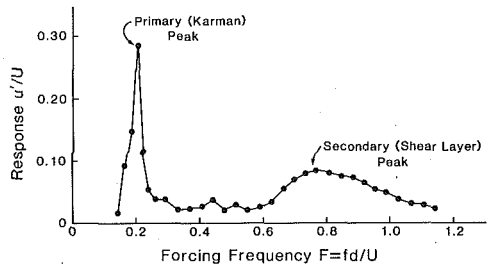

Fig. 12 A typical frequency response curve showing the normalized velocity response amplitude as a function of the forcing frequency for Re = 920, the vibration parameter $\Omega_1 = 0.14$, and $d = 1.27$ cm; from Filler et al. (1991)

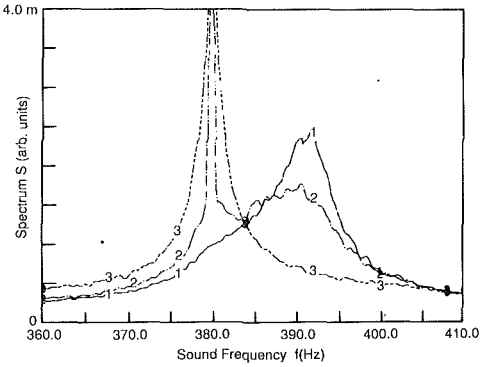

Fig. 13 Entrainment of natural or unforced vortex shedding at 392 Hz by sound at 380 Hz. The vertical scale is the same for all three spectra; from Blevins (1985).

when the oscillations are near the Karman vortex shedding frequency. When the Reynolds number is greater than about Re = 500, oscillations of higher frequency also can excite the Bloor-Gerrard (Bloor, 1964) frequency of instability in the shear layers separating from the cylinder. This excitation of the B-G instabilities is likely to be caused by inflow perturbations and other types of imposed body oscillations as well.

A series of photographs of vortex lock-on at increasing values of the oscillation Strouhal number St_f are shown in Fig. 11. The oscillation parameter $\Omega_1 = v_1/U$, where v is the peak circumferential velocity, was kept fixed during the sequence of conditions shown in this figure, from Tokumaru and Dimotakis (1991). The experiments were performed in a CalTech water channel at a Reynolds number of Re = 15,000, and the flow was visualized by introducing a mixture of colored food dye into the water upstream of the cylinder. The dye mixture was made neutrally buoyant by diluting it with ethyl alcohol (P.E. Dimotakis, private communication). In all of the cases shown the vortex shedding is locked-on in the classical manner with the imposed rotational oscillations. When the oscillation Strouhal number was increased to $St_f = 1.5$, the wake forcing went through a transition to the Bloor-Gerrard shear layer forcing. For a fixed value of oscillation Strouhal number of $St_f = 1$, the transition to shear layer forcing takes place at an oscillation parameter of approximately $\Omega = 16$.

A plot of the velocity u' in the wake from Filler et al. (1991) as a function of the oscillation Strouhal number St_f is shown in Fig. 12. Here the oscillation parameter $\Omega_1 = \omega_1 d/2U$, where ω_1 is the frequency of the rotational oscillations. At the lower frequencies near the usual Karman shedding frequency a large resonant peak is seen when the oscillations are in that range. However, at the higher imposed frequencies there is a secondary broad peak in the range of the shear layer instability frequencies. In the Karman frequency range of vortex shedding the wake behaves like a nonlinear oscillator near resonance. This behavior is well known (Bishop and Hassan, 1964; Bearman, 1984) and has been explored by numerous investigators for the cases of cross-flow and in-line oscillations. The forced Bloor-Gerrard shear layer instabilities are simply convected downstream in the near wake. An important finding by Tokumaru and Dimotakis (1991) is that active control of the near-wake vortex formation and flow physics by rotational oscillations of the cylinder can reduce the drag on the cylinder by as much as a factor of six! This decrease in the drag coefficient C_D is accompanied by a comparable decrease in the wake displacement thickness δ^* (a factor of five) as defined by an integral of the cross-stream wake velocity distribution over the height of the channel.

There are very few studies of rotational oscillations on wake flow control and vortex resonance or lock-on. Examples from the two most recent have been given here. For earlier examples the reader should refer to the work of Okajima et al. (1975) and of Taneda (1978). This is a new and potentially exciting approach to the active control of vortex formation and bluff body wake flows.

The Effects of Sound

The application of an appropriate sound field to the flow about a rigid cylinder can induce vortex lock-on and resonance in the wake. There are even fewer reported studies of the effect of sound than of rotational oscillations, the principal example of the former being that of Blevins (1985). The only other directly related work is that of Okamoto et al. (1981). As noted by Blevins, the effect on the vortex shedding of an acoustic wave propagating along the axis of a circular cylinder was examined by the latter. Only a minor influence was observed for sound excitation levels above 20 Pa.

The experiments performed by Blevins were at Reynolds numbers in the range Re = 20,000 to 40,000 in a wind tunnel that allowed a transverse sound field to be applied such that the cylinder was located at the node of the acoustic pressure field. This is the point of maximum induced velocity due to the sound. It was observed by Blevins that the vortex lock-on was induced by the velocity rather than the pressure.

An example of the results reported by Blevins (1985) is shown in Fig. 13. The frequency of the vortex shedding was $f_s = 392$ Hz, and the frequency of the applied sound field was $f = 380$ Hz. Thus the lock-on occurred at a frequency less than the Strouhal frequency. The average spectral output from a flush-mounted hot-film probe mounted on the cylinder is plotted for the three test runs. The spectrum labeled 1 shows the typical averaged spectrum for a rigid cylinder in a uniform flow, with the broad peak in this case centered at the vortex shedding frequency of 392 Hz. When a 100 Pa sound field is applied two peaks are present—a sharp peak at 380 Hz induced by the applied sound, and a broader reduced and shifted peak due to vortex shedding. An increase in the applied sound field to 250 Pa produces a typical lock-on spectrum with a single sharp peak at the frequency of the sound. The lock-on frequency here is less than the Strouhal frequency, and it was observed by Blevins that the induced resonance always was stronger at the reduced frequencies as compared to frequencies higher than the Strouhal frequency. The sound field and the vortex shedding were phase locked over a range of phase angles which varies nearly linearly with the applied sound frequency.

An additional observation by Blevins (1985) was that turbulence in the free stream suppressed the influence of sound on the vortex shedding. The results suggest that the induced sound field velocity must exceed the turbulence velocities in order for the sound to influence the vortex shedding. Also, the introduction of sound substantially increased the coherence of the vortex shedding along the span of the cylinder as is usually found when a circular cylinder is oscillated.

The Near-Wake Flow Field

There is a physical dependence between the wake width d' at the end of the vortex formation region of a bluff body and

Table 1 Legend for data plotted in Fig. 14

Symbol	Bluff body type	Method	Investigators
◗	Half cylinder (D-section)	Wind tunnel experiment	Armstrong et al. (1986, 1987)
⊢	Flat plate	Wind tunnel experiment	Armstrong et al. (1986, 1987)
●	Circular cylinder	Wind tunnel experiment	Armstrong et al. (1986, 1987)
◑	Circular cylinder	Wind tunnel experiment	Barbi et al. (1986)
◩□■ ■⊢	Wide splitter plate (D-section)	Computation	Grinstein et al. (1991)
◀	Hydrofoil	Wind tunnel experiment	Blake et al. (1977)
+	D-section cylinder	Wind tunnel experiment	Simmons (1975)
▽⊢ ▽	D-section cylinder with and w/o splitter plate	Wind tunnel experiment	Bearman (1965)

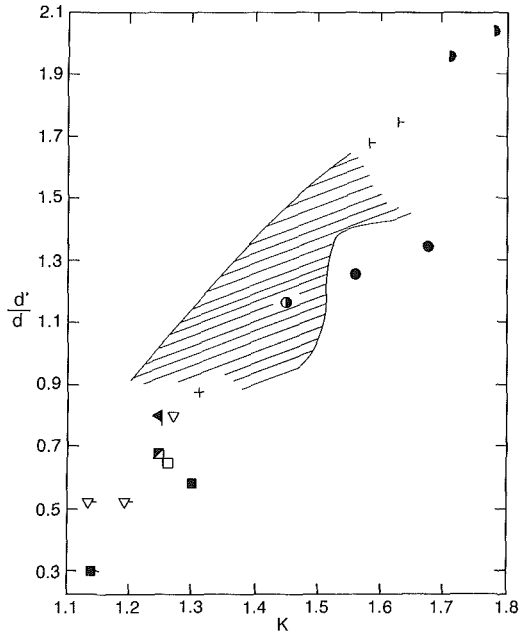

Fig. 14 Wake width d'/d as a function of the base pressure parameter or velocity ratio K. The legend is given in Table 1. The shaded area in the figure corresponds to a variety of body geometries and flow conditions given in Griffin (1989).

the base pressure coefficient $-C_{pb}$ or the related velocity ratio K. As discussed earlier, these are important characteristic physical parameters of the bluff body wake. In general, the bluffness of a given body shape is represented by a wider wake, and corresponding lower base pressure or higher velocity ratio. For a cylinder vibrating normal to the incident flow, the variation of both the measured base pressure and wake width with the frequency ratio f/f_{so} over the lock-on regime show the same resonant behavior (Griffin, 1989). Both $-C_{pb}$ and d' increase to a maximum value and then gradually decrease as the upper limit of the lock-on range of frequencies is reached. Only the base pressure variation was measured by Armstrong et al., but the wake width can be estimated as a function of $U/f_{so}d$, using the wake similitude relationships summarized earlier in the paper and measured values of St and C_{pb} (or K). For the range of Reynolds numbers corresponding to the experiments of Armstrong et al., the wake Strouhal number St* is essentially constant at a value of 0.16, so that

$$d'/d = (\mathrm{St}^*/\mathrm{St})K$$

from Eq. (4*a*).

The wake widths for several cylinders and flow conditions are plotted as a function of K in Fig. 14. The legend for the data in the figure is given in Table 1. This range of the base pressure parameter or separation velocity ratio K represents the entire regime over which vortex shedding takes place over bluff bodies, whether the shedding is natural or unforced, or the shedding is controlled or modified by some means such as oscillations, in-flow perturbations, sound, and wake splitter plates. The shaded area represents a host of results for oscillating circular cylinders, D-section cylinders, and flat plates under a wide variety of conditions (Griffin, 1989). There is generally good agreement between the new perturbed and steady flow results and the earlier data, except for the two circular cylinder results from Armstrong et al. which are displaced to the right of the overall trend of the data set. This departure from the overall trend of the results is due to the much reduced base pressure measured on the circular cylinder in those experiments, as previously mentioned. In the experiments of Armstrong et al. the circular cylinder and flat plate base pressures were virtually the same under otherwise unvarying conditions of blockage, incident flow, axial uniformity, etc. One might expect the base pressure coefficient for a circular cylinder at the Reynolds numbers studied to be closer to the values of $C_{pb} = -1$ to 1.1 measured by Barbi et al. and others at the same Reynolds numbers.

The wake widths for flow over a D-section cylinder computed by Grinstein et al. (1990, 1991) are also plotted in Fig. 14. The results shown represent a two-dimensional computation using the flux-corrected transport (FCT) algorithm, but comparable results were obtained with companion three-dimensional computations described by Grinstein et al. (1990). These computations were made for compressible flows with freestream Mach numbers in the range 0.3 to 0.6 at standard temperature and pressure conditions. However, for these Mach numbers compressibility effects are relatively small and reasonable comparisons can be made with incompressible flow experiments. The wake widths plotted in Fig. 14 were obtained directly from computed contour plots of rms velocity u' at the end of the vortex formation region. The results shown represent flow over the body both with and without a splitter plate attached and they agree remarkably well with the experimental results of Blade et al. (1977), Simmons (1975) and Bearman (1965). The D-section bluff body results overall represent the lowest regime of K which has been observed thus far.

A comprehensive experimental study of the effects of wake splitter plates on vortex shedding from a circular cylinder was made recently by Unal and Rockwell (1988b). The experiments were conducted in the Reynolds number range $\mathrm{Re} = 140$ to 5000, and the primary objective was to study the effects of the passive wake interference on the formation region of the vortices. An unusual aspect of these experiments was the ratio of the plate thickness h to the cylinder diameter d, which was approximately 0.5. Also, the plate length was approximately $l_p = 24d$ cylinder diameters, in contrast to the splitter plate

Table 2 Longitudinal vortex spacing or wavelength in the near-wake of a circular cylinder vibrating in-line with an incident uniform flow

Vibration frequency, f(Hz)	Frequency ratio, f/f_{so}	Vortex spacing, λ/d	Relative change, $\Delta\lambda/\lambda$	Vortex convection speed, $1/2f\lambda/U$
	Reynolds number = 190			
69.2	1.88	5.2	+0.07	0.94
73.6	2.00	4.9	0	0.93
75.6	2.06	4.7	−0.05	0.91
78.9	2.14	4.7	−0.04	0.96
80.4	2.18	4.4	−0.09	0.92
				Average = 0.93

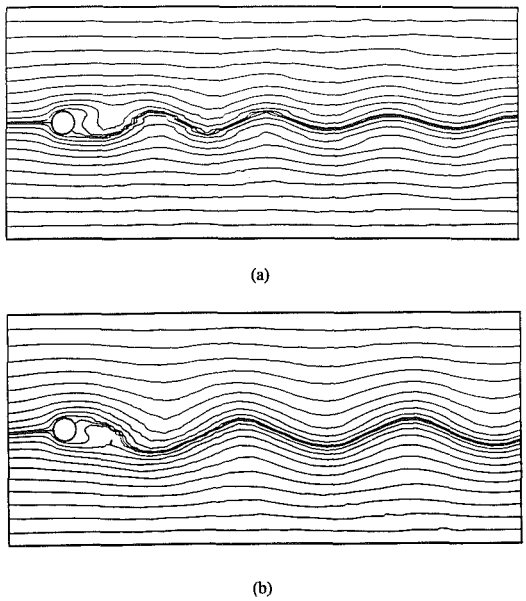

(a)

(b)

Fig. 15 (*a*) Instantaneous streamlines at Re = 100 for natural shedding. (*b*) Instantaneous streamlines at Re = 100 and near-wake forcing at the excitation frequency, $f_e = 0.75 f_s$ (a lock-in state); from Karniadakis and Triantafyllou (1989).

geometries discussed above. The leading edge of the plate had a tapered and sharply pointed configuration.

These experiments yielded several important conclusions and reinforced those previously reached by other investigators. The first is a reiteration of the importance of the dynamics of the formation region to the overall near-wake flow and the possibility of control and modification of the vortex wake. Second, the wake formation is dominated by an absolute instability and there is a close relation between the vortex formation process and the dynamics of the near-wake Karman vortex street. Other conclusions are the importance of Reynolds number to the wake formation, at least over the range examined, but that no locking-on or vortex resonance occurs in the presence of the passive wake interference. Nonetheless, the results of these and the other experiments and computations discussed here have demonstrated the potential importance of both passive and active control to the flow physics of bluff body wakes.

The downstream vortex spacing or wavelength is a valuable and important diagnostic parameter for the state of the spatial structure and development of the near-wake. Measurements of the spacing for a variety of in-line and cross-flow oscillations, and also for the unforced wakes of stationary cylinders were reported originally by Griffin and Ramberg (1976). These can be compared to the direct numerical simulations of Karniadakis and Triantafyllou (1989) and our recent NRL simulations (Hall and Griffin, 1992). The vortex spacing or longitudinal wavelength can be employed as a measure of the spatial state of the flow as compared to phase plane diagrams of the streamwise and cross stream components of the wake velocity fluctuations which can be employed comparably to assess the temporal state of the near-wake.

Two examples from Karniadakis and Triantafyllou are shown in Fig. 15. The upper instantaneous streamline pattern corresponds to the unforced wake at Re = 100 while the lower pattern corresponds to a wake forced by a spatially localized acceleration which varied with time in the near-wake vortex formation region with normalized amplitude and frequency, respectively, of $A = 0.10$ and $f/f_{so} = 0.75$, and which decayed exponentially in the far field. The center of the disturbance was located at $x = 2$, $y = 0$, measured in multiples of cylinder diameter. This is a unique form of control disturbance which had not been investigated in any previous work. For the unforced wake $\lambda = 5d$ and for the forced wake $\lambda = 7d$, an increase of forty percent. A similar example from the NRL perturbed flow computations is given in Fig. 6.

Comparable measurements were made at Re = 190 by Griffin and Ramberg (1976). The results are summarized in Table 2. The cylinder oscillations were in-line with the flow over a range of frequencies near twice the Strouhal frequency (as in Fig. 1) and, for the cases shown, a single vortex was shed during each oscillation cycle. Thus this basic forced wake pattern shared many of the same overall features of the wake forced with the cross-flow oscillations. The measured changes in the forced wake vortex spacing correspond directly with those from the direct numerical simulations; for $f < 2f_{so}$ the wavelength is increased while for $f > 2f_{so}$ the wavelength is decreased as shown in Table 2. Extrapolating the measured results in the table to the case shown in Fig. 15 using a least-squares straight line given by Griffin and Ramberg (1976), the vortex spacing is $\lambda = 6.2d$. This compares reasonably well with the computed results of $\lambda = 7d$. The measured vortex spacing for the stationary cylinder at Re = 190 ($\lambda = 4.9d$) is virtually identical to the computed value at Re = 100 ($\lambda = 5d$).

The vortex street wavelengths computed by Karniadakis and Triantafyllou and more recently at NRL are compared further with measured street wavelengths for both forced and unforced conditions in the range of Reynolds numbers from 100 to 2000 in Fig. 16. The computations fit well with the overall trend of the measured data, which show only a very slight dependence on Reynolds number in this range. The vertical scale in the figure essentially is a normalized form of the convection speed of the vortices, or the downstream speed of the vortex cores. The constant phase or convection speed is representative of a non-dispersive physical system.

Several measurements of the vortex phase or convection speed, i.e., the speed at which the vortex cores travel downstream, are given in Table 2. Though there is some scatter, the data generally are grouped around the average value of $U_\phi = 0.93U$. This gives some evidence that both forced and unforced or natural periodic vortex wakes have the same basic non-dispersive properties.

The experiments of Tokumaru and Dimotakis (1991) also included measurements of the vortex street wavelength λ over a wide range of the oscillation Strouhal number $St_f = fd/U$.

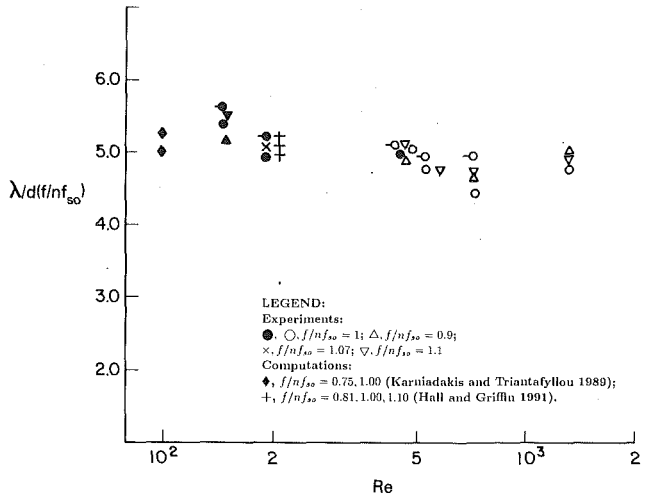

Fig. 16 Longitudinal vortex spacing $\lambda/d(f/nf_{so})$ as a function of Reynolds number Re. All of the measurements were made in the wakes of stationary and oscillating cylinders. Data points at Re = 190 and 200 correspond to in-line oscillations and flow perturbations with $n = 2$; all other results correspond to cross-flow oscillations (experiments) and near-wake perturbations (computations) with $n = 1$.

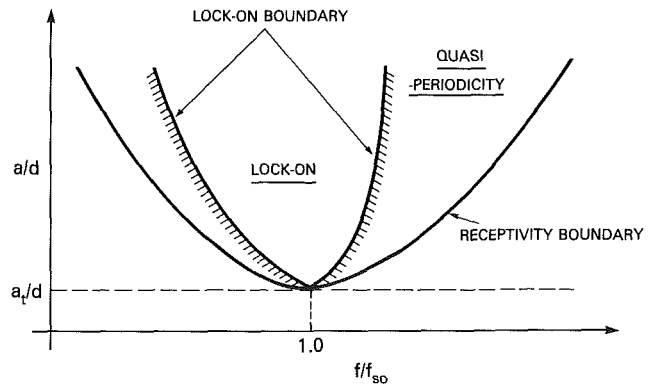

Fig. 17 State selection (amplitude versus frequency) diagram for laminar wakes. The plot should only be interpreted in a qualitative sense; from Karniadakis and Triantafyllou (1989).

For the observed range of lock-on where $St_f = 0.3$ to 1.0, the geometry of the vortex street adjusted in terms of the wavelength λ and the frequency f to form yet again an essentially non-dispersive street pattern, though there is some slight scatter in the measurements. The lateral spacing of the near-wake vortex street also decreased with increasing St_f over this lock-on range. The Reynolds number for these experiments was Re = 15,000, and some complementary smooth cylinder experiments were conducted at a lower Reynolds number of Re = 3,300 and with surface roughness added to the cylinder at the higher Reynolds number. The results were similar in both cases. These observations for the case of active control with rotational oscillations confirm and extend the conclusions drawn earlier for both forced and unforced wakes.

Near-Wake Flow Stability

The introduction of the absolute/convective theory of fluid dynamic stability has led to a promising new approach and a new theoretical framework for understanding the physics of vortex formation and near-wake flow development (Koch, 1985; Triantafyllou et al., 1986, 1987; Monkewitz and Nguyen, 1987; Rockwell, 1987; Chomaz et al., 1988; Unal and Rockwell, 1988a, b; Ongoren and Rockwell, 1988a, b; Karniadakis and Triantafyllou, 1989; Oertel, 1990; Huerre and Monkewitz, 1990; Rockwell, 1990). A flow is said to be absolutely unstable when an initial infinitesimally small disturbance grows exponentially in place at the location where it is introduced. In the case of a convective instability the initially small disturbance is transported or convected away from the point of its introduction, leaving behind an undisturbed region of flow. Chomaz et al. (1988) have introduced the term *global instability*. They note that the existence of a local absolute instability is only a necessary, but not sufficient, condition for the existence of a global instability in a shear flow, and that the localized region of absolute instability must physically grow to a large size to become globally unstable.

Recent stability calculations based upon computed and measured mean velocities in the wakes of stationary circular cylinders suggest that the vortex formation region is absolutely unstable while the fully-formed vortex street is convectively unstable. The vortex formation region is thought to be a complex global region of upstream and downstream propagating vorticity waves, self-excitation of the flow, and modal competition and interaction (Rockwell, 1990). This region of self-excited oscillations and flow resonance plays an important role in frequency selection, and thus in programming and control of the flow separation and the overall unsteady flow. More extensive stability calculations of this nature may also lead to better understanding of bluff body wakes, and their active control and modification by any of the means discussed here. A better understanding of passive wake control and modification, e.g., by splitter plates and base bleed, may be achieved in the same manner. The most recent and comprehensive discussions of absolute/convective and local/global instabilities for spatially developing shear flows, including bluff body wakes, are given by Huerre and Monkewitz (1990), Oertel (1990), and Rockwell (1990).

Karniadakis and Triantafyllou (1989) conducted a linear stability analysis of the time-averaged flow in the near-wake which was derived from their direct numerical simulation of the cylinder wake at Re = 100. The flow was assumed to be locally parallel and slowly varying in the downstream direction. The averaged flow was found to be absolutely unstable for approximately 2.5 diameters downstream from the cylinder. This corresponds generally to the length scale of the vortex formation region at subcritical Reynolds numbers below 10^4 (Bloor and Gerrard, 1966), a wide range of Reynolds numbers. At greater downstream distances the flow is convectively unstable. Thus the continuous formation of the vortex street is thought to be sustained by the near-wake absolute instability. Good global agreement was found between the stability analysis and the computation in that the Strouhal number was St = 0.179 in both cases. This is slightly higher than most experiments (Roshko, 1954; Williamson, 1988), which may be due partly to finite grid size and the extent of the computational domain, and to the three-dimensional effects which invariably exist in a cylinder wake. Williamson (1988) has shown the importance of the spanwise variation of the cylinder wake flow.

Summary and Concluding Remarks

Previous observations of vortex resonance or lock-on for bluff body near-wakes which have been accumulated by numerous researchers over the years now have been extended to several additional types of imposed disturbances of both fundamental and practical importance—a bluff body in a perturbed incident flow consisting of a mean flow with a periodic component superimposed upon it, rotational oscillations of the body, and sound. And the first of these cases has been shown to be fundamentally identical, under appropriate conditions, to the lock-on or vortex resonance of a cylinder oscillating in line with an incident uniform flow. The vortex lock-on results from the periodic flow exhibit a particularly strong form of resonance, with a relative perturbation amplitude of $2\Delta U/\omega D = 0.014$ resulting in a reduction in base pressure from

$C_{pb} = -1.44$ to -1.85, or 22 percent, for a circular cylinder (Armstrong et al., 1986, 1987). For a circular cylinder oscillating in cross-flow, as noted earlier, a peak-to-peak vibration amplitude of $2a/d = 0.20$ to 0.30 is required to provide a comparable reduction in C_{pb} (Stansby, 1976). Conditionally-averaged wake velocity measurements by Armstrong et al. (1987) have indicated that the strength of the vortices was increased by 29 percent and the spacing was decreased by 25 percent for the largest perturbation levels of their experiments.

These are quite remarkable modifications of the near-wake flow for such a relatively small perturbation amplitude. Thus, seemingly small perturbations of the basic wake flow can produce large changes in vortex strength, base pressure and drag on a bluff circular cylinder or other cross-section. Modification and control of the basic formation or instability mechanisms of the wake thus can provide a means for making substantial changes in the near-wake vortex pattern, and possibly even the middle- and far-wake patterns as well (Cimbala et al., 1988, Browne et al., 1989).

Karniadakis and Triantafyllou (1989) have characterized the state of both the forced and unforced vortex wakes by means of a state diagram as sketched in Fig. 17. At a small but finite amplitude the transitions corresponding to the upper and lower limits of the lock-on are given by two bounding frequencies; within these limits only periodic lock-on states exist. Two quasi-periodic regions are thought to develop at frequencies well above and below the lock-on regime, together with chaotic states in narrow regions immediately adjacent to the lock-on boundaries. These are conceptually similar in overall appearance to the vortex resonance or lock-on measurements of Koopmann (1967) for cross-flow oscillations of a cylinder, reproduced here in Fig. 7, and for the in-line flow perturbations and cylinder oscillations shown in Figs. 1 and 2.

As the threshold amplitude a_t is approached, these finite regions shrink to a single frequency f_e. For cross flow oscillations of the cylinder $f_e = f_{so}$ while for in-line oscillations of the body and periodic perturbations of the mean flow $f = 2f_{so}$ as shown in Fig. 2. The small amplitude perturbations introduced by Armstrong et al. (1986, 1987) correspond qualitatively to those discussed by Karniadakis and Triantafyllou. The relatively large amplitude cylinder oscillations and flow perturbations investigated by Koopmann (1967), Griffin and Ramberg (1974, 1976) and Barbi et al. (1986) and shown in Figs. 1 and 7 introduce nonlinearities and complex changes in the near-wake flow field as shown by the flow visualization studies of Griffin and Ramberg (1974, 1976), Williamson and Rashko (1988), and Ongoren and Rockwell (1988a, b). At the largest amplitudes of oscillation, highly complex vortex flow patterns were observed; and a more extensive kaleidoscope of complex vortex patterns over an even wider range of frequencies and amplitudes was observed experimentally by Williamson and Roshko (1988).

Further research based upon these new analytical and computational approaches described herein is likely to lead to new and more complete fundamental understanding of the near-wake vortex dynamics and vortex lock-on, which until now have been studied mostly by using the more traditional modeling approaches combined with experiments. The results discussed in this paper suggest that modification and control of the basic instability or formation mechanisms of the wake by imposed oscillations, i.e., cross-flow, in-line and rotational, incident flow perturbations, and an imposed sound field provide a means for making substantial alterations to the near-wake vortex pattern, and possibly to the middle- and far-wake flow patterns as well which exist relatively far downstream from the wake-generating body.

Acknowledgments

This study was conducted as part of a research program in fluid dynamics and bluff body flows supported by the Naval Research Laboratory and the Office of Naval Research. We are grateful to Dr. George Karniadakis of Princeton University for several helpful discussions on the spectral element computations and absolute/convective stability concepts. We are also grateful to our colleagues who provided figures and photographs from their research, and to the referees and editors who made numerous constructive and helpful comments to us.

References

Armstrong, B. J., Barnes, F. H., and Grant, I., 1986, "The Effect of a Perturbation on the Flow Over a Cylinder," *Phys. Fluids*, Vol. 29, pp. 2095–2102.

Armstrong, B. J., Barnes, F. H., and Grant, I., 1987, "A Comparison of the Structure of the Wake Behind a Circular Cylinder in a Steady Flow With That in a Perturbed Flow," *Phys. Fluids*, Vol. 30, pp. 19–26.

Barbi, C., Favier, D. P., Maresca, C. A., and Telionis, D. P., 1986, "Vortex Shedding and Lock-On of a Circular Cylinder in Oscillatory Flow," *J. Fluid Mech.*, Vol. 170, pp. 527–544.

Bearman, P. W., 1965, "Investigation of the Flow Behind a Two Dimensional Model With a Blunt Trailing Edge and Fitted With Splitter Plates," *J. Fluid Mech.*, Vol. 21, pp. 241–255.

Bearman, P. W., 1967, "On Vortex Street Wakes," *J. Fluid Mech.*, Vol. 28, pp. 625–641.

Bearman, P. W., 1984, "Vortex Shedding From Oscillating Bluff Bodies," *Ann. Rev. Fluid Mech.*, Vol. 6, pp. 195–222.

Bearman, P. W., and Currie, I. G., 1979, "Pressure Oscillation Measurements on an Oscillating Circular Cylinder," *J. Fluid Mech.*, Vol. 91, pp. 661–677.

Bearman, P. W., and Davies, M. E., 1975, "The Flow About Oscillating Bluff Structures," *Proc. 4th Int. Conf. Wind Eff. Build. Struct.*, ed. K. J. Eaton, pp. 285–295, Cambridge Univ. Press.

Bishop, R. E. D., and Hassan, A. Y., 1964, "The Lift and Drag Forces on a Circular Cylinder," *Proc. R. Soc., London, Series A*, Vol. 277, pp. 51–75.

Blevins, R. D., 1985, "The Effect of Sound on Vortex Shedding From Cylinders," *J. Fluid Mech.*, Vol. 161, pp. 217–237.

Blake, W. K., Maga, L. J., and Finkelstein, G., 1977, "Hydroelastic Variables Influencing Propellor and Hydrofoil Singing," *Noise and Fluids Engineering*, ASME: New York, pp. 191–199.

Bloor, M. S., 1964, "Transition to Turbulence in the Wake of a Circular Cylinder," *J. Fluid Mech.*, Vol. 19, pp. 290–304.

Bloor, M. S., and Gerrard, J. H., 1966, "Measurements on Turbulent Vortices in a Cylinder Wake," *Proc. Roy. Soc., Lond., Series A*, Vol. 294, pp. 319–342.

Browne, L. W. B., Antonia, R. A., and Shah, D. A., 1989, "On the Origin of the Organized Motion in the Turbulent Far-Wake of a Cylinder," *Exp. Fluids*, Vol. 7, pp. 475–480.

Chomaz, J. M., Huerre, P., and Redekopp, L. T., 1988, "Bifurcations to Local and Global Modes in Spatially Developing Flows," *Phys. Rev. Let.*, Vol. 60, pp. 25–28.

Cimbala, J. M., Nagib, H. M., and Roshko, A., 1988, "Large Structure in the Far Wakes of Two-Dimensional Bluff Bodies," *J. Fluid Mech.*, Vol. 190, pp. 265–298.

Ffowcs Williams, J. E., and Zhao, B. C., 1989, "The Active Control of Vortex Shedding," *J. Fluids Struct.*, Vol. 3, pp. 115–122.

Filler, J. R., Marston, P. L., and Mih, W. C., 1991, "Response of the Shear Layers Separating From a Circular Cylinder to Small Amplitude Rotational Oscillations," *J. Fluid Mech.*, Vol. 231, pp. 481–499.

Gerrard, J. H., 1966, "The Mechanics of the Formation Region of Vortices Behind Bluff Bodies," *J. Fluid Mech.*, Vol. 25, pp. 401–413.

Griffin, O. M., 1978, "A Universal Strouhal Number for the 'Locking-On' of Vortex Shedding to the Vibrations of Bluff Cylinders," *J. Fluid Mech.*, Vol. 85, pp. 591–606.

Griffin, O. M., 1981, "Universal Similarity in the Wakes of Stationary and Vibrating Bluff Structures," ASME JOURNAL OF FLUIDS ENGINEERING, Vol. 103, pp. 52–58.

Griffin, O. M., 1989, "Flow Similitude and Vortex Lock-On in Bluff Body Near-Wakes," *Phys. Fluids A*, Vol. 1, pp. 697–703.

Griffin, O. M., and Ramberg, S. E., 1974, "The Vortex Street Wakes of Vibrating Cylinders," *J. Fluid Mech.*, Vol. 66, pp. 553–576.

Griffin, O. M., and Ramberg, S. E., 1976, "Vortex Shedding From a Cylinder Vibrating in Line With an Incident Uniform Flow," *J. Fluid Mech.*, Vol. 75, pp. 257–271.

Grinstein, F. F., Boris, J. P., Griffin, O. M., Hussain, F., and Oran, E. S., 1990, "Coherent Structure Dynamics in Spatially Evolving Near Wakes," 28th Aerospace Sciences Meeting (Reno), AIAA Paper 90-0507.

Grinstein, F. F., Boris, J. P., and Griffin, O. M., 1991, "A Numerical Study of Passive Pressure-Drag Control in a Plane Vortex Street Wake," *AIAA J.*, Vol. 29, in press.

Hall, M. S., and Griffin, O. M., 1992, "Vortex Shedding and Lock-On in a Perturbed Flow," in preparation.

Hatfield, H. M., and Morkovin, M. V., 1973, "Effect of an Oscillating Free Stream on the Unsteady Pressure on a Circular Cylinder," ASME JOURNAL OF FLUIDS ENGINEERING, Vol. 95, pp. 249–254.

Huerre, P., and Monkewitz, P., 1990, "Local and Global Instabilities in Spatially Developing Flows," *Ann. Rev. Fluid Mech.*, Vol. 22, pp. 473–537.

Karniadakis, G. E., and Triantafyllou, G. S., 1989, "Frequency Selection and Asymptotic States in Laminar Wakes," *J. Fluid Mech.*, Vol. 199, pp. 441–469.

Karniadakis, G. E., and Triantafyllou, G. S., 1990, "Direct Numerical Simulation of the Three-Dimensional Vortex Street," 28th Aerospace Sciences Meeting (Reno), AIAA Paper 90-0113.

Koch, W., 1985, "Local Instability Characteristics and Frequency Determination of Self-Excited Wake Flows," *J. Sound Vib.*, Vol. 99, pp. 53, 83.

Koopmann, G. H., 1967, "The Vortex Wakes of Vibrating Cylinders at Low Reynolds Numbers," *J. Fluid Mech.*, Vol. 28, pp. 501–512.

Mansingh, V., 1986, "Experimental Investigation of the Effects of Splitter Plates on the Flow Behind a Rectangular Cylinder," Ph.D. thesis, Queen's University, Kingston, Ontario, Canada.

Meier-Windhorst, A., 1939, "Flatterschwingungen von Zylindern im gleichmassungen Flussigkeitsstrom," Mitteilungen des Hydraulischen Instituts der Technichen Hochscule, Munchen, Heft 9, pp. 9–39.

Monkewitz, P. A., and Nguyen, L., 1987, "Absolute Instability in the Near-Wakes of Two-Dimensional Bluff Bodies," *J. Fluids Struct.*, Vol. 1, pp. 165–184.

Morkovin, M. V., 1964, "Flow Around Circular Cylinders. A Kaleidoscope of Challenging Fluid Phenomena," ASME *Symposium on Fully Separated Flows*, ASME, New York.

Oertel, H., 1990, "Wakes Behind Blunt Bodies," *Ann. Rev. Fluid Mech.*, Vol. 22, pp. 539–564.

Okajima, A., Takata, H., and Asanuma, T., 1975, "Viscous Flow Around a Rotationally Oscillating Circular Cylinder," *Inst. Space and Aero. Sci.* (U. Tokyo), Report No. 532.

Okamoto, S., Hirosi, T., and Adachi, T., 1981, "The Effect of Sound on the Vortex Shedding From a Circular Cylinder," *Bull. Japan Soc. Mech. Engrs.*, Vol. 24, pp. 45–53.

Ongoren, A., and Rockwell, D., 1988a, "Flow Structure From an Oscillating Cylinder. Part 1: Mechanisms of Phase Shift and Recovery in the Near Wake," *J. Fluid Mech.*, Vol. 191, pp. 197–223.

Ongoren, A., and Rockwell, D., 1988b, "Flow Structure From an Oscillating Cylinder. Part II: Model Competition in the Near Wake," *J. Fluid Mech.*, Vol. 191, pp. 225–245.

Rockwell, D., 1987, "Unpublished Manuscript: A View of Hypotheses and Issues on Bluff Body Near-Wake Instabilities," Lehigh University.

Rockwell, D., 1990, "Active Control of Globally-Unstable Separated Flows," ASME *International Symposium on Nonsteady Fluid Dynamics* (*Proceedings*), FED-Vol. 92, pp. 379–394.

Roshko, A., 1954, "On the Drag and Shedding Frequency of Two-Dimensional Bluff Bodies," Nat. Adv. Comm. for Aero., Washington, DC, Technical Note 3169.

Roshko, A., 1955, "On the Wake and Drag of Bluff Bodies," *J. Aero. Sci.*, Vol. 22, pp. 124–132.

Sarpkaya, T., 1979, "Vortex Induced Oscillations: A Selective Review," ASME *Journal of Applied Mechanics*, Vol. 46, pp. 241–258.

Simmons, J. E. L., 1975, "Effect of Separation Angle on Vortex Streets," *Proc. ASCE, J. Eng. Mech.*, Vol. 101, pp. 649–661.

Stansby, P. K., 1976, "Base Pressure of Oscillating Cylinders," *Proc. ASCE, J. Eng. Mech.*, Vol. 104, pp. 591–600.

Taneda, S., 1978, "Visual Observations of the Flow Past a Circular Cylinder Performing a Rotatory Oscillation," *J. Phys. Soc. Japan*, Vol. 45, pp. 1038–1043.

Tanida, Y., Okajima, A., and Watanabe, Y., 1973, "Stability of a Circular Cylinder Oscillating in Uniform Flow or in a Wake," *J. Fluid Mech.*, Vol. 61, pp. 769–784.

Tatsuno, M., 1972, "Vortex Streets Behind a Circular Cylinder Oscillating in the Direction of Flow," *Bull. Res. Inst. Appl. Mech.*, Kyushu University, Vol. 36, pp. 25–37 (in Japanese).

Tokumaru, P. T., and Dimotakis, P. E., 1991, "Rotary Oscillation Control of a Cylinder Wake," *J. Fluid Mech.*, Vol. 224, pp. 77–90.

Triantafyllou, G., Triantafyllou, M., and Chrissostimidis, C., 1986, "Stability Analysis to Predict Vortex Street Characteristics and Forces on Circular Cylinders," ASME *J. Offshore Mech. and Arctic Engineering.*, Vol. 109, pp. 148–154.

Triantafyllou, G., Kupfer, K., and Bers, A., 1987, "Absolute Instabilities and Self-Sustained Oscillations in the Wakes of Circular Cylinders," *Phys. Rev. Let.*, Vol. 59, pp. 1914–1917.

Unal, M. F., and Rockwell, D., 1988a, "On Vortex Formation From a Cylinder. Part 1. The Initial Instability," *J. Fluid Mech.*, Vol. 190, pp. 491–512.

Unal, M. F., and Rockwell, D., 1988b, "On Vortex Formation From a Cylinder. Part 2. Control by Splitter Plate Interference," *J. Fluid Mech.*, Vol. 190, pp. 513–529.

West, G. S., and Apelt, C. J., 1982, "The Effects of Tunnel Blockage and Aspect Ratio on the Mean Flow Past a Circular Cylinder With Reynolds Numbers Between 10^4 and 10^5," *J. Fluid Mech.*, Vol. 114, pp. 361–377.

Williamson, C. H. K., and Roshko, A., 1988, "Vortex Formation in the Wake of an Oscillating Cylinder," *J. Fluids Struct.*, Vol. 2, pp. 355–381.

Williamson, C. H. K., "Defining a Universal and Continuous Strouhal-Reynolds Number Relationship for the Laminar Vortex Shedding of a Circular Cylinder," *Phys. Fluids*, Vol. 31, pp. 2742–2744.

Zdravkovich, M. M., 1982, "Modification of Vortex Shedding in the Synchronization Range," ASME JOURNAL OF FLUIDS ENGINEERING, Vol. 104, pp. 513–517.

Some Aspects of Uncertainty in Computational Fluid Dynamics Results

U. B. Mehta
NASA Ames Research Center,
Moffett Field, Calif. 94035

Uncertainties are inherent in computational fluid dynamics (CFD). These uncertainties need to be systematically addressed and managed. Sources of these uncertainties are identified and some aspects of uncertainty analysis are discussed. Some recommendations are made for quantification of CFD uncertainties. A practical method of uncertainty analysis is based on sensitivity analysis. When CFD is used to design fluid dynamic systems, sensitivity-uncertainty analysis is essential.

Introduction

The commonly used word uncertainty means lack of sureness or reliability about someone or something. This word also means an error, but it does not mean a mistake. In a number of endeavors, the value of uncertainty is determined and decisions are made based on this value. The following are some examples of these endeavors: nuclear reactor analysis (Lewins and Becker, 1982), structural engineering (Hart, 1982), experimental measurements (Coleman, 1989), psychology (Kahneman et al., 1982) and artificial intelligence (Lemmer and Kanal, 1988). Uncertainties in risk assessment and management are of concern to people in various fields (Covello et al., 1987): decision analysts, aircraft designers, safety engineers, epidemiologists, toxicologists, chemists, biologists, economists, political scientist, sociologists, and lawyers. In computational fluid dynamics (CFD), uncertainties are not systematically addressed and managed. (CFD is used herein to encompass a range of related areas, in which computations are done, such as computational aerodynamics, combustion, rarefied gas dynamics, and computational aerothermodynamics.) The objective of this paper is to identify uncertainties in CFD, discuss some aspects of uncertainty analysis, and to make some recommendations to quantify these uncertainties. Although this objective is met using examples taken from computation of hypersonic flight estimates, the essence of the presented discussions is applicable to all speed regimes.

The significance of uncertainty in experimental measurements is illustrated by the "Statement of Experimental Uncertainty" in every issue of the *Journal of Fluids Engineering*. This statement requires that "all papers considered for publication in this journal must contain an adequate statement of the uncertainty of experimental data." This journal also provides guidelines for estimating and presenting uncertainty. On the other hand, a statement of computational uncertainty along with standards for quantifying and presenting uncertainties is yet to be made. Celik (1989), Ferziger (1989), and Roache (1990) have attempted recently to address uncertainty due to numerical accuracy. But computational fluid dynamics uncertainties need to be addressed. Further, the computational fluid dynamicists are often concerned only about computation rather than about computation and fluids dynamics, abdicating responsibility for the latter to the experimenters.

In the field of reactor analysis, because of the responsibility placed on computer codes, a systematic effort was made to develop a practical uncertainty analysis method beginning in the early 1970s (Ronen, 1988). A frequently used method of conducting uncertainty analysis is based on sensitivity analysis. Once the uncertainty is determined, the credibility of the computed results can be established. Further, it is possible to design with a margin built in to reduce the risk associated with this uncertainty. Likewise, it is recommended that a systematic effort is required in CFD, particularly for design application which is the ultimate utility of CFD.

Use is made of examples taken from computation of flight estimates for the manned, single-stage-to-orbit space plane with an air-breathing propulsion system (Williams, 1988; Mehta, 1990a; Barthelemy, 1989; and Gregory, 1989a). This plane depends on two critical technologies related to its components: an engine that can propel this plane at hypervelocities

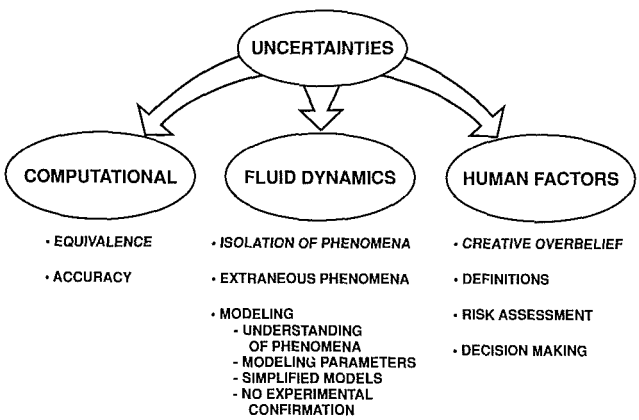

Fig. 1 Sources of uncertainties in computational fluid dynamics results

Contributed by the Fluids Engineering Division for publication in the JOURNAL OF FLUIDS ENGINEERING. Manuscript received by the Fluids Engineering Division March 19, 1990.

with little or no rocket assist and lightweight structural materials that can withstand high temperatures and high stress. On the other hand, among the various design tools, CFD is the only critical one at Mach numbers above eight. This is because of fundamental difficulties in creating complete flight simulations in ground-based facilities (whether existing, to-be-refurbished, or planned) (NRC, 1988; NRC, 1989; and Harsha and Waldman, 1989) and because rules for extrapolations from ground-based tests to flight conditions are difficult to develop and verify. On the other hand, it is the temperature requirements imposed on structural materials that are primarily determined by the fluid dynamics. The common bond between the engine technology and the material technology is the necessity of knowing the fluid dynamics at flight conditions. This knowledge is sought primarily through CFD. Therefore, the CFD technology is a critical enabling technology that the space plane relies on.

Uncertainties in Computational Fluid Dynamics

As the phrase indicates, *computational fluid dynamics* encompasses two disciplines, computation and fluid dynamics. Together, these disciplines are used to numerically simulate the real fluid dynamics through modeling. This numerical simulation is acceptable if it accurately reproduces the reality. Frequently, this cannot be achieved because both fluid dynamics and computation contain uncertainties that affect the computed results. The reason for this situation is obvious: numerical simulation attempts to describe natural reality, but by definition simulation is not reality. Moreover, an additional uncertainty is introduced by the human element. These uncertainties are summarized in Fig. 1, and they are discussed below.

The lack of knowledge about the degree of credibility (confidence level) of results generated by a computer code introduces uncertainties and that about proper usage of this code creates mistakes. These uncertainties are not treated separately as they are related to the CFD uncertainties. The credibility is established by addressing the computational fluid dynamics uncertainties and quantifying them. This process of establishing credibility also determines reliability and limits of applicability of the code.

Fluid Dynamics Uncertainties. There are three sources of uncertainties related to physics and chemistry. First, the uncertainty is caused by isolation of fluid dynamics phenomena, either deliberate or unavoidable. In order to understand certain phenomena, it is customary to set up a unit (that is, a benchmark or building-block) problem demonstrating these phenomena, assuming that there is either absolutely no influence or perfectly known influence on these phenomena of other natural phenomena. Sometimes lack of knowledge leads to isolation of phenomena. On the other hand, unavoidable isolation of phenomena takes place when it is not possible to address all relevant phenomena simultaneously. In either case, an approximation or an uncertainty is introduced. Second, the uncertainty is caused by the insertion of extraneous phenomena. When the reality of interest either cannot be simulated or is difficult to simulate, sometimes an alteration other than a simplification (isolation) of this reality is made so that this modified reality can be simulated. This introduction of extraneous phenomena may perturb the manifestation of existing phenomena. Third, the uncertainty is caused by improper modeling of the phenomena under consideration. A model describes reality in mathematical and/or empirical terms. The uncertainty is related to the validity of the model. Specifically, the sources of modeling uncertainty are the following: (i) The phenomenon under investigation is not thoroughly understood. (ii) Parameters used in the model are known with some degree of uncertainty. (iii) Appropriate models are simplified introducing uncertainty. (iv) An experimental confirmation of the model is not possible or not available.

In the design of the space plane, "aeropropulsion dynamics" is the most significant discipline. It includes aerodynamics, aerothermodynamics, propulsion, and aerodynamic-propulsive integration. Five phenomena are critical in aeropropulsion dynamics at hypervelocities: boundary layer characteristics, shock wave/boundary layer interaction, mixing of fuel and air, chemical kinetics, and low density effects at intermediate (say from 40 km to 80 km) and high (above 80 km) altitudes. Each of these phenomena may be further fragmented or isolated by imposing some constraints on them. The following are some examples: (i) The boundary layer transition from a laminar to turbulent flow is considered to depend on Mach number, Reynolds number, and the wall temperature without considering chemical kinetics. (ii) Different types of shock wave/boundary layer interaction phenomena are identified as incident shock interaction, compression corner interaction, corner flow interaction, glancing interaction, shock train interaction, shock/shock interaction, and shock/cooling layer interaction. Some of these interactions may occur side by side, which may cause them to influence each other. (iii) The effect of combustion instability on the mixing process is not considered. (iv) In chemical kinetics, an idealization is based on which initiation, branching, and termination reactions are considered between H_2 and O_2. (v) The low-density effects in the nose region and leading-edge region are neglected when the rest of the flow can be handled by the continuum, no-slip assumption.

A consequence of the isolation of phenomena illustrated in example (v) is explained as follows. There may be a mixed flow, continuum transitional flow around the nose region and continuum flow downstream of this region. The shock structure and chemical kinetics taking place in this region would have an impact on transition location, the length of the transition region, and the characteristic of the flow entering the engine.

Isolation of phenomena may also occur under the following condition: Design problems involve more phenomena than those considered in unit problems. Modeling of phenomena associated with unit problems and those associated with design problems may differ. The overall effect of the interaction of phenomena associated with different unit problem is unlikely to be simply additive.

Since the ground-based facilities cannot fully simulate hypervelocity flight conditions (NRC, 1988; NRC, 1989; and Harsha and Waldman, 1989), they may produce phenomena other than those of interest. An example of extraneous phenomena uncertainty is the simulation of ground-based combustor flow with chemical reactions in addition to those expected under flight conditions.

There are various sources of uncertainty of modeling: the basic flow equations, transition model, transition length model, relaminarization model, turbulence model (momentum and heat fluxes), relationship between viscous stress and strain rate, relationship between the first and second coefficient of viscosity, chemical reaction rates, vibrational and radiation excitation rates, surface chemical reaction rates (surface catalysis), gas and transport properties, and upstream flow conditions. The modeling uncertainty includes the uncertainty of the range of validity of the model. The term "basic flow equations" considers basic models for continuum, continuum transitional, and rarefied flows, dimensionality, etc. Further, transition and turbulence modeling of both attached and free shear layers are considered.

Computational Uncertainties. Once the modeling equations (which include the initial and boundary conditions) are determined, numerical algorithms are developed to solve them and computer codes are constructed. There are two sources of

uncertainties of computation: equivalence and numerical accuracy. Further, a computer code may contain mistakes.

The computational model needs to describe the "reality" contained in the theoretical (mathematical and/or empirical) model. A departure from equivalence of the two realities introduces errors. At times, this departure is caused by the need for an efficient and robust numerical algorithm. Examples of this departure are the following: (i) The fitting of strong shock waves, such as the bow shock wave at intermediate and high altitudes, would not resolve the shock structure, thereby altering the flow around the nose and the flow downstream of it. (ii) Numerical algorithms for complex problems often use the one-dimensional Riemann solver without taking into account multi-dimensional wave propagation. Under certain conditions, these algorithms may produce a contact discontinuity instead of a shock wave, and vice versa. (iii) The computational model may produce an asymptotic (steady-state, periodic, or chaotic), global solution that is a spurious solution of the theoretical model. Some numerical algorithms (time discretization schemes and/or nonlinear schemes for spatial discretization schemes) produce such solutions (Yee et al., 1990). Nonequilibrium, hypervelocity flows are typically governed by reaction-convection-diffusion equations containing nonlinear source terms. These equations may exhibit a nonlinear dynamical behavior; for example, they may have well-separated multiple solution. The discrete (computational) model should be able to determine the solution that corresponds to that of the differential (theoretical) model.

There are three sources of uncertainty related to numerical accuracy. First, an algorithm consists primarily of an approximation of the mathematical model owing to discretization. In the limit of the spatial and temporal grid sizes approaching zero, a consistent discretization would not have any discretization errors. In practice, this limit cannot be taken. For instance, algorithms for combustor flows may modify the combustion phenomena owing to numerical dissipation (diffusion). Further, the solution procedure for the inviscid part of the Navier-Stokes equations requires numerical damping (see for example Mehta and Lomax, 1982, and Hänel, 1989), thereby influencing viscous solutions. Second, a solution procedure used in an algorithm may contain an approximation. For example, the solution accuracy is dependent on the convergence criteria used in any iterative procedure. Third, techniques used for presentation of computed results is a source of uncertainty. An example is the presentation and interpretation of results using graphical techniques, which have inherent errors. (See also Buning, 1988).

A computer code can be a source of errors. The logic of the code involves the following: consistency of computer instructions with the numerical algorithm (model) and data management (internal and input/output). Coding errors are mistakes, not uncertainties. These mistakes can be eliminated by either checking the logic or by developing independently another code to confirm the results. (Computer hardware errors are not considered.)

Human Factor Uncertainties. There are four types of human factor uncertainties: phenomenon of creative overbelief (Morkovin, 1974), uncertainties about definitions, uncertainties about risk assessment, and uncertainties in decision making. The first two types can be eliminated with systematic questioning, whereas the latter two types of uncertainties are difficult to eliminate. These two principally arise when CFD is used in the design process.

Usually a person develops an emotional attachment to his creation which tends to visualize this creation as a reality based on insufficient evidence. The competitive market generally encourages overselling and fostering of creative overbelief. Uncertainties about definitions are caused by ambiguity concerning meaning and interpretation. Two examples are discussed below. Uncertainties about risk assessment arise from disagreements concerning what constitutes a risk and what is considered to be an acceptable risk. For example, what are acceptable risks due to fluid dynamic uncertainties and computational uncertainties within the flight envelope of the space plane? Uncertainties in decision making arise because of insufficient information. For example, how does one determine some of the fluid dynamics and computational uncertainties without flight test data?

Consider the following definition of CFD code calibration reported by Bradley (1988): "The comparison of CFD code results with experimental data for realistic geometries that are similar to the ones of design interest;" this comparison is "made in order to provide a measure of the code's capability to predict specific parameters that are of importance to the design objectives without necessarily verifying that all the features of the flow are correctly modeled." In this definition, the phrase "to provide a measure of the code's capability to predict" is ambiguous. A comparison between computed results and experimental data for a design-like geometry is not sufficient to justify declaring the code to be a calibrated code.

Referring to definitions of code validation and code calibration as reported by Bradley (1988), Marvin (1989) states the following: "Such definitions refer mainly to the completeness of the process. For the purposes of this paper, validation will refer to the overall process with the understanding that completeness will be evidenced in the depth and scope of carrying out the process." This quote illustrates uncertainty caused by interpretation and that due to meaning. The definition of code validation (Bradley, 1988) explicitly contains the phrase "validation can occur only when." This definition spells out the conditions under which a code can be considered to be a validated code. However, the above quote interprets code validation to be a process. Having different meanings of "validation" introduces uncertainties. When a claim is made that "code validation is done," what does one understand by it? The code may have undergone the process of validation or the code has achieved the status of being a validated code. There must be a generally accepted meaning of validation. On the other hand, consider the second sentence of the above quote, which defines validation. In this definition, the following phrase is meaningless: "completeness will be evidenced in the depth and scope of carrying out the process." What is the status or credibility of a code, if completeness is not achieved? In addition to this ambiguity, "carrying out the process" does not necessary lead to a validated code.

Uncertainty Analysis

Generally, uncertainty analysis is defined as the analysis of the effect of uncertainties involved in all stages of a process on the final responses. This process, for example, may be an experimental process or a computational process with the responses being experimental data or computed results, respectively. With respect to the computational process, there are two approaches to conducting the uncertainty analysis: experimental and computational. In CFD, the experimental approach is used more often than the computational approach. In nuclear reactor analysis, the computational approach is extensively used (Ronen, 1988). The other examples are air quality studies for protecting the environment (for example, Gelinas and Vajk, 1979) and nuclear waste isolation studies (for example, Worley, 1987 and Maerker,1988). Both approaches need to be fully and systematically exploited. They are equally essential for establishing the credibility of the CFD results.

Experimental Approach. Since CFD numerically simulates fluid dynamics reality through modeling, the obvious uncertainty analysis method consists of comparisons between com-

puted results and measurements. This experimental approach has its own limitations, primarily the following: the capability for conducting relevant tests, measurement uncertainties, and insufficiency of data.

Uncertainties are also inherent in experimental fluid dynamics. Both fluid dynamics and measurement contain uncertainties. The fluid dynamics uncertainties arise when ground-based testing is done is simulate flight reality. Two sources of uncertainties related to fluid dynamics are phenomena of isolation and extraneous phenomena. In case of measurements, groundbase or flight, there are interference uncertainties and data uncertainties. *Unless these measurement uncertainties are known, uncertainties of computed results cannot be determined with test data. (More important, the credibility of a design based on test data whose credibility is not established by indicating fluid dynamics and measurement uncertainties is questionable.)* Further, there are uncertainties introduced by the human element, in particular those related to creative overbelief and definitions. An example of the former is the attitude that measurements are the reality. An example of the latter is the false assignment of significance to what has been measured. (Uncertainties due to risk assessment and decision making need to be considered, if test data are to be used for design purposes.)

The fluid dynamics uncertainties are illustrated as follows. The chemical phenomena associated with air under flight conditions are not addressed when ground-based aerodynamic tests are conducted in a nitrogen wind tunnel at high hypersonic Mach numbers. Sometimes the heat transfer boundary condition in ground-based facilities are different from those observed in flight. In some instances, the ground-based facilities introduce phenomena that are not likely to occur in flight. For example, alterations may be caused in the flow owing to effects of additional chemical species, unsteadiness, and disturbances during propulsion tests. Moreover, the interference or interaction between the test device and the flow of interest and the manner in which measurements are taken influence the measured quantities, introducing interference uncertainties. There are two types of interference uncertainties associated with the measuring system, system disturbance uncertainties and system-sensor interaction uncertainties.

In most of the existing hypersonic ground-based facilities, flow conditions upstream of the test section (freestream conditions) are not sufficiently well known (NCR, 1989). *Without knowing the freestream conditions, meaningful computations cannot be done for comparison with test data.* Under such circumstances, the CFD that "confirm" the ground-based tests may be uncertain for estimating flight quantities. Another source of uncertainty is the process of extrapolating from ground-based test conditions to flight conditions. The result of an extrapolation involving a change in fluid dynamics is more uncertain that that of an interpolation without any such change.

Data uncertainties are the residual errors after all corrections have been made to the measured quantities. The uncertainty in a measurement is generally defined as the difference between measured value and the true value of the quantity being measured. There are three types of uncertainties: fixed, random, and variable but deterministic (Moffat, 1988). These uncertainties are also categorized as bias (fixed) and precision (random and variable but deterministic) uncertainties. A standard measurement uncertainty method has been recommended by a number of organizations such as SAE, ASME, AIAA, and JANNAF. Discussions of measurement uncertainty analysis may be found in several references, such as: Coleman (1989), Moffat (1988), ANSI/ASME Standards on Uncertainty (1983 and 1985), and Thompson et al. (1987).

If the levels of measurement uncertainties are acceptable and there is an acceptable level of agreement between the computed results and measurements, then the computer code providing these results is credible. This means that both the fluid dynamics model and numerics are satisfactory. If the level of agreement is not acceptable, then the code may still be acceptable. A possible source of this unacceptable level of agreement is the manner in which the code is being used. Alternatively, fluid dynamics and/or numerics is unsatisfactory and/or the numerical algorithm (model) may not be programmed properly. What are considered as "acceptable" computed results is determined by the accuracy requirements for these results. These are set by the utility of these results. When the experimental approach is used, the uncertainties in the computed results are the differences between measurements and computed results. This definition assumes that the computed results are numerically accurate.

The experimental approach by itself is of limited utility for flight estimates because of the following reasons: (i) There is insufficiency of data, ground-based or flight. It is not always possible to measure all quantities of interest, those necessary, and as often as required for a proper uncertainty analysis. (ii) Sometimes the relevant tests are not possible to carry out. Further, ground-based facilities may introduce fluid dynamics uncertainties, as illustrated above. (iii) This approach does not account for uncertainties in computation, that is, the accuracy of the computed results without a consideration of the experimental data. These uncertainties need to be identified when computed results are compared with measurements. Almost invariably, an excellent comparison between computed results and measurements is used to justify the validity of the computational model, without demonstrating, for example, the effect of grid refinement on the computed result. (iv) The experimental approach provides some, but not a sufficient, guidance for obtaining computed results with the same uncertainties or accuracy at conditions other than those considered, but with the same fluid dynamics.

Computational Approach. The second approach to conducting the computational fluid dynamics uncertainty analysis is the computational approach. This approach essentially does not utilize test measurements. In this case, uncertainties in modeling, uncertainties caused by input parameters, uncertainties in equivalence, and uncertainties in numerical accuracy are determined separately. Modeling uncertainties are generally conducted by those concerned with fluid dynamics. Input uncertainties are usually investigated by those interested in design and safety. Equivalence uncertainties and accuracy uncertainties are mainly of concern to people who are developing algorithms. However, all of these uncertainties are important. For example, the determination of modeling uncertainties is inconclusive without accuracy uncertainties. The theoretical model, the computational model, and the input parameters fix the accuracy that can be obtained.

When a test confirmation is not possible or available, it is sometimes possible to obtain an estimate of the uncertainty by computing the result in question with different models. For example, the intermediate and high altitude shock-on-shock heating on a cowl lip may be investigated by the Navier-Stokes (NS) equations, continuum equations more advanced than the NS equations (different forms of the Burnett equations), and the Boltzmann equation. The sensitivity of different transition models on heat transfer and skin friction and consequently on the take-off gross weight (TOGW) of the space plane can be studied to determine the uncertainty due to transition model. Similarly, uncertainties of turbulence models may be studied by considering models of increasing complexity. Although comparative studies involving different turbulence models are being done from the point of view of fluid dynamics in unit problems, they need to be done also for design-like problems and for determining the uncertainties in the design, for example in the TOGW.

Sometimes a simplified model is used although an accurate

model is available. For example, the parabolized NS equations may be used rather than full NS equations. Another example is the use of a smaller set of finite rate (chemical) reactions than those considered necessary. There are two ways of estimating uncertainties resulting from the use of a simplified model. The obvious procedure for obtaining the uncertainties is to compute using both the simplified and complex model and determine the difference between the two sets of results. Another way is to determine, if feasible, the perturbation operator, which is the difference between the complex model operator and the simplified model operator. Then it may be possible to obtain the uncertainty based on the perturbation theory (Gandini, 1988) or functional analysis (Ronen, 1988).

A practical uncertainty analysis method for determining the uncertainties of the input parameters is based on sensitivity analysis. These parameters include the computational model parameters and specifications, for example, grid spacing, turbulence model constants, the order of numerical scheme, and initial and boundary conditions. A sensitivity is a measure of the influence of a given input parameter on the computed results, primarily performance estimates in design applications. Generally, sensitivity analysis is defined as the procedure to determine sensitivities of input parameters on output results. This analysis provides guidance with respect to the identification of the important contributors to uncertainty, helps to assess confidence levels in computed results, and assists in further development of the computational model. This analysis is particularly useful when large computer codes are used for modeling complex phenomena. It is being used, for instance, in problems exhibiting phenomena associated with heat and mass transfer, chemical kinetics, and nuclear reactor physics. Further, sensitivity analysis can be used in selecting solution-adaptive space and time steps (see for example, Reuven et al., 1987).

Sensitivity analysis is crucial for establishing the credibility of a design and for design optimization. Assume that the computational model is appropriate. The acceptability of computed performance estimates is determined by the sensitivities of specifications to these estimates for the system under consideration. The requirements of acceptable accuracy for these estimates are set by their sensitivities to uncertainties in computed estimates. Some examples of sensitivities of space plane designs to performance estimates are discussed by Gregory (1988), Mehta (1990a), and Gregory (1989b). It is relatively convenient to conduct sensitivity analysis and design improvements with computers, but rather difficult to do so with test facilities, ground-based or flight.

Different methods are available for conducting sensitivity analysis: the brute force method, statistical methods, and deterministic methods. In the brute force method with N input parameters, a linear sensitivity and a nonlinear sensitivity, respectively, require $N+1$ and $2N^2+2N+1$ different computer solutions in order to determine sensitivities of one computed result. The other two methods greatly reduce the number of solutions needed. The response surface method, the Monte Carlo method and the Fourier Amplitude Sensitivity Test are examples of statistical methods. The adjoint method is an example of a deterministic method. Once the sensitivities are determined the uncertainty analysis is carried out to obtain uncertainties. Further, it is possible to obtain uncertainties in a new system, close to that in which uncertainties are known, without conducting the uncertainty analysis for this new system. The theoretical basis for the various sensitivity analysis methods and the uncertainty analysis is given in the book entitled *Uncertainty Analysis* and edited by Ronen (1988). The application of these sensitivity-uncertainty analysis methods to computational fluid dynamics is a new research activity.

Two major concerns of people who are developing numerical algorithms are the equivalence between theoretical and computational models and about computational accuracy. Uncertainties due to a lack of this equivalence and those due to a lack of numerical accuracy are rarely quantified for equations other than model equations used in the development of numerical methods. The only way the former uncertainties can be determined is by comparing two computed results, one with equivalence and one without equivalence. The latter uncertainties related to discretization is done by computing grid-independent results. A grid sensitivity analysis provides the sensitivity of the computed results to the grid size. But the Taylor series analysis for obtaining the leading truncation terms due to discretization does not quantify uncertainties. Algorithms to solve ordinary differential equations usually contain relative error estimates. These algorithms are not of concern here.

A Procedure for Estimating the CFD Uncertainty

Before CFD uncertainties are estimated, the purpose for determining CFD results must be established and a statement of criteria for a successful computation must be formulated. For example, the purpose may be the use of results in a design process and the statement of criteria may include the level of uncertainty that may be acceptable for fulfilling the purpose of the computation. Subsequently, the various sources of relevant CFD uncertainties need to be identified and estimated, as discussed previously.

Both computational and experimental approaches for establishing the credibility of CFD results are used as follows. First, the computational approach is used to determine the computational uncertainties. Then the experimental approach is undertaken to determine the uncertainties resulting from physical modeling by comparing these results with measurements that incorporate known measurement uncertainties and for the same flow conditions. These measurements may be related to unit, benchmark, or design-like problems or to flight problems. Only measurements related to problems of interest allow modeling uncertainties to be determined directly. If there are no measurements available for the flows of interest, fluid-dynamics uncertainties of the computed results are determined, as suggested previously while discussing the computational approach. Those models, which have been validated, should be shown to be applicable to the flows of interest. Further, uncertainties are sometimes associated even with these validated models. Whether these uncertainties can be transferred to the problem of interest needs to be investigated. When measurements are not available and the computational uncertainties are determined but the fluid-dynamics uncertainties are hard to determine, then a subjective process of establishing the credibility is carried out by submitting the results to a team of experts for evaluation.

In the field of nuclear reactor analysis, numerous examples are available to illustrate how sensitivity and uncertainty analysis may be carried out for determining uncertainties due to input parameters (Ronen, 1988). Only one study appears to be done in the field of computational fluid dynamics. Finley (1990) has illustrated quantification of CFD uncertainties and the sensitivity of a design to these uncertainties, following some suggestions presented by Mehta (1990b). Finley has presented a statistical technique for quantifying the credibility level in CFD drag predictions and determined the effect of this credibility on the space-vehicle fuel fraction required to achieve orbit.

Concluding Remarks

A consideration of the computational accuracy uncertainty only partially addresses computational fluid dynamic uncertainties. These uncertainties are related to both computation and fluid dynamics parts of computational fluid dynamics. These are introduced by a lack of equivalence of theoretical

and computational models, unsatisfactory computational accuracy, isolation of fluid dynamics phenomena, extraneous phenomena, improper modeling of phenomena, and by the human element. These uncertainties need to be addressed systematically and properly managed. There are two approaches of uncertainty analysis, experimental and computational. Both of these are equally important. In the experimental approach, measurement uncertainties must be known for determining the uncertainties in the computed results. In the computational approach, the use of sensitivity-uncertainty analysis is suggested. Although these aspects of uncertainty in computational fluid dynamics are discussed with examples taken from hypervelocity aeropropulsion dynamics problems of space planes, the essence of this discussion is applicable to other speed regimes and to other fluid dynamic systems. The credibility of CFD codes is established by code certification (Mehta, 1990a), which is a process for eliminating mistakes in codes and for determining their reliability and applicability.

The ultimate utility of CFD is in the design of fluid dynamic systems. In order to reduce uncertainties in CFD results used for design, the sensitivity of computed performance estimates to CFD uncertainties need to be quantified. In other words, the sensitivity-uncertainty analysis is essential for developing credibility of any design and for defining a safe design margin to account for uncertainties.

References

ANSI/ASME Standards on Uncertainty: "Measurement Uncertainty for Fluid Flow in Closed Conduits," ANSI/ASME MFC-2M-1983; and "Measurement Uncertainty, Part 1, Instruments and Apparatus," ANSI/ASME PTC 19.1-1985.

Barthelemy, R., 1989, "The National Aero-Space Plane Program," AIAA Paper No. 89-5001, AIAA First National Aero-Space Plane Conference, Dayton, OH.

Bradley, R. G., 1988, "CFD Validation Philosophy," *Symposium on Validation of Computational Fluid Dynamics*, Paper No. 1, AGARD CP-437.

Buning, P. G., 1988, "Sources of Error in the Graphical Analysis of CFD Results," *Journal of Scientific Computing*, Vol. 3, No. 2, pp. 149–164.

Celik, I., 1989, "Numerical Uncertainty in Fluid Flow Calculations," Forum on Methods for Estimating Uncertainty Limits in Fluid Flow Computations, ASME Winter Annual Meeting, San Francisco, CA.

Coleman, H. W., 1989, *Experimentation and Uncertainty Analysis for Engineers*, Wiley, New York.

Covello, V. T., Lave, L. B., Moghissi, A., and Uppuluri, V. R. R., 1987, Eds., "Uncertainty in Risk Assessment, Risk Management, and Decision Making," *Advances in Risk Analysis*, Vol. 4, Plenum Press, New York.

Ferziger, J. H., 1989, "A Note on Numerical Accuracy," Forum on Methods for Estimating Uncertainty Limits in Fluid Flow Computations, ASME Winter Annual Meeting, San Francisco, CA.

Finley, D., 1990, "Hypersonic Aerodynamics Considerations and Challenges," AIAA Paper 90-5222, AIAA Second International Aerospace Planes Conference, Orlando, FL.

Gandini, A., 1988, "Uncertainty Analysis and Experimental Data Transposition Methods Based on Perturbation Theory," *Uncertainty Analysis*, Ed. Y. Ronen, CRC Press, Inc., Boca Raton, FL.

Gelinas, R. J., and Vajk, J. P., 1979, "Systematic Sensitivity Analysis of Air Quality Simulation Models," EPA-600/4-79-035, Environmental Sciences Research Laboratory, Office of Research and Development, U. S. Environmental Protection Agency.

Gregory, T. J., 1988, "National Aero-Space Plane Design Fundamentals and Evaluation," AIAA Paper 88-4504, AIAA, AHS, and ASEE Aircraft Design, Systems, and Operations Meeting, Atlanta, GA.

Gregory, T. J., 1989a, "The Hypersonic Challenge," 33rd International Aerospace Fluid Power Conference, Jackson, Miss.

Gregory, T. J., 1989b, "Credibility of NASP," *Aerospace America*, Sept., pp. 42–44, and 46.

Hänel, D., 1989, "Computation of Compressible Viscous Flows," AGARD-FDP-VKI Special Course on 3-D Supersonic and Hypersonic Flows Including Separation.

Harsha, P., and Waldman, B., 1989, "The NASP Challenge: Testing for Validation," AIAA Paper No. 89-5005, AIAA First National Aero-Space Plane Conference, Dayton, OH.

Hart, G. C., 1982, *Uncertainty Analysis, Loads, and Safety in Structural Engineering*, Prentice-Hall, Inc. Englewood Cliffs, N. J.

Kahneman, D., Slovic, P., and Tversky, A., 1982, Eds., *Judgment Under Uncertainty: Heuristics and Biases*, Cambridge University Press.

Lemmer, J. F., and Kanal, L. N., 1988, Eds., *Uncertainty in Artifical Intelligence 2*, Machine Intelligence and Pattern Recognition, Vol. 5, North-Holland, Elsevier Science Publishers B. V.

Lewins, J., and Becker, M., 1982, Eds., "Sensitivity and Uncertainty Analysis of Reactor Performance Parameters," *Advances in Nuclear Science and Technology*, Vol. 14, Plenum Press, New York.

Maerker, R. E., 1988, "Comparison of Results Based on a Deterministic Versus a Statistical Uncertainty Analysis," ORNL/TM-10773, Oak Ridge National Laboratory.

Marvin, J., 1989, "Validation for NASP," *Proceedings of the Seventh National Aero-Space Plane Technology Symposium*, Vol. II, NASP CP-7041.

Mehta, U. B., and Lomax, H., 1982, "Reynolds Averaged Navier-Stokes Computations of Transonics—the State-of-the-Art," *Transonic Aerodynamics*, D. Nixon, Ed., Progress in Astronautics and Aeronautics, Vol. 81, AIAA, pp. 297–375.

Mehta, U. B., 1990a, "Computational Requirements for Hypersonic Flight Performance Estimates," *Journal of Spacecraft and Rockets*, Vol. 27, No. 2, pp. 103–112. (Also AIAA Paper 89-1670.)

Mehta, U. B., 1990b, "Some Aspects of Uncertainty in Computing Hypersonic Flight Estimates," NASA TM-102804.

Moffat, R. J., 1988, "Describing the Uncertainties in Experimental Results," *Experimental Thermal and Fluid Sciences*, Vol. 1, pp. 3–17.

Morkovin, M. V., 1974, "A Harangue to Young Authors by a Weary Reviewer," Guest Editorial, ASME JOURNAL OF FLUIDS ENGINEERING, Vol. 96, No. 2, pp. 82–83.

NRC, 1988, *Review of Aeronautical Wind Tunnel Facilities*, Committee on Assessment of National Aeronautical Wind Tunnel Facilities, Aeronautics and Space Engineering Board, National Research Council, National Academy Press, Washington, DC.

NRC, 1989, *Hypersonic Technology for Military Application*, Committee on Hypersonic Technology for Military Application, Air Force Studies Board, National Research Council, National Academy Press, Washington, DC.

Reuven, Y., Smooke, M. D., and Rabitz, H., 1987, "Sensitivity Analysis of One-Dimensional Mixed Initial-Boundary Value Problems: Application to Freely Propagating Premixed Laminar Flames," *Journal of Scientific Computing*, Vol. 2, No. 4, pp. 345–370.

Roache, P., 1990, "The Need for Control of Numerical Accuracy," *Journal of Spacecraft and Rockets*, Vol. 27, No. 2, pp. 98–102.

Ronen, Y., 1988, Editor, *Uncertainty Analysis*, CRC Press Inc., Boca Raton, FL.

Thompson Jr., J. W., Kimzey, W. F., and Boals Jr., W. O., 1987, "An Overview of the Application of Standard Measurement Uncertainty Methodology to Propulsion Testing," *Aerodynamic Data Accuracy and Quality: Requirements and Capabilities in Wind Tunnel Testing*, Paper No. 8, AGARD CP-249.

Williams, R., 1988, "Forces of Change and Future of Hypersonic Flight," *Proceedings of the First International Conference on Hypersonic Flight in the 21st Century*, University of North Dakota, p. 1–27.

Worley, B. A., 1987, "Deterministic Uncertainty Analysis," ORNL-6428, Oak Ridge National Laboratory.

Yee, H. C., Sweby, P. K., and Griffiths, D. F., 1990, "Dynamical Approach Study of Spurious Steady-State Numerical Solutions of Nonlinear Differential Equations, Part I. The Dynamics of Time Discretization and Its Implication for Algorithm Development in Computational Fluid Dynamics," *Journal of Computational Physics*, Vol. 97, 1991. See also NASA TM-102820.

A Numerical Model to Predict the Nonlinear Response of External Flow Over Vibrating Bodies (Planar Flow)

N. Kolluru Venkat[1]
Assoc. Mem. ASME

Malcolm Spaulding
Professor of Ocean Engineering.
Mem. ASME

Department of Ocean Engineering,
The University of Rhode Island,
Kingston, RI 02881

A model is developed to simulate two-dimensional laminar flow over an arbitrarily shaped body, a portion of which is subjected to time varying harmonic motion. The model is tested by comparison to previous numerical simulations for flow over a square cavity, oscillatory flow through a wavy channel and boundary layer flow along a flat plate. The model is applied to predict the flow over a flat plate with a section forced in simple sinusoidal motion. The dimensionless vibration amplitude, H_0, *and the Reynolds number,* Re *are maintained at 0.1 and 1000, respectively. The Strouhal number,* St, *defined as the ratio of the flow advective time scale to the plate oscillation period, is varied in the range* $0.0 \leqq \mathrm{St} \leqq 1.0$. *The friction and pressure coefficients over the vibrating portion of the body are analyzed using Fast Fourier Transform techniques. For low frequency vibrations (low Strouhal number) the pressure and friction coefficients match the steady state results for flow over a fixed sinusoidal bump. A small amplitude pressure wave generated by the oscillating plate propagates downstream with the flow. For high frequency vibrations (high Strouhal number) the pressure and friction coefficients over the vibrating portion of the body deviate from the steady state results and a high amplitude pressure wave propagates downstream. The pressure at one chord length upstream is also affected. As* St *increases the flow becomes highly nonlinear and harmonics appear in the downstream velocity and pressure fields. The nonlinearity is controlled by the convective acceleration term near the vibrating plate surface.*

1 Introduction

Engineering applications of unsteady boundary layers are numerous and of great importance in hydro and aero dynamics (Telionis 1981). Machines which operate inside a body, such as a submarine or torpedo, may cause a part of the body surface to vibrate at varying frequencies and modes. It is not generally understood how these vibrations affect the fluid flows over the surface of the vibrating body. In many cases of technological interest, solid boundaries appear to play a direct role in the sound generation process and their presence often results in a large increase in the radiated sound (Goldstein, 1974).

There is little information available to understand the process of sound generation if the perturbations that arise in the flow come from flexible boundaries (e.g., vibration of the body) rather than from the flow itself (e.g., turbulent flow). Most of the early work focussed on the interaction of free stream fluctuations with a stationary body. Lighthill (1954) derived the unsteady boundary layer equations using a small perturbation theory for fluctuations imposed on the free stream. Most of the subsequent investigations of this type of problem are based on expansions in powers of $\omega L/U$, where ω is the angular frequency of fluctuations in the fluid, L the characteristic length of the body, and U is the velocity of mean flow over the body. Expansions for small or large values of this parameter were carried out by numerous investigators (Telionis, 1981).

Telionis (1981) thoroughly reviewed unsteady boundary layers for separated and attached flows. In most of the research work summarized in this review, Prandtl boundary layer equations were used. The equations were solved using small perturbation theory. These methods however cannot be used for large body fluctuations and arbitrary shapes or for high Reynolds numbers where the interaction between the outer inviscid flow and inner boundary layer (Carter, 1975) may be quite significant.

Hurlburt (1978) developed a numerical model of fluid-structure interaction for a rigid circular cylinder in forced motion using the Marker and Cell method. This method is computationally inefficient and alternate schemes are presently available to simulate the flow over arbitrarily shaped bodies (Fasel, 1980).

Very little information is available on the response of the external laminar or turbulent flow to the unsteady vibrations

[1]Formerly research assistant, currently working as a consultant to SEA, Inc., Rhode Island.

Contributed by the Fluids Engineering Division for publication in the JOURNAL OF FLUIDS ENGINEERING. Manuscript received by the Fluids Engineer Division October 8, 1990.

of the outer surface of the body. In this paper, we focus our attention on developing a model to study the response of the fluid flowing externally over a body at low to moderate Reynolds numbers when a portion of the body surface is vibrating at high amplitudes and Strouhal numbers.

2 Mathematical Formulation

In the present work, the fluid-structure interaction problem is decoupled and the hydrodynamic region is solved using the two dimensional incompressible Navier–Stokes equations and conservation of mass equation in an x-y coordinate system, formulated in terms of vorticity and stream function. The flexible structure influence comes through the know time dependent boundary condition at the wall. The physical domain is shown in Fig. 1(*a*).

The flow equations and the associated boundary conditions are described in detail in Venkat (1991), only a brief description of the formulation is given here. The governing equations, in dimensionless form, are given by

$$\frac{\partial\omega}{\partial t}+\frac{\partial\psi}{\partial y}\frac{\partial\omega}{\partial x}-\frac{\partial\psi}{\partial x}\frac{\partial\omega}{\partial y}=\frac{1}{\mathrm{Re}}\left[\frac{\partial^2\omega}{\partial x^2}+\frac{\partial^2\omega}{\partial y^2}\right] \tag{1}$$

$$\left[\frac{\partial^2\psi}{\partial x^2}+\frac{\partial^2\psi}{\partial y^2}\right]=-\omega \tag{2}$$

The dimensionless variables (lower case) are defined as:

$$x=\frac{X}{L},\ y=\frac{Y}{L},\ u=\frac{U}{U_\infty},\ v=\frac{V}{U_\infty},\ p=\frac{P}{\rho U_\infty^2}$$

$$t=\frac{TU_\infty}{L},\ \omega=\frac{\Gamma L}{U_\infty},\ \psi=\frac{\Psi}{U_\infty L},\ \mathrm{Re}=\frac{LU_\infty}{\nu}\ \text{and}\ \mathrm{St}=\frac{fL}{U_\infty}$$

The velocity profile for a given Reynolds number at the upstream boundary is calculated using the Blasius equation (White, 1991) assuming that the leading edge of the plate (section FA) is located at a distance, x_s from the entry region of the model domain. In the present analysis, x_s is made equal to 1. Top boundary (section FE) is kept sufficiently far away such that $u = 1$ and $\omega = 0$ (Fletcher, 1988). An alternate frictionless "wind tunnel" boundary condition is to specify $u = 1$ and $v = 0$ on FE. This effectively imposes a Dirichlet boundary condition $\psi_{FE} = \psi_F$. As long as FE is sufficiently far from the vibrating section the global solution will be relatively insensitive to the particular boundary condition specification on FE. The normal second or higher order derivatives of stream function and vorticity are assumed zero at the downstream boundary (section DE; Fletcher, 1988).

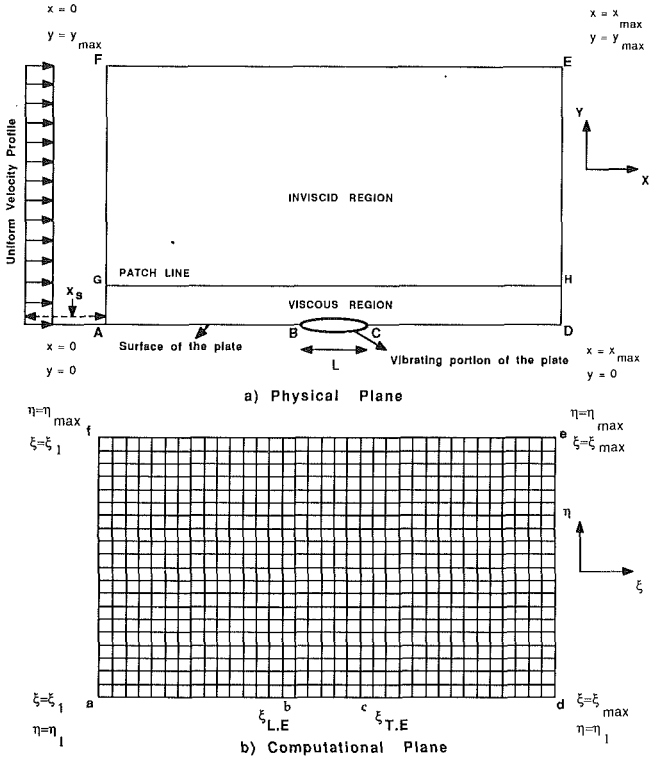

Fig. 1 Physical and computational planes for viscous flow over a vibrating body

On the plate surface, a section vibrates in simple harmonic motion (section BC). The equation for plate deflection is given by

$$y_w(x,t)=H_0\ \mathrm{Sin}\ (2\pi t\mathrm{St})\ \mathrm{Sin}\ (n\pi x)\quad x_{\mathrm{L.E.}}\leqq x\leqq x_{\mathrm{T.E.}} \tag{3}$$

On the remainder of the plate (sections AB and CD)

$$y_w(x,t)=0.0\quad 0<x<x_{\mathrm{L.E.}}\ \text{and}\ x_{\mathrm{T.E.}}<x<x_{\max} \tag{4}$$

The stream function on the vibrating section of the plate is calculated by integrating the velocity of vibration along the plate surface. Simultaneously the derivative of the stream function in the y direction is set to zero to satisfy the no slip boundary condition ($\partial\psi/\partial y = 0$). On the rest of the plate surface the stream function is constant and $\partial\psi/\partial y$ is zero. There are several methods available to handle the indirect boundary con-

Nomenclature

a = body vibration amplitude, m
$C_f(x,y=y_w,t)$ = friction coefficient on the plate surface
$C_p(x,y=y_w,t)$ = pressure coefficient on the plate surface
f = plate vibration frequency, Hz
H_0 = nondimensional body vibration amplitude ratio (a/L)
J = Jacobian of the metric coefficients in the boundary fitted plane
L = characteristic length of the vibrating portion of the body, m
n = plate vibration mode
p = dimensionless pressure ($p=P/\rho U^2$)
P = fluid pressure, kg/m^2
Re = Reynolds number ($U_\infty L/\nu$)
Re_x = local Reynolds number ($U_\infty x/\nu$)
St = Strouhal number (fL/U_∞)
T = dimensional time (s)
t = dimensionless time ($t=TU/L$)
u, v = dimensionless horizontal and vertical velocities ($u=U/U_\infty$, $v=V/U_\infty$)
U, V = horizontal (along plate/cylinder) and vertical velocities (normal to plate/cylinder), m/s
U_∞ = free-stream velocity
x, y = nondimensional coordinates in the physical plane ($x=X/L$, $y=Y/L$)
$x_{\mathrm{L.E.}}, x_{\mathrm{T.E.}}$ = leading and trailing edges of the vibrating section of the plate in the physical plane
$x_{\max}$ = length of the computational domain in the physical plane
x_s = nondimensional distance between the leading edge of the

dition for wall vorticity (Roache, 1972; Peyret and Taylor, 1983; Fletcher, 1988). For problems solved with numerical mapping, Isreli (1970), Thames (1975) and Ehrlich (1981) used a coupling procedure between the wall vorticity and the no slip boundary condition. In the present approach we followed Ehrlich's approach to determine wall vorticity.

Since there is a moving boundary on the body surface, a boundary fitted coordinate system was selected (Thompson, 1982) for numerically generating the grids and subsequently solving the time dependent flow problem. This transformation allows problems with time dependent boundaries to be solved with relative ease (Wang, 1986 and Venkat 1987). The transformed grid and flow equations and the associated boundary conditions are given in Venkat (1991).

3 Numerical Method

The Line Gauss Seidel method of Napolitano and Walters (1986) is adopted for the present numerical simulations. The flow and the grid generation equations in the transformed plane are discretized using second order finite differences and the resulting algebraic equations along with the transformed boundary conditions (Venkat, 1991) are solved using a Thomas Tri Diagonal Matrix Algorithm (Bringen and McMillan, 1980; Napolitano and Walters, 1986) from upstream to downstream for each time step. The time step is evaluated based on the stability analysis given in Roache (1972), Peyret and Taylor (1983) and Fletcher (1988) for incompressible flows. The discretization procedure is given in Venkat (1991).

A viscous-inviscid domain splitting approach described in Halim (1986) is adopted in the present numerical model. The patch line between the viscous and inviscid regions (Fig. 1a) is selected such that it is well above the boundary layer thickness. Substantial computational savings are achieved using this inviscid-viscous approach compared to a fully viscous approach.

The unperturbed boundary layer solution is used as an initial guess for the stream function and the vorticity variables. Because of the nonlinearities in the flow equations the vorticity on the body and in the domain is under-relaxed to avoid instability for high frequency plate vibrations while the stream function in the domain is over-relaxed to speed the convergence. Absolute convergence criteria are used for both variables. The converged stream function and vorticity values for each time step are used to calculate the friction and pressure coefficients ($C_f(\xi,\eta=\eta_1,t)$, $C_p(\xi,\eta=\eta_1,t)$) on the plate surface. They are given by

$$C_f(\xi,\eta=\eta_1,t) = -\frac{2}{\mathrm{Re}}\left[\omega_w + \frac{2}{J}\left(\frac{\partial y}{\partial \xi}\frac{\partial v}{\partial \eta} - \frac{\partial y}{\partial \eta}\frac{\partial v}{\partial \xi}\right)\right] \quad (5)$$

$$C_p(\xi,\eta=\eta_1,t) = P_\xi - P_{\xi_1} = \int_{\xi_1}^{\xi}\left\{\frac{1}{J\mathrm{Re}}\left(\beta\frac{\partial \omega}{\partial \xi} - \gamma\frac{\partial \omega}{\partial \xi}\right) - \frac{\partial x \partial u}{\partial \xi \partial t} - \frac{\partial y \partial v}{\partial \xi \partial t} - \frac{1\partial(u^2+v^2)}{2\partial \xi} + v\omega\frac{\partial x}{\partial \xi} - u\omega\frac{\partial y}{\partial \xi}\right\} d\xi' \quad (6)$$

The plate is moved to the next time step and the numerical procedure described above is repeated. The simulations are performed until the solution reaches steady state, repeats from one cycle to the next.

The spectral characteristics of the flow field are analyzed by applying Fast Fourier Transform (Newland, 1975) on the discrete numerical data (C_p) obtained from the numerical model. The data (2048) points for the FFT analysis use the last cycle (steady state) of the time series C_p data. In this approach, any subharmonics created during the transient stage are not included in the spectral analysis.

4 Model Testing

Before applying the model to the problem of interest it was compared with several conventional fluid mechanics problems for which known solutions exist. In addition, the sensitivity of the numerical solutions to the size of the computational domain, grid resolution and location of the patch line were investigated.

The model has been tested against cavity flow (Figs. 2 and 3), oscillatory flow in a channel with wavy walls (Figs. 4, 5, and 6) and Blasius flow over a flat plate (Fig. 10). In each case the model predictions compared well with analytic solutions (Blasius flat plate results; White, 1991), other numerical (cavity flow modeling; Morris, 1975) or experimental observations (oscillatory flow over fixed wavy walls; Sobey, 1982). These applications are described in detail in Venkat (1991). The test simulations show that the present numerical model can handle arbitrary shaped bodies and time dependent boundary conditions with reasonable accuracy.

The model was tested for the influence of the location of up and downstream (sections FA and ED) and top free-stream boundaries (section FE) on the numerical results. All the test runs were performed for Re = 1000, H_0 = 0.15 and St = 0 (steady flow). After some trail runs, the up and downstream and top free stream boundaries are located as shown in Fig. 8.

Next the impact of the bump grid resolution in the x direction

Nomenclature (cont.)

plate and the model entry domain
X, Y = dimensional coordinates in the physical plane
$y_{\max}$ = height of the computational domain in the physical plane
y_w = plate deflection in y-direction
Γ = dimensional vorticity, 1/s
ρ = fluid density
Ψ = dimensional stream function, m^2/s
β, γ = metric coefficients in the boundary fitted plane
ξ, η = coordinates in the boundary fitted computational domain
$\xi_{\max}$ = length of the computational domain in the boundary fitted plane
ξ_1, η_1 = coordinates of the origin in the boundary fitted plane
$\eta_{\max}$ = height of the computational domain in the boundary fitted plane
$\xi_{\mathrm{L.E.}}, \xi_{\mathrm{T.E.}}$ = leading and trailing edges of the vibrating section of the body in the boundary fitted computational plane
ψ, ω = dimensionless stream function ($\psi = \Psi/LU_\infty$) and vorticity ($\omega = \Gamma L/U_\infty$)
ω_w = wall vorticity
$\delta_{\mathrm{L.E.}}$ = boundary layer thickness at the leading edge of the vibrating plate section
δ_e = boundary layer thickness at the downstream end of the domain
p_{ξ_1} = reference pressure at $\xi' = \xi_1$
p_ξ = pressure at $\xi' = \xi$

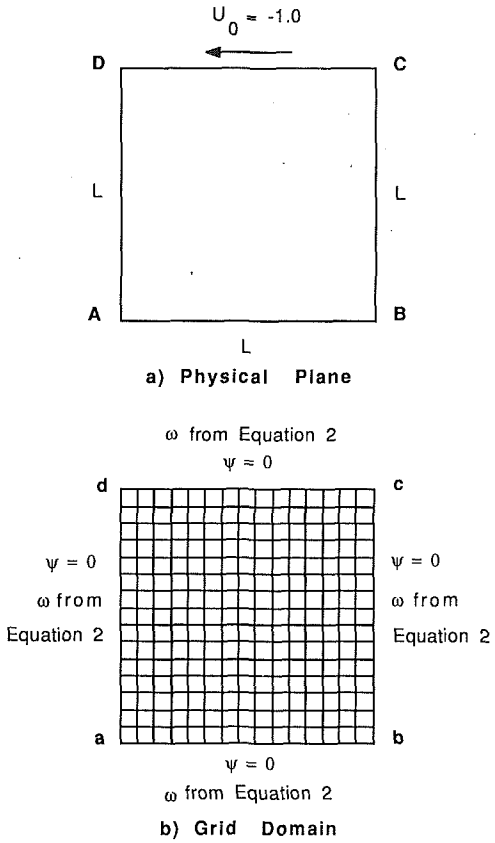

Fig. 2 Physical plane and the grid domain for a square cavity problem

on the model predictions was analyzed. C_f at the maximum amplitude position ($x = 8.25$) versus dy/dx ratios is plotted in Fig. 7 (dx-grid size in the x direction on the bump; dy-grid size between the bump and $\eta = 2$ line). Friction coefficient is plotted as $C_f\sqrt{\text{Re}}$ in all the figures. The dy/dx ratio at which C_f at the bump decreases and reaches an asymptote was chosen for the subsequent grid spacing in the x direction on the bump.

Finally, the number of grids on either side of the bump in the x direction were decreased to determine the minimum number of grids to maintain an accurate solution. This ultimately decreases the computational time. The final grid domain consists of 61 and 41 grids in x and y directions, respectively (Fig. 8). Similar analysis is performed for unsteady flow over a vibrating plate.

The flow was next simulated to test the sensitivity to the patch line location. C_f versus x for various patch line locations is shown in Fig. 9. Table 1 shows the number of iterations and CPU time for the various patch line location. In general, as the patch line is moved closer to the body both the CPU time and the number of iterations decrease. When the patch line is located at $y = 0.75L$ ($1.15\delta_e$), just above the boundary layer region, the friction coefficient remains the same as in the previous cases however the computational time and the number of iterations increase substantially. As a rule of thumb the patch line is located at least $1.5\delta_e$ from the body surface. Uncertainties in the numerical results were estimated by comparing the computations using different mesh sizes (81×51, 71×51, 61×51, 61×41). A detailed description of sensitivity analysis is given in Venkat (1991).

5 Results and Discussions

(a) Steady Flow. A fixed sinusoidal bump (Bump 1) with amplitude, $H_0 = 0.1$ is created on the plate between $x = 8.0$ and 9.0. The Reynolds number based on distance from the leading edge of the plate to the leading edge of the vibrating

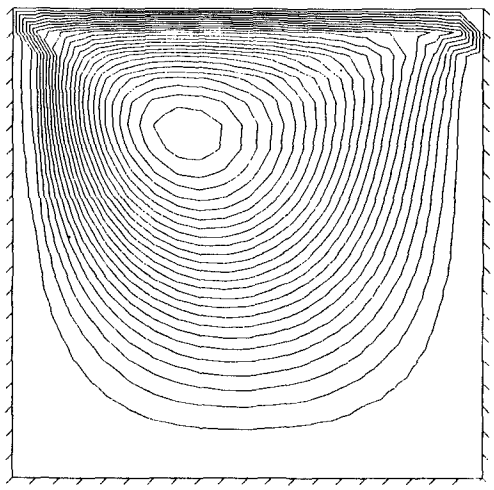

Fig. 3(a) Contour plot of stream function for the flow in the square cavity at Re = 100

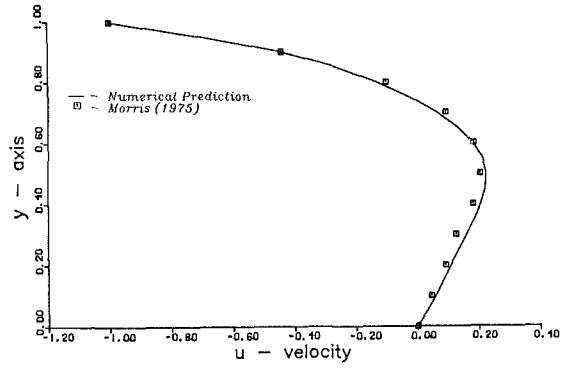

Fig. 3(b) Comparison of horizontal velocity (u) profile through the center of the vortex with the numerical solution of Morris (1975) for Re = 100

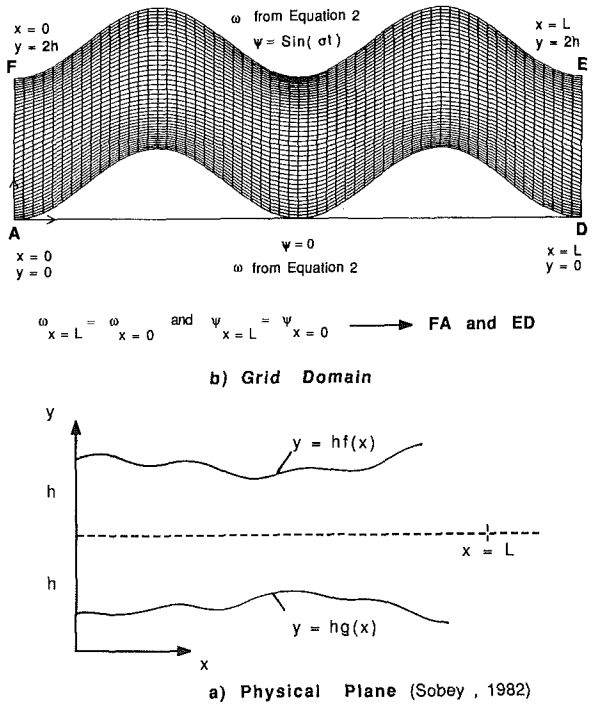

Fig. 4 Physical plane, grid domain and the associated boundary conditions for simulating oscillating flow through a rigid wavy (sinusoidal) channel

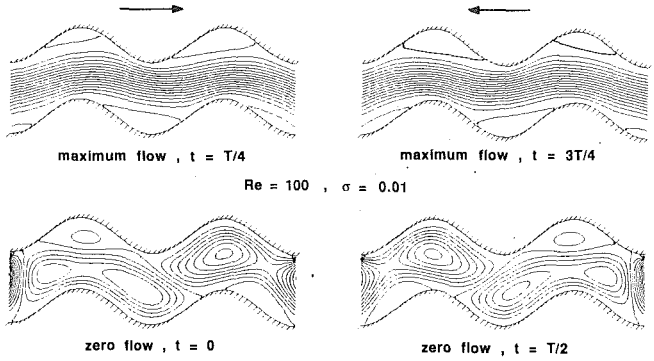

Fig. 5 Contour plot of stream function for the oscillatory flow in the wavy (sinusoidal) channel

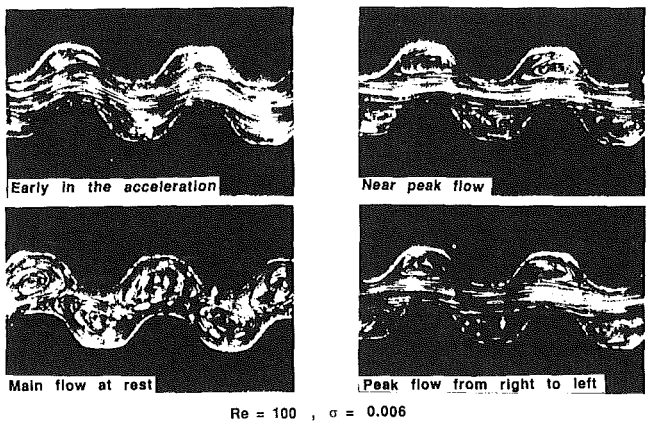

Fig. 6 Experimental flow pictures of oscillatory flow in the wavy (sinusoidal) channel by Sobey (1982)

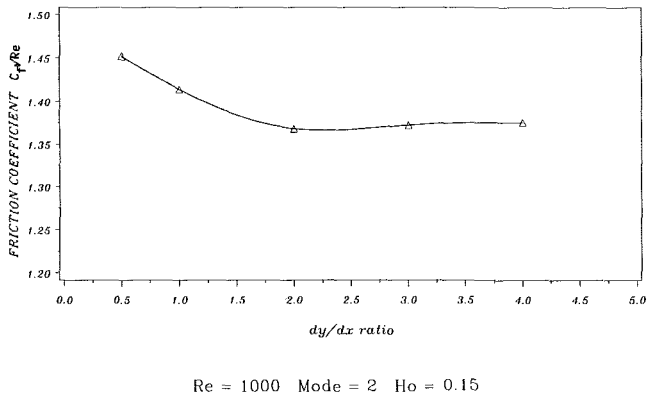

Fig. 7 Variation of friction coefficient with *dy/dx* ratio at the maximum amplitude position (x = 8.25)

section, Re_x, is 9000. This gives a boundary layer thickness ($\delta_{L.E.}$) to vibrating plate length (L) ratio of 0.4743 at the leading edge of the vibrating section and hence the boundary layer is relatively thick compared to the plate length. The ratio of H_0 to $\delta_{L.E.}$ is 0.21. The model predicted steady state variation of friction coefficient along the plate with the fixed bump is shown in Fig. 10. C_f changes rapidly at the position where the bump is created. Its value, however, slowly approaches the flat plate results far downstream.

The pressure coefficient is plotted in Fig. 11 together with the flat plate results. The pressure coefficient decreases markedly at the beginning of the bump and then remains almost constant downstream of the bump.. There is little pressure recovery in this region and hence a net pressure loss. A contour plot of stream function for this case is shown in Fig. 12. Figure 12(a) clearly shows that there is a separation bubble in the trough of the bump which is responsible for the lack of pressure recovery.

The flow is simulated for the same values of H_0 and Re for a second sinusoidal bump (Bump 2), 180 out of phase with the first. The variation of friction coefficient over the plate for this case is shown in Fig. 10. The flat plate case provides a reference. This case is very similar to the earlier simulation. The exception is that the separation bubble appears in the front part of the bump (Fig. 12(b)). Once again there is no downstream pressure recovery.

(b) **Unsteady Flow.** The plate (section BC), located between x equal to 8 and 9 is forced to vibrate in simple harmonic motion with mode n = 2 (Fig. 1(a)). The amplitude of vibration, H_0 and the Reynolds number, Re are maintained at 0.1 and 1000, respectively. The Strouhal number, St is fixed at 0.05 (low frequency vibration). Based on the stability analysis given in Roache (1972), one cycle of vibration is divided into 80 time steps. Figure 13 shows the shear stress, C_f, envelope. (The envelope is defined as the maximum and minimum values between which the value varies in time) for St = 0.05 and Re = 1000. The steady flow results for the flat plate and fixed sinusoidal shape cases are also included for comparison. The variation of skin friction coefficient over the vibrating portion of the plate is similar to the steady state results obtained for sinusoidal bumps with H_0 = 0.1. Upstream the shear envelope deviates little from the flat plate results. Moving downstream from the trailing edge of the bump the C_f minimum curve slowly returns to the Blasius solution after two plate lengths (2L) whereas the C_f maximum curve returns after one half plate length (0.5L). The flow returns more quickly to the Blasius solution when the body oscillates with positive (upward) velocity in the first half of the vibrating section than when the velocity is negative (downward). The location of the downstream boundary condition, eight wavelengths away from the trailing edge of the vibrating portion of the plate, provides a good representation of the flow.

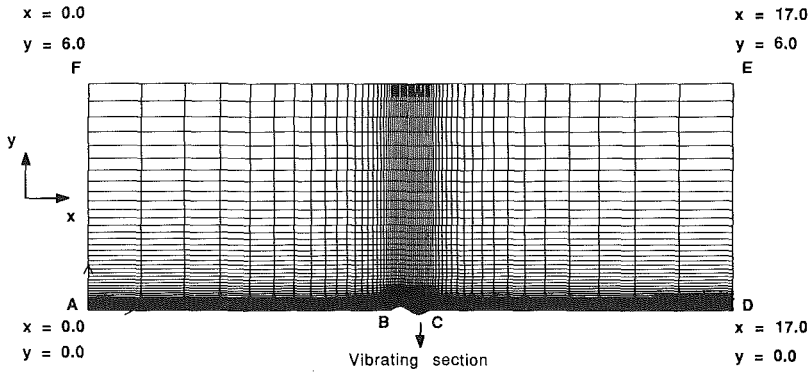

Fig. 8 Grid domain (61 × 41) for simulating steady and unsteady flows over the vibrating plate

Table 1 Central Processor Unit (CPU) time for different patch line locations

PATCH LINE LOCATION	CPU TIME (Minutes)	NUMBER OF ITERATIONS
6.00L	31:46	896
3.40L	29:36	802
1.00L	24:32	700
0.75L	32:08	955

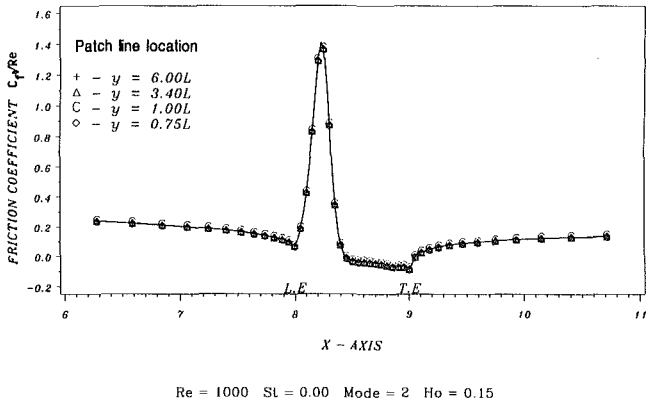

Fig. 9 Effect of patch line location on the distribution of friction coefficient over the fixed sinusoidal bump

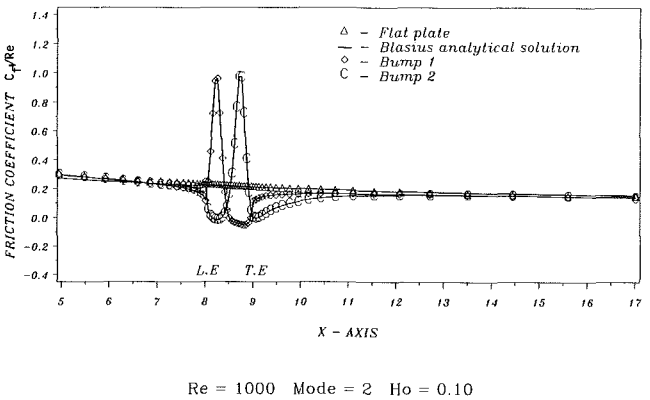

Fig. 10 Variation of friction coefficient over the plate with the fixed sinusoidal bump for Re = 1000. The analytical solution due to Blasius is also shown for comparison.

The pressure envelope for the unsteady case as well as the steady state numerical results for the flat plate and fixed sinusoidal bumps are shown in Fig. 11. Over the vibrating section, the C_p maximum and minimum curves deviate little from the steady state results. Downstream, their values are the same as the fixed sinusoidal bump cases both showing a net pressure drop compared to the Blasius result.

The variation of pressure coefficient with the instantaneous amplitude of the vibrating plate at $x = 8.25$ is shown in Fig. 14. This figure clearly shows that C_p varies linearly with the instantaneous amplitude of vibration of the plate for St = 0.05. The time variation of the velocity of vibration is very small and hence the amount of fluid displaced into the incoming flow is small. The incoming flow has sufficient time to sense the deflection of the plate and therefore the C_p envelope follows the steady state results. A perspective view of the pressure coefficient along the plate versus time for St = 0.05 is shown in Fig. 15*a*. Very small amplitude pressure waves propagate downstream; upstream pressure propagation is minimal.

Next the Strouhal number St is increased to 0.25 while maintaining Re and H_0 at previous values. For this case, one cycle of vibration is divided into 80 time steps. The shear and pressure envelope for St = 0.25 and Re = 1000 are shown in Figs. 16 and 17, respectively. The pressure envelope deviates considerably from the steady flow results. Unlike the St = 0.05 case, the pressure envelope increases considerably over the vibrating section and remains fixed and large as one moves downstream. The maximum, minimum, and mean values of

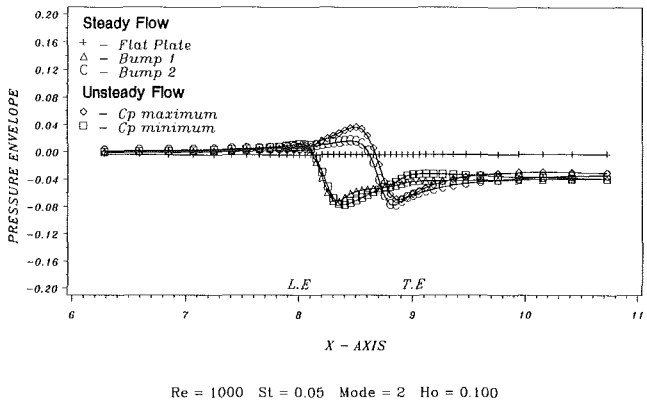

Fig. 11 Variation of pressure coefficient along the vibrating plate for Re = 1000 and St = 0.05. Steady flow results are also shown for comparison.

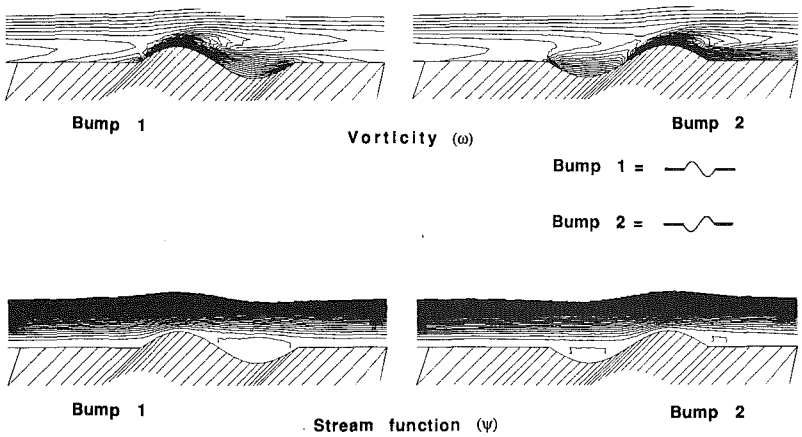

Fig. 12 Contour plot of stream function and vorticity in the vicinity of the fixed sinusoidal bump for Re = 1000

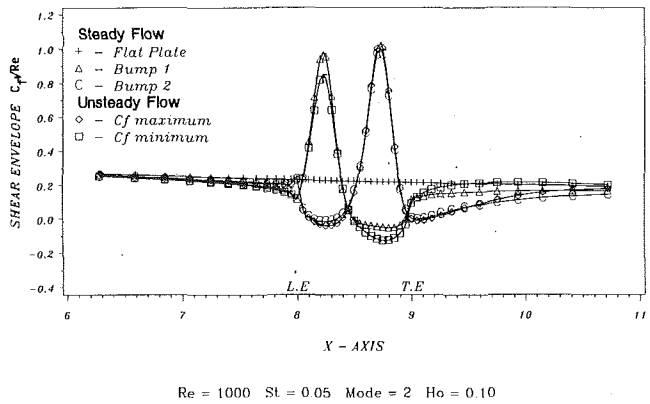

Fig. 13 Variation of friction coefficient along the vibrating plate for Re = 1000 and St = 0.05

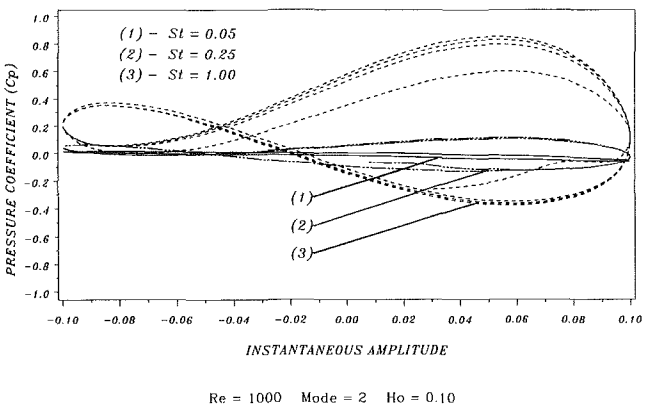

Fig. 14 Variation of pressure coefficient with the instantaneous amplitude of vibration at x = 8.25 and St = 0.05 0.25, and 1.0

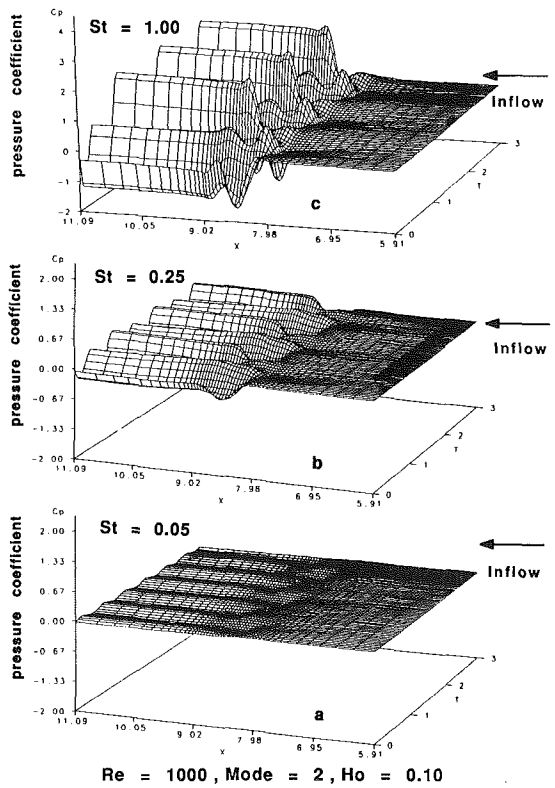

Fig. 15 Variation of pressure coefficient along the vibrating plate as a function of time for Re = 1000 and St = 0.05, 0.25, and 1.0

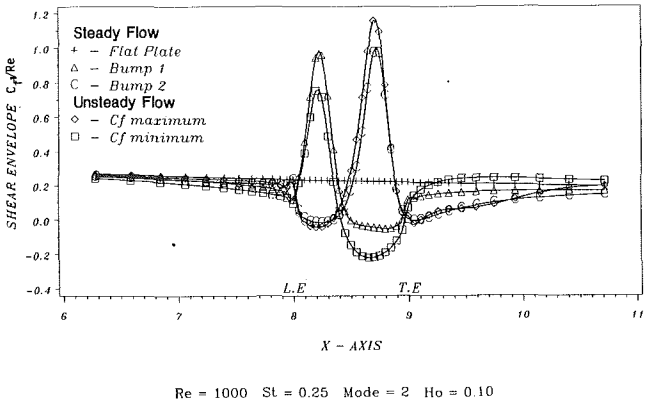

Fig. 16 Variation of friction coefficient along the vibrating plate for Re = 1000 and St = 0.25

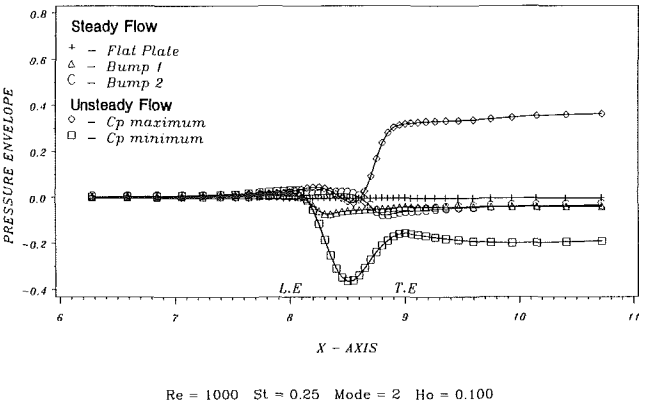

Fig. 17 Variation of pressure coefficient along the vibrating plate for Re = 1000 and St = 0.25

C_p at x = 10.71 (1.71L from T.E.) are shown in Table 2 while similar values for C_f are shown in Table 3. The drastic increase in the pressure envelope can be better described if the stream function contours in the vicinity of the vibrating section are shown as a function of time through a typical vibration cycle. It is shown in Fig. 18. At $t = T$, the vibrating section achieves maximum velocity and zero plate deflection. The fluid on the leading half of the vibrating section moves upwards and penetrates into the external flow. This displaced fluid forms a circulation cell with the downward moving fluid on the later half of the plate as shown in Fig. 18(*a*). This flow pattern creates a pseudo surface displacement in the neighborhood of the vibrating section and ultimately deflects the incoming flow. As the plate moves to the T/8 position, in addition to the plate velocity, the deflection of the plate displaces the fluid upward. This is clearly illustrated in Fig. 18(*b*). Because of this, there is increased interaction between the external flow and the vibrating section. The C_p minimum curve for St = 0.25 occurs at t = 0.12T, just prior to T/8. The flow pattern closely resembles that at $t = T$ and clearly explains the increase in the pressure envelope shown in Fig. 17. As time progresses the velocity of vibration decreases and the deflection of the plate increases. At $t = T/4$ the plate velocity is zero however the deflection is maximum. In this case, the flow has separated from the forward portion of the plate (bump) and a separation bubble is created in the trough section of the vibrating plate (Fig. 18(*c*)). The leading edge of this rearward cavity (unsteady separation location) moves upstream compared to the fixed bump case (compare Fig. 12 to Fig. 18(*d*)). As the plate moves through the second quarter period the cavity disappears and the fluid over the first half of the vibrating section is displaced downward (Fig. 18(*d*) to 18(*f*)). This downward moving fluid on the first half of the plate, in the absence of the external

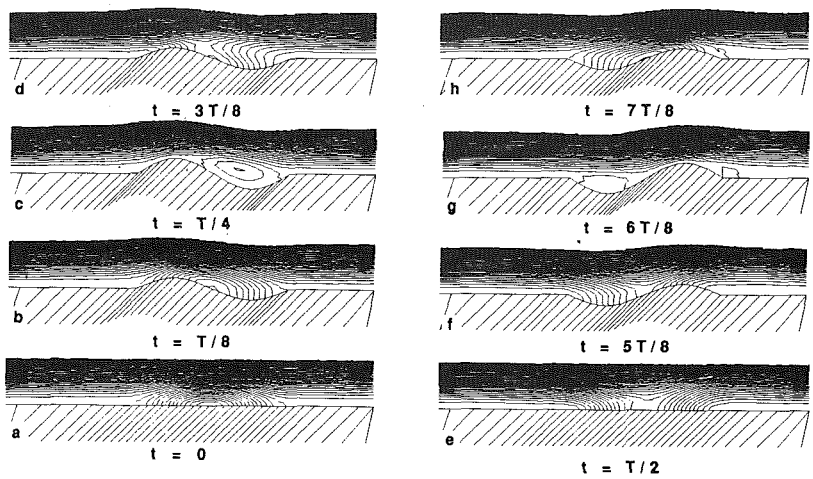

Fig. 18 Contour plot of stream function in the vicinity of the vibrating section of the plate for one complete cycle of vibration at $T/8$ time interval for Re = 1000 and St = 0.25

Table 2 Mean and amplitude of downstream pressure wave at x = 10.71 for various Strouhal numbers. Steady flow results are also included for comparison (x = 10.71, Re = 1000, n = 2, H_0 = 0.10).

CASE	STROUHAL NUMBER St	Cp MAXIMUM	Cp MINIMUM	Cp MEAN	Cp AMPLITUDE
UNSTEADY FLOW	0.05	-0.0307	-0.0308	-0.0351	0.0044
	0.25	0.3615	-0.1916	0.0850	0.2766
	0.50	0.7849	-0.3783	0.2033	0.5816
	0.80	1.3390	-0.7164	0.3112	1.0277
	1.00	1.8468	-0.8418	0.5025	1.3442
	1.20	2.4842	-0.8520	0.8161	1.6681
STEADY FLOW FLAT PLATE	0.00	0.0000	0.0000	0.0000	0.0000
BUMP 1	0.00	-0.0400	-0.0400	-0.0400	0.0000
BUMP 2	0.00	-0.0358	-0.0358	-0.0358	0.0000

x = 10.71 , Re = 1000 , Mode = 2 , Ho = 0.100

Table 3 Maximum and minimum values of C_f envelope for various Strouhal numbers (Re = 1000, n = 2, H_0 = 0.10)

CASE	STROUHAL NUMBER St	Cf MAXIMUM	Cf MINIMUM
UNSTEADY FLOW	0.05	-0.12677	1.00560
	0.25	-0.21946	1.15645
	0.50	-0.52231	1.18334
	0.80	-0.93382	1.32721
	1.00	-1.27209	1.46214
	1.20	-1.71253	1.65324
STEADY FLOW BUMP 1	0.00	-0.05250	0.95785
BUMP 2	0.00	-0.01612	0.97050

Re = 1000 , Mode = 2 , Ho = 0.10

flow, will form a circulation cell similar to Fig. 18(a) with the upward moving fluid on the second half of the vibrating section. In the presence of the external flow, however, the upward moving fluid over the second half of the vibrating section is in fact advected downstream. At the same time the incoming external fluid is drawn into the low pressure region created by the downward moving fluid on the first half of the vibrating section. Because of this, no separation bubble is formed over the first half of the plate. This response is clearly illustrated when the plate reaches its zero deflection and maximum velocity position ($t = T/2$, Fig. 18(e)). When the plate moves to 5T/8 position, the influence of plate velocity slowly decreases and the deflection of the plate draws some external fluid into the first half while fluid is displaced on the second half of the vibrating section (Fig. 18(f)). At $t = 3T/4$ the plate velocity is zero and the plate has reached its maximum amplitude. Two cavities are formed, one in the trough portion and the other at the trailing edge of the vibrating section of the plate (Fig. 18(g)). The sizes of these two cavities are larger than the steady flow results. As the plate moves into the fourth quarter time period, the upward moving fluid on the first half begins to form a circulation cell similar to $t = T$ with the downward moving fluid on the second half (Fig. 18(h)). In this process, the separation bubbles formed at the end of the third quarter time period are eliminated (Fig. 18(g)).

A perspective view of pressure coefficient along the plate versus time for St = 0.25 is shown in Fig. 15(b)). The pressure coefficient over the vibrating section and at the downstream has increased considerably compared to the low Strouhal number (St = 0.05) case. One can also clearly see a high amplitude pressure wave travelling downstream. In addition to the control exerted by the vibration amplitude the velocity of vibration also affects the pressure (Fig. 14). Although there is some upstream influence, it's impact on the pressure coefficient is insignificant.

Time series plots of the pressure coefficient and its corresponding Fast Fourier Transform (FFT; Newland 1975) at x = 6.0, 8.0, 9.0 and 17.0 are shown in Fig. 19 for St = 0.25. At x = 6 (upstream of the vibrating section) there is no variation of pressure with time (Fig. 19(a)). The pressure coefficient at the leading edge of the vibrating section (x = 8.0) however does oscillate with time (Fig. 19(b)). The pressure wave however is nonsinusoidal. The FFT for this pressure wave has a peak amplitude 0.02 at the fundamental frequency and another very small peak at the first harmonic. There are no other harmonics present in the flow. As one moves downstream the amplitude of the pressure wave increases (Fig. 19(b)). Far downstream (x = 17), the spectral amplitude at the fundamental frequency decreases to 0.015 and the second harmonic increases to 0.12 (Fig. 19(b)). Spectral amplitude at higher harmonics are minimal.

The existence and amplitude of the pressure variations at the first harmonic is caused by energy transfer from the input

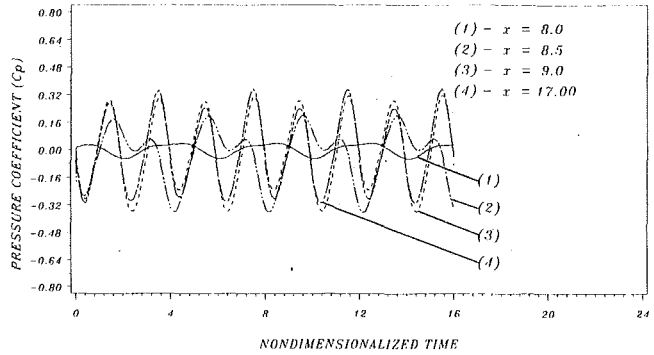

Fig. 19(*a*) Time series plot of pressure coefficient at x = 6.0, 8.0, 9.0, and 17.0 for Re = 1000 and St = 0.25

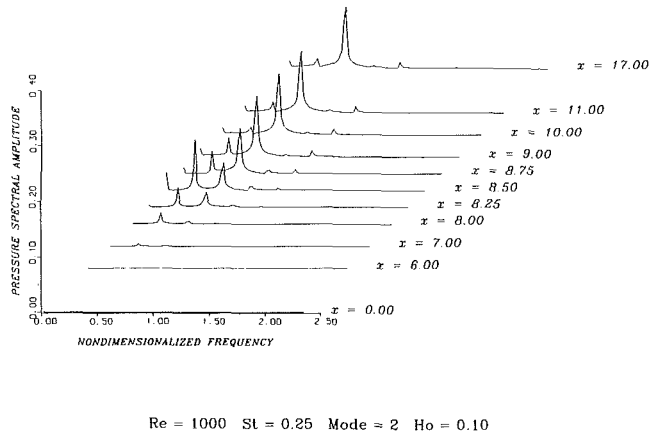

Fig. 19(*b*) Pressure coefficient versus frequency at x = 6.0, 8.0, 9.0, and 17.0 for Re = 1000 and St = 0.25

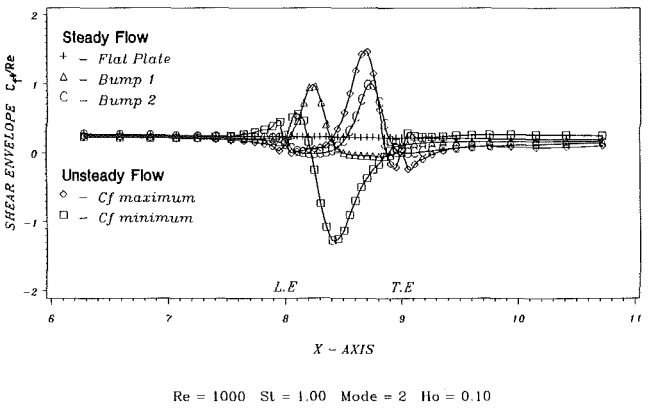

Fig. 20 Variation of friction coefficient along the vibrating plate for Re = 1000 and St = 1.0

frequency to higher harmonics by the nonlinear advective terms $u\ \partial u/\partial x$, $v\ \partial u/\partial y$ in the Navier-Stokes equations. This can be explained by assuming that the plate is vibrating in simple harmonic motion with a known fundamental frequency and amplitude ($a = H_0 \text{ Sin } kx \text{ Sin } 2\pi ft$). For small amplitudes the $\partial u/\partial y$ term approximately follows the shape of the vibrating section with only a small phase shift. This term therefore oscillates at the fundamental frequency. The vertical velocity v also oscillates with the same fundamental frequency but 180 deg out of phase with the amplitude of the vibrating plate ($v = H_0\ 2\pi f \text{ Sin } kx \text{ Cos } 2\pi ft$). The product of these two terms is $A_1 (\text{Sin } kx)^2 \text{ Sin } 2\pi ft \text{ Cos } 2\pi ft$. This can be written as $A_2 (1 - \text{Cos } 2kx) (\text{Sin } 4\pi ft)$ where A_1 and A_2 are known constants. It is seen clearly that when the body vibrates at the known

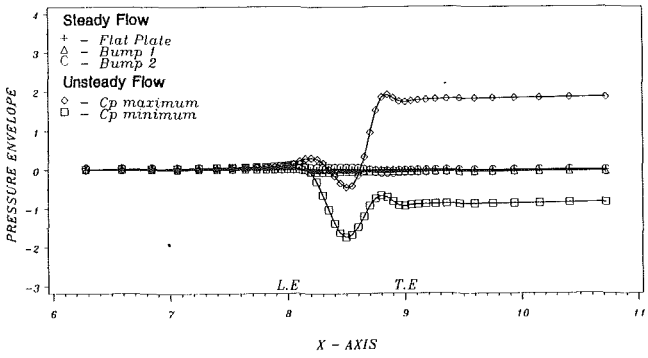

Fig. 21 Variation of pressure coefficient along the vibrating plate for Re = 1000 and St = 1.0

fundamental frequency the nonlinear term $v\ \partial u/\partial y$ transfers energy to the first harmonic.

To investigate the flow for high Strouhal numbers, a value of St equal to 1.0 was selected (high frequency of vibration). For this case the plate oscillation period is the same as the external flow advective time scale. The model predicted shear and pressure envelopes are shown in Figs. 20 and 21, respectively. The shear envelope differs considerably from the steady state results. This is due to the second term in Eq. (5) becoming significant for high Strouhal numbers. Downstream of the vibrating plate the pressure envelope range is considerably higher than for the low and medium Strouhal number cases. This increase in the C_p envelope range is due to increased vertical advection of flow by the vibrating plate. The stream function contour is shown in Fig. 22 for one complete cycle of vibration at every T/8 time intervals, respectively. At $t = T$, the displaced fluid creates a large circulation cell in the neighborhood of the vibrating section, compared to the St = 0.25 case (Fig. 22(*a*)). The vibrating fluid disturbs the external flow considerably both up and downstream. When $t = T/2$ the leading edge of the recirculation cavity moves upstream compared to the St = 0.25 case (Fig. 22(*b*)). As the plate moves to the second quarter period, the flow pattern on the vibrating section deviates from the St = 0.25 case. In addition to the external fluid flowing onto the vibrating section (similar to St = 0.25 case), a small circulation cell is also formed around the mid point of the vibrating plate (Fig. 22(*d*)). This flow pattern is more clearly illustrated when the plate moves into the third quarter period (Figs. 22(*e*) to 22(*f*)). At $t = 3T/4$, two separation bubbles are formed one on the first half and the other near the trailing edge of the vibrating section, similar to the St = 0.25 case (Fig. 22(*g*)). These bubbles however are considerably larger than the St = 0.25 cavities, especially the one at the trailing edge. With subsequent motion of the plate to the fourth quarter time period, the fluid displaced upward on the first half and downward on the second half fills the cavities created at $t = 3T/4$, there by forming a circulation cell as seen at $t = T$. These flow patterns show that the interaction between the external flow and the vibrating plate increases with increasing Strouhal number.

The variation of C_p with the instantaneous amplitude of the vibrating section at x = 8.25 is shown in Fig. 14. This figure clearly shows that the C_p amplitude is considerably large for St = 1.0 compared to low St cases. A perspective view of pressure coefficient versus time and distance along the plate is shown in Fig. 15(*c*) for the St = 1.0 case. The pressure propagates one plate length upstream. The increase in the downstream pressure wave is clearly depicted in Fig. 15(*c*) for high Strouhal frequency.

The time series plot of pressure coefficient for St = 1.0 at x = 6.0, 8.0, 9.0, and 17.0 and their corresponding FFT are

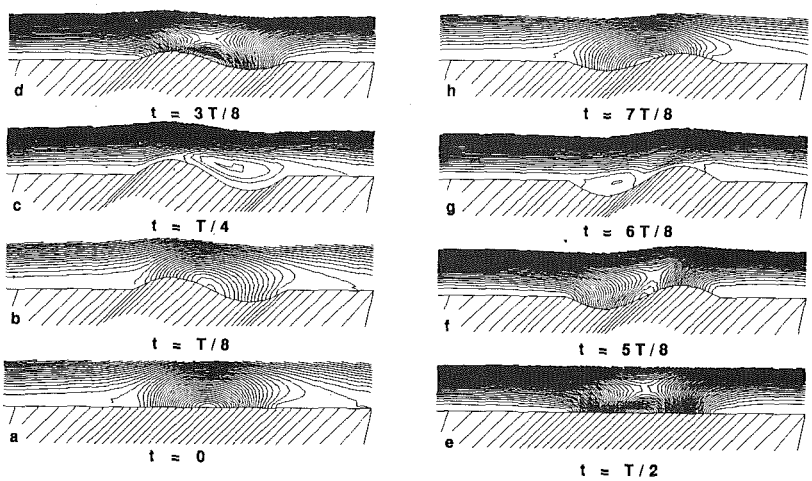

Fig. 22 Contour plot of stream function in the vicinity of the vibrating section of the plate for one complete cycle of vibration at $T/8$ time interval for Re = 1000 and St = 1.0

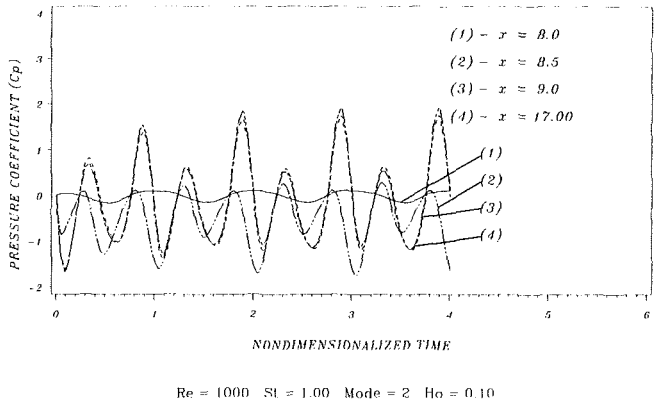

Fig. 23(*a*) Time series plot of pressure coefficient at x = 6.0, 8.0, 9.0, and 17.0 for Re = 1000 and St = 1.0

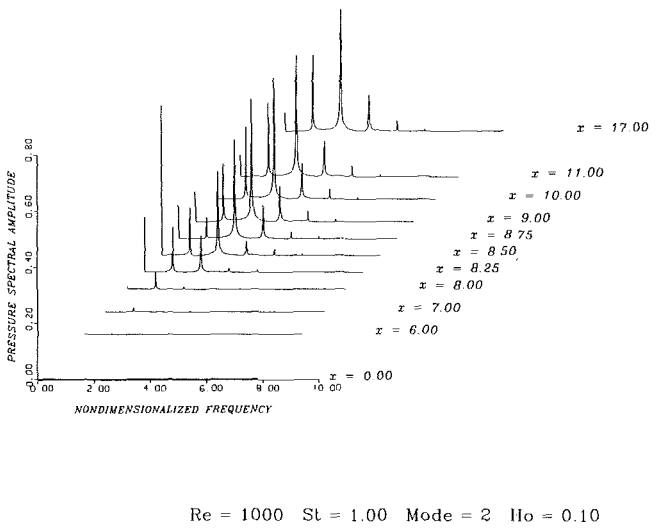

Fig. 23(*b*) Pressure coefficient versus frequency at x = 6.0, 8.0, 9.0, and 17.0 for Re = 1000 and St = 1.0

shown in Fig. 23. As explained previously the pressure wave becomes nonlinear as one moves downstream, through the vibrating section. Far downstream (x = 17.0) the spectral amplitude at the fundamental frequency is 0.26 while the first harmonic has a value of 0.44 (Fig. 23(*b*)). Unlike the low Strouhal case the spectral amplitude at the second harmonic is considerable and its value is half that of the first harmonic. As the fluid flows over the vibrating portion of the plate the spectral amplitude at the first and second harmonics increase continuously due to nonlinear interaction between the oscillating fluid and the external flow in the vicinity of the vibrating section.

6 Conclusion

For very low frequencies, very little energy transfer takes place. The fluid flowing over the vibrating section doesn't sense this low vibrational energy and hence very little nonlinear interaction between the flow and the vibrating body is observed. The pressure varies linearly with the instantaneous amplitude of the vibrating plate.

The pressure and hence the normal force acting on the vibrating flat plate is highly nonlinear and the nonlinearity predominates at higher frequencies (high Strouhal numbers). The nonlinearity in the pressure coefficient is controlled by the $v\ \partial u/\partial y$ term and increases with increasing Strouhal number. For medium and high Strouhal numbers, the incoming flow senses the disturbance created due to the vibration of the body and receives energy at the characteristic vibration frequency. After energy transfer the displaced fluid interacts with the main flow in the neighborhood of the vibrating section due to the nonlinear terms in the governing equations (e.g., $u\ \partial u/\partial x$, $v\ \partial u/\partial y$ etc.). This energy, received at the input frequency, is transferred to higher harmonics. The amplitude of the higher harmonics increase with increasing Strouhal number. The stream function and velocity vector plots clearly show that for high Strouhal numbers more fluid is advected into the mainflow. The displaced fluid penetrates one plate length upstream.

Acknowledgment

This research work was funded by the Office of Naval Research under contract no. 535413.

References

1 Bringen, S. H., and McMillan, O. J., 1980, "Calculation of Two-Dimensional Inlet Flow Fields in a Supersonic Free Stream-Program Documentation and Test Cases," NASA CP-3221.

2 Carter, J. E., and Wornom, S. F., 1975, "Solutions for Incompressible Boundary Layers Including Viscous-Inviscid Interaction, Aerodynamic Analysis Requiring Advanced Computers," NASA SP-347, pp. 125–150.

3 Curle, N., 1955, "The Influence of Solid Boundaries upon Aerodynamic Sound," *Proceedings of the Royal Society of London*, Series A, Vol. 231, pp. 505–514.

4 Ehrlich, W. L., 1981, "The Numerical Solution of a Navier–Stokes Prob-

lem in a Stenoised Tube: A Danger in Boundary Approximations of Implicit Marching Schemes," *Computers and Fluids*, Vol. 6, pp. 247–256.

5 Fasel, H., 1980, "Recent Developments in the Numerical Solution of the Navier–Stokes Equations and Hydrodynamic Stability Problems," Computational Fluid Dynamics, McGraw-Hill, New York, pp. 168–279.

6 Fletcher, C. A. J., 1988, *Computational Fluid Dynamics*, Vol. 1 and 2, Springer-Verlag, New York.

7 Goldstein, M. E., 1974, "Aeroacoustics," NASA SP-346.

8 Halim, Ahmad A. M., 1986, "Development of an Iterative Boundary Layer Type Solver for Axisymmetric Separated Flow," *AIAA Journal*, Vol. 24, No. 8, Aug. pp. 1298–1304.

9 Hurlburt, S., 1978, "A Numerical Model of Fluid-Structure Interaction for Circular Cylinders," M. S. Thesis, Ocean Engineering, University of Rhode Island.

10 Isreli, M., 1970, "A Fast Implicit Numerical Method for Time Dependent Viscous Flows," *Studies in Applied Mathematics*, Vol. 49, pp. 327–349.

11 Lighthill, M. J., 1954, "The Response of Laminar Skin Friction and Heat Transfer to Fluctuations in the Stream Velocity," *Proceedings of Royal Society of London*, Series A, Vol. 224, pp. 1–23.

12 Morris, D.J., 1975, "Solution of the incompressible Driven Cavity Problem by the Alternating-Direction Implicit Method," NASA SP-378, pp. 47–59.

13 Napolitano, M., and Quartapelle, L., 1985, "Block ADI Methods for Steady Natural Convection in Two Dimensions," *Numerical Methods in Heat Transfer*, ed. by R. W. Lewis and K. Morgan, Wiley, Vol. III, pp. 125–148.

14 Napolitano, M., and Walters, R. W., 1986, "An Incremental Block Line Gauss Seidal Method for the Navier–Stokes Equations," *AIAA Journal*, Vol. 24, No. 5, pp. 770–776.

15 Newland, D. E., *An Introduction to Random Vibrations and Spectral Analysis*, Longman Group Ltd., 1975.

16 Roache, P. J., 1972, *Computational Fluid Dynamics*, Hermosa Publishing, Albuquerque, N.M.

17 Sobey, Ian J., 1982, "Oscillatory Flows at Intermediate Strouhal Number in Asymmetric Channels," *Journal of Fluid Mechanics*, Vol. 125, pp. 359–373.

18 Peyret, P., and Taylor, T. D., 1983, *Computational Methods for Fluid Flow*, Springer-Verlag, New York.

19 Telionis, D. P., 1981, "Unsteady Viscous Flows," *Springer Series in Computational Physics*, Springer-Verlag, New York.

20 Thames, F. C, 1975, "Numerical Solution of the Incompressible Navier–Stokes Equations About Arbitrary Two-dimensional Bodies," Ph.D. Thesis, Mississippi State University, Mississippi State, Miss.

21 Thompson, J. F., 1982, *Numerical Grid Generation*, North-Holland.

22 Vemuri, V., and Karplus, Walter J., 1981, *Digital Computer Treatment of Partial Differential Equations*, Prentice-Hall.

23 Venkat, N. K., 1987, "Numerical Simulation of Nonlinear Free Surface Flows Generated by Moving Bodies of Arbitrary Cross Sectional Shape," M. S. thesis, Ocean Engineering, University of Rhode Island, Kingston, R.I.

24 Venkat, N. K., 1991, "Numerical Simulation of Planar and Axisymmetric Unsteady Flows Over Vibrating Bodies," Ph.D dissertation, Manuscript # 1, pp. 1–36, Department of Ocean Engineering, University of Rhode Island, Kingston, R.I.

25 Wang, X. M., 1986, "A Two Dimensional Nonlinear Hydrodynamic Model of the Wave Field Generated by a Heaving Body," M.S. Thesis, Ocean Engineering, University of Rhode Island, Kingston, R.I.

26 White, F. M., 1991, *Viscous Fluid Flow*, McGraw-Hill.

Numerical Analysis of Laminar Flow in Curved Elliptic Ducts

Z. F. Dong

M. A. Ebadian
Mem. ASME

Department of Mechanical Engineering,
Florida International University,
Miami, Florida 33199

The complete form of the Navier-Stokes equations is solved in this paper for a steady, incompressible, fully developed laminar flow in a curved duct of elliptic cross section. This is achieved by the use of the control volume-based finite difference method via the numerically generated boundary fitted coordinate system. The curvature ratio is included in the primitive variable governing equations, which are solved based on the SIMPLE algorithm. Solutions are obtained for the minor-axis to major-axis ratios of the elliptic duct, 0.2, 0.5, and 0.8, and for Dean numbers ranging from 11.41 to 635.7. It is found that only one pair of vortices appears on the cross-section, even at a Dean number of 635.7. The friction factor and the ratios of the curved duct to straight duct are tabulated and the correlation equation is developed. Furthermore, the distribution of the axial velocity is displayed graphically to illustrate its variations with the Dean number and the minor-axis to major-axis ratio of the elliptic duct on the horizontal symmetry line and on the half-vertical symmetry line. The present method is also applied to solve for a fully developed laminar flow in a curved square flow. The results are compared with the data available in the literature and very close agreement is observed.

Introduction

Flow through curved passages occurs in heat exchangers, turbo machinery blade passages, and aircraft intakes. Recently, the flow of blood through human arteries is also being modeled as flow through curved passages. The salient feature of flow in curved ducts is the presence of cross-stream recirculation in the twin counter-rotating vortices. These are generated due to the action of centrifugal forces on the primary flow. For the flow and heat transfer in a curved pipe, some review articles have been published by Berger et al. (1983) and Shah et al. (1987). Primarily, these investigations are mainly restricted to curved ducts with circular and rectangular cross sections. However, the scant information dealing with elliptic cross sections is obtained from these investigations.

For flows through curved pipes of elliptical cross section, very few theoretical and experimental investigations are available. The relevant studies are by Thomas and Walters (1965), Srivastava (1980), and Takami and Sudou (1984). In these analyses, the secondary flow is investigated by using Dean's (1927, 1928) formulation in which either the simplified forms of momentum and continuity equations have been used, or by using the boundary layer approximation approach. Recently, Topakoglu and Ebadian (1985, 1987) investigated the flow in curved elliptic pipes using the double expansion method of Topakoglu (1967). Some explicit expressions have been presented for flow rate. However, their results are limited by the finite number of calculated terms of the expansions. To the authors' best knowledge solutions for a laminar, fully developed flow in curved elliptic ducts based on a complete Navier-Stokes equation have not been reported in the literature to data. Therefore, it is necessary to obtain a numerical solution of the Navier-Stokes equations, which governs the steady, fully developed laminar flow in a curved elliptic duct, including the curvature ratio effect. An accurate numerical solution for the flow problem is a fundamental step toward studying convective heat and mass transfer.

The objective of this work is to present numerical results for flow in a curved duct of elliptic cross-section. Additionally, the flow is considered to be steady, incompressible laminar flow and is also assumed to be fully developed. The solutions are obtained by solving the Navier-Stokes equations in which the curvature ratio is included. The numerically generated boundary-fitted coordinate system is used to overcome the difficulties of discretizing the computational domain, and in addition, a general computer program is developed. Three minor-axis to major-axis ratios of the elliptic duct are calculated and the Dean number is varied up to 635.7. The secondary stream function contour and axial velocity distribution are numerically calculated and illustrated graphically. Furthermore, a correlation for the friction factor ratio of the curved elliptic duct to straight elliptic duct is also established for engineering applications.

Problem Formulation

The curved pipe geometry is shown in Fig. 1 where the toroidal coordinate system is used. The elliptical cross-section considered here has a semi-major axis, a, and a semi-minor axis, b. In addition, the section is oriented in such a way that the major axis is along the direction of the curvature of the curved pipe, and the minor axis is along the direction of the axis of symmetry of the curved pipe. The governing equations

Contributed by the Fluids Engineering Division for publication in the JOURNAL OF FLUIDS ENGINEERING. Manuscript received by the Fluids Engineering Division June 7, 1990.

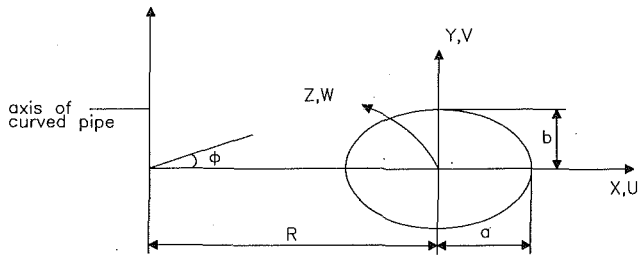

Fig. 1 Geometry and coordinate system

for the steady, fully developed, incompressible laminar flow can be written as:

Continuity Equation:

$$\frac{\partial U}{\partial X}+\frac{\partial V}{\partial Y}+\frac{U}{R+X}=0 \tag{1}$$

Momentum Equation:

$$U\frac{\partial U}{\partial X}+V\frac{\partial U}{\partial Y}-\frac{W^2}{R+X}=-\frac{1}{\rho}\frac{\partial P}{\partial X}+\nu\left[\frac{\partial^2 U}{\partial X^2}+\frac{\partial^2 U}{\partial Y^2}+\frac{1}{R+X}\frac{\partial U}{\partial X}-\frac{U}{(R+X)^2}\right] \tag{2}$$

$$U\frac{\partial V}{\partial X}+V\frac{\partial V}{\partial Y}=-\frac{1}{\rho}\frac{\partial P}{\partial Y}+\nu\left[\frac{\partial^2 V}{\partial X^2}+\frac{\partial^2 V}{\partial Y^2}+\frac{1}{R+X}\frac{\partial V}{\partial X}\right] \tag{3}$$

$$U\frac{\partial W}{\partial X}+V\frac{\partial W}{\partial Y}+\frac{UW}{R+X}=-\frac{R}{(R+X)\rho}\frac{\partial P}{\partial Z}+\nu\left[\frac{\partial^2 W}{\partial X^2}+\frac{\partial^2 W}{\partial Y^2}+\frac{1}{R+X}\frac{\partial W}{\partial X}-\frac{W}{(R+X)^2}\right] \tag{4}$$

Because of the symmetry of the flow, a half of a cross section of an elliptic duct is chosen as the solution domain. Therefore, the associated boundary conditions are:

$$U=V=W=0 \quad \text{at the wall} \tag{5}$$

$$V=\frac{\partial U}{\partial Y}=\frac{\partial W}{\partial Y}=0 \quad \text{along the line of symmetry, } Y=0 \tag{6}$$

where U, V, and W are the velocity components of the X, Y, and Z directions, respectively, as shown in Fig. 1. Also, P, ν, ρ, and R are pressure, dynamic viscosity, density of fluid, and the radius of the curvature, respectively. In the fully developed flow, the pressure gradient varies only in the cross-section of the curved duct. Therefore, the pressure gradient in the axial direction, $\partial P/\partial Z$, in Eq. (4) remains constant.

Introducing the dimensionless variables defined in the Nomenclature, one obtains the following governing equations:

$$\frac{\partial u}{\partial x}+\frac{\partial v}{\partial y}+\frac{u}{r+x}=0 \tag{7}$$

$$\frac{\partial(uu)}{\partial x}+\frac{\partial(uv)}{\partial y}-\frac{w^2}{r+x}=-\frac{\partial p}{\partial x}+\frac{\partial^2 u}{\partial x^2}+\frac{\partial^2 u}{\partial y^2}+\frac{1}{r+x}\frac{\partial u}{\partial x}-\frac{u}{(r+x)^2}-\frac{u^2}{r+x} \tag{8}$$

$$\frac{\partial(uv)}{\partial x}+\frac{\partial(vv)}{\partial y}=-\frac{\partial p}{\partial y}+\frac{\partial^2 v}{\partial x^2}+\frac{\partial^2 v}{\partial y^2}+\frac{1}{r+x}\frac{\partial v}{\partial x}-\frac{uv}{r+x} \tag{9}$$

$$\frac{\partial(uw)}{\partial x}+\frac{\partial(vw)}{\partial y}+\frac{uw}{r+x}=-\frac{r}{r+x}\frac{dp}{dz}+\frac{\partial^2 w}{\partial x^2}+\frac{\partial^2 w}{\partial y^2}+\frac{1}{r+x}\frac{\partial w}{\partial x}-\frac{w}{(r+x)^2}-\frac{uw}{r+x} \tag{10}$$

The boundary conditions are restated as follows:

$$u=v=w=0 \quad \text{at the wall} \tag{11}$$

$$v=\frac{\partial u}{\partial y}=\frac{\partial w}{\partial y}=0 \quad \text{at } y=0 \tag{12}$$

At this point, a numerical solution is the only approach for solving the above three simultaneous quasi-linear, second-order partial differential equations. The expression for the product of the friction factor and the Reynolds number can be obtained by considering the overall force balance for the

Nomenclature

a = semi-major axis of the curved elliptic duct
b = semi-minor axis of the curved elliptic duct
De = Dean number, $\mathrm{Re}(D_h/R)^{1/2}$
D_h = hydraulic diameter
f = friction factor
J = Jacobian of transformation, Eq. (26)
P = pressure, Pa
p = dimensionless pressure, $P/(\rho\nu^2/D_h^2)$
R = radius of the curvature of the centerline of the duct, Fig. 1
Re = Reynolds number, $D_h\,\overline{W}/\nu=\overline{w}$
r = dimensionless radius of curvature, R/D_h
U, V, W = velocity components in the X, Y, and Z directions
u, v, w = dimensionless velocity components $(U, V, W)/(\nu/D_h)$
$\overline{W}$ = average axial velocity
$\overline{w}$ = dimensionless average axial velocity
$\overline{U}$ = contravariant velocity defined by Eq. (26)
$\overline{V}$ = contravariant velocity defined by Eq. (26)
X, Y = transversal coordinates, Fig. 1 and Fig. 2(*a*)
x, y = dimensionless transversal coordinates $(X, Y)/D_h$
Z = axial coordinate, Fig. 1
z = dimensionless axial coordinate, Z/D_h
α = coefficient defined by Eq. (19), minor-axis to major-axis ratio of elliptic duct, $2b/2a$
β = coefficient defined by Eq. (20)
γ = coefficient defined by Eq. (21)
ν = kinematic viscosity
ξ, η = transversal coordinates in computational plane, Fig. (2*b*)
ϕ = coefficient defined in Eq. (22)
ξ_Q = rate of flow defined by Eq. (15)
ρ = density
ψ = coefficient defined by Eq. (23)

Subscripts

c, s = values for curved and straight ducts, respectively
i, j = space subscripts of a grid point
w = wall

differential axial length as given by Cheng et al. (1976):

$$f\mathrm{Re} = -\left(\frac{dp}{dz}\right)\Big/(2\overline{w}). \tag{13}$$

Another parameter involved here is the ratio of the flow rate in the duct. This ratio can be defined in terms of the fRe as:

$$\frac{Q_c}{Q_s} = \frac{(f\mathrm{Re})_s}{(f\mathrm{Re})_c}, \tag{14}$$

where in the above equation, subscripts, "s" and "c," refer to the straight and curved ducts, respectively. Furthermore, this equation can be written as:

$$\xi_Q = 1 - \frac{Q_c}{Q_s} = 1 - \frac{(f\mathrm{Re})_s}{(f\mathrm{Re})_c}, \tag{15}$$

where $(f\mathrm{Re})_s$ is calculated by the equation (Kakac et al., 1987):

$$(f\mathrm{Re})_s = 2(1+\alpha^2)\left(\frac{\pi}{E(m)}\right)^2. \tag{16}$$

In the above equations, $m = 1-\alpha^2$ and $E(m)$ is the complete elliptic integrals of the second kind.

Solution Procedure

Grid Generation. For purposes of the symmetrical flow field, a half domain is considered as the computational domain for this problem. Generally speaking, the discretization of this computational domain is tedious and difficult for the development of a general computer program. Fortunately, this difficulty can be resolved by the use of the numerically generated boundary-fitted coordinate system. The essential idea of a boundary-fitted coordinate system is such that it requires a computational domain boundary to coincide with the coordinate line. One of the methods often used was suggested by Thompson et al. (1974). The grid point distribution is controlled according to the method suggested by Thomas et al. (1982). Therefore, the domain transformation between the physical coordinates (x, y) and the boundary-fitted coordinates (ξ, η) is achieved by solving the following two coupled equations:

$$\alpha\left(\frac{\partial^2 x}{\partial \xi^2} + \phi\frac{\partial x}{\partial \xi}\right) - 2\beta\frac{\partial^2 x}{\partial \xi \partial \eta} + \gamma\left(\frac{\partial^2 x}{\partial \eta^2} + \psi\frac{\partial x}{\partial \eta}\right) = 0 \tag{17}$$

$$\alpha\left(\frac{\partial^2 y}{\partial \xi^2} + \phi\frac{\partial y}{\partial \xi}\right) - 2\beta\frac{\partial^2 y}{\partial \xi \partial \eta} + \gamma\left(\frac{\partial^2 y}{\partial \eta^2} + \psi\frac{\partial y}{\partial \eta}\right) = 0 \tag{18}$$

where

$$\alpha = \left(\frac{\partial x}{\partial \eta}\right)^2 + \left(\frac{\partial y}{\partial \eta}\right)^2, \tag{19}$$

$$\beta = \frac{\partial x}{\partial \xi}\frac{\partial x}{\partial \eta} + \frac{\partial y}{\partial \xi}\frac{\partial y}{\partial \eta}, \tag{20}$$

$$\gamma = \left(\frac{\partial x}{\partial \xi}\right)^2 + \left(\frac{\partial y}{\partial \xi}\right)^2. \tag{21}$$

On the left and right boundaries of the domain in the computational plane:

$$\psi = -\left(\frac{\partial^2 y}{\partial \eta^2}\frac{\partial y}{\partial \eta} + \frac{\partial^2 x}{\partial \eta^2}\frac{\partial x}{\partial \eta}\right)\Big/\left(\left(\frac{\partial x}{\partial \eta}\right)^2 + \left(\frac{\partial y}{\partial \eta}\right)^2\right) \tag{22}$$

On the top and bottom boundaries of the domain in the computational plane:

$$\phi = -\left(\frac{\partial^2 x}{\partial \xi^2}\frac{\partial x}{\partial \xi} + \frac{\partial^2 y}{\partial \xi^2}\frac{\partial y}{\partial \xi}\right)\Big/\left(\left(\frac{\partial x}{\partial \xi}\right)^2 + \left(\frac{\partial y}{\partial \xi}\right)^2\right) \tag{23}$$

The ϕ and ψ values on the internal grid points are determined by linear interpolation from the boundary values. The resulting grid construction in the physical plane and in the computational plane is shown in Figs. 2(*a*) and 2(*b*), respectively.

Transformation of Governing Equations and Method of Solution. The dimensionless governing Eqs. (7) through (10), can be written in terms of the following general conservation form:

$$\frac{\partial(u\phi)}{\partial x} + \frac{\partial(v\phi)}{\partial y} = \frac{\partial}{\partial x}\left(\Gamma_\phi\frac{\partial \phi}{\partial x}\right) + \frac{\partial}{\partial y}\left(\Gamma_\phi\frac{\partial \phi}{\partial y}\right) + R_\phi(x, y) \tag{24}$$

For the general dependent variable, $\phi = 1, u, v, w$, Eq. (24) refers to continuity and momentum equations in the x, y, and z directions, respectively. Γ_ϕ and $R_\phi(x, y)$ are correspondingly diffusivity coefficients and source terms. After some mathematical transformation, this equation is written as:

$$\frac{\partial}{\partial \xi}(\overline{U}\phi) + \frac{\partial}{\partial \eta}(\overline{V}\phi) = \frac{\partial}{\partial \xi}\left[\frac{\Gamma_\phi}{J}\left(\alpha\frac{\partial \phi}{\partial \xi} - \beta\frac{\partial \phi}{\partial \eta}\right)\right] + \frac{\partial}{\partial \eta}\left[\frac{\Gamma_\phi}{J}\left(-\beta\frac{\partial \phi}{\partial \xi} + \gamma\frac{\partial \phi}{\partial \eta}\right)\right] + JS_\phi(\xi, \eta) \tag{25}$$

where

$$\overline{U} = u\frac{\partial y}{\partial \eta} - v\frac{\partial x}{\partial \eta}$$

$$\overline{V} = v\frac{\partial x}{\partial \xi} - u\frac{\partial y}{\partial \xi}$$

$$J = \frac{\partial x}{\partial \xi}\frac{\partial y}{\partial \eta} - \frac{\partial x}{\partial \eta}\frac{\partial y}{\partial \xi} \tag{26}$$

The general dependent variable, ϕ, the diffusion coefficient, Γ_ϕ, and the source term, S_ϕ, in the ξ, η coordinate system, are defined in Table 1 for each conservative equation.

The governing Eq. (25) is approximated with finite difference equations by a control volume-based finite difference method for the dependent variables u, v, and w. The convection terms are discretized by a power-law scheme (Patankar, 1980) which is an approximation of the exponential scheme and a second-

Table 1 Variables in the conservation equations

Equation	ϕ	Γ_ϕ	S_ϕ
Continuity	1	0	$-\dfrac{u}{r+x}$
u-momentum	u	1	$-\dfrac{1}{J}\left(\dfrac{\partial p}{\partial \xi}\dfrac{\partial y}{\partial \eta} - \dfrac{\partial p}{\partial \eta}\dfrac{\partial y}{\partial \xi}\right)$ $+\dfrac{1}{r+x}\dfrac{1}{J}\left(\dfrac{\partial u}{\partial \xi}\dfrac{\partial y}{\partial \eta} - \dfrac{\partial u}{\partial \eta}\dfrac{\partial y}{\partial \xi}\right)$ $-\dfrac{u}{(r+x)^2} + \dfrac{w^2}{r+x} - \dfrac{u^2}{r+x}$
v-momentum	v	1	$-\dfrac{1}{J}\left(-\dfrac{\partial p}{\partial \xi}\dfrac{\partial x}{\partial \eta} + \dfrac{\partial p}{\partial \eta}\dfrac{\partial x}{\partial \xi}\right)$ $+\dfrac{1}{r+x}\dfrac{1}{J}\left(\dfrac{\partial v}{\partial \xi}\dfrac{\partial y}{\partial \eta} - \dfrac{\partial v}{\partial \eta}\dfrac{\partial y}{\partial \xi}\right)$ $-\dfrac{uv}{(r+x)}$
w-momentum	w	1	$-\dfrac{r}{r+x}\dfrac{\partial p}{\partial z}$ $+\dfrac{1}{r+x}\dfrac{1}{J}\left(\dfrac{\partial w}{\partial \xi}\dfrac{\partial y}{\partial \eta} - \dfrac{\partial w}{\partial \eta}\dfrac{\partial y}{\partial \xi}\right)$ $-\dfrac{w}{(r+x)^2} - \dfrac{2uw}{r+x}$

order central-difference formula is used to approximate the diffusion terms. A staggered grid system is employed for the transverse velocity components, u and v, as well as contravariant velocities, $\overline{U}$ and $\overline{V}$. Here, a combined use of the Cartesian velocity components and the contravariant velocity components is devised. In the momentum equation, the Cartesian components are treated as the primary variables, while in the continuity equation, the contravariant velocity components are first updated directly to satisfy the continuity equation. In the discretizing process, the cross-derivative terms, $\partial^2/\partial\xi\partial\eta$ are treated as additional source terms and the standard second-order central-difference approximation is also applied to the computation of α, β, γ, and J. The solutions are obtained by an iterative scheme, which is a modified SIMPLE algorithm in a boundary-fitted coordinate system (Shyy et al., 1985). A brief description of the main steps of this numerical procedure is given here for convenience.

For a given ratio, α, of the minor-axis to major-axis of the curved elliptic duct, curvature ratio, r, and the axial pressure gradient, dp/dz, the velocity contributions (u, v, and w) and pressure distribution p_A, are initially guessed and the momentum equations for u and v are then solved to get new velocity fields for u and v. Generally, these transverse velocity fields with the initial guessed pressure field, cannot satisfy the continuity equation. Thus, the pressure correction equation is solved and then u, v, and p are corrected accordingly. Furthermore, $\overline{U}$ and $\overline{V}$ are updated and the momentum equation for w is solved based on the corrected transversal velocity and pressure fields. Thus, one iteration cycle is completed. The iteration is repeated until the following convergence criterion is satisfied for all nodes:

$$\frac{\|\phi_{ij}^{k+1} - \phi_{ij}^{k}\|_\infty}{\|\phi_{ij}^{k+1}\|_\infty} \le 10^{-5}, \tag{27}$$

where ϕ stands for u, v, and w. Subscripts, i and j, represent the ξ and η coordinates, and superscript, k, represents the kth iteration. $\|\bullet\|_\infty$ is the infinite norm.

It is necessary to use an underrelaxation factor in solving the transversal momentum equations and pressure correction equation in order to make the solution converge. A relaxation factor ranging from 0.15 to 0.3 has been used for different computation cases.

In order to consider the effects of grid size, four grids of 20×10, 30×15, 40×20, and 50×30 have been tested to choose an independent grid. The results of comparing the finer 50×30 grid with the coarser 30×15 grid indicates a maximum discrepancy of less than 4 percent, and the maximum deviation occurs in the case of a small curvature ratio. The results of comparing 40×20 grid and the 30×15 grid show a maximum discrepancy of less than 3.5 percent. The computation time needed for the 30×15 grid is several times less than the one needed for the finer grids of 40×20 or 50×30. Depending on the different cases being considered, and from the viewpoint of compromising computational time and numerical accuracy, the 30×15 grid is used in the calculation. In addition, this present method is also applied to numerically analyze the flow in a curved square duct. The results are compared with Cheng et al. (1976) and Duh et al. (1989) and they are documented in Table 2. It is seen from this table that the maximum deviation between present results and the results of Cheng et al. (1976) is 2.45 percent with the same grid size of 20×10. However, the higher deviation exists between the present conclusions and the results of Duh et al. (1989). Perhaps this is due mainly to the different convergence criteria used in each study. Furthermore, all of the computations have been conducted on a MicroVax 8800.

Discussion of Results

Secondary Flow. Laminar flow in the curved elliptic duct is characterized by a secondary flow in the cross sectional plane perpendicular to the axial flow direction. The nature of this phenomenon depends upon the Dean number, which represents the ratio of the centrifugal force to the viscous force. The geometry is another factor effecting the secondary flow. The effects of the Dean number, De, and geometry parameter, α, on the secondary flow pattern in the form of stream function

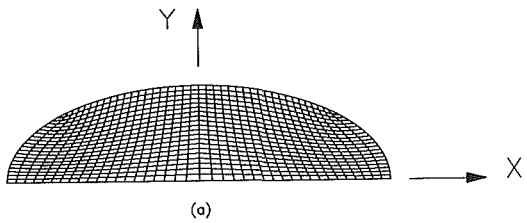

(a)

Fig. 2(*a*) Physical domain

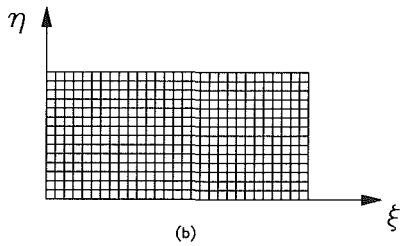

(b)

Fig. 2(*b*) Computational domain

Fig. 2 Grid configuration

Table 2 Comparison of numerical results for the curved square duct

$\frac{\partial P}{\partial z}$	r	Grid	De			f_c/f_s		
			Cheng et al. (1976)	Present Study	Duh et al. (1989)	Cheng et al. (1976)	Present Study	Duh et al. (1989)
-4×10^3	100	20×10	13.9	14.1	13.9	1.01	1.0	1.01
-4×10^4	100	20×10	100.0	99.1	—	1.41	1.42	—
-1.1×10^5	100	20×10	202.6	201.4	218.5	1.91	1.92	1.78
-8×10^4	10	20×10	368.1	358.4	—	2.42	2.48	—
-8×10^4	10	40×20	364.3	376.6	—	2.44	2.36	—
-2.5×10^4	4.0	20×10	214.8	211.5	233.4	2.04	2.08	1.89
-8.0×10^4	4.0	20×10	488.4	480.9	—	2.88	2.92	—
-9.0×10^4	4.0	20×10	520.2	523.7	—	3.04	3.02	—
-1.1×10^5	4.0	20×10	618.8	606.5	—	3.12	3.19	—
-1.4×10^5	4.0	20×10	715.4	726.4	—	3.43	3.39	—

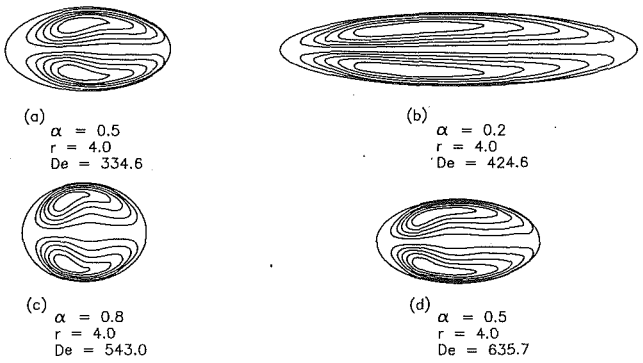

Fig. 3 (*a*) Stream-function contours for elliptic duct, $\alpha = 0.5$, De = 334.6; (*b*) Stream-function contours for elliptic duct, $\alpha = 0.2$, De = 424.6; (*c*) Stream-function contours for elliptic duct, $\alpha = 0.8$, De = 543.0; (*d*) Stream-function contours for elliptic duct, $\alpha = 0.5$, De = 635.7

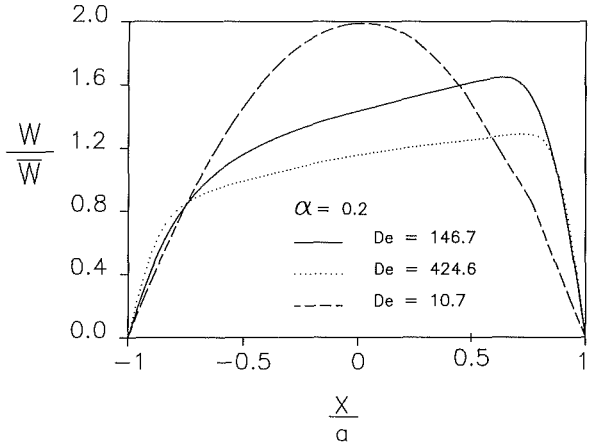

Fig. 4(*a*) Horizontal symmetry line

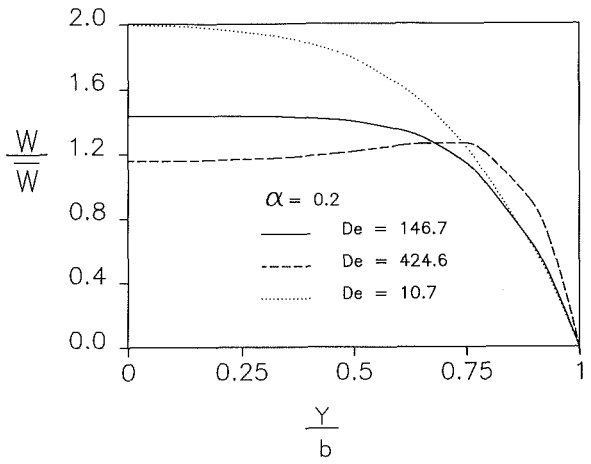

Fig. 4(*b*) Vertical symmetry line

Fig. 4 Axial velocity distribution for elliptic duct, $\alpha = 0.2$

contour, are shown in Fig. 3 for the fully developed flow in a curved elliptic duct.

It is observed from comparing Figs. 3(*a*) through 3(*d*) that only one pair of vortices occurs in the elliptic cross section in spite of the Dean number varying from 334.6 to 635.7. Furthermore, it is found that the location of the vortex center shifts as the Dean number varies. Due to centrifugal instability (Daskopoulos et al., 1989; Cheng et al., 1976; Mille et al.,

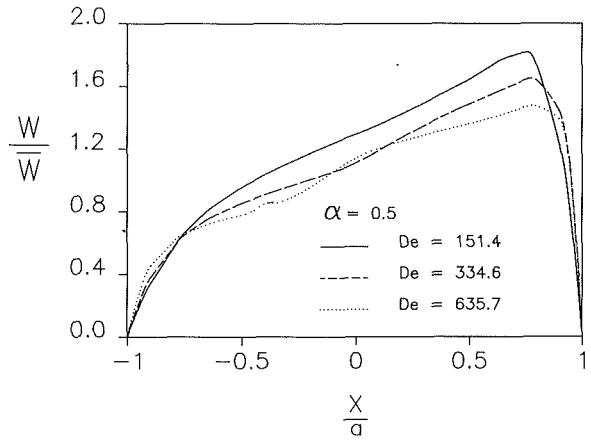

Fig. 5(*a*) Horizontal symmetry line

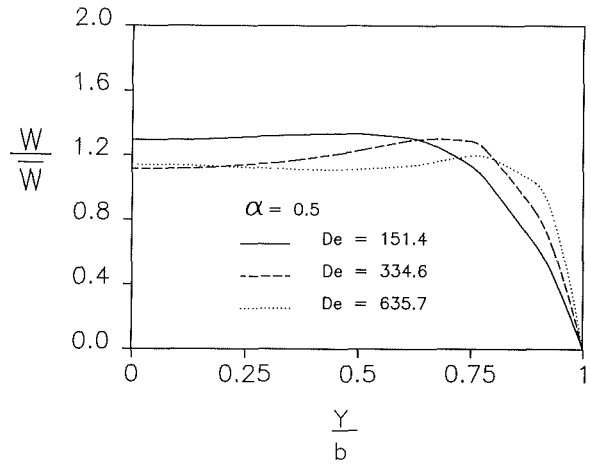

Fig. 5(*b*) Vertical symmetry line

Fig. 5 Axial velocity distribution for elliptic duct, $\alpha = 0.5$

1985; and Ghia et al., 1987), the secondary vortex takes place near the central outer wall in the curved rectangular duct and circular pipe. Whereas, the flow in the curved elliptic duct remains stable in the range of this computation.

Axial Velocity Distributions. The axial velocity profiles along the horizontal and vertical centerlines are shown in Figs. 4-6 for the minor-axis to major-axis ratios of $\alpha = 0.2$, 0.5, and 0.8 with the Dean number as a parameter. The effect of the Dean number on the axial velocity profiles is seen to be rather regular, indicating a stable flow field. The behavior of the axial velocity profile is qualitatively similar to each other, indicating that axial velocity is independent of α. The location of the maximum axial velocity on the horizontal symmetry line moves progressively toward the outer wall and its magnitude decreases as the Dean number increases (Figs. 4(*a*), 5(*a*), and 6(*a*)). For the velocity distribution on the vertical symmetry line, the maximum velocity occurs on the center point and the velocity is decreased monotonously along the positive vertical when the Dean number decreases. However, the maximum value of the axial velocity appears near the outer wall for a larger Dean number (Figs. 4(*b*), 5(*b*), 6(*b*)). From these three figures, it is also seen that the axial velocity distribution, regardless of whether it is on the horizontal or the vertical symmetry line, tends to be full as the Dean number increases.

The Friction Factor. The fully developed laminar flow in a curved duct of elliptic cross section is computed by a nu-

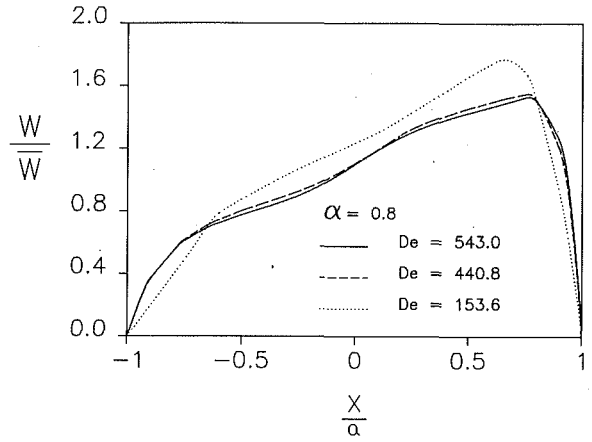

Fig. 6(*a*) Horizontal symmetry line

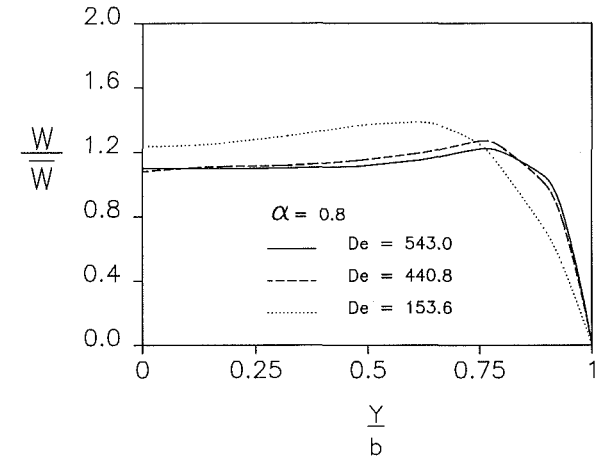

Fig. 6(*b*) Vertical symmetry line

Fig. 6 Axial velocity distribution for elliptic duct, $\alpha = 0.8$

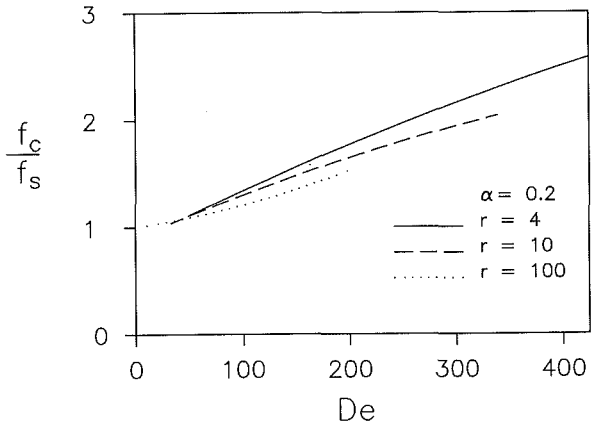

Fig. 7 Friction factor ratio versus Dean number for $\alpha = 0.2$

merical method considering the curvature ratio effect in the governing equations. Three minor-axis to major-axis elliptic duct ratios are taken into account. The numerical results for the friction factor and rate of flow are tabulated and given in Tables 3 through 5 for different axial pressure gradients, curvature ratios, and minor-axis to major-axis ratios of the elliptic duct. The data shown in these tables are also used to draw the curves in Figs. 7 through 12. The ratios of the friction factor for the curved elliptic duct, f_c, to the straight elliptic duct, f_s,

Table 3 Numerical results for friction factor, $\alpha = 0.2$

$\frac{\partial p}{\partial z}$	r	Re	De	f_c/f_s	ξ_Q	fRe
-8×10^4	4	849.2	424.6	2.58	0.612	47.11
-4×10^3	4	98.6	49.3	1.11	0.098	20.28
-2.5×10^4	4	390.7	195.4	1.75	0.428	31.99
-4×10^3	10	105.2	33.3	1.04	0.038	19.02
-2.5×10^4	10	463.8	146.7	1.47	0.321	26.95
-8×10^4	10	1074.3	339.7	2.04	0.509	37.23
-4×10^3	100	107.4	10.7	1.02	0.018	18.62
-8×10^4	100	1581.1	158.1	1.38	0.277	25.30
-1.1×10^5	100	1977.6	197.8	1.52	0.342	27.81

Table 4 Numerical results for friction factor, $\alpha = 0.5$

$\frac{\partial p}{\partial z}$	r	Re	De	f_c/f_s	ξ_Q	fRe
-4×10^3	4	98.7	49.4	1.20	0.170	20.26
-8×10^3	4	169.7	84.7	1.40	0.288	23.61
-8×10^4	4	867.7	433.8	2.74	0.635	46.10
-1.4×10^5	4	1271.3	635.7	3.27	0.695	55.06
-4×10^3	10	108.8	34.4	1.09	0.085	18.38
-8×10^4	10	1058.0	334.6	2.25	0.555	37.81
-1.1×10^5	10	1308.7	413.9	2.50	0.600	42.03
-4×10^3	100	114.4	11.41	1.04	0.038	17.49
-8×10^4	100	1514.1	151.4	1.57	0.363	26.42
-1.1×10^5	100	1921.4	192.1	1.70	0.413	28.63

Table 5 Numerical results for friction factor, $\alpha = 0.8$

$\frac{\partial p}{\partial z}$	r	Re	De	f_c/f_s	ξ_Q	fRe
-4×10^3	4	99.4	49.7	1.25	0.200	20.13
-8×10^4	4	881.67	440.8	2.82	0.645	45.37
-1.1×10^5	4	1085.9	543.0	3.15	0.682	50.65
-1.4×10^5	4	1269.4	634.7	3.43	0.708	55.14
-4×10^3	10	110.3	34.9	1.13	0.112	18.14
-8×10^3	10	193.4	61.2	1.28	0.221	20.68
-8×10^4	10	1072.7	339.2	2.32	0.568	37.29
-1.1×10^5	10	1336.4	422.6	2.56	0.609	41.16
-4×10^3	100	118.6	11.9	1.05	0.046	16.87
-8×10^3	100	233.5	23.4	1.06	0.060	17.13
-8×10^4	100	1536.1	153.6	1.62	0.382	26.04
-1.1×10^5	100	1941.4	194.1	1.76	0.432	28.33

are presented in Figs. 7, 8, and 9 for $\alpha = 0.2$, 0.5, and 0.8, respectively. From these figures, it is seen that the friction factor is increased as the Dean number increases and decreases as the curvature ratio increases. However, the effect of the curvature ratio on the friction factor is not clearly observed from these figures since the curvature is also included in the definition of the Dean number. In addition, analysis of these data shows that the friction factor increases as the minor-axis to major-axis ratio increases. However, the Dean number has a greater effect on the friction factor than the minor-axis to major-axis ratio. Tables 3 through 5 clearly indicate that the present computation covers the Dean numbers ranging from $10.7 \sim 424.6$ for $\alpha = 0.2$, $11.41 \sim 635.7$ for $\alpha = 0.5$, and $11.9 \sim 634.7$ for $\alpha = 0.8$, Three curvature ratios, $r = 4$, 10, 100 are also used here. Based on the present numerical results and using the least squares method, the correlation equation of the

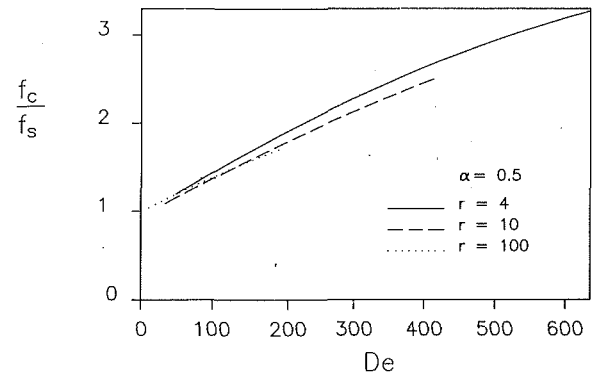

Fig. 8 Friction factor ratio versus Dean number for $\alpha = 0.5$

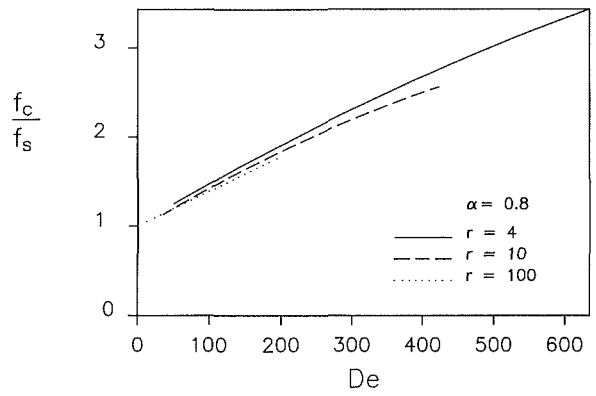

Fig. 9 Friction factor ratio versus Dean number for $\alpha = 0.8$

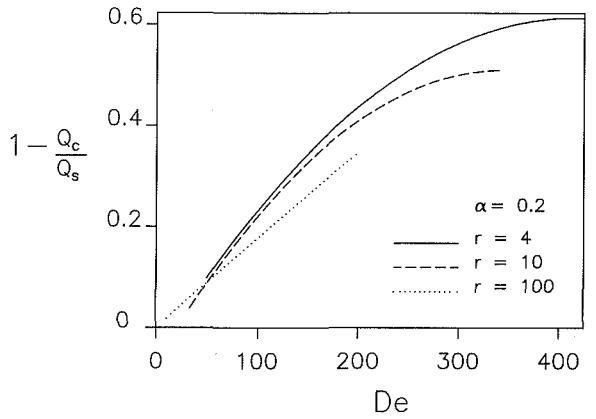

Fig. 10 ξ_Q versus Dean number for $\alpha = 0.2$

friction factor results for the curved elliptic duct is obtained as:

$$\frac{f_c}{f_s} = 1 + 0.0031\,\alpha^{0.3}\,\mathrm{De}^{1.07} \tag{28}$$

The maximum deviation of Eq. (28) from the numerically predicted values is 15 percent. This equation can be used for engineering design purposes.

The next three figures show the variation of ξ_Q with the Dean number at different minor-axis to major-axis ratios, $\alpha = 0.2, 0.5$, and 0.8, of the elliptic duct. Because of the relation between f_c/f_s and ξ_Q, a detailed discussion is not necessary here.

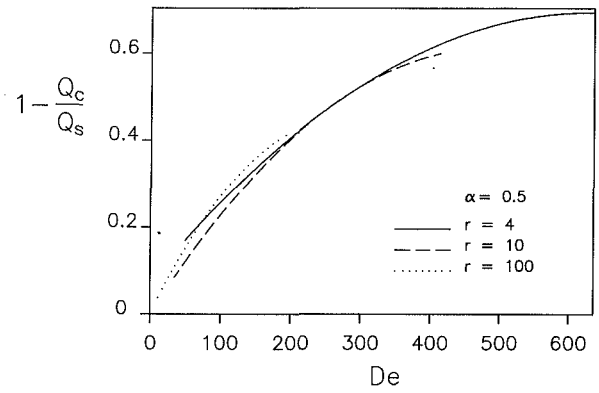

Fig. 11 ξ_Q versus Dean number for $\alpha = 0.5$

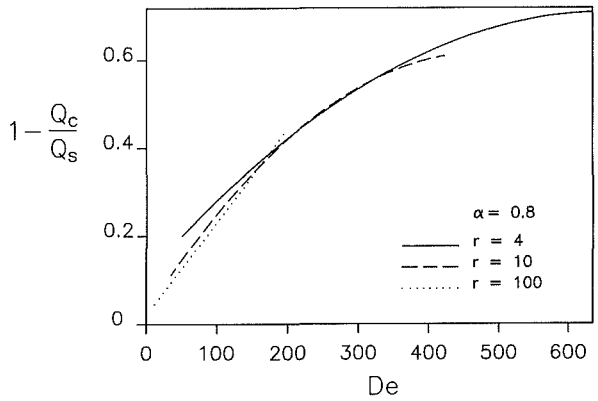

Fig. 12 ξ_Q versus Dean number for $\alpha = 0.8$

Conclusion

The fully developed laminar flow in the curved duct with an elliptic cross section is investigated by a control volume based finite difference method via the numerically generated boundary-fitted coordinate system. The effect of the curvature ratio on the flow is considered in the complete Navier-Stokes equations.

The present analysis reveals that only one pair of secondary vortices occurs on the cross section in all the computation cases. The location of the vortex center shifts toward the negative abscissa direction as the Dean numbers increase. No secondary pair of vortices appear up to a Dean number of 635.7. This indicates that the flow in the curved elliptic duct is stable in the computed cases.

The axial velocity results are shown graphically to illustrate the variations along the horizontal and vertical symmetry lines. It is seen that as the Dean number increases, the distribution of the axial velocity becomes full and the maximum value moves to the proximity of the outer wall.

It is found that the friction factor increases as the Dean number increases and as the curvature ratio decreases. The minor-axis to major-axis ratio of the elliptic duct also effects the friction factor, but it is not as strong as the Dean number. However, for the purposes of engineering design, the friction factor ratio of the curved elliptic duct to the straight elliptic duct is given in the form of Eq. (28), which is obtained from all the computed data by using the least square curve-fitted method. The ξ_Q, concerned with flow rate of the curved elliptic duct, is tabulated for engineering reference, as well. The solution of flow and heat transfer in the curved elliptic duct is essential to various engineering problems.

Acknowledgment

The results presented in this paper were obtained in the course of research sponsored by the National Science Foundation under Grant No. CTS-9017732.

References

Berger, S. A., Talbot, L., and Yao, L. S., 1983, "Flow in Curved Pipes," *Ann. Rev. Fluid Mech.*, Vol. 15, pp. 461–512.

Cheng, K. C., Lin, R. C., and Ou, J. W., 1976, "Fully Developed Laminar Flow in Curved Rectangular Channels," ASME JOURNAL OF FLUIDS ENGINEERING, Mar., pp. 41–48.

Daskopoulos, P., and Lenhoff, A. M., 1989, "Flow in Curved Ducts: Bifurcation Structure for Stationary Ducts," *J. Fluid Mech.*, Vol. 203, pp. 125–148.

Dean, W. R., 1927, "Note on the Motion of Fluid in a Curved Pipe," *Phil. Mag.*, Vol. 20, pp. 208–223.

Dean, W. R., 1928, "The Streamline Motion of Fluid in a Curved Pipe," *Phil. Mag.*, Vol. 30, pp. 673–695.

Duh, T. Y., and Shih, Y. D., 1989, "Fully Developed Flow in Curved Channels of Square Cross Sections Inclined," ASME JOURNAL OF FLUIDS ENGINEERING, Vol. III, pp. 172–177.

Ghia, K. N., Ghia, Li, and Shin, C. T., 1987, "Study of Fully Developed Incompressible Flow in Curved Ducts, Using a Multi-Grid Technique," ASME JOURNAL OF FLUIDS ENGINEERING, Vol. 109, pp. 226–236.

Kakac, S., Shah, R. K., and Aung, W., 1987, *Handbook of Single-Phase Convection Heat Transfer*, Wiley Interscience, New York.

Mille, P., Vehrenkamp, R., and Schulz-Dubois, E. O., 1985, "The Development and Structure of Primary and Secondary Flow in a Curved Square Duct," *J. Fluid Mech.*, Vol. 151, pp. 219–241.

Patankar, S. V., 1980, *Numerical Heat Transfer and Fluid Flow*, Hemisphere, Washington, D.C.

Shah, R. K., and Joshi, S. D., 1987, "Convective Heat Transfer in Curved Duct," *Handbook of Single-Phase Convective Heat Transfer*, ed., Kakac, S., et al., Wiley Interscience, New York.

Shyy, W., Tong, S. S., and Correa, S. M., 1985, "Numerical Recirculating Flow Calculation Using a Body-Fitted Coordinate System," *Numer. Heat Transfer*, Vol. 8, pp. 99–113.

Srivastava, R. S., 1980, "On the Motion of a Fluid in a Curved Pipe of Elliptical Cross-Section," *J. of Applied Mathematics and Physics* (ZAMP), Vol. 31, pp. 297–303.

Takami, T., and Sudou, K., 1984, "Flow through Curved Pipe with Elliptic Cross Sections," *Bull. JSME*, Vol. 27, pp. 1176–1181.

Thomas, P. D., and Middlecoff, J. F., 1980, "Direct Control of Grid Point Distribution in Meshes Generated by Elliptic Equation," *AIAA J.*, Vol. 18, pp. 652–656.

Thomas, R. M., and Walters, K., 1965, "On the Flow of an Elastico-Viscous Liquid in a Curved Pipe of Elliptic Cross Section Under a Pressure-Gradient," *J. Fluid Mech.*, Vol. 21, Part 1, pp. 173–182.

Thompson, J. F., Thames, F., and Mastin, C., 1974, "Automatic Numerical Generation of Body-Fitted Curvilinear Coordinate System for Field Containing any Number of Arbitrary Two-Dimensional Bodies," *J. Comput. Phys.*, Vol. 24, pp. 299–319.

Topakoglu, H. C., 1967, "Steady Laminar Flows of an Incompressible Viscous Fluid in Curved Pipes," *J. of Mathematics and Mechanics*, Vol. 16, pp. 1321–1337.

Topakoglu, H. C., and Ebadian, M. A., 1987, "Viscous Laminar Flow in a Curved Pipe of Elliptical Cross-Section," *J. Fluid Mech.*, Vol. 184, pp. 571–580.

Topakoglu, H. C., and Ebadian, M. A., 1985, "On the Steady Laminar Flow of an Incompressibel Viscous Fluid in Curve Pipoe of Elliptical Cross-Section," *J. Fluid Mech.*, Vol. 184, pp. 571–580.

A Numerical Study of Laminar 90-Degree Bend Duct Flow With Different Discretization Schemes

R. W. Yeo

P. E. Wood

A. N. Hrymak

Department of Chemical Engineering,
McMaster University,
Hamilton, Ontario, Canada L8S 4L7

Three different discretization schemes were used to study the flow in a 90-degree bend square duct. The numerical method consists of a general curvilinear coordinate formulation of the governing equations and a non-staggered grid for the variables. A stable method of implementing the higher-order schemes is proposed. The second-order upwinding and QUICK schemes give results which compare more favourably with the experimental data than the first-order upwinding method. In 3-D flow problems, the grid-refinement is severely limited by the amount of computer storage and the use of higher-order upwinding schemes provides a better alternative in obtaining accurate flow predictions.

1 Introduction

Many practical engineering problems require solutions to the complete Navier-Stokes equations in three-dimensional form, often in a complex domain. Solutions to the elliptic form of the 3-D Navier-Stokes equations are difficult to obtain since the amount of computer memory and CPU time can be quite extensive. For 2-D flows, the accepted practice has been to use a second-order finite difference analog for the diffusion terms and, for stability reasons, a first-order upwinding analog for the convection terms. Although it solves the stability problem, first-order upwinding degrades the accuracy of the solution due to numerical diffusion. Therefore, extensive grid refinement is required for complex flow problems (De Vahl and Mallinson, 1976). For 2-D flows this is not a serious obstacle since the grid-refinement is not costly but grid refinement can be expensive for 3-D flows. In order to capture the details of the flow field, the number of grid points must be increased in all three directions, and often the maximum number of grid points is limited by the available amount of computer memory or reasonable CPU times. An alternative approach, which is computationally more intensive, is to use a more accurate, higher-order numerical approximation for the convective terms. Higher order methods can give significantly more accurate results using reasonable grid densities compared to the first-order methods.

The necessity for more accurate, higher-order upwinding schemes is clearly shown in the 3-D elliptic treatment of curved duct problems (Regio and Camarero, 1987; Humphrey et al., 1977). Due to the presence of a centrifugal force created as the fluid travels through the bend, a helical secondary flow pattern develops which persists for several hydraulic diameters downstream of the bend. Previous numerical results (Regio and Camarero, 1987; Humphrey et al., 1977), using the first-order upwinding and hybrid methods, showed that only qualitative agreement could be achieved between the numerical and experimental results.

In this paper, two different higher-order upwinding methods are evaluated. QUICK (Leonard, 1979) (Quadratic Upstream Interpolations for the Convective Kinematics) is a third order accurate method (Pollard and Siu, 1982; Huang et al., 1985; Shyy, 1985). For many complex flow problems, QUICK provides accurate results without extensive grid refinement. The existing literature for the QUICK scheme applied to 3-D flows is not extensive. Only a few papers, which consider the cubic cavity problem in the Cartesian coordinate system are available (Freitas et al., 1985; Gaskell et al., 1987). The alternate higher order method is the second-order upwinding method explored by Shyy (1985) for 1-D and 2-D test problems and compared to other discretization schemes.

The test problem considered in this work is the 90-degree bend square duct which has been studied experimentally and numerically by Humphrey et al. (1977). Their numerical results show that even with extensive grid refinement, the results were only in "reasonable" agreement with the experimental data. Especially at the 60 and 90-degree positions, from the beginning of the bend, the discrepancy between the experimental and numerical results was significant.

The problem is solved using generalized curvilinear coordinates with a non-staggered arrangement for the primitive variables on the grid nodes. The momentum interpolation method (Rhie and Chow, 1983) was used to determine the correct cell face velocities. The SIMPLEC (Van Doormaal and Raithby, 1984) algorithm, a variant of the SIMPLE algorithm (Patankar, 1981), was used to find the pressure and velocities which satisfy continuity.

The main issues addressed in this paper are the accurate modelling of the 3-D flow phenomena and the higher-order discretization of the convective terms. In the next section a brief description of the numerical method is given and the three discretization schemes (first-order upwinding, second-

Contributed by the Fluids Engineering Division for publication in the JOURNAL OF FLUIDS ENGINEERING. Manuscript received by the Fluids Engineering Division October 26, 1989.

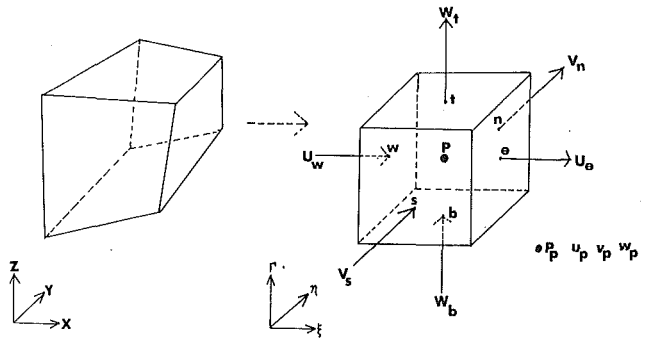

Fig. 1 Control volumes in the physical space (x, y, z) and transformed space (ξ, η, Γ)

order upwinding and QUICK) are discussed. A method of discretizing the higher-order schemes is presented. A more comprehensive description of the method used and the results of 2-D test problems are given in Yeo (1989). Finally, the numerical results obtained using the different discretizations will be compared to the available experimental data.

2 Governing Equations and the Model Problem

The flow field considered is laminar and steady. The governing equations, representing the conservation of mass and momentum, in the Cartesian coordinate system are

Continuity

$$\frac{\partial}{\partial x_i}(\rho u_i) = 0 \tag{1}$$

Momentum

$$\frac{\partial}{\partial x_i}(\rho u_i u_j) = -\frac{\partial P}{\partial x_i} + \frac{\partial}{\partial x_i}\left(\mu \frac{\partial u_j}{\partial x_i}\right) \tag{2}$$

Equations (1) and (2) can be put into a more general form.

$$\frac{\partial}{\partial x_i}(\rho u_i \Phi) = \frac{\partial}{\partial x_i}\left(\Gamma^{\Phi} \frac{\partial \Phi}{\partial x_i}\right) + s^{\Phi} \tag{3}$$

For the momentum equations, Γ^{Φ} represents the viscosity, s^{Φ} the pressure gradient source terms, while in the continuity equation $\phi = 1$ and $s^{\Phi} = 0$.

Equations (1)–(3) as written above, can only be used to solve problems in Cartesian coordinates. The equations can be transformed to the generalized curvilinear coordinate system by applying the general transformation $\epsilon_i = \epsilon_i(x_i)$ which is illustrated in Fig. 1.

For the source terms (by chain rule differentiation) of Eq. (3),

$$\frac{\partial F}{\partial x_i} = \frac{\partial F}{\partial \epsilon_j}\frac{\partial \epsilon_j}{\partial x_i} \tag{4}$$

For the transport terms (conservative transformation) (Thompson et al., 1985) of Eq. (3),

$$\frac{\partial F}{\partial x_i} = \frac{1}{J}\left[\frac{\partial}{\partial \epsilon_j}\frac{\partial \epsilon_j}{\partial x_i}(JF)\right] \tag{5}$$

where J is the Jacobian of the transformation defined as the determinant of the Jacobian matrix (Aris, 1962)

$$J = \frac{(x,y,z)}{(\epsilon,\eta,\Gamma)} \tag{6}$$

The resulting transformed Eq. (3) is

$$\frac{\partial}{\partial \epsilon_i}(\rho U_i \Phi) = \frac{\partial}{\partial \epsilon_i}\left(\Gamma^{\Phi} g^{ij} J \frac{\partial \Phi}{\partial \epsilon_j}\right) + s^{\Phi} J \tag{7}$$

U_i represents the contravariant velocities scaled by the Jacobian (J) and g^{ij} is the contravariant metric tensor defined by

$$U_i = J \frac{\partial \epsilon_i}{\partial x_j} u_j \tag{8}$$

$$g^{ij} = \frac{\partial \epsilon_i}{\partial x_k}\frac{\partial \epsilon_j}{\partial x_k} \tag{9}$$

The continuity equation becomes

$$\frac{\partial}{\partial \epsilon_i}(U_i) = 0 \tag{10}$$

The advantage of the above formulation is that problems in any arbitrary domain can be solved on a regular grid system. For a more detailed discussion of the transformation and the metric tensors see Thompson et al (1985) and Aris (1962).

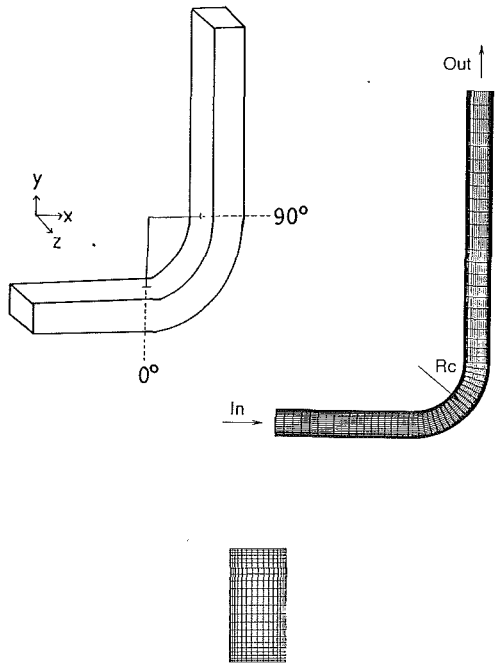

Fig. 2 90-degree bend square duct

90-Degree Bend Square Duct. Humphrey et al. (1977) carried out a detailed experimental analysis of laminar flow in a 90-degree bend (Fig. 2). Their velocity measurements will be compared with the numerical predictions of this study. Numerical comparisons to these experiments have also been made by Humphrey et al. (1977) and Rhie (1985), who used 60 × 15 × 10 and 50 × 22 × 15 grids respectively. The Reynolds number of the flow, based on the hydraulic diameter, was 790. The Dean number was $De = Re(d/2R_c)^{1/2} = 368$ where d is the hydraulic diameter and R_c is the mean radius of curvature. The longitudinal velocities were measured using a laser doppler anemometer, but the other velocity components were not measured.

At $x = -5$, (5 hydraulic diameters before the bend) a fully developed velocity profile was observed. As the fluid travelled through the bend, there was an acceleration towards the outer radius wall and deceleration near the inner radius wall. A small longitudinal recirculation was observed immediately into the bend, near the outer corners of the duct. The secondary flow pattern was not experimentally investigated; only numerical results were given. Numerical results on the 90-degree plane showed the presence of two counter-rotating vortices each filling half of the plane.

In this work, the presence of a symmetry plane is taken into consideration and only half of the domain is discretized. The boundary conditions are:

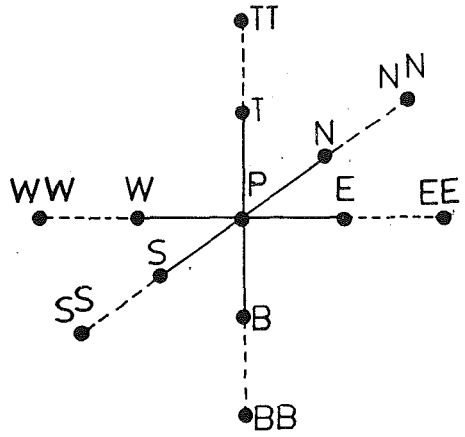

Fig. 3 Computational molecule with points on solid lines used in TDMA sweep and points on dotted lines used with source terms

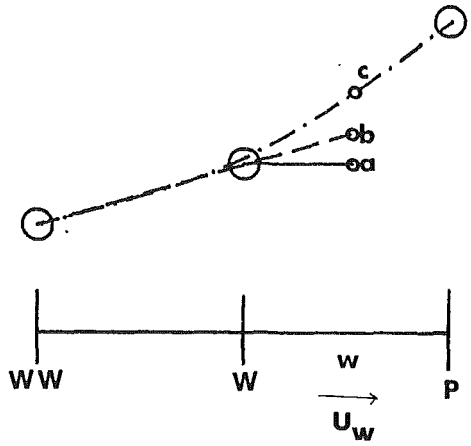

Fig. 4 Points used in discretization schemes: (*a*) first order upwinding, (*b*) second-order upwinding, (*c*) QUICK

at the inlet ($x = -5$): U, V, W = fully developed laminar profile

at the walls: U, V, $W = 0.0$

at the symmetry plane ($z = 0$):

$$\frac{\partial U}{\partial \Gamma} = 0.0, \frac{\partial V}{\partial \Gamma} = 0.0, \; W = 0.0$$

at the exit ($y = 10$): $\dfrac{\partial U}{\partial \epsilon} = 0.0, \dfrac{\partial V}{\partial \epsilon} = 0.0, \dfrac{\partial W}{\partial \epsilon} = 0.0$

Three different grid densities are used to solve the problem: $40 \times 17 \times 11$ ($\epsilon \times \eta \times \Gamma$), $61 \times 23 \times 17$, and $70 \times 25 \times 19$. The highest grid density is used to check the grid independence of the predicted velocities.

3 Numerical Method

The solution domain is divided into a number of control volumes (Fig. 1). In the physical space coordinates a control volume can take any arbitrary shape, while in the transformed domain, a control volume is rectangular parallelepiped with a uniform grid spacing ($\Delta\epsilon = \Delta\eta = \Delta\Gamma = 1.0$).

In order to obtain the discretized equation set, Eq. (7) must be integrated over the control volume. The integration process is illustrated using the convection and diffusion terms.

$$\int_b^t \int_s^n \int_w^e \frac{\partial}{\partial \epsilon}\left(\Gamma^\Phi g^{11} \mathrm{J} \frac{\partial \Phi}{\partial \epsilon}\right) d\epsilon d\eta d\Gamma = \left[\left(\Gamma^\Phi g^{11} \mathrm{J} \frac{\partial \Phi}{\partial \epsilon}\right)_e - \left(\Gamma^\Phi g^{11} \mathrm{J} \frac{\partial \Phi}{\partial \epsilon}\right)_w\right] \Delta\eta \Delta\Gamma \quad (11)$$

The derivatives in Eq. (11) are approximately by second-order central differences

$$\left(\frac{\partial \Phi}{\partial \epsilon}\right)_e = \frac{\Phi_E - \Phi_P}{\Delta\epsilon}.$$

The cross derivatives which arise in Eq. (7), as the result of nonorthogonality of the grid, are treated in a similar manner as Eq. (11). However, in order to retain the 7-point computational molecule shown in Fig. 3 which can be conveniently treated by TDMA (tridiagonal matrix algorithm) based iterative solvers, the nonorthogonality terms are included with the source term.

For the first convection term,

$$\int_b^t \int_s^n \int_w^e \frac{\partial}{\partial \epsilon} (\rho U \Phi) d\epsilon d\eta d\Gamma = [(\rho U \Phi)_e - (\rho U \Phi)_w] \Delta\eta \Delta\Gamma \quad (12)$$

The discretized equation will have the following form.

$$(B_P^\Phi - s_b^\Phi)\Phi_P = \sum A_i^\Phi \Phi_i + s_a^\Phi \quad i = E, W, N, S, T, B \quad (13)$$

The coefficients B_P^Φ, A_i^Φ and s_a^Φ will depend upon the method used to approximate Φ_e and Φ_w in Eq. (13). Different methods discretizing the convection terms are discussed later.

The coupled set of Eqs. (13) are solved iteratively and in order to obtain convergence must be under-relaxed. Using the relaxation factor α (0.7 in this work)

$$\Phi_P = \alpha \Phi_P^{\text{new}} + (1 - \alpha)\Phi_P^{\text{old}} \quad (14)$$

In the solver, the block correction procedure is carried out in alternating directions before the line-by-line sweep also in alternating directions (Patankar, 1981). In the line-by-line sweep, a method similar to Stone's partial cancellation was used to accelerate convergence (Van Doormal and Raithby, 1984). Only a couple of sweeps were necessary to obtain a significant reduction in the residual. The requirements for the convergence of the solution are diagonal dominance and positive matrix coefficients (Patankar, 1981).

In order to obtain the solution to the elliptic form of Navier-Stokes equations some method which enforces continuity must be used. The SIMPLEC (SIMPLE Consistent) method obtains corrections to the velocities and pressure by solving a Poisson-type equation (Van Doormal and Raithby, 1984). With a non-staggered grid system, a special treatment is required to obtain the cell face convection quantities to prevent the "checkerboard" type oscillation (Patankar, 1981). The cell face contravariant velocities are obtained using momentum interpolation (Rhie and Chow, 1983; Mujamdar, 1988). The coefficients are linearly interpolated, but neighboring cell node pressures are used rather than averaging the pressure gradients for the control volumes. This enforces strong velocity-pressure coupling. The cell face convection quantities are also relaxed (Mujamdar, 1988) to obtain convergence.

First-Order Upwinding. Central differencing of the convection terms results in coefficients which become negative when the flow is convection dominated. As a result, the diagonal dominance criterion can not be met and this scheme could not be used with the TDMA based solvers. While converged solutions may be obtained with other types of solvers, which do not require diagonal dominance, the solutions contain unrealistic oscillations (Leonard, 1979; Shyy, 1985). The first-order upwinding method was proposed as a method to overcome the difficulties with central differencing. The resulting discretized equations are diagonally dominant and give physically smooth solutions. In Fig. 4, the first order upwinding method is graphically presented. For the west cell face, the cell face value is assumed to be the value of the upstream node. For the east and west faces

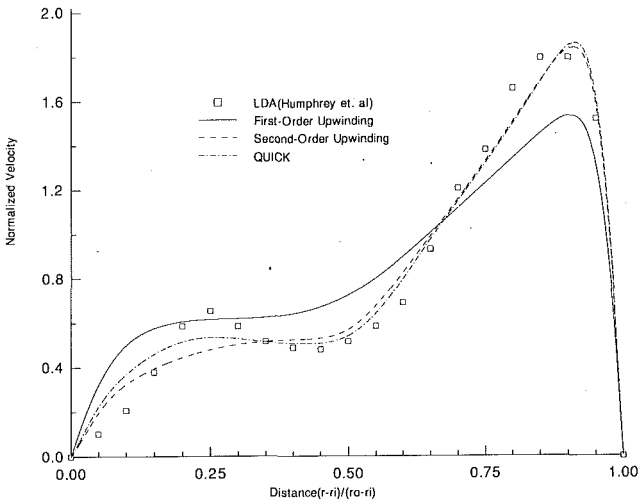

Fig. 5(*a*) Comparison of results at the 90-degree plane along the central (symmetry) plane within the duct

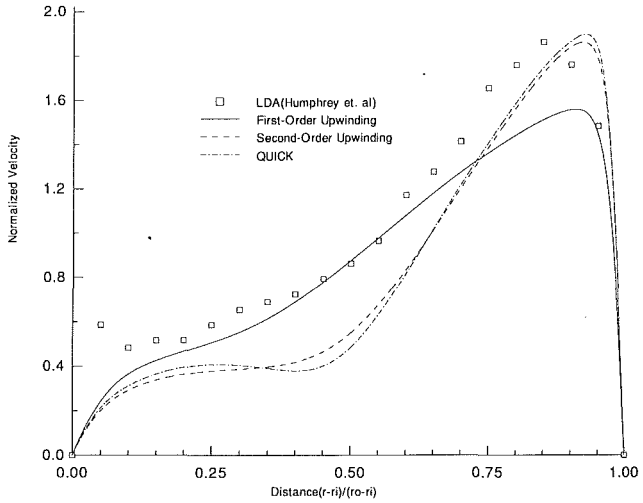

Fig. 6(*a*) Comparison of results at the 60-degree plane along the central (symmetry) plane within the duct

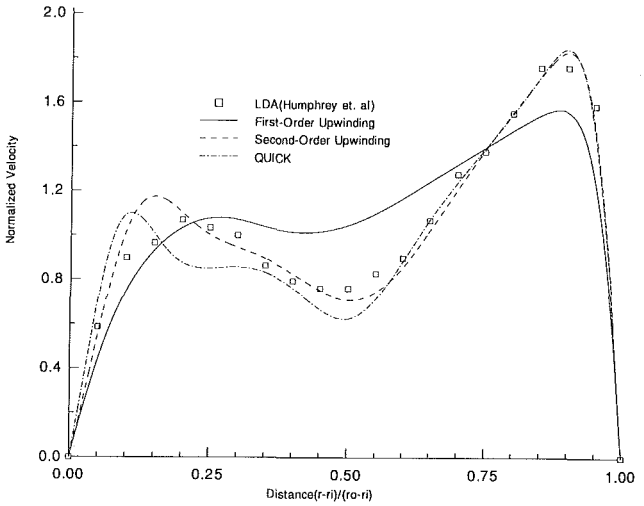

Fig. 5(*b*) Comparison of results at the 90-degree plane along the plane halfway between the symmetry plane and the outside wall within the duct

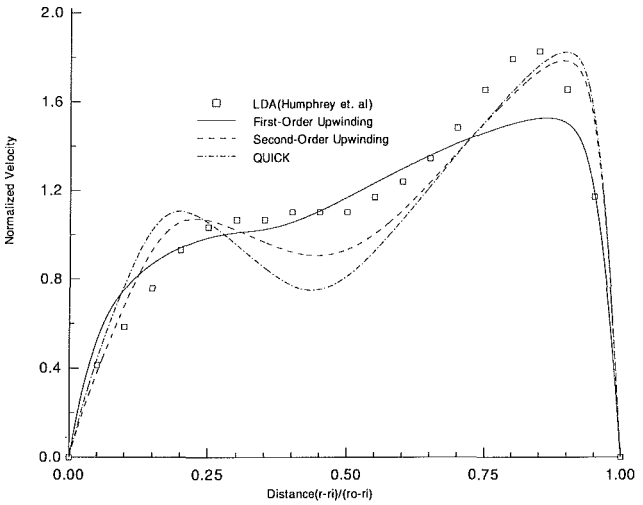

Fig. 6(*b*) Comparison of results at the 60-degree plane along the plane halfway between the symmetry plane and the outside wall within the duct

$$\Phi_e = \begin{matrix} \Phi_P & U_e > 0 \\ \Phi_E & U_e < 0 \end{matrix}$$

$$\Phi_w = \begin{matrix} \Phi_W & U_w > 0 \\ \Phi_P & U_w < 0 \end{matrix} \tag{15}$$

The coefficients in Eq. (13) will be

$$A_E^\Phi = D_e + [-CE, 0.0]$$
$$A_W^\Phi = D_w + [CW, 0.0]$$
$$A_N^\Phi = D_n + [-CN, 0.0]$$
$$A_S^\Phi = D_s + [CS, 0.0]$$
$$A_T^\Phi = D_t + [-CT, 0.0]$$
$$A_B^\Phi = D_b + [CB, 0.0]$$
$$B_P^\Phi = \sum A_i^\Phi \tag{16}$$

where

[ ] maximum operator

D_x diffusion coefficient, e.g., $D_e = (\Gamma^\Phi g^{11} J)_e$

CX convection coefficient, e.g., $CE = (\rho U)_e$

Although smooth converged solutions can be obtained with first order upwinding, extensive studies (De Vahl Davis and Mallinson, 1976; Huang et al., 1985; Shyy, 1985) indicate that the method fails to give accurate solutions at high Re numbers. Due to false diffusion, the strength of motion is under-predicted. For recirculating flows, the method predicts weaker vortices and sometimes an incorrect flow field (De Vahl Davis and Mallinson, 1976).

Second-Order Upwinding. A better approximation of the cell face value would be to use two upstream nodal values to determine the cell face value (Fig. 4). For the east and west faces

$$\Phi_e = \begin{matrix} 1.5\Phi_P - 0.5\Phi_W & U_e > 0 \\ 1.5\Phi_E - 0.5\Phi_{EE} & U_e < 0 \end{matrix}$$

$$\Phi_w = \begin{matrix} 1.5\Phi_W - 0.5\Phi_{WW} & U_w > 0 \\ 1.5\Phi_P - 0.5\Phi_E & U_w < 0 \end{matrix} \tag{17}$$

An upwinding formulation was used when implementing this method in the computer code. The coefficients are the same as Eq. (12). The equations for Φ_e, Φ_w and s_a^Φ are

$$\Phi_e = \begin{matrix} \Phi_P + S_e; & S_e = 0.5(\Phi_P - \Phi_W) & U_e > 0 \\ \Phi_E + S_e; & S_e = 0.5(\Phi_E - \Phi_{EE}) & U_e < 0 \end{matrix}$$

$$\Phi_w = \begin{matrix} \Phi_W + S_w; & S_w = 0.5(\Phi_P - \Phi_W) & U_w > 0 \\ \Phi_P + S_w; & S_w = 0.5(\Phi_P - \Phi_E) & U_w < 0 \end{matrix} \tag{18}$$

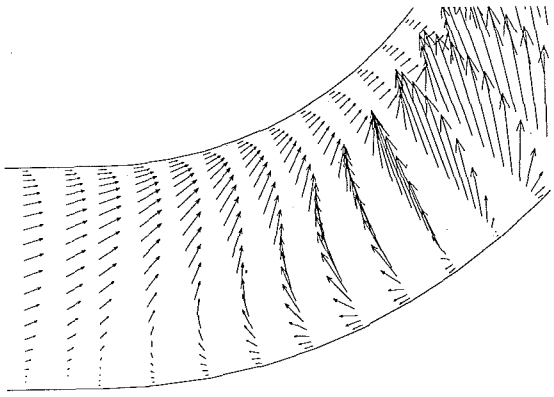

Fig. 7 Velocity vectors in the plane z = 0.485 showing logitudinal recirculation (between 0 degree and 20 degree planes along the duct)

$$s_a^\Phi = s_a^\Phi + (CW \cdot S_w - CE \cdot S_e) + (CS \cdot S_s - CN \cdot S_n) + (CB \cdot S_b - CT \cdot S_t) \quad (19)$$

QUICK. In the second-order method two upstream nodes are used. If a third node (see Fig. 4) is included, a better approximation can be obtained, and is equivalent to fitting a polynomial, $\Phi_e = C_1 + C_2\epsilon + C_3\epsilon^2$, with upstream weighting. The truncation error is third order and the false diffusion error is reduced significantly with this method (Leonard, 1979; Pollard and Siu, 1982; Huang et al., 1985). For east and west faces the approximations for Φ are

$$\Phi_e = \begin{cases} \frac{1}{2}(\Phi_E + \Phi_P) - \frac{1}{8}(\Phi_E + \Phi_W - 2\Phi_P) & U_e > 0 \\ \frac{1}{2}(\Phi_E + \Phi_P) - \frac{1}{8}(\Phi_P + \Phi_{EE} - 2\Phi_E) & U_e < 0 \end{cases}$$

$$\Phi_w = \begin{cases} \frac{1}{2}(\Phi_W + \Phi_P) - \frac{1}{8}(\Phi_P + \Phi_{WW} - 2\Phi_W) & U_w > 0 \\ \frac{1}{2}(\Phi_W + \Phi_P) - \frac{1}{8}(\Phi_W + \Phi_E - 2\Phi_P) & U_w < 0 \end{cases} \quad (20)$$

The QUICK scheme, depending on the method of implementation may yield coefficients which can become negative and lead to convergence problems. In order to obtain convergence, a false transient term must be added or a very small relaxation factor must be used (Pollard and Siu, 1982; Freitas et al., 1985). In order to achieve stability the scheme must be recast into a diagonally dominant form. An upwinding type formulation was used (Eq. (21)) to overcome the stability problem. The source term due to QUICK is sufficiently small and will not significantly hinder convergence. This approach is much less complicated than the QUICKE or QUICKER formulations of Pollard and Siu (1982).

$$\Phi_e = \begin{cases} \Phi_P + S_e; \quad S_e = \frac{1}{8}(3\Phi_E - 2\Phi_P - \Phi_W) & U_e > 0 \\ \Phi_E + S_e; \quad S_e = \frac{1}{8}(3\Phi_P - 2\Phi_E - \Phi_{EE}) & U_e < 0 \end{cases}$$

$$\Phi_w = \begin{cases} \Phi_W + S_w; \quad S_w = \frac{1}{8}(3\Phi_P - 2\Phi_W - \Phi_{WW}) & U_w > 0 \\ \Phi_P + S_w; \quad S_w = \frac{1}{8}(3\Phi_W - 2\Phi_P - \Phi_E) & U_w < 0 \end{cases} \quad (21)$$

4 Results and Discussion

The numerical results at the 90 degree and 60 degree planes are plotted in Fig. 5 and 6 for the 61 × 21 × 17 grid with the experimental results of Humphrey et al. (1977). At the 90 degree and 60 degree planes the first order upwinding method

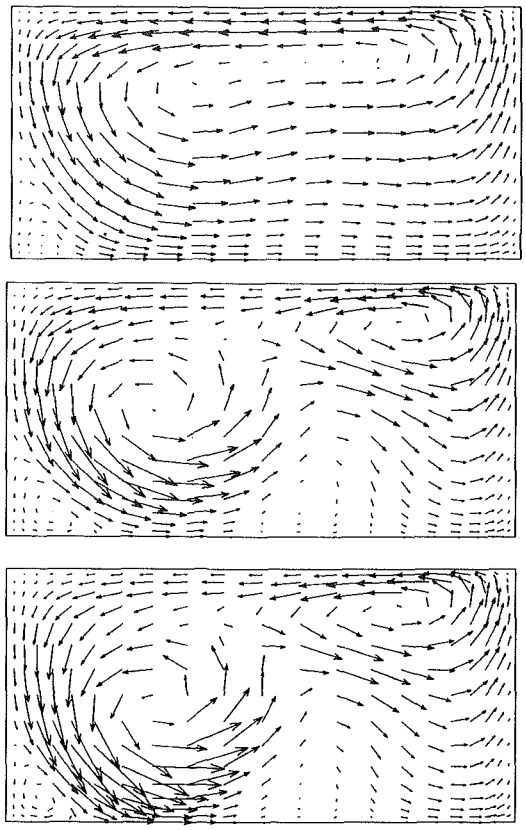

Fig. 8 Secondary flows in the 90-degree plane (left side is inner wall, *right side is outer wall and bottom is symmetry plane): top, first-order* upwinding; middle, second-order upwinding; bottom, QUICK

results are consistent with previous work, i.e., the velocity profiles were not steep and the peak velocities were consistently under-predicted (Humphrey et al., 1977; Rhie, 1985). The results obtained with the higher order methods are in excellent agreement with the observed experimental values at the 90 degree plane. The higher-order methods under-predict the velocity in the symmetry line at the 60 degree plane [Fig. 6(*a*)]. The experimental results show a sharp rise in the velocity profile near the inner radius wall. In order to capture the sharp velocity profile, a much finer grid in the vicinity of the wall may be needed.

The weak longitudinal recirculation zone, which was observed experimentally, is also determined numerically with all three discretization schemes. The streamwise velocity vector plot is given in Fig. 7 for the QUICK scheme.

In Fig. 8 the vector plots of the secondary flow in the 90-degree plane are given. The upwinding result indicates the presence of one vortex, while the higher-order schemes indicate a cellular-type flow pattern with weak secondary vortices. The upwinding result is consistent with other published results (Humphrey et al., 1977; Mujamdar, 1988). The higher-order upwinding results indicate a more complicated flow pattern which is consistent with the phenomenon first studied by Dean (1927). If a critical Dean number (which indicates the ratio of the curvature effect to the viscous effect) is exceeded, the secondary flow field is unstable and results in the development of a second stable laminar flow pattern which consists of several vortices superimposed on the main flow (Nandakumar and Masiliyah, 1986). This phenomenon was observed by Cheng et al. (1977) using flow visualization studies which showed complex flow patterns at high De numbers.

In Fig. 9 the effect of grid refinement for the three schemes is shown at the 90 degree symmetry plane. The first-order upwinding scheme solution is not grid-independent and changes

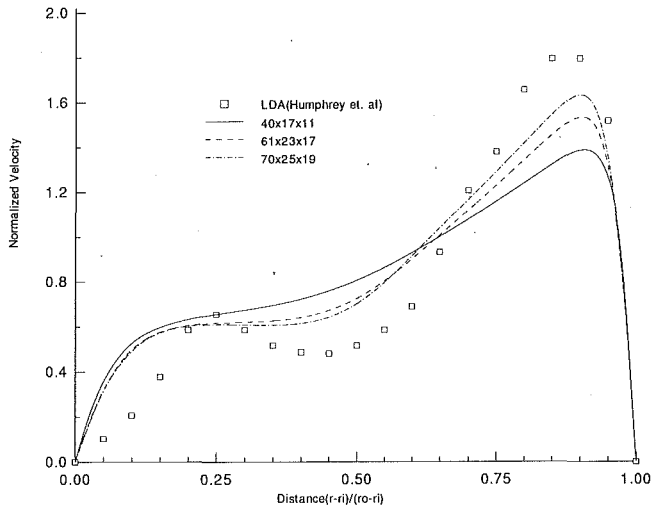

Fig. 9(*a*) Effect of grid refinement in the 90-degree plane for first-order upwinding

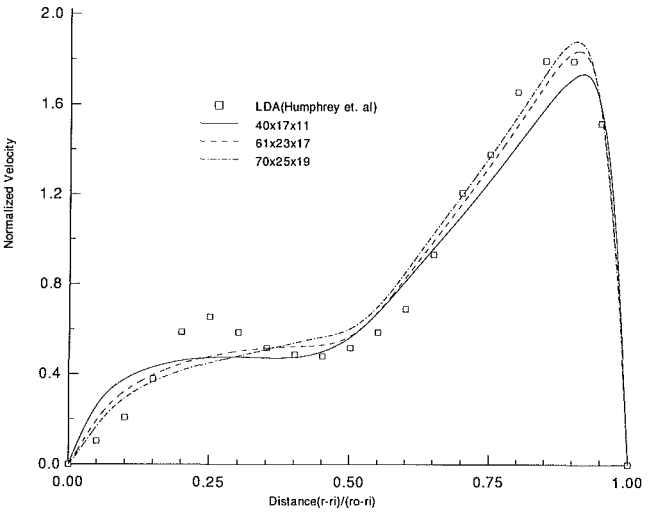

Fig. 9(*b*) Effect of grid refinement in the 90-degree plane for second-order upwinding

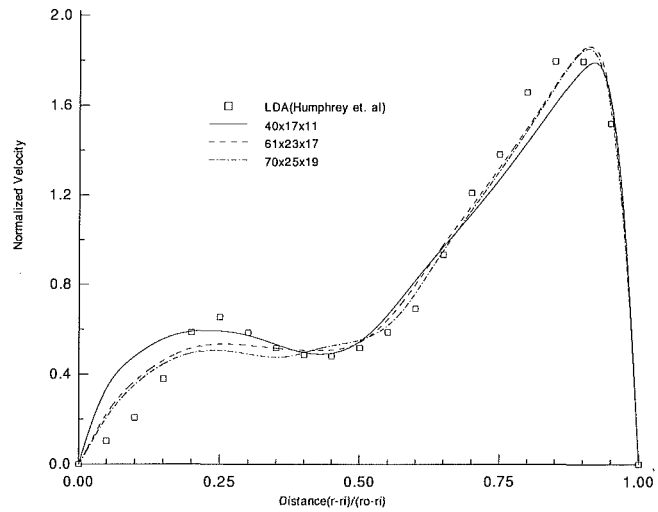

Fig. 9(*c*) Effect of grid refinement in the 90-degree plane for QUICK

significantly as the grid is refined. The higher-order upwinding scheme solutions at the lowest grid density are very similar to those at the highest grid density and the 61 × 21 × 17 grid shows near grid independence of the solutions. It is difficult to achieve grid independence, especially with highly convected flows in 3-D.

Conclusions

A stable method of discretizing higher-order schemes was used to study the flow in a 90-degree bend. The results show that the higher-order schemes were able to predict the experimentally observed trends more accurately than previous numerical solutions. Although the higher-order schemes are more expensive computationally, the accuracy obtained with the schemes makes them a worthwhile alternative method. The advantage is especially true in 3-D flows in which the grid-refinement is limited by the available computer memory.

Acknowledgments

The authors would like to acknowledge the financial support of the Natural Sciences and Engineering Research Council of Canada.

References

Aris, R., 1962, *Vectors, Tensors and the Basic Equations of Fluid Mechanics*, Prentice-Hall, Englewood Cliffs, N.J.

Cheng, K. C., Nakayama, J., and Akiyama, M., 1977, "Effect of Finite and Infinite Aspect Ratios of Flow Patterns in Curved Rectangular Channels," *Proceedings of the International Symposium on Flow Visualization*, Tokyo, Japan, pp. 109–114.

Dean, W. R., "Note on the Motion of Fluid in a Curved Pipe," *Philosophical Magazine*, Vol. 4, pp. 208–223.

De Vahl Davis, G., and Mallinson, G. D., 1976, "An Evaluation of Upwind and Central Difference Approximations by a Study of Recirculating Flow," *Computers and Fluids*, Vol. 4, pp. 29–43.

Freitas, C. J., Street, R. L., Findikakis, A. N., and Koseff, J. R., 1985, "Numerical Simulation of Three-Dimensional Flow in a Cavity," *International Journal Numerical Methods in Engineering*, Vol. 5, pp. 561–575.

Gaskell, P. H., Lau, A. K., and Wright, N. G., 1987, "Two Efficient Solution Strategies for Use with Higher Order Discretisation Schemes, in the Simulation of Fluid Flow Problems," *Numerical Methods in Laminar and Turbulent Flow: Proceedings of the 5th International Conference*, Montreal, Ed. C. Taylor, W. G. Habashi, M. M. Hafez, Swansea, U. K., Pineridge Press, pp. 210–220.

Huang, P. G., Launder, B. E., and Leschziner, M. A., 1985, "Discretisation of Nonlinear Convection Processes: A Broad-Range Comparison of Four Schemes," *Computer Methods in Applied Mechanics and Engineering*, Vol. 48, pp. 1–24.

Humphrey, J. A. C., Taylor, A. M. K., and Whitelaw, J. H., 1977, "Laminar Flow in a Square Duct of Strong Curvature," *Journal of Fluid Mechanics*, Vol. 83, pp. 509–527.

Leonard, B. P., 1979, "A Stable and Accurate Convective Modelling Procedure Based on Quadratic Upstream Interpolation," *Computer Methods in Applied Mechanics and Engineering*, Vol. 19, pp. 59–98.

Mujamdar, S., 1988, "Role of Under-Relaxation in Momentum Interpolation for Calculation of Flow with Non-Staggered Grids," *Numerical Heat Transfer*, Vol. 13, pp. 125–132.

Nandakumar, K., and Masiliyah, J. H., 1986, "Swirling Flow and Heat Transfer in Coiled and Twisted Pipes," *Advances in Transport Processes*, Halsted Press, Ed. by Mujumdar, A. and Mashelkar, R. A., Vol. 4, pp. 49–112.

Patankar, S. V., 1981, "A Calculation Procedure for Two-Dimensional Elliptic Situations," *Numerical Heat Transfer*, Vol. 4, pp. 409–425.

Pollard, A., and Siu, A. L. W., 1982, "The Calculation of Some Laminar Flows Using Various Discretisation Schemes," *Computer Methods in Applied Mechanics and Engineering*, Vol. 35, pp. 293–313.

Regio, M., and Camarero, R., 1987, "A Calculation Scheme for Three-Dimensional Viscous Incompressible Flows," ASME JOURNAL OF FLUIDS ENGINEERING, Vol. 109, pp. 345–352.

Rhie, C. M., 1985, "A Three-Dimensional Passage Flow Analysis Method Aimed at Centrifugal Impellers," *Computers and Fluids*, Vol. 13, pp. 443–460.

Rhie, C. M., and Chow, W. L., 1983, "A Numerical Study of the Turbulent Flow Past an Isolated Airfoil with Trailing Edge Separation," *AIAA Journal*, Vol. 21, pp. 1525–1532.

Shyy, W., 1985, "A Study of Finite Difference Approximations to Steady-State, Convection-Dominated Flow Problems," *Journal of Computational Physics*, Vol. 57, pp. 415–438.

Taylor, A. M. K. P., Whitelaw, J. H., and Yianneskis, M. J., 1982, "Curved Ducts with Strong Secondary Motion: Velocity Measurements of Developing Laminar and Turbulent Flow," JOURNAL OF FLUIDS ENGINEERING, Vol. 104, pp. 350–359.

Thompson, J. F., Warsi, Z. U. A., and Mastin, C. W., 1985, *Numerical Grid Generation, Foundations and Applications*, North Holland, New York, New York.

Van Doormaal, J. P., and Raithby, G. D., 1984, "Enhancements of the SIMPLE Method for Predicting Incompressible Fluid Flows," *Numerical Heat Transfer*, Vol. 7, pp. 147–163.

Yeo, R. W., 1989, "Modelling of Fluid Flow in a Complex Domain," Internal Report, Department of Chemical Engineering, McMaster University, Hamilton, Ontario, Canada.

Katsumasa Suzuki
Associate Professor.

Takayuki Taketomi[1]
Graduate Student.

Sanroku Sato
Professor.

Department of Mechanical Engineering,
Musashi Institute of Technology,
Tamazutsumi Setagayaku,
Tokyo 158, Japan

Improving Zielke's Method of Simulating Frequency-Dependent Friction in Laminar Liquid Pipe Flow

Zielke's technique of using a method of characteristics to simulate transient phenomena of a liquid transmission line is accurate, easy to apply to complicated systems and therefore, frequently used. However, it requires a very large amount of computation time and computer storage to simulate frequency-dependent friction in a transient liquid flow. Searching for a way to counteract these disadvantages, the authors took note of the fact that the weighting function, which is the root of the above problems, is given by exponential functions or other functions depending on dimensionless time. In order to perform mathematically equivalent calculation without approximations, they have developed a new method which requires much less computation time and computer storage than Zielke's method. The calculation process is shown by a block diagram to facilitate visual understanding of the method.

1 Introduction

The characteristics of a transient pipe flow influence the dynamic performance of an oil hydraulic system. It is thus important to clarify transient flow in an oil hydraulic pipeline. This topic has been studied by many researchers. A model which considers transient two-dimensional laminar flow predicts experimental results accurately and is therefore often used (Goodson and Leonard, 1972). There have been two basic approaches based on this model for determining the dynamic response of a liquid pipeline: an analytical method developed by Brown (1962) which utilizes Laplace transformation, and a computer simulation developed by Zielke (1968) using the method of characteristics. The effect of fluid viscosity is completely taken into account by including a frequency-dependent friction term at the wall. Zielke related the headloss due to the friction to the instantaneous mean velocity and to weighted past velocity changes.

The simulation method can be applied easily to a pipeline with complicated boundary conditions and is therefore very useful (Suzuki, 1989 and 1990). However, much computer time and a large amount of storage are required when the headlosses due to fluid friction are calculated. Furthermore, the computer running time and storage required to perform each time step increase without limit as the number of time steps increases. Elimination of this shortcoming is desirable. Trikha (1975) approximated the weighting function which causes this shortcoming, by a summation of exponential functions which decreased the amount of calculation and the required computer storage to a low level. Bratland (1986) proposed a new method without using a method of characteristics. He discretized the physical system first, and then established a mathematical model of the discrete system. This model, known as the cylinder-model is simple, however, it can produce instabilities in the solution because it does not use a method of characteristics as Zielke's does.

The weighting function of Zielke's method is expressed by a summation of exponential functions or other functions depending on the value of dimensionless time τ. In this paper, calculations mathematically equivalent to Zielke's is performed in a much shorter computation time with much less computer storage than in Zielke's method. Such calculations can be handled easily by a personal computer. The three kinds of calculation methods are shown by a block-diagram representation of discrete time systems to facilitate visual understanding of the calculation process and to clarify the differences among them.

2 Fundamental Equations

The equation of motion and the equation of continuity for a one-dimensional model of a pipeline are given by

$$\frac{\partial V}{\partial t}+g\frac{\partial H}{\partial x}+gh_f=0, \tag{1}$$

$$\frac{\partial H}{\partial t}+\frac{a^2}{g}\frac{\partial V}{\partial x}=0, \tag{2}$$

where h_f is the headloss due to fluid friction per unit length. Equations (1) and (2) become identical to equations of the two-dimensional frequency-dependent model if $h_f(t)$ is given by the following equation, derived from the analysis of transient

[1]Present address: Yokogawa Electric Company, Nakamachi, Musashinoshi, Tokyo 180.

Contributed by the Fluids Engineering Division for publication in the JOURNAL OF FLUIDS ENGINEERING. Manuscript received by the Fluids Engineering Division March 8, 1990.

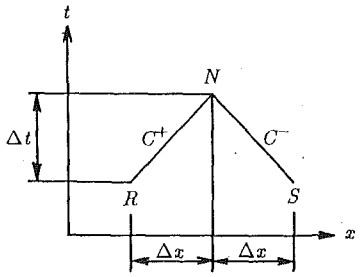

Fig. 1 Characteristic lines on the x-t plane

two-dimensional laminar flow (Zielke, 1969):

$$h_f(t)=\frac{8\nu}{gR^2}V(t)+\frac{4\nu}{gR^2}\int_0^t W(t-u)\frac{\partial V}{\partial t}(u)du$$
$$=\frac{8\nu}{gR^2}V(t)+\frac{4\nu}{gR^2}\int_0^t W(u)\frac{\partial V}{\partial t}(t-u)du, \quad (3)$$

where

$$\tau\equiv\nu t/R^2,$$
$$W(t)\equiv\overline{W}(\tau),$$
$$\overline{W}(\tau)\equiv\overline{W}_1(\tau)$$
$$=0.282095\tau^{-1/2}-1.250000+1.057855\tau^{1/2}$$
$$+0.937500\tau+0.396696\tau^{3/2}-0.351563\tau^2$$
$$\text{for } \tau\le\tau_0=0.02, \quad (4)$$

and

$$\overline{W}(\tau)\equiv\overline{W}_2(\tau)$$
$$=e^{-26.3744\tau}+e^{-70.8493\tau}+e^{-135.0198\tau}+e^{-218.9216\tau}+e^{-322.5544\tau}$$
$$=\sum_{i=1}^{5}e^{-\eta_i\tau} \quad \text{for } \tau>\tau_0=0.02. \quad (5)$$

Through use of the method of characteristics (Streeter and Wylie, 1967), the partial differential Eqs. (1) and (2) can be converted into a pair of total differential equations,

$$\frac{dV}{dt}\pm\frac{g}{a}\frac{dH}{dt}+gh_f=0, \quad (6)$$

$$\frac{dx}{dt}=\pm a. \quad (7)$$

As shown in Fig. 1, Eqs. (6) and (7) are integrated along the characteristic lines C^+ and C^-, respectively. A first-order finite difference-approximation is applied to Eqs. (6) and (7),

$$V_N-V_R+\frac{g}{a}(H_N-H_R)+g\Delta th_{fR}=0 \quad (8)$$

$$V_N-V_S-\frac{g}{a}(H_N-H_S)+g\Delta th_{fS}=0, \quad (9)$$

where $\Delta t=\Delta x/a$, $\Delta x=L/n$. The subscripts N, R, and S indicate the points at which the values of the variables are specified. With algebraic Eqs. (8) and (9), the unknown V_N and H_N are obtained from the known values at the points R and S. The computation time is controlled mainly by the calculation for h_f given by Eq. (3).

3 Calculation Method for h_f

3.1 New Method. Integrating Eq. (3) at $t=K\Delta t$ by a first-order approximation, we obtain

$$h_f(K\Delta t)=\frac{8\nu}{gR^2}V(K\Delta t)+\frac{4\nu}{gR^2}\sum_{J=1}^{K}[V((K-J+1)\Delta t)$$
$$-V((K-J)\Delta t)]W\left(\left(J-\frac{1}{2}\right)\Delta t\right). \quad (10)$$

In Zielke's paper, a first-order difference approximation is used for the time interval of $2\Delta t$, increasing J two units at a time. For simple treatment and accuracy, in this paper J is increased unit by unit, and a first-order difference approximation is applied to the interval of Δt. If Eq. (10) is calculated faithfully in the conventional manner, all past velocities at each point until $t=K\Delta t$ are required, and these repeated calculation of the velocities takes quite a long time. Moreover, the amount of computer storage and computation time required to perform each time increment step increases without limit as the number of time steps, K, is increased. A method of eliminating this shortcoming is proposed in this paper.

The quantity $W((J-1/2)\Delta t)$ in Eq. (10) is given by Eq. (4) or (5) according to the value of τ. If JT is defined as the integer J which corresponds to the boundary $\tau_0=0.02$,

$$\frac{\nu\Delta t}{R^2}\left(JT-\frac{1}{2}\right)\le 0.02<\frac{\nu\Delta t}{R^2}\left(JT-\frac{1}{2}+1\right);$$

therefore

$$JT=\text{trunc}\left(\frac{0.02R^2}{\Delta t\nu}+\frac{1}{2}\right), \quad (11)$$

where trunc(x) denotes the maximum integer which does not exceed x.

Thus, Eq. (10) becomes

$$h_f(K\Delta t)=\frac{8\nu}{gR^2}V(K\Delta t)+h_{f1}(K\Delta t)+h_{f2}(K\Delta t), \quad (12)$$

where $h_{f1}(K\Delta t)$ and $h_{f2}(K\Delta t)$ are distinguished by whether $\overline{W}_1(\tau)$ or $\overline{W}_2(\tau)$ is used as the weighting function. Defining $W_1(t)\equiv\overline{W}_1(\tau)$ and $W_2(t)\equiv\overline{W}_2(\tau)$, we obtain

Nomenclature

a = sonic velocity in fluid
C^+, C^- = characteristic line
D = inner diameter of line
g = acceleration due to gravity
H = head
h_f = headloss due to fluid friction per unit length
JT = integer given by Eq. (11)
K = number of time steps
L = length of line
N = subscript denoting point N
n = number of nodes along line
R = inner radius of line
R = subscript denoting point R
S = subscript denoting point S
t = time
u_J = state variable defined by Eq. (15)
V = average fluid velocity at line section
V_0 = initial value of average fluid velocity at the line section
W = weighting function
x = coordinate in axial direction of the line
y_i = state variable
z^{-1} = one-step delay
Δt = time increment, equal to $\Delta x/a$
Δx = increment in distance, equal to L/n
η_i = constant given by Eq. (5)
η_i' = $\eta_i\times\nu\Delta t/R^2$
ν = kinematic viscosity of fluid
τ = dimensionless time, equal to $\nu t/R^2$

$$h_{f1}(K\Delta t)=\frac{4\nu}{gR^2}\sum_{J=1}^{JT}[V((K-J+1)\Delta t) - V((K-J)\Delta t)]W_1\left(\left(J-\frac{1}{2}\right)\Delta t\right) \quad (13)$$

$$h_{f2}(K\Delta t)=\frac{4\nu}{gR^2}\sum_{J=JT+1}^{K}[V((K-J+1)\Delta t) - V((K-J)\Delta t)]W_2\left(\left(J-\frac{1}{2}\right)\Delta t\right). \quad (14)$$

If $u_J(K\Delta t)$ is defined by Eq. (15) as JT state variables which denote each velocity change at each point from the present to JT time intervals before,

$$u_J(K\Delta t)=V((K-J+1)\Delta t)-V((K-J)\Delta t) \quad (J=1\sim JT), \quad (15)$$

then the following relations are obtained.

$$u_1(K\Delta t)=V(K\Delta t)-V((K-1)\Delta t) \quad (16)$$

$$u_J((K+1)\Delta t)=u_{J-1}(K\Delta t) \quad (J=2\sim JT) \quad (17)$$

Using the definition of Eq. (15), we convert Eq. (13) into Eq. (18).

$$h_{f1}(K\Delta t)=\frac{4\nu}{gR^2}\sum_{J=1}^{JT}u_J(K\Delta t)W_1\left(\left(J-\frac{1}{2}\right)\Delta t\right). \quad (18)$$

Using Eq. (5) for $W_2(t)$ in Eq. (14) and defining $\eta_i' \equiv \eta_i \times \frac{\nu}{R^2}\Delta t$, we obtain

$$h_{f2}(K\Delta t)=\frac{4\nu}{gR^2}\sum_{J=JT+1}^{K}[V((K-J+1)\Delta t) - V((K-J)\Delta t)]\sum_{i=1}^{5}e^{-\eta_i'\left(J-\frac{1}{2}\right)}=\frac{4\nu}{gR^2}\sum_{i=1}^{5}y_i(K\Delta t), \quad (19)$$

where $y_i(K\Delta t)$ are five state variables defined by

$$y_i(K\Delta t)=\sum_{J=JT+1}^{K}[V((K-J+1)\Delta t) - V((K-J)\Delta t)]e^{-\eta_i'\left(J-\frac{1}{2}\right)}. \quad (20)$$

Therefore, from Eqs. (12), (18), and (19),

$$h_f(K\Delta t)=\frac{8\nu}{gR^2}V(K\Delta t)+\frac{4\nu}{gR^2}\sum_{J=1}^{JT}u_J(K\Delta t)W_1\left(\left(J-\frac{1}{2}\right)\Delta t\right)+\frac{4\nu}{gR^2}\sum_{i=1}^{5}y_i(K\Delta t) \quad (21)$$

$$h_f((K+1)\Delta t)=\frac{8\nu}{gR^2}V((K+1)\Delta t)+\frac{4\nu}{gR^2}\sum_{J=1}^{JT}u_J((K+1)\Delta t)W_1\left(\left(J-\frac{1}{2}\right)\Delta t\right)+\frac{4\nu}{gR^2}\sum_{i=1}^{5}y_i((K+1)\Delta t). \quad (22)$$

Then, assuming $J' = J - 1$, from Eq. (20), we obtain

$$\begin{aligned}y_i((K+1)\Delta t)&=\sum_{J'=JT}^{K}[V((K-J'+1)\Delta t) - V((K-J')\Delta t)]e^{-\eta_i'\left(J'-\frac{1}{2}+1\right)}\\&=[V((K-JT+1)\Delta t)-V((K-JT)\Delta t)]e^{-\eta_i'\left(JT-\frac{1}{2}+1\right)}\\&\quad+\sum_{J'=JT+1}^{K}[V((K-J'+1)\Delta t) - V((K-J')\Delta t)]e^{-\eta_i'\left(J'-\frac{1}{2}\right)}\times e^{-\eta_i'}. \quad (23)\end{aligned}$$

Applying the relations given by Eqs. (15) and (20) to Eq. (23), we obtain

$$y_i((K+1)\Delta t)=y_i(K\Delta t)e^{-\eta_i'}+u_{JT}(K\Delta t)e^{-\eta_i'\left(JT+\frac{1}{2}\right)}. \quad (24)$$

Therefore, $y_i((K+1)\Delta t)$ of Eq. (22) is obtained from $u_{JT}(K\Delta t)$ and the value of y_i at the previous time step. This computation is much easier than that of Eq. (20). The relations described by Eqs. (16), (17), (21), and (24) are shown in Fig. 2 by utilizing a block diagram expression for a discrete-time system. Here, z^{-1} represents a one-step delay. This block diagram is composed of a nonrecursive part on the left side and a recursive part on the right side.

Zielke's original method is shown in Fig. 3 using the relations described by Eqs. (12), (13), and (14). This block diagram is composed of only a nonrecursive part. Blocks of z^{-1} continue rightwards without limit.

3.2 Comparison With Other Methods. The new method is compared with other reported methods by showing them as block-diagram expressions for a discrete-time system.

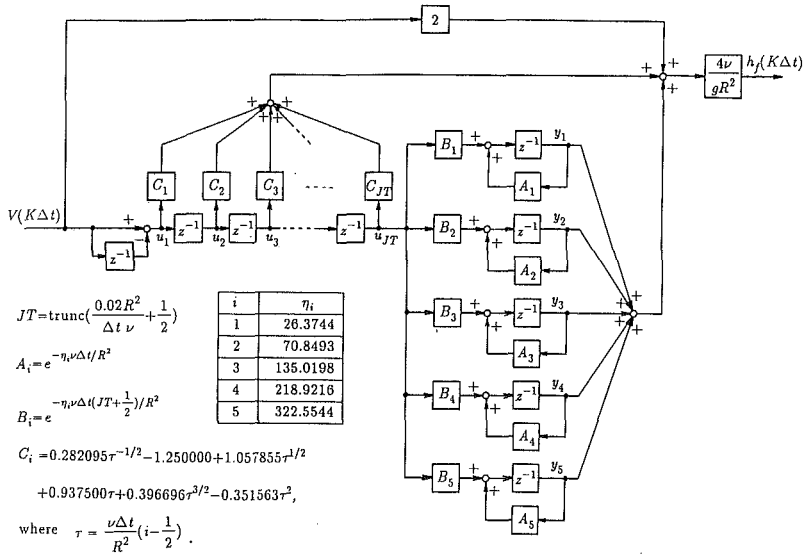

Fig. 2 Block-diagram representation of the new method

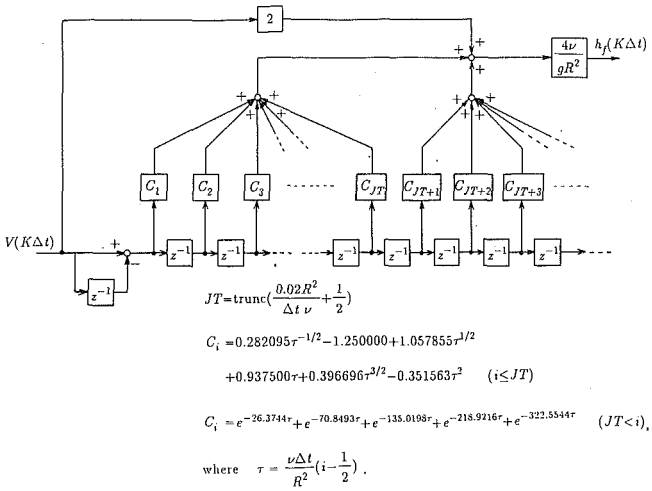

Fig. 3 Block-diagram representation of Zielke's method

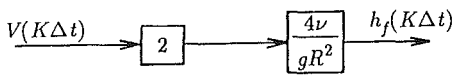

Fig. 4 Block-diagram representation of headloss of steady laminar flow friction

3.2.1 Steady-State Friction. If the headloss due to fluid friction per unit length, h_f, is taken to be steady-state laminar headloss, it is given by Eq. (25), using only the first term of the right side of Eq. (3).

$$h_f(t)=\frac{8\nu}{gR^2}V(t) \tag{25}$$

The relationship between h_f and V of this equation is shown by block-diagram expression in Fig. 4.

3.2.2 Trikha's Method. Trikha (1975) approximated Zielke's weighting function by three terms as shown by

$$\overline{W}(\tau)\approx\overline{w}_1(\tau)+\overline{w}_2(\tau)+\overline{w}_3(\tau). \tag{26}$$

Each term is the product of a constant and an exponential function as shown by

$$\overline{w}_i(\tau)=m_ie^{-n_i\tau} \quad (i=1,2,3), \tag{27}$$

where m_i and n_i are determined, so that the error will be small, by satisfying the conditions given by Trikha. The values are given in the table of Fig. 5.

Then, $y_i(t)$ is defined by

$$y_i(t)=\int_0^t m_ie^{-n_i(\nu/R^2)(t-u)}\frac{\partial V}{\partial t}(u)du \quad (i=1,2,3). \tag{28}$$

By Eqs. (26), (27), and (28), Eq. (3) becomes

$$h_f(t)=\frac{8\nu}{gR^2}V(t)+\frac{4\nu}{gR^2}[y_1(t)+y_2(t)+y_3(t)]. \tag{29}$$

Therefore, $h_f(t+\Delta t)$ is given by

$$h_f(t+\Delta t)=\frac{8\nu}{gR^2}V(t+\Delta t)+\frac{4\nu}{gR^2}[y_1(t+\Delta t)+y_2(t+\Delta t)+y_3(t+\Delta t)]. \tag{30}$$

Substituting $t+\Delta t$ instead of t of Eq. (28), rearranging it and assuming $\Delta t \ll 1$, we obtain

$$y_i(t+\Delta t)=y_i(t)e^{-n_i(\nu/R^2)\Delta t}+m_ie^{-n_i(\nu/R^2)(\Delta t/2)}\times[V(t+\Delta t)-V(t)]. \tag{31}$$

Assuming $\left|n_i\frac{\nu}{R^2}\frac{\Delta t}{2}\right| \ll 1$ and $e^{-n_i(\nu/R^2)(\Delta t/2)}\approx 1$, we derive

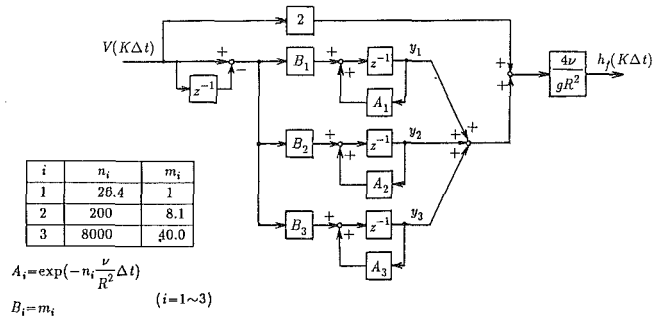

i	n_i	m_i
1	26.4	1
2	200	8.1
3	8000	40.0

Fig. 5 Block-diagram representation of Trikha's method

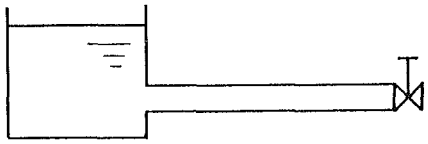

Fig. 6 Pipeline system

$$y_i(t+\Delta t)=y_i(t)e^{-n_i(\nu/R^2)\Delta t}+m_i[V(t+\Delta t)-V(t)]. \tag{32}$$

The $h_f(t)$ is calculated at high speed using the relations given by Eqs. (29) and (32). This computation process is shown in Fig. 5 by a block-diagram expression.

4 Results of Simulation

Figure 7 shows the pressure fluctuation simulated by each method at the downstream end of the simple pipeline system shown in Fig. 6 when a valve at the downstream end is shut instantaneously. Parameter values are shown in the table in Fig. 8. The microcomputer NEC PC9801VM2 is used for computation. The language is Microsoft MS-FORTRAN. Double precision is used. It is well known that the agreement between experimental results and calculated results by Zielke's method is very good. In the figure, no difference can be distinguished between the results of the new method and those of Zielke's method. The results of Trikha's method and the method which uses steady-state headloss both differ greatly from those of the aforementioned two methods. The values at intervals of 50 time increment steps are shown in Table 1 to distinguish in detail the difference between the two methods. It is seen that the results obtained by the new method and by Zielke's method agree for all the figures output by the computer. Therefore, it is confirmed by the simulation that the new method is mathematically equivalent to Zielke's, as was already deduced theoretically in section 3.1. By contrast, Trikha's method is an approximation of Zielke's.

Figure 8 shows the relationship between computation time and number of time steps, K, where the times for compilation and linking are excluded. The new method requires more computation time than Trikha's, but much less time than Zielke's. The computation time for Zielke's method increases exponentially with the number of time steps, K. It increases linearly with K in the new method, as in the other methods. The reason is as follows. When h_f is calculated by Zielke's method at each divided point along a pipeline, the required computation time increases exponentially because the velocity change, which must be multiplied by C_i and summed, increases with the number of time steps. Furthermore, the flow velocity (change), which must be stored, increases with the number of time steps until it finally exceeds the available capacity of the computer storage, and computation can no longer be continued.

In the new method, however, only the JT flow changes from u_1 to u_{JT} and the five variables from y_1 to y_5, for a total of $(JT+5)$ so-called state variables, need to be stored for each divided point along a pipeline. Because they give all the in-

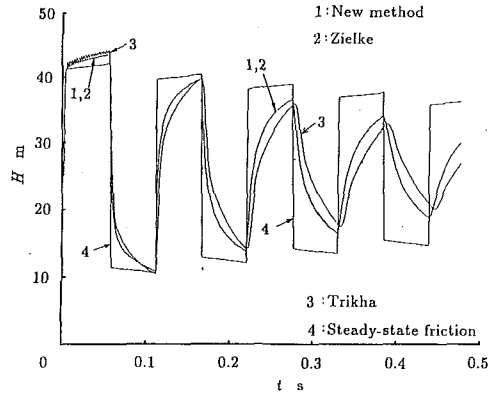

Fig. 7 Head fluctuation at valve after instantaneous valve closure

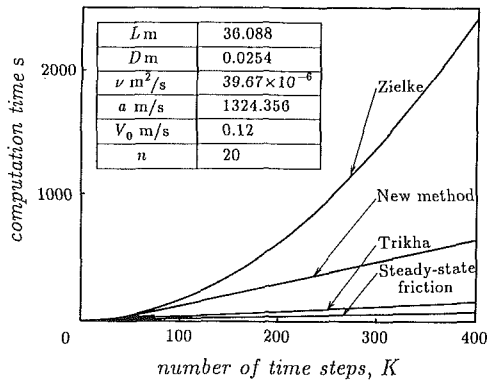

Fig. 8 Comparison of computation time (1)

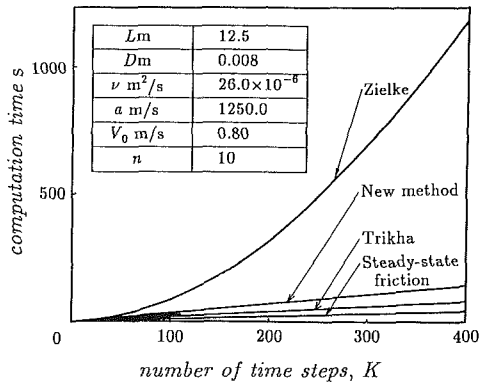

Fig. 9 Comparison of computation time (2)

formation required by Zielke's method, the amount of required computer storage does not increase to more than a constant. Each time-lag element shown by z^{-1} in Fig. 2 requires one unit of computer storage. Therefore, problems such as having to abandon the computation halfway because of a shortage of computer storage capacity are avoided. Computation time does not increase exponentially because h_f is obtained by multiplications and additions concerning a constant number of these state variables and the current flow velocity.

Table 1 Comparison of simulated results

	Head H m	
K	New method	Zielke
50	14.6394926066112	14.6394926066112
100	37.4583217988436	37.4583217988436
150	14.9335334239241	14.9335334239241
200	36.6867184170422	36.6867184170423
250	26.1166441615528	26.1166441615527
300	22.6642561308133	22.6642561308133
350	30.3956083019248	30.3956083019248
400	20.7437216511604	20.7437216511604

Figure 9 shows the computation time for a different parameter. The computation time is reduced drastically only by the new method. This is because the value of JT calculated by Eq. (11) becomes smaller and the number of iterations of calculation is reduced. Thus this method can especially be used to advantage in the case of the parameter which makes JT small.

5 Conclusions

Zielke's technique of using the method of characteristics to simulate transient phenomena of a liquid pipeline is accurate and widely used. However, it requires very much computation time and computer storage because evaluation of all past velocity changes is required when headloss is calculated taking transient laminar flow into consideration.

In this paper, it is clarified that a mathematically equivalent calculation without approximation can be computed in a shorter time and with less computer storage by improving Zielke's method. The new method eliminates the shortcoming of Zielke's method wherein the amounts of computer storage and computation time required to increase each time step increase without limit as the number of time steps increases. As a result, calculations which formerly required a large computer can now be performed easily on a personal computer. The calculation process is shown by block-diagram representation for a discrete-time system to make this concept more readily comprehensible.

References

Bratland, O., 1986, "Frequency-Dependent Friction and Radial Kinetic Energy Variation in Transient Pipe Flow," 5th International Conference on Pressure Surges, Hannover F. R. Germany, Paper D2, pp. 95–101.

Brown, F. T., 1962, "The Transient Response of Fluid Lines," ASME *Journal of Basic Engineering*, Vol. 84, No. 4, pp. 547–553.

Goodson, R. E., and Leonard, R. G., 1972, "A Survey of Modeling Techniques for Fluid Line Transients," ASME *Journal of Basic Engineering*, Vol. 94, No. 2, pp. 474–482.

Streeter, V. L., and Wylie, E. B., *Hydraulic Transients*, McGraw-Hill, New York, 1967.

Suzuki, K., 1989, "Application of a New Pressure Intensifier Using Oil Hammer to Pressure Control of a Hydraulic Cylinder," ASME *Journal of Dynamic Systems, Measurement, and Control*, Vol. 111, No. 2, pp. 322–328.

Suzuki, K., 1990, "A New Hydraulic Pressure Intensifier Using Oil Hammer," ASME JOURNAL OF FLUIDS ENGINEERING, Vol. 112, No. 1, pp. 56–60.

Trikha, A. K., 1975, "An Efficient Method for Simulating Frequency-Dependent Friction in Transient Liquid Flow," ASME JOURNAL OF FLUIDS ENGINEERING, Vol. 97, No. 1, pp. 97–105.

Zielke, W., 1968, "Frequency-Dependent Friction in Transient Pipe Flow," ASME *Journal of Basic Engineering*, Vol. 90, No. 1, pp. 109–115.

V. C. Patel
Professor.
Fellow ASME

J. Tyndall Chon
Graduate Research Assistant.

J. Y. Yoon
Graduate Research Assistant.

Department of Mechanical Engineering
and Iowa Institute of Hydraulic Research,
The University of Iowa,
Iowa City, Iowa 52242

Laminar Flow Over Wavy Walls

The boundary layer over a wavy wall and fully-developed flow in a duct with a wavy wall are considered. Numerical solutions of the Navier-Stokes equations have been obtained to provide insights into the various steady flow regimes that are possible, and to illustrate the nuances of predicting flows containing multiple separation and reattachment points.

Introduction

The literature in computational fluid dynamics abounds in studies related to the prediction of laminar separated flows by solution of the Navier-Stokes equations. By and large, most definitive studies have been confined to simple rectangular geometries, such as the driven cavity, forward- and backward-facing steps, and obstructions in ducts. In many of these problems, the point of primary separation is fixed by the geometry, and solutions are often obtained at rather small Reynolds numbers. For the classical problem of predicting boundary-layer separation from a curved surface at large Reynolds numbers, however, there are very few reliable Navier-Stokes solutions of flows involving separation and reattachment. Such flows are analyzed, instead, by inverse and interactive solutions of the boundary layer equations. In the development of general and versatile numerical methods for Navier-Stokes equations it is obviously of interest to consider flows of the boundary layer type at high Reynolds numbers. The present study is motivated, in part, by this need. Therefore, we consider flows which could be regarded as more demanding test cases for numerical methods. This study also serves as a prelude to a companion study of turbulent flow, which is reported separately (Patel et al., 1991).

We consider two model problems. The first is the flow past a flat plate with a sinusoidal cavity, as shown in Fig. 1, and the second is the flow in a straight duct with one of the walls becoming wavy after a development length sufficient to establish a fully developed flow, as shown in Fig. 2.

The reason for choosing the first problem is that, by suitable choice of the cavity depth, it is possible to examine flows with different separation patterns. In some respects this problem resembles the driven cavity, but the differences are more significant. Here we are dealing with a flow that originates from a well-known initial condition, namely, the Blasius solution.

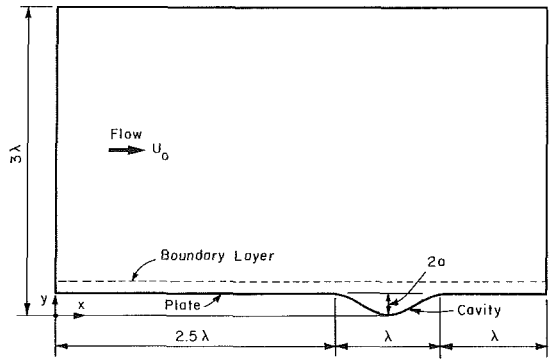

Fig. 1 Boundary layer on a wall with a cavity; solution domain and notation

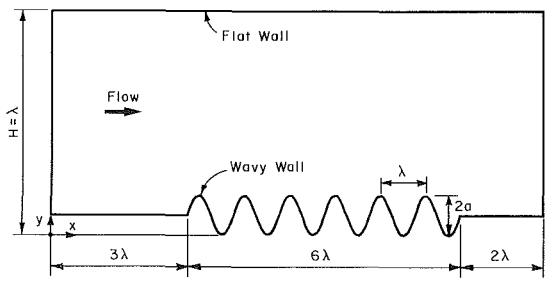

Fig. 2 Flow in a channel with a wavy wall; solution domain and notation (not to scale)

Also, it is a high Reynolds number external flow, with boundary layer separation and reattachment points not known a priori. The recovery of the boundary layer downstream of reattachment is also of basic interest. There exists a limited amount of experimental data (Saidi et al., 1987) for this con-

Contributed by the Fluids Engineering Division for publication in the JOURNAL OF FLUIDS ENGINEERING. Manuscript received by the Fluids Engineering Division October 23, 1990.

figuration and, therefore, comparisons can be made to evaluate some aspects of the calculations.

The second model problem is one of internal flow. Here again, the upstream conditions are well known and easily defined. The geometry is also relatively simple. The flow features of particular concern, both from numerical as well as physical viewpoints, are the adjustment of the initially fully developed flow to a spatially periodic condition and, for specific amplitudes, the occurrence of repeated separation bubbles. Such configurations are of interest in drag reduction and heat-transfer enhancement. While there is no detailed experimental data for this model problem, it serves to introduce the corresponding problem of turbulent flow, which poses additional challenges and for which quite extensive data have been gathered.

The numerical method used here is basically that described by Chen and Patel (1987). The version employed here solves the full Navier-Stokes equations in primitive variables for unsteady, two-dimensional, incompressible flow in generalized, nonorthogonal coordinates. The momentum equations are discretized using analytic solutions of the linearized equations in each numerical cell, and the pressure-velocity coupling is made through the continuity equation using a modified version of the SIMPLER algorithm. Although the numerical method solves the unsteady-flow equations in a time-marching scheme, the present work is confined to steady flows; time is used as an iteration parameter to seek the steady-state solution.

Boundary Layer on a Wall With a Sinusoidal Cavity

Consider the geometry shown in Fig. 1, which is similar to the configuration in the experiments of Saidi et al. (1987). The boundary layer develops on a flat plate with a sinusoidal cavity of depth $2a$ and wave length λ, beginning at a distance 3λ from the plate leading edge. In the experiments, $2a/\lambda = 0.2$, and the Reynolds number $U_0\lambda/\nu = 10{,}760$, U_0 being the freestream velocity and ν the kinematic viscosity.

The selected solution domain is shown in Fig. 1. The upstream boundary ($x = 0$), where the velocity components are specified according to the Blasius solution, is located at a distance of 0.5λ from the plate leading edge. The downstream boundary is at $x = 4.5\lambda$, which allows a recovery length of one wave length beyond the cavity. At this boundary, the parabolic condition of zero streamwise pressure gradient is imposed. In the direction normal to the plate, the boundary is placed at $y = 3\lambda$, y being measured from the bottom of the cavity. It was verified that this is sufficiently far from the plate for the effects of the cavity to be negligible and uniform-flow conditions to be applied. On the plate itself, the no-slip condition is applied. Due to the ellipticity of the equations and the time-marching scheme used, initial conditions at every point in the flow field are formally required. In the approach used here, the solution is initiated by carrying out a parabolic march, starting from the upstream section $x = 0$, with the pressure set to zero throughout.

The numerical grids were generated by solving two Poisson equations, following the method of Knight (1982). For the geometry of Saidi et al., solutions were obtained with 69×35, 128×70, and 134×82 points, in the longitudinal and normal directions, respectively. The first grid was judged to be too coarse, while the last was the finest that could be accommodated on a CRAY XMP/48 supercomputer. In the finest grid, the points nearest the wall were placed at a nondimensional distance (y/λ) of the order of 10^{-5}. Solutions obtained with the finest grid will be presented here, but the results with the intermediate one, as noted later, were not substantially different. 550 iterations were performed, which took 12 minutes of CPU time. Satisfactory convergence was achieved in about 450 iterations.

Figure 3 shows the solutions for the pressure and friction coefficients on the wall. All quantities are normalized by the

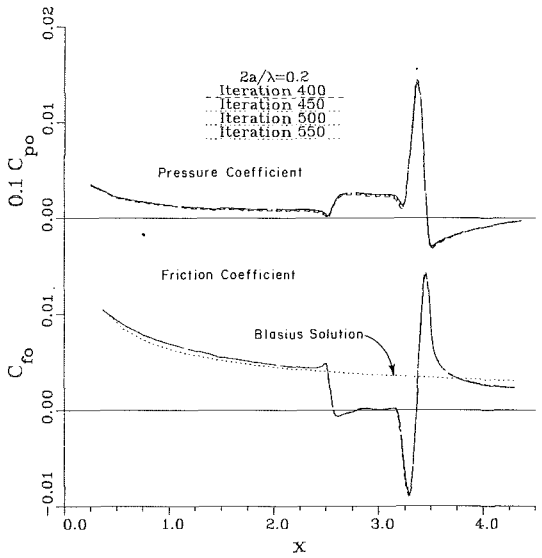

Fig. 3 Distributions of pressure and friction coefficients; note convergence history

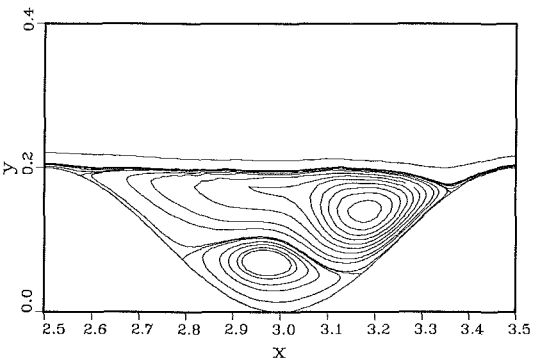

Fig. 4 Streamlines of flow in the cavity

reference velocity U_0 and the wavelength λ. The results may be compared with the Blasius solution ($C_{po} = 0$, $C_{fo} = 0.664\, R_x^{-1/2}$) to gage the influence of the initial conditions and recovery of the boundary layer downstream of the cavity. The streamlines are shown in Fig. 4.

First of all, it is seen that there exists a small favorable pressure gradient almost up to $x = 2.0$, well ahead of the cavity. Such a gradient is observed also in the absence of the cavity and is associated with viscous-inviscid interaction which cannot be ignored at these low Reynolds numbers. In other words, first-order boundary-layer theory is still not applicable at these Reynolds numbers. The Blasius solution used as an initial condition is, therefore, an approximation. Figure 3 shows, however, that the friction coefficient and therefore the velocity profile through the boundary layer is not affected much by this assumption. The influence of the start of the cavity, at $x = 2.5$, is seen to extend only a short distance upstream, as a slight favorable pressure gradient. Once the flow enters the cavity, however, it meets an adverse pressure gradient, and shortly thereafter separates, as evidenced by the region of negative skin friction and backflow. As seen more clearly from Fig. 4, a second eddy also forms, so that the flow in the region $2.797 < x < 3.160$ is again in the positive direction at the boundary, although isolated from the main flow above the cavity. Where this secondary separation zone ends, there is again a very strong adverse pressure gradient, and backflow at the wall causes another region of negative skin friction. Shortly before $x = 3.50$, which marks the end of the cavity,

the pressure gradient becomes favorable and reattachment of the primary separation occurs. Thus, the region of separated flow is very large, as it occupies almost the entire cavity. The flow separates first at $x = 2.585$, and the last point of attachment is at $x = 3.358$. Here we note that the separation and reattachment points predicted with the less finer (intermediate) grid were within 0.002 of the values quoted above for the finest grid.

Figure 5 shows the profiles of the Cartesian velocity component u at eight x stations along the wall. The variable n is dimensionless distance along the curvilinear coordinate normal to the boundary. The data of Saidi et al. (1987) are also shown in the figure. It should be noted that these measurements were made with a single channel laser-Doppler velocimeter, without a Bragg cell to sense flow direction, and therefore, only the magnitude of u was determined. Consequently, the data are suspect at points within the cavity.

The first profile shown is at a station ($x = 1.96$) before the influence of the cavity is felt, and exhibits the expected flat plate boundary layer behavior. The next station is at the beginning of the cavity ($x = 2.50$). The third station shown, $x = 2.60$, is just after the predicted primary separation point, and the calculations indicate slightly negative u velocity component close to the wall. At the following two stations, $x = 2.81$ and 2.99, the flow near the wall is again in the forward direction, since it is within the secondary eddy, while the rest of the flow in the cavity is reversed. A strong shear layer is clearly evident around $n = 0.15$. By $x = 3.20$, the flow nearest the wall as well as in the cavity is again reversed, since this is beyond the zone of the secondary eddy. Finally, at $x = 3.50$, which marks the end of the cavity, the flow recovers from separation. As shown in Fig. 3, the recovery to Blasius conditions is not completed until much later, around $x = 4.50$. The agreement of the computed values of the Cartesian velocity component u with the experimental data is satisfactory at the start of the cavity, but thereafter the two disagree greatly within the cavity, presumably due to the lack of directional sensitivity in the experimental data as noted earlier. The comparison of $x = 2.60$ suggests that the calculations predict a somewhat earlier separation than that observed in the experiments.

A parametric study was performed next, to determine the effect of varying the cavity depth while keeping the cavity location fixed. Three values of the quantity $2a/\lambda$ were used: 0.02, 0.10, and 0.40. The smallest cavity showed no separation while the next indicated a single eddy. This is to be compared with the two eddies observed in the case $2a/\lambda = 0.20$ discussed above. In all of these cases, no difficulty was encountered in obtaining a converged steady-state solution. This was not the case, however, for the deepest cavity considered, $2a/\lambda = 0.40$.

For this case, numerous calculations performed with different grids and time steps failed to yield a stationary solution. Instead, in all attempts, the solution tended to become periodic, with a regular frequency, after an initial transient period. The periodicity, however, was confined to the flow in the cavity, with the flow upstream and downstream being independent of time. Within the cavity itself, two to three eddies were observed at various times in the oscillation cycle. Recall that a time-marching numerical method capable of predicting time-varying flow is employed here. In the present case, the unsteadiness is self induced but its origin is not clear. The numerical tests performed, and the regularity of the solutions obtained, suggested the existence of two steady-state solutions, between which the numerical solution oscillated.

In a recent paper, Rubin and Himansu (1989) have reported a similar behavior of numerical solutions for flow in sinusoidal cavities and tentatively attributed the oscillations to a physical instability, i.e., the tendency of the flow to amplify small disturbances. Somewhat related to this is the work of Nayfeh et al. (1988), who used interactive laminar boundary-layer theory to calculate the flow past bulges (hills) and dips (cavities)

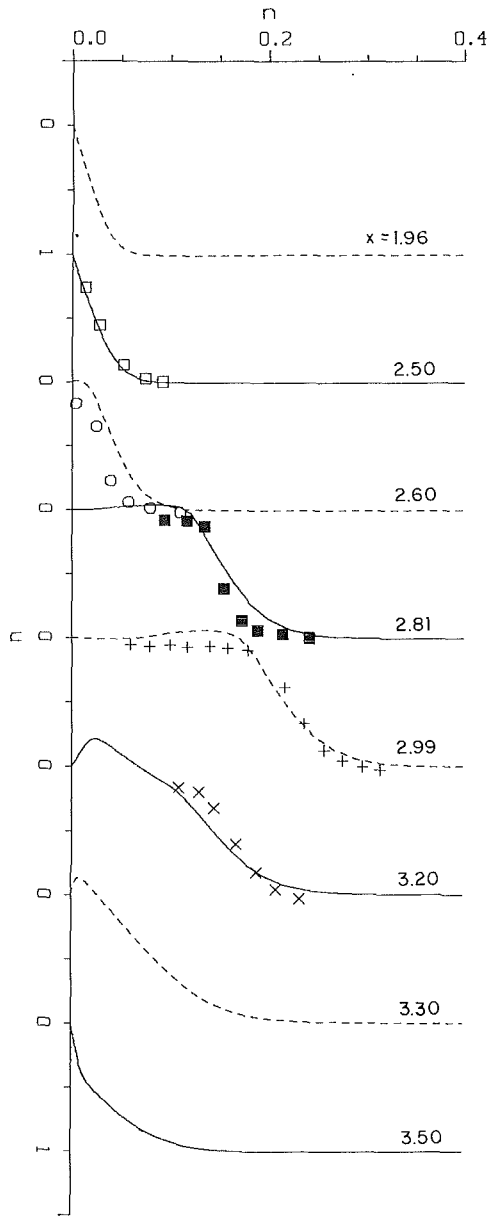

Fig. 5 Velocity profiles; lines: calculations; symbols: data of (Saidi et al., 1987)

in a flat plate and then applied linear stability theory to observe the response to small disturbances. Among other things, they showed that increasing the size of the separation bubble, by increasing either the height-to-wavelength ratio or the Reynolds number, led to increased growth rates of disturbances and earlier transition to turbulence. Obviously, these are issues requiring considerable further work. The numerical method employed here is a useful tool for the investigation of these aspects.

Channel With a Wavy Wall

Next, consider the internal flow in the duct of Fig. 2. Calculations were performed with two upstream conditions; developing flow with thin boundary layers at entry, and fully-developed flow with a parabolic velocity profile at entry. Insofar as the effects of the wavy wall are concerned, the two sets of results are qualitatively similar and, therefore, only the second case will be discussed here.

Calculations were performed for a channel Reynolds number, $UH/\nu = 10{,}760$, where U is the average velocity and $H(=\lambda)$ is the channel height. This is the same value as in the case of the single cavity considered above. It should be noted, however, that this value is considerably higher than the Reynolds number at which transition is observed in a plane channel. Indeed, the value chosen here is of the same order as those used in studies of turbulent flow (see Patel et al., 1991). Therefore, the present solution should be regarded as an experiment designed to test numerical methods for separated flows. The solution domain is shown in Fig. 2. Six sinusoidal waves, with a depth-to-wavelength ratio $2a/\lambda = 0.20$, are located on the lower wall in the region $3.0 < x < 9.0$. The straight sections upstream and downstream of the wavy section are 3H and 2H long, respectively. At the upstream boundary ($x = 0$), the velocity distribution is parabolic and the flow is parallel. At the downstream boundary, the streamwise pressure gradient is assumed to be zero, corresponding to an exit into a reservoir. No-slip condition is applied at both walls. The grid in this case had 328 × 99 points, 50 along each of the six waves, and 99 across the channel. The points nearest the walls are again at nondimensional distances of the order of 10^{-5}. This grid is comparable to the one used in the previous example, and similar level of grid independence of separation and reattachment points was observed.

As Fig. 6 shows, satisfactory convergence to steady state was achieved after about 550 iterations. This figure also shows a number of other important aspects of the flow. First, on the flat wall, the effect of the waves in the opposite wall is felt only through an increased pressure gradient and increased friction coefficient. The total drop in pressure due to the wavy section indicates a substantial increase in resistance over that in fully-developed flow in a flat-walled channel. From the waveform of the pressure and friction distributions on the wavy wall, it is seen that the solution becomes spatially periodic after about the third wave. Note that, in the case of pressure, there is a superimposed constant pressure gradient. The spatial periodicity was ascertained by comparing distributions of velocity components at corresponding locations in successive waves. This periodicity suggests that, if upstream and downstream effects of a wavy segment are not of interest, solutions for a single wave could be obtained by use of periodic boundary conditions, as has been done in many previous studies, for example, by Garg and Maji (1988) and Ralph (1987).

An examination of the friction distribution reveals multiple sign reversals, indicating several zones of separation and eddies. In fact, there is a region of separation just ahead of the first wave and two eddies in each of the six wave cavities. This is seen from Fig. 7 in which are plotted the pressure and friction distributions, and the corresponding streamlines, over one wave, from the fifth peak to the sixth peak, i.e., $7.25 < x < 8.25$. The pressure in the eddies is nearly uniform except for changes associated with the primary separation and reattachment. The first separation takes place in a moderate adverse pressure gradient while there is strong adverse pressure gradient just before and after the last reattachment. The lack of strong pressure gradients accompanying the secondary separation and reattachment indicates that the secondary eddy is very weak. The friction coefficient under the eddies is very small except in a region ahead of reattachment, where it is large and negative.

Because the numerical solutions give the distributions of friction and pressure on both walls of the channel, it is of interest to evaluate the components of resistance associated with the two walls. Integration of friction and pressure coefficients on the lower, wavy wall over a wavelength gives a resistance coefficient, based on bulk velocity and channel height, of 0.00982. Of this, 0.00108 is due to friction and 0.00874 to pressure. From the flat wall there is a contribution only from friction, and this is 0.00289. The total channel resistance over a wavelength, therefore, is 0.01271. This may be compared with the well known plane Poiseuille solution for laminar flow in a channel, which yields, for the present Reynolds number, a value of 0.00223, with equal contributions from friction on the two walls. Thus, the wavy wall results in (*a*) an increase in friction on the opposite flat wall, (*b*) a decrease in average friction on the wavy wall, and (*c*) a significant pressure or form drag on the wavy surface.

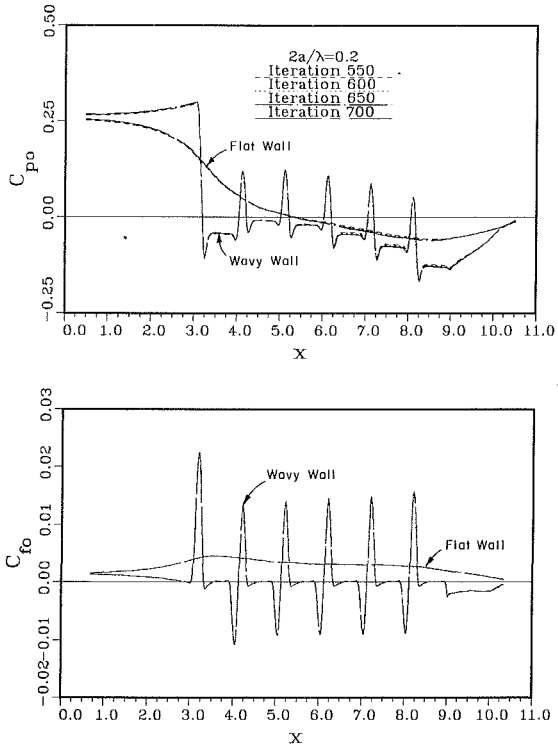

Fig. 6 Convergence of pressure and friction coefficients on the channel walls

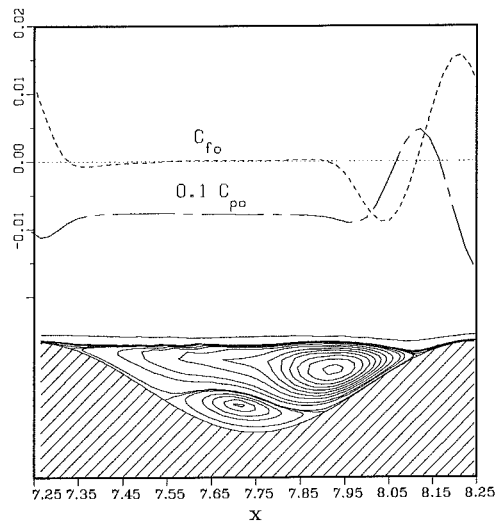

Fig. 7 Pressure and friction coefficients, and flow streamlines in the fifth wave cavity

The results shown in Fig. 7 are, in general, quite similar to those observed in the case of the developing boundary layer over a single cavity considered above. The detailed velocity profiles were also found to have similar features and, therefore, are not shown here. Finally, it is of interest to note that, insofar

as the flow in a single cavity is concerned, the present results are consistent with those calculated by others (Sobey, 1980; Garg and Maji, 1988; Ralph, 1987), using quite different numerical methods, albeit for different amplitude-to-wavelength ratios and much lower Reynolds numbers.

Conclusions

Two flows involving wavy boundaries, a boundary layer and a channel, have been studied through numerical solutions of the Navier-Stokes equations. These flows were selected to minimize the usual uncertainties associated with the prescription of boundary conditions because the upstream and downstream states are well known. Thus, it has been possible to isolate the problems of predicting separation and reattachment points. The range of flow phenomena observed suggests that these two problems are very effective test cases for numerical methods.

The method employed in the present study yielded stable and steady solutions for flows with multiple separation bubbles. In the case of the boundary layer over a plate with a single sinusoidal cavity, the results compared favorably with the limited data that are available. At comparable Reynolds number and cavity depth, stable laminar solutions were also obtained in channel flow. However, there is no experimental data to validate these solutions but, as transition is known to occur at much smaller Reynolds numbers in a plane channel, it is unlikely that this flow is stable in reality. A parametric study revealed that for deep enough cavities, the flow tends to become unsteady, presumably as a result of an instability and transition to turbulence. This feature of the problem deserves a more detailed analysis to separate the numerical and physical aspects.

Acknowledgments

This research was partially supported by the Office of Naval Research, under Contract N00014-88-K-0001. The calculations were performed on the CRAY XMP/48 of the National Center for Supercomputing Applications (NCSA), Champaign, Ill.

References

Chen, H. C., and Patel, V. C., 1987, "Laminar Flow at the Trailing Edge of a Flat Plate," *AIAA J.*, Vol. 25, pp. 920–928.

Garg, V. K., and Maji, P. K., 1988, "Laminar Flow and Heat Transfer in a Periodically Converging-Diverging Channel," *Int. J. Numer. Methods in Fluids*, Vol. 8, pp. 579–597.

Knight, D. D., 1982, "Application of Curvilinear Coordinate Generation Techniques to the Computation of Internal Flows," *Numerical Grid Generation*, Elsevier Sci. Publ. Co., pp. 357–384.

Nayfeh, A. A., Ragab, S. A., and Al-Maaitah, A. A., 1988, "Effect of Bulges on the Stability of Boundary Layers," *Phys. Fluids*, Vol. 31, pp. 796–806.

Patel, V. C., Chon, J. T., and Yoon, J. Y., 1991, "Turbulent Flow in a Channel with a Wavy Wall," ASME JOURNAL OF FLUIDS ENGINEERING, published in this issue pp. 579–586.

Ralph, M. E., 1987, "Steady Flow Structures and Pressure Drops in Wavy-Walled Tubes," ASME JOURNAL OF FLUIDS ENGINEERING, Vol. 109, pp. 255–261.

Rubin, S. G., and Himansu, A., 1989, "Convergence Properties of High Reynolds Number Separated Flow Calculations," *Int. J. Numer. Methods in Fluids*, Vol. 9, pp. 1395–1412.

Saidi, C., Legay-Desesquelles, F., and Prunet-Foch, B., 1987, "Laminar Flow Past a Sinusoidal Cavity," *Int. J. Heat & Mass Transf.*, Vol. 30, pp. 649–661.

Sobey, I. J., 1980, "On Flow Through Furrowed Channels. Part 1. Calculated Flow Patterns," *J. Fluid Mech.*, Vol. 96, pp. 1–26.

V.C. Patel
Professor,
Fellow ASME

J. Tyndall Chon
Graduate Research Assistant.

J.Y. Yoon
Graduate Research Assistant.

Department of Mechanical Engineering
and Iowa Institute of Hydraulic Research,
The University of Iowa
Iowa City, Iowa 52242

Turbulent Flow in a Channel With a Wavy Wall

A numerical method for the solution of the Reynolds-averaged Navier-Stokes equations, together with a two-layer turbulence model, has been used to describe steady flow in a two-dimensional channel with a wavy wall. Comparisons of calculations with experiments demonstrate the effects of alternating pressure gradients induced by alternating surface curvatures, and multiple separations and reattachments. The numerical method and the turbulence model are shown to capture the overall features of such a flow, including the breakdown of the logarithmic law of the wall in strong pressure gradients and in separated flow.

Introduction

The study of flow over a wavy boundary is hardly a recent undertaking. It is of interest in the generation of water waves by wind, evolution of sand dunes in deserts and sediment dunes in rivers, melting of ice covers on rivers, enhancement of heat and mass transfer, and possibly drag reduction. There is extensive previous work in most of these areas. Theoretical approaches have included applications of linear stability theory, boundary-layer theory, solutions of the Navier-Stokes equations, and solutions of the Reynolds-averaged Navier Stokes equations with different types of turbulence closure models. Periodicity is generally assumed so that solutions are obtained only for a single wave. Experimental studies have included field observations and laboratory investigations. In the latter, internal and external flows have been considered in addition to flow in open channels.

From the perspective of viscous-flow theory, the flow over a wavy boundary, whether laminar or turbulent, is much more complex than that over a flat surface because of the additional parameters and flow phenomena that are involved. For example, for fully developed flow in a channel or pipe, we have, in addition to the Reynolds number, the ratios λ/H and a/λ, where a is wave amplitude, λ is the wavelength, and H the channel height or pipe diameter. For developing boundary-layer flows, the conditions of the boundary layer upstream and the number of waves must be considered. In either case, for wave amplitudes greater than some critical value at any Reynolds number, the flow involves multiple regions of separation and reattachment. Description of turbulent flow past a wavy surface involves a number of challenges. In addition to the effects of the alternating favorable and adverse pressure gradients, and convex and concave surface curvatures on the turbulence, there is the difficulty of predicting the separation and reattachment points. For laminar as well a turbulent flows, there exists the possibility of self-induced unsteadiness of the flow in the cavities and associated vortex shedding. To all of these complications must be added problems associated with moving and deforming boundaries, such as those at the surface of a liquid or at a sedimentary bed, and the evolution of waveforms of arbitrary shape.

The present study is concerned with numerical solutions of steady turbulent flow in a two-dimensional channel with a fixed sinusoidally wavy wall. The study was motivated by the need for more comprehensive numerical models for some of the practical applications noted above. Of particular concern here is the description of the mean flow in the neighborhood of the wall in the presence of successive separations and reattachments. The channel configuration was selected, as against developing boundary-layer flows, for several reasons, the most important being that it has been studied rather extensively over a number of years in a series of experiments conducted by Hanratty and his students (see Table 1). Another compelling reason is that this geometry represents an excellent test case for numerical methods and turbulence models as it avoids the usual uncertainties concerning initial and boundary conditions.

The numerical method used here is a derivative of that described by Chen and Patel (1987) and Richmond and Patel (1991) for the solution of the Reynolds-averaged Navier-Stokes equations for unsteady flow in generalized, nonorthogonal coordinates. No simplifications or approximations are made in these equations other than those implicit in the turbulence model. The two-layer approach to turbulence modeling suggested by Chen and Patel (1988) has been used. In this approach, the standard two-equation k-ϵ turbulence model is combined with a simpler, one-equation model for the flow close to the wall. The momentum and turbulence transport equations are discretized using analytic solutions of the linearized equations, and the pressure-velocity coupling is made through the continuity equation using the SIMPLER algorithm. Applications of this numerical method to other configurations with laminar flow are described in Patel et al. (1991). Turbulent flows over convex and concave surfaces are discussed in Richmond and Patel (1991) where it is shown that

Contributed by the Fluids Engineering Division for publication in the JOURNAL OF FLUIDS ENGINEERING. Manuscript received by the Fluids Engineering Division October 23, 1990.

Table 1 Summary of the Experiments of Hanratty et al.

References	Measurements Made	Re	2a/λ	Flow Features Observed
Zilker et al. (1977)	wall pressure, wall shear,	6,000– 64,000	0.0125 0.03125	linear shear stress response linear shear stress response
Zilker et al. (1979)	mean velocity, turbulent velocity, flow visualizations		0.05 0.125 0.20	instantaneous flow reversal separated flow separated flow
Thorsness et al. (1978)	wall shear mean velocity	11,000– 64,000	0.0114 0.0125	linear shear stress response linear shear stress response
Buckles et al. (1984)	mean and fluctuating velocities and wall pressure	24,000	0.02	separated flow
Abrams et al. (1981, 1986)	mean and fluctuating wall shear	11,940– 245,000	0.014	linear shear stress response
Frederick et al. (1986, 1986)	mean and fluctuating velocities	12,800 77,600	0.03125* 0.05	linear shear stress response nonlinear stress response
Kuzan (1986)	wall pressure, mean and fluctuating velocities, flow visualization	96,000 17,000 8,160	0.125 0.05 0.20*	instantaneous flow reversal instantaneous flow reversal separated flow

*Present calculations were performed for these two cases.

the turbulence model used here tends to overpredict the convex wall skin friction and underpredict that on the concave wall. Unfortunately, it is not possible to separate the curvature effects from those of pressure gradients in the present case. Therefore, explicit curvature corrections are not included in the present work.

Experimental Information

As noted above, there have been a number of previous experimental studies in turbulent flows with wavy boundaries. Examples of those limited to fixed boundaries include the work of Sigal (1971), Cary et al. (1980), who studied boundary layers, Hsu and Kennedy (1971) and Chauve and Schiestel (1985), who considered fully developed flow in circular pipes, and the extensive work of Hanratty et al., summarized in Table 1, in two-dimensional channels. Even for this last case considered here, there is a large body of experiments in which various aspects of the flow were studied. These experiments were all conducted in the same water-channel facility, although there were variations in the measurement techniques. In a rectangular channel, 2 in. high, 24 in. wide, and 35 ft. long, removable wavy surfaces were placed in the last 27 inches of the bottom wall. In all cases, a wavelength of 2 in. was used, with ten waves in the test section. The waves were sinusoidal, so that the surface height y_s was defined by $y_s = a \sin \alpha x$, where $\alpha = 2\pi/\lambda$ is the wave number. Fully developed flow was obtained in the channel before the test section, and in all cases, spatially periodic conditions were found to have been established early in the wavy test section. Therefore, most detailed measurements were made only over a single wave.

Table 1 summarizes the measurements made and the parameters used in the various experiments, including the ratio $2a/\lambda$ and the Reynolds number, $\mathrm{Re} = UH/\nu$, based on the bulk velocity U, channel height H (= 2 in.), and the kinematic viscosity ν. Note that $H/\lambda = 1$ in all the experiments. Table 1 also notes the most important flow characteristics observed in the experiments. Depending upon the Reynolds number and wave amplitude, different flow regimes are possible. Figure 1, adapted from Frederick (1986), shows the boundaries between these regimes; $\alpha\nu/u_\tau$ being the reciprocal of the Reynolds number based on the length $\lambda/2\pi$ and the wave-averaged wall shear velocity u_τ. As expected, a linear response is observed for small amplitudes and low Reynolds numbers. As both increase, a nonlinear response is observed. At any Reynolds number, there is a wave amplitude above which separated flow is observed. Needless to say, the experimentally established boundaries between the regimes are not precise.

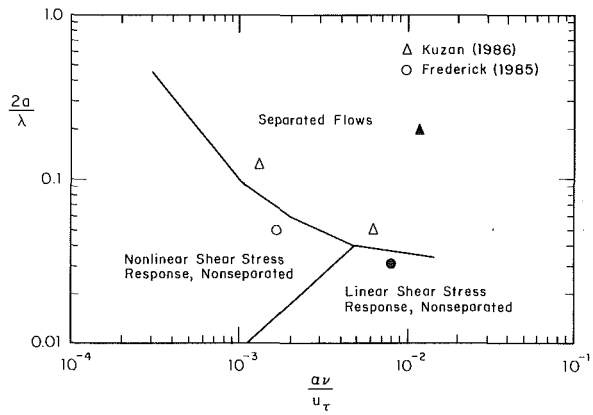

Fig. 1 Regimes of flow in the experiments of Hanratty et al.; after Frederick; conditions for present calculations indicated by solid symbols.

Calculations and Results

Two sets of calculations, corresponding to an experiment of Frederick (1986) in the linear response regime, and one of Kuzan (1986) in the nonlinear separated-flow regime, have been performed. These cases are identified in Table 1 and Fig. 1. Each calculation was performed in two parts, one for the upstream straight channel to establish the proper initial conditions and the other for a portion of the straight and the wavy sections.

For the straight portion, a length of 80H was used, and calculations were made with a grid of 81 streamwise and 99 cross-stream nodes, with the first grid point off the walls at y^+ ($= u_\tau y/\nu$) around 0.01. Starting with approximate initial conditions at time zero, converged steady state solutions were obtained in about 100 iterations (time steps). Note that the distributions of velocity and turbulence parameters in fully-developed flow at sufficiently large distances from entry, typically 60 channel heights, should be independent of the initial conditions and become invariant with distance. This was ascertained in the present calculations. The velocity field and turbulence parameters thus calculated in the fully developed flow were used as the initial conditions for the subsequent wavy-wall calculations. The same distribution of grid across the channel was maintained in both calculations so that the initial conditions could be used without interpolation. It should be emphasized that this method of establishing initial conditions requires the specification of only the channel Reynolds

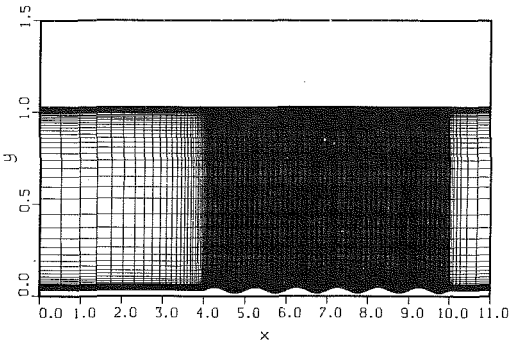

Fig. 2 Solution domain and grid for $2a/\lambda = 0.03125$

number, all other information being generated consistently from the solution of the governing equations. This removes the usual uncertainties about initial conditions and makes the present calculations truly predictive.

In the presentation of the results, all quantities, including pressure and friction coefficients, are normalized by the bulk velocity (U) in the channel, the wave length ($\lambda = H$), and the fluid properties (density ρ, and kinematic viscosity ν).

Wavy Wall With $2a/\lambda = 0.03125$, Re = 12,800; Attached Flow. The solution domain and grid used for this case are shown in Fig. 2. In the solution domain, an upstream section, 4λ in length, allows the flow to adjust to the wavy section, and a downstream section, of length λ, is used for flow recovery. The wavy section begins with a positive slope to match the experimental configuration. The initial conditions were applied at $x = 0$. Note that the distance y across the channel is measured from the bottom of the waves.

The grid was generated by solving two Poisson equations, with a two-step transformation, following the method of Knight (1982). There are 328 × 99 grid points. Over each of the six sinusoidal waves in the lower boundary, there are 50 nodes. As will become evident from the results, the distance of the first grid point from each wall is such that there are several points within the viscous sublayer. It should be noted here that extensive grid-dependency tests have been performed in the course of previous studies employing this combination of numerical method and turbulence model (see, for example, Chen and Patel (1988), Richmond and Patel (1991), and Patel et al. (1991)), and the present grid was chosen on the basis of these studies to ensure that the results obtained were insensitive to grid refinement.

Six hundred iterations were used, taking approximately 60 minutes on a Cray XMP-48. Figure 3 shows the pressure and friction coefficients calculated after 450 iterations, at intervals of 50 iterations. The results are practically indistinguishable and show that satisfactory convergence was achieved after about 450 iterations. It is also seen that there is a pressure drop along the channel, superimposed on the changes in pressure over the boundary waves. Initially the pressure and friction coefficients on both the upper and lower boundaries coincide, as would be expected in a duct with flat walls. The influence of the wavy section is seen to begin upstream of its origin, which is at $x = 4.0$. Conditions at the upper boundary appear to be little affected by the wavy section. The behavior of both the pressure and the friction coefficients in the straight exit section imply that this section was not long enough to allow for complete recovery of the flow to straight-duct conditions.

Figure 3 indicates that the flow becomes spatially periodic rather quickly, establishing almost fully-periodic conditions by the second or third wave. The spatial periodicity was ascertained by comparing the profiles of velocity components and turbulence parameters, such as the turbulent kinetic energy (k), the rate of energy dissipation (ϵ), and the Reynolds shear stress ($\overline{uv}$), at corresponding positions on successive waves.

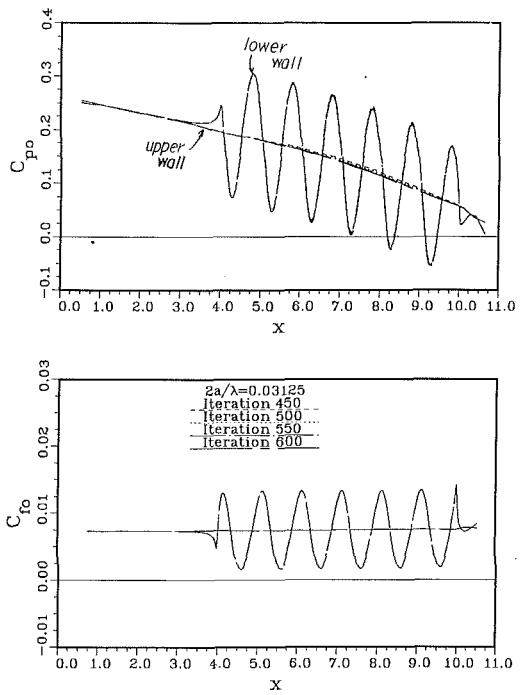

Fig. 3 Convergence of pressure and friction coefficients, $2a/\lambda = 0.03125$. Note: Results for different iterations are indistinguishable in most respects.

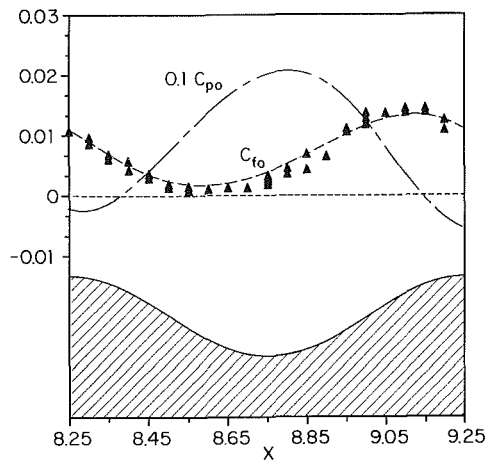

Fig. 4 Pressure and friction coefficients over a single wave. Lines: calculations; symbols: experiment.

The observed periodicity suggests that, if upstream and downstream effects of a wavy segment are not of interest, solutions for a single wave could be obtained by use of periodic boundary conditions. However, such boundary conditions cannot be established without prior knowledge of the flow, particularly with regard to the turbulent quantities. Calculations of the type performed here are indeed necessary to obtain the proper boundary conditions if solutions are to be restricted to a single wave.

The distributions of pressure and friction coefficients over the fifth wave, $8.25 < x < 9.25$, are shown in Fig. 4, along with the wave profile. The pressure and friction coefficients show a phase shift with respect to the surface. The pressure lags the surface profile by about 200 deg whereas the friction anticipates it by almost 45 deg. The agreement between the calculated and measured values (Frederick, 1986; Frederick and Hanratty, 1986) of the friction coefficient is good except in the region $8.50 < x < 8.95$, where the predicted values are larger.

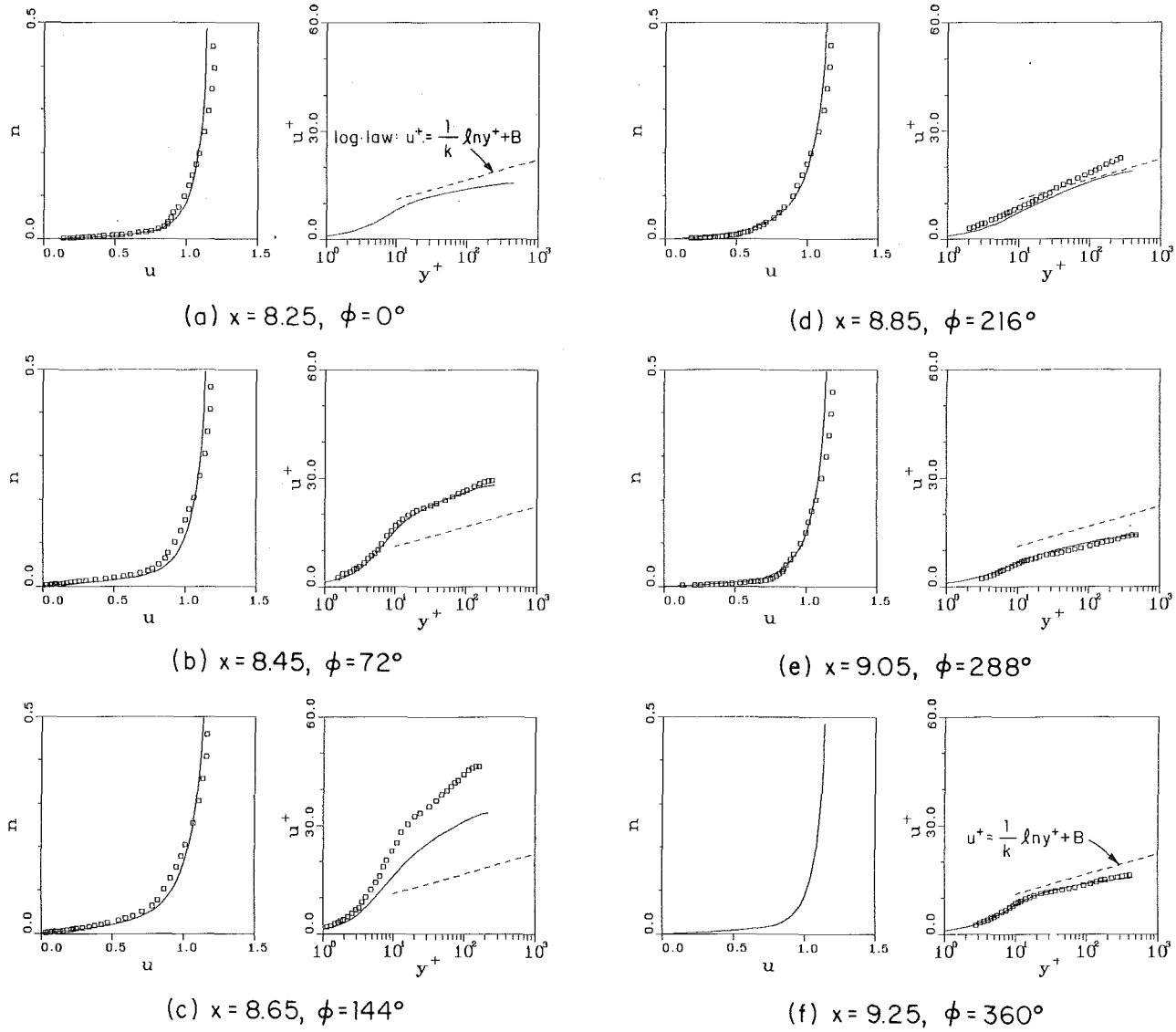

Fig. 5 Velocity profiles at selected positions in a single wave. Solid lines: calculations; symbols: experiment.

As in the laminar-flow calculations of Patel et al. (1991), it is of interest to evaluate the friction and pressure components of resistance associated with the two walls of the channel. Integration of friction and pressure coefficients on the lower, wavy wall over a wavelength gives a resistance coefficient, based on bulk velocity and channel height, of 0.00940. Of this, 0.00718 is due to friction and 0.00222 to pressure. From the flat wall there is a contribution only from friction, and this is 0.00756. The total channel resistance over a wavelength, therefore, is 0.01696. This may be compared with the value of 0.01554 for fully developed turbulent flow in a plane channel at Re = 12,800. Thus, the wavy wall results in (*a*) a slight (2.7 percent) decrease in friction on the opposite flat wall, (*b*) a somewhat greater decrease (7.6 percent) in average friction on the wavy wall, and (*c*) a significant pressure or form drag on the wavy surface. The net increase in total resistance over a plane channel is 9.1 percent. It is of interest to note here that the foregoing observations concerning the frictional and pressure contributions to the total drag of the wavy surface confirm the experimental findings of Cary et al. (1980) and Lin et al. (1984), who concluded that none of the sinusoidal models they tested resulted in a net drag reduction, over the range of parameters they investigated.

Figure 5 shows the axial velocity profiles at stations one-fifth of a wave length (72 deg) apart, beginning with the peak of the fifth wave at $x = 8.25$ and ending with the peak of the sixth at $x = 9.25$. Both linear and logarithmic plots are shown. In the latter, $u^+ = u/U_\tau$ and $y^+ = U_\tau y/\nu$, where U_τ is the friction velocity based on the *local* wall shear stress. The data are those of Frederick (1986) and Frederick and Hanratty (1986), gathered over the eighth of ten waves. The profiles are shown only to about the middle of the channel, $n = 0.5$, n being the distance along the grid line originating from the wavy wall at the appropriate x station. The difference between this and the normal distance y is insignificant. In the experiments for this configuration, measurements did not extend into the top half of the channel. The first and last stations, labelled $\phi = 0$ and 360 deg, respectively, correspond to the wave crests.

From the linear plots in Fig. 5 it is seen that the measured velocities are larger than the calculated ones for n greater than about 0.2. Because the duct used in the experiments had an aspect ratio (channel width to mean-depth ratio) of only 12, with an approach section 70 hydraulic diameters long and a test section 29 wavelengths long, it is possible that end-wall effects are responsible for these higher core velocities. Closer to the wall, but still outside the law-of-the-wall region, the

agreement of the calculated and experimental results is good until about the trough of the wave, and thereafter the velocities are slightly overpredicted.

It is important to emphasize here that the logarithmic plots of the calculated and measured velocity profiles in Fig. 5 were made using the calculated and measured local friction velocities, respectively. This is different from the plots made by some previous investigators, for example, Chauve and Schiestel (1985), who employed the constant, wave-averaged shear velocity. While such plots are of interest in assessing the overall effects of the wavy wall on the velocity distribution, it is the format used here that reveals the validity or breakdown of the law of the wall. The present format provides the most direct comparison between predictions and measurements with respect to the wall shear stress and the near-wall velocity distribution. Also shown in Fig. 5, by the dashed lines, is the standard logarithmic law:

$$u_+ = \frac{1}{\kappa} \ln y^+ + B \tag{1}$$

with $\kappa = 0.418$ and $B = 5.5$. The first significant observation is that the standard law is clearly not applicable in regions of strong adverse and favorable pressure gradients. The calculated profiles follow the experimental trends rather well but do not completely match the data at all stations. Initially, at $\phi = 0$ deg, the pressure gradient is mildly favorable (see Fig. 4) and the velocity distribution lies below the logarithmic law. By the next station, $\phi = 72$ deg, the pressure gradient is adverse and the profile lies above the logarithmic law. At the following station, $\phi = 144$ deg, the adverse gradient is strong and the friction velocity is near its minimum. Here, we observe the greatest departures from the logarithmic law as well as the greatest disagreement between the calculated and experimental values. This disagreement occurs in the region of strongest adverse pressure gradients and very low local wall-shear stresses, and stems from the difference between the calculated and measured wall shear stress. In fact, the velocity profiles can be reconciled if the larger calculated value for the shear velocity is also used to plot the data. If difficulties of measuring wall shear stresses so close to separation are taken into account, the disagreement between the calculated and measured velocity profiles even in the region of strong adverse pressure gradients is not of great practical significance. As the peak in the adverse pressure gradient is passed, the velocity profile begins to shift back toward the logarithmic law, until $\phi = 216$ deg, where agreement is reestablished due to near zero pressure gradient at this location. At the next two stations, $\phi = 288$ and 360 deg, the favorable pressure gradient causes departures of the velocity profiles below the logarithmic law, which the calculations predict faithfully. These departures are quite similar to those which precede relaminarization of turbulent boundary layers under the influence of strong favorable pressure gradients (Patel and Head, 1968; Finnicum and Hanratty, 1988). Finally, note that the solution at the last station was found to be in excellent agreement with that at the first, confirming the spatial periodicity of the flow.

In order to make a more detailed assessment of the turbulence model used in the present study, it is of interest to examine some further aspects of the results. Figure 6 shows the distributions of velocity (u^+), the turbulent kinetic energy ($k^+ = k/U_\tau^2$), its rate of dissipation ($\epsilon^+ = \epsilon\nu/U_\tau^4$), and the Reynolds shear stress ($\overline{uv}^+ = \overline{uv}/U_\tau^2$), in wall coordinates, at three locations along the wave. The three stations were selected not simply to avoid duplicating the results of Fig. 5, but because they depict the flow details where the local pressure gradient is nearly zero ($\phi = 36$ deg), where it is adverse and strong enough to cause a significant departure from the logarithmic law as well as differences between the experiments and calculations ($\phi = 108$ deg), and where the pressure gradient is favorable ($\phi = 324$ deg).

From the results of Fig. 6 it is clear that the turbulence parameters vary rapidly normal to the wall, through the sublayer and the buffer layer, into the logarithmic region. There are also very rapid changes along the wall. The large gradients normal to the wall have presented great difficulties in the numerical integration of turbulence-model equations, particularly the equation for ϵ, in the so-called low Reynolds number or near-wall models (Patel et al., 1985). Replacement of the ϵ equation by a specified length scale in the near-wall region, following the suggestion of Chen and Patel (1988), has obviously alleviated this difficulty. In fact the results show no discontinuities stemming from the combination of a one-equation near-wall treatment with the standard two-equation (k-ϵ) model farther out. This is due to the manner in which the two models are matched in the fully-turbulent region. There is little direct experimental evidence to confirm all of the predicted changes taking place in the near-wall distributions of the three turbulence quantities. However, at $\phi = 36$ deg, where the local pressure gradient is nearly zero, the results are similar to those found in a flat-plate turbulent boundary layer. For example, the peak values of k^+ and ϵ^+, as well as the locations of those peaks, are in agreement with available near-wall data (Patel et al., 1985). Finally, it is of interest to note the implications of the present results for the so-called "wall-function treatment" that is frequently employed to avoid numerical solution of the equations in the near-wall region. In this approach, the boundary conditions are prescribed at some point in the full turbulent region, beyond the sublayer and the buffer layer, typically $y^+ > 60$, by assuming that the velocity is given by the logarithmic law, Eq. (1), and the turbulence is in local equilibrium, resulting in $k^+ = C_\mu^{-1/2}$ and $\epsilon^+ = (\kappa y^+)^{-1}$, where C_μ ($= 0.09$) is a constant. Obviously, the present results do not support such a practice. It is seen that pressure gradients have a very strong influence not only on the velocity distribution but also on the turbulence parameters.

Wavy Wall With $2a/\lambda = 0.20$, Re = 8,160; Separated Flow. The calculations for this extreme case (see Fig. 1) were carried out with the solution domain and grid numbers similar to those used in the first case, except that the upstream and downstream straight sections were 3λ and 2λ, respectively (Fig. 7). This change allowed a longer downstream recovery length. Figure 8 shows the pressure and friction coefficients after 550 iterations, at intervals of 50 iterations. As in the previous case, the results are practically indistinguishable after 550 iterations. Again the solutions on the upper and lower walls are in agreement initially, but in this case the solution on the upper wall appears to vary more from a standard straight-duct behavior than in the previous case shown in Fig. 3. Recovery in the downstream section is more closely achieved. However, it is clear that a much longer section is required to reestablish straight-channel conditions.

Comparison of Fig. 3 and 8 clearly indicates the additional complexities of the second case. Harmonic analysis of the two sets of results would confirm the classification of Hanratty et al. (Fig. 1), that the former shows nearly linear response while the latter is highly nonlinear. The calculations for the present case of $2a/\lambda = 0.20$ indicate flow separation not only in the wave cavities but also ahead of the first wave. The distributions of pressure and friction coefficients, and the calculated streamlines, over the fifth wave, $7.25 < x < 8.25$, are shown in Fig. 9. Separation (S) is predicted at $x = 7.33$ and reattachment (R) at $x <= 7.98$. Measuring from the top of the upstream crest ($x = 7.25$), these points are located at Δx of 0.08 and 0.73, respectively. Kuzan (1986) measured separation point at $\Delta x = 0.12$, with reattachment at $\Delta x = 0.77$. For the same configuration but a different Reynolds number, Buckles et al. (1984) measured separation at $\Delta x = 0.14$ and reattachment at $\Delta x = 0.69$. Thus, the predicted positions are in fairly good agreement with data.

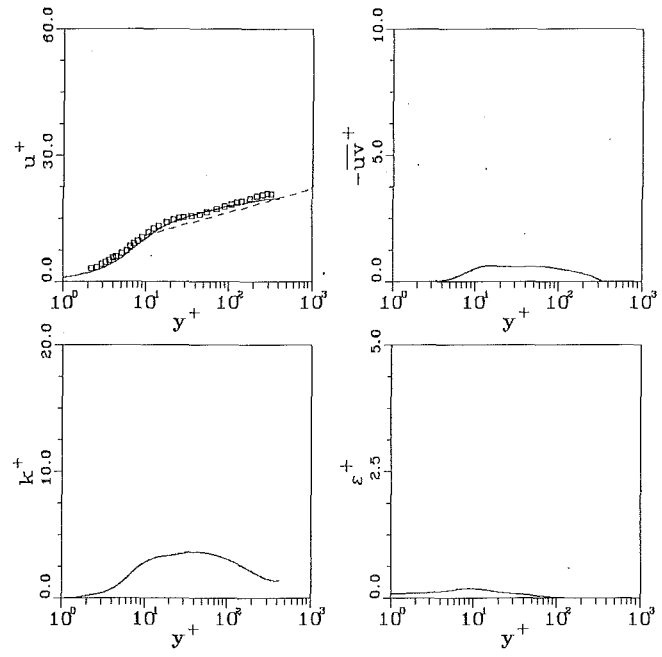

(a) x = 8.35, ϕ = 36°

(c) x = 9.15, ϕ = 324°

Fig. 6 Distributions of velocity *(u)*, turbulent kinetic energy *(k)*, Reynolds stress $\overline{uv}$, and energy dissipation rate (ϵ) in wall coordinates

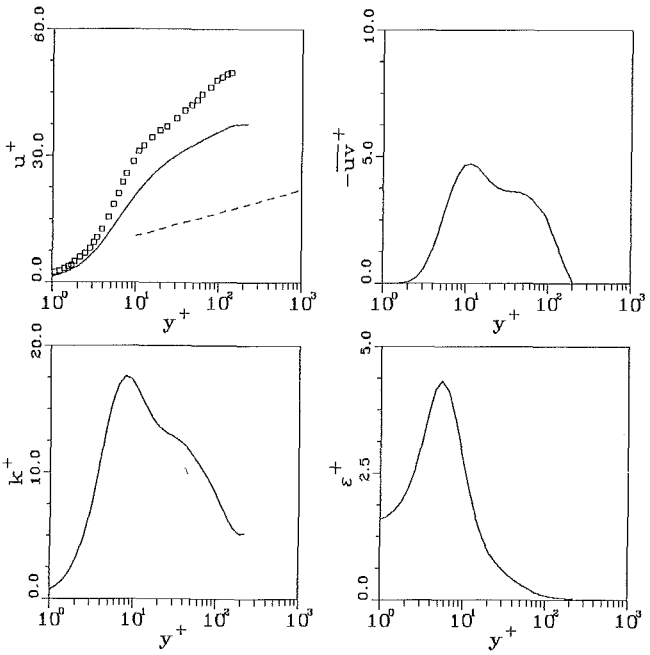

(b) x = 8.55, ϕ = 108°

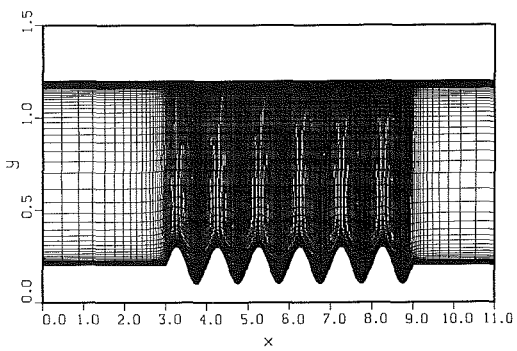

Fig. 7 Solution domain and grid for 2a/λ = 0.20

Integration of friction and pressure coefficients on the wavy wall over one wavelength gives a resistance coefficient of 0.06972, of which, 0.00144 is due to friction and 0.06828 to pressure. Integration of friction on the flat wall gives 0.01224, and therefore, the total channel resistance over a wavelength is 0.08196. For fully developed turbulent joint in a plane channel at Re = 8,160, the resistance coefficient is 0.01676. Thus, in the presence of separation, there is (*a*) a substantial (46 percent) increase in friction on the opposite flat wall, (*b*) a dramatic decrease (almost by a factor of six) in average friction on the wavy wall, and (*c*) a pressure drag on the wavy surface that dominates the contributions from friction. The total resistance of the channel with a wavy wall is almost five times that of a plane channel. This is quite different from the situation in the previous case where the flow remained attached throughout the channel.

The velocity profiles at a few representative locations along the fifth wave are shown in Fig. 10. The data are due to Kuzan (1986). In these experiments, the measurements extended all the way to the opposite flat wall of the channel. In addition to the usual linear plots of velocity, Fig. 10 also shows the logarithmic plots. In these, only the results on the wavy-wall side, up to the velocity maximum, are shown, and the friction velocity U_τ is now based on the magnitude of the local wall shear stress, because it is negative in separated flow. It should be noted that this choice is made for convenience in the present context and should not be construed to give support to the existence of a law of the wall in separated flow. As before, to ensure most meaningful and critical comparisons, measured wall shear stresses were used to normalize the experimental data while calculated stresses were used to normalize the predicted results. The usual logarithmic law, Eq. (1), is again included for reference.

Figure 9 indicates that the flow at the first station, the wave crest, ϕ = 0 (and 360) deg, is attached but recovering from a strong favorable pressure gradient (acceleration) that follows reattachment on the previous wave. From Fig. 10(*a*) it is seen

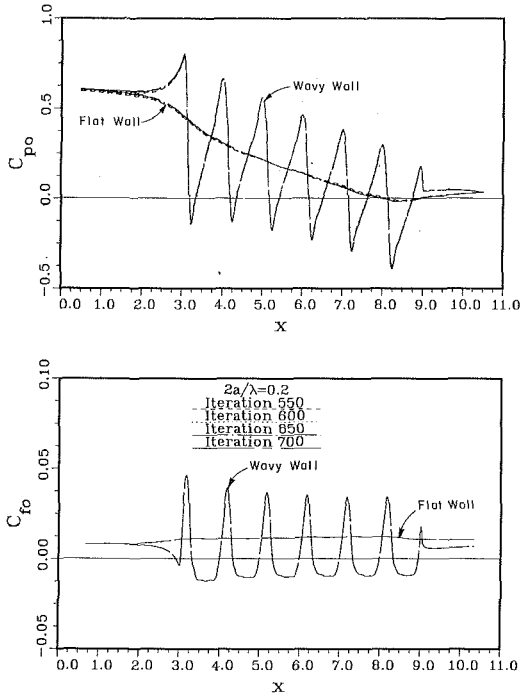

Fig. 8 Convergence of pressure and friction coefficients, $2a/\lambda = 0.20$. Note: Results for different iterations are indistinguishable in most respects.

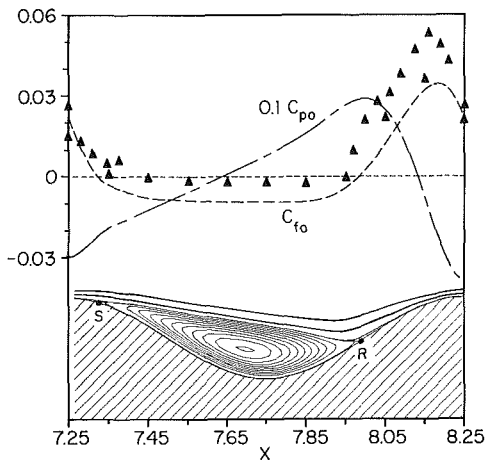

Fig. 9 Pressure and friction coefficients, and streamlines over a single wave. Lines: calculations; symbols: experimental friction coefficient.

that the velocity profile at the crest is predicted rather well except in the region close to the wall where much higher velocity is predicted. The plot in wall coordinates indicates only qualitative agreement between the calculations and experiment. The observed differences may be due to local relaminarization as a result of the strong flow acceleration ahead of this station. At the next station, $\phi = 36$ deg, the local pressure gradient is adverse, and the flow is on the verge of separation. The predictions are in good agreement with experiment except when compared in the format of the law of the wall. The relatively large discrepancies observed in the latter is due, in very large measure, to the differences between the predicted and measured wall shear stresses, as was also noted in the previous case. As seen from Fig. 9, the magnitudes of both are rather small, but the differences in them are magnified in the logarithmic plots. In the final analysis, these plots may not be the best gage of success, but they are useful in examining the near-wall details. The next station, $\phi = 180$ deg, lies at the middle of the wave and in separated flow. Here also there is a strong adverse pressure gradient. The velocity profile is predicted rather well except within the separated zone. The extent of the separated region is underpredicted while the reverse flow velocity is overestimated. This is presumably related to the performance of the turbulence model for separated flow. The logarithmic plot for this station clearly shows the region of flow reversal although quantitative differences between the calculated and measured profiles persist due to the differences in the calculated and measured wall shear stresses. The next station, $\phi = 252$ deg, was selected because here the flow has just reattached. Again there is good agreement between the calculations and measurements. Because the local wall shear is very small at this location, the logarithmic plot is not particularly reliable. However, the reattachment is clearly seen and the agreement in the sublayer is indicative of the numerical resolution of the flow very close to the wall. Finally, the results at the last section, $\phi = 324$ deg, located in a region of strong favorable pressure gradient, are quite similar to those at the wave crest ($\phi = 0$ and 360 deg).

Before closing this section, it is important to make some general observations concerning the results shown in Fig. 10. First, the breakdown of the usual logarithmic law, Eq. (1), observed in the first case, where the flow remained attached everywhere, is underscored by the results in separated flow. Thus, the use of wall functions is turbulent-flow calculations, which is even more prevalent for complex and separated flows, is a questionable practice. Secondly, the near-wall treatment used in the present turbulence model seems to reproduce all of the trends observed in the experiments. Thirdly, the disagreement seen in the near-wall velocity distributions when viewed in law-of-the-wall coordinates are due more to the disagreement in the wall shear stress than a failure of the turbulence model in general. The wall shear measurements were made by determining the slope of the velocity profile at the wall, a procedure that is known to be prone to large errors, especially when the slope is small and the flow is not steady, as is the case in separated flow.

Conclusions

The flow in a channel with a wavy wall is obviously a challenging test case for numerical methods and turbulence models because a variety of flow phenomena can be considered by changing the amplitude-to-wavelength ratio and there exist few, if any, uncertainties concerning the proper initial and boundary conditions required to carry out a truly predictive calculation. Although it has not been possible to separate the effects of surface curvatures from those of the strong pressure gradients that are present in this flow, the results presented here show that the present numerical method is quite successful in calculating flows with multiple separations and reattachments with a reasonable amount of computer time, and the two-layer turbulence model of Chen and Patel (1988) appears to capture most of the important physical features of such flows. The results also demonstrate, quite conclusively, the breakdown of the standard law of the wall in strong adverse and favorable pressure gradients, well before the onset of separation or relaminarization, and therefore suggest that the wall-function approach should be abandoned in favor of direct integrations to the wall. In this respect, as an alternative to wall functions, even simpler turbulence models, such as an eddy-viscosity model, are to be preferred. Finally, the overall numerical approach described here is general enough to begin a more in-depth study of the physics of flows over wavy walls of sinusoidal or arbitrary shape and extend the method to consider the many practical flow phenomena which involve wavy boundaries. An extensive parametric study will be required, however, to explicate all of the effects of wavy boundaries in a turbulent flow.

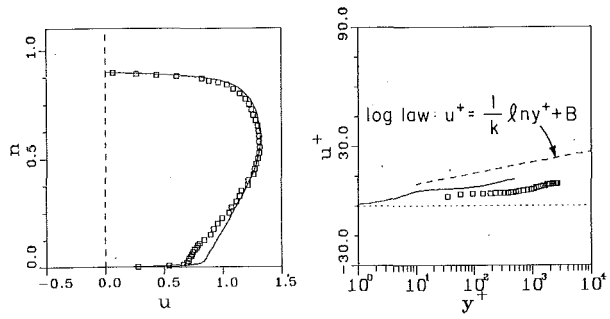

(a) x = 7.25, ϕ = 0°

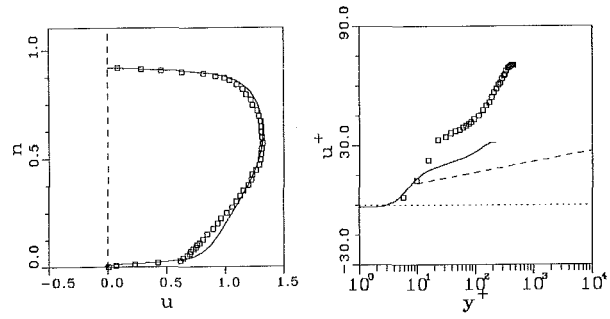

(b) x = 7.35, ϕ = 36°

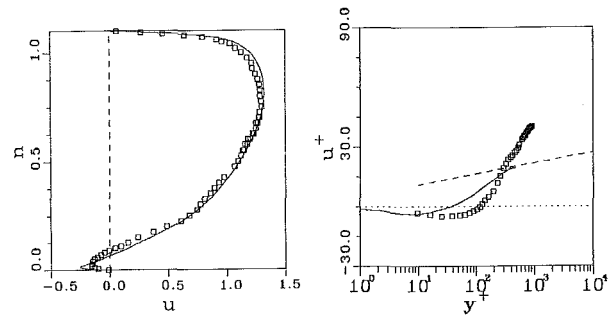

(c) x = 7.75, ϕ = 180°

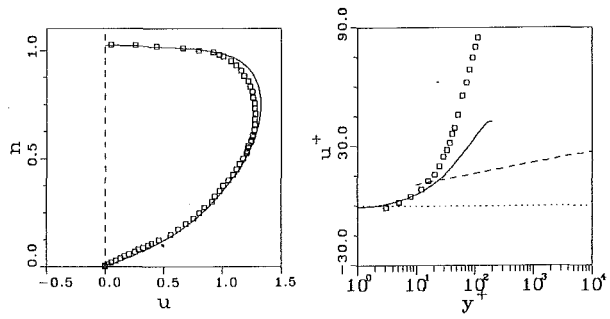

(d) x = 7.95, ϕ = 252°

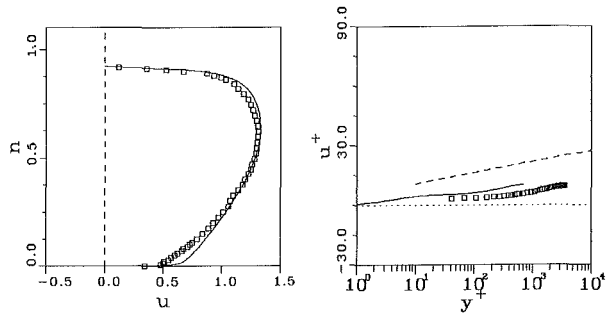

(e) x = 8.15, ϕ = 324°

Fig. 10 Velocity profiles at selected positions in a single wave. Solid lines: calculations; symbols: experiment.

Acknowledgments

This research was partially supported by the Office of Naval Research, under Contract N0014-88-K-0001. The calculations were performed on the CRAY XMP/48 of the National Center for Supercomputing Applications, Champaign, Illinois.

References

Abrams, J., 1984, "Turbulent Flow over Small Amplitude Solid Waves," Ph.D. Thesis, Dept. Chem. Engr., Uni. Illinois, Urbana, Ill.

Abrams, J., and Hanratty, T. J., 1985, "Relaxation Effects Observed for Turbulent Flow over a Wavy Surface," *J. Fluid Mech.*, Vol. 151, pp. 443–455.

Buckles, J., Hanratty, T. J., and Adrian, R. J., 1984, "Turbulent Flow over Large Amplitude Wavy Surfaces," *J. Fluid Mech.*, Vol. 140, pp. 27–44.

Cary, A. M. Jr., Leonard, L. M., and Bushnell, D. M., 1980, "Drag Reduction Characteristics of Small Amplitude Rigid Surface Waves," *Viscous Flow Drag Reduction*, ed. G. R. Hough, AIAA, New York, pp. 144–167.

Chauve, M. P., and Schiestel, R., 1985, "Influence of Weak Wall Undulations on the Structure of Turbulent Pipe Flow: an Experimental and Numerical Study," *J. Fluid Mech.*, Vol. 160, pp. 47–75.

Chen, H. C., and Patel, V. C., 1987, "Laminar Flow at the Trailing Edge of a Flat Plate," *AIAA J.*, Vol. 25, pp. 920–928.

Chen, H. C., and Patel, V. C., 1988, "Near-Wall Turbulence Models for Complex Flows Including Separation," *AIAA J.*, Vol. 26, pp. 641–648.

Finnicum, D. S., and Hanratty, T. J., 1988, "Effect of Favorable Pressure Gradients on Turbulent Boundary Layers," *A.I.Ch.E. Journal*, Vol. 34, pp. 529–540.

Frederick, K. A., 1986, "Velocity Measurements for Turbulent Nonseparated Flow over Solids Waves," Ph.D. thesis, Dept. Chem. Engr., Uni. Illinois, Urbana, Illinois.

Frederick, K. A., and Hanratty, T. J., 1986, "Velocity Measurements for a Turbulent Nonseparated Flow over Solids Waves," *Expts. Fluids*, Vol. 6, pp. 477–486.

Hsu, S. T., and Kennedy, J. F., 1971, "Turbulent Flow in Wavy Pipes," *J. Fluid Mech.*, Vol. 47, pp. 481–502.

Knight, D. D., 1982, "Applications of Curvilinear Coordinate Generation Techniques to the Computation of Internal Flows," *Numerical Grid Generation*, Elsevier Sci. Publ. Co., pp. 357–384.

Kuzan, J. D., 1986, "Velocity Measurements for Turbulent Separated and Near Separated Flow over Solids Waves," Ph.D. thesis, Dept. Chem. Engr., Uni. Illinois, Urbana, Illinois.

Lin, J. C., Walsh, M. J., and Balasubramanian, R., 1984, "Drag of Two-Dimensional Small-Amplitude Symmetric and Asymmetric Wavy Walls in Turbulent Boundary Layers," NASA Tech. Paper 2318.

Patel, V. C., Chon, J. T., and Yoon, J. Y., 1991, "Laminar Flow over Wavy Walls," JOURNAL OF FLUIDS ENGINEERING, published in this issue pp. 574–578.

Patel, V. C., and Head, M. R., 1968, "Reversion of Turbulent to Laminar Flow," *J. Fluid Mech.*, Vol. 34, pp. 371–392.

Patel, V. C., Rodi, W., and Scheuerer, G., 1985, "Turbulence Models for Near-Wall and Low Reynolds Number Flows: A Review," *AIAA.*, Vol. 23, pp. 1308–1319.

Richmond, M. C., and Patel, V. C., 1991, "Convex and Concave Surface Curvature Effects in Wall-Bounded Turbulent Flows," *AIAA J.*, Vol. 29, pp. 895–902.

Sigal, A., 1971, "An Experimental Investigation of the Turbulent Boundary Layer over a Wavy Wall," Ph.D. thesis, Calif. Inst. Tech., Pasadena, Calif.

Thorsness, C. B., Morrisroe, P. E., and Hanratty, T. J., 1978, "A Comparison of Linear Theory with Measurements of the Variation of Shear Stress Along a Solid Wave," Chem. Eng. Sci., Vol. 33, pp. 579–592.

Zilker, D. P., Cook, G. W., and Hanratty, T. J., 1977, "Influence of the Amplitude of a Solid Wavy Wall on a Turbulent Flow. Part 1. Nonseparated Flows," *J. Fluid Mech.*, Vol. 82, pp. 29–51.

Zilker, D. P., Cook, G. W., and Hanratty, T. J., 1979, "Influence of the Amplitude of a Solid Wavy Wall on a Turbulent Flow. Part 2. Separated Flows," *J. Fluid Mech.*, Vol. 90, pp. 257–271.

Application of V Shape Riblets to Pipe Flows

Shin-ichi Nakao
Senior Research Scientist,
Fluid Measurement Section,
National Research Laboratory of Metrology,
Ibaraki, Japan

Pipes with V shape riblets were tested at Reynolds numbers between 5×10^3 and 4×10^4. All riblet pipes indicated some drag reduction. The model with $h = 0.55$ mm and $h/S = 0.483$ showed the maximum drag reduction of 8 percent and the widest range of Reynolds number over which the riblet reduces drag. The riblet shape desirable for drag reduction in pipe flows was almost the same as that in flat plate boundary layers, but the value of S^+ which provided the maximum drag reduction was quite different; $S^+ = 23$ for pipe flows and $S^+ = 12$ for flat plate boundary layers.

1 Introduction

The fact that the riblet can reduce turbulent frictional drag has been ascertained by many studies (Walsh, 1982, 1983; Pulles et al., 1989) and some flow models have been proposed to explain the mechanisms of the drag reduction by riblets (Bacher and Smith, 1985; Nakao, 1990). One of the next interesting steps is to apply the riblet to some industrial fields. In particular, application to pipelines is expected to provide major energy savings. However, most of the riblet studies were carried out in flat plate boundary layers with few works for pipe flows. Liu et al. (1989) tested pipes lined with riblet film and reported reduced frictional drag of 5 to 7 percent in the fully developed turbulent flow of water. However, they did not discuss the uncertainty of the results.

The purposes of the present work was to investigate the performance of riblets for drag reduction in pipe flows through comparisons of riblet pipes results with those from a smooth pipe and study of the optimum riblet shape in pipe flows.

2 Experimental Apparatus

The experiments were carried out with air flow in PVC pipes. The Reynolds number of the present experiments varied from $Re = 5 \times 10^3$ to 4×10^4. The schematic picture of the apparatus is shown in Fig. 1. The length of the test section was 40 D and the upstream side of the test section had the length of 120 D where D is the pipe diameter. The 14 pressure taps were positioned at 10 D along the smooth pipe to measure the pressure gradient along the pipe axis. The measured linear pressure gradients at the test section indicated the flow was fully developed and turbulent. The flow rate Q was regulated by the orifice plate placed after the blower and measured by the turbine meter placed 40 D downstream of the test section. The flow rate, the static pressures, and the temperature and the humidity of the air were measured for each experiment. An experiment comprised two steps: the smooth pipe experiment and the riblet pipe as inserts into the test section. These two sections were interchanged five times for each riblet model.

Contributed by the Fluids Engineering Division for publication in the JOURNAL OF FLUIDS ENGINEERING. Manuscript received by the Fluids Engineering Division January 3, 1991.

The riblet pipes were made by the extrusion process. The cross sections of the riblet pipes and the smooth pipe were carefully measured at four different places by the profile projector with the resolution of ±0.001 mm. The averaged values of the height (h), the spacing (S) of the groove, and the diameter (D) of each pipe are summarized on Table 1. The precision

Table 1 The sizes and the configuration of riblet pipes tested

MODEL	h(mm)	s(mm)	D(mm)	h/S
1	0.86	1.81	51.3	0.474
2	0.68	0.71	50.7	0.96
3	0.40	1.70	48.6	0.235
4	0.55	1.14	51.2	0.483
5	0.64	1.61	50.6	0.4
6	0.55	2.04	51.3	0.27
SMOOTH	---	---	51.1	---

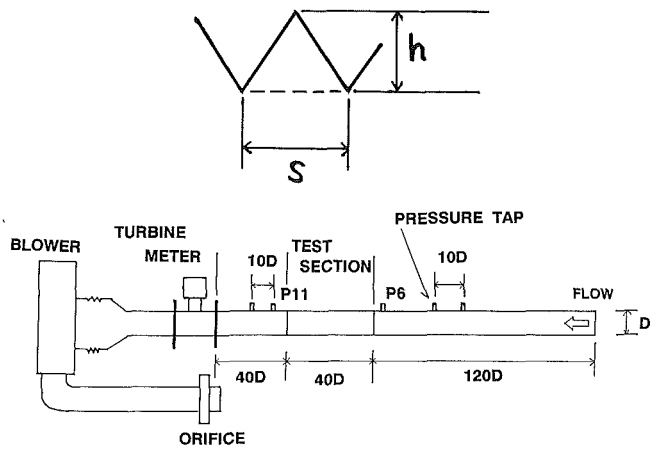

Fig. 1 Schematic picture of experimental apparatus

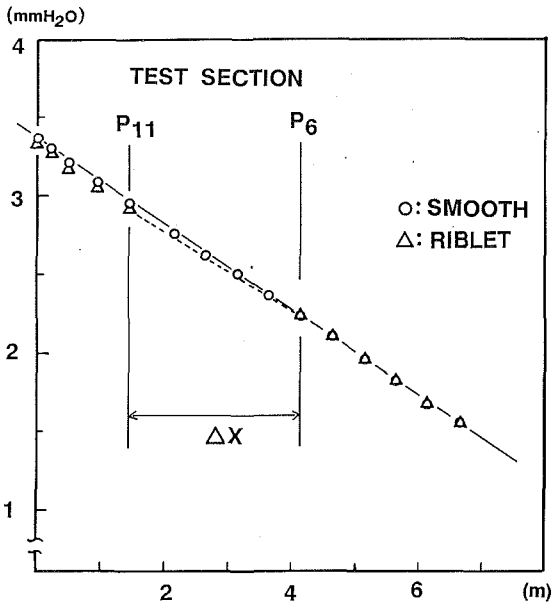

Fig. 2 Pressure distributions along the axis of the smooth pipe and the riblet pipe. (Uncertainty of the static pressure: 0.105 percent for 95 percent coverage. The bias error was not discussed in this figure because of the comparative measurements.)

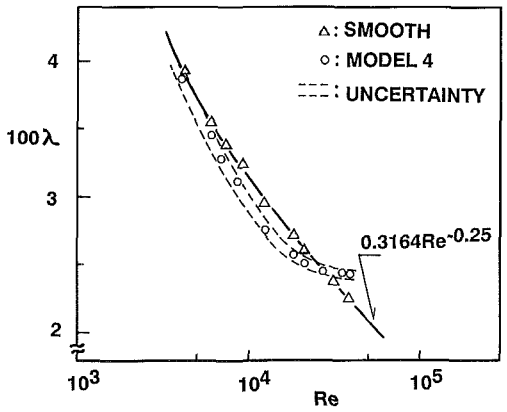

Fig. 3 Comparison between the frictional resistances for the smooth pipe and those of the riblet pipe, MODEL 4 (Uncertainty for 95 percent coverage. The smooth pipe : ±1.32 percent, MODEL 4 : ±1.42 percent.)

error limit of D calculated according to ANSI/ASME (1986) was 0.12 mm.

3 Measurement of Frictional Resistance and Its Uncertainty

The frictional resistance of a pipe, λ, in fully developed turbulent flow is obtained from the following equation.

$$\lambda = 2DA/(\rho U^2)$$

where A is the pressure gradient along the pipe axis, ρ is the density of the air, and U is the mean velocity of the pipe, which was calculated from the flow rate Q measured by the turbine meter as follows;

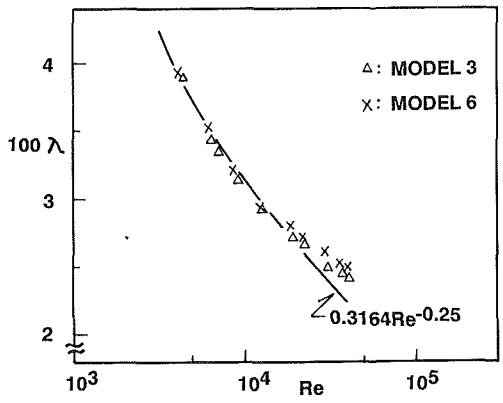

Fig. 4(*a*) M 3:h/S = 0.235, M 6:h/S = 0.27

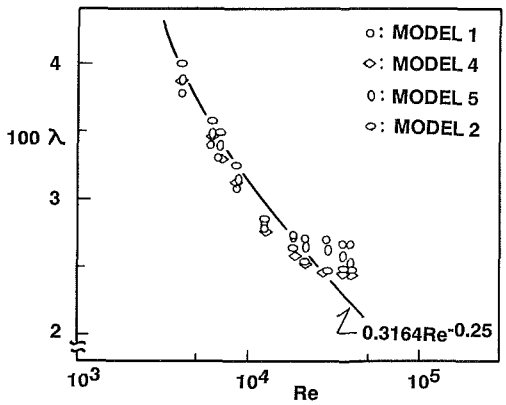

Fig. 4(*b*) M 1:h/S = 0.474, M 2:h/S = 0.96, M 4:h/S = 0.48, M 5:h/S = 0.4. (Uncertainty for 95 percent coverage. M 1 : ±1.48 percent, M 2 : ±1.49 percent, M 3 : ±1.36 percent, M 4 : ±1.64 percent, M 5 : ±1.58 percent, M 6 : ±1.97 percent.)

Fig. 4 Variation of the frictional resistances of the riblet pipes versus the Reynolds number

$$U = Q/(\pi D^2/4)$$

The test section is between P6 and P11, as shown in Fig. 1, and A was determined from the values of these pressure taps in all experiments.

The uncertainty of λ is calculated according to ANSI/ASME (1986). The main sources of the bias error are the errors in D and the static pressures. For the latter, only the error caused by the shape of the pressure hole is considered. The other sources are very small compared with these and therefore are not discussed here. The error in D was considered as the major bias error as it was a constant during all experiments and was ±0.24 percent from the result in the last section. The bias error limit of λ based on D therefore becomes ±1.2 percent from the relation $\lambda \propto D^5$. The other source, the errors caused by the shape of the pressure hole, were neglected herein for the following reason. As the static pressures are measured on the same pressure holes, the errors involved in the measuring values would be the same at all cases and would cancel out each other when the pressure gradient is calculated. Accordingly, the source of the bias error limit of λ was only the error

Nomenclature

A = the pressure gradient
D = the diameter of pipe
h = the height of groove (shown in Table 1)
S = the spacing of groove (shown in Table 1)
Q = the flow rate
U = the mean velocity of pipe
λ = the frictional resistance
Re = Reynolds number based on the pipe diameter, DU/ν

Superscript

\+ = law of the wall variable

Subscript

RIB = of the riblet pipe
0 = of the smooth pipe

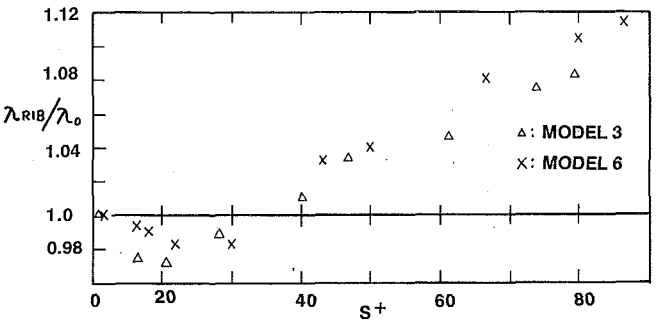

Fig. 5(*a*) M 3 : h/S = 0.235, M 6 : h/S = 0.27

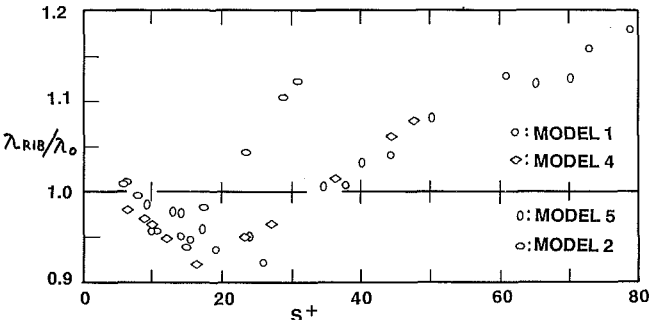

Fig. 5(*b*) M 1 : h/S = 0.474, M 2 : h/S = 0.96, M 4 : h/S = 0.48, M 5 : h/S = 0.4 (Uncertainty for 95 percent coverage. M 1 : ±1.58 percent, M 2 : ±1.58 percent, M 3 : ±1.47 percent, M 4 : ±1.73 percent, M 5 : ±1.67 percent, M 6 : ±2.04 percent.)

Fig. 5 Variation of the drag reduction versus the spacing of the groove

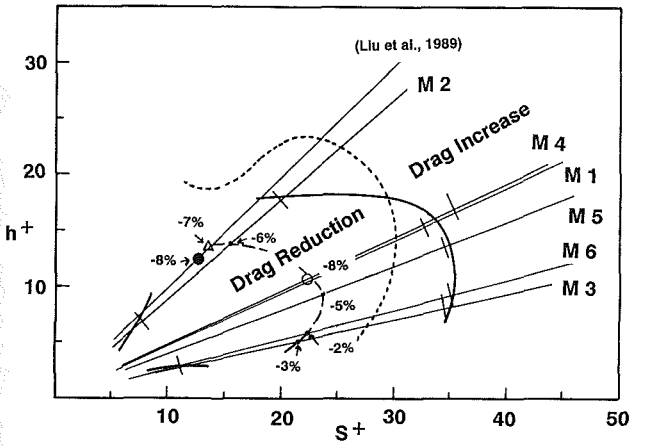

Fig. 6 Drag reduction region of $h+$ and $S+$.
———:the boundary of drag reduction in the pipe flows
---- :the boundary of drag reduction in the flat plate boundary layers (Walsh, 1983)
— — — :the positions that give maximum drag reduction on each riblet pipe
○ :the position of the maximum drag reduction in the present experiments
● :the position of the maximum drag reduction in the flat plate boundary layers
△ :the position of the maximum position of the (Liu et al., 1989)

on D. Next, the precision error limit for λ was calculated based on a statistical analysis of repeated independent measurements and was determined to be a maximum of 1.6 percent. Finally, from both the bias error limit and the precision error limit, the uncertainty of λ was estimated as 2.0 percent for 95 percent coverage.

4 Experimental Results

Figure 2 is a typical example of the measured pressure distributions. The static pressures of the riblet pipe are on a straight line with the same slope as that of the smooth pipe until P6. However, the pressure at P11 just after the test section is clearly smaller than that of the smooth pipe; that is to say, the pressure loss becomes smaller on the riblet pipe than on the smooth pipe.

Figure 3 shows the variation of the frictional resistance of MODEL 4 versus the Reynolds number. λ of the smooth pipe is on the solid line, which is the Blasius formula. λ of MODEL 4 is below that line up to Re = 2.8×10^4, but after that the riblet acts as roughness and the drag of MODEL 4 increases more than that of the smooth pipe. The two broken lines in this figure present the 95 percent coverage obtained in the last section. From this figure, the drag reduction of MODEL 4 is found to be significant even with consideration of the uncertainty.

The frictional resistances of the riblet pipes are compared in Figs. 4. Figure 4 (*a*) shows the results of the riblet pipes with $h/S \leq 0.27$, which are slightly below the Blasius formula around Re = 10^4, and after Re = 2×10^4 they show drag increase. These models indicate similar behavior, although their sizes are rather different. Figure 4 (*b*) shows the results of the models with $h/S \geq 0.4$. These models indicate significant drag reductions. As the Reynolds number becomes smaller, the effects of the riblet are relaxing because the height of the riblet becomes small in comparison with the sublayer thickness, and the frictional resistance becomes close to the Blasius. All models exhibit such behavior, but some of them seem still to work in those smaller Reynolds numbers. On the models with the similar value of h/S (=0.483 and 0.474), MODEL 4 with smaller h (h=0.55 mm) exhibited drag reduction over a wider Reynolds number range than MODEL 1 (h = 0.86 mm). Therefore, the value of h seems to be important as far as the range of Reynolds number over which the riblet works. Figure 5 indicates the relationship between drag reduction and spacing of the riblet. Figure 5 (*a*), for $h/S \leq 0.27$, shows that MODEL 3 and MODEL 6 reduce the frictional drag about 3 and about 2 percent respectively. All models with $h/S \geq 0.4$ shown in Fig. 5 (*b*) indicate drag reductions of 5 to 8 percent, with maximum drag reductions occurring at $S^+ = 15 - 25$, which is in agreement with flat plate results. This figure also shows that the other models except MODEL 2 reduce drag successfully up to about $S^+ = 35$; The reason that MODEL 2 does not reduce drag above $S^+ = 20$ could be related to the value of h/S, because the riblet pipe tested by Liu et al. (1986) exhibited similar behavior and the h/S of both cases is about 1.0. These figures suggest that h/S is one of the important parameters and the riblet with $h/S = 0.4 - 0.5$ is optimum for drag reduction.

Figure 6 shows the drag reduction region of h^+ and S^+. This figure includes the boundary between drag reduction and drag increase in the present experiments, for the results of Liu et al. (1986) and the corresponding boundary for the flat plate case (Walsh, 1983), which is shown by the dotted line. As Walsh (1990) indicated, the S^+ range for drag reduction extends up to about 35 when $h/S \leq 0.5$. The broken line indicates the positions that give the maximum drag reduction in each model of the present experiments, and the solid circle presents the position of the maximum drag reduction in the flat plate boundary layers while the triangle indicates the position of the maximum drag reduction obtained by Liu et al. (1989). The maximum drag reduction obtained in both flows is almost the same (8 percent). However, the value of S^+ that provides the maximum drag reduction seems to be different in pipe and boundary layer; $S^+ \approx 12$ for the flat plate boundary layers and $S^+ \approx 22$ for the pipe flows. Some of this difference may be due to changes in riblet shape details such as peak sharpness.

5 Discussion and Conclusions

Six riblet pipes were tested in fully developed turbulent flows.

MODEL 4 with $h = 0.55$ mm and $h/S = 0.48$ indicated the maximum drag reduction of 8 percent and worked over the widest range of Reynolds number. The present results also showed that the value of h/S is important for an overall drag performance with an optimum value of $0.4 - 0.5$.

It was found from the present results that the riblet shape desirable for drag reduction in the pipe flows can be roughly estimated from the results in flat plate boundary layers, but the optimum riblet shape for maximum drag reduction in the former is different according to the present results. The height and the spacing of the groove which are desirable for drag reduction in both pipe and flat plate are $S^+ = 15 - 25$ and $h^+ = 7 - 15$, respectively. As the optimal height of the riblets is considered to be directly connected with the sublayer thickness, it is expected to have a similar value in both flat plate boundary layers and pipe flows. On the other hand, the meaning of S^+ is still not as clear as h^+. Of possible interest is that both the S^+ of the zero drag reduction point and the structural scale of the streaks in the near wall region are similar in both the pipe flows (Bakewell and Lumely, 1967) and the flat plate boundary layer. This suggests that the proper size of the riblet spacing has some relation to the structural scale of the wall streaks.

References

ANSI/ASME PTC19.11-1985, "Measurement Uncertainty Part I," Instruments and Apparatus.

Bacher, E. V., and Smith, C. R., 1985, "A Combined Visualization-Anemometry Study of the Turbulent Drag Reducing Mechanisms of Triangular Micro-Groove Surface Modifications," AIAA Paper 85-0548.

Bakewell, Jr. H. P., and Lumely, J. L., 1967, "Viscous Sublayer and Adjacent Wall Region in Turbulent Pipe Flow," The *Phy. Fluids*, Vol. 10, pp. 1880–1889.

Liu, K. N., Christodoulou, C., Riccius, O., and Joseph, D. D., 1989, "Drag Reduction in Pipes Lined with Riblets," *IUTAM Symposium Structure of Turbulence and Drag Reduction*, pp. 545–551.

Nakao, S., 1990, "Turbulent Boundary Layer Developing on Drag Reducing Riblet," *Theoretical and Applied Mechanics*, Vol. 39, pp. 303–308.

Pulles, C. J. A., Prasad, K. K., and Nieuwstadt, F. T. M., 1989, "Turbulent Measurements over Longitudinal Micro-Grooved Surfaces," *Appl. Scientific Research*, Vol. 46, pp. 197–208.

Walsh, M. J., 1982, "Turbulent Boundary Layer Drag Reduction using Riblets," AIAA paper 82-0169.

Walsh, M. J., 1983, "Riblets as a Viscous Drag Reduction Technique," *AIAA J.*, Vol. 21, pp. 485–486.

Walsh, M. J., 1990, "Riblets," *Viscous Drag Reduction in Boundary Layer, Progress in Astro. and Aero.*, Vol. 123, p. 203–261.

A. A. Al-Maaitah
Department of Mechanical Engineering,
Mutah University,
Jordan

A. H. Nayfeh

J. A. Masad[1]

Department of Engineering Science and Mechanics,
Virginia Polytechnic Institute and State University,
Blacksburg, VA 24061

Effect of Suction on the Stability of Supersonic Boundary Layers. Part I—Second-Mode Waves

The effect of suction on the second (Mack) mode of instability in supersonic and hypersonic two-dimensional boundary layers is investigated. The results show that suction has a stabilizing effect on these waves; it reduces the peak amplification and shifts it toward a higher frequency. In the presence of suction, the most amplified Mack mode remains two-dimensional. The effectiveness of suction in stabilizing Mack waves decreases as the Mach number increases. Variations of the growth rates of the most amplified Mack mode and the corresponding frequencies and wave numbers with mass flux are found to be almost linear. The frequencies and wave numbers corresponding to the most amplified Mack mode increase by increasing the suction level.

Introduction

The design of advanced aerodynamic vehicles, such as the high-speed civil transport HSCT aircraft and the hypersonic National Aerospace Plane (NASP), requires knowledge of the location and streamwise extent of laminar-turbulent transition in boundary-layer flows. In most cases, only a knowledge of the transition location is required to "switch" from the laminar to the turbulent options of the computer codes. In other cases, such as turbine blades, transition can extend over major parts of the chord. Advanced vehicles to operate at hypersonic speed and high altitudes will likely experience transitional flow. However, the flow properties in the transition region can be obtained neither from laminar nor turbulent flow models, yet influence the performance (Herbert, 1991). Bogdanoff (1987) ranked the transition issue as a first-order problem in hypersonic vehicle design.

The compressible stability theory of laminar boundary layers differs in many ways from the incompressible theory (Mack, 1969, 1984; Nayfeh, 1988). The most important feature of the stability of supersonic laminar boundary layers is that there can be more than one growing mode of instability. Using extensive numerical calculations, Mack found that there are multiple values of wave numbers for a single disturbance phase velocity c_r whenever there is a region in which the mean flow relative to the disturbance phase velocity is supersonic; that is $M_r^2 > 1$, where, $M_r = (U - c_r)/a$, U is the streamwise velocity, and a is the local speed of sound. The first mode of instability is similar to the Tollmien-Schlichting instability mode of incompressible flows, while the second and higher unstable modes are unique to compressible flows. Mack called these modes higher modes and we will call them Mack modes. For the inviscid case, Mack found that the lowest Mach number at which the higher modes exist in the boundary layer on an insulated flat plate is 2.2. The lowest of these modes is the second mode and it is the most amplified of the higher modes. The numerical results of Mack show that two-dimensional second and higher-mode (Mack) waves are more unstable than their corresponding three-dimensional waves. The maximum growth rate of second-mode waves drops sharply as the wave angle increases from zero. For the viscous case, the lowest Mach number at which Mack was able to calculate two-dimensional second-mode waves is $M_\infty = 3.0$, at which the minimum critical Reynolds number is 13,900. Moreover, the inviscid instability increases rapidly with increasing Mach number and hence one would expect the minimum critical Reynolds number to decrease rapidly to lower values as the Mach number increases. In fact, Mack found that the minimum critical Reynolds number drops to 235 as the Mach number increases to 4.5. Moreover, at high Mach numbers, Mack waves have much higher growth rates than oblique first-mode waves.

The effect of heat transfer on the stability of compressible boundary layers has been studied by many researchers. Using temporal inviscid and viscous theories, Mack (1969, 1975) came up with most of what we know about the effect of heat transfer on the stability of compressible boundary layers. Mack found that while cooling stabilizes first-mode waves it destabilizes second-mode waves. Lysenko and Maslov (1984) confirmed experimentally and by integrating the stability equations in the Dunn-Lin approximation that surface cooling destabilizes second-mode (high frequency) disturbances: the amplification rates increase and the unstable frequency range expands and is shifted to the region of larger frequencies. Lysenko and Maslov found that the experimental results are in qualitative agreement with the predictions of the theory of hydrodynamic stability.

Malik (1989) found that favorable pressure gradients stabilize both first and second-modes of instability. Zurigat et al.

[1]Present address: High Technology Corporation, Hampton, VA 23666

Contributed by the Fluids Engineering Division for publication in the JOURNAL OF FLUIDS ENGINEERING. Manuscript received by the Fluids Engineering Division November 5, 1990.

(1990) studied the effect of favorable and adverse pressure gradients on the stability of compressible boundary layers. In addition to confirming the findings of Malik (1989), they found that the effectiveness of favorable pressure gradients on natural laminar flow control decreases at hypersonic Mach numbers. The stabilizing effect of favorable pressure gradients on three-dimensional first-mode waves is much larger than on two-dimensional first-mode waves.

Malik (1989) studied the effect of self-similar suction distributions on second-mode waves. He found that suction shifts the band of unstable frequencies to higher values and reduces the peak amplification. Mack (1989) showed that suction is also stabilizing according to the inviscid theory, although the effect is not as strong as in Malik's example. We note that Malik's results are for a single Reynolds number ($R = 1500$) and a single Mach number ($M_\infty = 4.5$). In this paper and its companion Part II, we present a detailed study of the effect of self-similar as well as uniform-suction distributions on the stability of supersonic boundary layers. Since, as we pointed out earlier, the most amplified second-mode waves are two dimensional, whereas the most amplified first-mode waves in supersonic flows are three dimensional, we consider the simpler problem of second-mode waves in this paper and we consider first-mode waves in Part II (Masad et al., 1991).

The Mean Flow

We consider a two-dimensional compressible flow of an ideal calorically perfect gas over an adiabatic flat plate. The basic flowfield is goverened by the nondimensional two-dimensional boundary-layer equations:

x-momentum equation

$$\rho u \frac{\partial u}{\partial x} + \rho v \frac{\partial u}{\partial y} = \frac{\partial}{\partial y}\left(\mu \frac{\partial u}{\partial y}\right) \tag{1}$$

continuity equation

$$\frac{\partial(\rho u)}{\partial x} + \frac{\partial(\rho v)}{\partial y} = 0 \tag{2}$$

energy equation

$$\rho u \frac{\partial T}{\partial x} + \rho v \frac{\partial T}{\partial y} = \frac{1}{\mathrm{Pr}} \frac{\partial}{\partial y}\left(\mu \frac{\partial T}{\partial y}\right) + (\gamma - 1)\mathrm{M}_\infty^2 \mu \left(\frac{\partial u}{\partial y}\right)^2 \tag{3}$$

In these equations,

$$x = \frac{x^*}{L^*},\ y = \sqrt{\mathrm{Re}}\,\frac{y^*}{L^*},\ u = \frac{u^*}{U_\infty^*},\ v = \sqrt{\mathrm{Re}}\,\frac{v^*}{U_\infty^*},$$

$$\rho = \frac{\rho^*}{\rho_\infty^*},\ T = \frac{T^*}{T_\infty^*},\ \mu = \frac{\mu^*}{\mu_\infty^*} \tag{4}$$

$$\mathrm{Re} = \frac{U_\infty^* L^* \rho_\infty^*}{\mu_\infty^*},\ \mathrm{Pr} = \frac{\mu_\infty^* C_p^*}{\kappa_\infty^*},\ \text{and}\ \gamma = \frac{C_p^*}{C_v^*}$$

where the subscript ∞ indicates free-stream values, L^* is a reference length, and C_p^* and C_v^* are the gas specific heat coefficients at constant pressure and volume, respectively. For a perfect gas, the non-dimensional equation of state takes the form

$$\rho T = 1 \tag{5}$$

Away from the wall, the boundary conditions are

$$u \to 1 \text{ and } T \to 1 \text{ as } y \to \infty$$

Moreover, the temperature gradient at the wall should vanish for adiabatic wall conditions; that is,

$$\frac{\partial T}{\partial y} = 0 \text{ at } y = 0 \tag{6a}$$

Here, we consider the case of continuous wall suction. Assuming that the suction velocity is directed normal to the plate, we have

$$u = 0 \text{ and } v = v_w \text{ at } y = 0 \tag{6b}$$

where v_w can vary with x in general. However, there are two restrictions on the suction velocity. First, v_w should not be too large so as to invalidate the boundary-layer assumptions. Second, v_w should not vary abruptly, as in the case of suction strips. In the latter case, the conventional boundary-layer equations cannot predict the upstream influence of the abrupt changes. Instead one should use a triple-deck formulation or the interactive boundary-layer equations or the Navier-Stokes equations.

It is convenient to reformulate the problem by using the Levy-Lees variables

$$\xi = x \text{ and } \eta(x, y) = \frac{\sqrt{Re}}{\sqrt{2\xi}} \int_0^y \rho dy \tag{7}$$

and transforming Eqs. (1)–(6) into

$$2\xi F F_\xi + V F_\eta - \frac{\partial}{\partial \eta}\left(\theta \frac{\theta F}{\partial \eta}\right) = 0 \tag{8}$$

$$2\xi F_\xi + V_\eta + F = 0 \tag{9}$$

$$2\xi F Q_\xi + V Q_\eta - \frac{\partial}{\partial \eta}\left(\frac{\theta}{\mathrm{Pr}} \frac{\partial Q}{\partial \eta}\right) - (\gamma - 1)\mathrm{M}_\infty^2 \theta F_\eta^2 = 0 \tag{10}$$

where

$$F = u,\ Q = T,\ \theta = \rho\mu \tag{11a}$$

$$V = \sqrt{2\xi}\ [\sqrt{\mathrm{Re}}\ \rho v + \eta_x \sqrt{2\xi}\ F] \tag{11b}$$

The boundary conditions become

$$F \to 1 \text{ and } Q \to 1 \text{ as } \eta \to \infty \tag{12a}$$

$$F = 0,\ \frac{\partial Q}{\partial \eta} = 0, \text{ and } V\sqrt{2\xi Re}\ \rho(0) v_w \text{ at } \eta = 0 \tag{12b}$$

Equations (7)–(12) represent the nonsimilar boundary-layer equations. Under certain conditions, these equations admit self-similar solutions. These conditions include flows over an adiabatic flat plate with no suction or blowing. In the case of uniform suction distributions, V_w varies along the plate and hence self-similar solutions do not exist. However, when V_w is constant, and hence the physical suction velocity v_w is proportional to $\xi^{-1/2}$, Eqs. (7)–(12) admit self-similar solutions for flows over adiabatic flat plates. In the latter case, $F_\xi = 0$ and $Q_\xi = 0$. Letting $V = -f(\eta)$ and solving Eq. (9), we have $F = f'$. Then, using Eq. (5), we rewrite Eqs. (8) and (10) as

$$\left(\frac{\mu}{T} f''\right)' + f f'' = 0 \tag{13}$$

$$\left(\frac{\mu}{T\mathrm{Pr}} T'\right)' + f T' + (\gamma - 1)\mathrm{M}_\infty^2 \frac{\mu}{T} (f'')^2 = 0 \tag{14}$$

where the prime denotes the derivative with respect to η. The boundary conditions (12) become

$$f' \to 1 \text{ and } T \to 1 \text{ as } \eta \to \infty \tag{15}$$

$$f' = 0,\ T' = 0, \text{ and } f = \sqrt{2}\ V_w \text{ at } \eta = 0 \tag{16}$$

where

$$V_w = \frac{\sqrt{\xi \mathrm{Re}}}{T(0)} v_w = \text{constant} \tag{17}$$

Thus, the physical wall velocity must be proportional to $T(0)/\sqrt{\xi}$. In the self-similar calculations, we specify V_w instead of v_w. We note from Eqs. (17) and (5) that V_w is proportional to the mass-flow rate and we will refer to it as the mass flux.

Equations (7)–(12) are solved using central differences in the transverse direction and three-point backward differencing in the streamwise direction, whereas Eqs. (13)–(17) are solved using the finite-difference code BVPFD (Pereyra, 1976).

Stability Analysis

To study the stability of the calculated two-dimensional mean flow, we superimpose on it a small disturbance and express the total-flow quantities in the form

$$\hat{q}(x, y, z, t) = q_m(y) + q(x, y, z, t) \tag{18}$$

where q stands for u, v, w, ρ, p, μ, and T; the hat stands for the total-flow quantities; and the subscript m stands for the mean-flow quantities. Substituting Eq. (18) into the compressible Navier-Stokes equations, recalling that the mean flow satisfies the Navier-Stokes equations, and linearizing with respect to q, we obtain the disturbance equations

$$\frac{\partial \rho}{\partial t} + \rho_m \frac{\partial u}{\partial x} + u_m \frac{\partial \rho}{\partial x} + \frac{\partial}{\partial y}(\rho_m v) + \rho_m \frac{\partial w}{\partial z} = 0 \tag{19}$$

$$\rho_m \left(\frac{\partial u}{\partial t} + u_m \frac{\partial u}{\partial x} + v \frac{du_m}{dy}\right) = -\frac{\partial p}{\partial x} + \frac{1}{R}\left\{\mu_m \frac{\partial}{\partial x}\left(r \frac{\partial u}{\partial x} + m \frac{\partial v}{\partial y} + m \frac{\partial w}{\partial z}\right) + \frac{\partial}{\partial y}\left[\mu_m\left(\frac{\partial u}{\partial y} + \frac{\partial v}{\partial x}\right) + \mu \frac{du_m}{dy}\right] + \mu_m \frac{\partial}{\partial z}\left(\frac{\partial w}{\partial x} + \frac{\partial u}{\partial z}\right)\right\} \tag{20}$$

$$\rho_m \left(\frac{\partial v}{\partial t} + u_m \frac{\partial v}{\partial x}\right) = -\frac{\partial p}{\partial y} + \frac{1}{R}\left\{\frac{\partial}{\partial x}\left[\mu_m\left(\frac{\partial u}{\partial y} + \frac{\partial v}{\partial x}\right) + \mu \frac{du_m}{dy}\right] + \frac{\partial}{\partial y}\left[\mu_m\left(m \frac{\partial u}{\partial x} + r \frac{\partial v}{\partial y} + m \frac{\partial w}{\partial z}\right)\right] + \mu_m \frac{\partial}{\partial z}\left(\frac{\partial v}{\partial z} + \frac{\partial w}{\partial y}\right)\right\} \tag{21}$$

$$\rho_m \left(\frac{\partial w}{\partial t} + u_m \frac{\partial w}{\partial x}\right) = -\frac{\partial p}{\partial z} + \frac{1}{R}\left\{\mu_m \frac{\partial}{\partial x}\left(\frac{\partial w}{\partial x} + \frac{\partial u}{\partial z}\right) + \frac{\partial}{\partial y}\left[\mu_m\left(\frac{\partial v}{\partial z} + \frac{\partial w}{\partial y}\right)\right] + \mu_m \frac{\partial}{\partial z}\left(m \frac{\partial u}{\partial x} + m \frac{\partial v}{\partial y} + r \frac{\partial w}{\partial z}\right)\right\} \tag{22}$$

$$\rho_m \left[\frac{\partial T}{\partial t} + u_m \frac{\partial T}{\partial x} + v \frac{dT_m}{dy}\right] = (\gamma - 1)\mathrm{M}_\infty^2 \left[\frac{\partial p}{\partial t} + u_m \frac{\partial p}{\partial x} + \frac{1}{\mathrm{R}} \phi\right] + \frac{1}{R\mathrm{Pr}}\left\{\mu_m \frac{\partial^2 T}{\partial x^2} + \frac{\partial}{\partial y}\left(\mu_m \frac{\partial T}{\partial y} + \mu \frac{dT_m}{dy}\right) + \mu_m \frac{\partial^2 T}{\partial z^2}\right\} \tag{23}$$

$$\phi = 2\mu_m \left(\frac{\partial u}{\partial y} + \frac{\partial v}{\partial x}\right) \frac{du_m}{dy} + \mu \left(\frac{du_m}{dy}\right)^2 \tag{24}$$

where

$$r = 2 + \frac{\lambda}{\mu} \text{ and } m = \frac{\lambda}{\mu}$$

The local Reynolds number R in Eqs. (19)–(24) is based on a reference length $\delta_r^* = \sqrt{\nu_\infty^* x_r^* / U_\infty^*}$, which is the order of the boundary-layer thickness, where x_r^* is the distance from the leading edge to the location where the stability calculations are performed. Velocities are normalized with respect to the free-stream velocity U_∞^* and lengths are normalized with respect to δ_r^*. Hence,

$$\mathrm{R} = \frac{U_\infty^* \delta_r^*}{\nu_\infty^*} = \sqrt{\frac{U_\infty^* x_r^*}{\nu_\infty^*}} = \sqrt{\mathrm{Re}_x} = \sqrt{x\mathrm{Re}}$$

The boundary conditions at the wall are

$$u = v = w = 0 \text{ and } T = 0 \text{ at } y = 0 \tag{25}$$

Away from the wall,

$$u, v, w, T, p \text{ are bounded as } y \to \infty \tag{26}$$

We assume that μ is a function of temperature only; hence

$$\mu = T \frac{d\mu_m}{dT}(T_m) = T\mu_m'(T_m) \tag{27}$$

Moreover, the linearized equation of state takes the form

$$p/p_m = T/T_m + \rho/\rho_m \tag{28}$$

Because the mean flow is assumed to be quasiparallel, we seek a solution in the form of three-dimensional traveling waves as

$$[u, v, p, T, w] = [\zeta_1(y), \zeta_3(y), \zeta_4(y), \zeta_5(y), \zeta_7(y)] \exp[i(\int \alpha dx + \beta z - \omega t)] \tag{29}$$

where α and β are the streamwise and spanwise wave numbers, respectively, and ω is the frequency. Substituting Eqs. (28) and (29) into Eqs. (19)–(24), we obtain

$$D\zeta_3 + i\alpha\zeta_1 - \frac{DT_m}{T_m}\zeta_3 + i(\alpha u_m - \omega)\left(\gamma \mathrm{M}_\infty^2 \zeta_4 - \frac{\zeta_5}{T_m}\right) + i\beta\zeta_7 = 0 \tag{30}$$

$$i(\alpha u_m - \omega)\zeta_1 + \zeta_3 Du_m + i\alpha T_m \zeta_4 - \frac{T_m}{\mathrm{R}}\{-\mu_m(\mathrm{r}\alpha^2 + \beta^2)\zeta_1 - \alpha\beta\mu_m(m+1)\zeta_7 + i(m+1)\alpha\mu_m D\zeta_3 + \mu_m' DT_m D\zeta_1 + i\alpha\mu_m' DT_m\zeta_3 + \mu_m D^2\zeta_1 + D(\mu_m' Du_m)\zeta_5 + \mu_m' Du_m D\zeta_5\} = 0 \tag{31}$$

$$i(\alpha u_m - \omega)\zeta_3 + T_m D\zeta_4 - \frac{T_m}{R}\{i(m+1)\alpha\mu_m D\zeta_1 + im\alpha\mu_m' DT_m\zeta_1 - (\alpha^2 + \beta^2)\mu_m\zeta_3 + r\mu_m' DT_m D\zeta_3 + im\beta\mu_m' DT_m\zeta_7 + i\alpha\mu_m' Du_m\zeta_5 + r\mu_m D^2\zeta_3 + i(m+1)\beta\mu_m D\zeta_7\} = 0 \tag{32}$$

$$i(\alpha u_m - \omega)\zeta_7 + i\beta T_m\zeta_4 - \frac{T_m}{\mathrm{R}}\{-(\mathrm{m}+1)\alpha\beta\mu_m\zeta_1 + i\beta\mu_m' DT_m\zeta_3 + \mu_m i(m+1)\beta D\zeta_3 - \mu_m(\alpha^2 + r\beta^2)\zeta_7 + \mu_m' DT_m D\zeta_7 + \mu_m D^2\zeta_7\} = 0 \tag{33}$$

$$i(\alpha u_m - \omega)\zeta_5 + \zeta_3 DT_m - i(\gamma - 1)T_m \mathrm{M}_\infty^2 (\alpha u_m - \omega)\zeta_4 - (\gamma - 1)\mathrm{M}_\infty^2 \frac{T_m}{R}\left[2\mu_m Du_m(D\zeta_1 + i\alpha\zeta_3) + \mu_m'(Du_m)^2\zeta_5\right] - \frac{T_m}{\mathrm{RPr}}\left[-\mu_m(\alpha^2 + \beta^2)\zeta_5 + D(\mu_m D\zeta_5) + \mathrm{D}(\mu_m' DT_m\zeta_5)\right] = 0 \tag{34}$$

$$\zeta_1 = \zeta_3 = \zeta_5 = \zeta_7 = 0 \text{ at } y = 0 \tag{35}$$

$$\zeta_n \text{ are bounded as } y \to \infty \tag{36}$$

where the prime denotes the derivative with respect to the argument and $D = d/dy$.

In this work, we consider the case of spatial stability so that ω is real. Because the mean flow is two-dimensional, β is real and α complex so that

$$\alpha = \alpha_r + i\alpha_i \tag{37}$$

Moreover, we compute ω from the nondimensional frequency F as

$$\omega = \mathrm{R}F \tag{38a}$$

and compute the wave angle ψ as

$$\psi = \tan^{-1}(\beta/\alpha_r) \tag{38b}$$

Letting $\mathrm{R} \to \infty$ in Eqs. (30)–(34) yields the inviscid stability problem. The resulting equations can be combined into either (Mack, 1969; Nayfeh, 1988)

$$D^2\zeta_4 - D(\ln D\mathrm{M}_r^2)D\zeta_4 - k^2(1 - \mathrm{M}_r^2)\zeta_4 = 0 \tag{39}$$

or

$$D^2\chi + D\left[\ln \frac{\mathrm{M}_r^2}{1 - \mathrm{M}_r^2}\right] D\chi - \mathrm{k}^2(1 - \mathrm{M}_r^2)\chi = 0 \tag{40}$$

where

$$\chi=\frac{\zeta_3}{\alpha U_m-\omega},\ \mathrm{M}_r=\frac{(\alpha U_m-\omega)\mathrm{M}_\infty}{k\sqrt{T_m}},\ k=(\alpha^2+\beta^2)^{1/2} \quad (41)$$

Thus, M_r can be interpreted as the local Mach number of the mean flow in the direction of the vector $\mathbf{k} = \alpha\mathbf{i} + \beta\mathbf{j}$ relative to the phase velocity ω/k. In general, M_r is complex and it is only real for neutral disturbances. Outside the boundary layer, $U_m = 1$ and $T_m = 1$ and hence

$$\mathrm{M}_r=\mathrm{M}_f=\frac{(\alpha-\omega)\mathrm{M}_\infty}{k}$$

and Eqs. (39) and (40) reduce to

$$D^2\zeta_4-k^2(1-\mathrm{M}_f^2)\zeta_4=0 \quad (42)$$

and

$$D^2\chi-k^2(1-\mathrm{M}_f^2)\chi=0 \quad (43)$$

Therefore, neutral disturbances decay outside the boundary layer if and only if $\mathrm{M}_f^2 < 1$; these disturbances are termed subsonic waves. When $\mathrm{M}_f^2 > 1$, neutral disturbances do not vanish in the freestream and they represent sound waves or Mach waves of the relative flow; they are termed supersonic waves. When $\mathrm{M}_f^2 = 1$, the disturbances are termed sonic waves. These classifications are due to Lees and Lin (1946). Because subsonic waves are the most unstable disturbances (Mack, 1969), we consider in this paper only subsonic waves and hence replace Eq. (36) with

$$\zeta_n\to 0 \text{ as } y\to\infty \quad (44)$$

The eigenvalue problem given by Eqs. (30)–(35) and (44) consists of a system of homogeneous differential equations subject to homogeneous boundary conditions. The solution to this eigenvalue problem is obtained numerically using a combination of an adaptive finite-difference scheme (Pereyra, 1976) and a Newton-Raphson iteration procedure. Our code was validated for the case of impermeable flat plate by comparing its results with those obtained using the fundamental matrix method and the computer code SUPPORT (Asfar et al., 1990).

The advantages of using the adaptive finite-difference scheme is that it is easy to program, highly accurate, and can solve a nonlinear problem. One of its disadvantages is the large amount of memory required if too many grid points are used, which will be the case if a high accuracy is required. Other disadvantages are that the code might not converge even for linear problems and that it is not recommended for a number of equations exceeding 20.

In all the computations done in Parts I and II of this paper, 801 points were used in the normal direction. The value of y where the free-stream boundary conditions were applied was increased with increasing M_∞. At $\mathrm{M}_\infty = 8.0$, it was set equal to 40.0. The tolerance specified for all the computations is 10^{-6}, which means that the computations stop when

$$|\tau|/\max(|\zeta|)<10^{-6}$$

where τ is the estimated error for any ζ at any grid point.

Results

The quasiparallel assumption for the flow under consideration is justified because the wavelengths of the most amplified disturbances are very small compared to the development length χ_r^* of the boundary layer. For second-mode (Mack) waves of instability at $R=\sqrt{\mathrm{Re}_x} = 1500$, where $\mathrm{Re}_x=U_\infty^* x_r^*/\nu_\infty^*$, the results presented in this paper for the most amplified waves show that $\alpha_r^*\delta_r^* > 0.0945$ for all Mach numbers between 3.8 and 8, where α_r^* is the most amplified streamwise wave number and $\delta_r^* = \sqrt{\nu_\infty^* x_r^*/U_\infty^*}$. Thus, $\alpha_r^* x_r^* > 0.0945\sqrt{\mathrm{Re}_x}$.

The instability of compressible boundary layers is both viscous and inviscid in nature. The inviscid stability theory of compressible boundary layers revealed two important parameters. Equations (39) and (40) show explicitly one of these parameters, namely, M_r, the local Mach number of the mean flow in the direction of the wave number vector relative to the phase velocity ω/k. The second parameter is the so-called generalized inflection point, which corresponds to y_s where

$$D(\rho_m DU_m)=0 \quad (45)$$

Lees and Lin (1946) demonstrated that a sufficient condition for the existence of amplified inviscid disturbances is the presence of a generalized inflection point at some transverse position $y_s > y_o$ where y_o is the transverse location where $U_m = 1 - \mathrm{M}_\infty^{-1}$. In contrast with incompressible flow over an insulated flat plate which does not have inflection points and hence is stable to inviscid disturbances, compressible flow over an insulated plate has generalized inflection points and hence is unstable to inviscid disturbances.

At low supersonic Mach numbers, the instability is of the viscous type as in the incompressible case except that the most amplified waves are oblique rather than two-dimensional. As the Mach number increases, the generalized inflection point moves farther away from the wall, as in the case of incompressible boundary layers with adverse pressure gradients, except that compressibility has a stabilizing effect. Using extensive numerical calculations, Mack (1969) found that the destabilizing influence of viscosity decreases as the Mach number increases and that above a Mach number of about 4, the influence of viscosity is only stabilizing.

Using extensive numerical calculations, Mack (1979) established the existence of an infinite sequence of discrete wave numbers corresponding to an infinite sequence of discrete modes when $\mathrm{M}_r^2 > 1$ somewhere in the boundary layer. The first mode of instability is similar to the Tollmien-Schlichting instability mode of incompressible flows, while the second and higher modes are unique to compressible flows. In contrast with the first inviscid mode whose existence depends on the presence of a generalized inflection point, the higher inviscid modes exist whenever $\mathrm{M}_r^2 > 1$, irrespective of the presence of a generalized inflection point. The lowest Mach number at which the higher modes exist in the boundary layer on a flat plate is 2.2. It turns out that this is also the lowest Mach number at which subsonic higher mode disturbances exist. The lowest of the subsonic modes is called the second mode and it is the most amplified of the higher modes. The lowest Mach number at which Mack was able to calculate viscous two-dimensional second-mode waves is $\mathrm{M}_\infty = 3.0$ at which the minimum critical Reynolds number is 13,900. As pointed out earlier, the inviscid instability increases rapidly with increasing Mach number and hence one would expect the minimum critical Reynolds number to decrease rapidly to lower values as the Mach number increases. In fact, Mack found that the minimum critical number drops to 235 as M_∞ increases to 4.5. Moreover, at high Mach numbers second-mode waves have much higher growth rates than oblique first-mode waves.

As suction is applied to the plate, the original generalized inflection point moves toward the wall and a second generalized inflection point appears for $U_m<1-\mathrm{M}_\infty^{-1}$; the latter is not associated with any inviscid instabilities. As the suction level increases, the two generalized inflection points move toward each other and then disappear, resulting in the disappearance of the inviscid instability.

In this paper, we investigate the effect of suction on second-mode waves, whereas in Part II, we investigate the effect of suction on first-mode waves. As pointed out earlier, at Mach numbers above 3.0, a second mode of instability emerges. As the Mach number increases, this mode becomes more unstable than the first mode. Malik (1989) showed that the maximum growth rate $-\alpha_i$ of second-mode waves at $\mathrm{M}_\infty = 4.5$ and R = 1500 decreases with suction and the frequency of the most amplified wave is shifted considerably toward higher values. Since our formulation and results are for a constant Prandtl

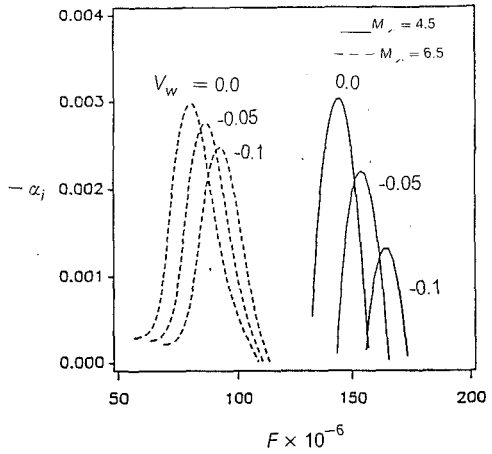

Fig. 1 Effect of self-similar suction distributions on the variation of the growth rate of two-dimensional second-mode waves with frequency when R = 1550, T_∞ = 120°K and Pr = 0.72

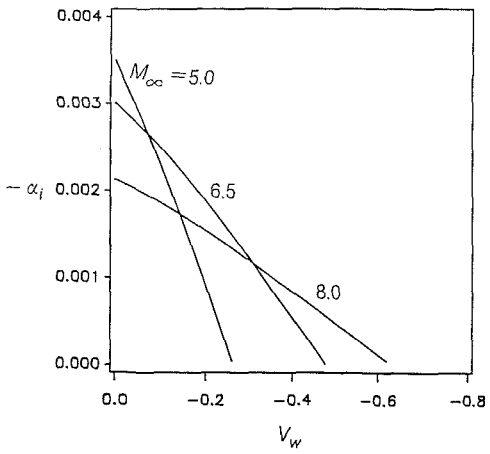

Fig. 2 Variation of the maximum growth rate with mass flux for the case of self-similar suction distributions: R = 1550, T_∞ = 120°K, and Pr = 0.72

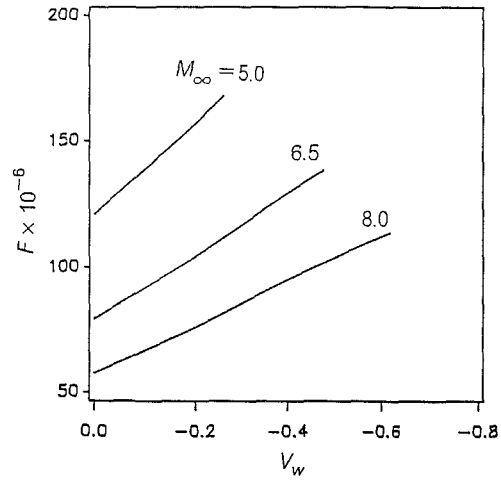

Fig. 3 The frequencies corresponding to the maximum growth rates of Fig. 2

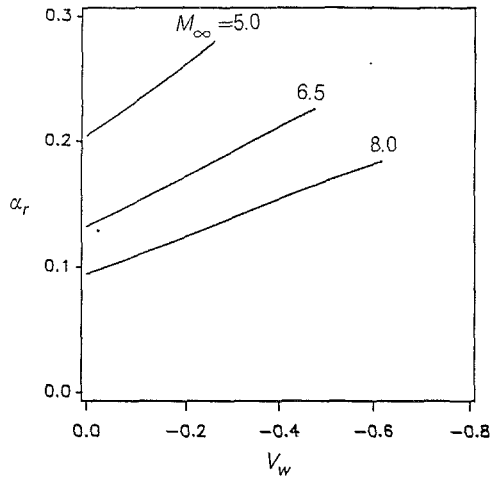

Fig. 4 The wave numbers corresponding to the maximum growth rates of Fig. 2

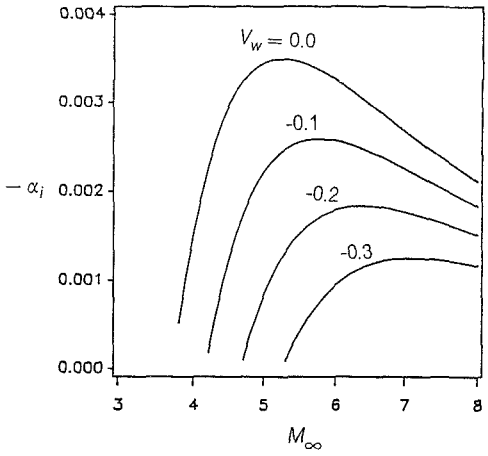

Fig. 5 Variation of the maximum growth rate of two-dimensional second-mode waves with Mach number for the case of self-similar suction distributions when R = 1500, T_∞ = 120°K, and Pr = 0.72

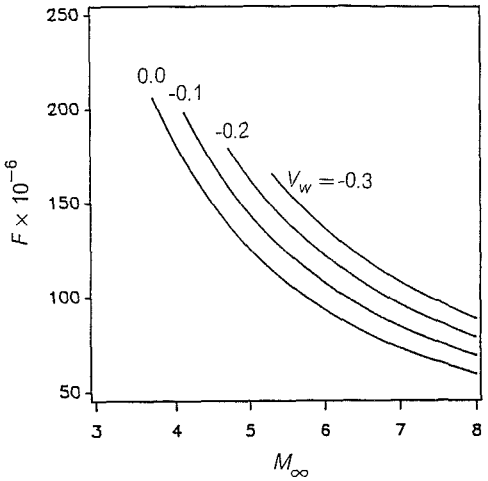

Fig. 6 The frequencies corresponding to Fig. 5

number, whereas those of Malik are for a variable Prandtl number, it is not possible to compare our results with his. However, Fig. 1 shows a set of results similar to those of Malik for the two Mach numbers 4.5 and 6.5 at R = 1500. The considered waves are two-dimensional. We note that as the Mach number increases, the band of unstable frequencies shifts considerably toward lower frequencies. Moreover, at both Mach numbers, suction reduces the peak amplification and shifts it toward a higher frequency. However, suction is much less effective in stabilizing second-mode waves at M_∞ = 6.5 than at M_∞ = 4.5.

Figure 2 shows variation of the maximum growth rates with

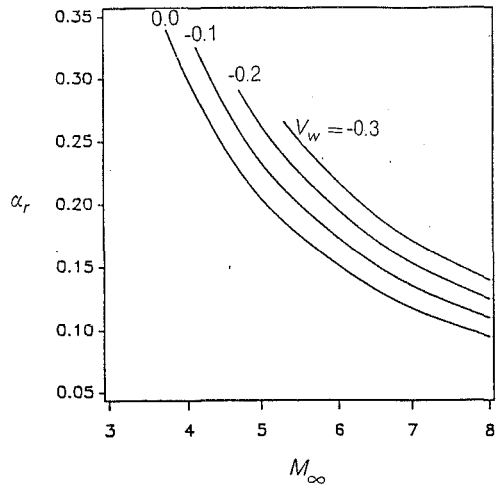

Fig. 7 The wave numbers corresponding to Fig. 5

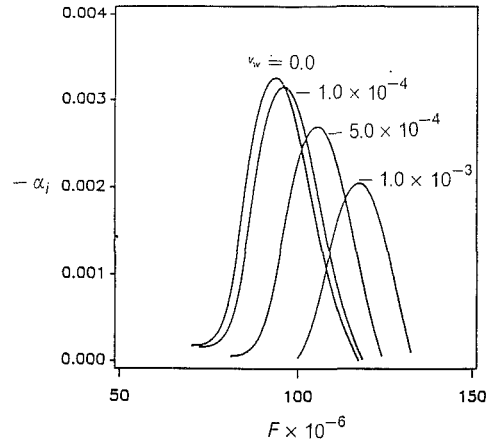

Fig. 8 Effect of uniform suction distributions on the variation of the growth rate of two-dimensional second-mode waves with frequency: R = 1500, Re = 10^8, x = 0.0225, M_∞ = 6.0, T_∞ = 120°K, and Pr = 0.72

mass flux for the three Mach numbers M_∞ = 5, 6.5, and 8 at R = 1550. For all three Mach numbers, the maximum growth rates decrease monotonically with mass flux. In fact the maximum growth rate decreases approximately linearly with mass flux. Figure 2 also shows that, although in the presence of no suction the maximum growth rates of second-mode waves at high Mach numbers are less than those at lower Mach numbers, it takes more suction to stabilize them. This is true at any suction level, as we can tell by comparing the slopes of the lines. This indicates clearly that the effectiveness of suction in stabilizing second-mode (Mack) waves decreases drastically as the Mach number increases. The corresponding frequencies increase approximately linearly with mass flux, as shown in Fig. 3. Moreover, the corresponding wave numbers also increase approximately linearly with mass flux, as shown in Fig. 4. We note here that in computing the results shown in Fig. 2, we maximized the growth rate over both frequencies and wave angles with the steps in frequency F and spanwise wave number β being 0.01 × 10^{-6} and 0.0001, respectively. The results show that the wave angle remained zero, which means that in the presence of suction, the most unstable second-mode (Mack) waves remain two dimensional.

Figure 5 shows variation of the maximum growth rate with M_∞ for different suction levels. The critical Mach number at which unstable second-mode waves exist increases with suction. Without suction, the critical Mach number is M_∞ = 3.8, whereas with V_w = − 0.3, the critical Mach number increases to M_∞ = 5.3. In addition, suction is very effective in decreasing the maximum growth rates of Mach waves at low Mach numbers. Figure 6 shows that the frequencies corresponding to the maximum growth rates decrease with Mach number but increase as the suction level increases, in agreement with the results of Figs. 1 and 3. The wave numbers corresponding to the maximum growth rates decrease as the Mach number increases but increase as the mass flux increases, as shown in Fig. 7, in agreement with the results of Fig. 4.

Figure 8 shows variation of the growth rate with frequency for different levels of uniform suction distribution at M_∞ = 6.0. As in the case of self-similar suction distributions, uniform suction distributions reduce the peak amplifications and shift them toward higher frequencies.

We mention here that at hypersonic Mach numbers, transition is more likely to take place due to the second mode rather than the first mode. It seems that controlling disturbances at hypersonic Mach numbers is a very difficult task. There are three main known methods to control disturbances, namely, heat transfer, pressure gradient (or wall shaping), and suction. Mack (1969) showed that wall heating stabilizes the second mode. However, wall heating is very unlikely to be used to control the flow at hypersonic speeds because available materials can hardly sustain the surface temperatures even in the presence of no heating. Moreover, Masad et al. (1991) showed that the effect of heat transfer on the stability of compressible boundary layers deteriorates at hypersonic speeds. Zurigat et al. (1990) showed that the effectiveness of wall shaping on stabilizing the flow also decreases at high Mach numbers. In this work we showed that suction behaves similarly. Thus, all three main known methods of controlling boundary layers become ineffective at hypersonic speeds, and there might be a need to explore other methods to control the flow at high speeds.

In summary, suction is more effective in stabilizing second-mode (Mack) waves at low Mach numbers. The peak amplifications of Mack waves are always reduced by suction and shifted toward higher frequencies. In the presence of suction, the most amplified Mack waves remain two dimensional. The maximum growth rates of second-mode (Mack) waves and their corresponding frequencies and wave numbers vary almost linearly with mass flux. The frequencies and wave numbers corresponding to the most amplified second-mode waves increase by increasing the mass flux.

Acknowledgment

This work was supported by the Office of Naval Research under grant No. N00014-85-0011, NR 4325201.

References

Asfar, O. R., Masad, J. A., and Nayfeh, A. H., 1990, "A Method for Calculating the Stability of Boundary Layers," *Computers & Fluids*, Vol. 18, pp. 305–315.

Bogdanoff, S., 1987, "Concluding Remarks," NASA/ICASE Workshop on Stability and Transition of High Mach Number Shear Layers, Hampton, VA.

Herbert, Th., 1991, "Boundary-Layer Transition-Analysis and Prediction Revisited," AIAA Paper No. 91-0737.

Lees, L., and Lin, C. C., 1946, "Investigation of the Stability of the Laminar Boundary Layer in a Compressible Fluid," NACA Technical Note No. 1115.

Lysenko, V. I., and Maslov, A. A., 1984, "The Effect of Cooling on Supersonic Boundary-Layer Stability," *Journal of Fluid Mechanics*, Vol. 147, pp. 39–52.

Mack, L. M., 1969, "Boundary-Layer Stability Theory," Jet Propulsion Laboratory, Pasadena, CA, Document No. 900-277, Rev. A.

Mack, L. M., 1975, "Linear Stability Theory and the Problem of Supersonic Boundary-Layer Transition," *AIAA Journal*, Vol. 13, pp. 278–289.

Mack, L. M., 1984, "Boundary-Layer Linear Stability Theory," in Special Course on Stability and Transition of Laminar Flow, AGARD Report No. 709.

Mack, L. M., 1989, "On Inviscid Acoustic-Mode Instability in Supersonic Shear Flows," *Fourth Symposium on Numerical and Physical Aspects of Aerodynamic Flows*, Long Beach, CA.

Malik, M. R., 1989, "Prediction and Control of Transition in Hypersonic Boundary Layers," *AIAA Journal*, Vol. 27, pp. 1487–1493.

Masad, J. A., Nayfeh, A. H., and Al-Maaitah, A. A., 1991, "Effect of

Suction on the Stability of Supersonic Boundary Layers II. First-Mode Waves," ASME JOURNAL OF FLUIDS ENGINEERING, published in this issue, pp.

Masad, J. A., Nayfeh, A. H., and Al-Maaitah, A. A., 1991, "Effect of Heat Transfer on the Stability of Compressible Boundary Layers," in press, *Computers & Fluids*.

Nayfeh, A. H., 1988, "Stability of Compressible Boundary Layers," *Transonic Symposium: Theory, Application, and Experiment* (NASA-Langley Research Center, Hampton, VA), NASA Conf. Pub. 3020, Vol. 1, pp. 629–689.

Pereyra, V., 1976, "PASVA3: An Adaptive Finite Difference Fortran Program for First Order Nonlinear, Ordinary Boundary Problems," *Lecture Notes in Computer Science*, Vol. 76, pp. 67–88.

Zurigat, Y. H., Nayfeh, A. H., Masad, J. A., 1990, "Effect of Pressure Gradient on the Stability of Compressible Boundary Layers," AIAA Paper No. 90-1451.

J. A. Masad[1]

A. H. Nayfeh

Department of Engineering Science and Mechanics,
Virginia Polytechnic Institute and State University,
Blacksburg, VA 24061

A. A. Al-Maaitah
Department of Mechanical Engineering,
Mutah University,
Jordan

Effect of Suction on the Stability of Supersonic Boundary Layers. Part II—First-Mode Waves

The effect of suction on the first mode of instability of compressible two-dimensional boundary layers is investigated. Suction is found to be more effective in stabilizing the viscous instability, and hence it is more effective at low Mach numbers. Suction decreases the amplification rates at all frequencies and narrows down the band of unstable frequencies. Moreover, for a given frequency, suction decreases the amplification rates at all streamwise locations. Variations of the growth rates of the most amplified first-mode waves with mass flux are found to be almost linear.

Introduction

The stability theory of compressible laminar boundary layers differs in many ways from that of incompressible boundary layers (Mack, 1969, 1984a; Nayfeh, 1988). Whereas the incompressible flat-plate boundary layer has no inflection points and hence is stable to inviscid disturbances, the compressible flat-plate boundary layer has generalized inflection points and hence is unstable to inviscid disturbances. The generalized inflection point is defined as the point where $D(\rho_m DU_m)=0$. As the Mach number increases, the generalized inflection point moves away from the wall and the inviscid instability increases.

The most important feature of the stability of supersonic laminar boundary layers is that there can be more than one growing mode of instability. Using extensive numerical calculations, Mack found that there are multiple values of wavenumbers for a single disturbance phase velocity whenever there is a region of supersonic mean-flow velocity relative to the disturbance phase velocity; that is, $M_r^2>1$, where $M_r=M-c/a$, M is the local wavenumber, c is the phase speed, and a is the local speed of sound. The first mode is similar to the Tollmien-Schlichting instability mode of incompressible flows, while the second and higher modes are unique to supersonic flows.

It is an interesting facet of compressible two-dimensional boundary layers that the most unstable first-mode wave need not be parallel to the free stream as the Mach number approaches unity. In contrast with incompressible stability theory, three-dimensional first-mode waves at supersonic speeds are more unstable than their corresponding two-dimensional waves.

Again, using extensive numerical calculations, Mack investigated the influence of Mach number on the viscous instability of compressible flows past flat plates. He found that viscosity is stabilizing for both two-dimensional and three-dimensional first-mode waves when $M_\infty \geq 3.8$; that is, the maximum amplification rate (over all frequencies and waveangles at a constant Reynolds number) decreases with decreasing Reynolds number. At $M_\infty=1.6$, Mack found that compressibility drastically reduces the viscous instability. As the Mach number increases beyond 1.6, the viscous instability continues to weaken although the effect of the increase in the inviscid instability continues to extend to lower and lower Reynolds numbers. When M_∞ reaches 3.8, the viscous instability disappears and viscosity acts only to damp out the inviscid instability. This result was disputed by Wassan et al. (1984) who did not find a transition from viscous to inviscid instability with increasing Mach number but found that the viscous instability persists to $M_\infty=6.0$. Mack (1984b) reconfirmed his calculations for the case of temporal stability and obtained spatial stability results that agree with his earlier conclusions on the influence of viscosity on compressible stability. Recently, Reed and Balakumar (1990) also reconfirmed the results of Mack. Our results are in full agreement with those of Mack and Reed and Balakumar.

Malik (1989) investigated the influence of self-similar suction distributions on second-mode waves at $M_\infty=4.5$ and $R=\sqrt{\mathrm{Re}_x}=1500$. He found that suction reduces the peak amplification and shifts it to a higher frequency. Mack (1989) showed that suction is also stabilizing according to the inviscid theory, although the effect is not as strong as in Malik's example. In this paper, we present a detailed study of the effect of suction on first-mode waves in supersonic boundary layers. Second-mode waves are treated in Part I (Al-Maaitah et al., 1991), which also contains the problem formulation.

Results

The quasiparallel assumption for the flow under consideration is justified because the wavelengths $2\pi/\alpha_r^*$ of the most amplified first-mode instability waves are very small compared to the development length x_r^* of the boundary layers. In fact, the results presented in this paper show that $\alpha_r^* x_r^* > 0.0239\sqrt{\mathrm{Re}_x}$ for Mach numbers varying from zero to 7.0 and for $V_w=0.0$, -0.1, and -0.2, where Re_x is the Reynolds number based on x_r^* and V_w is the self-similar mass flux.

[1]Present address: High Technology Corporation, Hampton, VA 23666.

Contributed by the Fluids Engineering Division for publication in the JOURNAL OF FLUIDS ENGINEERING. Manuscript received by the Fluids Engineering Division November 5, 1990.

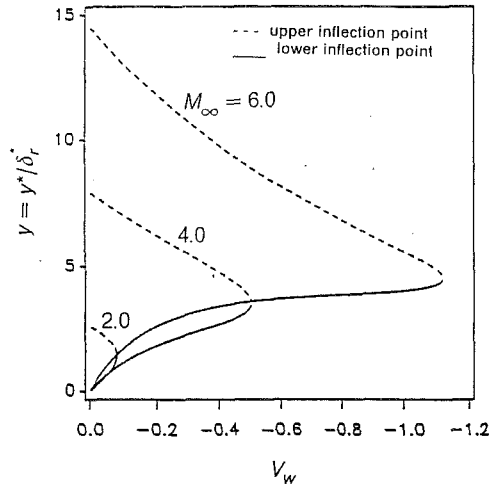

Fig. 1 Variation of the locations of the generalized inflection points with suction level for the three Mach numbers at $T_\infty = 150°K$ and Pr = 0.72.

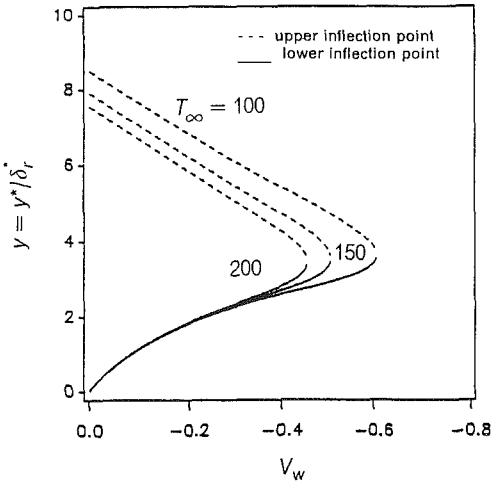

Fig. 2 Effect of T_∞ on the variation of the locations of the generalized inflection points with suction level at $M_\infty = 4.0$ and Pr = 0.72.

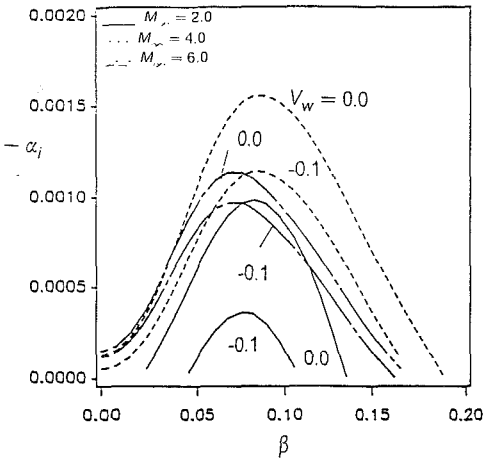

Fig. 3 Effect of suction on the variation of the growth rate with spanwise wavenumber when $R = 1500$, $F = 20 \times 10^{-6}$, Pr = 0.72, and $T_\infty = 150°K$

A great deal of the physics of the stability problem can be understood by studying the effect of suction on the mean-flow characteristics. Whereas the incompressible Blasius profile does not have an inflection point and hence it is stable to inviscid disturbances, an important characteristic of the compressible boundary layer on an adiabatic flat plate is the existence of a generalized inflection point inside the boundary layer and hence

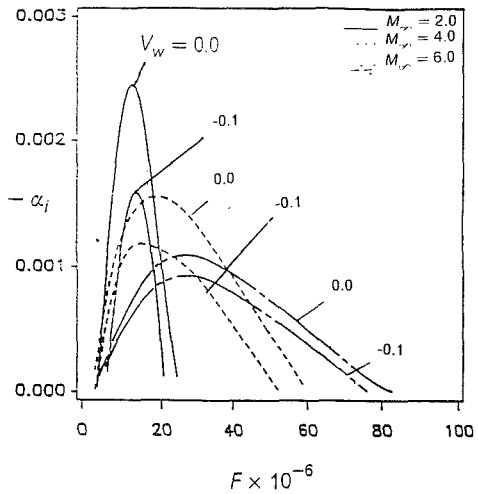

Fig. 4 Effect of suction on the variation of the growth rate with frequency when $R = 1500$, $\beta = 0.09$, Pr = 0.72, and $T_\infty = 150°K$

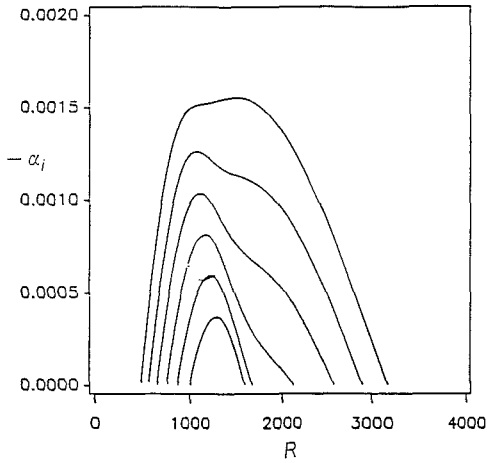

Fig. 5 Effect of suction on the variation of the growth rate with streamwise location when $F = 20 \times 10^{-6}$, $M_\infty = 4.0$, $T_\infty = 150°K$, Pr = 0.72, and $\beta = 0.06R/1000$. The values of V_w proceeding downwards are: 0.0, −0.1, −0.2, −0.3, −0.4, and −0.5.

the compressible boundary layer is unstable to inviscid disturbances. The inflection point is defined as the point y_s where $D(\rho_m DU_m) = 0$. Lees and Lin (1946) established that a sufficient condition for the existence of amplified inviscid disturbances is the presence of a generalized inflection point at $y_s > y_0$, where y_0 is the point where $U_m = 1 - M_\infty^{-1}$. As the Mach number increases, the generalized inflection point moves away from the wall and hence the inviscid instability increases.

In the absence of suction, there is one generalized inflection point y_s inside the compressible boundary layer. Because $y_s > y_0$, this generalized inflection point is associated with an inviscid instability. Suction decreases y_s and creates another generalized inflection point y_{s_1} near the wall. In Fig. 1 we show our results for variation of the locations of the inflection points with the level of the self-similar wall suction distribution when $M_\infty = 2.0$, 4.0, and 6.0. Because $y_{s_1} < y_0$, the second generalized inflection point is not associated with an inviscid instability. As the suction level increases, the two generalized inflection points move closer to each other until they meet and then disappear, as shown in Fig. 1. The minimum suction level needed to eliminate the generalized inflection points increases rapidly as the Mach number increases. Therefore, the suction level needed to stabilize the inviscid mechanism increases rapidly as the Mach number increases. The influence of T_∞ on the locations of the generalized inflection points is shown in Fig. 2. Our results in

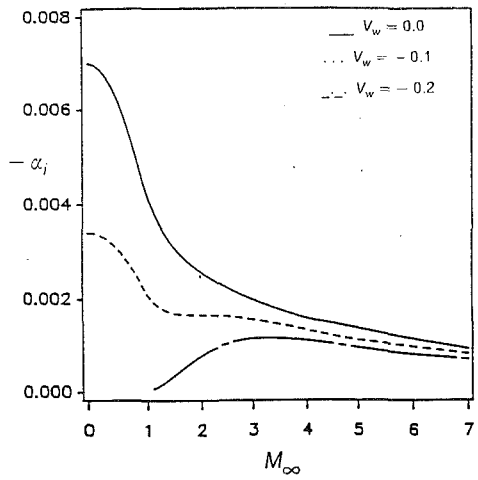

Fig. 6 Effect of suction on variation of the maximum growth rate with Mach number when $R = 1500$, Pr = 0.72, and $T_\infty = 150°K$

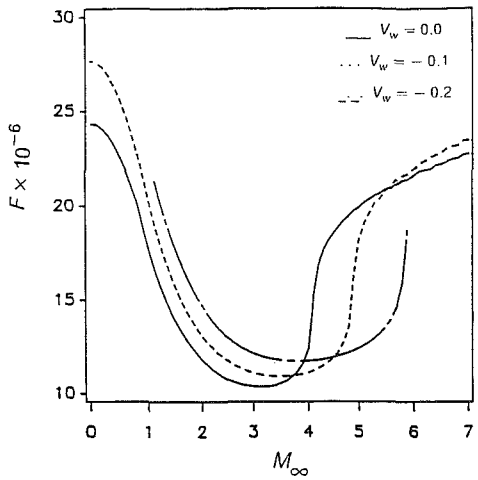

Fig. 7 The frequencies corresponding to Fig. 6

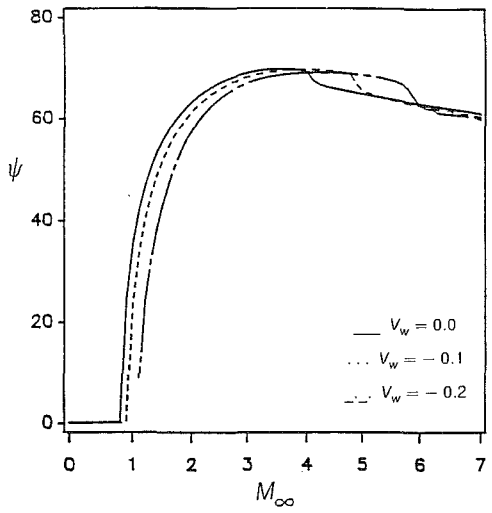

Fig. 8 The waveangles corresponding to Fig. 6

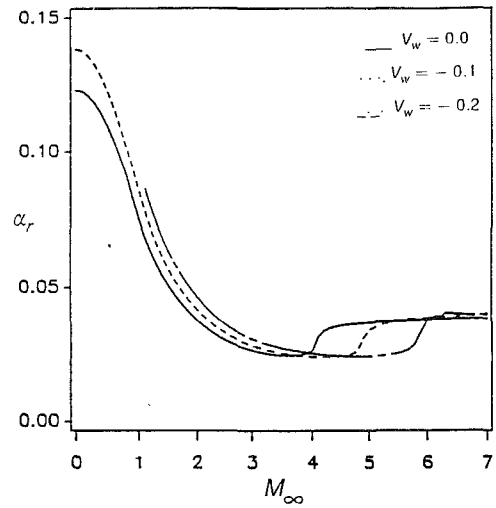

Fig. 9 The wavenumbers corresponding to Fig. 6

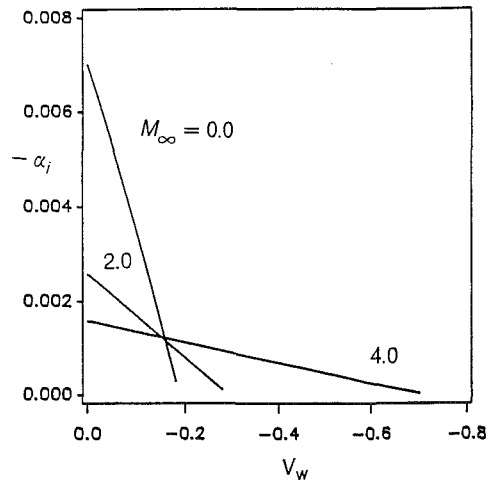

Fig. 10 Variation of the maximum growth rate with suction level when $R = 1500$, Pr = 0.72, and $T_\infty = 150°K$

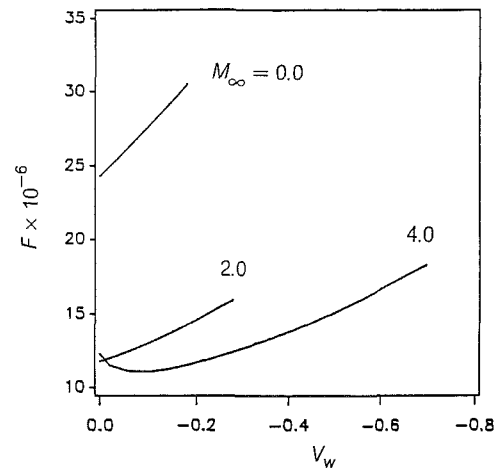

Fig. 11 The frequencies corresponding to Fig. 10

Fig. 2 show clearly that the suction level needed to eliminate the generalized inflection points increases by decreasing T_∞.

Mack (1969) found that oblique first-mode waves are more unstable than two-dimensional first-mode waves. In Fig. 3, we show the effect of suction on variation of the growth rate with spanwise wavenumber β for the Mach numbers 2.0, 4.0, and 6.0. Clearly, suction has a stabilizing influence on two-dimensional and three-dimensional waves and its effect decreases as the Mach number increases. Moreover, suction slightly changes the most amplified spanwise wavenumber.

In Fig. 4, we show variation of the growth rate with frequency for the Mach numbers 2.0, 4.0, and 6.0. It is clear that, for all three Mach numbers, suction decreases the band of frequencies receiving amplification and reduces the growth

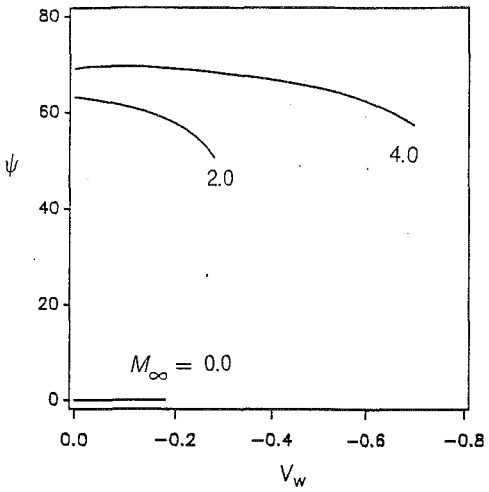

Fig. 12 The waveangles corresponding to Fig. 10

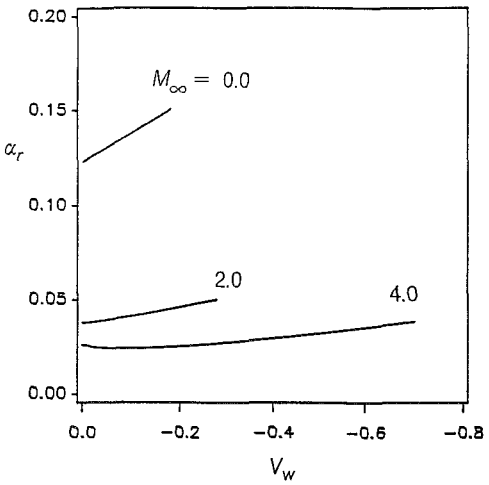

Fig. 13 The wavenumbers corresponding to Fig. 10

rates at all frequencies. However, it is also clear that the unstable band of frequencies greatly increases by increasing Mach number. As we have seen in Fig. 3, Fig. 4 indicates that the effect of suction on stabilizing first-mode waves decreases as Mach number increases. Figure 4 shows that there is no consistent trend in the shift of the peak amplification as suction is applied, which means that the shift depends on Mach number.

For a given frequency and following a certain wave with a specific dimensional spanwise wavenumber as it propagates downstream, suction decreases the growth rates of first-mode waves at all streamwise locations, as shown in Fig. 5. Suction increases the critical Reynolds number and decreases the Reynolds number corresponding to the second neutral point. It is clear that the amplification factors (areas under the curves) decrease as the mass flux increases.

Variation of the maximum growth rate (maximized over all waveangles and frequencies) with Mach number is shown in Fig. 6. In performing the maximizations over the frequencies and waveangles, we took the steps in the frequency F and spanwise wavenumber β to be 0.001×10^{-6} and 0.00001, respectively. In the absence of suction, the maximum growth rate decreases monotonically with Mach number. Suction is more effective at low Mach numbers because it reduces the viscous instability, which is dominant at low Mach numbers. However, suction is not as effective in stabilizing the inviscid mechanism, which is dominant at higher Mach numbers, because high levels of suction are needed to eliminate the generalized inflection points at such Mach numbers. Figure 7 shows the frequencies corresponding to the maximum growth rates of Fig. 6, whereas Figs. 8 and 9 show the corresponding waveangles and wavenumbers, respectively.

Mack studied the effect of suction on the stability of compressible boundary layers on two transonic wings of infinite span. He considered stationary (zero-frequency) disturbances to represent cross-flow instability as well as disturbances with the wavenumber vector aligned with the local flow direction to represent traveling-wave instability. Mack found that, for both types of disturbances, the maximum amplification rate varies almost linearly with the suction magnitude up to at least the point where the amplification rate is halved. Our results show that, for our configuration, the growth rates decrease almost linearly with suction level as shown in Fig. 10, in which variation of the maximum growth rate is plotted against the suction level for the three Mach numbers $M_\infty = 0.0$, 2.0, and 4.0 at $R = 1500$. Figure 11 shows the frequencies corresponding to Fig. 10, whereas Figs. 12 and 13 show the corresponding waveangles and wavenumbers.

In summary, first-mode waves are always stabilized by suction. Suction is found to be more effective in stabilizing the viscous stability, and hence it is more effective at low Mach numbers. Variation of the growth rate of the most amplified first-mode wave with mass flux is found to be almost linear.

Acknowledgment

This work was supported by the Office of Naval Research under Grant No. N00014-85-K-0011/NR 4325201.

References

Al-Maaitah, A. A., Nayfeh, A. H., and Masad, J. A., 1991, "Effect of Suction on the Stability of Supersonic Boundary-Layers. Part I—Second-Mode Waves," ASME JOURNAL OF FLUIDS ENGINEERING, published in this issue, pp. 591–597.

Lees, L., and Lin, C. C., 1946, "Investigation of the Stability of the Laminar Boundary Layer in a Compressible Fluid," NASA Technical Note No. 1115.

Mack, L. M., 1969, "Boundary-Layer Stability Theory," Jet Propulsion Laboratory, Pasadena, CA, Document No. 900-277, Rev. A.

Mack, L. M., 1975, "Linear Stability Theory and the Problem of Supersonic Boundary-Layer Transition," *AIAA Journal*, Vol. 13, pp. 278–289.

Mack, L. M., 1982, "Compressible Boundary-Layer Stability Calculations for Sweptback Wings with Suction," *AIAA Journal*, Vol. 20, pp. 363–369.

Mack, L. M., 1984a, "Boundary-Layer Linear Stability Theory," *Special Course on Stability and Transition of Laminar Flow*, AGARD Report No. 709.

Mack, L. M., 1984b, "Remarks on Disputed Numerical Results in Compressible Boundary-Layer Stability Theory," *Physics of Fluids*, Vol. 27, pp. 342–347.

Mack, L. M., 1989, "On Inviscid Acoustic-Mode Instability in Supersonic Shear Flows," *Fourth Symposium on Numerical and Physical Aspects of Aerodynamic Flows*, Long Beach, CA.

Malik, M. R., 1989, "Prediction and Control of Transition in Hypersonic Boundary Layers," *AIAA Journal*, Vol. 27, pp. 1487–1493.

Nayfeh, A. H., 1988, "Stability of Compressible Boundary Layers," *Transonic Symposium: Theory, Application, and Experiment* (NASA-Langley Research Center, Hampton, VA), NASA Conf. Pub. 3020, Vol. 1, pp. 629–689.

Reed, H. L., and Balakumar, P., 1990, "Compressible Boundary-Layer Stability Theory," *Physics of Fluids A*, Vol. 1, No. 8, pp. 1341–1349.

Wazzan, A. R., and Taghavi, H., and Keltner, G., 1984, "The Effect of Mach Number on the Spatial Stability of Adiabatic Flat Plate Flow to Oblique Disturbances," *Physics of Fluids*, Vol. 27, pp. 331–341.

N. T. Obot
Fluid Mechanics, Heat and Mass Transfer Laboratory,
Department of Chemical Engineering,
Clarkson University,
Potsdam, NY 13699-5705.
Mem. ASME

J. A. Jendrzejczyk
Mem. ASME.

M. W. Wambsganss
Mem. ASME.

Materials and Components Technology Division,
Argonne National Laboratory,
Argonne, Ill. 60439

Direct Determination of the Onset of Transition to Turbulence in Flow Passages

Easily applied methods are proposed, based on tests with air and water, for direct determination of the onset of transition in flow passages using static and dynamic wall pressure data. With increasing Reynolds number from laminar flow, the characteristic feature of transition is the change from steady to oscillating pressure readings. It is established that the power spectral density (psd) representations exhibit a distinctive change in profile at transition. Further, it is shown that the root-mean-square (rms) values of the wall pressure fluctuations rise sharply at transition. The critical Reynolds numbers recorded via the change from steady to unsteady pressure readings are almost the same as those deduced from the psd and rms pressure data or from the familiar friction factor-Reynolds number plots.

Introduction

The process of transition from laminar to turbulent flow in pipes, which involves the presence of alternating patches of laminar and turbulent flow with time, was successfully traced by Reynolds (1883) more than a century ago. Since then, this important problem has attracted the attention of many researchers and will probably continue to interest investigators for many years to come. The presence of turbulent slugs/spots has been confirmed (Lindgren, 1957; Paterson and Abernathy, 1972; Wygnanski and co-workers, 1973; 1975; to mention a few) and is now considered to be an integral part of the transition process. However, the problem is that there is no simple and direct method for accurate determination of the onset of transition; notably for situations that involve heat transfer.

To date, flow visualization is by far the most common method for obtaining data on the transition or critical Reynolds number. Alternatively, a hot-wire probe can be used to detect the discontinuity in velocity signal between laminar flow and the turbulent slugs (Karnitz et al., 1974). The hot wire technique can also be used to determine the intermittency coefficient as a function of the flow Reynolds number, from which the values of the lower and upper critical Reynolds number can be determined (Kaupas et al., 1989). Even for isothermal channel flows, these experimental techniques are somewhat limited, not to mention the complication introduced by the presence of heat transfer. Also, these techniques do not afford direct determination of the corresponding pressure drop, and hence the critical friction factor, at transition. Indirectly, the critical Reynolds number at the onset of transition is usually deduced from the friction factor-Reynolds number plots, an approach that requires extensive experimentation as well as data reduction. The advantage of the indirect approach is that it can give accurate estimates of the critical Reynolds number and the critical friction factor.

Besides the occurrence of turbulent slugs/spots, there are clear indications that the onset of transition is accompanied by significant unsteadiness in pressure drop readings (Reynolds, 1883; Paterson and Abernathy, 1972; Jones, 1976; and Fukano et al., 1989). In the experiments to determine the critical Reynolds number, Reynolds observed very steady differential pressure readings for low flowrates, with marked pressure oscillations at a particular flowrate for a given tube. These results, which were documented in sufficient detail, led Reynolds to conclude that "to each critical velocity, of course, there corresponds a value of the critical pressure." He also postulated that the general cause of the change from steady to eddying motion was the consequence of an instability in laminar flow. Paterson and Abernathy used the intermittency of the pressure transducer signal to study pipe flow transition for water and dilute solutions of polyethylene oxide.

The results of Jones (1976) indicated that the scatter in the measured friction factors was significantly greater in turbulent than laminar flow, especially in the transition region. More recently, Fukano et al. (1989) presented time traces of the differential pressure signals for laminar, transitional and turbulent flow. Their profiles showed roughly the same general trend for laminar and turbulent flow, with significant fluctuations within the transition region. Specifically, the traces have periods with large and small amplitudes, which is indicative of the intermittent nature of the flow within the transition region. Although it would seem from this discussion that the onset of transition may be determined by simply monitoring the pressure drop readings with increasing flowrate to detect the change from steady to unsteady readings, it appears that no systematic investigation has been made to provide a consistent basis for the use of such a method.

The work described in this paper grew out of preliminary single-phase pressure drop measurements that were performed

Contributed by the Fluids Engineering Division for publication in the JOURNAL OF FLUIDS ENGINEERING. Manuscript received by the Fluids Engineering Division May 31, 1990.

to qualify the two-phase flow experimental facility at Argonne National Laboratory. The rather unique features of transition that were observed during these measurements prompted extension of the data processing to include computation of both the power spectra of the wall differential pressures and the associated rms values of the pressure fluctuations. Based on these results, direct experimental methods are proposed for determining the onset of transition of turbulent flow in flow passages.

Experimental Facility and Test Procedures

It should be mentioned at the outset that the air experiments were performed on a circular tube and a rectangular channel, while the water data were obtained only with the latter. For the air experiments, compressor air was passed through one of three rotameters (depending on the desired flowrate), a flexible hose and a straight 7.75 mm I.D. stainless steel tube or a rectangular channel of width and height 3.18 and 19.05 mm, respectively. For any particular rotameter, the air flowrate was varied by regulating the rotameter inlet pressure over the range of values between 101.3 kPa and 653.0 kPa. Air temperature at a rotameter inlet was measured by a resistance temperature detector. All air rotameters were calibrated using a dry gas test meter and appropriate corrections were applied to account for differences between calibration and actual test conditions. The estimated uncertainty in flowrate measurement was ± two percent. For water, the fluid was similarly metered by one of three calibrated rotameters prior to passing it through the rectangular channel. Additional details of the test facility are given in Wambsganss et al. (1991) and will not be repeated here.

For the stainless steel tube, the pressure taps, spaced 0.69 m apart, were located 0.305 m from one end of the tube and 3.88 m from the other end. By reversing the flow direction it was possible to obtain pressure drop data for two entrance lengths (L_e/D_e = 39.3 and 500). The pressure taps were made by welding a 3.2 mm I.D. housing to the outside surface of the tube and drilling a 0.25 mm hole through the tube wall. For the rectangular channel, the upstream and downstream pressure taps were located at L_e/D_e = 135 and 198. Two holes, 3.2 mm in diameter, were drilled through the vertical side of the channel wall to afford almost flush mounting of the piezoresistive transducers.

For the air experiments, the pressure measurements were made using two types of transducers: a Statham unbonded strain gauge transducer (range: ± 1.03 kPa) and two Endevco piezoresistive transducers (range: 0–13.8 kPa). The latter fitted directly into the upstream and downstream pressure taps and provided pressure data relative to the ambient. For the Statham transducer which was used only with air at low pressures, and was the reference for the other calibrations, clear tubings (1.59 mm internal diameter) were used to link the two transducer ports to the adaptors inserted into the pressure tap openings. It is noted that preliminary pressure drop measurements were also made using a Meriam Instrument Company (Model 40HE35) inclined manometer.

The rms values of the differential pressure fluctuations were obtained with the Statham transducer for the circular and rectangular ducts and, consistent with the details in the preceding paragraph, these data are presented as Δp_{rms}. For the small Endevco transducers, which were used mostly for both air and water with the rectangular passage and for limited circular tube tests with air, the rms data are presented as p_{rms} and Δp_{rms}; the latter was obtained by taking the difference of the two point measurements. The signal processing of the wall pressure fluctuations was carried out using a Hewlett-Packard Model 5451C FFT (Fast Fourier Transform) Analyzer, averaging 5.12-second "lengths" of time signal; the total sampling time was 51.2 seconds.

Results and Discussion

Visual Determination of the Critical Reynolds Number. It is instructive to begin the presentation with an overview of the dominant features that were observed during the single phase pressure drop measurements, since these observations prompted the dynamic pressure analysis. It is noted that the trends that are given in the following discussion were in evidence with all pressure transducers and the inclined manometer mentioned in the preceding section. Also, for a given flowrate, the output of the pressure transducers was displayed simultaneously on the Hewlett-Packard 3466A and Fluke 8060A digital multimeters.

In laminar flow, the characteristic feature was one of very steady pressure drop readings. With increasing flowrate, there was always one flow setting at which very significant variations in pressure drop reading were observed for either duct geometry, even when the rotameter setting was as steady as can be maintained. The most remarkable thing about this flow setting was that by lowering it by 0.5 mm on the rotameter scale, which amounted to a Reynolds number decrease on the order of 50, one was back again into the steady pressure drop regime. From the very extensive flow calibration data it was established that the flow setting, which marked the onset of unsteady differential pressure readings, corresponded rather closely to that for transition to turbulence, based of course on the location of the minimum in plots of friction factor versus Reynolds number. With increasing flowrate from the value for the initiation of unsteady pressure drop readings, the marked variations in these readings persisted and then diminished in magnitude when one was well into the turbulent regime, an indication that there may be a well defined transition region.

Although the general trends outlined above were the same for the circular and rectangular cross-sections, there was one notable difference, that is, the magnitudes of the variations in pressure drop readings were more pronounced with the rectangular channel than with the circular tube. Interestingly, for either duct, the flowrate corresponding to this initiation point (hereafter referred to as the critical or transition Reynolds number) remained unchanged whether it was approached beginning from laminar or turbulent flow. In the latter case, this is the flow rate below which there exists steady pressure drop readings.

At the onset of transition, the differences between the lowest and the highest pressure drop readings were quite significant. For example, the maximum peak-to-peak values recorded with the circular tube were 20.2 Pa for L_e/D_e = 39.3, and 52.4 Pa for L_e/D_e = 500. For each Reynolds number within the transition region and inclusive of the Re range up to 5000, calculations of the average pressure drop and the attendant

Nomenclature

A = cross sectional flow area, m^2
D_e = equivalent (hydraulic) diameter, m
f = frequency (Hz)
L_e = entrance length, m
m = mass flowrate, kg/s
p_{rms} = rms value of wall pressure relative to ambient, Pa
Δp_{rms} = rms value of wall differential pressure, Pa
Re = Reynolds number, $mD_e/A\mu$
$\bar{V}$ = average flow velocity, m/s
μ = fluid viscosity, Pa s
ρ = fluid density, kg/m^3

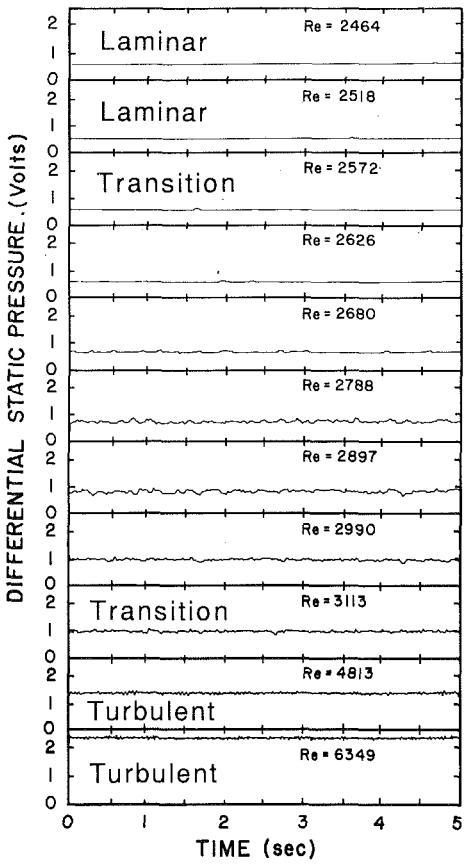

Fig. 1 Typical time traces of the pressure drop signal (with 1 volt = 68.95 Pa, uncertainty in pressure drop = ± 1.0 Pa and in time = ± 1 percent)

standard deviation were made using twenty-five readings. In all cases, the values for the standard deviation were largest within the transition region. Also, the percentage variations about the average pressure drop were greatest at the Reynolds number that corresponded to the onset of transition. The observations in the preceding paragraphs prompted calculation of both the power spectral density and the rms values of the wall differential pressure fluctuations.

To shed further light on the above discussion of the visual observations, time traces of the differential pressure signals are given in Fig. 1 for the L_e/D_e = 39.3 stainless steel tube location. For convenience and in order to consolidate this information into a single figure, the ordinate is in volts and the appropriate conversion is 1 volt = 68.95 Pa. Beginning with the lowest Reynolds number of 2464 in laminar flow, the pressure drop-time history are shown for eleven values of Reynolds number. These results require only several comments beyond the elaborate discussion in the preceding paragraphs. The first is that the distinct change from steady to fluctuating profile is observed around Re = 2572. Also, the shape of the turbulent profiles (Re = 4813 and 6349) are markedly different from those in laminar flow or within the transition region. With regard to the onset of transition, attention is directed to the presence of a "hump" between 1.5 and 2 seconds for Re = 2572 and several "humps" for Re = 2626.

In summary, the present observations on the change from steady to unsteady differential pressure readings, the connection between this phenomenon and transition to turbulence and the fact that the transition region is the seat of marked oscillations in differential pressure are qualitatively in agreement with the findings of other investigators (Reynolds, 1883; Jones, 1976; Fukano et al., 1989). Although the connection between the onset of unsteady pressure drop readings and the occurrence of turbulent slugs/spots was not addressed in this study, it appears, at least based on the observations of Reynolds on eddy formation, that the two phenomena may be indicative of the same process.

Dynamic Wall Pressure Data. We begin this presentation by considering the real time signals of the differential pressure fluctuations (the "d.c. contribution" has been removed), Fig. 2, and the power spectral density (psd) of the wall differential pressures (Fig. 3) because, as with the wall differential pressure signals of Fig. 1, the characteristics of these representations with increasing Reynolds number afford direct determination of the onset of transition. Figures 2 and 3 complement Fig. 1 in that the test conditions were the same and the data were obtained using the Endevco transducers; but the conversion for Fig. 2 or 3 is 1 volt = 6.895 Pa. The corresponding nondimensional value ($p'_{rms} = \Delta p_{rms}/\rho V^2$) of the rms differential pressure fluctuations is also given for each Reynolds number on Fig. 3.

It is evident from the general characteristics of these representations that the transition region, inclusive of the Reynolds number at which the process begins, is a special case. For instance, the amplitudes of the differential pressure fluctuations of Fig. 2 are generally small in laminar flow. In the vicinity of the transition point, as well as within the transition region, oscillations of very high amplitude are observed to occur; but their amplitude decreases as one moves into turbulent flow. Similarly, Fig. 3 establishes that the low frequency contributions (f < 18 Hz) are primarily responsible for the dramatic increase in the rms differential pressure fluctuations in the transition region; here, the reader's attention is called to the changes in scale factor on the "y axis." Frequency contributions in the range 18 to 70 Hz are most likely inherent to the test channel/measurement system. It is expected that they are present in the transition region but are not detectable on the spectral plots of Fig. 3 because of the two orders or magnitude increase in scale factor. For the moment, it is also worthy of note that the normalized value of the rms differential pressure fluctuations rises sharply at transition (Fig. 3).

The most important conclusion that can be drawn from the results of Figs. 1–3 is that there are characteristic changes in amplitude and/or shape of the profiles. Thus, by fine tuning the fluid flowrate and simultaneously monitoring the differential pressure signals, the wall differential pressure fluctuations, or the power spectral density profiles, this distinctive feature can be used to determine the onset of transition with a high degree of accuracy and consistency. The real advantage of these methods is one of simplicity; requiring little additional instrumentation beyond what is usually needed for pressure measurements.

To carry the presentation a step further, the root-mean-square (rms) values of the wall pressure fluctuations, together with the frequency range over which the data were averaged, are presented on Figs. 4–6 for air and on Fig. 7 for water. The upper plot of Fig. 4 shows the circular tube Δp_{rms} data for L_e/D_e = 39.3 and 500, while the nondimensional representations (scaled with ρV^2) of the same data are given in the lower plots. The results obtained on the rectangular passage are presented on Figs. 5–7. The dimensional and nondimensional data across the length over which the pressure drop was measured are given in Fig. 5 where, for the purpose of comparison, the Statham transducer data are also included, Fig. 5(c). By contrast, the rms pressure profiles at the upstream and downstream tap locations, with the ambient pressure as the reference, are shown in Fig. 6. For water, the upstream and downstream data as well as Δp_{rms} are given on Fig. 7.

On each of Figs. 4 through 6, the points that are identified with arrows along with the letter 'V' are those at which the change from steady to unsteady oscillatory pressure readings were observed visually from the transducer output. Since preliminary tests with water indicated a similar change from steady

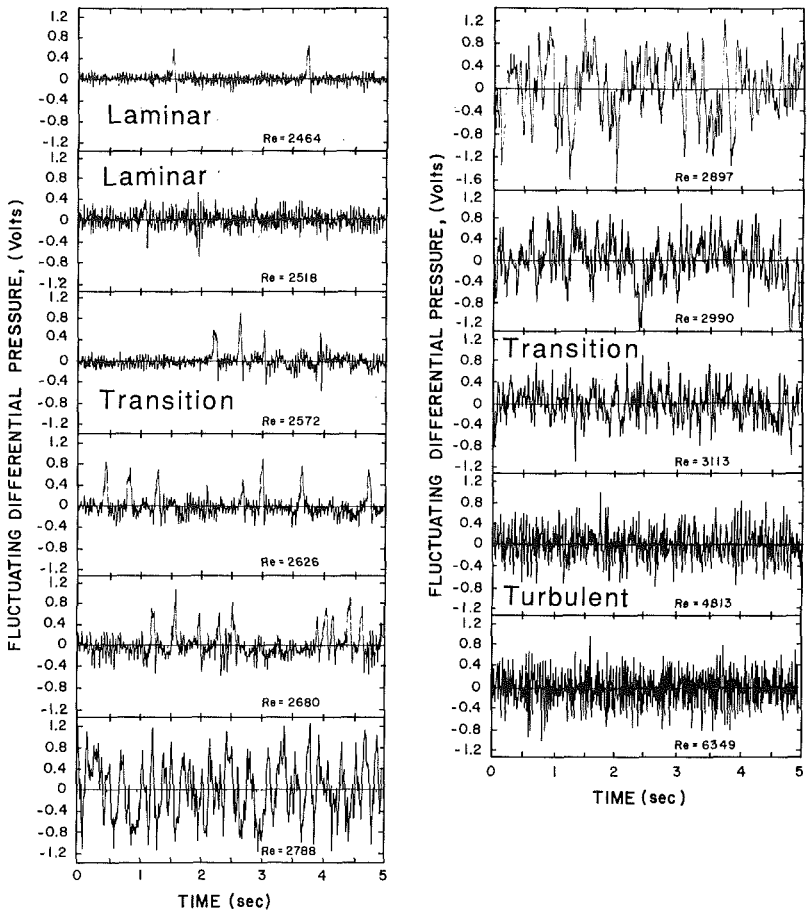

Fig. 2 Typical time (± 1 percent) traces of the wall differential pressure fluctuations (± 7 percent)

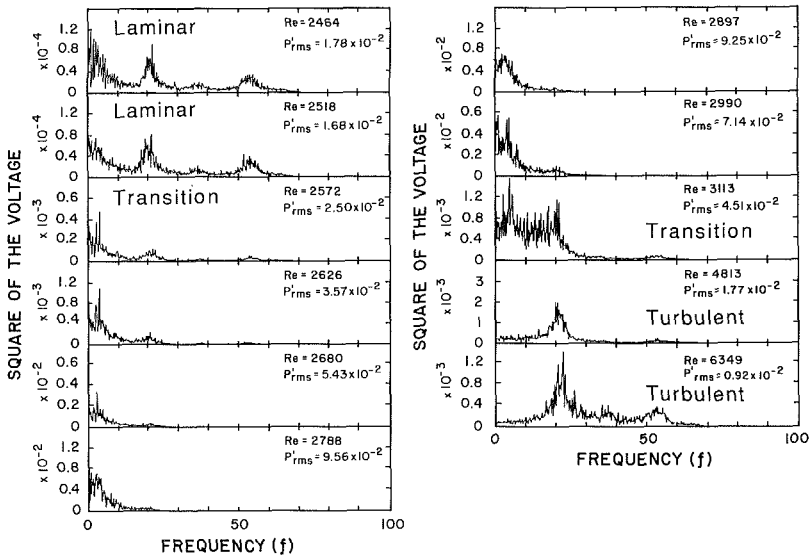

Fig. 3 Typical power spectral density profiles of the wall differential pressures (uncertainty in p'_{rms} = ± 8 percent and in frequency = ± 1 percent)

to unsteady differential pressure readings, as well as the same general trend for the rms pressure fluctuations as with air, the visually observed transition Reynolds number was not recorded during tests for which the results are given on Fig. 7.

It was determined, based on the location of the minimum in the friction factor versus Reynolds number curves, that the sudden change from steady to unsteady differential pressure readings is exhibited by a sharp rise in the rms value of the differential pressure fluctuations. It follows that the peak value of Δp_{rms} does not occur at the transition Reynolds number, but rather at a Reynolds number greater than that at transition. The friction factor data are given in the paper by Wambsganss et al. (1991). Another useful result of this study is that the same conclusion is reached with a single pressure tap as with differential data over a specified length (Figs. 6 and 7).

From the time traces of the static and dynamic pressure

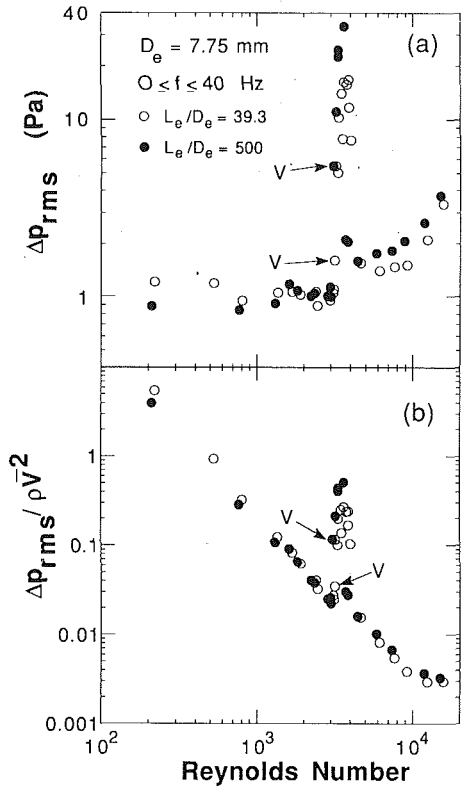

Fig. 4 RMS values of the differential pressure for circular tube with air (uncertainty in Δp_{rms} = ± 7 percent, in $\Delta p_{rms}/\rho V^2$ = ± 8 percent)

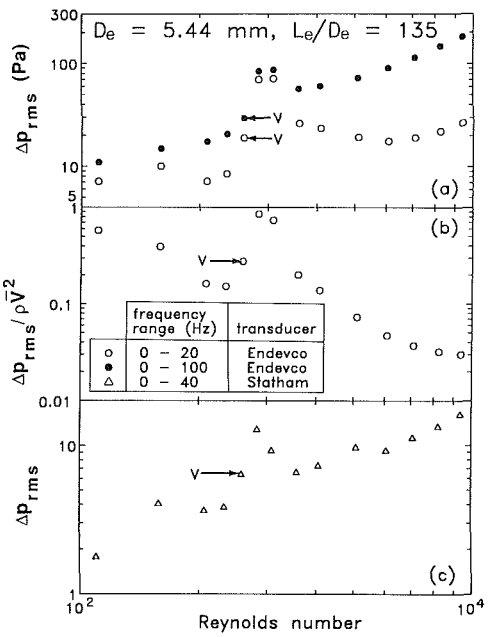

Fig. 5 RMS values of the differential pressure for rectangular channel with air (same uncertainties as in Fig. 4)

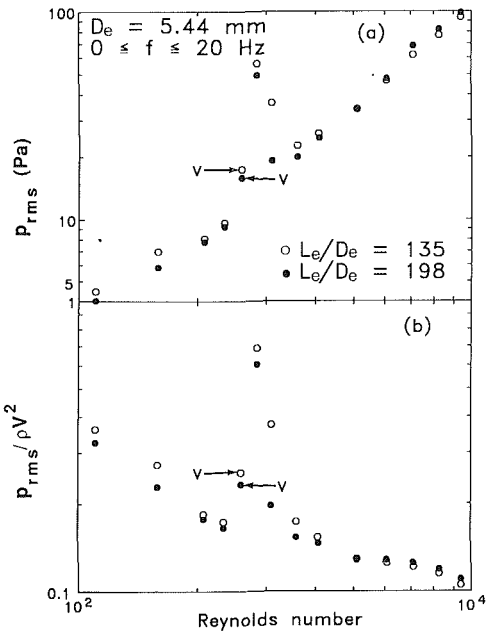

Fig. 6 Upstream and downstream rms pressure profiles for rectangular channel with air (uncertainty in p_{rms} = ± 4 percent)

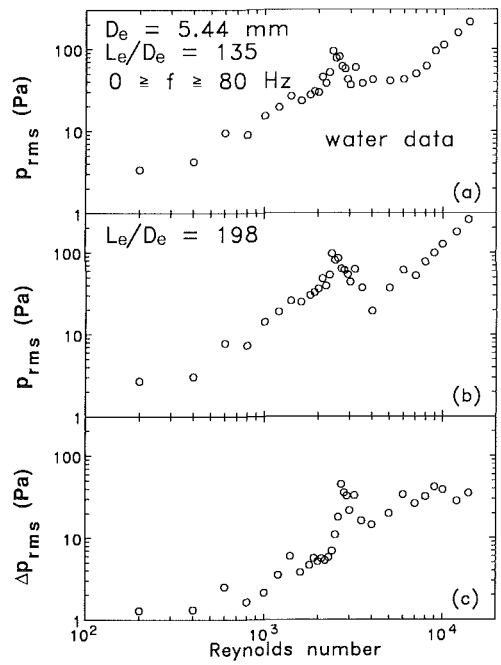

Fig. 7 RMS pressure data for rectangular channel with water (uncertainty in p_{rms} = ± 4 percent, in Δp_{rms} = 7 percent).

signals, the power spectral density plots and the attendant rms pressure profiles, it is correct to state that there exists a well defined transition region, the extent of which is, unlike that for either laminar or turbulent flow, confined to a very narrow Re range. Although the indication is that the onset of transition is almost abrupt in nature, it appears that fully turbulent flow occurs only after the p_{rms} or Δp_{rms} value has dropped from its maximum to its lowest value. On this basis, the results of this study indicate that the transition region extends to about 1.4 times the critical Reynolds number for both circular and rectangular ducts.

Comparison of the transition Reynolds number determined from Figs. 1–3 with that deduced from Fig. 4 for the same L_e/D_e shows that the latter value is higher by about 15 percent. This is a reflection of the effect of temperature that is not adequately accounted for by the Reynolds number similarity. The results on Figs. 1–3 were obtained during the winter for an air temperature of 16.6°C, while the air temperature for the data of Fig. 4 was 29.0°C.

It was noted earlier, during the discussion of the visual observations, that the magnitudes of the variations in the differential pressure readings were more pronounced in the rectangular channel than the circular tube. This fact is established

from comparison between Figs. 4(*a*) and 5(*c*) which give results obtained with the same transducer (Statham) for the same (0–40 Hz) frequency range. In laminar flow, Δp_{rms} (Fig. 4(*a*)) is independent of Re for the circular tube. By contrast, p_{rms} (Fig. 6(*a*)) or Δp_{rms} (Fig. 5(*a*)) increases with increasing Re for the rectangular channel with air or water (Fig. 7). Since there is hardly any effect of L_e/D_e on Δp_{rms}^{max} or on Δp_{rms} (Fig. 4) in the laminar or turbulent flow range, it may then be noted that, although the peak Δp_{rms} is roughly about the same for both cross-sections, Δp_{rms} values in both laminar and turbulent flow are significantly higher with rectangular than with circular geometry.

For a given duct cross-section and tranducer, p_{rms}^{max} or Δp_{rms}^{max} is almost independent of the frequency range over which the data were averaged, Fig. 5(*a*). As can be determined from Fig. 3, this is a direct consequence of the dominance of the low frequency content of the psd profile at this Reynolds number. In laminar or turbulent flow, values of p_{rms} or Δp_{rms} vary widely with frequency since, given the shape of the psd profiles of Fig. 3, a large frequency range allows for additional contributions to the rms values. Also, it is noted that the small diameter Endevco transducers give rms values that are much higher than those obtained with the Statham unbonded strain gauge transducer. This is due to the fact that since the local pressure is made up of both nearfield and farfield components, the latter with inherently long wavelengths are effectively nulled out in the subtraction process; also, the longer lines associated with the differential transducer tend to act as a 'filter' for high frequencies.

It is evident from Figs. 4(*b*) and 5(*b*) that $\Delta p_{rms}/\rho\overline{V^2}$ decreases monotonically with Re in laminar flow, with a minimum and maximum very close to the transition point and midway within the transition region, respectively, and then continues to decrease with increasing Re. For the circular tube, since Δp_{rms} is almost independent of Re in laminar flow, it follows that $\Delta p_{rms}/\rho\overline{V^2} \propto Re^m$, where m must have a value close to -2.0. Using the $L_e/D_e = 39.3$ data, a value of -2.02 was deduced by regression. It is noted that the use of ρU_τ^2 ($U_\tau = (\tau_w/\rho)^{1/2}$, friction velocity) instead of $\rho\overline{V^2}$ as the scaling factor for Δp_{rms} does not alter the general trend on Fig. 4(*b*) or 5(*b*). Specifically, $\Delta p_{rms}/\rho U_\tau^2$ decreases steadily from 2.37 at Re = 5870 to 0.9 at Re = 15710 for the circular tube.

Conclusions and Recommendations

In summary, to determine the onset of transition beginning from laminar flow, it is necessary to fine-tune the flow while observing the characteristic change from steady to unsteady wall pressure readings. Given the magnitudes of the static pressure variations, it should be possible to detect the phenomenon even with an inclined manometer similar to that used in this study, not to mention the use of a pressure transducer which affords monitoring of the digital display of the output. Alternatively, the graphical display of the wall pressure fluctuations and the power spectral density of the wall pressures can be viewed with increasing Reynolds number to detect the characteristic change in both the magnitude and shape, an indication of the sharp rise in the rms value of the pressure fluctuations. Although the use of p_{rms} (or Δp_{rms}) versus Re profiles affords very accurate determination of the critical Reynolds number, this approach is, as with the friction factor versus Reynolds number plots, indirect in that the rms values of the pressure fluctuations must be calculated from the psd data for the entire Re range.

Although the present results were obtained in the absence of heat transfer, there is no reason that the method should not be used for situations involving surface heating or cooling. This observation is reinforced by the fact that the effects of surface cooling or fluid heating on pressure drop are most pronounced within the transition region. In laminar or turbulent flow, the relative magnitudes of the effect of heat transfer on pressure drop are small but, in the transition region, the pressure drop is much greater with than without heat transfer for a given Reynolds number (Obot et al., 1991). Also, since the onset of transition is determined largely by conditions occurring in the immediate vicinity of a surface, these methods should be applicable to other types of boundary layer flows. Finally, the availability of easily applied experimental methods should aid the design of full-scale investigations of the origin and mechanism of transition to turbulence.

Acknowledgments

This work was performed as part of the Thermal Science Research Program sponsored by the U.S. Department of Energy, Office of Conservation and Renewable Energy, Division of Advanced Industrial Concepts. The continuing encouragement and support of M.E. Gunn, Jr. is gratefully appreciated. We thank R. K. Smith for his assistance with the setup and Professor J. B. McLaughlin of Clarkson for very valuable discussion. N. T. Obot was supported as a Faculty Research Participant by the Argonne Division of Educational Programs.

References

Fukano, T., Kariyasaki, A., and Kagawa, M., 1989, "Flow Patterns and Pressure Drop in Isothermal Gas-Liquid Concurrent Flow in a Horizontal Capillary Tube," *American Nuclear Society Proceedings*, 1989 National Heat Transfer Conf., pp. 153–161.

Jones, O. C., Jr., 1976, "An Improvement In the Calculation of Turbulent Friction In Rectangular Ducts," ASME JOURNAL OF FLUIDS ENGINEERING, Vol. 98, pp. 173–181.

Karnitz, M. A., Potter, M. C., and Smith, M. C., 1974, "An Experimental Investigation of Transition of a Plane Poiseuille Flow," ASME JOURNAL OF FLUIDS ENGINEERING, Vol. 96, pp. 384–388.

Kaupas, V. E., Poškas, P. S., and Vilemas, V. J., 1989, "Heat Transfer to a Transition-Range Gas Flow in a Pipe at High Heat Fluxes (2. Heat Transfer in Laminar to Turbulent Flow Transition)," *Heat Transfer-Soviet Research*, Vol. 21, No. 3, pp. 340–351.

Lindgren, E. R., 1957, "The Transition Process and Other Phenomena in Viscous Flow," *Arkiv för Fysik*, Vol. 12, pp. 1–169.

Obot, N. T., Esen, E. B., and Rabas, T. J., 1991, "Pressure Drop and Heat Transfer for Spirally Fluted Tubes Including Validation of the Role of Transition," Fouling and Enhancement Interactions, HTD-Vol. 164, ed T. J. Rabas and J. M. Chenoweth, American Society of Mechanical Engineers, pp. 85–92.

Paterson, R. W., and Abernathy, F. H., 1972, "Transition to Turbulence in Pipe Flow for Water and Dilute Solutions for Polyethylene Oxide," *J. Fluid Mech.*, Vol. 51, p. 177–185.

Reynolds, O., 1883, "An Experimental Investigation of the Circumstances which Determine Whether the Motion of Water Shall be Direct or Sinuous, and of the Law of Resistance in Parallel Channels," *Phil. Trans. Roy. Soc. London*, Vol. 174, Series A, pp. 935–982.

Wambsganss, M. W., Jendrzejczyk, J. A., France, D. M., and Obot, N. T., 1991, "Frictional Pressure Gradients in Two-phase Flow in a Small Rectangular Channel," *Experimental Thermal Fluid Sci.*, (in press).

Wygnanski, I., Sokolov, M., and Friedman, D., 1975, "On Transition in a Pipe. Part 2. The Equilibrium Puff," *J. Fluid Mech.*, Vol. 69, Part 2, pp. 283–304.

Wygnanski, I. J., and Champagne, F. H., 1973, "On Transition in a Pipe. Part 1. The Origin of Puffs and Slugs and the Flow in a Turbulent Slug," *J. Fluid Mech.*, Vol. 59, Part 2, pp. 281–335.

Prediction of Three-Dimensional Developing Turbulent Flow in a Square Duct With an Anisotropic Low-Reynolds-Number k-ϵ Model

Hyon Kook Myong
Senior Research Scientist,
Air Conditioning and Environmental Control Lab.,
Korea Institute of Science and Technology,
Seoul 130-650, Korea

Toshio Kobayashi
Professor,
Institute of Industrial Science,
The University of Tokyo,
Tokyo 106, Japan

Three-dimensional developing turbulent flow in a square duct involving turbulence-driven secondary motion is numerically predicted with an anisotropic low-Reynolds-number k-ϵ turbulence model. Special attention has been given to both regions close to the wall and the corner, which are known to influence the characteristics of secondary flow a great deal. Hence, the no-slip boundary condition at the wall is directly used in place of the common wall function approach. The resulting set of equations simplified only by the boundary layer assumption are first compared with previous algebraic stress models, and solved with a forward marching numerical procedure for three-dimensional shear layers. Typical predicted quantities such as mean axial and secondary velocities, friction coefficients, turbulent kinetic energy, and Reynolds shear stress are compared with available experimental data. These results indicate that the present anisotropic k-ϵ turbulence model performs quite well for this complex flow field.

Introduction

Turbulent flow in noncircular ducts, commonly encountered in engineering practice, is characterized by the everpresent secondary motions in the plane perpendicular to the streamwise direction, and thus always of a three-dimensional nature for the mean velocity field. In general, the secondary motion is caused by two different mechanisms. The pressure-induced secondary motion (of Prandtl's first kind) exists in curved (circular) ducts and its magnitude can be quite large, say of the order of 20–30 percent of the streamwise mean velocity. On the contrary, the secondary motion encountered in straight noncircular ducts is caused by the turbulence and thus this secondary flow is present even under fully-developed conditions. The present paper is concerned with this turbulence-driven secondary motion (of Prandtl's second kind). Although the magnitude of turbulence-driven secondary motion is smaller than the root-mean-square value of turbulence intensity, this motion distorts the streamwise mean velocity and temperature contours toward the corners a great deal and thus can have important consequences. Therefore, this particular secondary flow phenomenon has been a topic of interest to those who study complex, three-dimensional flows.

From the experimental investigations Brundrett and Baines (1964) and Perkins (1970) have shown that the turbulence-driven secondary flows in noncircular ducts result from the anisotropy of each Reynolds stress in the cross-sectional plane. Thereafter, a considerable number of experimental investigations have been carried out to understand in detail turbulent flows in a straight square duct as the simplest geometry in which turbulence-driven secondary flows arise (see e.g., Melling and Whitelaw, 1976; Gessner et al., 1979). In addition, since these particular flow situations provide a natural vehicle for examining the validity of existing turbulence models, turbulence-driven secondary flows in a straight square duct are of special interest to modelers, and hence numerical investigations have also been carried out to accurately predict them by Launder and Ying (1973), Gessner and Emery (1981), Nakayama et al. (1983), and Demuren and Rodi (1984). Since the widely used (isotropic) k-ϵ model has no built-in mechanism for the development of secondary flow due to its inherent isotropic characteristics, most of their methods are based on the algebraic Reynolds stress models. However, all these models are simplified for their original Reynolds stress models with several drastic assumptions which have not yet been verified. Also, they all have used the wall function approach as a wall boundary condition, whose validity is still unclear, at least, near the corner (e.g., Gessner, 1982). Moreover, since both regions close to the wall and the corner are known to influence the characteristics of secondary flow a great deal, this approach seems to be less than desirable from the standpoint of numerical prediction.

Recently, the first author (Myong, 1988; Myong and Kasagi, 1990a) has proposed an anisotropic low-Reynolds-number k-ϵ turbulence model which is valid right up to the wall. It is just an extended form of its isotropic version (Myong, 1988; Myong and Kasagi, 1990b), but broadens the range of applicability whilst maintaining most of popular features of the

Contributed by the Fluids Engineering Division for publication in the JOURNAL OF FLUIDS ENGINEERING. Manuscript received by the Fluids Engineering Division December 5, 1990.

latter. This model has already been found capable of predicting the anisotropic normal Reynolds stresses up to the wall with the correct wall-limiting behavior, and also proven to perform satisfactorily in several flow situations, including turbulent pipe and channel flows, two-dimensional boundary layer flows with and without pressure gradients (Myong and Kasagi, 1990a, c; Myong et al., 1990). These results suggest a possibility that this model can be used to predict more complex flows influenced by the anisotropy of Reynolds stresses, e.g., secondary flows in noncircular ducts and separated flows.

The purpose of the present paper is to demonstrate that this anisotropic k-ϵ model is useful for the prediction of three-dimensional developing turbulent flows in a square duct involving turbulence-driven secondary flow. We will not use the wall function approach commonly adopted in the previous models, but use directly the no-slip boundary condition at the wall, since the regions close to the wall and the corner play an important role in the characteristics of secondary flow a great deal as mentioned above. The resulting set of equations are simplified only by the boundary layer approximation and compared with previous algebraic stress models. Then they are solved with a forward marching numerical procedure for three-dimensional shear layer. It will be shown that the present anisotropic k-ϵ model performs quite well for this complex flow field.

The paper goes beyond the experimental investigation by paying particular attention to the predictions in both regions close to the corner and the wall, where little experimental data have been reported due to the difficulty of experimental measurement. These predictions are interesting in themselves and also provide a body of material which future modelers and/or experimenters may wish to compare with their own results.

Mathematical Model

Reynolds Averaged Navier-Stokes Equations. The coordinate system and pertinent variables, as they apply for developing flows in a square duct, are shown in Fig. 1. The three-dimensional Reynolds averaged Navier-Stokes equations governing the distribution of the mean velocity components in a straight duct are expressed as follows:

Continuity equation:

$$\frac{\partial U}{\partial x}+\frac{\partial V}{\partial y}+\frac{\partial W}{\partial z}=0 \tag{1}$$

Streamwise (or longitudinal) momentum equation:

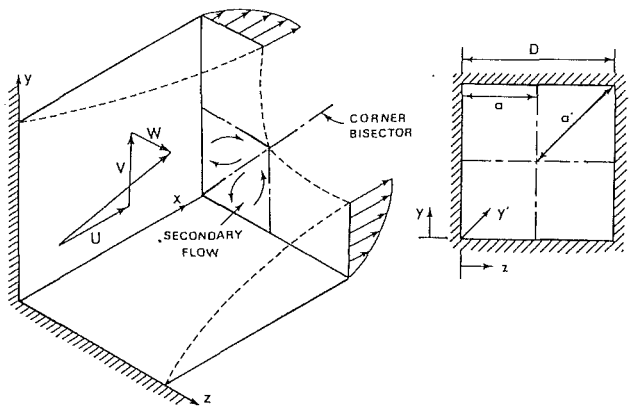

Fig. 1 Coordinate system and pertinent variables in a straight square duct

$$U\frac{\partial U}{\partial x}+V\frac{\partial U}{\partial y}+W\frac{\partial U}{\partial z}= -\frac{1}{\rho}\frac{\overline{dP}}{dx}-\frac{\overline{\partial uv}}{\partial y}-\frac{\overline{\partial uw}}{\partial z}+\nu\left(\frac{\partial^2 U}{\partial y^2}+\frac{\partial^2 U}{\partial z^2}\right) \tag{2}$$

Momentum equations governing the secondary velocities V and W:

$$U\frac{\partial V}{\partial x}+V\frac{\partial V}{\partial y}+W\frac{\partial V}{\partial z}= -\frac{1}{\rho}\frac{\partial P}{\partial y}-\frac{\overline{\partial v^2}}{\partial y}-\frac{\overline{\partial vw}}{\partial z}+\nu\left(\frac{\partial^2 V}{\partial y^2}+\frac{\partial^2 V}{\partial z^2}\right) \tag{3}$$

$$U\frac{\partial W}{\partial x}+V\frac{\partial W}{\partial y}+W\frac{\partial W}{\partial z}= -\frac{1}{\rho}\frac{dP}{dz}-\frac{\overline{\partial vw}}{\partial y}-\frac{\overline{\partial w^2}}{\partial z}+\nu\left(\frac{\partial^2 W}{\partial y^2}+\frac{\partial^2 W}{\partial z^2}\right) \tag{4}$$

It is noted that, using the boundary layer approximation, the streamwise momentum fluxes have been neglected, and the pressure gradient $\partial P/\partial x$ originally appearing in Eq. (2) has been replaced by the cross-sectional average pressure gradient $\overline{dP/dx}$, following the method of Patankar and Spalding (1972). By these boundary layer approximations the above equations become parabolic in the streamwise direction and consequently

Nomenclature

a = duct half width (Fig. 1)
a' = diagonal half width (Fig. 1)
C_1, C_2, C_3 = turbulence model constants for anisotropy
C_f = friction factor ($C_f \equiv 2\overline{\tau_w}/(\rho U_b^2)$)
$C_{\epsilon 1}$, $C_{\epsilon 2}$, C_μ = turbulence model constants
D = hydraulic diameter (Fig. 1)
f_μ, f_2 = modification function in k-ϵ model
k = thermal conductivity or turbulent kinetic energy
P = mean static pressure or turbulent kinetic energy production
Re = Reynolds number ($\mathrm{Re} \equiv U_b D/\nu$)
R_t = turbulent Reynolds number ($R_t \equiv k^2/(\nu\epsilon)$)
$\overline{u^2}$, $\overline{v^2}$, $\overline{w^2}$ = Reynolds normal stress components
$\overline{uv}$, $\overline{uw}$, $\overline{vw}$ = Reynolds shear stress components
u_τ = friction velocity ($u_\tau \equiv \sqrt{\tau_w/\rho}$)
U^+ = dimensionless velocity ($U^+ \equiv U/u_\tau$)
U, V, W = mean velocity components (Fig. 1)
V' = mean velocity component along diagonal
x, y, z = cartesian coordinates (Fig. 1)
y' = cartesian coordinate along diagonal (Fig. 1)
y^+, z^+ = dimensionless wall coordinate ($y^+ \equiv u_\tau y/\nu$)
δ_{ij} = Kronecker delta
ν = kinematic viscosity
ν_t = eddy diffusivity of momentum
ρ = density
σ_k, σ_ϵ = turbulence model constants for diffusion of k and ϵ
ϵ = dissipation rate of k
τ_w, $\overline{\tau_w}$ = local and average wall shear stress, respectively

Subscripts

b = bulk-mean
c = center
w = wall

are amenable to an efficient numerical forward marching solution procedures which are particularly economic. The viscous stress terms appearing in the momentum equations are not neglected, since, in the present calculation procedure, the no-slip boundary condition at the wall is directly used in place of the common wall function approach as discussed above.

From momentum equations of Eqs. (3) and (4) governing the secondary motion, it can be easily seen that the Reynolds stresses $\overline{v^2}$, $\overline{w^2}$, and $\overline{vw}$ play an important role in the secondary motion. Therefore, special attention is given to these stresses in the following sections introducing the turbulence model.

Anisotropic k-ϵ Turbulence Model. As a turbulence model for determining the Reynolds stresses appearing in the momentum equations above, the anisotropic low-Reynolds-number k-ϵ turbulence model of the first author (Myong, 1988; Myong and Kasagi, 1990a) is introduced in the present study. This model is generally expressed as follows:

$$\frac{Dk}{Dt}=\frac{\partial}{\partial x_j}\left[\left(\nu+\frac{\nu_t}{\sigma_k}\right)\frac{\partial k}{\partial x_j}\right]-\overline{u_iu_j}\frac{\partial U_i}{\partial x_j}-\epsilon \tag{5}$$

$$\frac{D\epsilon}{Dt}=\frac{\partial}{\partial x_j}\left[\left(\nu+\frac{\nu_t}{\sigma_\epsilon}\right)\frac{\partial \epsilon}{\partial x_j}\right]-C_{\epsilon 1}\frac{\epsilon}{k}\overline{u_iu_j}\frac{\partial U_i}{\partial x_j}-C_{\epsilon 2}f_2\frac{\epsilon^2}{k} \tag{6}$$

where:

$$\overline{u_iu_j}=\frac{2}{3}k\delta_{ij}-\nu_t\left(\frac{\partial U_i}{\partial x_j}+\frac{\partial U_j}{\partial x_i}\right)+\frac{k}{\epsilon}\nu_t\sum_{\beta=1}^{3}C_\beta\left(S_{\beta ij}-\frac{1}{3}S_{\beta\alpha\alpha}\delta_{ij}\right)+\frac{2}{3}\nu\frac{k}{\epsilon}\left(\frac{\partial\sqrt{k}}{\partial x_n}\right)^2W_{ij}(n,m) \tag{7a}$$

$$S_{1ij}=\frac{\partial U_i}{\partial x_\gamma}\frac{\partial U_j}{\partial x_\gamma} \tag{7b}$$

$$S_{2ij}=\frac{1}{2}\left(\frac{\partial U_\gamma}{\partial x_i}\frac{\partial U_j}{\partial x_\gamma}+\frac{\partial U_\gamma}{\partial x_j}\frac{\partial U_i}{\partial x_\gamma}\right) \tag{7c}$$

$$S_{3ij}=\frac{\partial U_\gamma}{\partial x_i}\frac{\partial U_\gamma}{\partial x_j} \tag{7d}$$

$$\nu_t=C_\mu\sqrt{k}L=C_\mu f_\mu\frac{k^2}{\epsilon} \tag{8}$$

$$f_\mu=(1+3.45/\sqrt{R_t})[1-\exp(-y^+/70)] \tag{9}$$

$$f_2=\{1-(2/9)\exp[-(R_t/6)^2]\}[1-\exp(-y^+/5)]^2 \tag{10}$$

$$W_{ij}(n,m)=-\delta_{ij}-\delta_{in}\delta_{jn}+4\delta_{im}\delta_{jm} \tag{11}$$

$$\sigma_k=1.4,\ \sigma_\epsilon=1.3,\ C_{\epsilon 1}=1.4,\ C_{\epsilon 2}=1.8,\ C_\mu=0.09 \tag{12}$$

Note that the indices n and m denote the coordinate normal to the wall and the streamwise coordinate, respectively: summation convention does not apply to n and m.

From the trial test for the two-dimensional fully developed channel flow, the present model is known to resolve two serious weaknesses common to previous k-ϵ models. That is, it reproduces correctly all the major turbulence quantities such as Reynolds shear stress $-\overline{uv}$, turbulent kinetic energy k and its dissipation rate ϵ near the wall with the correct wall-limiting behavior. And, the present model also works well for the distribution of eddy diffusivity of momentum ν_t even in the region far from the wall (Myong, 1988; Myong and Kasagi, 1990b). In addition, compared with the common (isotropic) k-ϵ model, the present model has additive third and fourth nonlinear quadratic terms on the right-hand side in the Reynolds stress tensor of Eq. (7). The third term is important to exhibit the anisotropic characteristics of each Reynolds stresses across the whole region. In contrast, the fourth one is crucial to reproduce the strong anisotropy in the near-wall region and also to satisfy the wall-limiting condition of normal Reynolds stresses. Note that the ν_t in Eq. (7) is the same as that in the isotropic near-wall k-ϵ model. Thus, the present anisotropic k-ϵ model is supplemented with the original transport equations of k and ϵ, but broadens the range of applicability while maintaining most of its popular features. These and other features of the model are described in more detail elsewhere (Myong, 1988; Myong and Kasagi, 1990a, c).

Application of the Anisotropic k-ϵ Model to Square Duct Flow. Since the turbulent flows in a square duct have the corner regions where both walls influence the flow field, this fact should be taken into account in the present anisotropic k-ϵ model. First, the wall coordinate y^+ appearing in the modification functions of Eqs. (9) and (10) should be modified to take the effect of both walls into account. Up to the present, the correct form obtained theoretically does not still exist, although there are several proposals for this one (see e.g., Demuren and Rodi, 1984). In the present study, we replace it with the wall coordinate using the smaller value between perpendicular distances from each wall; i.e. $y^+=min(y^+, z^+)$. Second, the fourth term on the right-hand side of Eq. (7), which is crucial to satisfy the wall limiting condition of normal Reynolds stresses, is expressed as a superposition of terms that are attained by considering each wall independently.

Based on the above consideration, the present model can be applicable to the turbulent flow in a square duct. In the present study, we can simplify further the transport equations of Eqs. (5) and (6) and each component of Reynolds stresses using the boundary layer approximations consistent with the above consideration for the momentum equations. Consequently, Eqs. (5)-(7) are expressed as follows:

$$U\frac{\partial k}{\partial x}+V\frac{\partial k}{\partial y}+W\frac{\partial k}{\partial z}=\frac{\partial}{\partial y}\left[\left(\nu+\frac{\nu_t}{\sigma_k}\right)\frac{\partial k}{\partial y}\right]+\frac{\partial}{\partial z}\left[\left(\nu+\frac{\nu_t}{\sigma_k}\right)\frac{\partial k}{\partial z}\right]+P-\epsilon \tag{13}$$

$$U\frac{\partial \epsilon}{\partial x}+V\frac{\partial \epsilon}{\partial y}+W\frac{\partial \epsilon}{\partial z}=\frac{\partial}{\partial y}\left[\left(\nu+\frac{\nu_t}{\sigma_\epsilon}\right)\frac{\partial \epsilon}{\partial y}\right]+\frac{\partial}{\partial z}\left[\left(\nu+\frac{\nu_t}{\sigma_\epsilon}\right)\frac{\partial \epsilon}{\partial z}\right]+C_{\epsilon 1}\frac{\epsilon}{k}P-C_{\epsilon 2}f_2\frac{\epsilon^2}{k} \tag{14}$$

where

$$P=-\overline{uv}\frac{\partial U}{\partial y}-\overline{uw}\frac{\partial U}{\partial z}-\overline{v^2}\frac{\partial V}{\partial y}-\overline{w^2}\frac{\partial W}{\partial z} \tag{15}$$

$$\overline{u^2}=\frac{2}{3}k+\frac{1}{3}\nu_t\frac{k}{\epsilon}(2C_1-C_3)\left[\left(\frac{\partial U}{\partial y}\right)^2+\left(\frac{\partial U}{\partial z}\right)^2\right]+2\nu\frac{k}{\epsilon}\left[\left(\frac{\partial\sqrt{k}}{\partial y}\right)^2+\left(\frac{\partial\sqrt{k}}{\partial z}\right)^2\right] \tag{16}$$

$$\overline{v^2}=\frac{2}{3}k-2\nu_t\frac{\partial V}{\partial y}-\frac{1}{3}\nu_t\frac{k}{\epsilon}\left[(C_1-2C_3)\left(\frac{\partial U}{\partial y}\right)^2+(C_1+C_3)\left(\frac{\partial U}{\partial z}\right)^2\right]-\nu\frac{k}{\epsilon}\left[\frac{4}{3}\left(\frac{\partial\sqrt{k}}{\partial y}\right)^2+\frac{2}{3}\left(\frac{\partial\sqrt{k}}{\partial z}\right)^2\right] \tag{17}$$

$$\overline{w^2}=\frac{2}{3}k-2\nu_t\frac{\partial W}{\partial z}$$
$$-\frac{1}{3}\nu_t\frac{k}{\epsilon}\left[(C_1-2C_3)\left(\frac{\partial U}{\partial z}\right)^2+(C_1+C_3)\left(\frac{\partial U}{\partial y}\right)^2\right]$$
$$-\nu\frac{k}{\epsilon}\left[\frac{4}{3}\left(\frac{\partial\sqrt{k}}{\partial z}\right)^2+\frac{2}{3}\left(\frac{\partial\sqrt{k}}{\partial y}\right)^2\right] \quad (18)$$

$$\overline{uv}=-\nu_t\frac{\partial U}{\partial y}, \qquad \overline{uw}=-\nu_t\frac{\partial U}{\partial z} \quad (19,20)$$

$$\overline{vw}=-\nu_t\left(\frac{\partial W}{\partial y}+\frac{\partial V}{\partial z}\right)+C_3\nu_t\frac{k}{\epsilon}\left(\frac{\partial U}{\partial y}\right)\left(\frac{\partial U}{\partial z}\right) \quad (21)$$

The model constants C_1, C_2, and C_3 are set equal to 0.8, 0.45, and -0.15, respectively, which are the same values as those proposed previously for boundary layer flows (Myong and Kasagi, 1990a, c). Note that one model constant C_2 does not appear in the present case. Also, note here that, contrary to the previous Reynolds (or algebraic) stress models, the present anisotropic model is substantially derived from the standard (isotropic) k-ϵ turbulence model; i.e., the standard k-ϵ model is obtained in the limit as $C_i\to 0$.

It should be valuable to note here that, in the process of attaining the above simplified results from Eq. (7), the terms not having both the gradients of primary velocity among the nonlinear terms of velocity gradient are neglected by the usual order of estimation, while those of secondary velocity gradients in the linear terms are retained, because the same order of estimation between the linear and nonlinear terms of velocity gradient are generally not applicable. This is indirectly confirmed by Demuren and Rodi (1984); they showed that the secondary velocity gradients in the linear terms play an important role in the formation of secondary flows.

Here, we briefly discuss the resulting forms of Reynolds stresses, comparing with those of the previous representative algebraic stress models of Demuren and Rodi (1984, hereafter DR) and of Launder and Ying (1973, LY). First, the expressions for the primary Reynolds shear stresses $\overline{uv}$ and $\overline{uw}$ of Eqs. (19) and (20) in the present model happen to be identical to those for eddy diffusivity formulation in the common isotropic k-ϵ model, and also the same forms as those of both DR and LY models. However, they are obtained only by boundary layer approximation in the present model, but by drastic assumptions in the latter models. On this point of view, the present model seems likely to confirm, to some extent, the usefulness of the eddy diffusivity concept for the primary Reynolds shear stresses usually adopted in the previous algebraic stress models with little theoretical foundation. Second, in the present model the separation of secondary normal Reynolds stresses $\overline{w^2}-\overline{v^2}$ is expressed as follows:

$$\overline{w^2}-\overline{v^2}=2\nu_t\left(\frac{\partial V}{\partial y}-\frac{\partial W}{\partial z}\right)-C_3\nu_t\frac{k}{\epsilon}\left[\left(\frac{\partial U}{\partial y}\right)^2-\left(\frac{\partial U}{\partial z}\right)^2\right]$$
$$+\frac{2}{3}\nu\frac{k}{\epsilon}\left[\left(\frac{\partial\sqrt{k}}{\partial y}\right)^2-\left(\frac{\partial\sqrt{k}}{\partial z}\right)^2\right] \quad (22)$$

This term as well as that of the secondary Reynolds shear stress $\overline{vw}$ of Eq. (21) is generally known to play an important role in the vorticity (or secondary flow) generation. Except for the third term in Eq. (22), both expressions of Eqs. (21) and (22) are in general similar to those of DR model which is known to be superior to any other existing models. In the DR model, however, they are obtained by using several ad-hoc assumptions with unknown validity. In contrast, the present model has obtained these forms only by the boundary layer approximation as discussed above. In particular, the present model also confirms validity two different mechanisms that contribute to the generation of secondary shear stress $\overline{vw}$ identified by Perkins (1970); the first mechanism is associated with the gradients of the secondary velocities, and its contributions to $\overline{vw}$ can be represented in terms of an isotropic eddy diffusivity, while the second one is associated with the primary velocity gradients because of its close relation with the distortion of the primary stress field in the corner. Note that the importance to represent both these processes in a model is also reported by Demuren and Rodi (1984). Third, both secondary normal Reynolds stresses $\overline{v^2}$ and $\overline{w^2}$ of Eqs. (17) and (18) in the present model have the gradient terms of primary velocity in both y and z directions. On the contrary, most of the algebraic stress models involving the DR and LY models have only one directional gradient term of primary velocity for each secondary normal Reynolds stress, which is clearly unreasonable on the physical ground. As a consequence, the above expressions for Reynolds stresses in the present model have strong similarities to those of previous algebraic stress models, but seem likely to be more appropriate on the physical ground. Furthermore, in contrast to the previous models the present model is directly applicable right up to the wall.

Solution Procedure and Boundary Conditions. An efficient forward marching solution procedure is employed to solve the above equations, since they are parabolic in the streamwise direction. This procedure requires only two-dimensional storage of the dependent variables at each forward step, starting from given inlet conditions over the duct cross section. In the present study, a revised version of the three-dimensional parabolic finite difference procedure of Patankar and Spalding (1972) is employed; in particular, the SIMPLER algorithm of Patankar (1980) is substituted for the original SIMPLE algorithm in an attempt to improve its rate of convergence. As the initial conditions, an essentially uniform distribution of all variables is prescribed at the duct inlet, following the available experimental conditions. For example, the secondary velocities V and W are set to zero, and the turbulent kinetic energy and mean streamwise velocity are given uniformly over the duct across section except for the vicinity of the wall, based on the experimental data. The dissipation rate ϵ is assigned to small values such that the eddy diffusivity ν_t is several times the molecular viscosity ν. Starting from these initial (or inlet) conditions, the step-by-step integration is carried out up to a location 100 duct hydraulic diameters downstream, where the nominally fully-developed flow is attained. At each step, the momentum equations are solved first with the SIMPLER algorithm, which consists of solving the pressure equation to obtain the pressure field and solving the pressure-correction equation only to correct the velocities. A more detailed procedure of the SIMPLER is described by Patankar (1980). Subsequently, the Reynolds stresses are determined from the algebraic expressions of Eqs. (16)–(21) with the eddy diffusivity relation of Eq. (8), and finally the k- and ϵ-equations of Eqs. (14) and (15) are solved.

The forward step size is initially 0.01 percent of the duct hydraulic diameter D but progressively enlarged to a maximum level of 1 percent of D. At each step several iterations are carried out to reduce the residuals to negligible levels. The mesh typically comprises of a 66×66 grid points distributed nonuniformly over a cross section quadrant: the clustering function stretches the mesh in y and z directions by using the geometric progression, and three or four grid lines are, at least, within $y^+<5$ (or $z^+<5$). These meshes are concentrated in the sublayer and buffer regions near the wall. Validation of the numerical procedure is achieved through comparisons between the numerical results with different grid spacing and forward step sizes. For example, additional computations are also made with a 80×80 grid points, and all predicted turbulence quantities are found to be differed from those with a 66×66, at most, by 0.3 percent. It should be valuable to note

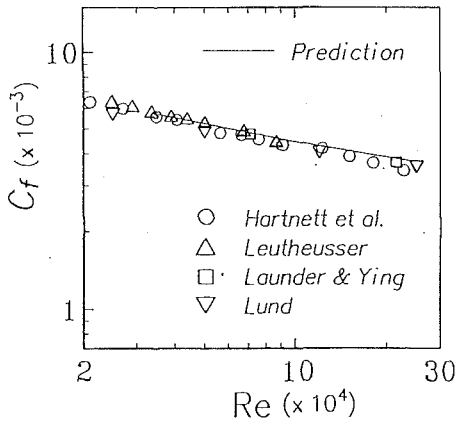

Fig. 2 Friction coefficient for fully-developed flows in a square duct

here that the condition of three or four grid lines, at least, in the sublayer mentioned above is crucial to the convergence and numerical accuracy.

Boundary conditions are prescribed at symmetry planes and at solid walls, since the calculation is made in one quadrant only. At symmetry planes, the velocity component normal to the symmetry plane is set equal to zero, while for all other quantities the gradients normal to this plane are taken as zero. At the solids walls, all of the velocity components and Reynolds stresses are set equal to zero, and the dissipation rate is set equal to $\nu(\partial^2 k/\partial y^2)_w$ or $\nu(\partial^2 k/\partial z^2)_w$.

Results and Discussion

The predicted distributions of the friction coefficient C_f for full developed flow in a square duct are compared with the experimentally determined values in Fig. 2. Note that the data shown, which were selected on the basis of a recent survey of corner flow data by Gessner, are cited from Gessner and Emery (1981). It is generally known that the predictions for C_f with the previous models have been somewhat unsatisfactory (Gessner and Emery, 1981). From the figure it can be seen that the present predictions agree quite well with the experimental results over a wide range of Reynolds number. It is informative to mention here the following facts. In the present model the average wall shear stress $\overline{\tau_w}$ is calculated directly from the local wall shear stress $\tau_w = \mu(\partial U/\partial y)_w$, which is discussed below. Therefore, the present results seem likely to indicate indirectly the adequacy of the present model for near-wall turbulence, since this affects strongly C_f.

Hereafter, among the available experimental data those of Gessner et al. (1979) and Gessner and Emery (1981) are mainly compared with the predictions, largely due to the facts that these data are known to be relatively accurate and also adopted at the 1980-81 Stanford Conference (Kline et al., 1982).

Figure 3 shows the predicted streamwise variation of the axial mean velocity component along the wall bisector $x/a = 1.0$ at several fixed distances from the wall over the interval $0.02 \le y/a \le 1.0$. The experimental data are included for comparison. The data indicate that the velocities in the central region increase first with streamwise distance, reach local peak values, and then decrease to asymptotic values. The local peak in the central region is due to the increased core flow acceleration induced by simultaneous boundary layer development on all four walls. On the contrary, the velocities near the wall directly decrease to their asymptotic values without increasing, due to the presence of the wall. In particular, the peak of the centerline velocity occurs downstream of the location where the boundary layers begin to merge ($x/D \fallingdotseq 32$), indicating that further adjustment of the flow takes place after the core flow becomes nonexistent. This is presumably due to the shear layer

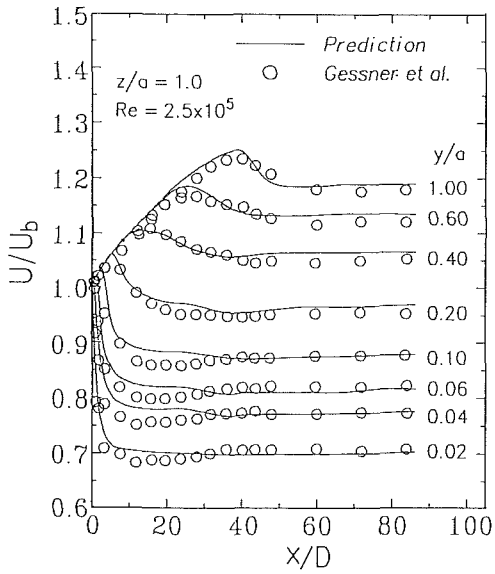

Fig. 3 Predicted axial mean velocity distributions at various streamwise locations along the wall bisector $x/a = 1$

interaction effects which lead to a non-equilibrium condition at about $x/D = 32$ (Gessner and Emery, 1981). The present predictions agree fairly well with experimental data over the entire calculation domain from the uniform distributions at the inlet to asymptotic ones at fully developed state, confirming the experimental evidence mentioned above.

Figure 4 shows predicted axial mean velocity distributions along the wall and corner bisectors of a square duct at various streamwise locations. Note that the difference between the two sets of Gessner and Emery (1981) and Gessner et al. (1979) is a good measure of the experimental scatter, since they were obtained in the same experimental apparatus and under similar conditions. It can be seen that the predicted distributions along both the wall and corner bisectors are in good agreement with their experimental counterparts as a whole.

Comparisons between predicted and experimental secondary velocity profiles are shown in Fig. 5 at various streamwise locations. Along both bisectors the present model predicts fairly well the secondary velocity, although it underpredicts a little the secondary velocity at $x/D = 84$. Note that the experimental data indicate that the maximum velocity increases slightly from $x/D = 40$ to 84, but the present calculation shows the opposite trend; V and V' decrease slightly there. This behavior is also observed by Demuren and Rodi (1984). Considering this fact and reminding that there is considerable disagreement among the previous experimental data, particularly along the corner bisector, the present model's predictions seem likely to agree quite well with experimental data as a whole.

The existence of secondary flow and its initial location in the developing region have been of the controversial problem in both experimental and numerical analyses. In experimental analysis this is mainly attributed to the fact that most experimenters conjecture the existence of the secondary flow from the isovel results of axial mean velocity without direct measuring the secondary flow (see e.g., Melling and Whitelaw, 1976; Ahmed and Brundrett, 1971), while in numerical analysis this is mainly attributed to the near-wall spatial resolution (see e.g., Gessner and Emery, 1981). The present predictions as shown in Fig. 5 shows that the secondary flow appears early near the corner in the entrance region ($x/D = 8$) and its influence consistently increases laterally as the flow progresses downstream. And, their presence is felt across the entire duct cross section when the flow is fully developed. This is consistent with the experimental evidence of Ahmed and Brundrett (1971). Note

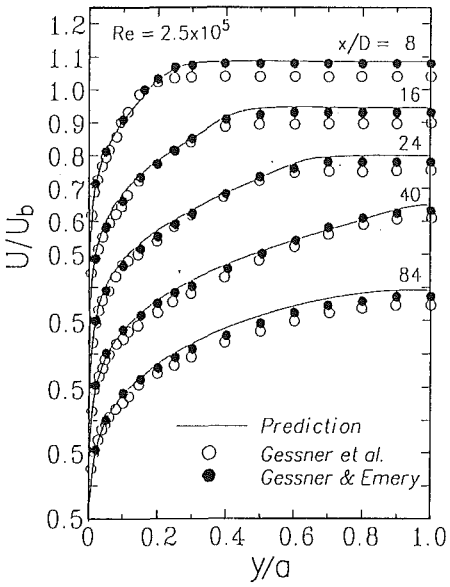

Fig. 4(*a*) Along the wall bisector

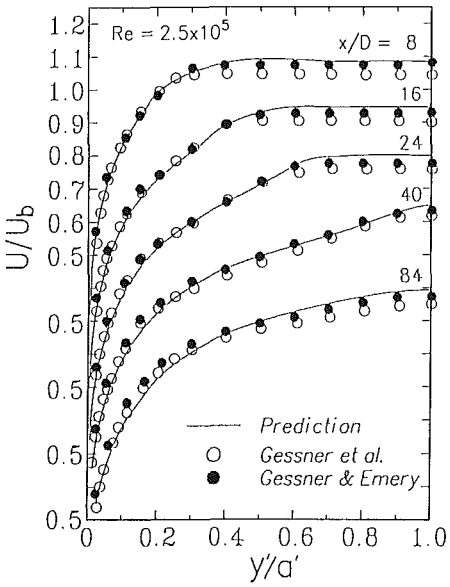

Fig. 4(*b*) Along the corner bisector

Fig. 4 Velocity profiles at various streamwise locations

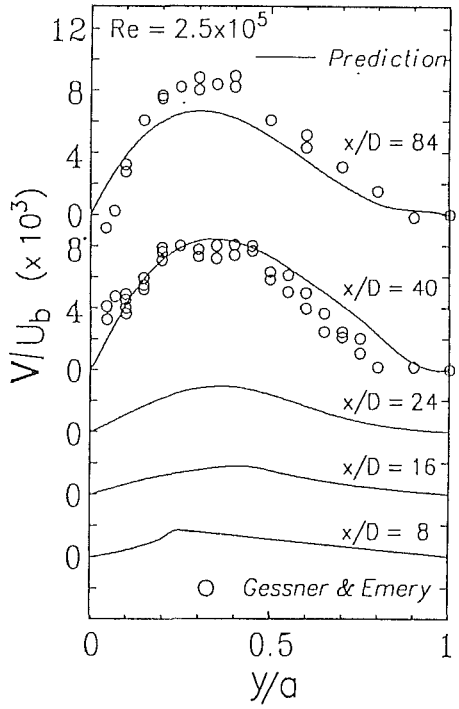

Fig. 5(*a*) Along the wall bisector

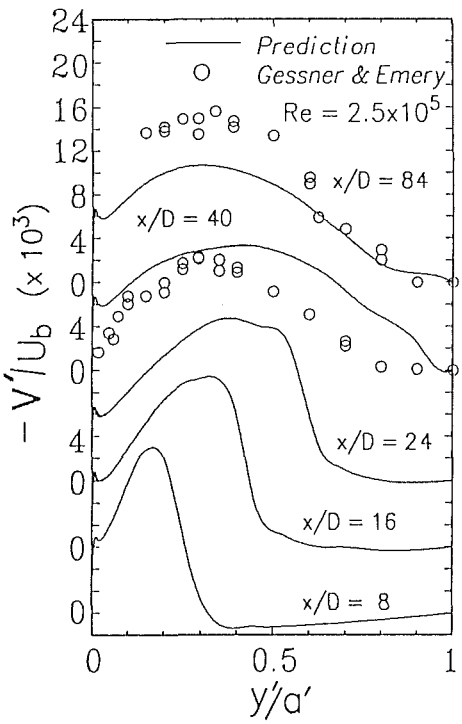

Fig. 5(*b*) Along the corner bisector

Fig. 5 Secondary velocity profiles at various streamwise locations

that an inflection point close to the corner is found in the present prediction, although the cause of this fact is not clear at present.

Figure 6 shows the predicted local wall shear stress distributions along the duct perimeter for fully-developed flow in a square duct. The experimental data are also included for comparison. Experimental data indicate that the wall shear stress first rises from the symmetry plane toward the corner with the peak shear stress about midway between the corner and the mid-point of the duct sides, and then falls again near the corner, approaching zero at the corner. Most previous models tend to predict local overshoot behavior of wall shear stress away from the corners and underpredict values in the near-corner regions (see Gessner and Emery, 1981). The present model, however, simulates the above mentioned experimental behavior excellently. Also, from Fig. 6 the present results bring out well the tendency of the secondary motion to smooth out variations in wall shear stress around the perimeter of the duct. It should be valuable to note here that the present result also lends support to the claim that the secondary motion has been simulated reasonably well by the model, since the occurrence of a local maximum in the wall shear stress distribution is due to the secondary motion.

The predicted velocity profiles in wall coordinates are shown in Fig. 7, at four positions in the z direction, which are normalized by the local wall friction velocities at each position. It is generally acknowledged from the experimental investigations that, except near the corner regions, the usual inner logarithmic law of the wall is valid with a little scatter in the involved constants, while no universal defect laws are found

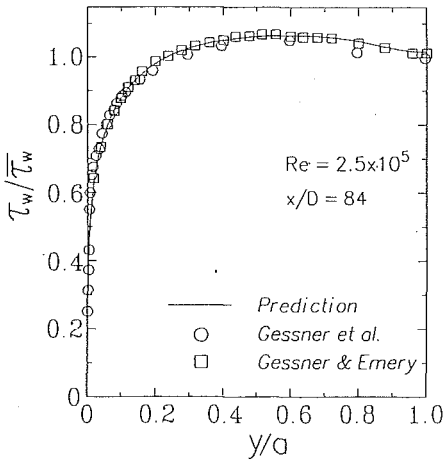

Fig. 6 Local wall shear stress distributions for fully-developed flow in a square duct

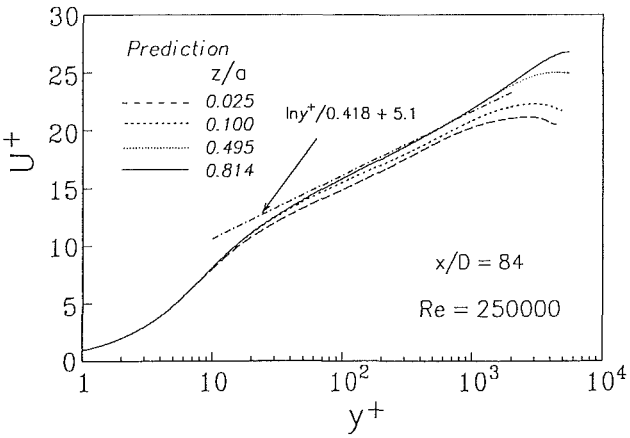

Fig. 7 Mean velocity profiles for fully-developed flow

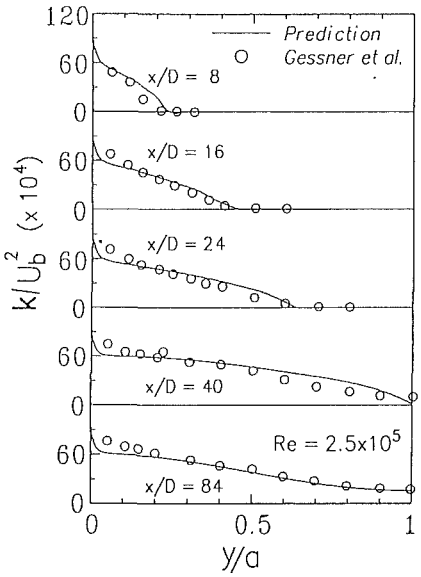

Fig. 8(*a*) Along the wall bisector

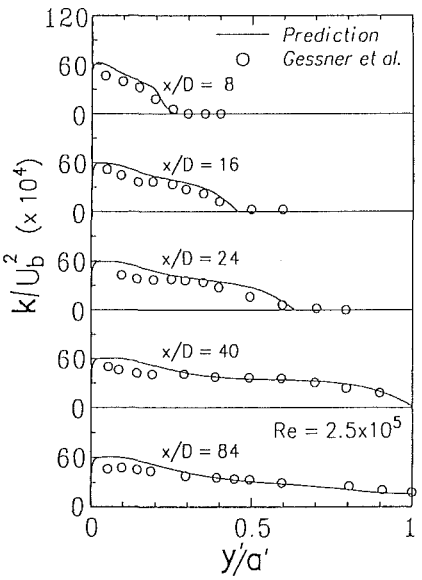

Fig. 8(*b*) Along the corner bisector

Fig. 8 Turbulent kinetic energy profiles at various streamwise locations

for the outer region (e.g., Leutheusser, 1963). The present prediction confirms clearly these experimental evidence as a whole. It also indicates that, although velocity profiles even near the corner region ($z/a=0.025$) exhibit slightly wakelike behavior, the usual inner logarithmic law of the wall is still a good approximation, as experimentally reported by Gessner (1982), but the involved constants should be consistently varied over the relatively wide range of corner region.

Figure 8 compares the predicted and measured distributions of the turbulent kinetic energy k along the wall and corner bisectors in the developing flow region of a square duct. The present prediction simulates excellently the experimental distributions of turbulent kinetic energy over a whole calculation domain. The present model also predicts fairly well the experimentally observed plateau-like behavior along a corner bisector (Fig. 8(b)). Furthermore, it can be seen from the figure that, as a whole predicted turbulent kinetic energy values decrease a little between the shear layer interaction region ($x/D=40$) and the nominally fully-developed region ($x/D=84$), which is in accord with the experimental evidence. Note that, along the wall bisector the present model predicts the similar behavior of k with a sharp peak in the vicinity of the wall to that for two-dimensional channel flow, while along the corner bisector it does not predict this characteristic behavior, perhaps due to the secondary motion.

The predicted and measured development of Reynolds shear stress $\overline{uv}$ along the wall and corner bisectors are shown in Fig. 9. The present model works fairly well along the wall bisector (Fig. 9(a)), but the distributions along the corner bisector (Fig. 9(b)) are somewhat overpredicted, particularly near the corner region, although the model prediction shows qualitatively pretty well their behavior over a whole calculation domain. Here, it is valuable to mention that the values of Reynolds shear stress $\overline{uv}$ near the corner region change rapidly along the tranverse (see e.g., Gessner, 1982) and thus the experimental data in this region may have somewhat large measurement uncertainties.

Concluding Remarks

Three-dimensional developing turbulent flows in a straight square duct involving turbulence-driven secondary flow are numerically investigated with the anisotropic low-Reynolds-number k-ϵ turbulence model. Contrary to most of the previous models, the present model has used directly the no-slip boundary conditions at the wall in place of the common wall function approach. The resulting set of equations are also simplified only by the boundary layer assumption and solved with a forward marching numerical procedure for three-dimensional

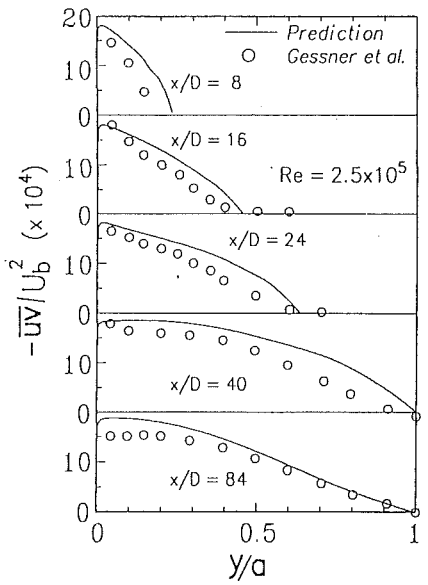

Fig. 9(*a*) Along the wall bisector

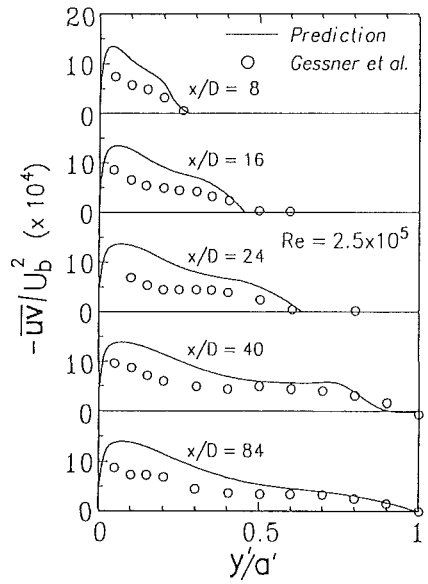

Fig. 9(*b*) Along the corner bisector

Fig. 9 Primary shear stress profiles at various streamwise locations

shear layers. The predicted quantities such as axial mean velocity, friction coefficients, local wall shear stresses and Reynolds stresses are all in good agreement with the available experimental data. Secondary flow velocity profiles are also predicted well over the entire region. The present results show that the present anisotropic k-ϵ model offers a viable alternative to higher-order closure models for predicting complex turbulent flows influenced by the anisotropy of Reynolds stresses.

Finally, it should be noted the following facts. Most of the previous (algebraic stress) models used the wall functions approach as the boundary condition, which is discussed above. This means that the mean velocity is artificially fitted to the universal velocity profile at the first grid point away from the wall. Consequently, they can yield a pretty good prediction near the wall region. However, generally this method is likely to be less than desirable from the standpoint of numerical prediction. In contrast, the present model uses directly the no-slip condition at the wall and thus has no restricted conditions. Furthermore, all of the present results discussed above are by no means inferior to those of the previous higher-order models such as the DR model, although not shown here.

Acknowledgments

The present work was mainly undertaken at both the Institute of Industrial Science (IIS) and Research Center for Advanced Science and Technology (RCAST) of the University of Tokyo. The first author gratefully acknowledges the support of both IIS and RCAST.

References

Ahmed, S., and Brundrett, E., 1971, "Turbulent Flow in Non-Circular Ducts. Mean Flow Properties in the Developing Region of a Square Duct," *Int. J. Heat Mass Transfer*, Vol. 14, pp. 365–372.

Brundrett, E., and Baines, W. D., 1964, "The Production and Diffusion of Vorticity in Duct Flow," *J. Fluid Mech.*, Vol. 19, pp. 375–394.

Demuren, A. O., and Rodi, W., 1984, "Calculation of Turbulence-Driven Secondary Motion in Non-Circular Ducts," *J. Fluid Mech.*, Vol. 140, pp. 189–222.

Gessner, F. B., 1982, "Corner Flow (Secondary Flow of the Second Kind)," In Kline et al., pp. 182–212.

Gessner, F. B., and Emery, A. F., 1981, "The Numerical Predictions of Developing Turbulent Flow in Rectangular Ducts,' ASME JOURNAL OF FLUIDS ENGINEERING, Vol. 103, pp. 445–455.

Gessner, F. B., Po, J. K., and Emery, A. F., 1979, "Measurements of Developing Turbulent Flow in a Square Duct," *Turbulent Shear Flows I* (ed. by Durst, et al.) Springer-Verlag, New York, pp. 119–136.

Kline, S. J., Cantwell, B., and Lilley, G. M. (eds.), 1982, *Proc. 1980–1981 AFORS-HTTM Stanford Conf. on Complex Turbulent Flows*, Stanford University.

Launder, B. E., and Ying, W. M., 1973, "Prediction of Flow and Heat Transfer in Ducts of Square Cross-Section," *Proc. Inst. Mech. Engrs.*, Vol. 187, pp. 455–461.

Leutheusser, H. J., 1963, "Turbulent Flow in Rectangular Ducts," *J. Hydraulics Div., Proc. ASCE*, Vol. 89(HY3), pp. 1–19.

Melling, A., and Whitelaw, J. H., 1976, "Turbulent Flow in a Rectangular Duct," *J. Fluid Mech.*, Vol. 78, pp. 289–315.

Myong, H. K., 1988, "Fundamental Studies on Two-Equation Turbulence Model for Numerical Predictions of Wall-Bounded Shear Flow and Heat Transfer," Dr. Eng. Thesis, The University of Tokyo, Tokyo.

Myong, H. K., and Kasagi, N., 1990a, "Prediction of Anisotropy of the Near-Wall Turbulence with an Anisotropic Low-Reynolds-Number k-ϵ Turbulence Model," ASME JOURNAL OF FLUIDS ENGINEERING, Vol. 112, pp. 521–524.

Myong, H. K., and Kasagi, N., 1990b, "A New Approach to the Improvement of k-ϵ Turbulence Model for Wall-Bounded Shear Flows," *JSME Int. J.*, Ser. II, Vol. 33, pp. 63–72.

Myong, H. K., and Kasagi, N., 1990c, "A Proposal for an Anisotropic k-ϵ Turbulence Model Satisfying the Wall-Limiting Condition of Turbulence," *Trans. Japan Soc. Mech. Engrs.* (in Japanese), Vol. 56B(531), pp. 3298–3304.

Myong, H. K., Kasagi, N., and Kobayashi, T., 1990, "Numerical Prediction of Boundary Layer Flows with the Anisotropic k-ϵ Turbulence Model," *Trans. Japan Soc. Mech. Engrs.* (in Japanese), Vol. 56B(531), pp. 3305–3312.

Nakayama, A., Chow, W. L., and Sharma, D., 1983, "Calculation of Fully Developed Turbulent Flows in Ducts of Arbitrary Cross-Section," *J. Fluid Mech.*, Vol. 128, pp. 199–217.

Patankar, S. V., and Spalding, D. B., 1972, "A Calculation Procedure for Heat, Mass and Momentum Transfer in 3-D Parabolic Flows," *Int. J. Heat Mass Transfer*, Vol. 15, pp. 1787–1806.

Patankar, S. V., 1980, *Numerical Heat Transfer and Fluid Flow*, Hemisphere, New York.

Kline, S. J., Cantwell, B., and Lilley, G. M. (eds.), 1982, *Proc. 1980–1981 AFORS-HTTM Stanford Conf. on Complex Turbulent Flows*, Stanford University.

Perkins, H. J., 1970, "The Formation of Streamwise Vorticity in Turbulent Flow," *J. Fluid Mech.*, Vol. 44, pp. 721–740.

R. A. Antonia

D. K. Bisset
Department of Mechanical Engineering,
University of Newcastle,
N.S.W., 2308, Australia

J. Kim
Center for Turbulence Research,
NASA-Ames Research Center,
Moffett Field, CA, 94035

An Eddy Viscosity Calculation Method for a Turbulent Duct Flow

The mean velocity profile across a fully developed turbulent duct flow is obtained from an eddy viscosity relation combined with an empirical outer region wake function. Results are in good agreement with experiments and with direct numerical simulations in the same flow at two Reynolds numbers. In particular, the near-wall trend of the Reynolds shear stress and its variation with Reynolds number are similar to those of the simulations. The eddy viscosity method is more accurate than previous mixing length or implicit function methods.

1 Introduction

It is useful to have a simple means of obtaining reliable mean velocity distributions in turbulent wall flows. Such distributions may, for example, serve as input for engineering calculations such as integral and differential methods (e.g., Dean, 1976) and for calculations of heat and mass transfer.

It is well known that a turbulent wall layer can be described in terms of four regions (in order of increasing distance from the wall): a viscous sublayer, buffer, logarithmic, and wake-like regions. The mean velocity distribution can be written in the form (e.g., Coles, 1956)

$$\overline{U}^+ = f(y^+) + g\left(\frac{y}{\delta}\right) \tag{1}$$

where $f(y^+)$ represents the distribution across the inner region, which includes the sublayer, buffer, and logarithmic regions. Spalding (1961) proposed an implicit analytic relation in the form $y^+ = f_1(\overline{U}^+)$, while Dean (1976) obtained a single analytic relation for the whole layer by combining f_1 with an expression for g. Other approaches use a mixing length distribution, usually a modified form of van Driest's (1956) formulation, to determine $f(y^+)$. The van Driest damping function has an exponential form which asymptotically merges into the log region. Granville (1989) reviewed a number of the van Driest type formulae that are used for turbulent boundary layers in pressure gradients and noted that many of these fail to match either the slope or intercept (or both) of the log law. He proposed a relation that satisfied both requirements but which (like most other proposals, including Dean's formula) did not exhibit the correct limiting behaviour for the Reynolds shear stress at the wall, i.e., $-\overline{u^+v^+} \sim y^{+3}$ (Chapman and Kuhn, 1986; Kim et al., 1987). This was remedied in Granville's (1990) eddy viscosity formula for turbulent boundary layers with pressure gradients which was also compatible with the slope and intercept of the log law. We show here that this formula can, with minor modification, be successfully applied to a fully developed duct flow over a range of Reynolds numbers. The addition of a suitable wake function $g(y/h)$ provides the complete velocity profile from wall to centerline.

There were two reasons for selecting a duct flow: (i) the distribution of the total shear stress is known theoretically; and (ii) the direct numerical simulation (DNS) data of Kim et al. (1987) form a very useful basis for comparison, especially in the near-wall region where reliable experimental data on the Reynolds shear stress are scarce. Correct mean velocity and Reynolds shear stress distributions in this region should be important pre-requisites for heat transfer calculations. As the DNS data have been obtained at low Reynolds numbers, where Reynolds number effects are greatest, they represent a fairly severe test for the calculation method.

2 Description of Method

The total shear stress τ in a parallel planar duct is given by

$$\tau^+ \equiv (1+\nu_T^+)\frac{d\overline{U}^+}{dy^+} = 1 - \frac{y^+}{h^+} = -\overline{u^+v^+} + \frac{d\overline{U}^+}{dy^+} \tag{2}$$

and Eq. (1) is replaced by

$$\overline{U}^+ = \int_0^{y^+} \frac{\tau^+}{1+\nu_T^+}\, dy^+ + g\left(\frac{y}{h}\right) \tag{3}$$

where h, the duct half-width is used instead of δ. The assumed eddy viscosity ν_T^+, based on that used by Granville (1990), is

$$\nu_T^+ = \kappa y^+ \tau^+ \left\{1 - e^{-\left(\frac{y^+}{\lambda_0^+}\right)^2} + A_1\left[e^{-\left(\frac{y^+}{\lambda_0^+}\right)^3} - e^{-A_2\left(\frac{y^+}{\lambda_0^+}\right)^3}\right]\right\}, \tag{4}$$

with $A_1 = 0.06$ and $A_2 = 70$. The term in square brackets (not used by Granville) will be discussed in Section 4. Granville replaced λ_0^+ by $\lambda^+/\sqrt{1+a\hat{p}^+}$, $\hat{p}^+$ being the nondimensional pressure gradient which governs the behavior of τ^+ at the wall, viz.

$$\tau^+ = 1 + \hat{p}^+ y^+. \tag{5}$$

He found that particular values of the slope ($\kappa = 0.4$) and intercept ($C = 5.23$) of the log law, viz.

$$\overline{U}^+ = \kappa^{-1} \ln y^+ + C, \tag{6}$$

could be matched with (constant) $\lambda^+ = 24$ and a equal to 14.5 ($\hat{p}^+ > 0$) or 18.0 ($\hat{p}^+ < 0$) but we preferred to specify κ and

Contributed by the Fluids Engineering Division for publication in the JOURNAL OF FLUIDS ENGINEERING. Manuscript received by the Fluids Engineering Division October 17, 1990.

C values directly and calculate the appropriate λ_0^+. The y^{+2} term in Eq. (4) ensures the correct y^{+3} variation of ν_T^+ near the wall while giving approximately the correct rate of decay for the damping function, and the combination $\kappa y^+ \tau^+$ allows the slope of the log law to be matched. Note that Eq. (2) represents the correct shear stress distribution throughout the duct flow, whereas in the case of a boundary layer with pressure gradient, Eq. (5) is valid only near the wall.

In Granville's paper, the focus was primarily on the wall region so that the wake function term in (3) was not considered. The wake function adopted here is based on that suggested by several investigators (Dean, 1976; Finley et al., 1966; Granville, 1976), i.e.,

$$g = \frac{1}{\kappa}(1 + 6\Pi)\left(\frac{y}{h}\right)^2 - \frac{1}{\kappa}(1 + 4\Pi)\left(\frac{y}{h}\right)^3 \tag{7}$$

where Π depends on the Reynolds number, and h replaces the boundary layer thickness δ. The origin for the wake function is moved slightly away from the wall, however, to $y_1^+ = (h^+/10) - 10$, with $g = 0$ for $y < y_1$ and $(y - y_1)/(h - y_1)$ replacing y/h in Eq. (7). This is because dg/dy^+, though small, is larger than $-u^+v^+$ close to the wall, and would cause errors when $-u^+v^+$ is calculated from Eq. (2).

The value of λ_0^+ for Eq. (4) is determined (in a computer program) by ensuring that the calculated distribution of $\overline{U}^+$ satisfies input values of both κ and C, as follows. If

$$\frac{d\overline{U}^+}{dy^+} = \frac{\tau^+}{1 + \nu_T^+} = \frac{1}{\kappa y^+}$$

at some point $y^+ = y_0^+$ near the beginning of the log region, then

$$\lambda_0^{+2} = -\frac{y_0^{+2}}{\ln\left\{\frac{1}{\kappa y_0^+ \tau^+} + A_1\left[e^{-\left(\frac{y_0^+}{\lambda_0^+}\right)^3} - e^{-A_2\left(\frac{y_0^+}{\lambda_0^+}\right)^3}\right]\right\}}, \tag{8}$$

which is solved iteratively to obtain λ_0^+ for a specified y_0^+. At y_0^+, $\overline{U}^+$ is given by Eq. (6) so that

$$C = \int_0^1 \frac{\tau^+}{1 + \nu_T^+}\, dy^+ + \int_0^{\ln y_0^+} \left(\frac{\tau^+ y^+}{1 + \nu_T^+} - \frac{1}{\kappa}\right) d(\ln y^+). \tag{9}$$

An initial guess for y_0^+ is made in the program, and λ_0^+ and C are calculated from Eqs. (8) and (9). The guess is refined until the calculated C is equal to the specified value ± 0.001, which usually requires no more than three iterations. In general, $y_0^+ \approx 50$.

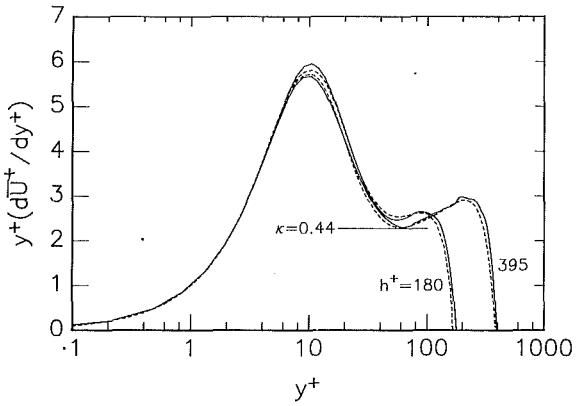

Fig. 1 Product $y^+ d\overline{U}^+/dy^+$ ($h^+ = 180$ and $h^+ = 395$). - - -, present calculation; ———, DNS.

3 Results: Comparison With DNS Data

Mean velocity distributions were calculated for the same conditions as the available DNS data in a fully developed turbulent duct flow. The DNS were carried out at two Reynolds numbers, Re = 3300 and 7900, or equivalently, for $h^+ = 180$ and 395. Details of these simulations are given by Kim et al. (1987) and Kim (1989).

Apart from h^+, the program requires κ, C, and Π as inputs. The existence of these parameters hinges on the existence of a logarithmic region. For the relatively small values of h^+ at which the DNS were performed, the existence of a logarithmic region may be in doubt, especially for $h^+ = 180$. This aspect has been discussed in some detail by Spalart (1988) who suggested that the logarithmic layer, or the "apparent logarithmic layer" for very low Reynolds numbers, can be found by seeking the minimum of $y\, d\overline{U}/dy$ versus y. The minimum should have a magnitude of κ^{-1}, and the value of C can be determined at this position. As for Spalart's boundary layer distributions of $y\, d\overline{U}/dy$, the present DNS distributions for the duct (Fig. 1) exhibit narrow minima and imply different values of κ^{-1}. At low Reynolds numbers, however, the value of y at which the logarithmic region begins ($y^+ \approx 40$) exceeds the value at which the wake region becomes significant ($y \approx 0.15h$). Thus it is reasonable to assume a lower value of κ^{-1} than implied by the $y\, d\overline{U}/dy$ plot in such cases, and allow the wake function to make up the difference. Huffman and Bradshaw (1972) found no evidence that κ varied with Reynolds number for several wall-bounded flows, but pointed out that there is some freedom in selecting the actual value of the constant κ. They found that C can be Re-dependent, however. For the present comparison

Nomenclature

a = pressure gradient coefficient of Granville (1990)
A_1, A_2 = constants in Eq. (4)
A^+ = van Driest damping length scale
C = log-law intercept, Eq. (6)
d_1 = coefficient in series expansion of $\overline{U}^+$
f, f_1 = inner region mean velocity functions
g = wake function
h = duct half-height
l = mixing length
$\hat{p}$ = non-dimensional pressure gradient, Eq. (5)
Re = Reynolds number $\equiv U_1 h/\nu$
$\overline{U}$ = mean velocity in x direction
U_1 = centerline velocity
U_τ = friction velocity ($\equiv\sqrt{\tau_w}$)
u, v = velocity fluctuations in x, y directions
x, y = longitudinal and normal-to-the-wall coordinates
y_0 = y value where calculated $\overline{U}$ matches the log-law
y_1 = origin for wake function
α_1, β_1 = coefficients in series expansion of $-\overline{u^+v^+}$
δ = boundary layer thickness
κ = von Kármán constant, Eq. (6)
λ, λ_0 = eddy viscosity damping parameters
λ_1 = mixing length damping parameter
ν = kinematic viscosity
ν_T = eddy viscosity = $-\overline{uv}/(\partial\overline{U}/\partial y)$
Π = wake parameter, Eq. (9)
τ = kinematic total shear stress

Superscript

$+$ = normalization by wall variables (U_τ and/or ν)

Subscript

w = value at the wall

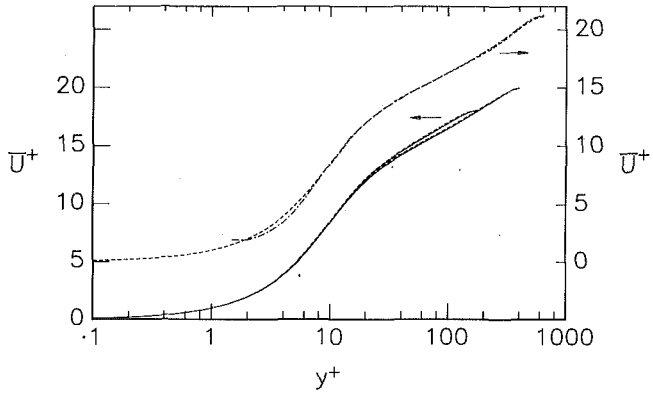

Fig. 2 Mean velocity distributions. ———, DNS (h^+ = 180 and h^+ = 395); —·—, experimental (R_θ = 13800, $h^+ \approx$ 650) from Hussain and Reynolds (1975); - - -, present calculation

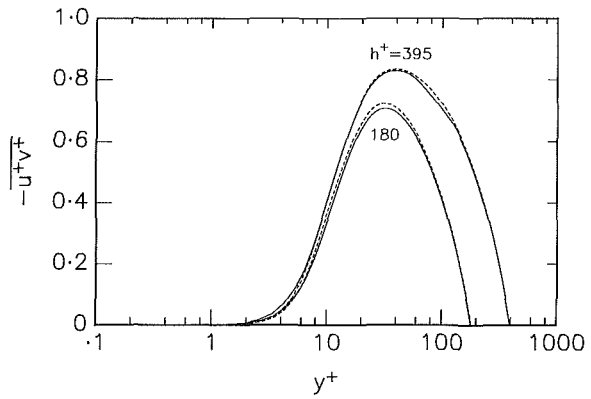

Fig. 3 Reynolds shear stress distributions (h^+ = 180 and h^+ = 395). - - -, present calculation; ———, DNS.

with DNS results, κ is assumed constant at 0.44, but the value of C varies (see below).

The calculated distributions of $y^+ d\overline{U}^+/dy^+$ are shown in Fig. 1 and they follow the DNS distributions quite well. The quality of agreement with the DNS results is partly due to the term in square brackets in Eq. (4): without this term, the calculation results are slightly high at $y^+ \approx 10$, and low by more than 10 percent at $y^+ \approx 30$. The form of this term is chosen because of its effect on $\overline{uv}$ (discussed further in relation to Fig. 4).

Figure 2 shows distributions of $\overline{U}^+$ for the DNS and the calculation, and also shows pitot tube measurements (Hussain and Reynolds, 1975) at Re = 13800 compared with calculation results for $h^+ = 650$. The values of C and Π used in calculations were C = 6.2, 6.0, 5.8 and Π = 0.04, 0.09, 0.16 corresponding to h^+ = 180, 395 and 650. The presentation in Fig. 2 (which is the one commonly used in the literature) is not as sensitive as that in Fig. 1 in terms of emphasizing differences between the calculations and the DNS (or experimental) data, but the agreement is clearly very good.

Distributions of $-\overline{u^+v^+}$, inferred from the mean velocity calculation via Eq. (2), agree closely with the DNS distributions (Fig. 3). The magnitude of the differences would be well within the uncertainty in any experimental data. The limiting behavior of $-\overline{u^+v^+}$ near the wall (Chapman and Kuhn, 1986; Kim et al., 1987) may be analyzed with the aid of Taylor series expansions (e.g., Antonia and Kim, 1991b):

$$-\overline{u^+v^+} = \alpha_1 y^{+3} + \beta_1 y^{+4} + \cdots$$

$$\overline{U}^+ = y^+ - \frac{1}{2h^+} y^{+2} + d_1 y^{+4} + \cdots$$

where $\alpha_1 = -4d_1$ [this follows from Eq. (2)]. Therefore,

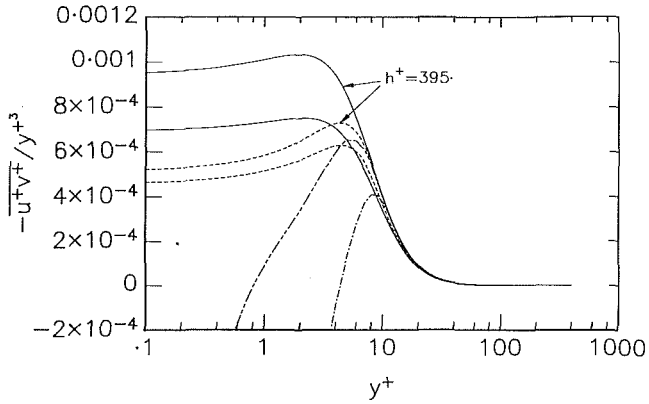

Fig. 4 Ratio $-\overline{u^+v^+}/y^{+3}$ (h^+ = 180 except where indicated). - - -, present calculation; ———, DNS; — - - —, mixing length; —·—, Dean (1976).

$$\nu_T^+ \equiv -\overline{u^+v^+}\left(\frac{d\overline{U}^+}{dy^+}\right)^{-1} = \alpha_1 y^{+3} + \left(\frac{\alpha_1}{h^+} + \beta_1\right) y^{+4} + \cdots .$$

For our choice of ν_T^+, Eq. (4),

$$\nu_T^+ = \frac{\kappa}{\lambda_0^{+2}} y^{+3} + \kappa\left(A_1 \frac{A_2 - 1}{\lambda_0^{+3}} - \frac{1}{\lambda_0^{+2} h^+}\right) y^{+4} + \cdots$$

so that $\alpha_1 \equiv \kappa/\lambda_0^{+2}$. Plotting $-\overline{u^+v^+}/y^{+3}$ (Fig. 4) indicates that the values of α_1 are lower for the calculation than the DNS, but the general shape of the curves and their behavior with increasing h^+ are similar. This is partly because of the square brackets term in Eq. (4). The form of this term was specifically chosen for its effect on the value of β_1, but the constants A_1 and A_2 were selected for best agreement in the $y^+ dU^+/dy^+$ results (which emphasizes the interdependence of $\overline{U}^+$ and $-\overline{u^+v^+}$). If the square brackets term is omitted (i.e., $A_1 = 0$), β_1 is negative, although α_1 may be somewhat improved. The present method (with positive β_1) yields substantially more accurate values of $-\overline{u^+v^+}$ for $y^+ \gtrsim 3$.

The results presented so far apply to a fairly restricted range of Reynolds numbers, and ideally that range could be extended by means of comparisons with experimental data. Unfortunately, published velocity profiles show significant variations (see Fig. 14 of Hussain and Reynolds, 1975, for example), which means that definitive values of κ, C, and Π cannot be given at this stage. The data of Shah (1988) cover the range 3300 ≤ Re ≤ 33000 (180 ≤ h^+ ≤ 1350) and agree adequately with the results presented so far where they overlap, and therefore they can at least indicate the trend at higher Re. These data suggest that with κ = 0.44, C and Π are constant at 5.7 and 0.3, respectively, for Re ≥ 17000 ($h^+ \gtrsim 750$), although the value of Π implied for $h^+ = 650$ is a bit larger ($\approx$0.25) than the value of 0.16 used for the uppermost curve in Fig. 2. Thus the eddy viscosity calculation method requires only one input parameter at $h^+ \gtrsim 750$, viz. h^+ itself.

The damping parameter λ_0^+ varies only a little with Re, decreasing from 30.98 at $h^+ = 180$ to an asymptotic value of about 27.4 at high Re. This behavior is qualitatively similar to the variation of A^+ with h^+ obtained by Huffman and Bradshaw (1972). These authors used a modified van Driest mixing length distribution with a constant value for κ and obtained reasonable agreement (up to $y \approx 0.2\ h$) with the experiments of Patel and Head (1969), mainly in the range $h^+ < 180$. However, the van Driest mixing length distribution has an incorrect limiting wall behavior and although the results obtained with it (Antonia and Kim, 1991a) compare favorably with the DNS data over a major part of the flow, the comparison is not as good as with the present method. The suggestion that there is negligible Re-dependence of the wake region in the duct (Huffman and Bradshaw, 1972) is not borne

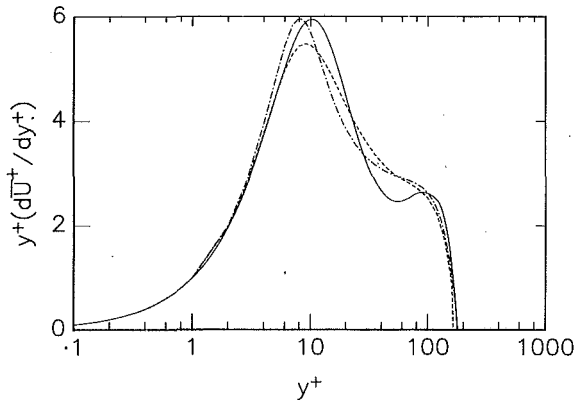

Fig. 5 Product $y^+ d\overline{U}^+/dy^+$, obtained with Granville's (1989) mixing length distribution or Dean's (1976) formula, for $h^+ = 180$. - - -, mixing length; — - —, Dean (1976); ———, DNS

out by the present results, although the dependence appears to be less than that in a zero-pressure gradient boundary layer.

4 Other Methods

Results from an assumed mixing length distribution and from the relation proposed by Dean (1976) are now compared with the DNS data.

The mixing length distribution

$$l^+ = \kappa y^+ \tau^{+1/2}\left(1 - e^{-\frac{y^+}{\lambda_l^+}}\right) \tag{10}$$

is very similar to that used by Granville (1989) for boundary layers with pressure gradients. The details of the calculation are very similar to those outlined in Section 2, Eq. (10) being used instead of Eq. (4) as the starting point for the determination of $\overline{U}^+$ in the inner region and Eq. (7) retained for the outer region wake function. The magnitude of λ_l^+ was obtained iteratively in order to match the slope and intercept of the logarithmic region.

Dean's (1976) implicit relation is given by

$$y^+ e^{\kappa g} = f_1(\overline{U}^+) \tag{11}$$

with g given by expression (7) and $f_1(\overline{U}^+)$ given by

$$f_1(\overline{U}^+) = \overline{U}^+ + e^{-\kappa C}\left[e^{\kappa\overline{U}^+} - 1 - \kappa\overline{U}^+ - \frac{(\kappa\overline{U}^+)^2}{2} - \frac{(\kappa\overline{U}^+)^3}{3!} - \frac{\kappa\overline{U}^+)^4}{4!}\right].$$

Newton's iteration method was applied to Eq. (11) to obtain $\overline{U}^+$ for any given y^+. Equations (10) and (11) were applied to the DNS conditions using the input values obtained directly from the DNS curves, i.e., κ, C, and $\Pi = 0.4$, 5.37, -0.055 ($h^+ = 180$) or 0.43, 5.72, 0.072 ($h^+ = 395$). Distributions of $y^+ d\overline{U}^+/dy^+$ for $h^+ = 180$ (Fig. 5) indicate that agreement with the DNS data is not of the same quality as in Fig. 1, especially with regard to the lack of a local minimum at $y^+ \approx 50$. Note also that Dean's relation underestimates the y location of the main local maximum in $y^+ d\overline{U}^+/dy^+$. Results are only slightly better at $h^+ = 395$. Both relations have a limiting wall behavior which is incorrect, as is evident in the $-\overline{u^+v^+}/y^{+3}$ distributions for $h^+ = 180$ in Fig. 4. The errors, in particular the negative values, are caused partly by the fact that the wake function, Eq. (7), has its origin at the wall, but when the wake function is made exactly zero for $y^+ < 10$ the curves are still incorrect, implying that $-\overline{u^+v^+}$ varies as y^{+4}. This does not cause practical errors, since $-\overline{u^+v^+} << \tau^+$ near the wall, but a method (such as the present one) which has the correct limiting behavior is likely to be more robust in general.

5 Conclusions

The present approach, which combines an eddy-viscosity based calculation for the inner region with a specific choice of wake function in the outer region, yields mean velocity and Reynolds shear stress distributions which are in close agreement with direct numerical simulation of a fully developed turbulent duct flow. In particular, the wall-limiting behavior and Reynolds number dependence of the Reynolds shear stress are in qualitative agreement with the simulations, which is not the case for the mixing length approach or the implicit relation used by Dean (1976). The eddy-viscosity approach should be valid for all Reynolds numbers for which a logarithmic region can be identified, and should also be valid in pipe flows. For fully developed channel flow, the von Kármán constant κ is assumed to be fixed at 0.44, while the log-law C and the wake parameter Π vary at low Reynolds numbers only.

Acknowledgment

RAA acknowledges the support of the Australian Research Council.

References

Antonia, R. A., and Kim, J., 1991a, "Reynolds Shear Stress and Heat Flux Calculations in a Fully Developed Turbulent Duct Flow," *International Journal of Heat and Mass Transfer*, Vol. 34, pp. 2013–2018.

Antonia, R. A., and Kim, J., 1991b, "Turbulent Prandtl Number in the Near-Wall Region of a Turbulent Channel Flow," *International Journal of Heat and Mass Transfer*, Vol. 34, pp. 1905–1908.

Chapman, D. R., and Kuhn, G. D., 1986, "The Limiting Behaviour of Turbulence Near a Wall, *Journal of Fluid Mechanics*, Vol. 170, pp. 265–292.

Coles, D., 1956, "The Law of the Wake in the Turbulent Boundary Layer," *Journal of Fluid Mechanics*, Vol. 1, pp. 191–226.

Dean, R. B., 1976, "A Single Formula for the Complete Velocity Profile in a Turbulent Boundary Layer," ASME JOURNAL OF FLUIDS ENGINEERING, Dec., pp. 723–727.

Finley, P. J., Khoo, C. P., and Chin, J. P., 1966, "Velocity Measurements in a Thin Turbulent Water Layer," *La Houille Blanche*, Vol. 21, pp. 713–721.

Granville, P. S., 1976, "A Modified Law of the Wake for Turbulent Shear Layers," ASME JOURNAL OF FLUIDS ENGINEERING, Sept., pp. 578–580.

Granville, P. S., 1989, "A Modified van Driest Formula for the Mixing Length of Turbulent Boundary Layers in Pressure Gradients," ASME JOURNAL OF FLUIDS ENGINEERING, Vol. 111, pp. 94–97.

Granville, P. S., 1990, "A Near-Wall Eddy Viscosity Formula for Turbulent Boundary Layers in Pressure Gradients Suitable for Momentum, Heat or Mass Transfer," ASME JOURNAL OF FLUIDS ENGINEERING, Vol. 112, pp. 240–243.

Huffman, G. D., and Bradshaw, P., 1972, "A Note on von Kármán's Constant in Low Reynolds Number Turbulent Flows," *Journal of Fluid Mechanics*, Vol. 53, pp. 45–60.

Hussain, A. K. M. F., and Reynolds, W. C., 1975, "Measurements in Fully Developed Turbulent Channel Flow," ASME JOURNAL OF FLUIDS ENGINEERING, Vol. 97, pp. 568–578.

Kim, J., 1989, "On the Structure of Pressure Fluctuations in Simulated Turbulent Channel Flow," *Journal of Fluid Mechanics*, Vol. 205, pp. 421–451.

Kim, J., Moin, P., and Moser, R., 1987, "Turbulence Statistics in Fully Developed Channel Flow at Low Reynolds Numbers," *Journal of Fluid Mechanics*, Vol. 177, pp. 133–166.

Patel, V. C., and Head, M. R., 1969, "Some Observations on Skin Friction and Velocity Profiles in Fully Developed Pipe and Channel Flows," *Journal of Fluid Mechanics*, Vol. 38, pp. 181–201.

Shah, D. A., 1988, "Scaling of the 'Bursting' and 'Pulse' Periods in Wall Bounded Turbulent Flows," Ph.D. thesis, University of Newcastle, Australia.

Spalart, P. R., 1988, "Direct Simulation of a Turbulent Boundary Layer up to $R_\theta = 1410$," *Journal of Fluid Mechanics*, Vol. 187, pp. 61–98.

Spalding, D. B., 1961, "A Single Formula for the Law of the Wall," ASME *Journal of Applied Mechanics*, Vol. 83, pp. 455–458.

van Driest, E. R., 1956, "On Turbulent Flow Near a Wall," *Journal of Aeronautical Science*, Vol. 23, pp. 1007–1012

Mean and Turbulence Characteristics of a Class of Three-Dimensional Wall Jets—Part 1: Mean Flow Characteristics

G. Padmanabham
Department of Aeronautical Engineering,
Madras Institute of Technology,
Anna University,
Madras 600 044, India

B. H. Lakshmana Gowda
Fluid Mechanics Laboratory,
Department of Applied Mechanics,
Indian Institute of Technology,
Madras 600 036, India

This paper reports experimental investigations on mean and turbulence characteristics of three-dimensional, incompressible, isothermal turbulent wall jets generated from orifices having the shapes of various segments of a circle. In Part 1, the mean flow characteristics are presented. The turbulence characteristics are presented in Part 2. The influence of the geometry on the characteristic decay region of the wall jet is brought out and the differences with other shapes are discussed. Mean velocity profiles both in the longitudinal and lateral planes are measured and compared with some of the theoretical profiles. Wall jet expansion rates and behavior of skin-friction are discussed. The influence of the geometry of the orifice on the various wall jet properties is presented and discussed. Particularly the differences between this class of geometry and rectangular geometries are critically discussed.

1 Introduction

Wall jets can be recognized as an example of the interaction between free jets and boundary layer types of flows. These have been attracting a great deal of attention of research workers and they are being increasingly investigated. Glauert (1956) analyzed the turbulent wall jet by dividing the flow regime into two parts: the region between the wall and the point of maximum velocity as a normal boundary layer, called the inner layer; and the rest of the wall jet with the features of a free jet, called the outer layer. He matched the solutions for these two layers at the point of maximum velocity of the profile where the shear stress was assumed to be zero. Since Glauert's pioneering work, many studies have been conducted on plane, axisymmetric, and radial wall jets and a complete review of the wall jet has been given by Launder and Rodi (1981). Three-dimensional wall jets, which occur more often in practical situations, have started receiving attention only in recent times. These flows can be found in many fields of engineering such as the boundary layer control of airfoils, effective film cooling of turbine blades, and in the design of air vents for ventilation purposes.

When the aspect ratio of the orifice from which the jet issues onto a solid boundary is finite, the wall jet becomes three-dimensional. The variation of flow properties should then be considered not only in the longitudinal direction but also in the lateral direction. The first published work on three-dimensional wall jets is the experimental study undertaken by Sforza and Herbst (1970). They investigated wall jets formed on a flat plate by jets issuing from rectangular orifices of various eccentricities. The eccentricities (height/length) of the orifice used by them were 0.025, 0.05, 0.1, and 1.0. Based on the detailed velocity profile measurements, they divided the flow field into three regions depending on the maximum velocity decay along the axial direction: (*a*) the potential core (PC) region, where the maximum velocity U_m is equal to or is very close to the jet exit velocity U_j; (*b*) the characteristic decay (CD) region, where the decay of the maximum velocity depends on the geometry of the orifice, and (*c*) the radial decay (RD) region, where the flow field becomes independent of the geometry of the orifice and the maximum velocity decays at the same rate as that for a radial wall jet (Bakke, 1957). Three-dimensional wall jets have been generated by using orifice geometries other than rectangular (e.g., circular, semi-circular, square, and elliptic geometries). A summary of these investigations is given in Part 2 of the paper in which the turbulence results are also presented.

Three-dimensional wall jets produced by various orifices of different aspect ratios have their own characteristics in the CD region. Particularly the investigations of Sforza and Herbst brought out the properties of wall jets generated by rectangular shapes which have flat sides. Another class of nozzle geometries which can be used to generate three-dimensional wall jets are the segments of a circle. In this case, the nozzle shape across the cross-section changes continuously when compared to the nozzles having the shape of rectangular geometry. It was felt important to study the flow fields (mean and turbulence) of three-dimensional wall jets produced by this class of geometries. A comparison of these characteristics with those obtained by the use of rectangular nozzles would then give information which could be useful to understand the growth and interaction of shear layers emanating from different orifice shapes and which could also be effectively used in many practical applications. For example, the difference in the spread rates could

Contributed by the Fluids Engineering Division for publication in the JOURNAL OF FLUIDS ENGINEERING. Manuscript received by the Fluids Engineering Division April 25, 1991.

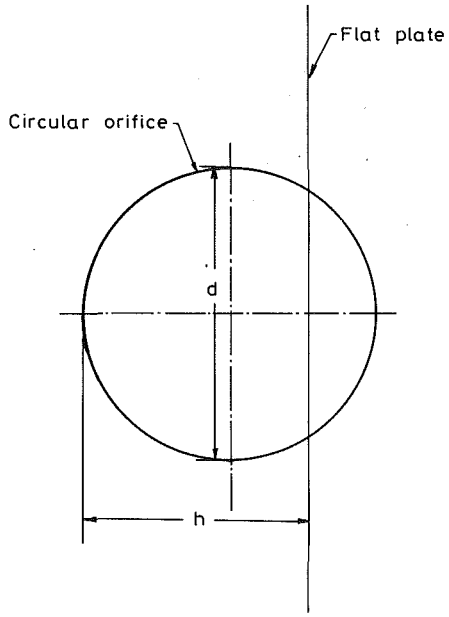

Fig. 1 Definition sketch of orifice configuration (h/d) employed. (*a*) $h/d = 0.1$; (*b*) $h/d = 0.8$; (*c*) $h/d = 0.5$; (*d*) $h/d = 0.23$.

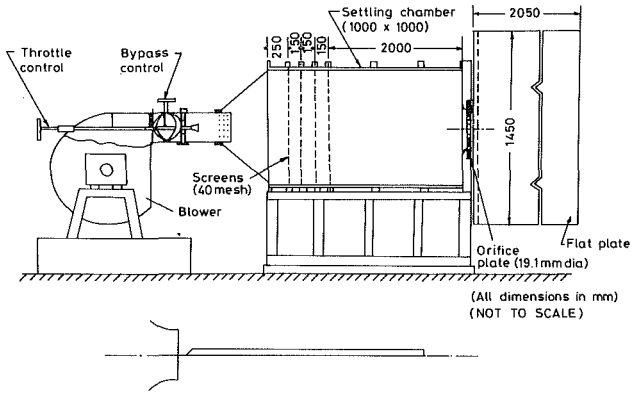

Fig. 2 Schematic diagram of experimental setup.

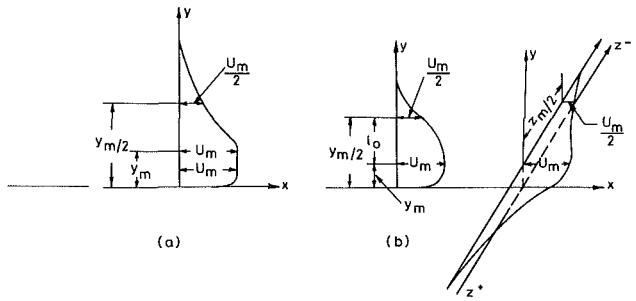

Fig. 3 Schematic representation of three-dimensional wall jet flow field. Velocity profiles in (*a*) PC region; (*b*) CD and RD regions; *x*-axis orifice plate centerline.

be advantageously utilized in air-venting systems and drying processes.

For these reasons, investigations are carried out in the developing and fully developed regions of three-dimensional wall jets generated by the impingement of free jets issuing tangentially onto a smooth flat plate from the orifices having geometries of various segments of a circle (see Fig. 1). The different orifice geometries defined in terms of h/d ratios were obtained by laterally moving a flat plate positioned vertically in front of a circular orifice. The dimension "h" is the distance normal to the plate from one edge of a circular orifice in the diametral plane and "d" is the diameter of the circular orifice. The different h/d ratios employed in the present investigation were 1.0, 0.8, 0.5, and 0.23. The corresponding values of $h/\sqrt{A}$, where A is the area of the respective segments, are 1.19, 0.98, 0.80, and 0.60. The various geometries will be referred to in terms of h/d ratios.

The mean flow measurements made in the present investigations include mean velocity profiles, maximum velocity decay, growth rates in the longitudinal and spanwise directions, and skin-friction estimates covering an axial distance up to one hundred orifice slot widths along the jet axis. The results obtained are discussed in relation to the available data for other geometries. The results of the turbulence measurements are presented in Part 2 of the paper.

2 Experimental Procedure

2.1 The Test Setup. All the measurements reported were performed using the low speed jet tunnel of the Fluid Mechanics Laboratory, Indian Institute of Technology, Madras. Figure 2 shows schematically the jet tunnel and the general layout of the experimental arrangement. Air is supplied from a centrifugal blower and it is controlled by a throttle placed in the inlet section. The air stream is led into a settling chamber through a set of four screens. An orifice plate was positioned

Nomenclature

A = cross-sectional area of a segment of a circle
A = constant appearing in law-of-the wall
B = constant appearing in law-of-the wall
c_f = skin-friction coefficient
d = diameter of circular orifice
e = eccentricity of rectangular orifice (height/width; dimensionless)
h = distance normal to the plate from one edge of the circular orifice, see Fig. 1
K = constant as given in Eq. (3)
l_0 = $(y_{m/2} - y_m)$ as shown in Fig. 3
N = constant as given in Eq. (3)
n = exponent describing the decay of maximum velocity in Eq. (1)
Re_d = jet exit Reynolds number $(= U_j d/\nu)$; dimensionless
Re_{ym} = Reynolds number based on y_m $(= U_m y_m/\nu)$; dimensionless
U = mean velocity in x-direction
U_j = jet velocity at orifice exit
U_m = maximum velocity at any station along x-direction
U_* = wall shear stress velocity $(=\sqrt{\tau_0/\rho})$
U^+ = U/U_* (= dimensionless)
x_0 = virtual origin of the jet
y = transverse direction (normal to the plate)
y_m = value of y where $U = U_m$
$y_{m/2}$ = value of y for which $U = U_m/2$
y^+ = yU_*/ν (= dimensionless)
z = spanwise direction (parallel to the plate)
$z_{m/2}$ = value of z for which $U = U_m/2$
ν = kinematic viscosity of the air
ρ = density of air
α = constant in Glauert's profile
τ_0 = shear stress at the wall

Subscript

$(\bar{\ })$ = indicates normalization with h (e.g., $\bar{x} = x/h$)
CD = characteristic decay
DC = direct current
PC = potential core
RD = radial decay

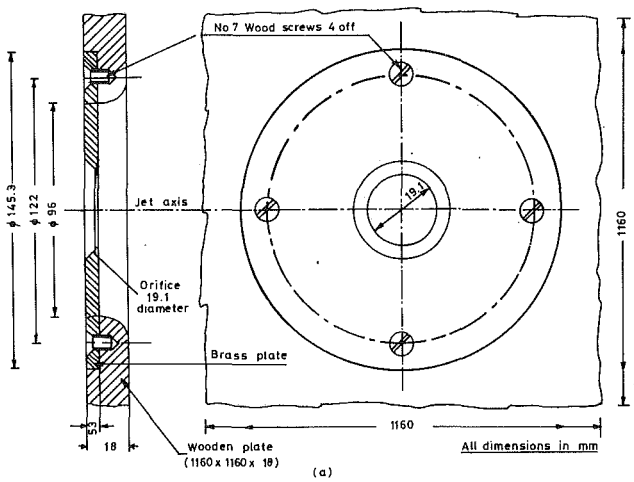

(a)

Fig. 4(*a*) Sketch showing nozzle assembly and jet axis

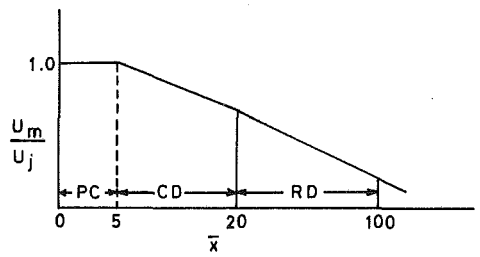

(b) h/d = 0.8

Fig. 4(*b*) Three regions of flow development of wall jet for $h/d = 0.8$

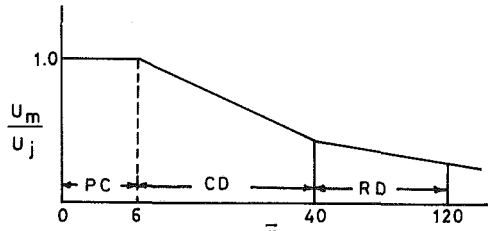

(c) h/d = 0.23

Fig. 4(*c*) Three regions of flow development of wall jet for $h/d = 0.23$

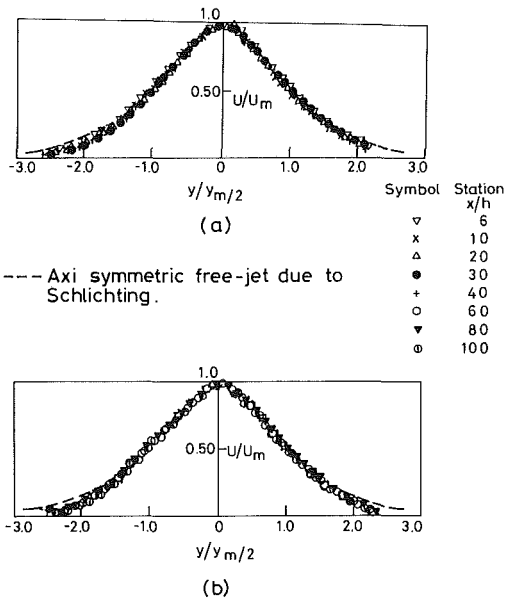

Fig. 5(*a,b*) Normalized free jet velocity profiles in *x-y* plane (uncertainty in $U = \pm 2$ percent in average; uncertainty in $y = 0.5$ mm). - - -, mean curve of axisymmetric free jet due to Schlichting (1968).

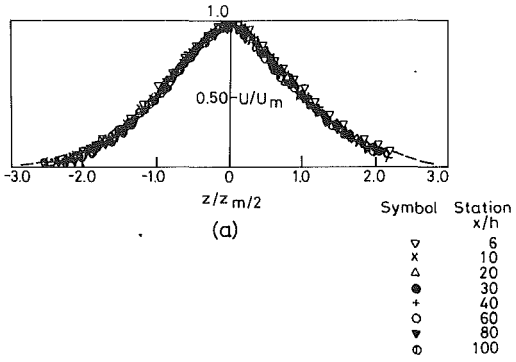

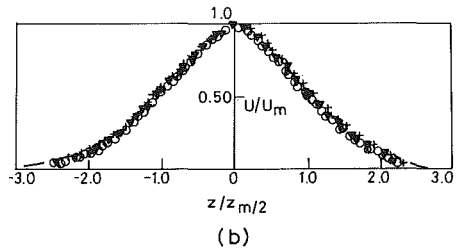

Fig. 6(*a,b*) Normalized free jet velocity profiles in *x-z* plane (uncertainty in $U = \pm 2$ percent in average; uncertainty in $z = 0.5$ mm). - - -, mean curve of axisymmetric free jet due to Schlichting (1968).

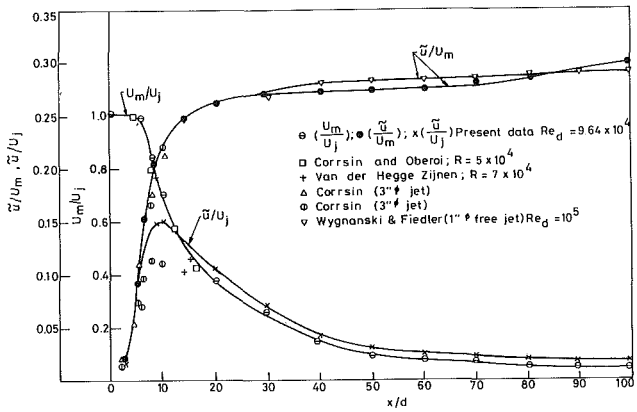

Fig. 7 Decay of centerline axial velocity and turbulence of 19.1 mm diameter free jet (uncertainty in $U = \pm 2$ percent; uncertainty in $x = 0.5$ mm; uncertainty in $u/U_m = \pm 10$ percent in average).

at the end of the settling chamber. This plate was made of brass with a 19.1 mm diameter orifice and conformed to Indian Standard-2952 (Fig. 4). Before carrying out the wall jet measurements, the characteristics of free jet issuing from the 19.1 mm dia orifice were determined. These are shown in Figs. 5(*a,b*) and 6(*a,b*), and 7. It can be seen from these figures that the flow field characteristics of the jet correspond to those of standard free jets (Abramovich, 1963; Schlichting, 1968).

The different orifice geometries, defined in terms of h/d ratios (Fig. 1), were obtained by moving laterally (normal to jet axis) a flat plate kept vertically in front of the circular orifice plate. Further details of orifice plates employed are given in Table 1.

A smooth polished flat plate of size 1.45 m × 2.05 m × 18 mm and made of teak wood was used to generate the wall jets. The plate was fixed vertically to an apparatus having three degrees of freedom to facilitate easy alignment and movement of the flat plate. The leading edge of the plate was chamfered to 45 deg (to avoid pressure-gradient effects due to a rounded

Table 1 Details of various orifice shapes used

	Serial number	h (mm)	d (mm)	h/d	$h/\sqrt{A}$
*	1	19.10	19.1	1.00	1.12
*	2	15.28	19.1	0.80	0.98
*	3	9.55	19.1	0.50	0.80
**	4	4.45	19.1	0.23	0.60

*Serial numbers 1, 2, and 3 were generated from the circular orifice plate of 19.1 mm diameter.
**Serial number 4 has been fabricated independently to have the shape of $h/d = 0.23$.
A = Area of the various segments of the circle (mm^2).

leading edge) and was placed at a distance of 2 mm from the face of the orifice so as to facilitate smooth lateral movement of the plate in order to generate different h/d ratios.

A traversing mechanism (make: AVA, Göttingen) with three translatory degrees of freedom and two rotational degrees of freedom was used for probe traverse. Displacement of the probes larger than 1 mm, and away from the wall, was measured by scales fixed to the traversing mechanism. Near-wall measurements were made by using dial gauges (least count: 0.01 mm) mounted on magnetic bases. The symmetry of the flow was checked by taking a few measurements on either side of the jet axis at equidistant points from the jet axis. During the experiments the wall static pressure indicated by a Betz manometer was used to monitor the jet exit velocity. Over the duration of any run (which lasted about 4 hours) the change in the temperature of the jet was about 2° to 3°C. This variation has been neglected in analyzing the experimental data. All the measurements for each h/d ratio, were carried out at a jet exit velocity of 80 m/s. Corresponding to this velocity the exit Reynolds number (Re_d) is 9.54×10^4. With the velocity of 80 m/s, the exit Mach number is about 0.25 which is rather high for tests in the incompressible regime. Still, the compressibility effects will be quite small.

A total pressure probe was used to obtain the mean velocity profiles at all the stations along the jet axis where it was proposed to make the hot wire measurements at a later time. The static pressure was assumed to be everywhere equal to the measured still air value. The probe was of standard design and made out of stainless steel tubing of 1 mm outer diameter. Prandtl manometer and an inclined tube manometer (make: AVA, Göttingen) whose inclination could be varied in steps, were used to record the pressure from the total pressure probe.

A cartesian coordinate system, as shown in Fig. 3, was chosen with the origin located at the center of the orifice plate with the x-axis oriented along with the centerline of the jet. This figure also shows the velocity and length scales for PC, CD, and RD regions used in the present investigations.

2.2 Comments on the Data. In the present investigation, the plate used (on which wall jets have been generated) is made of wood (nonconducting) and as such wall correction was not applied to the measured data. Bhatia et al. (1982) have found such corrections are not required if the material of the plate is nonconducting. The difference between the readings of mean velocity obtained from total pressure probe measurements and those obtained from the d-c outputs of a hot wire anemometer (details of the hot wire anemometry used are given in Part 2 of the paper) showed a difference of 5 to 10 percent in the inner region and 12 percent in the outer region of the wall jet. Chao and Sandborn (1966) and Bandyopadhyay (1974) have observed a difference of the order of 10 percent between the mean values obtained by total probe and the hot wire results. Repeatability of mean velocities made with the total pressure probe was within 2 percent. Displacement correction required was performed using the formula of Macmillan (Pierce and Zimmerman, 1973) and it was found that there was hardly any difference between the velocity profiles obtained with and without correction. The velocity at the exit of the orifice plate was very uniform and the variation was less than 0.5 percent.

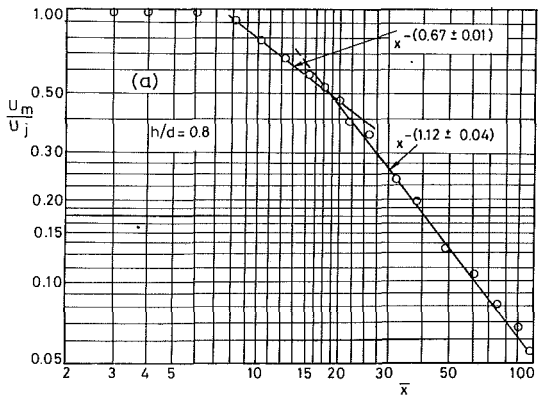

Fig. 8(*a*)

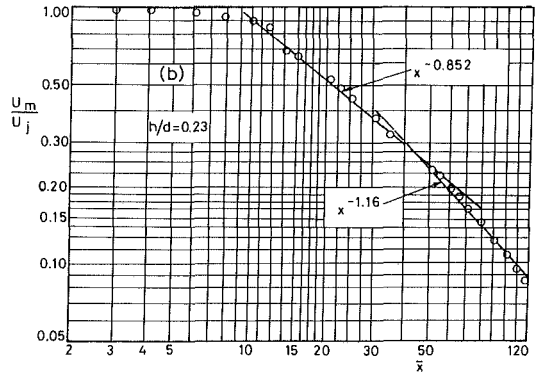

Fig. 8(*b*)

Fig. 8 Decay of maximum velocity in the plane of symmetry of the wall jet (*a*) $h/d = 0.8$; (*b*) $h/d = 0.23$ (uncertainty in $x = 0.5$ mm; uncertainty in $U = \pm 2$ percent in average).

The uncertainty levels in the measurements are indicated in each of the figures.

3 Results and Discussions

The important overall characteristics for a three-dimensional wall jet are expressed by (*a*) the rate of decay of the maximum axial velocity; (*b*) the mean velocity profile and its similarity form; and (*c*) the rate of expansion of the wall jet half-width. These are described in the same order in the subsequent sections, for all the four geometries tested. Axial distances "x" along the jet axis were normalized by the dimension "h". The velocity scale is U_m, the local maximum velocity at any station along the jet axis.

3.1 Decay Rate of Maximum Velocity. In a three-dimensional wall jet, the decay of the maximum velocity in the plane of symmetry can be expressed in a power-law form:

$$\frac{U_m}{U_j} = a(x/h)^{-n} \tag{1}$$

where U_m is the maximum velocity for any x and U_j is the jet efflux velocity. Sforza and Herbst (1970) have divided the flow field of a three-dimensional wall jet into three regions (PC, CD, and RD regions) depending on the decay rate of the maximum velocity as mentioned earlier.

The decay of the maximum velocity in these three regions for all the four geometries tested ($h/D = 1.0$, 0.8, 0.5, and 0.23) were obtained and the results for $h/d = 0.8$ and 0.23 are shown in Figs. 8(*a*) and 8(*b*), respectively. The decay-rate exponents for the different geometries in various regions of wall jets are

Table 2 Axial variation of U_m for two-dimensional and three-dimensional wall jets

Type of wall jet	Investigators	Date	h/d	e eccentricity	Streamwise variation of U_m in CD region	Streamwise variation of U_m in RD region	Length of CD region
Two-dimensional	Sigalla	1958	—	—	$x^{-0.50}$	—	—
	Bradshaw and Gee	1962	—	—	$x^{-0.53}$	—	—
	Schwarz and Cosart	1961	—	—	$x^{-0.55}$	—	—
	Myers et al.	1963	—	—	$x^{-(0.49\pm0.03)}$	—	—
Radial	Bakke	1957	—	—	—	$x^{-(1.12\pm0.03)}$	—
	Bradshaw and Love	1959	—	—	—	$x^{-1.12}$	—
	Poreh et al.	1967	—	—	—	$x^{-1.10}$	—
							X/We
Three-dimensional	Sforza and Herbst	1970	—	0.025	$x^{-0.41}$	$x^{-1.1}$	20 to 200
				0.050	$x^{-0.44}$	for all e	20 to 100
				0.100	$x^{-0.16}$		10 to 40
	Newman et al.	1972	1.00	—	—	$x^{-1.0}$	—
	Rajaratnam and Pani	1974	1.00	—	—	$x^{-1.0}$	—
	Gowda	1973	0.50	—	$x^{-0.54}$	—	—
	Swamy et al.	1975	0.50	—	$x^{-0.616}$	$x^{-1.1}$	—
	Torukoso and Hideo Ohashi	1982	0.50	—	—	$x^{-(1.27\pm0.02)}$	—
							x/h
	Present data		1.00	—	$x^{-(0.75\pm0.01)}$	$x^{-(1.15\pm0.02)}$	10.0 to 18.0
			0.80	—	$x^{-(0.67\pm0.01)}$	$x^{-(1.12\pm0.04)}$	10.0 to 22.5
			0.50	—	$x^{-(0.63\pm0.01)}$	$x^{-(1.15\pm0.01)}$	10.0 to 20.0
			0.23	—	$x^{-0.852}$	$x^{-1.16}$	10.0 to 30.0*

e = eccentricity = height of orifice/length of orifice. We = width or length of the rectangular orifice. * = length of transitional region.

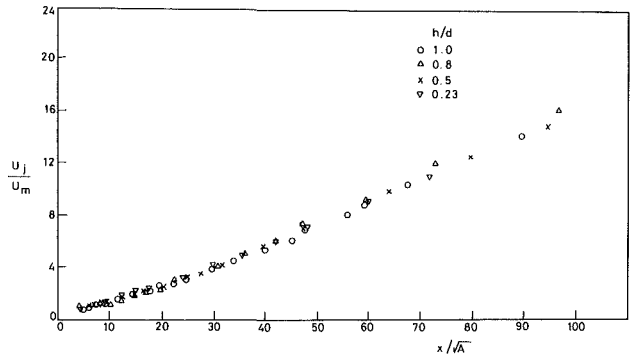

Fig. 9 Decay of maximum velocity in the plane of symmetry of the wall jets (with square root of the area of orifice as the parameter). (For uncertainty limits see the caption of Fig. 8).

shown in Table 2. This table also includes the data obtained by earlier investigators both for the three-dimensional and two-dimensional wall jets. For all the orifices tested, the influence of the geometry can be seen in the values of decay-rate exponents in the CD region. When the decay rates and the extent of the CD region for the present class of geometries and the rectangular shapes investigated by Sforza and Herbst are compared (Table 2), distinct difference between the two can be seen.

For the rectangular-shaped orifice, there are flat edges, one at the top and the other at the two sides. But for the present class of geometries, there are no well defined edges; there is a continuous change in the geometry along the span-wise direction. Thus, the generation and growth of the shear layers in these two cases can be expected to be quite different. The extent to which both PC and CD regions exist should depend upon the growth of these shear layers along the flow direction. In the case of rectangular geometries, the PC region extends to a point where the shear layers from the top and the bottom meet and the CD region extends until the shear layers from the sides meet on the jet axis. It is not this mechanism which gives rise to PC and CD regions for the present class of geometries. Both these regions are generated due to a continuous interaction of the boundary layer with shear layers from all along the edges of the orifice. It is difficult to see clearly the reason for the nonexistence of a well defined CD region for the geometry with $h/d = 0.23$. Though a curve has been fitted in the CD region for the maximum velocity decay in the case of $h/d = 0.23$ the value of the exponent for U_m decay is nearly equal to 1 and the CD region is not well defined.

In general, it can be expected that the influence of geometry will be much stronger in the case of orifices which have well defined edges because the shear layers from the sides (as explained earlier) merge along the centerline at different streamwise distances, whereas for the curved geometries the shear layers grow all along the contour at the same rate and converge at nearly the same location along the streamwise direction.

In the light of the above explanation, the length of the CD region can be expected to vary considerably with the change in the eccentricity (e) of a rectangular orifice (Table 2) whereas the length of the CD region can be expected to be more or less the same for the class of geometries where there is a continuous change of contour (e.g., circular, semi-circular, elliptical, etc.). This is borne out when the present results and those of Sforza and Herbst are compared. The exponent of U_m decay in the CD region (though distinctly different from that of the values of radial decay) is comparatively much closer to the exponent in the RD region for the present class of geometries than those for the rectangular orifices. Considering the length of the CD region for the present class of geometries (except for $h/d = 0.23$), the length of the CD region extends between $x/h = 10$ to 20 whereas this length varies considerably for the rectangular geometries as can be seen from the Table 2.

Another length scale parameter which could be considered instead of "h" is the square root of the area of various orifices. The variation of U_j/U_m when $\sqrt{A}$ is used as the length scale is shown in Fig. 9. This figure shows that the radial decay region starts from $x/\sqrt{A} \simeq 35$ irrespective of the geometry. In this respect $\sqrt{A}$ is a better scaling parameter than h. But the characteristics of individual orifices are masked. Geometry does influence the maximum velocity decay rates and the spread rates especially close to the exit of the orifice, trends which are not brought out when $\sqrt{A}$ is utilized.

For all the geometries tested in the present investigation, the decay-rate exponents of the maximum velocity in the RD region are shown in Table 2. In general, the exponents for the U_m decay in the RD region in the present study conform with those of earlier investigators.

3.2 Mean Velocity Profiles. In the present investigation, mean velocity profiles along the jet axis in the plane of symmetry ($z = 0$) have been measured up to $x/h = 100$ for $h/d = 1.0$ and 0.8 and up to $x/h = 120$ for $h/d = 0.5$ and 0.23, respectively. For all the geometries the mean velocity profiles have also been

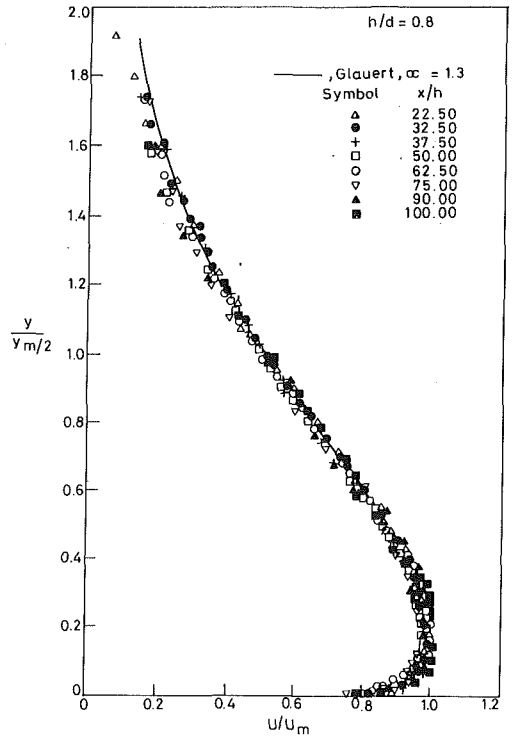

Fig. 10 Similarity of mean velocity profiles of the wall jet in the RD region for $h/d = 0.8$ (uncertainty in $U = \pm 2$ percent in average; uncertainty in $y = 0.5$ mm)

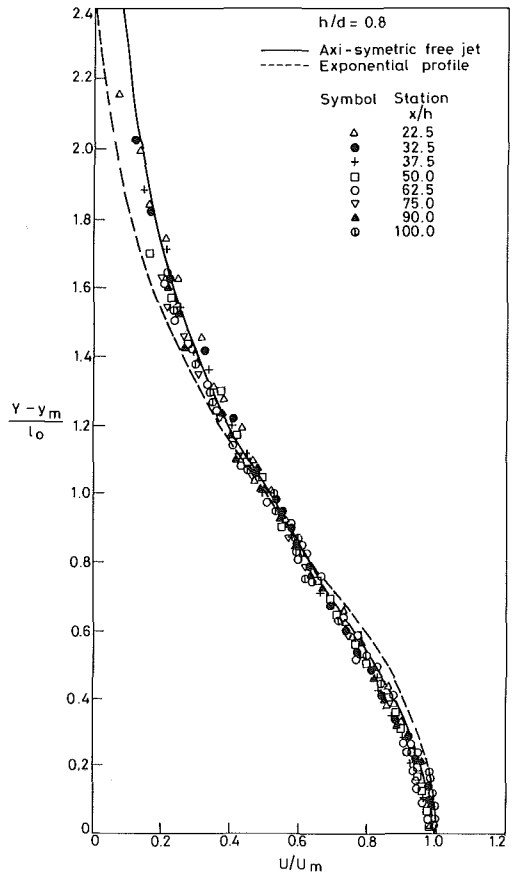

Fig. 11 Similarity of mean velocity profiles in the outer region of wall jet in the RD region for $h/d = 0.8$ (uncertainty limits are same as in Fig. 10)

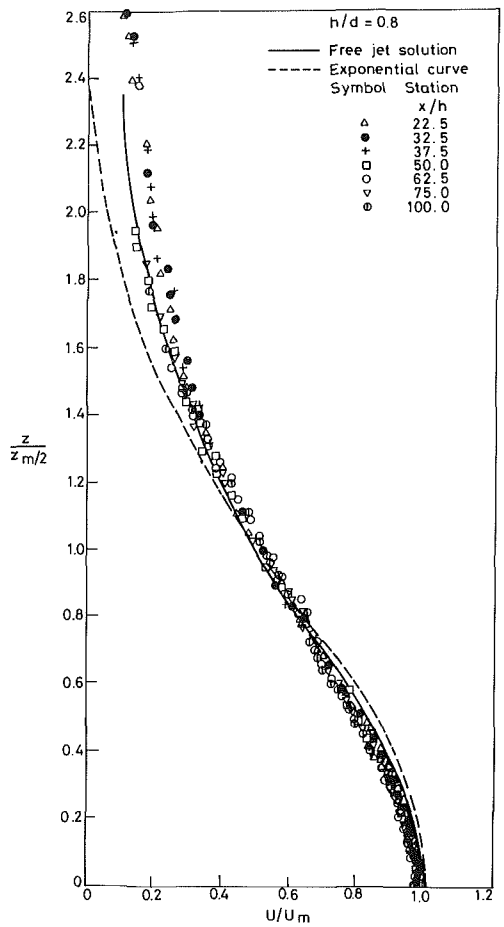

Fig. 12 Similarity of the spanwise velocity profiles at $y = y_m$ in the RD region of wall jet for $h/d = 0.8$ (uncertainty in $U = \pm 2$ percent in average; uncertainty in $z = 0.5$ mm). For further information see the caption of Fig. 11.

measured in the spanwise direction, at a distance $y = y_m$ from the wall, where the maximum velocity occurs. Only typical results for $h/d = 0.8$ are presented and discussed.

The velocity profiles in the RD region shown in Fig. 10 exhibit similarity (same was the case with other geometries). Glauert's profile for the radial well jet ($\alpha = 1.3$) is included for comparison. The agreement is very satisfactory. In Fig. 11 the velocity profile in the outer region is given and Fig. 12 shows the normalized spanwise velocity profile in the RD region. Similarity of the velocity profiles is observed in both figures. The profiles are compared with the exponential profile suggested by Newman et al. (1972) and Schlichting's axisymmetric (1968) free-jet solution. In general, it is seen that for the present class of geometries, the free-jet solution agrees better with the experimental data, whereas poor agreement is observed with the exponential profile.

3.3 Variation of Length Scales. The longitudinal variation of the length scales y_m, $y_{m/2}$, l_0 and $z_{m/2}$ are shown in Figs. 13(*a*) and 13(*b*). They have been normalized with h, e.g., $\bar{y}_m = (y_m/h)$. The corresponding spread rates in the RD region in both y and z directions are given in Table 3. The tabulated values show that in general a larger spread in z-direction compared to y-direction is a common feature for all the three-dimensional wall jets studied. Some of the earlier results relevant to the present investigation are included in Table 3.

Comparing the growth rates normal to the plate for all the h/d ratios in the present investigation, they are found to be nearly the same at sufficiently large distances downstream (Table 3). When a comparison is made between the spanwise spread rates for this class of geometries with those of rectan-

Table 3 Growth rates in the RD region and location of virtual origins for turbulent free jets and wall jets

Type of jet	Authors	Date	h/d	e	$dy_{m/2}/dx$	dl_0/dx	$dz_{m/2}/dx$	$dz_{m/2}/dx$	$dy_{m/2}/dx$	Virtual origin based on $y_{m/2}$ (x_0/h)	Virtual origin based on $z_{m/2}$ (x_0/h)
1	2	3	4	5	6	7	8	9		10	11
Three-dimensional wall	Present data		1.00	—	0.045	0.040	0.216	4.80		−19.5	+12.0
"	"		0.80	—	0.043	0.038	0.215	5.00		−18.5	+8.5
"	"		0.50	—	0.049	0.042	0.245	5.00		−17.5	+8.0
"	$(x/h<40)$		0.23	—	0.067	0.064	0.150	2.25		−20.5	+3.5
"	$(x/h>40)$		0.23	—	0.040	0.034	0.250	6.25		−65.0	+17.0
"	Newman et al.	1972	1.00	—	0.050	0.042	0.278	5.56		−19.0	+17.0
"	Rajaratnam and Pani	1974	1.00	—	0.045	—	0.210	4.80		−19.6	+11.0
"	Davis et al.	1980	1.00	—	0.037	—	0.320	8.60		−19.0	—
"	Swamy and Bandyopadhyay	1975	0.50	—	0.046	0.042	0.166	3.60		−17.5	+7.0
"	Sforza and Herbst	1970	—	0.10	—	—	0.140*	—		—	—
Three-dimensional wall jet	Sforza and Herbst		—	0.05	—	—	0.100*	—		—	—
"	Sforza and Herbst	1970	—	0.025	—	—	0.100*	—		—	—
Two-dimensional wall jet	Schwarz and Cosart	1961	—	—	0.068	—	—	—		—	—
"	Sigalla	1958	—	—	0.065	—	—	—		—	—
Free jet	Wygnanski and Fiedler	1969	—	—	0.083	—	0.083	1.00		0.00	0.0
"	Pani and Dash	1983	—	—	0.098	—	0.098	1.00		1.00	1.0
"	Present data		—	—	0.091	—	0.091	1.00		1.00	1.0

*Approximate values calculated from the data available.

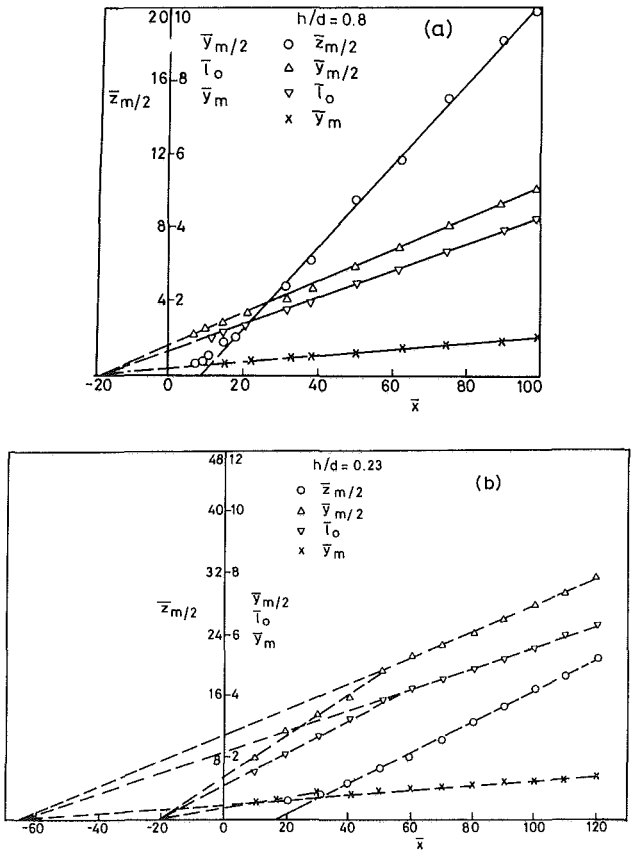

Fig. 13 Variation of length scales and location of virtual origins (*a*) $h/d = 0.8$, (*b*) $h/d = 0.23$ (uncertainty $x = 0.5$ mm; uncertainty in y and $z = 0.5$ mm). ×, $\bar{y}_m$; ▽, $\bar{l}_0$; △, $\bar{y}_{m/2}$; ○, $\bar{z}_{m/2}$

gular geometries investigated by Sforza and Herbst (given in Table 3), the present class of geometries exhibit in general higher growth rates. Further, the spanwise spread starts in the CD region itself (as seen from Figs. 13(*a*) and 13(*b*)), whereas in the case of rectangular geometries, the flow does not show any tendency to spread in the spanwise direction within the CD region. This has considerable practical implications. The large maximum-velocity decay rates close to the orifice exit observed for the present class of geometries (section 3.1) can also be attributed to this lateral spread of the flow in the CD region itself.

3.3.1 Virtual Origins. Figure 13(*a*) shows the two virtual origins for $h/d = 0.8$. The values given in Table 3 for $h/d = 1.0$ and 0.5 in the present investigation agree with the earlier results for the corresponding geometries. It is interesting to see that the geometry with $h/d = 0.23$ (for $x/h < 40$) has the virtual origin based on $z_{m/2}$ growth quite close to the exit of the orifice (+3.5) but for $x/h > 40$ it is located very much downstream (+17) compared to other geometries ($h/d = 1.0$, 0.8, and 0.5). Further, for $x/h > 40$ the virtual origin based on $y_{m/2}$ growth is located very much upstream ($x/h = -65$) of the exit of the orifice. It is difficult to give the exact reasons why two virtual origins exist for $h/d = 0.23$. These experiments were repeated and it was determined that this effect was not due to any experimental errors, rather the observation can be attributed to the differences in the geometry.

The virtual origin indicates the location of the origin of the spread of the wall jet. As far as the virtual origin based on the growth rate in the normal direction is concerned, it is the same for the various geometries (excluding $h/d = 0.23$ for $x/h > 40$). The virtual origin based on $z_{m/2}$ growth is located downstream of the orifice indicating that the spread in the spanwise direction starts much later than the spread normal to the plate.

Similar to Fig. 8 for maximum velocity decay, results were obtained for the length scale variation using $\sqrt{A}$ as the normalizing parameter and are shown in Figs. 14(*a*) and 14(*b*). From Figs. 14(*a*) and 14(*b*) it appears that the virtual origins for the geometries including $h/d = 0.23$ are the same although a closer examination reveals two slopes in the plot of the experimental points for $h/d = 0.23$. This trend is not as clear as in Fig. 13(*b*) and the details are masked when $\sqrt{A}$ is used as the scaling parameter.

3.4 Skin-friction Estimation. The skin-friction for a wall jet is normally expressed by its coefficient c_f and is defined as

Table 2 Wall-law constants for three-dimensional wall jets

Authors	h/d	A	B
Present	1.00	5.60	5.0
"	0.80	4.00	10.0
"	0.50	4.00	9.2
"	0.23	4.42	9.0
Gowda	0.50	5.60	5.5
Swamy and Bandyopadhyay	0.50	4.10	9.1

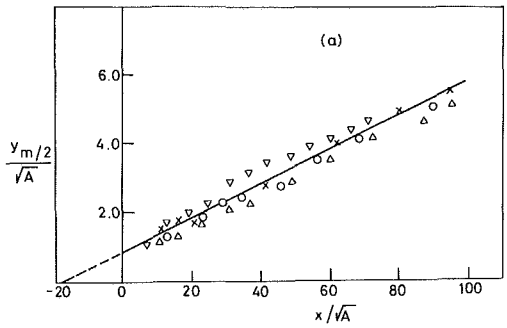

Fig. 14(*a*) Variation of length scales normal to the wall (with the square root of the area of the orifice as parameter) (uncertainty in $x = 0.5$ mm; uncertainty in $y = 0.5$ mm). For further information see the caption of Fig. 14(*b*).

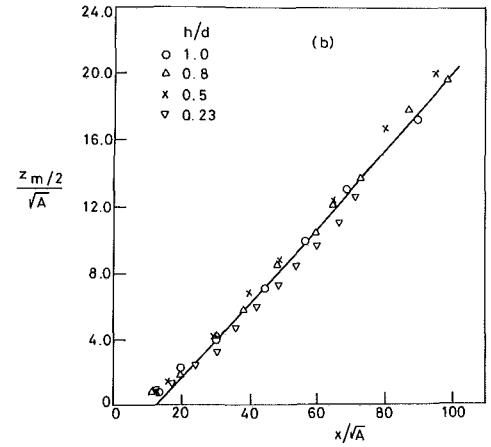

Fig. 14(*b*) Variation of length scales parallel to the wall (with the square root of the area of the orifice as parameter) (uncertainty in $x = 0.5$ mm; uncertainty in $z = 0.5$ mm).

$$c_f = \tau_0/(1/2\rho U_m^2) \tag{2}$$

where τ_0 is the shear stress at the wall.

Skin-friction measurements in three-dimensional wall jets are relatively few. Pani and Dash (1983) and Rajaratnam and Pani (1974), Swamy and Gowda (1974) and Swamy and Bandyopadhyay (1975) are the four investigators who have given c_f values for three-dimensional wall jets.

The skin-friction in the present investigation was estimated using Clauser's technique (1954) from the mean velocity profiles measured along the jet axis in the plane of symmetry. The values of A and B obtained in the form $U^+ = A \log y^+ + B$ are shown in Table 4. The values of A and B for $h/d = 1.0$ are surprisingly the same as those obtained for turbulent boundary layers. No other results for this geometry are available for comparison purposes. It is pertinent to mention that the value of the power law exponent obtained for $h/d = 1.0$ is 8 (details not reported here) which is quite close to the value for a turbulent boundary layer (7). For the other h/d ratios, A and B obtained are quite close to those typically observed for wall jets.

The variation in c_f along the centerline is shown in Fig. 15.

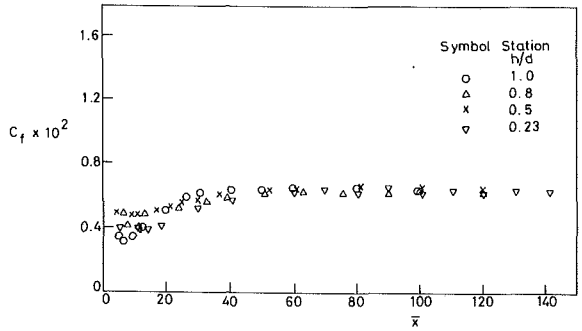

Fig. 15 Centerline skin-friction distribution for all h/d ratios (uncertainty in $c_f = \pm 0.0005$; uncertainty in $x = 0.5$ mm). For further information see the caption of Fig. 14(*b*).

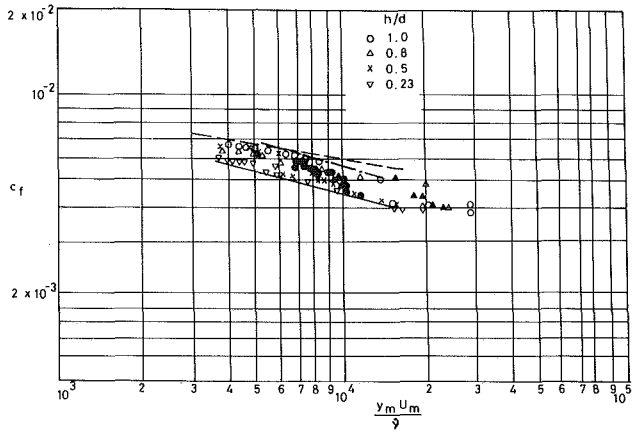

Fig. 16 Skin-friction distribution in the wall jet in the plane of symmetry for all h/d ratios (uncertainty in c_f as in Fig. 15). o, $h/d = 1.0$; Δ, $h/d = 0.8$; x, $h/d = 0.5$; ▽, $h/d = 0.23$; present data, $Re_d = 9.64 \times 10^4$. ▲, Gowda's data, $Re_d = 7.8 \times 10^4$ (1974): ●, Bandyopadhyay's data, $Re_d = 7.8 \times 10^4$ (1975); —, Mathieu and Tailland (1963); - - -, Bradshaw and Gee (1962); -·-·-, Sigalla (1958).

This figure shows a slight drop in c_f especially in the potential core region and thereafter a slight increase is observed. The rapid growth of the wall jet region is reflected in the reduction of c_f and subsequent gradual increase in c_f is associated with slow increase in y_m. c_f approaches a constant value of 0.0064 at large distances downstream from the orifice exit irrespective of the orifice geometry tested.

The variation of c_f with Reynolds number can be expressed as a power law:

$$c_f = K(\mathrm{Re}_{ym})^{-N} \tag{3}$$

where K = the constant of proportionality and $\mathrm{Re}_{ym} = (U_m y_m/\nu)$. Such variations are plotted in Fig. 16. The values of c_f in the present case are enclosed between the results for the two-dimensional wall jets.

4 Concluding Remarks

The results presented in this part on a class of three-dimensional wall jets have shown the differences in the mean velocity field between circular and rectangular geometries. The mechanism of generation of the CD region is different for these two classes of geometries. The circular geometries exhibit higher jet spread rates than those of the rectangular orifices and this may have considerable advantage in many practical applications.

The mean velocity profiles appear to be relatively unaffected by the orifice geometries and attain similarity at distances not far from the jet exit. The skin-friction coefficient approaches a constant value at large distances downstream irrespective of the orifice geometry.

References

Abramovich, G. N., 1963, *The Theory of Turbulent Jet*, M.I.T. Press.

Bakke, P., 1957, "An Experimental Investigation of a Wall Jet," *Journal of Fluid Mechanics*, Vol. 2, pp. 467–472.

Bandyopadhyay, P., 1974, "Some Studies on a Developing Three-Dimensional Incompressible Turbulent Wall Jet," Ph.D. thesis, Indian Institute of Technology, Madras, India.

Bhatia, J. C., Durst, P., and Jovasnovic, J., 1982, "Corrections of Hot Wire Anemometer Measurements Near Walls," *Journal of Fluid Mechanics*, Vol. 122, pp. 411–431.

Bradshaw, P., and Gee, M. T., 1962; "Turbulent Wall Jets With and Without an External Stream," Aeronautical Research Council R and M, No. 3252.

Chao, J. L., and Sandborn, V. A., 1966, "Evaluation of the Momentum Equation for a Turbulent Wall Jet," *Journal of Fluid Mechanics*, Vol. 26, Part 4, pp. 819–828.

Clauser, F. H., 1954, "Turbulent Boundary Layers in Adverse Pressure Gradient," *Journal of Aeronautical Sciences*, Vol. 21, pp. 91–108.

Corrsin, S., 1943, "Investigation of Flow in an Axially Symmetrical Heated Jet of Air," NACA War Time Report, W-94.

Corrsin, S., and Uberoi, M. S., 1950, "Further Experiments on the Flow and Heat Transfer in a Heated Turbulent Air Jet," NACA Report 998.

Glauert, M. B., 1956, "The Wall Jet," *Journal of Fluid Mechanics*, Vol. 1, pp. 625–643.

Launder, B. E., and Rodi, W., 1981, "The Turbulent Wall Jet," *Progress in Aerospace Sciences*, Vol. 19, pp. 81–123.

Mathieu, J., and Tailland, A., 1963, "E-tude d'un plan dirige' tangentiellement a une paroi," C. R. Academy of Sciences, Vol. 256, pp. 2768–2771.

Newman, B. G., Patel, R. P., Savage, S. B., and Tjio, H. K., 1972, "Three-Dimensional Wall Jet Originating from a Circular Orifice," *Aeronautical Quarterly*, Vol. 23, pp. 188–200.

Pani, B. S., and Dash, R. N., 1983, "Three-Dimensional Wall Jets from Multiple Outlets," *Proceedings Institution of Civil Engineers*, Vol. 75, Part 2, pp. 725–749.

Pierce, F. J., and Zimmerman, B. B., 1973, "Wall Shear Stress Influence from Two-Dimensional and Three-Dimensional Boundary Layer Velocity Profiles," ASME JOURNAL OF FLUIDS ENGINEERING, Vol. 95, pp. 61–67.

Rajaratnam, N., and Pani, B. S., 1974, "Three-Dimensional Turbulent Wall Jets," *Journal of Hydraulics Division*, Vol. 100, No. 1, pp. 69–83.

Schlichting, H., 1968, *Boundary Layer Theory*, 6th Edition, McGraw-Hill, New York.

Sforza, P. M., and Herbst, G., 1970, "A Study of Three-Dimensional Incompressible, Turbulent Wall Jets," *AIAA Journal*, Vol. 8, No. 2, pp. 276–283.

Sigalla, A., 1958, "Measurements of Skin-Friction in a Plane Turbulent Wall Jet," *Journal of Royal Aeronautical Society*, Vol. 62, pp. 873–877.

Swamy, N. V. C., and Gowda, B. H. L., 1974, "Characteristics of Three-Dimensional Wall Jets," *Zeitschrift Für Flugwissenschaften*, Bd. 22, pp. 314–323.

Swamy, N. V. C., and Bandyopadthyay, P., 1975, "Mean and Turbulence Characteristics of Three-Dimensional Wall Jets," *Journal of Fluid Mechanics*, Vol. 71, Part 1, pp. 541–562.

Van Der Hegge Zijnen, B. G., 1957, "Measurements of Turbulence in a Plane Jet of Air by Diffusion Method and by the Hot Wire Method," *Journal of Applied Scientific Research*, Vol. 7, pp. 256–276.

Wygnanski, I., and Fiedler, H., 1969, "Some Measurements in the Self-Preserving Jet," *Journal of Fluid Mechanics*, Vol. 28, Part 3, pp. 577–612.

G. Padmanabham
Department of Aeronautical Engineering,
Madras Institute of Technology,
Anna University,
Madras 600 044, India

B. H. Lakshmana Gowda
Fluid Mechanics Laboratory,
Department of Applied Mechanics,
Indian Institute of Technology,
Madras 600 036, India

Mean and Turbulence Characteristics of a Class of Three-Dimensional Wall Jets—Part 2: Turbulence Characteristics

The mean flow characteristics of three-dimensional, incompressible, isothermal turbulent wall jets generated from orifices having the shapes of various segments of a circle are presented in Part 1 of this paper. In this part, the turbulence characteristics are presented. Turbulence quantities measured include normal stresses and Reynolds shear stresses in the characteristic-decay and in the radial-decay regions of the wall jets investigated. These results are compared with those available for two-dimensional and three-dimensional wall jets. The presence of counter-gradient regions and the feature of "energy reveral" are discussed.

1 Introduction

Wall jets are generated when a jet of fluid strikes a surface at an angle. When the angle is 90 deg, a radial wall jet is formed and when this angle is tangential to the surface, a plane wall jet is generated. When the aspect ratio of the orifice from which the jet issues is finite, the wall jet becomes three-dimensional. Three-dimensional wall jets generated by using different orifice geometries (such as rectangular, square, circular, semi-circular, and elliptic geometries) have been studied. A summary of these investigations is listed in Table 1. All the orifice (or nozzle) geometries employed are given as defined by the respective investigators. Other quantities measured are also listed in this table.

The investigations of Sforza and Herbst (1970) dealt with properties of wall jets generated by orifices having rectangular geometries with flat sides. In the present study another class of geometries having the shape of various segments of a circle have been utilized to generate the wall jets. Here, the nozzle shape across the cross-section changes continuously when compared to rectangular nozzles. The mean flow characteristics of wall jets generated from this class of geometries are presented and discussed in Part 1 of the paper. The turbulence characteristics are presented and discussed in this part. It should be mentioned that comparatively less information is available on the turbulence characteristics of three-dimensional wall jets (Newman et al., 1972; Swamy and Bandyopadhyay, 1975; Davis and Winarto, 1980; and Torukoso and Ohashi, 1982). The present results are compared with published results for both two-dimensional and three-dimensional wall jets.

Contributed by the Fluids Engineering Division for publication in the JOURNAL OF FLUIDS ENGINEERING. Manuscript received by the Fluids Engineering Division April 25, 1991.

2 Experimental Arrangement

The experimental facility is the same as that utilized for the mean flow measurements.

Turbulence measurements in the wall jets were performed using a DISA 55D01 anemometer (constant temperature mode) and a DISA 55D15 linearizer. A normal-wire probe (DISA 55A22) was mainly used to measure the streamwise turbulence intensity $\tilde{u}$. Transverse turbulence intensity $\tilde{v}$ and Reynolds shear stress $\overline{uv}$ were measured using an inclined-wire probe (DISA 55P12). These probes were made of platinum-plated tungsten wire of 5 μm diameter and had an active length of 1.2 mm. The d-c and a-c components of the linearized output signals were measured with DISA 55D31 Digital d-c and DISA 55D35 rms volt-meters, respectively. The linearizations were carried out in two velocity ranges: (i) 80 m/s to 20 m/s and (ii) 16 m/s to 4 m/s. This procedure of linearization was adopted for both the normal and inclined-wire measurements. The hot wire probes were calibrated with the help of DISA 55D90 calibration equipment. Calibration was done after every run of approximately 4 hours. An integration time of 60 seconds was found to be adequate for both the normal and inclined-wire measurements. The probes were introduced with their prongs parallel to the main flow direction (x-axis) and their calibration was also performed in the same configuration. While taking measurements close to the wall, the probes were kept with their axes at a pitch angle of 3 to 5 deg to the wall depending on the location of measurement station along the x-axis. This inclined operation of the wire was extended up to a distance of 10 mm from the wall (normal to the plate). Beyond this, the wires were not pitched and they were operated in the normal position (with prongs parallel to main flow direction). The technique due to Vagt (1979) is used to evaluate the turbulence quantities $\tilde{v}$ and $\overline{uv}$. The detailed description of the measurement technique adopted, alignment procedures, calibration, etc. is given in Padmanabham (1986).

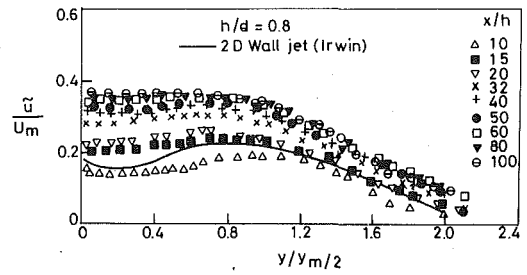

Fig. 1 Distribution of longitudinal turbulence intensity $\tilde{u}$ across wall jet in the plane of symmetry for $h/d=0.8$. △, $x/h=10$; ■, $x/h=15$; ▽, $x/h=20$; X, $x/h=32$; +, $x/h=40$; ●, $x/h=50$; □, $x/h=60$; ▼, $x/h=80$; ⊖, $x/h=100$. ——, mean data due to Irwin (1973) for two-dimensional wall jet (uncertainty in $\tilde{u}/U_m=\pm 10$ percent in average; uncertainty in $y=0.5$ mm).

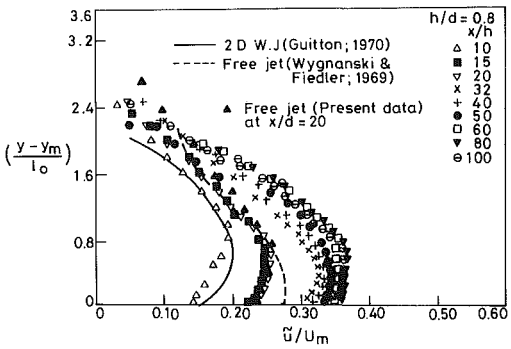

Fig. 2 Distribution of longitudinal turbulence intensity $\tilde{u}$ in the outer region of the wall jet in the plane of symmetry for $h/d=0.8$. (Uncertainty is same as in Fig. 1.) ▲, free jet data (19.1 mm dia) at $x/d=20$; ——, mean curve from Guitton's data for two-dimensional wall jet (1970); ----, mean curve from free jet due to Wygnanski and Fiedler (1969). For further information see the caption of Fig. 1.

No correction has been applied for turbulence intensities. In the present investigation the maximum turbulence levels recorded were approximately 35 percent. To apply corrections for these turbulence levels, higher order correlations are required which unfortunately were not obtained. For turbulence intensities of the order of 20 percent, a correction of the order of 5 percent is necessary (Irwin, 1973). Based on the care and repeatability checks, the uncertainty levels in the turbulence measurements could be taken at ±10 percent in the present investigation. The uncertainty levels are also indicated in each of the figures.

The turbulence measurements for each h/d ratio, (definition sketch given in Part 1) were carried out at a jet exit velocity of 80 m/s, and an exit Reynolds number (Re_d) of 9.54×10^4, the same condition as for the mean flow measurements.

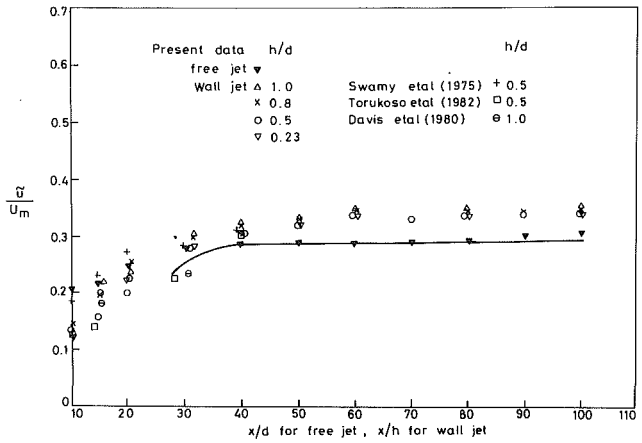

Fig. 3 Axial variation of longitudinal turbulence intensity at maximum velocity points. (Uncertainty in $x=0.5$ mm; uncertainty in $\tilde{u}/U_m=\pm10$ percent in average.) ——, mean curve of axisymmetric free jet due to Wygnanski and Fiedler (1969).

3 Results and Discussion

The turbulence quantities discussed in the following section were obtained for all the geometries tested. As in Part 1, only the results for $h/d=0.8$ are shown.

3.1 Normal Stresses

3.1.1 Variation of $\tilde{u}$ in the Plane of Symmetry. The distribution of longitudinal turbulence $\tilde{u}$ in the plane of symmetry at various stations along the jet axis and across the wall jet is shown in Fig. 1. The length and velocity scales are $y_{m/2}$ and U_m, respectively.

Referring to the figure it is observed that at the lower values of x/h (<30), the influence of the orifice geometry is still evident. This corresponds to CD region. Here, the turbulence parameters are still undergoing some changes. This region could thus be called an "evolutionary region." It is usual to compare the longitudinal turbulence intensity $\tilde{u}$ for a two-dimensional wall jet with the turbulence levels observed in this evolutionary region of the three-dimensional wall jet. In Fig. 1, the mean curve drawn through the experimental points of the data of Irwin (1973), for a two-dimensional wall jet is shown by a solid line. The profiles of $\tilde{u}/U_m$ for $h/d=0.8$ and all the other cases tested show the same trend as that of Irwin's data, even though the turbulence levels observed are different. Further, $\tilde{u}/U_m$ exhibits self-similarity from $x/h=60$ onwards, which was also the case for other geometries.

The distribution of longitudinal turbulence intensity $\tilde{u}$ in the outer region of the wall jet is shown in Fig. 2. The mean curve

Nomenclature

A = cross-sectional area of a segment of a circle
E = instantaneous voltage of hot-wire probe for nonlinearized operation
$\bar{E}$ = d-c voltage of hot-wire probe for nonlinearized operation
E_L = instantaneous voltage for linearized operation
$\bar{E}_L$ = d-c voltage for linearized operation
f = frequency
G = directional sensitivity coefficient of the hot-wire
k = directional sensitivity coefficient of hot wire or wave number
l = length of hot wire probe
l_0 = $(y_{m/2}-y_m)$
Re_d = jet exit Reynolds number $(=U_j d/\nu)$; dimensionless
S = calibration or sensitivity factor for linearized operation
$\tilde{u}$ = rms of velocity of fluctuations in x-direction
$\tilde{v}$ = rms of velocity of fluctuations in y-direction
$\overline{uv}$ = Reynolds shear stress
x = streamwise or longitudinal distance along the jet axis
y = transverse direction (normal to the plate)
y_m = value of y where $U=U_m$
z = spanwise direction (parallel to the plate)
π = rate of production of turbulent kinetic energy or 3.14159

Subscript

(-) = indicates normalization with h(e.g., $\bar{x}=x/h$)
CD = characteristic decay
DC = direct current
PC = potential core
RD = radial decay
rms = root mean square

Table 1 Three-dimensional wall jet experimental studies on plane surface in stagnant surroundings

Sl. no.	Author(s) and year	Shape of nozzle/ orifice	Slot dimensions (cm)	$10^3 \cdot Re_b$	Region of Measurement	$\frac{dl_0}{dx}$	$\frac{dy_{m/2}}{dx}$	$\frac{dz_{m/2}}{dx}$	$\frac{dz_{m/2}}{dx} / \frac{dy_{m/2}}{dx}$	Virtual origin (x_0/b) for $y_{m/2}$	Virtual origin (x_0/b) for $z_{m/2}$	Turbulence measurements taken	Streamwise variation of U_m
1	2	3	4	5	6	7	8	9	10	11	12	13	14
1	Sforza and Herbst (1970)	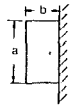	$a \times b = .0645$ cm^2 $b/a = e = 0.025$ 0.050 0.100 1.000		x/b 20–350 15–220 4–100 1–10		non-linear						CD region $x^{-0.41}$ $x^{-0.42}$ $x^{-0.16}$ RD region for all values of e $x^{-1.10}$
2	Newman, Patel, Savage, and Tjio (1972)		0.3175 0.2 $e = 1.0$ $(r/b = 1.0)$	$\frac{10^3 U_0 I_0}{\nu}$ 16.4 2.8	x/b 20–200 50–130	0.042	0.050	0.278	5.56	−19	+17	$\bar{u}$ measurements up to 175 slot diameters	RD region $x^{-1.0}$
3	Gowda, B. H. L. (1973)		$b = 10.0$ $(r/b = 0.5)$	118	x/r 5–14							$\bar{u}$ component measured in the inner layer at $x/r = 6$	CD region $x^{-0.54}$
4	Bandyopadhyay, P. (1974)		$b = 5.7$ $(r/b = 0.5)$	78	x/r 5–40	0.046	0.046	0.166	3.608	−17.5	+7	$\bar{u}$ up to $x/r = 40$ $\bar{v}$ and $\bar{w}$ at $x/r = 34$, 36 and 38 $\overline{uv}$ at $x/r = 36$ and 38	CD region $x^{-0.616}$ RD region $x^{-1.1}$
5	Rajratnam and Pani (1974)		0.95 $(e = 1.0)$	65.0	x/b 5–70		0.045	0.21	4.67	−19.6	+11		RD region $x^{-1.0}$
			0.98 $(e = 1.0)$	67.0	5–70		0.045	0.265	5.88	−19.6	+15		
			$B = 1.44$ $b = 1.27$ $(e = 1.1)$	86.0	x/B 4–43		0.042	0.208	4.90	−19.8	+11		
			$B = 1.45$ $b = 0.95$ $(e = 1.5)$	97.5	3–43		0.042	0.205	4.88	−19.5	+11		
			$B = 1.5$ $b = 0.9$ $(e = 0.667)$	59.5	3–43		0.040	0.205	5.20	−20.0	+11		
6	Hofer (1979)		0.5–0.75 $(r/b = 1.0)$	0.8–4.4									
7	Davis and Winarto (1980)		$b = 2.54$ $h/b = 0.5$ 1.0 2.0 4.0	170	x/b 5–60		0.037 0.036 0.039 0.046	0.32 0.33 0.29 0.23	9.4 9.8 7.4 5.0	−19.0 −21.0 −22.0 −25.5		$\bar{u}$ measured up to $x/b = 32$ for all h/b ratios $\bar{v}$, $\bar{w}$, $\overline{uv}$ and $\overline{uw}$ measured at $x/b = 32$ for $h/b = 0.5$ only	
8	Torukoso and Hideo Ohashi (1982)		$b_{eq} = 3.49$ $b = 5.0$ $r = 2.5$	66.2*	x/b_{eq} 5–45							$\bar{u}$ up to $x/b_{eq} = 20$ $\bar{v}$ and $\bar{w}$ at $x/b_{eq} = 10$ only $\overline{uv}$ and $\overline{uw}$ at $x/b_{eq} = 20$ only	RD region $x^{-(1.27 \pm 0.02)}$
9	Pani and Dash (1983)	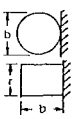	1.270 0.635 $r = 0.635$ $b = 0.953$	79.76 39.88 59.86	x/b 5–100 6–80								RD region $x^{-1.0}$ for all geometries

Notes: 1. e = height of orifice/width of orifice
2. *Reynolds number based on equivalent diameter b_{eq}

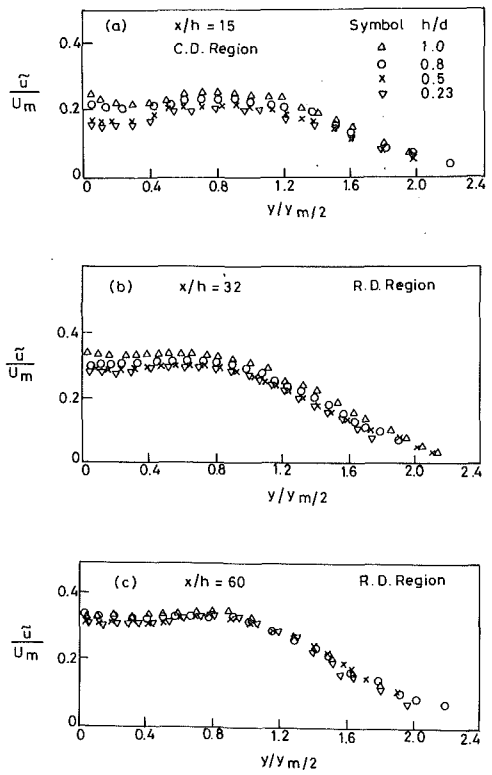

Fig. 4 Influence of orifice geometry (h/d) on longitudinal turbulence intensity $\tilde{u}$ (*a*) in CD region ($x/h = 15$); (*b*) in RD region ($x/h = 32$); (*c*) in RD region ($x/h = 60$). (Uncertainty in $y = 0.5$ mm; uncertainty in $\tilde{u}/U_m = \pm 10$ percent in average.) △, $h/d = 1.0$; ○, $h/d = 0.8$; X, $h/d = 0.5$; ▽, $h/d = 0.23$.

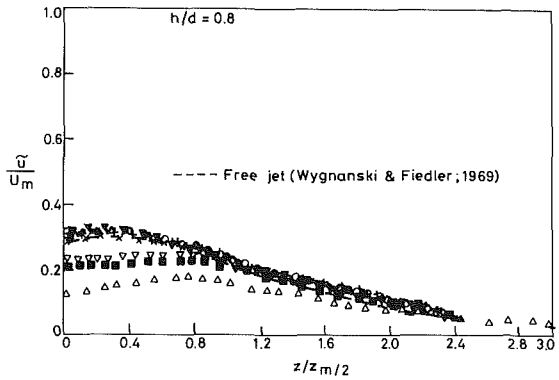

Fig. 5 Spanwise distribution, at the distance y_m from the wall, of longitudinal turbulence intensity $\tilde{u}$ in the wall jet for $h/d = 0.8$ (uncertainty in $z = 0.5$ mm, uncertainty in $\tilde{u}/U_m$ is ± 10 percent in average). For further information see caption of Fig. 1. ----, mean curve free jet due to Wygnanski and Fiedler (1969).

through the experimental data due to Guitton (1970) for the two-dimensional wall jet issuing into still air is also included for comparison purposes (shown by a solid line). The shape of the profiles for all the other geometries tested is the same as that of Guitton, but the magnitudes of $\tilde{u}$ turbulence are much higher. This is attributed to the lateral stretching of the eddies in three-dimensional wall jets (Newman et al., 1972). The mean curve drawn through the experimental points of Wygnanski and Fielder (1969) for a free jet obtained at large distances from the jet exit shows poor agreement with present results. However, when a similar comparison for the mean velocity profiles is made, it showed reasonably good agreement between the results for the outer region of the wall jet and free jet as mentioned in section 3.2, Part 1. It appears that the turbulence levels in the outer region are affected by the presence of the wall.

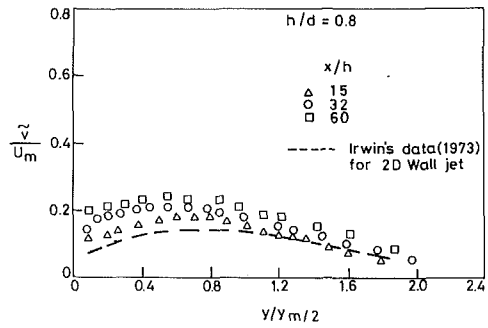

Fig. 6 Variation of $\tilde{v}$ turbulence across wall jet in the plane of symmetry for $h/d = 0.8$ (uncertainty in $y = 0.5$ mm; uncertainty in $\tilde{v}/U_m = \pm 10$ percent in average). △, $x/h = 15$; ○, $x/h = 32$; □, $x/h = 60$; ---, mean data due to Irwin for two-dimensional wall jet (1973).

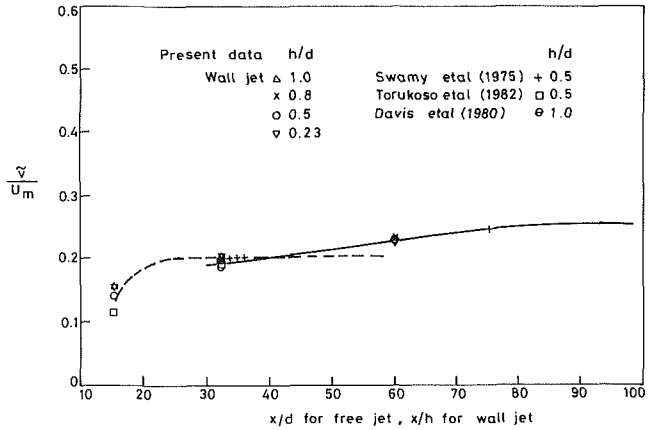

Fig. 7 Axial variation of $\tilde{v}$ turbulence at maximum velocity points (uncertainty in $x = 0.5$ mm, uncertainty in $\tilde{v}/U_m = \pm 10$ percent in average). ——, mean curve of free jet due to Wygnanski and Fiedler (1969); ---, mean curve of two-dimensional free jet due to Gutmark and Wygnanski (1976).

In Fig. 3 the variation of longitudial turbulence intensity $\tilde{u}/U_m$ along the axial direction measured at $y = y_m$ is presented. The levels of $\tilde{u}/U_m$ attained here in both wall jets and a free jet are comparable to those observed by earlier investigators. The results tend to flatten at $x/h = 60$ thereby indicating a tendency for similarity from this axial distance downstream. As stated earlier, a state of self-similarity of $\tilde{u}/U_m$ has been observed at $x/h = 60$ and beyond for all the three-dimensional wall jets investigated.

In order to bring out more clearly the effect of orifice geometry (h/d) on the longitudinal turbulence intensity $\tilde{u}$ along the jet axis, the distributions of $\tilde{u}/U_m$ across the wall jet both in the CD region ($x/h = 15$) and RD region ($x/h = 32$ and 60) have been compared. These are shown in Fig. 4(*a*) for the CD region and Figs. 4(*b*) and (*c*) for the RD region. The differences in the turbulence levels for the various geometries decrease with the distance from the orifice exit. As (x/h) increases, the lateral distance across which ($\tilde{u}/U_m$) remains constant increases. The overall levels of ($\tilde{u}/U_m$) also appear to be constant for the larger x/h values. It is interesting to see that geometry has a distinctive influence not only on the mean velocities but also on the turbulence levels. Beyond $x/h = 60$, the variation of $\tilde{u}/U_m$ for all the shapes can be expected to be negligible as self-similarity in $\tilde{u}/U_m$ is achieved.

3.1.2 Spanwise Variation of Longitudinal Turbulence $\tilde{u}$. The distribution of $\tilde{u}$ in the spanwise direction at $y = y_m$ from the wall are shown in Fig. 5. The length and velocity scales chosen are $z_{m/2}$ and U_m, respectively. The profiles of $\tilde{u}/U_m$ exhibit similarity from $x/h = 60$ onwards. The mean curve as given by Wygnanski and Fielder (1969) for a free jet is shown for comparison.

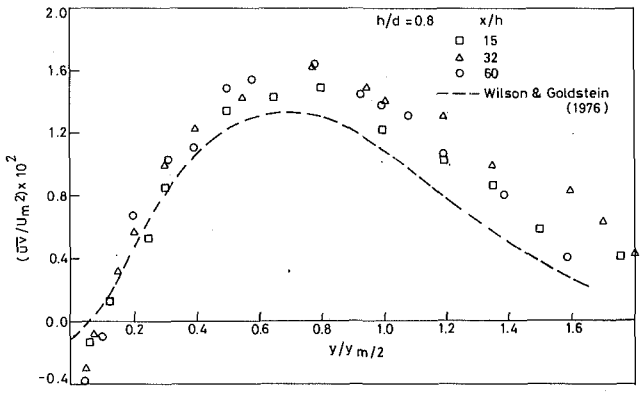

Fig. 8 Shear stress variation across wall jet in the plane of symmetry for $h/d = 0.8$ (uncertainty in $y = 0.5$ mm; uncertainty in $\overline{uv}/U_m^2 = \pm 10$ percent in average). ---, mean curve of two-dimensional wall jet due to Wilson and Goldstein (1976)

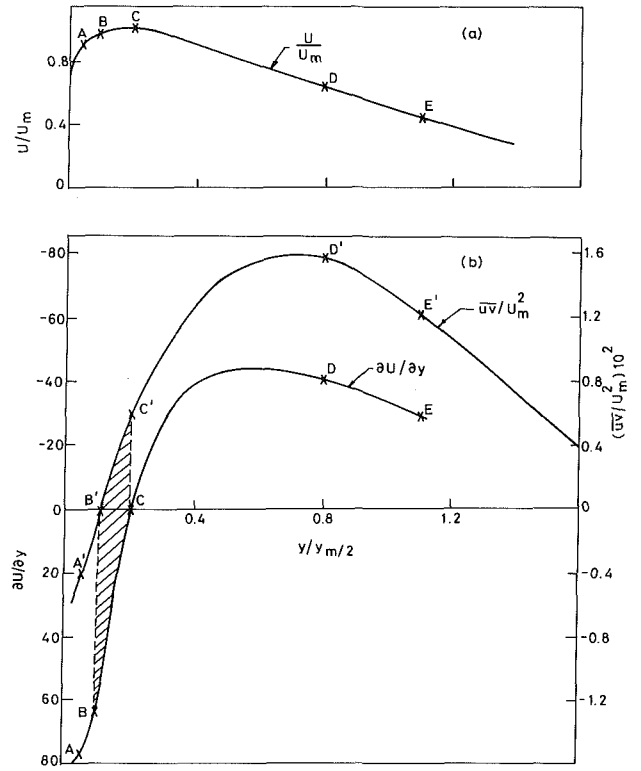

Fig. 9(*a*,*b*) Properties of three-dimensional wall jets for $h/d = 0.8$ at $x/h = 60$

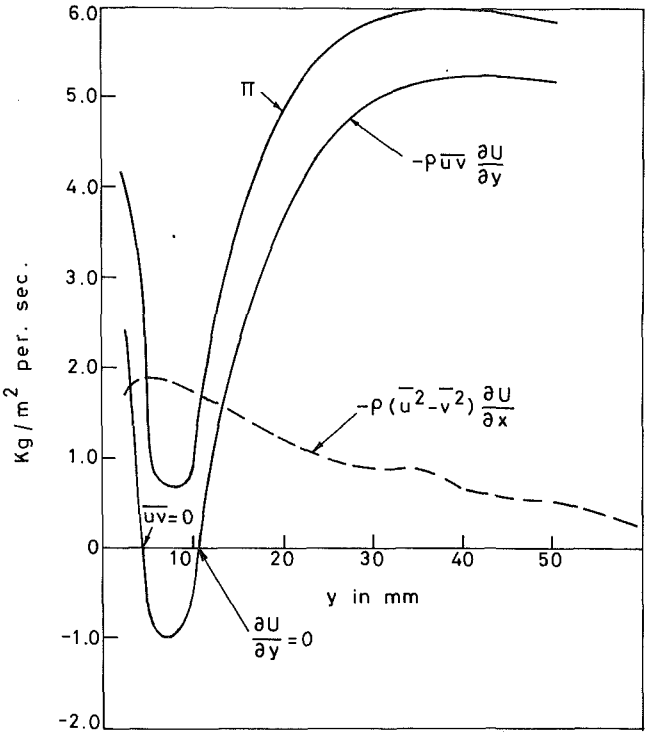

Fig. 10 Distribution of rate of turbulent kinetic energy production terms across wall jet in the plane of symmetry at $x/h = 60$ for $h/d = 0.8$

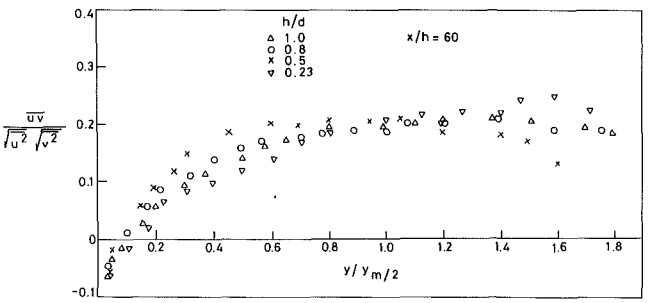

Fig. 11 Distribution of correlation coefficient at $x/h = 60$ for all (h/d) ratios (uncertainty in $y = 0.5$ mm; uncertainty in $\overline{uv}/\sqrt{\overline{u^2}}\cdot\sqrt{\overline{v^2}}$ is ± 10 percent in average)

It is observed that there is poor agreement between the turbulence ($\tilde{u}$) data for a free jet and that for the outer layer of wall jets measured in x-y plane (section 3.1.1). However, there is good agreement when the spanwise distributions are considered. This was also the case regarding the mean velocities in the spanwise direction (section 3.2; Part 1). It appears as through the flow history has a lesser influence in the spanwise direction than in the longitudinal direction.

3.1.3 Variation of Transverse Turbulence Intensity $\tilde{v}$. The normalized distributions of $\tilde{v}$ turbulence intensity across the wall jet at $x/h = 15$, 32, and 60 for $h/d = 0.8$ are shown in Fig. 6. In this figure the mean curve drawn through the experimental points of Irwin's data (two-dimensional wall jet) is also shown. The trend of the curves is the same in both cases. When the magnitudes of $\tilde{v}$ turbulence are compared with those of $\tilde{u}$ (Fig. 1), the former are found to be smaller. The maximum of $\tilde{v}/U_m$ occurs around $y/y_{m/2} = 0.8$. This was also the case with the other geometries.

The $\tilde{v}$ turbulence intensity obtained at maximum velocity points is shown in Fig. 7. The values of $\tilde{v}/U_m$ obtained agree with those of earlier investigators and the level of turbulence intensity is similar to that of a free jet.

3.2 Variation of Turbulent Shear Stress. The normalized distributions of $\overline{uv}$ at $x/h = 15$, 32, and 60 for $h/d = 0.8$ are shown in Fig. 8. The mean curve through Wilson and Goldstein's (1976) data for a plane wall jet is also included.

The most important feature noticed here is that the point of zero shear stress does not coincide with the point of maximum velocity. The point of zero shear stress is around $y/y_{m/2} = 0.13$ on the average for all the geometries tested, which is a typical value generally observed for both two-dimensional and three-dimensional wall jets. This feature is further discussed by choosing a typical case from the present results.

In Fig. 9(a) the mean velocity profile for $h/d = 0.8$ at $x/h = 60$ is shown (the curve plotted is an average curve through the experimental points). The positions of some typical points A, B, C, D, and E are considered. In Fig. 9(b) the variation

of turbulent shear stress $\overline{uv}/U_m^2$ and the velocity gradients $\partial U/\partial y$ across the width of the wall jet are shown. The corresponding points A, B, C, D, E and A′, B′, C′, D′, E′ are also shown in this figure. In the region AB-A′B′, $\partial U/\partial y$ is positive and $\overline{uv}$ is negative, causing the product $\overline{uv}.\ \partial U/\partial y$ to be negative. In the region CDE-C′D′E′, $\overline{uv}$ is positive but $\partial U/\partial y$ is negative and again the product is negative. But in the region BC-B′C′, $\partial U/\partial y$ is positive and $\overline{uv}$ is also positive i.e., the quantity $\overline{uv}$ is counter-gradient, with the result that the product $(\overline{uv}.\ \partial U/\partial y)$ is positive. This means that in this region, as far as this production term is concerned, it is positive for the mean velocity field and negative as far as the turbulence energy balance is concerned. This observation implies that turbulence feeds the mean field in this region, i.e., there is energy reversal in the region BC-B′C′. This is a typical feature of an asymmetric velocity profile and both Palmer and Keffer (1972) and Eskinazi and Erian (1969) have argued that there might be a transfer of kinetic energy from the turbulence to the mean flow. However, one has to be cautious to categorically come to this conclusion because turbulence production is comprised of other quantities in addition to the product $(\overline{uv}.\ \partial U/\partial y)$.

Considering all the production terms, the rate of turbulent kinetic energy π can be expressed as:

$$\pi = -\rho(\overline{u^2} - \overline{v^2}) \cdot \frac{\partial U}{\partial x} - \rho\overline{uv} \cdot \left(\frac{\partial U}{\partial y} + \frac{\partial V}{\partial x}\right) \tag{1}$$

The axial gradient of V is usually much smaller than that of U. Hence, Eq. (1) can be written as:

$$\pi = -\rho(\overline{u^2} - \overline{v^2}) \cdot \frac{\partial U}{\partial x} - \rho\overline{uv} \cdot \left(\frac{\partial U}{\partial y}\right) \tag{2}$$

In turbulent flows, bulk of the kinetic energy is supplied by the term $(-\overline{uv}.\ \partial U/\partial y)$. The two terms in Eq. (2) have been estimated (for the case of $h/d = 0.8$) and the combined results are shown in Fig. 10. As can be seen, most of the turbulent kinetic energy is supplied by the term $(-\overline{uv}.\ \partial U/\partial y)$. Though the production of turbulent kinetic energy due to work done by the rate of strain against the shear stress is negative over a substantial portion of the inner region, near the point of velocity maximum it is more than balanced by the contribution from the normal stresses. Hence, no region of negative production of turbulent kinetic energy exists in the flow field under investigation. The total production of the turbulent kinetic energy is positive over the entire width of the wall jet.

Hence, the concept of energy reversal, i.e., the idea of the turbulence feeding the mean flow rather than the opposite is not valid for this flow. Further, as there are regions of counter gradients (i.e., regions where both $\partial U/\partial y$ and $\overline{uv}$ have the same sign), the gradient-transport models are inadequate to predict such flows.

3.2.1 Shear Correlation Coefficient. The shear correlation coefficient at $x/h = 60$ is shown in Fig. 11. Such results were also obtained at $x/h = 15$ and 32. The trends were the same as that shown in Fig. 11, but there was considerable scatter at locations close to the nozzle exit. This is expected in that the shear correlation coefficient is a structure parameter (indicates momentum exchange between $\tilde{u}$ and $\tilde{v}$ fluctuations) and tends to an asymptotic value only at large downstream distances.

4 Concluding Remarks

From the results presented in this part on the turbulence characteristics of a class of three-dimensional wall jets it is seen that just as the mean velocity profiles (Part 1), the turbulence profiles are relatively unaffected by the orifice geometries. However, similarity for the turbulence quantities is achieved farther away from the jet exit compared to the mean flow quantities. Unfortunately turbulence data for the other class of geometries (e.g., rectangular) is not available and hence the comparisons with the present results were not possible. However, when the trends in the variation of turbulence levels for the various shapes measured in the present investigation are noted, the same order and trends for these quantities can be expected for other orifice geometries.

Turbulence measurements in off-the-plane of symmetry and spectral measurements are desirable.

References

Bandyopadhyay, P., 1974, "Some Studies on a Developing Three-Dimensional Incompressible Turbulent Wall Jets," Ph.D. thesis, Indian Institute of Technology, Madras, India.

Davis, M. R., and Winarto, H., 1980, "Jet Diffusion from a Circular Nozzle above a Solid Plane," *Journal of Fluid Mechanics*, Vol. 101, Part 1, pp. 201–221.

Eskinazi, S., and Erian, F., 1969, "Energy Reversal in Turbulent Flows," *The Physics of Fluids*, Vol. 12, No. 10, pp. 1988–1998.

Gowda, B. H. L., 1973, "Three-Dimensional Wall Jets," Ph.D. thesis, Indian Institute of Technology, Madras, India.

Guitton, D. E., 1970, "Some Contributions to the Study of Equilibrium and Non-Equilibrium Turbulent Wall Jets over Curved Surfaces," Ph.D. thesis, McGill University, Montreal, Canada.

Gutmark, E., and Wygnanski, I., 1976, "The Planar Turbulent Jet," *Journal of Fluid Mechanics*, Vol. 73, pp. 465–495.

Hofer, K., 1979, Nr 42, Eidenossiche Technische Hoch Schule, Zurich.

Irwin, H. P. A. H., 1973, "Measurements in a Self-preserving Plane Wall Jet in a Positive Pressure Gradient," *Journal of Fluid Mechanics*, Vol. 61, Part 1, pp. 33–63.

Newman, B. G., Patel, R. P., Savage, S. B., and Tjio, H. K., 1972, "Three-Dimensional Wall Jet Originating from a Circular Orifice," *Aeronautical Quarterly*, Vol. 23, pp. 188–200.

Padmanabham, G., 1986, "Mean and Turbulence Characteristics of Three-Dimensional Wall Jets," Ph.D. thesis, Indian Institute of Technology, Madras, India.

Palmer, M. D., and Keffer, J. F., 1972, "An Experimental Investigation of an Asymmetrical Turbulent Wake," *Journal of Fluid Mechanics*, Vol. 53, Part 4, pp. 593–610.

Pani, B. S., and Dash, R. N., 1983, "Three-Dimensional Wall Jets from Multiple Outlets," *Proceedings Institution of Civil Engineers*, Vol. 75, Part 2, pp. 725–749.

Rajaratnam, N., and Pani, B. S., 1974, "Three-Dimensional Turbulent Wall Jets," *Journal of Hydraulics Division*, Vol. 100, No. 1, pp. 69–83.

Sforza, P. M., and Herbst, G., 1970, "A Study of Three-Dimensional Incompressible, Turbulent Wall Jets," *AIAA Journal*, Vol. 8, No. 2, pp. 276–283.

Swamy, N. V. C., and Bandyopadthyay, P., 1975, "Mean and Turbulence Characteristics of Three-Dimensional Wall Jets," *Journal of Fluid Mechanics*, Vol. 71, Part 3, pp. 541–562.

Torukoso and Hideo Ohashi, 1982, "Turbulent Diffusion of a Three-Dimensional Wall Jet," *Bulletin, JSME*, Vol. 25, No. 200, pp. 173–181.

Vagt, J., 1979, "Hot Wire Probes in Low Speed Flows," *Progress in Aerospace Sciences*, Vol. 18, pp. 271–323.

Wilson, D. J., and Goldstein, R. J., 1976, "Turbulent Wall Jets with Cylindrical Streamwise Surface Curvature," ASME JOURNAL OF FLUIDS ENGINEERING, Series 1, Vol. 98, pp. 550–557.

Wygnanski, I., and Fiedler, H., 1969, "Some Measurements in the Self-Preserving Jet," *Journal of Fluid Mechanics*, Vol. 28, Part 3, pp. 577–612.

P. Merati
Associate Professor,
Department of Mechanical and Aeronautical Engineering,
Western Michigan University,
Kalamazoo, Mich. 49008

H. M. McMahon
Professor,
School of Aerospace Engineering.

K. M. Yoo
Research Assistant.

Georgia Institute of Technology,
Atlanta, GA 30332

Experimental Investigation of a Turbulent Flow in the Vicinity of an Appendage Mounted on a Flat Plate

Experimental measurements were carried out in an incompressible three-dimensional turbulent shear layer in the vicinity of an appendage mounted perpendicular to a flat plate. The thickness of the turbulent boundary layer as it approached the appendage leading edge was 76 mm or 1.07 times the maximum thickness of the appendage. As the oncoming boundary layer passed around the appendage, a strong secondary flow was formed which was dominated by a horseshoe root vortex. This secondary flow had a major effect in redistributing both the mean flow and turbulence quantities throughout the shear layer, and this effect persisted to a significant degree up to at least three chord lengths downstream of the appendage leading edge.

1 Introduction

Secondary or transverse flows are those which have mean flow components in a plane perpendicular to the main flow direction. Secondary flows can occur in both laminar and turbulent shear flows and in such diverse situations as the flow in ducts and the flow in junctures formed by bodies protruding from a wall.

The secondary flow problem considered here is that of a turbulent boundary layer on a flat plate which encounters an appendage of finite chord protruding from the plate. When the turbulent boundary layer is developing on the flat plate, the vortex lines in the boundary layer are straight and aligned perpendicular to the main flow and parallel to the plate. When the flow goes around the appendage, these vortex lines are skewed and stretched due to the three-dimensional curvature of the streamlines. Thus, streamwise vorticity is produced in the juncture formed by the plate and the appendage. This is illustrated schematically in Fig. 1.

Secondary flows caused by both skewing and blockage effects arise in wind-fuselage junctures, turbine cascades, and in the hull-appendage juncture of ships and submarines. Since the secondary flow persists downstream, it can have an important influence on the flow over aft fuselages and on the inflow to a ship's propulsive device.

The flow of a three-dimensional boundary layer approaching an upright wall mounted circular cylinder has been experimentally investigated by Angui and Andreopoulos (1990). They found that a mean separation point of the oncoming boundary layer was located 0.76 and 0.82 diameter upstream of the cylinder on the plane of symmetry at Reynolds numbers 10^5 and 2.2×10^5, respectively. A separation line which marked the horseshoe vortex, emerged from the mean separation point and wrapped the cylinder with a parabola like line.

Experimental investigations of turbulent flow about a strut-end wall configuration by Chang et al. (1990) showed that spanwise varying natural transition on the strut led to the formation of a secondary vortex which coexisted with horseshoe vortex generated by end wall flow separation upstream of the strut leading edge. Both vortices were similar in strength downstream of the strut trailing edge, and both distorted the primary flow and local turbulence structure in the wake end wall region. They indicated that conventional eddy viscosity and k-ϵ transport equation models are not wholly adequate for predicting the flow.

Devenport and Simpson (1990) examined the turbulent flow

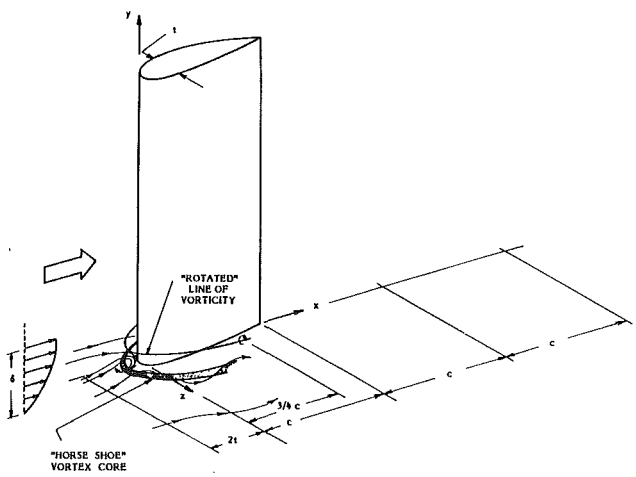

Fig. 1 Appendage flow schematic and location of measurement planes

Contributed by the Fluids Engineering Division for publication in the JOURNAL OF FLUIDS ENGINEERING. Manuscript received by the Fluids Engineering Division January 15, 1991.

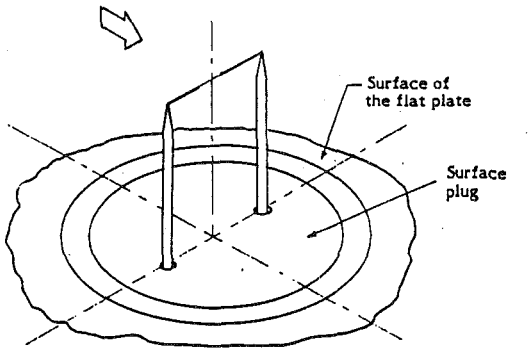

HORIZONTAL WIRE

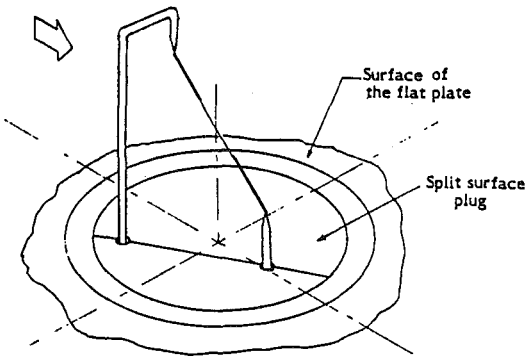

SLANT WIRE

Fig. 2 Details of hot-wire geometries

near the nose of a wing-body junction. They showed that flow in the plane of symmetry immediately upstream of a 3:2 elliptical nose is characterized by large-scale, low-frequency unsteadiness. This unsteadiness is bimodal in nature, with streamwise mean velocities near the wall alternating between large negative values and near-zero values. A relatively weak, counter-rotating recirculation pattern exists near the wall upstream of the primary recirculation pattern when the zero-flow mode is present. The time-dependent recirculation structures differ from those obtained by time-averaged measurements of Abid and Schmitt (1986) upstream of a semi-circular nose.

The mean flow structure upstream, around, and in the juncture formed by a finite-chord appendage with a cylindrical leading edge has been studied experimentally by Pierce et al. (1985, 1987) and by Abid and Schmitt (1986). Rood (1984) examined the large-scale temporal flow around several appendages with various elliptical leading edge geometries. Dickinson (1986a and 1986b) performed flow visualization, pressure measurements on the flat plate, and three-dimensional mean and fluctuating velocity measurements for two appendage shapes at zero angle of attack with a turbulent incoming boundary layer. Dickinson (1986a and 1986b) concluded that the radius of curvature of the leading edge affected the strength of the secondary vortex flow. The vortex was close to the wall, on the order of the momentum thickness of the incoming boundary layer, and had a flattened shape.

The numerical solution of the complete appendage flow problem is a very demanding task which has received attention only recently. The incompressible laminar flow case has been described numerically by Briley et al. (1984). There has been some success in predicting the development of turbulent flow in an appendage corner when starting downstream of the appendage leading edge with experimental data used as a starting condition. A steady, incompressible three-dimensional Reynolds equation solver was applied to the problem of flow past an appendage mounted on a flat plate by Burke (1987). The results of his numerical calculations were compared with wind tunnel experiments of Dickinson (1986a and 1986b). The observed and predicted pressure distributions on the flat plate agreed well, but the lateral extent of the horseshoe vortex was over predicted compared to the experimental data.

The primary aim of the experiments reported here was to carefully document the turbulent flow around an appendage with emphasis on the character of the flow downstream of the trailing edge. In addition, physical insights into the nature of the flow field were sought. Measurements were made in selected planes normal to the free stream as shown in Fig. 1. The data are intended to aid in formulating and evaluating numerical analyses of the turbulent appendage flow problem.

2 Facilities, Instrumentation, and Technique

The experiments were performed in an open return type wind tunnel with a test section of 6.1 m long and 1.07 × 1.09 m in cross-section. The wind tunnel free-stream turbulence intensity was measured to be 0.5 percent.

The appendage was a modified NACA 0020 airfoil. The standard airfoil was fitted with a 1.5:1 elliptical leading edge matched at the point of maximum thickness. The aft portion of the appendage was approximated by a straight line from the 0.86 chord location to the trailing edge, resulting in a trailing edge semi-vertex angle of 11.5 degrees. The appendage had a chord of 30.9 cm and a maximum thickness of 7.1 cm. The span of the appendage was 69.5 cm to ensure the two dimensionality of the appendage. The appendage was fitted with static pressure taps arranged in both a chordwise and spanwise pattern. Some taps were located symmetrically on either side of the appendage and were used to align the appendage with the free-stream. The appendage was fitted with a boundary layer trip wire 0.46 mm in diameter located at 8.2 percent chord.

The two-dimensional boundary layer was generated on a flat plate which was supported 30 cm above the wind tunnel floor. The flat plate spanned the wind tunnel. The plate leading edge was located 2.8 m upstream of the exit of the test section and extended 1.73 m beyond the exit. The appendage was mounted on the plate in the free jet downstream of the exit of the open return wind tunnel. The flat plate was fitted with a distributed sand roughness consisting of No. 16 floor-sanding paper which extended 0.61 m downstream from the plate leading edge.

All of the tests were run at a nominal free-stream velocity of 15.24 m/s corresponding to a chord Reynolds number of 307,000. The turbulent boundary-layer thickness on the flat plate at the streamwise location corresponding to the leading edge of the appendage was 76 mm, giving a ratio of boundary-layer thickness to appendage maximum thickness of 1.07. At this streamwise location the flat-plate Reynolds number based upon boundary layer momentum thickness was 6700.

In each of the measurement planes shown in Fig. 1, data were taken at 26 locations spaced vertically through the shear layer and at 10 or more transverse (z) stations.

Two wire geometries, horizontal and slant wires, used in making measurements near the plate surface are shown in Fig. 2. Since the needles supporting the hot-wire sensors protrude through the surface of the flat plate in order to minimize probe interference effects, the vertical travel of the sensors is limited. However, the thick shear layer under present investigation required surveys to be made to about 100 mm above the plate surface. In order to accomplish this, the two hot-wire geometries shown in Fig. 2 also were fabricated with the needles supported vertically by means of a tube 3.18 mm in diameter which protruded through the surface of the flat plate.

The measurements with the horizontal and slant wires were made sequentially and then the entire data set was assembled

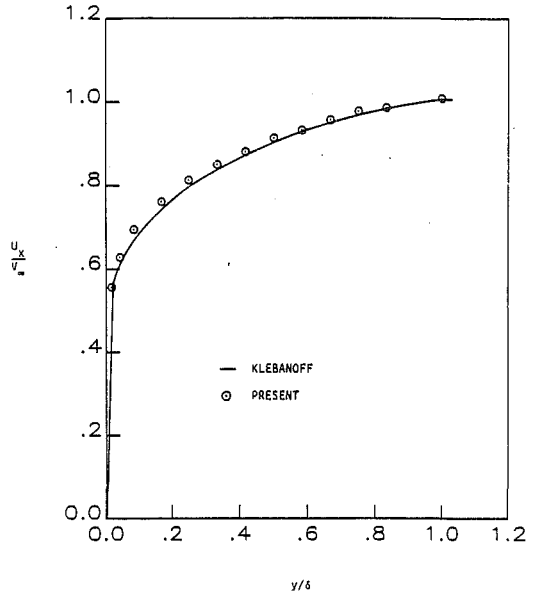

Fig. 3(*a*) Mean velocity (uncertainty in $U_x/v_\infty = \pm 0.014$ at 20:1 odds)

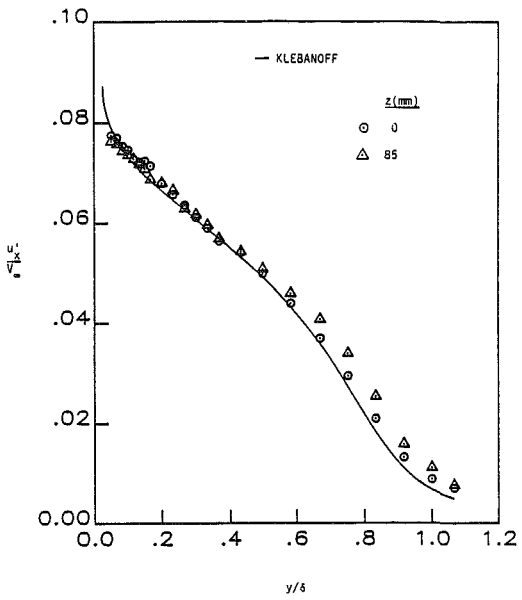

Fig. 3(*b*) Turbulent normal stress u_x' (uncertainty in $u_x'/v_\infty = \pm 0.0018$ at 20:1 odds)

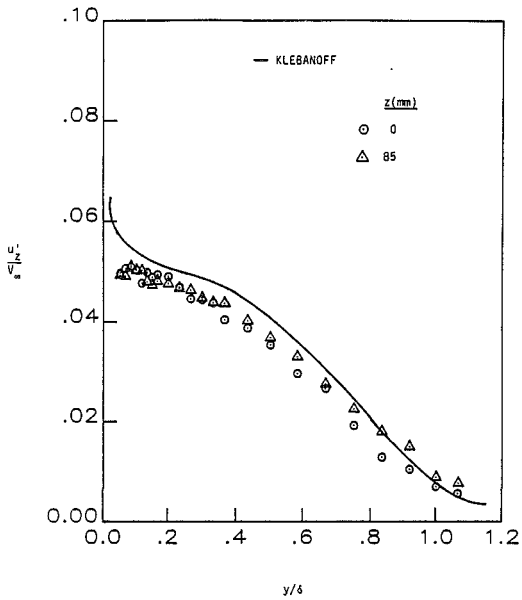

Fig. 3(*c*) Turbulent normal stress u_z' (uncertainty in $u_z'/v_\infty = \pm 0.002$ at 20:1 odds)

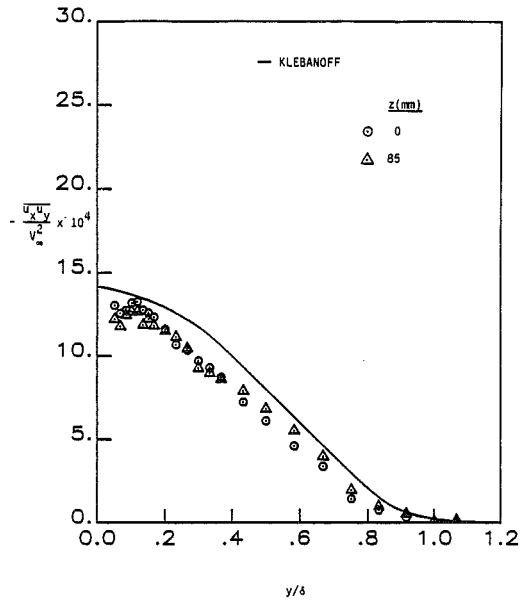

Fig. 3(*d*) Turbulent shear stress $-\overline{u_x u_y}$ (uncertainty in $-\overline{u_x u_y}/v_\infty^2 = \pm 0.22 \times 10^{-4}$ at 20:1 odds)

Fig. 3 Comparison of the present measurements with the data obtained by Klebanoff (1954) (uncertainty in $y/\delta = \pm 0.01$ at 20:1 odds)

in order to perform the data reduction for the required flow variables. Thus it was important that the sensor portion of each wire be located as nearly as possible at the same point in space when the probes were interchanged. This was accomplished by using special optics and techniques developed for this purpose as reported by McMahon et al. (1982).

Static pressures were measured on the surface of the appendage, on the plate surface using a static pressure tap device inserted into the probe positioning hole in the slide and in transverse measurement planes using a static pressure probe. The static pressure probe was rotated to match the known local flow yaw angle before the measurement was taken, so that no yaw correction was necessary. Previous measurements by Kubendran et al. (1986), had shown that pitch errors in the measurement of static pressure were negligible.

The three mean velocity components U_x, U_y, and U_z and the six turbulence quantities u_x', u_y', u_z', $-\overline{u_x u_y}$, $-\overline{u_y u_z}$, and $-\overline{u_x u_z}$ were measured. The measurement methods are described in a report by McMahon et al. (1982).

3 Results and Discussion

The principal results of this experimental investigation are measured values of the three mean velocity components U_x, U_y, and U_z and the six turbulence quantities u_x', u_y', u_z', $-\overline{u_x u_y}$, $-\overline{u_y u_z}$, and $-\overline{u_x u_z}$ at five streamwise stations near and downstream of the appendage. Static pressure distributions on the surface of the appendage, the flat plate and in the three dimensional boundary layer were measured.

3.1 Two-Dimensional Boundary Layer. Before any systematic data-taking was begun, the quality of the two-dimensional boundary layer on the flat plate was evaluated in the absence of the appendage. It was important that a fully developed turbulent boundary layer had been generated which exhibited proper behavior for both mean flow and turbulence characteristics.

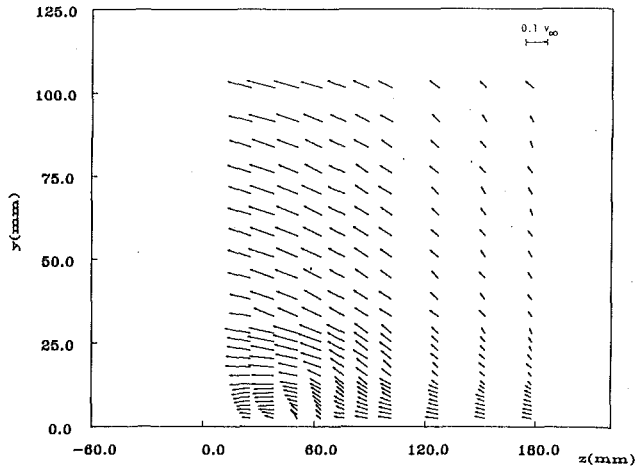

Fig. 4(*a*) $x/c = 0.75$

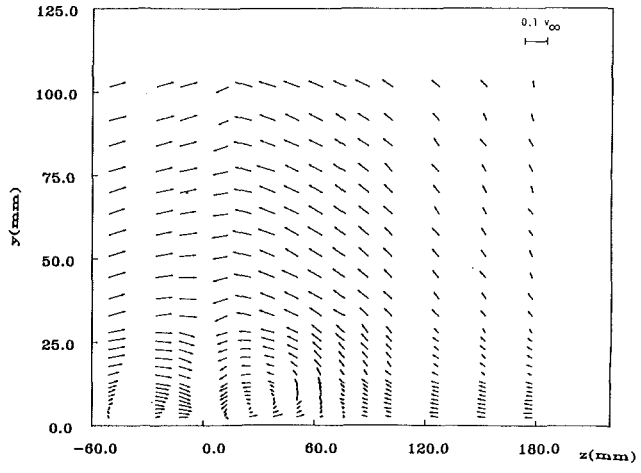

Fig. 4(*b*) $x/c = 1.0$

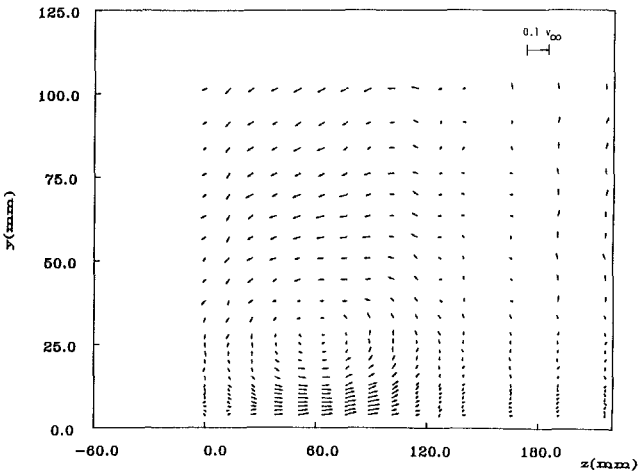

Fig. 4(*c*) $x/c = 3.0$

Fig. 4 Cross-flow velocity vectors (uncertainty in $y = \pm 0.8$mm, $z = \pm 1$mm, and in velocity vector $= \pm 0.001 v_\infty$ at 20:1 odds)

Hot-wire measurements were carried out in the turbulent boundary layer at $x = -142$ mm with the appendage removed and the results were compared with the classical data due to Klebanoff, 1954.

Comparison of the present profiles for U_x, u_x', u_z' and $-\overline{u_x u_y}$ with the data obtained by Klebanoff (1954) are shown in Fig. 3.

The agreement between the present values for U_x and the data by Klebanoff (1954) is satisfactory as shown by Fig. 3(*a*). The u_x' data taken here, Fig. 3(*b*), show the normal stress u_x' to be slightly larger near the outer edge of the boundary layer compared with the values reported by Klebanoff (1954). This small difference is due to the higher turbulence intensity in the free-stream for the present tunnel. Present data show lower values for u_z' and $-\overline{u_x u_y}$ near the wall compared to those obtained by Klebanoff (1954).

Pierce et al. (1985) and three other experimentalists cited by him measured lower values of u_z' and $-\overline{u_x u_y}$ being 10 to 12 percent lower for $-\overline{u_x u_y}$ compared to the data by Klebanoff (1954). The present results for $-\overline{u_x u_y}$ are lower than the data obtained by Klebanoff (1954) by 10 percent near $y/\delta = 0.2$.

It was concluded that the flat plate boundary layer generated for these experiments was satisfactorily two-dimensional and classical in behavior, and that the measured mean and turbulence quantities agree with reported values to a degree that gives confidence in the appendage measurement technique.

3.2 Investigation of Flow Symmetry. The two-dimensional turbulent boundary layer on the flat plate was surveyed at two different z-stations just upstream of the appendage leading edge, with the appendage removed, and was found to be at zero yaw angle within the accuracy of the measurement (± 1 degree).

The angle of attack was adjusted until the appendage surface static pressure pairs matched. To check the flow symmetry further, the local flow skew angles were measured at $x/c = 0.75$ on either side of the appendage in the shear layer near the plate surface ($y < 33$ mm) where the skew angle gradients were largest. The skew angles were measured at $z = \pm 25$ mm and $z = \pm 52$ mm. The data showed that the variation in skew angle with vertical distance, y, on either side of the appendage was similar but not symmetrical. It was necessary to change the appendage angle of attack by approximately 1.2 degrees (trailing edge toward the negative z direction) in order to achieve skew angle symmetry in the corner. This orientation of the appendage was fixed for the remainder of the tests.

3.3 Flow Upstream of the Appendage. The upstream measurement station for these tests was specified to be at $x/c = -0.47$, or 145 mm upstream of the appendage leading edge. At this location, the two-dimensional flow in the oncoming boundary layer was starting to turn to get around the appendage and the skew angle was quite uniform through the shear layer. The profile of the mean streamwise velocity component near the plane of symmetry ($z = 0$) was retarded compared to the profile at the most outboard location. This retarding effect was present to a measurable extent over a width of boundary layer that was almost three times the maximum width of the appendage, and the skewing effect was noted this far outboard as well. The presence of the appendage did not have a noticeable effect on the distribution of the turbulent normal and shear stresses in the boundary layer.

3.4 Flow in the Corner and Wake of the Appendage. The skewing of the vorticity lines in the oncoming two-dimensional boundary layer and the separation and roll-up of the boundary layer near the nose of the appendage result in a horseshoe vortex being formed. Each leg of this horseshoe vortex trails down either side of the appendage near the plate surface. The two legs of the horseshoe vortex redistribute the mean flow and the turbulence quantities in the corner and then proceed downstream in the wake of the appendage with only slightly diminished strength where they again cause a significant redistribution of the properties of the turbulent shear layer.

The presence of the secondary flow vortex in the shear layer is most vividly seen by examining vector plots of the resultants of the mean flow vectors U_y and U_z in the y-z plane. Such a

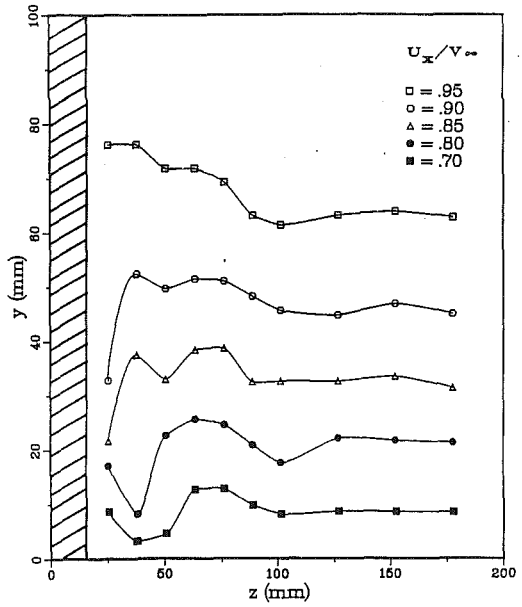

Fig. 5(*a*) x/c = 0.75

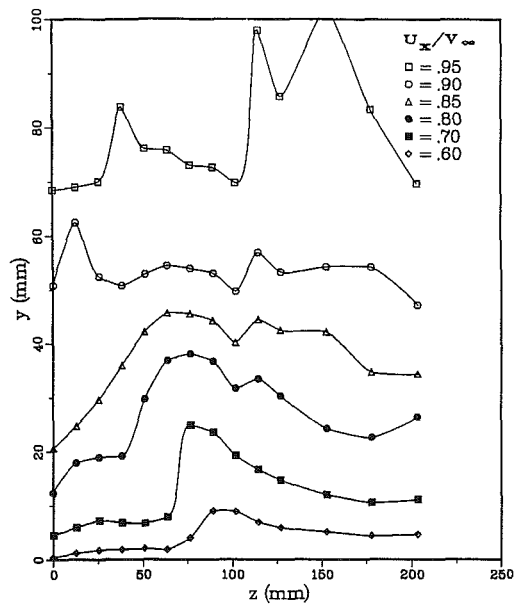

Fig. 5(*b*) x/c = 2.0

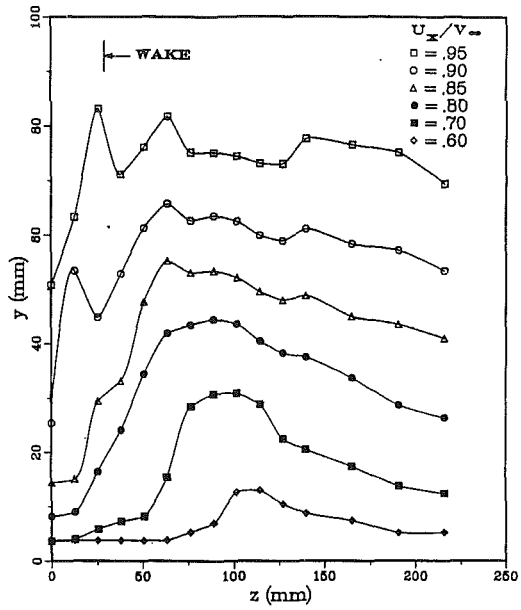

Fig. 5(*c*) x/c = 3.0

Fig. 5 Contours of mean velocity U_x (uncertainty in U_x/v_∞ = ±0.014 and in z = ±1mm at 20:1 odds)

presentation is seen in Fig. 4. All of the vector plots are constructed with a view looking downstream along the right (positive z) side of the appendage. The vector plot at x/c = 0.75 shown in Fig. 4(*a*) is in the region where the flow around the appendage was slowing down and the static pressure was increasing. At first glance, there is no vortex-like signature present in this figure. This is because there was a large cross flow in the negative z direction as the flow followed the narrowing of the appendage while approaching the trailing edge. This geometry-induced cross flow masks the presence of the vortex.

By the time the flow reached the trailing edge, Fig. 4(*b*), the velocity component U_z caused by geometrically-induced flow around the appendage had become much reduced, and the presence of the vortex is seen in the vector plot directly. As estimated from the vector plot of Fig. 4(*b*), the coordinates of the center of the root vortex at the trailing edge are at z = 28 mm and y = 7 mm. This location of the vortex core is at 40 percent of the appendage thickness away from the appendage chordline and 8 percent of the two-dimensional boundary layer thickness above the flat plate surface.

At two chord lengths downstream of the appendage leading edge, the vortex has moved away considerably from the plate surface and the vertical plane of symmetry. The coordinates of the vortex core at x/c = 2 are at z = 56 mm and y = 27 mm which corresponds to 80 percent of the appendage thickness from the appendage chordline and 29 percent of the undisturbed local shear layer thickness above the flat plate surface.

By three chord lengths downstream of the appendage leading edge, Fig. 4(*c*), the vortex core has moved outboard an additional increment of 8 mm from the plane of symmetry, which is small compared with its outward movement between one and two chord lengths, while its height above the plate surface has remained almost constant.

The contours of constant U_x in Fig. 5 correlate well with the location of the core of the trailing vortex as inferred from the vector plots of Fig. 4. There is a large positive gradient in the contour at about the center of the vortex. Inboard of this, the pumping action of the secondary flow vortex has brought high momentum fluid down near the plate surface from the outer regions of the shear layer. Outboard of the vortex center, the reverse is true. The effect of this pumping action is confined to approximately the lower half of the shear layer. The half width of the appendage wake outside the shear layer in the free stream as measured by a total pressure probe has been indicated schematically at x/c = 3.0. It was found that there is a conventional appendage wake present above the outer edge of the shear layer.

The action of the secondary flow in redistributing the turbulent normal stress, u_x', is seen in Fig. 6. Again, the peaks and valleys in the contours correlate with the vortex action centers as inferred from the vector plots. The presence of the appendage boundary layer is evident in the behavior of the data at x/c = .75 and at the trailing edge, where the contours rise for small values of z, Figs. 6(*a*) and 6(*b*). Downstream of the trailing edge, the pumping action of the secondary flow is still significant, and it greatly distorts the distribution of u_x' near the plane of symmetry (z = 0). The symmetrical behavior of the u_x' distribution through the shear layer about the plane of symmetry at x/c = 3.0 is noted.

For flow in the corner of the appendage of constant thickness as investigated by Kubendran et al. (1986), there was a marked similarity in the distribution of the turbulent normal stresses

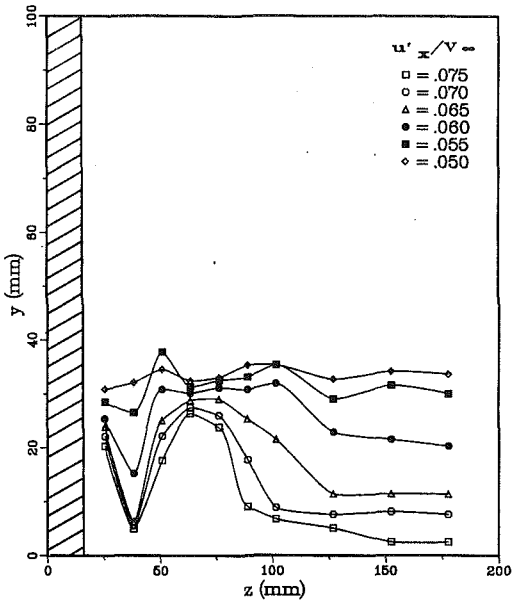

Fig. 6(*a*) *x/c* = 0.75

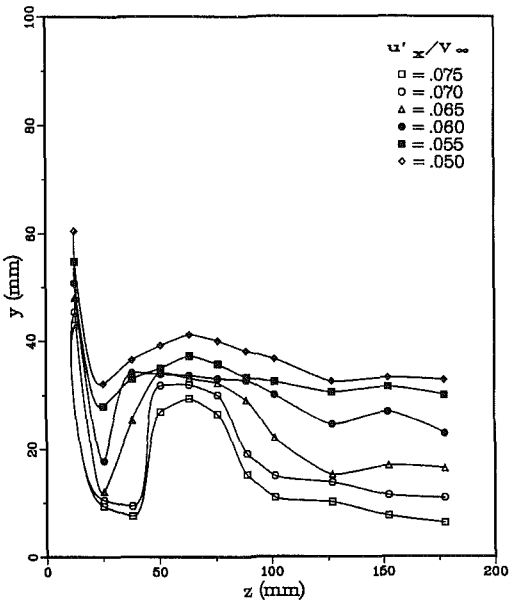

Fig. 6(*b*) *x/c* = 1.0

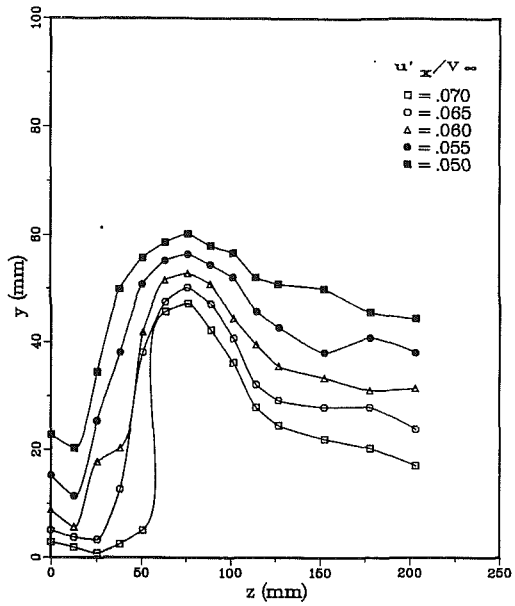

Fig. 6(*c*) *x/c* = 2.0

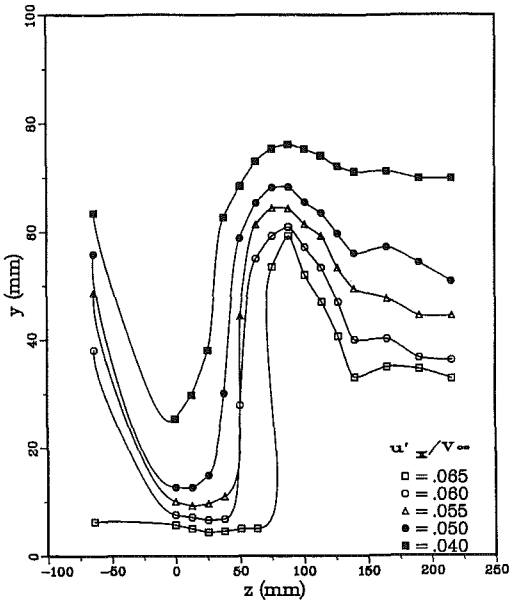

Fig. 6(*d*) *x/c* = 3.0

Fig. 6 Contours of constant normal stress u_x' (uncertainty in u_x'/v_∞ = ±0.0018 and in *z* = ±1mm at 20:1 odds)

u_x' and u_z' at the same z station for three streamwise measurement stations. Such a similarity is absent here, appearing neither in the juncture nor in the wake.

In general, the shear stress $-\overline{u_x u_y}$ at $x/c = 0.75$ and at $x/c = 1.0$ is minimally affected by the secondary flow except close to the appendage and near the plate surface, where the trailing vortex redistributes the turbulence. Downstream of the trailing edge as shown by Fig. 7, the shear stress profiles are redistributed by the root vortex especially near the plane of symmetry and near the center of the trailing vortex. In the plane of symmetry ($z = 0$) in the wake, $-\overline{u_x u_y}$ is zero over the outer two-thirds of the shear layer where U_x is almost constant.

The turbulent shear stress $-\overline{u_x u_z}$ was found to attain very large values in the juncture, but by two chord lengths downstream of the appendage leading edge the values were small at all values of z except near the plane of symmetry. By three chord lengths downstream of the appendage leading edge all the values have become much reduced.

The turbulent shear stress $-\overline{u_y u_z}$ was found to peak up in the juncture and diminish downstream similar to $-\overline{u_x u_y}$ and $-\overline{u_x u_z}$. In addition it was found that secondary flow produced regions of positive shear stresses $-\overline{u_y u_z}$ and $-\overline{u_x u_z}$. This was also observed in the juncture flow of an appendage of constant thickness investigated by Kubendran et al. (1986).

The pumping action of the secondary flow in redistributing the kinetic energy is also investigated. The secondary flow brings low turbulence level fluid from the edge of the shear layer down close to the plate surface and pushes high turbulence level fluid up from the vicinity of the plate surface further out into the shear layer.

3.5 Pressure Field. The flow accelerates as it goes around the point of maximum thickness on the appendage and then slows as it approaches the trailing edge. This is reflected in the measured chordwise pressure distribution on the appendage in the irrotational portion of the flow. However, this inviscid pressure distribution is modified somewhat by the presence of the shear layer on the plate and the resulting secondary flow.

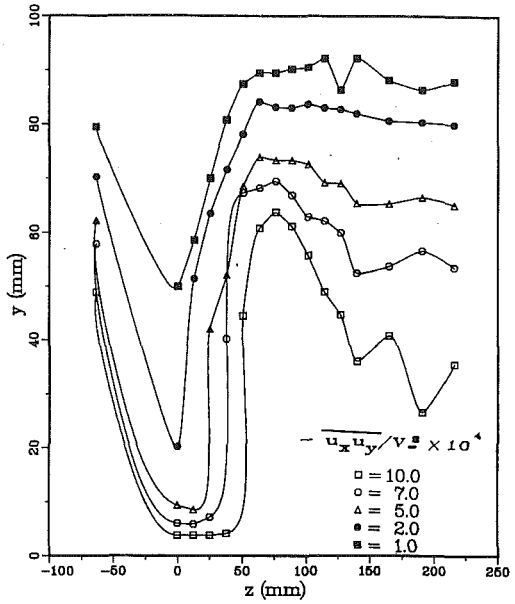

Fig. 7 Contours of constant turbulent shear stress $-\overline{u_x u_y}$ at $x/c = 3.0$ (uncertainty in $-\overline{u_x u_y}/V_\infty^2 = \pm 0.22 \times 10^{-4}$ and in $z = \pm 1$mm at 20:1 odds)

The variation in the spanwise pressure distribution on the appendage as measured at $x/c = 0.23$ and $x/c = 0.75$ is shown in Fig. 8(*a*). The variation is significant at the 23 percent chord station and is confined to the approximate thickness of the shear layer (the variation at large y is the effect of the appendage tip). At the 75 percent chord station, the spanwise pressure distribution as well as the pressure distribution on the plate surface in the transverse direction as shown in Fig. 8(*b*), is almost constant. At $x/c = 1$, the transverse pressure variation on the plate surface is significant as shown by Fig. 8(*b*). The pressure variation on the plate surface calculated using the two-dimensional panel code is also shown in Fig. 8(*b*). This code is a two-dimensional analysis in the x-z plane of this flow problem. The code does not include any secondary flow or viscous effects. The experimental data do not match the predicted values near the trailing edge because the inviscid theory predicts a relatively high pressure there. At the measurement stations downstream of the trailing edge, the transverse pressure distributions on the plate flatten out and the static pressure is at essentially the ambient value.

The static pressure gradient through the shear layer was found to be essentially zero at $x/c = 0.75$ and 1.0 except very near the plane of symmetry. The static pressure for $z = 25$ mm at the trailing edge was seen to decrease approaching the center of the trailing vortex. Excluding the results at $x/c = 1$ and $z = 25$ mm, the static pressure surveys made at the two streamwise stations of $x/c = 0.75$ and 1 showed that the static pressure gradients through the shear layer were small. The static pressure gradients through the shear layer were found to be negligible for flow downstream of the appendage.

4 Conclusions

Measurements of mean velocity components, turbulence stresses and pressure distributions have been carried out in the juncture and downstream of an appendage mounted on a flat plate. The turbulent boundary layer on the flat plate was fully developed and its thickness at a location corresponding to the appendage leading edge was 1.07 times the maximum thickness of the appendage. The appendage was symmetrical, was set at zero incidence with respect to the flow, and had an effectively infinite aspect ratio.

The presence of the appendage results in the formation of

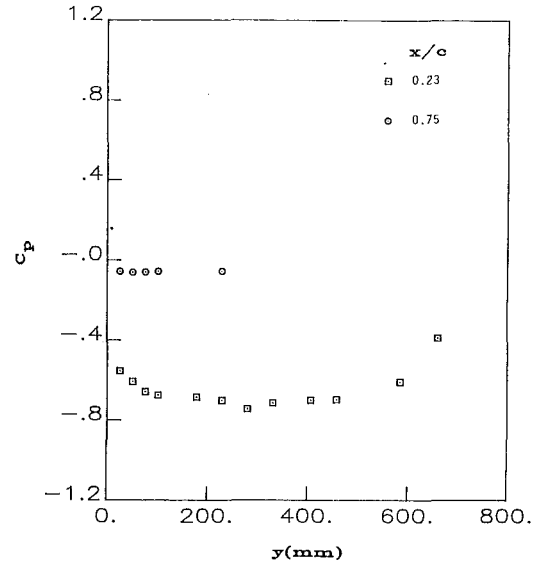

Fig. 8(*a*) Spanwise distribution on appendage

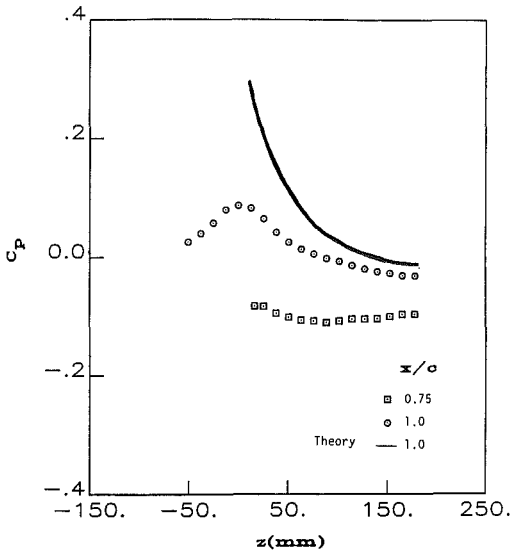

Fig. 8(*b*) Transverse distribution on plate surface

Fig. 8 Static pressure distribution on surfaces (uncertainty in $C_p = \pm 0.05$, in $y = \pm 0.8$mm and in $z = \pm 1$mm at 20:1 odds)

a streamwise root vortex which trails downstream in the corner and behind the appendage. The pumping action of the root vortex is such as to cause a significant redistribution of both the mean flow and turbulence properties in the shear layer. This redistribution is still significant three chord lengths downstream of the appendage leading edge.

The secondary flow has a considerable effect on the wake flow behind the appendage in the lower one-third of the shear layer on the flat plate. The center of the vortex-like secondary flow is located close to the plate surface at the appendage trailing edge at about 8 percent of the local thickness of the shear layer. The center is 40 percent of the appendage thicknesses away from the trailing edge. By the time the flow reaches $x/c = 3.0$, this center has risen to a height corresponding to 29 percent of the local shear layer thickness and has moved further away from the vertical plane of symmetry ($z = 0$) to a distance of 80 percent of the appendage thickness. The appendage turbulent boundary layer separates at the trailing edge and interacts with the trailing root vortex.

At $x/c = 0.75$ the pressure distribution on the plate and appendage surface is well represented by a potential flow de-

scription except in the immediate vicinity of the trailing vortex. Downstream of the appendage the secondary flow has only a small effect on the static pressure field. At all streamwise stations, the static pressure gradient through the shear layer is small.

Acknowledgments

Thanks are extended to Professor L. N. Sankar for his assistance in supplying the theoretical results. This work was supported by the Office of Naval Research.

References

Abid, E. A., and Schmitt, R., 1986, "Experimental Study of a Turbulent Horseshoe Vortex Using a Three-Component Laser Velocimeter," AIAA-86-1069.

Angui, J. H., and Andreopoulos, J., 1990, "Experimental Investigation of a Three-Dimensional Boundary Layer Flow in the Vicinity of an Upright Wall Mounted Cylinder," AIAA 21st Fluid Dynamics, Plasma Dynamics and Lasers Conference, Seattle, WA, pp. 1-12.

Briley, W. R., Buggeln, R. C., and McDonald, H., 1984, "Solution of the Three-Dimensional Navier Stokes Equations for a Steady Laminar Horseshoe Vortex Flow," Report R84-920014-F, Scientific Research Associates.

Burke, R. W., 1987, "Numerical Calculation of Appendage-Flat Plate Junction Flow," DTNSRDC-87/002, David Taylor Naval Ship Research and Development Center, Bethesda, Maryland, pp. 1-30.

Chang, P. S., Segundo, E. I., and Gessner, F. B., 1990, "Experimental Investigation of Flow About a Strut-Endwall Configuration," AIAA 21st Fluid Dynamics Plasma Dynamics and Lasers Conference, Seattle, WA, pp. 1-12.

Devenport, W. J., and Simpson, R. L., 1990, "Time Dependent and Time-Averaged Turbulent Structure Near the Nose of a Wing-Body Junction," *Journal of Fluid Mechanics*, Vol. 210, pp. 23-55.

Dickinson, S. C., 1986a, "Flow Visualization and Velocity Measurements in the Separated Region of an Appendage-Flat Plate Junction," DTNSRDC-86/020, David W. Taylor Naval Ship Research and Development Center, Bethesda, Maryland.

Dickinson, S. C., 1986b, "An Experimental Investigation of Appendage-Flat Plate Junction Flow, Volume I: Description," DTNSRDC-86/051, David W. Taylor Naval Ship Research and Development Center, Bethesda, Maryland, pp. 1-60.

Klebanoff, K. S., 1954, "Characteristics of Turbulence in Boundary Layer with Zero Pressure Gradient," NACA TN 3178.

Kubendran, L. R., McMahon, H. M., and Hubbart, J. E., 1986, "Turbulent Flow Around a Wing/Fuselage-Type Juncture," *AIAA Journal*, Vol. 24, No. 9, pp. 1447-1453.

McMahan, J. M., Hubbartt, J. E., and Kubendran, L. R., 1982, "Mean Velocities and Reynolds Stresses in a Juncture Flow," NACA CR 3605, pp. 1-118.

Pierce, F. J., Harsh, M. D., and Menna, J. D., 1985, "The Mean Flow Structure Around and Within a Turbulent Junction or Horseshoe Vortex," Report VPI-E-85-19, Virginia Polytechnic Institute and State University, Blacksburg, Virginia.

Pierce, F. J., Kim, C. M., and Harsh, M. D., 1987, "The Mean Flow Structure of a Turbulent Junction Vortex," Report VPI-E-87-6, Virginia Polytechnic Institute and State University, Blacksburg, Va.

Rood, E. P., 1984, "Experimental Investigation of the Turbulent Large Scale Temporal Flow in the Wing-Body Junction," Ph.D. thesis, Catholic University of America.

Maximum Pressure Head Due to Linear Valve Closure

Chyr Pyng Liou
Assistant Professor,
Department of Civil Engineering,
University of Idaho,
Moscow, Idaho 83843

The maximum pressure head resulting from one-speed closure of wide open valves is investigated. The dimensionless variables formulated in this study make the subtle effect of the initial valve head loss explicit and separate from that of the pipe frictional head loss. The maximum head is related to initial pipe frictional head loss, the initial valve head loss, the inherent flow characteristic of the valve, and the closure period by plots of dimensionless variables. The trends of the variation of the maximum pressure head are discussed. An example is used to illustrate the usage of the plots, and to show the advantage of having a global perspective of the phenomenon in the selection and sizing of valves from the water hammer point of view.

Introduction

Consider a valve at the outlet of a pipe discharging liquid from a constant head reservoir. Closure of the valve results in a pressure rise, which propagates toward the reservoir at a speed equal to the pressure wave speed of the pipe-liquid system. Subsequent reflections of this pressure wave at the pipe ends cause local pressures to fluctuate until the fluid motion is damped out by system friction. The maximum head occurs at the valve. An accurate calculation of the maximum pressure head rise due to valve closure is important in the design and operation of pressurized piping systems. Higher than expected water hammer pressure threatens the integrity of a piping system.

Several independent variables affect the magnitude of the maximum pressure rise. They are: closure period, head loss across the valve before closing, inherent hydraulic characteristic of the valve, pipe frictional head loss, and initial discharge. The combined effects of these variables on the maximum pressure head are nonlinear and difficult to visualize. This paper separates the effects of head losses of the pipe and the valve on the maximum pressure head, and presents a global perspective of the phenomenon.

Literature Review

Various aspects of the valve closure problem have been studied by many investigators (Joukowsky, 1904; Allievi, 1925; Dawson and Kalinske, 1939; Kerr, 1951; Parmakiam, 1963; Vallentine, 1965; Sharp, 1969, Jones and Wood, 1972). Many of these earlier studies assume the pipe to be frictionless. Sharp (1974) discussed the effect of pipe friction on the maximum surge pressure. Wood and Jones (1974) suggested adding the steady state frictional pressure drop to the maximum pressure for frictionless pipe as a rough estimation of the effect of pipe line friction.

More recently, Ruus and El-Fitiany (1980) presented comprehensive charts for water hammer due to valve closure. The maximum pressure head rises at the valve and at the midpoint of the pipe were plotted against the Allievi pipeline constant, the relative valve closure time, and the ratio of pipe frictional head loss versus reservoir static head. Using a similar approach, Karney and Ruus (1985) presented charts for maximum head resulting from closure of full open valves.

This study differs from the studies by Ruus and El-Fitiany (1980) and by Karney and Ruus (1985) in an important way. These two studies used the constant static reservoir head to nondimensionalize variables such as the pipe frictional head loss, the maximum head rise, and the pipeline constant. The steady-state valve head loss was treated as a part of the static reservoir head instead of as a separate variable. Consequently, the influence of the initial valve loss on the maximum head is not explicit in their plots. In this study, the initial head loss across the valve is treated as an independent variable. The dependence of the maximum head on the initial valve head loss is shown explicitly in a set of dimensionless plots.

Purpose and Scope

This study aims at providing an overall picture for the maximum pressure head as a result of valve closure at one speed from the full open position. The method enables the separate effects of the initial valve head loss and the pipe frictional head loss to be explicitly evaluated. Approximate minimum valve closure time periods and reasonable water hammer pressure allowances can be estimated with only a few simple calculations.

The plots presented here complement detailed computer simulations when the specific valve characteristic and closure speed are known and accurate maximum pressure head is desired.

Inherent Valve Characteristic

The flow rate through a valve is a function of pressure drop and valve opening. There are several ways to describe this relationship. This study uses the common valve flow coefficient. With a pressure drop of 1 psi (6.89 kPa) across the valve, the flow rate of 60°F (15.6°C) water in U.S. gpm at a given valve opening is called the flow coefficient C_v of the valve at

Contributed by the Fluids Engineering Division and presented at the Winter Annual Meeting Dallas, Texas, November 25–30, 1990 of THE AMERICAN SOCIETY OF MECHANICAL ENGINEERS. Manuscript received by the Fluids Engineering Division December 2, 1990.

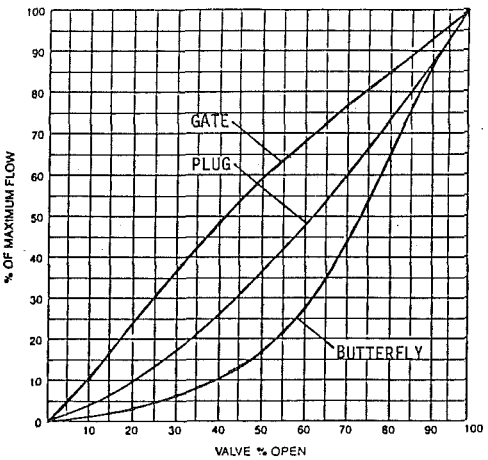

Fig. 1 Inherent flow characteristic of actual gate, plug, and butterfly valves

that opening. Flow coefficients are determined by standardized tests (Lyons and Askland, 1975).

The inherent hydraulic characteristic of valve is expressed by a curve showing C_v as a function of valve position in degrees or percentage of opening. Customarily, C_v is expressed as a percentage of C_{v0}, which is the C_v when the valve is wide open. C_{v0} can vary significantly with the valve's size, type, and manufacturer. It reflects the capacity of the valve and is routinely provided by manufacturers based on their tests or calculations. Figure 1 shows the inherent flow characteristic of a gate valve, a plug valve, and a butterfly valve.

Governing Equations and Numerical Solution Procedure

Assuming that the convective changes in cross-sectional average velocity and in pressure to be negligible, and that the density of the liquid and the pipe cross-sectional area to be constant except in the definition of the pressure wave speed, the equation of motion and the continuity equation governing one-dimensional transient flow are (Wylie, 1984, 1985):

$$g\frac{\partial H}{\partial X}+\frac{1}{A}\frac{\partial Q}{\partial T}+\frac{fQ|Q|}{2DA^2}=0 \tag{1}$$

$$\frac{\partial H}{\partial T}+\frac{a^2}{gA}\frac{\partial Q}{\partial X}=0 \tag{2}$$

in which H = piezometric head, Q = volumetric flow rate, D = pipe diameter, A = cross-sectional area of the pipe, g = gravitational acceleration, f = Darcy-Weisbach friction factor, a = pressure wave speed of the liquid-pipe system, X = distance, and T = time. The stated assumptions are valid when Q/A is much less than a, which is the case under consideration.

Represent the steady-state volumetric flow rate by Q_0 and the head rise due to sudden and complete stoppage of the velocity V_0 ($= Q_0/A$) by H_0. This head rise, called potential surge, can be expressed as (Wylie and Streeter, 1983)

$$H_0=\frac{aV_0}{g} \tag{3}$$

Let $v = Q/Q_0$, $h = H/H_0$, $x = XL$, and $t = aT/L$, L being the length of the pipe. Equations (1) and (2) take the following dimensionless form

$$\frac{\partial h}{\partial x}+\frac{\partial v}{\partial t}+Rv|v|=0 \tag{4}$$

$$\frac{\partial h}{\partial t}+\frac{\partial v}{\partial x}=0 \tag{5}$$

where

$$R=\frac{fLV_0}{2aD} \tag{6}$$

This choice of the dimensionless variables is motivated by the need to separate the initial valve head loss from the pipe wall frictional head loss. It deviates from the traditional Allievi's choice where the static reservoir head H_r was used to form the dimensionless head H/H_r and the dimensionless pipeline constant $aV_0/(2gH_r)$. Allievi's theory deals with water hammer in a frictionless pipe. With the presence of pipe wall friction, however, Allievi's dimensionless variables are not the best choice. In this case, the valve head loss (as a portion of the static reservoir head) appears in both the Allievi variables (see Ruus and El-Fitiany, 1980, and Karney and Ruus, 1985). As a result, the effect of valve head loss, which is very significant as demonstrated later, can not be shown explicitly.

Using the characteristics method, Eqs. (4) and (5) are transformed into a pair of total differential equations

$$\frac{dh}{dt}\pm\frac{dv}{dt}\pm Rv|v|=0 \tag{7}$$

which are valid along characteristics

$$\frac{dx}{dt}=\pm 1 \tag{8}$$

It is assumed that the velocity head and the entrance loss are negligible. With the datum for head taken at the downstream flange of the valve, the boundary condition at the reservoir end is

$$h(0,t)=h_f+h_v \tag{9}$$

where

$$h_f=R=\frac{H_f}{H_0} \tag{10}$$

and

Nomenclature

A = pipe cross-sectional area
a = wave speed
C_v = valve flow coefficient
C_{v0} = initial (full open) valve flow coefficient
D = pipe diameter
dt = time step size
f = Darcy-Wiesbach friction factor
g = gravitational acceleration
H = piezometric head
H_0 = potential surge
H_f = pipe frictional head loss
H_v = head loss across a valve
h = dimensionless piezometric head, $h = H/H_0$
h_f = dimensionless head loss due to pipe friction, $h_f = H_f/H_0$
h_v = dimensionless valve head loss, $h_v = H_v/H_0$
L = pipe length
N = number of computational reaches
Q = volumetric flow rate
Q_0 = initial steady state flow rate
R = a dimensionless constant defined by Eq. (6)
T = time
t = dimensionless time, $t = Ta/L$
V = average velocity over pipe cross-section
V_0 = steady state average velocity over pipe cross-section
v = dimensionless volumetric flow rate, $v = Q/Q_0$
X = distance along the pipe
x = dimensionless distance along the pipe, $x = X/L$
τ = dimensionless valve flow coefficient, $\tau = C_v/C_{v0}$

$$h_v = \frac{H_v}{H_0} \tag{11}$$

are the dimensionless head losses in the pipe and across the valve prior to the valve closure. H_f = the initial steady-state pipe frictional head loss, H_v = the initial steady-state head loss across the valve.

At the downstream end, it is assumed that the pipe extends beyond the valve for a short distance (about 10 diameters) to enable full pressure recovery before discharging the fluid into atmosphere. The discharge versus head loss relationship of the valve provides the downstream boundary condition

$$v(1,t) = \tau(t)\sqrt{\frac{h(1,t)}{h_v}} \tag{12}$$

where $\tau(t) = C_v(t)/C_{v0}$, and is shown as percentage of maximum flow in Fig. 1. At $t = 0$ the valve is wide open and $\tau = 1$. In the numerical solution process, each curve in Fig. 1 is represented by 11 equally spaced points. At any given moment, τ is obtained by linear interpolation.

The initial conditions are

$$v(x,0) = 1 \tag{13}$$

and

$$h(x,0) = h_f + h_v - Rx \tag{14}$$

Figure 2 depicts the finite difference approximation to Eq. (7). The pipe is divided into N computational reaches of equal length. At the interior point P, the unknown h and v are related to the known conditions at points A and B by

$$C^+: h_P - h_A + (v_p - v_A) + Rv_A|v_A|dt = 0 \tag{15}$$

$$C^-: h_P - h_B - (v_p - v_B) - Rv_B|v_B;|dt = 0 \tag{16}$$

where dt is the time step. These two equations yield a unique solution for h and v at P.

At the upstream end of the pipe, the head h_p is known from Eq. (9) and the flow v_p is solved from the C^- equation as

$$v_P = h_P - h_B + v_B - Rv_B|v_B|dt \tag{17}$$

At the downstream end, the C^+ equation and Eq. (12) enable the head and the flow to be solved

$$v_P = \frac{1}{2}\left[-\frac{\tau^2}{h_v} + \tau\sqrt{\frac{\tau^2}{h_v^2} + \frac{4}{h_v}(h_A + v_A - Rv_A|v_A|dt)}\right] \tag{18}$$

and

$$h_P = h_A - v_P + v_A - Rv_A|v_A|dt \tag{19}$$

The discretization error decreases with increasing N. Sufficiently accurate results were obtained with $N = 20$.

Ranges of Dimensionless System Variables

The preceding section shows that the dimensionless variables $h_f\,(=R)$, h_v, and $\tau(t)$ completely characterize the valve closure problem. The ranges of magnitude of these three parameters are now considered.

The lower limit for h_f approaches zero when the pipe is short, smooth, or the velocity is low. There is no upper limit for h_f. However, a value of 1.0 may be considered high, and is used as the upper limit. For a pipe 1 ft (0.3 m) in diameter and 5 miles (8.05 km) long with a Darcy-Weisbach friction factor of 0.02, a pressure wave speed of 3500 ft/s (1067 m/s), and an initial velocity of 7 ft/sec (2.13 m/s), the value for h_f is 0.53.

The range of h_v is from 0.0001 to 0.01. For an initial velocity of 7 ft/sec (2.13 m/s) and a pressure wave speed of 3500 ft/s (1067 m/s), and for a very large full open valve head loss of 10 velocity heads, h_v equals 0.01.

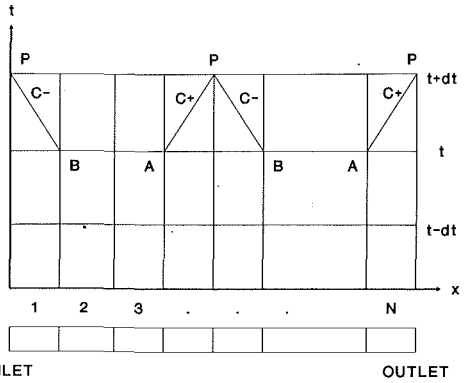

Fig. 2 Finite Difference approximations along the characteristics in the $x-t$ plane

The ranges of h_f and h_v cover most situations excepting those with unusually high pipe loss or with unusually low valve loss.

This study assumes the valve position to be a linear function of time. A dimensionless valve closure time t_c is defined as the closure clock time T_c divided by the travel time of a pressure wave over one pipe length (L/a):

$$t_c = \frac{aT_c}{L} \tag{20}$$

The t_c considered are 1, 5, and 10. $t_c = 1$ represents an "instantaneous" closure in the sense that the potential surge is realized. $t_c = 10$ represents a very slow closure.

Effects of Pipe Friction, Initial Valve Head Loss, Inherent Valve Characteristic, and Closure Time on Maximum Head

The calculated maximum pressure heads at the valve are shown in Fig. 3 for the gate valve, the plug valve, and the butterfly valve for $t_c = 1$, 5, and 10. Terms such as maximum head, valve head loss, and pipe friction loss used in Fig. 3 and in the ensuing discussions are the respective quantities nondimensionalized by the potential surge H_0.

The top row in Fig. 3 shows that for $t_c = 1$, the maximum head is essentially a linear function of pipe friction, and that the initial valve head loss has little influence on the maximum head. Since the initial valve head loss is small (less than one thousandth of the potential surge), the maximum heads shown are essentially the maximum head rises as well. The lowest value of the maximum head at the valve is unity and it occurs for a frictionless pipe. In dimensional terms, the lowest maximum head equals the potential surge. For pipes with frictional head loss, an additional head rise resulting from line pack (Wylie and Streeter, 1983) is added to the potential surge. This additional head rise is proportional to the initial pipe frictional head loss. The valve type and the inherent valve characteristic have negligible effect on the maximum head rise when the valve closure is sufficiently rapid. The closure is rapid when the valve is closed before the reflected wave from the reservoir arrives at the valve.

As the valve closure time increases, the maximum head surface becomes more warped (middle and bottom rows of Fig. 3). The effects of the initial valve head loss and the inherent valve flow characteristic become more significant for longer closure times. For a specified initial pipe loss, the maximum head decreases with increasing initial valve head loss. The rate of decrease changes with both pipe friction and valve loss. This variability is most pronounced for butterfly valves, moderately so for plug valves and less so for gate valves.

Table 1 lists the maximum head at the four corners of the surface plots. It presents the extreme values of the maximum head for the ranges of initial pipe friction loss and valve head

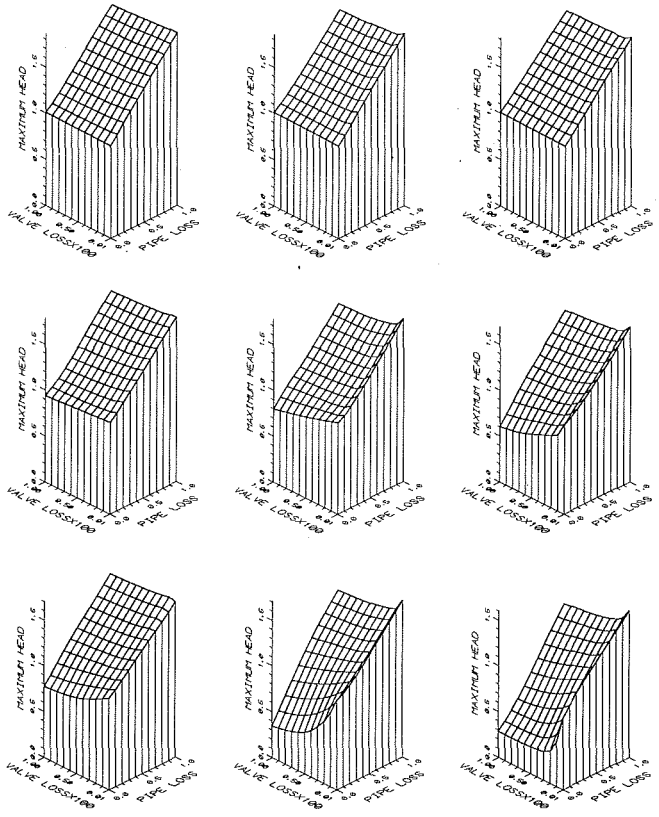

Fig. 3 Dimensionless maximum pressure heads at the valve for the gate valve (left column), the plug valve (middle column), and the butterfly valve (right column) at t_c = 1 (top row), t_c = 5 (middle row), and t_c = 10 (bottom row)

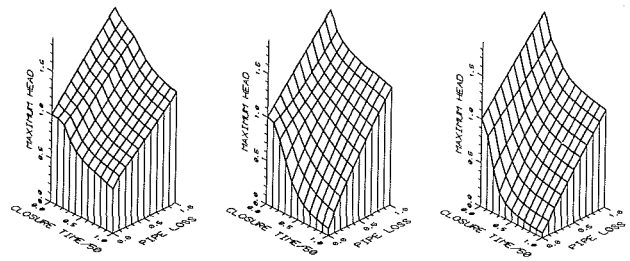

Fig. 4 Dimensionless maximum head for h_v = 0.001 for gate valve (left), plug valve (middle), and butterfly valve (right)

loss considered. For each type of valve, the highest maximum head occurs at maximum pipe friction loss and minimum valve head loss (column 4). This trend can be explained as follows. First, higher pipe wall friction results in more head rise due to line pack. Secondly, lower initial valve loss relative to the pipe frictional head loss makes the valve less effective in slowing down the flow during the initial stroke of the valve closure. The flow is unimpeded during the first portion of the closing stroke. The flow begins to slow down only after the flow area of the valve is sufficiently reduced to produce a more substantial head loss. Therefore, for valves with low initial head loss, the effective time period to stop the flow is shorter than the valve closure period, resulting in a higher maximum head rise.

Referring again to Table 1, the lowest maximum head "rise" occurs for zero pipe friction loss and maximum valve head loss (column 5). The reasons are opposite to those explained above. With the absence of pipe wall friction, there is no head rise due to line pack. With a larger initial valve head loss, the flow is reduced to zero over a longer time period, resulting in less head rise.

Table 1 Summary of maximum heads

t_0 (1)	Type (2)	h_v = .0001 h_f = 0.0 (3)	h_v = .0001 h_f = 1.0 (4)	h_v = .01 h_f = 0.0 (5)	h_v = .01 h_f = 1.0 (6)
1	gate	1.00	1.87	1.01	1.83
	plug	1.00	1.86	1.01	1.77
	butterfly	1.00	1.82	1.01	1.76
5	gate	1.00	1.79	0.94	1.73
	plug	1.00	1.77	0.80	1.59
	butterfly	0.98	1.69	0.61	1.52
10	gate	1.00	1.72	0.77	1.65
	plug	0.98	1.72	0.34	1.48
	butterfly	0.78	1.60	0.29	1.33

Wood and Jones (1974) suggested, in terms of notations used here, that the maximum head can be roughly estimated by adding h_f to the maximum head obtained with $h_f = 0$. It can be demonstrated that such a procedure does not always yield conservative results. When the frictional resistance to flow is significant, the maximum head so estimated can be either above or below the correct value, depending on the valve closure time.

Consider a steady state flow with $h_v = 0.01$ and $h_f = 1.0$. Suppose a plug valve is closed in L/a seconds. The resulting dimensionless maximum head shown in Table 1 is 1.77. Adding the steady state pipe frictional head loss (1.0) to the frictionless maximum head (1.01) yields a maximum head of 2.01, which overestimates the maximum head by 0.24 (2.01–1.77). This amounts to $0.24H_0$ or 24 percent of the potential surge.

However, suppose that the same valve is closed in $10L/a$ seconds. Table 1 shows a dimensionless maximum head of 1.48. Adding the steady state frictional head loss (1.0) to the frictionless maximum head (0.34) yields a maximum head of 1.34. The estimation now underestimates the maximum head by 0.14 (1.48–1.34) or 14 percent of the potential surge. Thus, not incorporating the pipe friction rigorously in the calculation may result in significant error in the maximum head.

Figure 4 shows the maximum head as a function of pipe frictional head loss and valve closure period for an initial dimensionless valve head loss of 0.001. This figure is useful in determining the shortest closure period so that the maximum head at the valve does not exceed a specified limit. It is seen that, with the initial valve head loss specified, the maximum head increases nearly linearly with increasing pipe friction loss. The maximum head decreases with a more variable rate as the valve closure period is lengthened. The rate of decrease is the greatest for butterfly valves with the shortest closure time.

Column separation may occur as a result of the valve closure. As an indication of the likelihood of column separation, the intersections of minimum head surfaces with the plane of zero head over the h_f versus h_v plane were obtained. The results indicate that, for horizontal pipes, systems with h_f less than approximately 0.6 are likely to have column separation. h_v has little impact on gate valves for the three closure speeds considered. Greater h_v (0.001 or higher) significantly reduces the likelihood of column separation for butterfly valve with t_c = 10. Full computer simulation should be carried out if column separation is suspected.

Application Example

Consider a 1 ft (0.3 m) steel pipe that delivers 3.5 cfs (0.099 m^3/s) of water for a distance of 10 miles (16.1 km). The Darcy-Weisbach coefficient is estimated to be 0.013, which gives H_f = 212 ft (64.6 m). Suppose a 1 ft (0.3 m) diameter plug valve with a wide open C_v value of 3455 at the pipe outlet is closed linearly in 76.5 seconds. With the valve wide open at the steady state, the initial head loss through the valve is calculated to be 0.48 ft (0.146 m). Assume the speed of the pressure wave in the system to be 3450 ft/sec (1052 m/s). The relevant param-

eters are: H_0 = 478 ft (146 m), h_f = 0.44, h_v = 0.001, and t_c = 5. Entering Fig. 3 (figure in the middle row and middle column) with these values, one finds the dimensionless maximum head to be 1.23. Therefore, the maximum head rise is $1.23H_0$ or 588 ft (180 m).

If the maximum head is limited to 400 ft (122 m), then the closure time must be lengthened if the same valve is to be used. The shortest closure time to satisfy this constraint can be found from Fig. 4. One enters Fig. 4 (middle figure) with a dimensionless maximum head of $400/H_0$ = 0.84 and a h_f value of 0.44 to find a dimensionless closure time of 30. Thus, the valve should be closed no faster than $30L/a$ or 459 s.

If this closure time is too long, then one should consider other types of valves. Figure 4 suggests that the butterfly valve is better suited to satisfy the maximum pressure requirement since its rate of decrease of the maximum pressure with closure period is the fastest. The capacity (i.e., C_{v0}) of the valve needs to be checked to see if it is comparable to that of the plug valve. If not, then curves similar to those in Fig. 4 but with different h_v values can be used to find the shortest closure time.

The precision of using the dimensionless plots to obtain the maximum pressure rise is limited by the physical size of the plots. For the calculations demonstrated here, plots twice as large as those shown were used. A direct calculation of the time history of the head at the valve in the example was made by solving Eqs. (1) and (2) using the method of characteristics (Wylie and Streeter, 1983). With twenty computational reaches, the calculated maximum pressure head at the valve was 585 ft. Comparing this value with the 588 ft obtained from Fig. 4, the error is less than one percent. This error can be reduced if Fig. 4 is presented with a larger physical dimension.

Summary and Conclusion

The valve closure problem of water hammer is investigated by a parametric study of the governing equations in a dimensionless form. The results are presented by a set of dimensionless plots. The plots show that the initial pipe friction head loss, the initial head loss across the valve (or, indirectly, the valve capacity), the inherent valve flow characteristic, the one-speed valve closure period, and the valve type all influence the maximum head in a nonlinear fashion. The effects of the initial valve head loss and the pipe frictional head loss on the maximum pressure head are explained and independently evaluated. An example is used to demonstrate the utilities of the plots.

References

Allievi, L., 1925, Theory of Water Hammer (in Italian, Translated by Halmos, E. E.), American Society of Mechanical Engineers, New York.

Bergeron, L., 1961, Water Hammer in Hydraulics and Wave Surges in Electricity (in French, translated by ASME), J. Wiley, New York.

Dawson, F. M., and Kalinske, A. A., 1939, "Methods of Calculating Water Hammer Pressures," *Journal of The American Water Works Association*, Vol. 31, No. 11, pp. 1835–1864.

Jones, S. E., and Wood, D. J., 1972, "Prediction and Control of Pressure Surges Due to Valve Closures," *Proceedings, First International Conference on Pressure Surges*, Canterbury, England, BHRA, Paper F1.

Joukowsky, N., 1904, "Water Hammer," (in Russian, translated by Simis, Miss O.), *Proceedings of The American Water Works Association*, Vol. 24, pp. 341–424.

Karney, B., and Ruus, E., 1985, "Charts for Water Hammer in Pipelines Resulting from Valve Closure from Full Opening Only," *Canadian Journal of Civil Engineering*, Vol. 12, pp. 241–264.

Kerr, S. L., 1951, "Water Hammer Control," *Journal of The American Water Works Association*, Vol. 43, No. 12, pp. 985–999.

Lyons, J. L., and Askland, C. L. Jr., 1975, *Lyons' Encyclopedia of Valves*, Van Nostrand Reinhold, New York.

Parmakian, J., 1963, *Waterhammer Analysis*, Dover Publications, Inc., New York.

Ruus, E., and El-Fitiany, F. A., 1980, "Charts for Water Hammer in Pipelines Resulting from Valve Closure," *Canadian Journal of Civil Engineering*, Vol. 7, pp. 243–255.

Sharp, B. B., 1969, "Water Hammer Gate Characteristics," *Water Power*, Sept. pp. 352–354.

Sharp, B. B., 1974, A Discussion to "Water-Hammer Charts for Various Types of Valves," *Journal of the Hydraulics Division*, Proceedings of the American Society of Civil Engineers, Vol. 100, No. HY2, pp. 323–327.

Vallentine, H. R., 1965, "Rigid Water Column Theory for Uniform Gate Closure," proceeding paper 4386, *Journal of the Hydraulics Division*, Proceedings of the American Society of Civil Engineers, Vol. 91, No. HY4, pp. 27–33.

Wood, D. J., and Jones, S. F., 1973, "Water-Hammer Charts for Various Types of Valves," proceeding paper 9500, *Journal of the Hydraulic Division*, Proceedings of the American Society of Civil Engineers, Vol. 99, No. HY1, pp. 167–178.

Wood, D. J., and Jones, S. E., 1974, Closure to Discussions on "Water-Hammer Charts for Various Valves," *Journal of the Hydraulic Division of American Society of Civil Engineers*, Vol. 100, HY9, pp. 1272–1274.

Wylie, E. B., and Streeter, V. L., 1983, *Fluid Transients*, FEB Press, Ann Arbor, Michn.

Wylie, E. B., 1984, "Fundamental Equations of Waterhammer," proceeding paper 18707, *Journal of Hydraulic Engineering*, Vol. 110, No. 4, pp. 539–542.

Wylie, E. B., 1985, Closure to discussions on "Fundamental Equations of Waterhammer," *Journal of Hydraulic Engineering*, Vol. 111, No. 8, pp. 1197–1200.

A. J. Hudson
Research Assistant.

P. A. Eibeck
Associate Professor.

Mechanical Engineering Department,
University of California at Berkeley,
Berkeley, CA 94720

Torque Measurements of Corotating Disks in an Axisymmetric Enclosure

Torque measurements, which can be related to viscous dissipation, were made in a simulated disk drive consisting of a single or multiple corotating disk stack enclosed in an axisymmetric shroud. The effects of rotational velocity, axial and radial spacing, and the position and thickness of simulated read/write arms between disks on torque were studied. Correlations are presented to describe the results of the unobstructed cases and the cases with the read/write arms at their innermost position, and a method is introduced to calculate the torque at intermediate arm positions.

Introduction

Thermal expansion in magnetic recording disks and other components of a disk drive can cause errors in positioning read/write heads over data tracks, resulting in limitations on the minimum spacing between data tracks written on a disk. Heat transfer from disks to the air inside the drive enclosure affects the thermal expansion of the components of a disk drive and is a problem of current interest (see Chang et al., 1988 and Torok and Gronseth, 1988). Eibeck et al. (1989) presented a thermal model which predicts the temperature distribution and resulting thermal expansions in an operating disk drive, and reported a lack of reliable information on viscous dissipation in disk drives. Sato et al. (1988) studied heat transfer in Helium-filled drive enclosures, and presented an approximate result for viscous dissipation which included only the effects of disk radius, rotational velocity, and fluid properties. Accurate measurements of viscous dissipation can benefit the computation of heat transfer in rotating disk systems by serving as a check on the accuracy of numerical solutions.

In current disk-drive systems, viscous dissipation, or aerodynamic heating, is a minor heat source and in many cases can be neglected in a thermal analysis of a disk drive. As rotational velocities are increased to reduce access time, viscous dissipation is expected to rise considerably, making it a significant heat source in a drive enclosure and an important consideration in disk-drive design.

A study of a single rotating disk in a housing was performed by Daily and Nece (1960). They state that the mode of flow between a rotating disk and the stationary housing only depends on disk Reynolds number and the ratio of the disk radius to the clearance between disk and housing. Daily and Nece suggested that four modes of flow can be present: Regime I in which laminar boundary layers on the disk and housing are merged; Regime II in which separate laminar boundary layers are present on the disk and housing surfaces; Regime III with turbulent, merged boundary layers; and Regime IV with turbulent, separate boundary layers. For a given axial clearance to disk radius ratio, the flow may or may not experience all four regimes over a practical Reynolds number range.

Daily and Nece (1960) present theoretical and experimental determinations of the nondimensional torque, or moment, coefficient, C_m. They found that the moment coefficient varies as Re^{-1}, $Re^{-1/2}$, $Re^{-1/4}$, and $Re^{-1/5}$ for the Regimes I through IV, respectively. While the moment coefficients presented in Daily and Nece can be used to predict the viscous dissipation for the case of a single shrouded disk, no information is available to predict the dissipation in multiple disk stacks.

Experimental Approach

In order to determine the viscous dissipation in systems relevant to disk-drive designers, torque measurements were made on an experimental disk drive which emulates basic disk-drive features. Torque measurements indicate viscous dissipation since the power required to rotate a disk stack at steady state is equal to the frictional losses between the disks and the air, i.e., the viscous dissipation, less any losses due to bearing friction. A disk stack and hub assembly were rotated within a smooth, sealed cylindrical shroud, with the effect of read/write arms on dissipation simulated by placing a bluff body of rectangular cross section into the gaps between disks. The results, presented in the form of dimensionless moment coefficients, reveal the dependence of torque on Reynolds number, disk spacing, tip clearance, and the placement of arms in the flow.

The shaft power input was determined by measuring the restraining torque necessary to prevent the rotation of the shroud. The apparatus, illustrated in Fig. 1, consists of the following main components: a drive assembly, shroud, torque balance, and supporting structure. The drive assembly is mounted vertically at the center of the base. The torque balance is suspended below the upper support plate and held the shroud

Contributed by the Fluids Engineering Division for publication in the JOURNAL OF FLUIDS ENGINEERING. Manuscript received by the Fluids Engineering Division October 8, 1990.

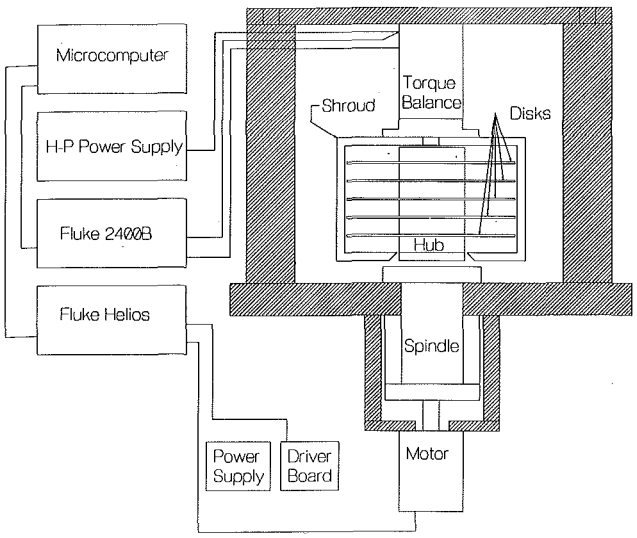

Fig. 1 Experimental apparatus

in position around the disks with the centerline of the shroud coincident with the axis of rotation of the disk stack. Details of this apparatus are available in Hudson (1989), and are summarized below.

The drive assembly includes a drive motor, grinder spindle, and disk-drive hub. The drive motor is a Pittman 5223 brushless DC motor (400 watt output at 10,000 rpm), capable of driving the spindle to 10,000 rpm (1047 rad/s). The spindle is a Gilman 1875 grinder spindle which can operate at speeds up to 10,000 rpm while limiting radial runout to 0.008 mm. The hub is a cylindrical shaft, permanently attached to the spindle, with an outside diameter matched to the inside diameter of the disks (radial clearance = 0.012 mm).

Figure 2 shows details of the hub, disk stack, and shroud. Actual magnetic recording disks were used (Iron Oxide media) with a 130 mm outside diameter, 40 mm inside diameter, and a thickness of 1.93 mm. The disks were separated on the hub by spacers having inside diameters that allow a slip fit over the hub (40.02 mm) and outside diameters of 50.80 mm. Three spacer sets were fabricated with different thicknesses; 12.70 mm, 6.35 mm, and 1.58 mm.

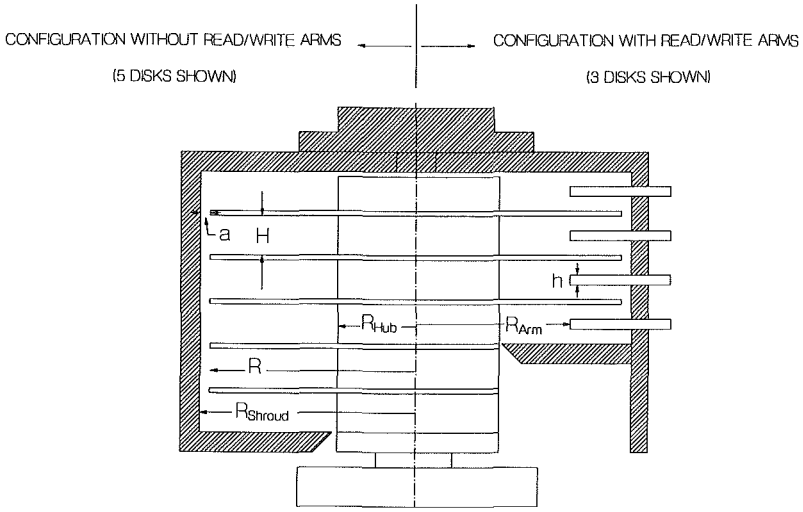

Fig. 2 Test section schematic

Nomenclature

a = radial clearance between disk tip and shroud
a/R = shroud clearance ratio (a/R_{disk})
B = blockage ratio (h/H)
C_m = moment coefficient $\left(\frac{T}{1/2\rho\omega^2 R_{disk}^5}\right)$
$C_{m\,gap}$ = gap moment coefficient $\left(\frac{T_{gap}}{1/2\rho\omega^2 R_{disk}^5}\right)$
$C_{m\,total}$ = moment coefficient based on total torque $\left(\frac{T_{total}}{1/2\rho\omega^2 R_{disk}^5}\right)$
$C_{m\,unobstructed}$ = C_m measured without arms
$C_{m\,obstructed}$ = C_m measured with arms at the innermost position
$C_{m\,comp}$ = composite moment coefficient at intermediate arm positions
F = force
h = axial height of the arms
H = axial height of shear gap or corotating gap
H/R = gap aspect ratio
r = radial coordinate
P_d = viscous dissipation power
R^* = dimensionless arm radius (R_{arm}/R_{disk})
R_{arm} = radial position of the arm tip
R_{shroud} = radius of shroud wall
R_{hub} = radius of hub
R = disk radius
R_{disk} = disk radius
Re = disk Reynolds number ($\omega R_{disk}^2/\nu$)
T = torque
T_{total} = measured shroud torque for multiple disk configurations
T_{gap} = torque acting on the two disk surfaces in a corotating gap
θ = temperature
ν = kinematic viscosity of air
ρ = density of air
τ = shear-stress component perpendicular to r, acting on the disk surface
Φ = viscous dissipation per unit volume
ω = angular velocity (Rad/s)

The shroud assembly, a circular cylinder with flat end plates, was suspended above the disk stack by the torque balance, enclosing the disk stack while allowing no physical contact with the disks or hub. The lower end plate is an annular disk, which fits around the bottom of the hub (radial clearance = 0.25 mm), at a vertical position adjusted to match the number of disks and the axial spacing. In all cases, the gap height between corotating disks is the same height as the gap between the end wall of the shroud and the adjacent disk surface.

To study the effect of read/write arms on torque, bluff bodies of rectangular cross section were inserted into the gaps between neighboring disks and between the disks and shroud end walls. Two sets of arms were fabricated, with thicknesses, represented by the parameter h, of 3.175 mm and 6.350 mm. The three arm positions defined in terms of R^*, the radial position of the tip of the arm relative to the disk radius, were: 0.933, 0.738, and 0.542.

The torque balance measured the moment about the axis of rotation of the shroud (coincident with the axis of rotation of the drive assembly) in order to determine the shaft power input to the disk drive.

The torque balance measured the restraining torque on the shroud by measuring the restraining force acting on a moment arm attached to the balance. The force transducer, with a 3 mV/V full scale sensitivity over a 500 gram range, used a 4 element strain-gage bridge on a bending member to determine the force applied to the moment arm.

The shroud was suspended in the correct position and orientation relative to the rotating disk stack on ball bearings with a contact diameter of approximately 1 mm (.040 in.), spaced 70 mm apart. Friction in these bearings was a limiting factor in the accuracy of the torque balance. When the speed of the drive was increased, the friction of the bearings acted in the same direction as the restraining torque, resulting in a reduced measured value of the shroud torque. When the drive speed was decreased, the bearing friction torque opposed the restraining torque, giving a measured value equal to the combined total of the shroud torque and the bearing friction torque. This hysteresis was found to be approximately 0.1 Newton-millimeters (N·mm).

Preliminary results suggested that the manufacturer's calibration of the transducer was insufficient to ensure accurate readings, therefore a calibration procedure was implemented. A calibration balance, which transmitted the vertical gravitational force acting on a weight to a horizontal force, provided a moment on the torque balance. The calibration procedure involved placing known weights on the calibration balance and measuring the force transducer output after the system had reached its equilibrium position. A typical calibration would show a linear relationship between applied torque and measured output voltage over the range 0–18 N·mm with a standard deviation of less than 0.05 N·mm for 18 calibration points.

The data acquisition system consisted of the following main components: a Fluke 2400B data logger with a high performance A/D converter with 1 microvolt precision for reading bridge excitation and bridge output voltages; a Fluke Helios datalogger with an analog output to set the motor speed and a counter/timer to measure rotational velocity (the motor was equipped with a 500 line per revolution optical shaft encoder); and finally, a microcomputer to coordinate the operation of the disk drive and data acquisition equipment.

During an experiment, the rotational velocity of the disk stack was set by ramping the driver board voltage to the appropriate value and then waiting 90 seconds to allow the apparatus to reach a steady rotational velocity. After this pause, the angular velocity was read by the counter/timer, recording the number of pulses from the shaft encoder over a period of .66 seconds. This was repeated twice at 5 second intervals. A variation in rotational velocity of more than 0.3 percent led to a reading being rejected.

Results

Torque measurements were made on the single disk and on a disk stack of 3 and 5 disks at nine test conditions consisting of the matrix of three gap aspect ratios (H/R of 0.195, 0.098, and 0.024 and three tip clearance ratios (a/R) of 0.015, 0.031, and 0.077. The results of the single disk studies are presented first and compared to the results of Daily and Nece (1960). The multiple disk torque measurements follow, leading to a general result for multiple disk configurations.

A portion of the experimental matrix was repeated with arms obstructing the flow. For 1 and 3 disks in a stack, torque measurements were made for arms positioned at $R^* = 0.54$, 0.74, and 0.93, where $R^* = R_{arm}/R_{disk}$. Tests were conducted for two arm blockage ratios ($B = h/H$) of 0.25 and 0.50 with a gap aspect ratio of $H/R = 0.195$. A gap ratio of $H/R = 0.098$ was also tested for the arm blockage ratio of 0.50.

All data are reported in the form of moment coefficients, C_m, as a function of Reynolds number, Re, where

$$\mathrm{Re} = \omega R_{disk}^2/\nu \tag{1}$$

and

$$C_m = \frac{T}{1/2\rho\omega^2 R_{disk}^5} \tag{2}$$

Uncertainty. The dominant uncertainty in the torque measurements arose as a result of the hysteresis in the torque balance due to bearing friction. The uncertainty was approximately constant throughout the experiments and was estimated to be ± 0.1 N·mm. This was determined from repeated tests with the speed increasing and then decreasing. This absolute level of uncertainty led to large relative uncertainties in the torque measurements at rotational velocities less than 3000 rpm. For this reason, the correlations presented in this paper will be based on the data measured at rotational velocities greater than 3000 rpm.

Single Disk. Figure 3 presents the torque measurements for the case of gap ratio of $H/R = 0.098$ and tip clearance of $a/R = 0.015$, compared with the correlations presented by Daily and Nece (1960) for their case of $H/R = 0.115$. The present data cover the Reynolds number range over which Daily and Nece observed a transition between laminar flow with separate boundary layers on each surface (Regime II) and turbulent, separate boundary layers (Regime IV). At high Reynolds numbers ($\mathrm{Re} \geq 80{,}000$), our measurements match Daily and Nece within 7 percent; however at low Reynolds numbers our measurements are significantly higher than those of Daily and Nece. In fact, as is shown by the dashed line in Fig. 4, the present data follow a Re^{-1} trend for $\mathrm{Re} \leq 40{,}000$, corresponding to laminar merged boundary layers (Regime I), rather than the $\mathrm{Re}^{-1/2}$ trend Daily and Nece observed (Regime II).

The discrepancies between the experimental results of Daily and Nece (1960) and our study may be attributed to geometric differences between the two experimental apparatuses. Daily and Nece had a tip clearance ratio (a/R) of 0.00637, which is significantly smaller than the 0.015 value of the present study. In addition, the ratio of hub to disk diameter is 0.39 for the present study, while Daily and Nece's ratio is 0.10. The greater blockage in the gap between the disk and housing caused by the larger diameter hub should influence the boundary layer development, and hence, the sensitivity of moment coefficient to Reynolds number.

The single disk experiments were repeated with larger tip clearance ratios of $a/R = 0.031$ and 0.077. Increasing the clearance between the single disk and the shroud increased torque a very slight amount. For $H/R = 0.024$ and 0.097, increasing a/R from 0.015 to 0.077 increased the moment

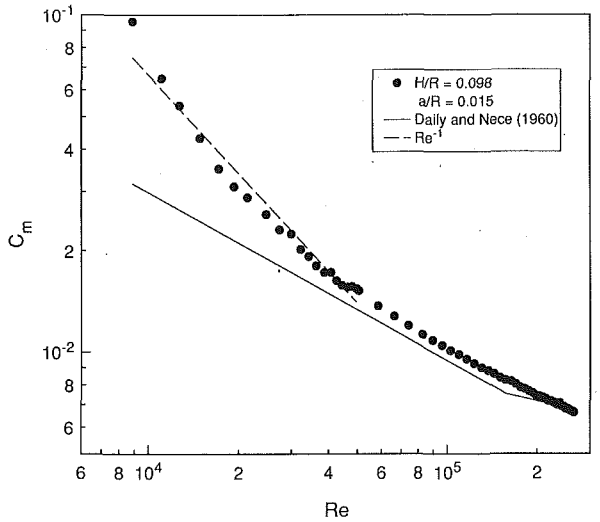

Fig. 3 Moment coefficient as a function of Reynolds number for the single disk. (Uncertainty at Re = 80,000 in $C_m = \pm 1.3 \cdot 10^{-3}$, in Re = ±240 and at Re = 280,000 in $C_m = \pm 1.1 \cdot 10^{-4}$, in Re = ±840.)

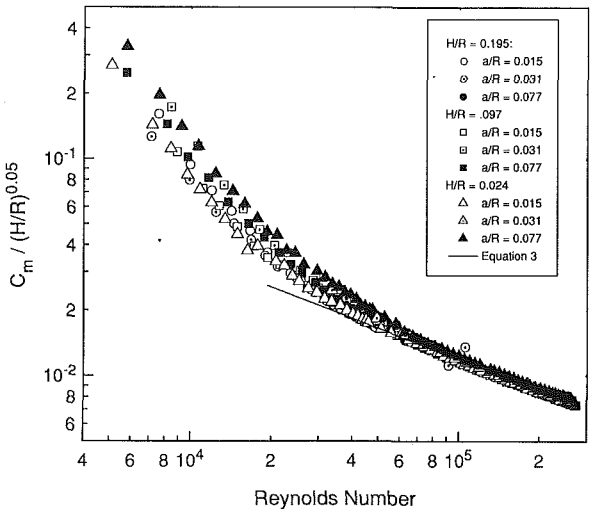

Fig. 4 Moment coefficient data and correlation for the single disk as a function of Reynolds number. (Uncertainty at Re = 80,000 in $C_m = \pm 1.3 \cdot 10^{-3}$, in Re = ±240 and at Re = 280,000 in $C_m = \pm 1.1 \cdot 10^{-4}$, in Re = ±840.)

coefficient by 2 to 3 percent, while the effect is less than one percent in the case where $H/R = 0.195$.

All moment coefficient data for the single disk collapse at high Reynolds numbers if they are scaled by $(H/R)^{0.05}$, as shown in Fig. 4. For Re ≥ 80,000, which is the range of most accurate data measurements, the moment coefficient varies logarithmically with Reynolds number. Neglecting the effects of tip clearance ratio, which was shown above to be a small effect, a correlation was developed for moment coefficient in this Reynolds number range.

$$C_m = 2.83\mathrm{Re}^{-.48}(H/R)^{.05} \tag{3}$$

This correlation fits the data for 80,000 ≤ Re ≤ 280,000 with a standard deviation of 2 percent.

Multiple Disks. The total torque on a stack of N disks is due to the frictional resistance generated by the air in the two shear gaps (i.e., the gaps between the shroud and the top and bottom disks) as well as by the air in the (*N*-1) gaps between corotating disks. If we neglect any interactions between the corotating gaps and the shear gaps, the torque generated by each corotating gap, T_{gap}, can be found by subtracting the torque of the single disk case (which has only shear gaps) from a multiple disk case and dividing by the number of corotating gaps.

This procedure was applied to both the 3 and 5 disk-stack data, and in all cases, the same gap-torque was calculated within experimental uncertainty. The results presented for gap torque are based on the 5-disk-stack case;

$$T_{gap} = (T_5 - T_1)/4 \tag{4}$$

since this case should have the lower experimental uncertainty. Typical corotating gap torques are approximately one half the magnitude of the single disk torque.

The moment coefficient based on gap torque ($C_{m\ gap}$) was calculated as a function of Reynolds number for all gap aspect ratios and tip clearance ratios tested. Figure 5 shows the results and a correlation over the valid Reynolds number range of 80,000 ≤ Re ≤ 280,000

$$C_{m\ gap} = 0.46\mathrm{Re}^{-.35}(H/R)^{0.5}(a/R)^{-0.07} \tag{5}$$

(The data for $H/R = 0.024$ and $a/R = 0.077$ were not used in defining the correlation due to probable experimental errors.) Note the larger coefficient on H/R in Eq. (5) (0.5) compared to Eq. (3) for the single disk case (0.05). This indicates

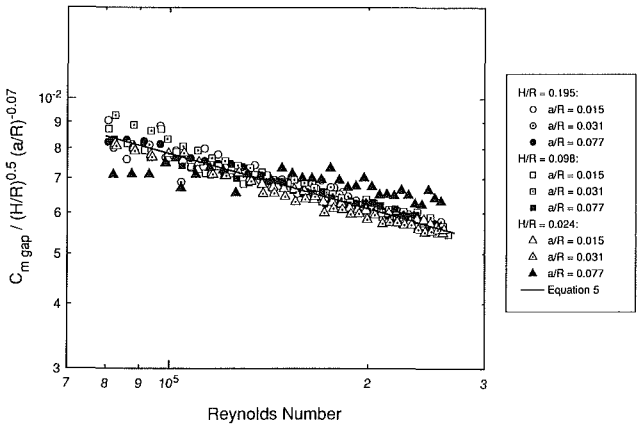

Fig. 5 Gap moment coefficient data and correlation as a function of Reynolds number. (Uncertainty at Re = 80,000 in $C_m = \pm 1.3 \cdot 10^{-3}$, in Re = ±240 and at Re = 280,000 in $C_m = \pm 1.1 \cdot 10^{-4}$, in Re = ±840.)

a greater sensitivity of the corotating gap torque to gap aspect ratio compared to the shear-flow gaps of the single disk case.

Equation (5) also shows a sensitivity to tip clearance, which was neglected in the correlation for the single disk. For the two largest gap spacings, $H/R = 0.195$ and 0.097, the effect of increasing the tip clearance from $a/R = 0.015$ to 0.077 is to decrease the gap torque by 10 percent. This effect is not as distinct in the smallest axial spacing case ($H/R = 0.024$) due to the greater sensitivity to experimental uncertainties at the lower magnitudes of moment coefficient. It should be noted that this trend for torque as a function of tip clearance encountered in the corotating gap flow is opposite to that seen in the single disk case, where increases in gap clearance led to small increases in gap torque. This is a subtle effect, and is observed at the limit of the uncertainty of our measurements for the single disk cases.

The torque on multiple disk stacks of *N* disks can be calculated by combining the moment coefficients for the single disk case and for the corotating gaps:

$$C_{m\ total} = C_{m\ single\ disk} + (N-1)C_{m\ gap} \tag{6}$$

Obstructed Disk Flow. The protrusion of read/write arms into the gaps between rotating disks will increase the torque

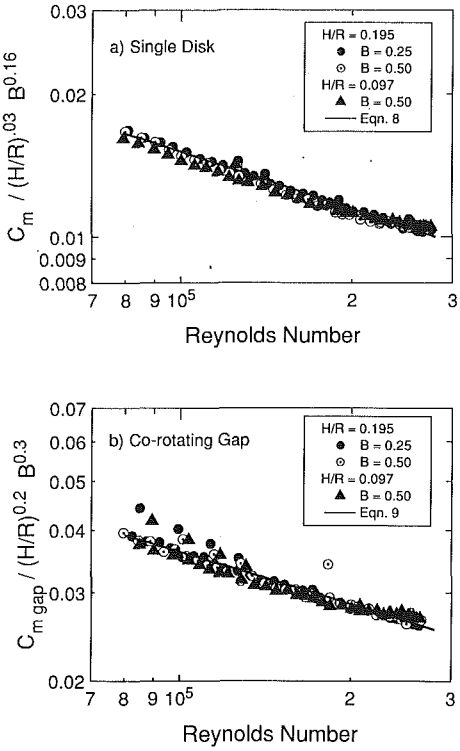

Fig. 6 Data and correlation for fully obstructed gaps (R* = 0.54); (*a*) Single disk moment coefficients; (*b*) Gap moment coefficients. (Uncertainty at Re = 80,000 in $C_m = \pm 1.3 \cdot 10^{-3}$, in Re = ±240 and at Re = 280,000 in $C_m = \pm 1.1 \cdot 10^{-4}$, in Re = ±840.)

of the system due to the frictional and pressure forces acting on the arms, as well as by changes in the flow patterns that alter the shear forces acting on the disk surfaces. Torque measurements were obtained with and without arms present in a 1 and 3 disk stack with a gap ratio of 0.195 and a tip clearance ratio of 0.015. The arm blockage ratio, B, was 0.5. Torque was measured at three arm positions: $R^* = 0.93$ (outermost position), $R^* = 0.74$ and $R^* = 0.54$ (innermost position). For the single disk rotating at 9400 rpm, the torque increased by 7, 16, and 24 percent over the unobstructed value when arms were present at $R^* = 0.93$, 0.74, and 0.54, respectively. The stack of 3 disks was more sensitive to the presence of the arms since its torque at 9400 rpm increased by 20, 58, and 82 percent as the arms were moved inward.

The greater sensitivity of the multiple disk stack to the presence of the arms suggest that the contributions to the total torque by the corotating gaps is significantly altered by the obstructions. Gap torque calculations, in this case defined as:

$$T_{gap} = (T_3 - T_1)/2 \tag{7}$$

show that the corotating gap torque approaches that of the single disk as the arms protrude into the gap. The ratio of corotating gap torque to single disk (shear-flow gap) torque increases from 0.45 in the unobstructed case to 0.89 in the case where $R^* = 0.54$.

The torque moment results for the fully obstructed case, i.e., when the arm is fully inserted into the gap ($R^* = 0.54$), are shown in Fig. 6(*a*) and 6(*b*) for a single disk and for the corotating gap, respectively. For the single disk in the fully obstructed configuration, the data correlation is

$$C_m = 1.51 \mathrm{Re}^{-.40} (H/R)^{.03} B^{.16} \tag{8}$$

and for a corotating gap,

$$C_{m\ gap} = 1.95 \mathrm{Re}^{-.35} (H/R)^{.2} B^{.3} \tag{9}$$

(Note that these correlations reflect estimates of the dependence of moment coefficients on H/R and B since only two values of aspect ratio and blockage were tested for the fully obstructed case.)

The effect of aspect ratio (H/R) on torque seems to be weaker in the fully obstructed cases (where $R^* = 0.54$) than in the unobstructed cases, as evidenced by the smaller coefficients on H/R in Eqs. (8) and (9) compared to Eqs. (3) and (5) that represent the unobstructed data. Also note that the effect of the blockage ratio is more pronounced than that of aspect ratio, for both the single and corotating cases.

For multiple disk configurations, Eq. (6) can be used to compute the total torque. Agreement between the multiple disk torque data and the torque predicted using Eqs. (6), (8), and (9) is within 2.3 percent.

The torque experienced by a disk stack with arms at intermediate positions can be estimated once the torque is known for the unobstructed and the fully obstructed cases. A composite torque (T_{comp}) can be estimated by assuming 1) the region of the disk adjacent to the arm is subjected to the same shear stresses as in the fully obstructed case; and 2) the region of the disk where $r < R_{arm}$ is subjected to the same shear stress as in the unobstructed case. The resulting expression for moment coefficient of a disk stack with arms protruding a distance R^* into the stack is:

$$C_{m\ comp} = C_{m\ unobstructed} (R^*)^4 + C_{m\ obstructed} (1 - (R^*)^4) \tag{10}$$

where $C_{m\ unobstructed}$ is the moment coefficient of the stack of disks without arms present, estimated using Eqs. (3), (5), and (6), and $C_{m\ obstructed}$ is the moment coefficient of the stack of disks with arms present, estimated using Eqs. (8), (9) and (6). (For details of the derivation of Eq. (10), see Hudson, 1989).

Comparison of the intermediate arm position data with the composite moment coefficients calculated in the manner described above shows a standard deviation of 2.6 percent and average error of less than 0.5 percent at the intermediate arm positions, suggesting that combining the unobstructed and fully obstructed data in this manner is adequate to describe the results within experimental uncertainty.

Viscous Dissipation. Once the torque of a disk stack is known, the total viscous dissipation that occurs within its housing can be determined. The power required to rotate the disks compensates for the viscous losses of the air, which are dissipated as heat. Total viscous dissipation is found from

$$P_d = T_{tot} \omega \tag{11}$$

where T_{tot} is the total torque for the disk drive.

For the four-disk configuration studied by Eibeck et al. (1989), calculations based on the correlations in the present paper reveal total viscous dissipation of 0.4 W for a speed of 1850 rpm and 2.9 W for a speed of 4000 rpm. Based on measurements by Eibeck et al. (1989) of the total power input to the disk-drive, which is all eventually dissipated as heat in one form or another, the viscous dissipation accounts for only 5 percent of the total thermal load for 1850 rpm and for 30 percent of the total thermal load for 4000 rpm. The greater importance of viscous dissipation at higher speeds demonstrates the need for accurate predictions of dissipation.

Summary

Shroud torque measurements were made in a simulated disk drive consisting of a single and multiple corotating disk stacks enclosed in an axisymmetric housing. The effects of rotational rate, axial and radial spacing, and the position and thickness of simulated read/write arms between disks were evaluated. Correlations were developed based on the experimental data for disk Reynolds numbers between 80,000 and 280,000.

The results indicated the following trends:

1. For a single disk without arms present, the correlation for moment coefficient is:

$$C_m = 2.83\mathrm{Re}^{-.48}(H/R)^{.05} \quad (12)$$

2. The moment coefficient generated within a single corotating gap in a stack of multiple corotating disks without arms present is:

$$C_{m\ \mathrm{gap}} = 0.46\mathrm{Re}^{-.35}(H/R)^{0.5}(a/R)^{-0.07} \quad (13)$$

3. For the single rotating disk with a read/write arm in the fully obstructed position, the moment coefficient correlation is:

$$C_m = 1.51\mathrm{Re}^{-.40}(H/R)^{.03}B^{.16} \quad (14)$$

4. For a corotating gap in a stack of disks with a read/write arm at the fully obstructed position, the moment coefficient correlation is:

$$C_{m\ \mathrm{gap}} = 1.95\mathrm{Re}^{-.35}(H/R)^{.2}B^{.3} \quad (15)$$

Relationships are presented to estimate the total moment coefficient and viscous dissipation for multiple disk stacks with read/write arms present and with arms at any radial position, based on these correlations.

Acknowledgments

The authors would like to thank IBM Almaden Research Center for their generous support of this research (Grant #811412). We would also like to thank Dr. Donald Wroblewski for his valuable technical assistance in preparation of this manuscript.

References

Chang, C. J., Schuler, C. A., Humphrey, J. A. C., and Greif, R., 1988, "Flow and Heat Transfer in the Space Between Two Co-rotating Disks in an Axisymmetric Enclosure," ASME *Journal of Heat Transfer*, Vol. 111, pp. 625–632.

Daily, J. W., and Nece, R. E., 1960, "Chamber Dimension Effects on Induced Flow and Frictional Resistance of Enclosed Rotating Disks," ASME *Journal of Basic Eng.*, Mar., pp. 217–232.

Eibeck, P. A., Clauss, N. S., and Cohen, D. J., 1989, "Prediction of Temperature Distributions and Thermal Expansions Within a Fixed Disk-Drive Storage System," ASME *Journal of Electronics Packaging*, Vol. 111, No. 3, pp. 220–227.

Judge, A. W., 1955, *The Testing of High Speed Internal Combustion Engines*, 4th ed. rev., London, Chapman and Hall.

Hudson, A., 1989, "Viscous Dissipation in Co-rotating disks in an Axisymmetric Enclosure," Master's project report, Department of Mechanical Engineering, University of California, Berkeley.

Sato, I., Otani, K., Oguchi, S., and Hoshiya, K., 1988, "Characteristics of Heat Transfer in Helium Gas Enclosed Disk Enclosures," *Proceedings Intersociety Conference on Thermal Phenomena in Fabrication and Operation of Electronic Components*, Los Angeles, CA, pp. 142–146.

Torok, D., and Gronseth, R., 1988, "Flow and Thermal Fields in Channels Between Co-rotating Disks," *Proceedings Intersociety Conference on Thermal Phenomena in Fabrication and Operation of Electronic Components*, Los Angeles, CA, pp. 162–170.

Air Test Flow Analysis of the Hydrogen Pump of Vulcain Rocket Engine

F. Bario
Research Engineer CNRS,
Laboratoire de Mécanique des Fluides & d'Acoustique (UA CNRS 263),
Ecole Centrale de Lyon, F69131 Ecully Cedex, France

L. Barral
Project Engineer SEP,
Société Européenne de Propulsion, F27207 Vernon, France

G. Bois
Engineer METRAFLU,
Société pour la Mesure et le Traitement des Milieux Fluides, F69134 Ecully Cedex, France

Within the framework of the technological development of the VULCAIN rocket engine (Ariane V European project), initiated by the Centre National d'Etudes Spatiales (CNES) for the Agence Spatiale Européenne (ESA), the Société Européenne de Propulsion (SEP) is in charge of the design and building of the liquid hydrogen turbopump. In order to characterize the hydraulic performance of the pump, an air test facility reproducing the pump geometry was built by SEP and fitted in the Laboratoire de Mécanique des Fluides et d'Acoustique of the Ecole Centrale de Lyon. Benefits and disadvantages of air tests of hydraulic pumps are discussed. The pump is composed of three stages. The first one is an axial inducer stage. The second and third ones are centrifugal stages with vaned diffusers and are separated by a U bend and a vaned return channel. Results of the first measurement campaign are presented. They consist of overall pressure, wall static pressure and velocity measurements. Local quantities (velocity triangle, pressure) and mean quantities (pressure rise, losses, efficiency) are given. Recirculating and wake flow analysis are included. The goals of the study are the understanding of the flow behavior and the improvement of the prediction methods. Predicted and measured quantities (losses, efficiency, kinetic momentum) are compared. The hydrogen performances are deduced, they agree with the specified performances of the pump. This validation is one of the main results achieved.

Introduction

The Vulcain engine hydrogen pump input power is 11,000 Kw. The rotation speed is 34,000 rpm. The turbopump mass is 240 Kg. Liquid hydrogen inlet temperature is 21 K (Thevenot and Borromee, 1988). To test and improve the design of such a pump, a cheap and simple way is to use a specially designed air test facility. For similar reasons Gorton and Lakshminarayana (1980) have developed air measurements of a model of an SSME inducer. Detailed measurements have been obtained in the rotating frame of the blade channels, showing a complex flow pattern: strong developments of 3-D viscous flow were observed (Lakshminarayana, 1982). It is related to the inducer axial geometries associated with moderate specific speed values such as 0.9 generally applied to helicocentrifugal impellers.

The idea of testing hydraulic machinery on air is not new and can be credited to Prandtl. Comparison of air and hydraulic (LO_x, LH_2) test results made by authors such as King (1968) shows a good agreement.

In our experiment the whole pump has been tested with air. The main objective applying to pump air tests are the following.

- The Reynolds numbers are quite different: $Re_{LH2} \sim 200.Re_{air}$.

This is related to the large difference in kinematic viscosity of the LH_2 and air fluids ($\nu_{air}/\nu_{LH_2} = 95$). Therefore, Reynolds numbers for air and LH_2 cannot be matched between the LH_2 turbopump and air test rig. The rotational speed of the test rig was chosen large enough to ensure a weak dependence of the wall friction coefficient on Reynolds number.

- The fluid compression between air and LH_2 will be different: air outlet/inlet density ratio is 1.14 in air test conditions to compare with 1.06 in liquid hydrogen. So the viscous flows will be different with a tendency to stall more pronounced in air. For a given inlet pump flow coefficient the various pump components will operate at slightly different flow coefficients between air and LH_2.

Nevertheless the Vulcain hydrogen pump development logic was organized as follows:

- hydrogen and air flow computations (KATSANIS meridional through flow method and nondimensional energy loss model)
- air test facility design.
- computed and measured performances comparison in air and energy loss prediction models checking.
- water test facility design and inducer cavitation test run (Desclaux et al., 1988).
- cavitation model checking.
- hydrogen turbopump testing in LH_2.

Air test measurements have been used to validate the flow angle deviation and energy loss models. The hydrogen pump performances have then been estimated.

Contributed by the Fluids Engineering Division for publication in the JOURNAL OF FLUIDS ENGINEERING. Manuscript received by the Fluids Engineering Division May 15, 1989.

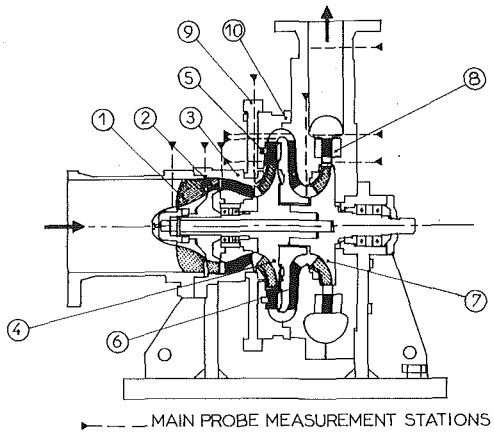

Fig. 1 Experimental setup

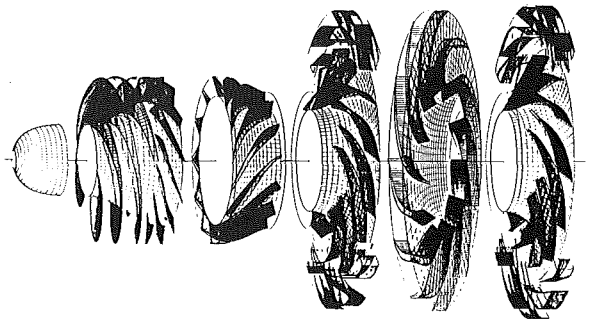

Fig. 2 Pump cut-away drawing

Experimental Set-Up

The experimental set-up for the three stage pump is shown in Fig. 1. The first axial stage is composed of a tandem blade row inducer (1, 2).[1] The stagger of the first inducer (1) with 4 unshrouded blades, relative to the second blade row (2) with 12 shrouded blades, can be changed to study its overall performance influence. The following stator (3) has 13 blades. The first centrifugal stage has a shrouded impeller (4) with 6 blades and 6 splitters, and a vaned diffuser (5) of 11 blades. It is followed by a 180 degree U-bend and a vaned return channel (6) of 11 blades. The last stage has a centrifugal shrouded impeller (7) similar to the first centrifugal stage one and a vaned diffuser (8) of 13 blades.

The stagger of the first centrifugal diffuser blades relatively to the return channel blades, and the stagger of the second centrifugal diffuser blades relatively to the volute tongue can be changed by rotating (5) and (8). One hundred static pressure measurements are possible. The number of probe locations is 25 (see Fig. 1). Probe measurements at different azimuthal locations at axial stator exit (3) can be done by rotating part (9). Similarly, probe measurements at the first centrifugal diffuser inlet and outlet can be done by rotating part (5) and (10) on which probe equipment is installed. A cut-away drawing of the pump is presented in Fig. 2.

Test Rig

The test rig is composed of an 18 Kw direct current electric motor fixed on a 1,800 Kg steel frame mounted on silent blocks. A gearbox of 3.5 velocity ratio and a torque/speed meter are connected to the motor. An electronic speed variator allows rotating speed control. The high speed shaft connected to the experimental set-up has a maximum speed of 10,800 rpm and is secured by calibrated shear-pins. The experimental set-up air intake is composed of a filter, a honeycomb structure, a convergent and a straight pipe. A Venturi flowmeter designed for nominal flow rate is placed on the exit line upstream of a needle-valve used to adjust the operating point. The air warmed in the set-up is ejected outside.

Table 1

MEASUREMENT	SENSOR	ACCURACY
V	3 or 5 hole probe	1%
Pt	"	0.5%
Ps	"	0.5%
wall static pressure Ps	pressure taps	0.5%
α, β	3 or 5 hole probe	± 0.5°
R		±0.0001m

Measurements and Data Acquisition

The test rig safety measurements are acquired and processed by a Hewlett Packard acquisition system and a microcomputer. Alarms and stop signals can be adjusted. A separate computer takes care of the data acquisition. Static pressure fields are acquired separately using a scanivalve system. Probe measurement is done semi-automatically for better acquisition in large gradient areas. Temperature, 3 hole pressure and 5 hole pressure probes are used to obtain an accurate flow picture. Typical data accuracy and measurement equipment are shown in Table 1.

[1] Numbers in parenthesis designate mechanical parts of the pump (see Fig. 1).

Nomenclature

C_p = static pressure coefficient
m_s = mass flow rate
P_s = static pressure
P_t = stagnation pressure
R = radius
Re = Reynolds number for inducer tip diameter $\mathrm{Re} = 2\,\omega R_t^2/\nu$
U = rotational speed $U = R\,\omega$
V = absolute velocity
Vu = tangential velocity ($\mathrm{sgn}(Vu) = \mathrm{sgn}(U)$)
W = relative velocity
α = absolute velocity angle relatively to meridional plan ($\mathrm{sgn}(\alpha) = \mathrm{sgn}(Vu)$)
β = relative velocity angle relatively to meridional plan ($\mathrm{sgn}(\beta) = \mathrm{sgn}(Vu - U)$)
$\Delta(\ )$ = for a difference
ϕ = mass flow coefficient at the pump inlet $\phi = \mathrm{ms}/\pi\rho_0\omega(R_t^2 - R_h^2)R_t$
ψ = stagnation pressure coefficient $\psi = \Delta P_T/\rho_0\omega^2 R_t^2$
η = isentropic efficiency
ρ = fluid density
ω = angular rotational speed
$\tilde{\omega}$ = loss coefficient $\tilde{\omega} = \Delta P_T/\frac{1}{2}\rho V^2$
ν = fluid kinematic viscosity

Subscripts

h = inducer hub
N = for nominal flow rate
t = inducer inlet tip
TH = for theoretical (computed) value
0 = upstream of the pump
1 = upstream of element
2 = downstream of element
( ) = mass averaged quantity.

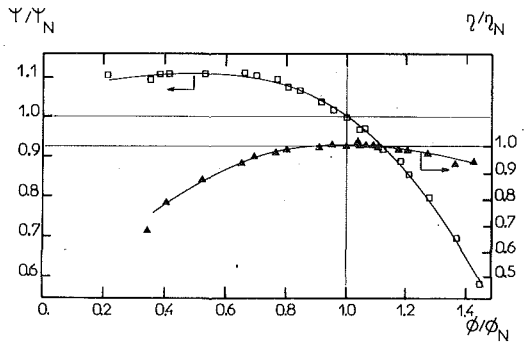

Fig. 3 Overall pump performance in air

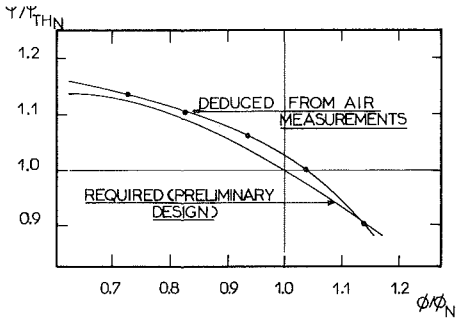

Fig. 4 Comparison between required and deduced from air test measurements LH_2 characteristics

Measurement Process

Measurements at each station are done with straight three hole probes fitted to near-shroud measurements, and with five hole cobra probes adapted to near-hub measurements. Reliability is demonstrated when measurements at mid-height with the two types of probes give the same values. The density is obtained by preliminary pressure and temperature measurements with a thermocouple probe. The mass flow rate was calculated from the probe measurements and was compared with the Venturi mass flow; this allows to decide the probe measurement validity.

Description and Analysis of Measurement Results

Pump Overall Quantities. The measured quantities are referred to nominal operating conditions with the subscript N in Fig. 3 or to theoretical nominal values with the subscript TH_N. Every parameter presented in Figs. 4, 5, 8(*b*), 10, and 11(*b*) are dimensionless in regard to a corresponding value calculated at nominal design conditions.

Air test stagnation pressure rise, mass flow characteristic are shown in Fig. 3. No hysteresis has been observed on the full measurement range. The head rise curve shows a continuous decrease with flow rate increase on the operating range from 0.7 to 1.1 ϕ_N.

Stability problems are not expected. Maximum pump isentropic efficiency is reached at the nominal flow rate condition (see Fig. 3). It has been deduced from stagnation temperature measurements.

LH_2 Pump Performance Prediction. The stagnation pressure characteristic is deduced for LH_2 from air test measurements applying the following method: The air density is calculated from pressure and temperature measurements at each pump element inlet and for different flow rates. The static pressure coefficient can then be obtained versus the flow coefficient for each pump element using wall static pressure measurements.

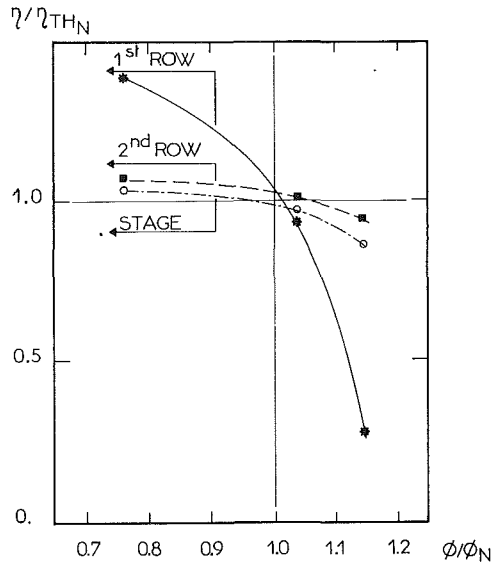

Fig. 5(*a*) First blade row, second blade row and stage efficiencies

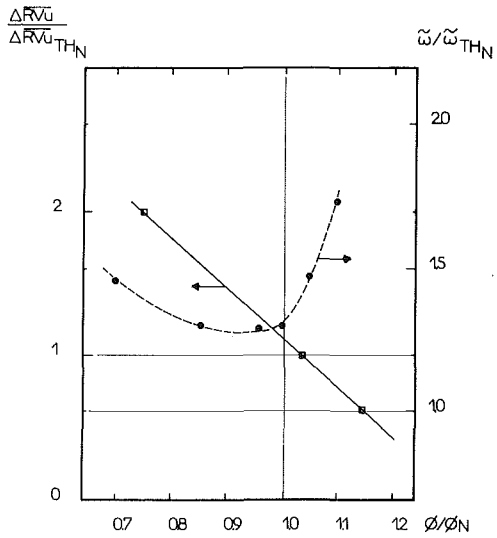

Fig. 5(*b*) Stator losses and kinetic momentum

Fig. 5 Inducer stage performance in air.

The LH_2 density is estimated using the meridional computation. The flow coefficient of each element operating in hydrogen is calculated for a given LH_2 mass flow rate. We compute the corresponding static pressure rise for air for every element assuming the dimensionless characteristic of each element is similar in air and LH_2. Then we use similarity laws and LH_2 density distribution to predict LH_2 static pressure rise for every element. The resulting overall stagnation pressure rise for a given LH_2 mass flow rate is the sum of the LH_2 static pressure rises and average exit velocity head rise.

The physical hypotheses of this method are mainly the following: the losses and deviation are not or weakly dependent on Reynolds number and the air and LH_2 compressibility effects are not so much different to induce strong differences in velocity distributions. The choice of the rotational speed has been made according to these two points.

It can be seen from Fig. 4 that the required performance will be reached in the operating range.

The comparison between test data and theoretical calculated values is in a good agreement from 0.7 to 1.1 ϕ_N. However, the measured characteristic becomes steeper as flow rate increases. This is related to the inducer behavior.

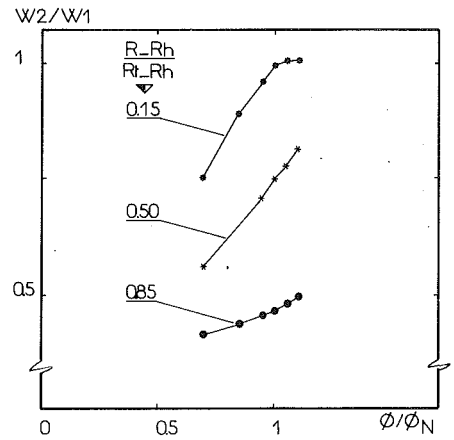

Fig. 6 Tandem inducer relative velocity deceleration (outlet/inlet relative velocity ratio (W_2/W_1)

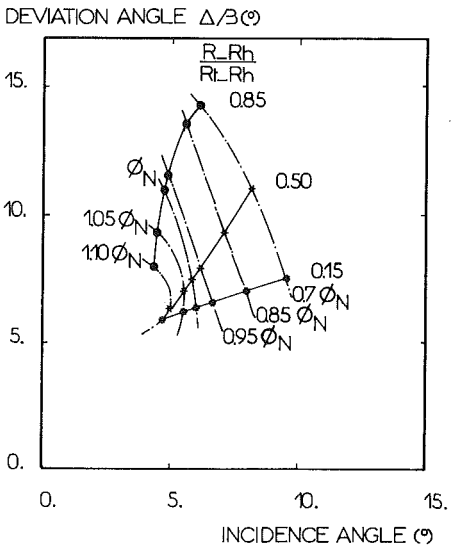

Fig. 7 Deviation angle at exit of tandem inducer versus incidence angle at leading edge

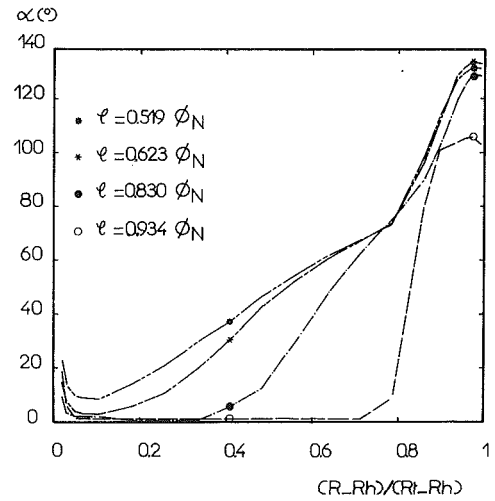

Fig. 8(*a*) Inducer probe measurements for various flow conditions. Inlet absolute angle measurements.

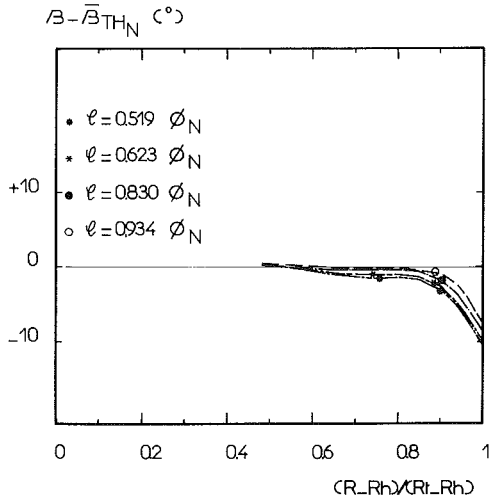

Fig. 8(*b*) Inducer probe measurements for various flow conditions. First blade row outlet relative angle

Inducer Overall Behavior. The tandem inducer overall performances are presented in Fig. 5.

The predicted performances are obtained with the help of a meridional and blade to blade inviscid method (KATSANIS) and a monodimensional energy loss model. The same method has been applied to the centrifugal stages. The first row, second row and tandem blade row efficiencies have been slightly under-estimated at nominal flow rate (Fig. 5(*a*)). The stator losses have been under-estimated (Fig. 5(*b*)). The resulting overall stage efficiency reaches the anticipated value. The strong decrease of the first row efficiency with increasing mass flow rate must be pointed out. The inducer first blade row is very sensitive to fluid incidence angle, blade loading decreasing strongly with increasing flow rate. It can be illustrated by the mean kinetic momentum $\Delta(\overline{R V_u})$ in Fig. 5(*b*). Besides, the first blade row has a large blade chord length leading to friction losses depending strongly on flow rate. The combination of reducing work and increasing energy loss brings an efficiency decrease with increasing flow rate.

Inducer Relative Velocity Analysis. The classical quasi three dimensional analysis of the flow used for axial pumps and compressors with short chord blades and high solidities is not sufficient to characterize the inducer blade channel flow. Nevertheless, we present the tandem inducer outlet/inlet velocity ratio W_2/W_1 in Fig. 6 as a function of flow coefficient. It can be seen that the W_2/W_1 ratio is larger at blade hub than near the tip and more sensitive to flow rate coefficient. This is related to the high blade loading at the periphery.

The outlet deviation angle $\Delta\beta_2$ is presented in Fig. 7 as a function of incidence angle $\Delta\beta_1$ for various radial locations. $\Delta\beta_2$ is a slip angle relatively to the second blade row pressure side exit. The incidence angle $\Delta\beta_1$ is the difference between the relative flow angle and the first blade row leading edge pressure side angle. It can be pointed out that blade tip incidence angles stay small and that deviation angles reach maximum values.

Inducer Detailed Flow Analysis. The analysis of the inducer inlet probe measurements shows evidence of an existing recirculation at the periphery for low flow rate. The absolute fluid angle α variation at the inducer first row inlet shows the occurrence of a recirculation in Fig. 8(*a*). Correlatively the static pressure measurements on the casing show the appearance of that recirculated flow at low flow rate. When the mass flow decreases, the static pressure immediately upstream of the inducer becomes higher than the upstream static pressure. The recirculation extends far upstream, the first static pressure tap being located more than one axial chord upstream of the leading edge (see Fig. 9). That higher pressure nearer to the inducer can be attributed to the centrifugal forces caused by the velocity tangential component.

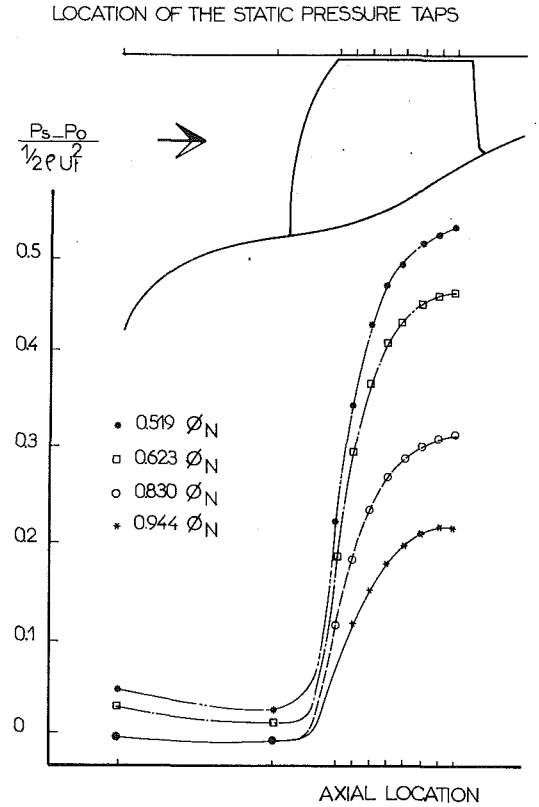

Fig. 9 Wall static pressure fields for the first inducer row

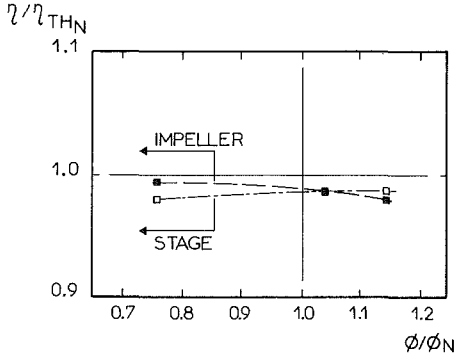

Fig. 10(*a*) Impeller and stage efficiencies

Between the two blade rows the relative angle measurements show no dependency on flow rate coefficient (see Fig. 8(*b*)).

First Centrifugal Stage Overall Behavior. The efficiencies at nominal mass flow rate have been slightly over-estimated for the impeller and for the whole stage as shown by Fig. 10(*a*). The centrifugal diffuser losses are well predicted at nominal flow rate (see Fig. 10(*b*)). The kinetic momentum rise from inlet to outlet of the impeller is slightly under-estimated (Fig. 10(*b*)).

Diffuser and U-Bend Detailed Flow Analysis. A complete picture of the loss distribution at the diffuser exit is given in Fig. 11(*a*) for the mass flow rate coefficient $\phi = 1.038\ \phi_N$. The probe measurements were realized at the exit of the diffuser at the same radius but with different azimuthal angles. A minimum of 7 probe measurements was necessary to build that blade to blade distribution. The blades, shown in Fig. 2, are thick, for this reason, there is an important curvature at the end of the pressure side. There exists a loss region near the pressure side, this is related to the trailing edge curvature which induces a decelerating flow at the pressure side. The local losses

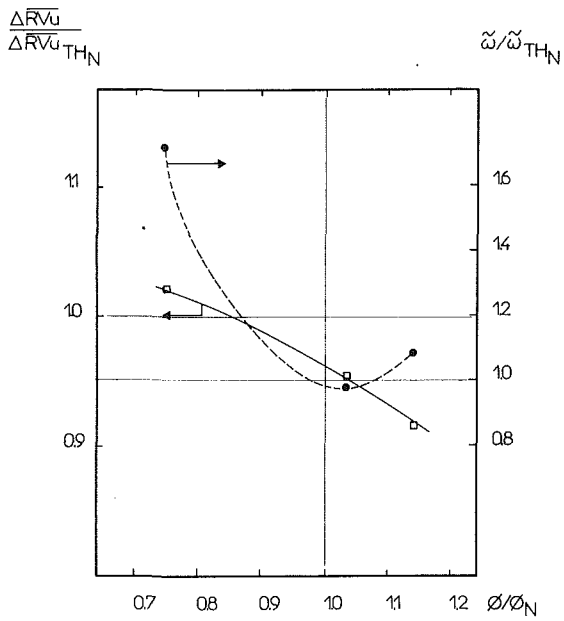

Fig. 10(*b*) Diffuser losses and kinetic momentum

Fig. 10 First centrifugal stage performance in air

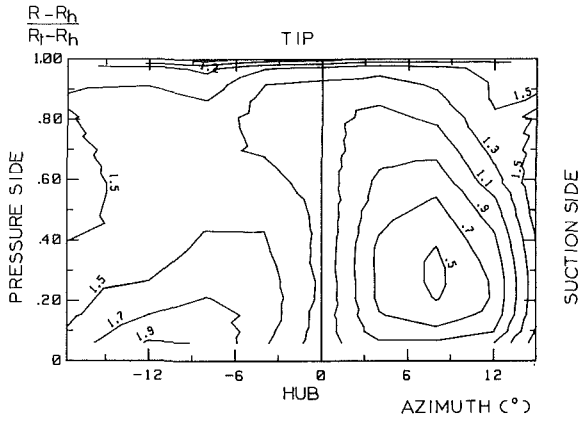

Fig. 11(*a*) Losses distribution $\tilde{\omega}/\bar{\tilde{\omega}}$ ($\bar{\tilde{\omega}}$ is the mean measured loss)

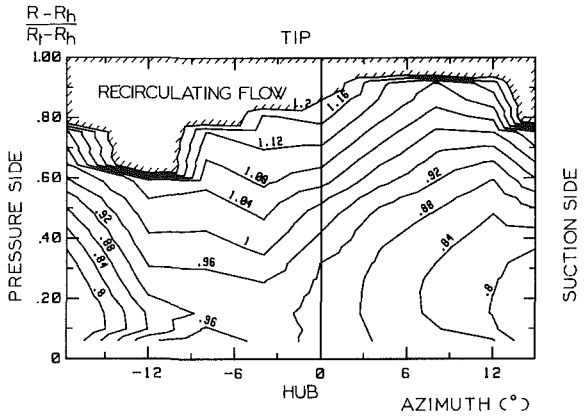

Fig. 11(*b*) Absolute angle distribution $\alpha/\overline{\alpha_{TH}}$

Fig. 11 Flow at the exit of the first diffuser at nominal flow rate

are divided by a mean diffuser loss averaged relatively to local mass flow. A low loss area is located near the blade exit suction side. Near the casing (shroud side) strong loss gradients are related to a recirculating flow region. The complete picture

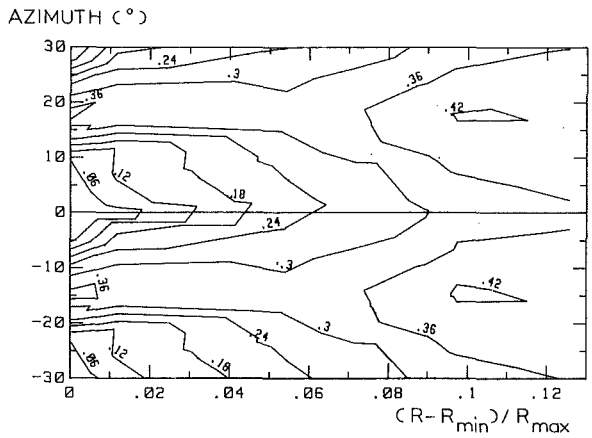

Fig. 12 Wall static pressure field in the U-bend behind the first centrifugal stage diffuser. Iso pressure coefficient C_p (two gaps). $C_p = P_s - P_{s\,mini}/ 1/2\,\rho\overline{V^2}$ ($P_{s\,mini}$ and $1/2\,\rho\overline{V^2}$ are the minimum static pressure and the mean dynamic pressure at the inducer exit radius R_{min}, R_{max} is the maximum radius of the U-bend wall)

acquired at the diffuser inlet by various azimuthal position probe measurements allows us to say that the recirculation observed has started inside the diffuser. No recirculation was observed at the impeller exit for this flow coefficient. Besides the energy loss distribution, the absolute angle distribution clearly brings into light the recirculating area (Fig. 11(*b*)).

In the vaneless diffuser part and in the U-bend channel the wall static pressure distribution is measured on the casing by rotating part (10) (equipped with 10 static pressure taps at various radii) relatively to the diffuser (5) for a minimum of 7 stagger angles. The picture obtained shows the existence of strong azimuthal gradients at the diffuser exit (Fig. 12). These gradients tend to disappear in the U-bend as the flow diffusion increases. It should result that no strong dependency of the vaned return channel performance with respect to the relative stagger angle of the diffuser (5) and the return channel blades (6) will be observed.

In other words, the diffuser exit wakes will not exist anymore at the return channel blade leading edge. These assumptions have been experimentally confirmed.

Conclusion

The measurements performed on an air test facility have been used to characterize the VULCAIN liquid hydrogen pump performance and flow picture. The head rise/mass flow rate characteristic does not show hysteresis in the full measurement range. The hydrogen pump performance calculated from air test results are in good agreement with the required performance. The head rise/flow rate characteristic trend is well predicted on the 0.7 to 1.1 ϕ_N operating flow coefficient range. Performance of the various components are generally well predicted at nominal mass flow rate. Nevertheless the measurements have shown the necessity to develop the effort initiated to understand the pump flow patterns, particularly in the inducer axial stage.

The first experimental results obtained at real conditions on the new SEP PF52 LH_2/LOX test rig confirm the good behavior of the turbopump in liquid hydrogen.

Acknowledgments

The authors wish to acknowledge the CNES and SEP for publication authorizations. The authors also wish to acknowledge the employees of METRAFLU and SEP who contributed to the development of the study. Grateful thanks to Ray Furst for helpful discussions and paper review.

References

Desclaux, J., Martignac, F., Bernard, R., and Rebattet, C., 1988, "Essais hydrauliques de l'inducteur hydrogène du moteur fusée VULCAIN," presented at Société Hydraulique de France, SHF Meeting, Paris.

Gorton, C. A., and Lakshminarayana, B., 1980, "Analytical and Experimental Study of Mean Flow and Turbulence Characteristics Inside the Passages of an Axial Flow Inducer," NASA contractor report 3333.

King, J. A., 1968, "Testing Pumps in Air," ASME *Journal of Engineering for Power*, Vol. 90, p. 97.

Lakshminarayana, B., 1982, "Fluid Dynamics of Inducers—A Review," ASME JOURNAL OF FLUIDS ENGINEERING, Vol. 104, pp. 411-427.

Thevenot, D., and Borromee, J., 1988, "Evolution des technologies et des méthodes de conception dans le développement du moteur VULCAIN," CNES/SEP contribution to the Ist symposium Europe in Space, Strasbourg.

LDV Measurements and Investigation of Flow Field Through Radial Turbine Guide Vanes

Hasan Eroglu

Widen Tabakoff

Department of Aerospace Engineering
and Engineering Mechanics,
University of Cincinnati,
Cincinnati, Ohio 45221

The results of LDV measurements and investigation of the detailed flow field in a radial inflow turbine nozzle are presented. The flow velocities were measured at upstream, inside and downstream of the nozzle blades for two different mass flow rates, using a three-component LDV system. Results are presented as contour plots of mean velocities, flow angles, and turbulence intensities. The flow field inside the nozzle blade passages was found to be influenced by the upstream scroll geometry. The flow turbulence increased in the downstream flow direction. The LDV mean flow results on the blade-to-blade midspan plane which is parallel to the end walls were also compared with an inviscid, "panel method" solution.

Introduction

In recent years, radial inflow turbines are finding a wide range of applications due to their ease of manufacture, low cost, and high efficiency. These benefits are especially evident at low Reynolds numbers. Some examples of these applications are turbochargers in automotive vehicles and gas turbines in aircraft and spacecraft auxiliary power units.

Recent efforts to improve the performance of radial inflow turbines concentrated on the development of computer programs to determine the flow field through various components (Choo and Civinskas, 1985; Hamed et al., 1978). Since the actual flow is three-dimensional in radial inflow turbines, and is complicated by the interaction between the scroll, nozzle and rotor, the need for reliable experimental data is of obvious importance. Tabakoff et al. (1983) obtained hot wire anemometer measurements in scrolls of different cross-sectional geometries that revealed the presence of two counter rotating vortices. Malak et al. (1986) measured the detailed flow field through a rectangular cross-section scroll using LDV. They observed only one vortex rather than the conventional two counter rotating vortices. The measured flow angle distribution at the scroll and nozzle exit displayed noticeable change especially in the vicinity of the jargon. The turbulence stresses were also measured and the results showed that the turbulence is anisotropic. Khalil et al. (1976) presented maps of the measured total pressure, Mach number and flow angles at the inlet and exit of a radial inflow vaned nozzle using wedge type pressure probes. The results were used to develop a theoretical model for loss prediction in both the vaned and the vaneless regions of the nozzle. The experimental results showed strong end wall cross flows and significant losses. Large mixing effects were observed at the exit of the nozzle. Hashemi et al. (1984) presented the results of total and static pressure measurements using conventional pressure probes at three radii downstream of the radial nozzle cascades. They also conducted flow visualizations in the air and water test rigs. These flow visualizations show that the radial turbine nozzles have different secondary flows from the axial flow turbine cascades because of the radial pressure gradients and the incidence effects. Although they show the existence of the leading edge vortices, the passage vortices are either too weak or they do not exist. The shape of leading edge vortices depends strongly on the incidence angle.

More extensive measurements are still needed in the radial turbine guide vanes, to provide a better understanding of the evolution of the three-dimensional flow and to serve as data base for validating the three-dimensional flow solutions. The errors introduced by the measuring probes can be significant inside the radial turbine guide vanes because of the small flow passages, and their correction is very difficult due to the high velocity gradients in the proximity of the walls. The noninstrusive, LDV and other laser velocimetry measuring techniques avoid these difficulties.

This paper presents the results of an experimental study conducted to obtain 3-D flow measurements through the guide vanes of a radial inflow turbine using a three-component LDV system. The same test rig, whose scroll flow field was investigated by Malak et al. (1986) was used at the same test conditions for the experiments. LDV measurements were obtained at five stations which are upstream, inside the blade passage and downstream of the cascade. Data were presented as contour plots of mean velocity, flow angle and turbulence intensity. LDV measurements were repeated upstream and downstream of the cascade at a higher mass flow rate. The experimental mean flow results on the blade-to-blade midspan

Contributed by the Fluids Engineering Division for publication in the JOURNAL OF FLUIDS ENGINEERING. Manuscript received by the Fluids Engineering Division August 25, 1989.

plane which is parallel to the end walls were compared with the inviscid, "panel method" solution to reveal the three-dimensional and viscous effects.

Experimental Configuration

The experimental configuration is shown schematically in Fig. 1. It consists of the test turbine, the seeding particle atomizer, the LDV optical and data acquisition systems.

Test Rig. Figure 2 shows the schematic of the experimental turbine. The turbine scroll has a cross-sectional area/radius ratio of 38.69 mm at the inlet. This value varies to 30.1, 17.14, 8.71, and 0 mm as the circumferential angle ϕ shown in Fig. 2 changes to 90, 180, 270, and 360 degrees, respectively. The scroll has an initial height/width ratio of 0.964. This value gradually increases and the height/width ratio reaches 1.105 maximum. It then decreases to 0.878 at $\phi = 315$ deg. Therefore, the scroll has nearly a square cross-section over most of the circumference. It is also unsymmetric, since the flow leaves the scroll through a flow channel located at one corner of the cross section as shown in Fig. 2. The details of the scroll geometry can be found in reference by Malak et al. (1986). The unsymmetric scroll cross-section location relative to the nozzle is such that one side of the square cross-section lines up with one of the nozzle end walls. This wall is made of 6.35 mm (0.25 in.), thick plexiglass, through which the LDV measurements were obtained. The nozzle end walls are parallel and are 12.7 mm (0.5 in.) apart. The outer radius of the nozzle is 137.3 mm (5.41 in.) with a vaneless region followed by nozzle vanes between 112 mm (4.41 in.) and 85 mm (3.35 in.) radii. There are eighteen slightly cambered nozzle vanes. The vane chord length is 50 mm (1.97 in.). The solidity based on the pitch at the trailing edge is 1.685, and the aspect ratio is 0.254.

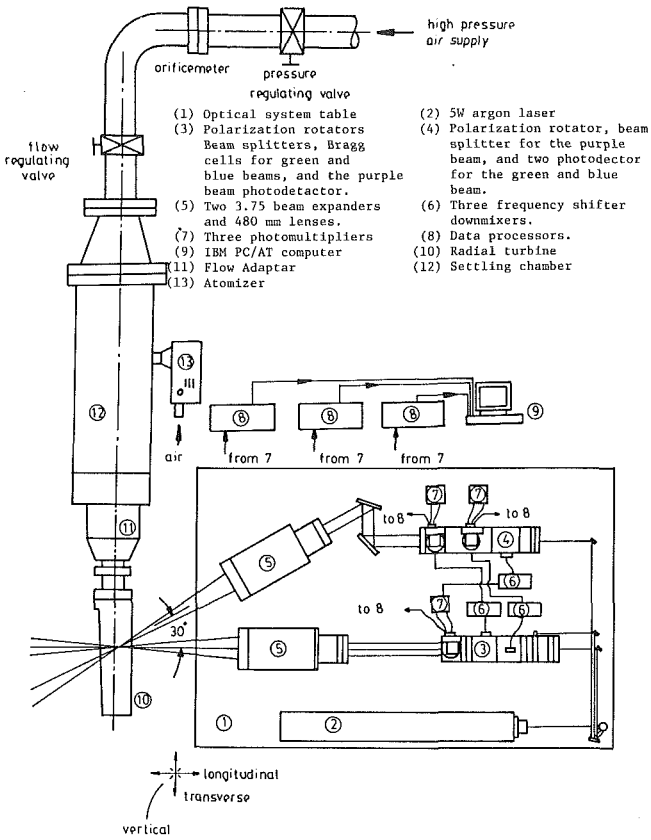

Fig. 1 Schematic showing the test rig and LDV system

Nomenclature

A = flow area
c = blade chord length
c_p = pressure coefficient $\left(\frac{p-p_1}{\frac{1}{2}\rho V_1^2}\right)$
c_r = radial chord length
g = gravitational acceleration in m/s^2
h = blade height
H = turbine specific work in m
k = turbulence intensity
$\dot{m}$ = mass flow rate
N = sample size, number of blades
N_s = specific speed $\left(\frac{\Omega\sqrt{Q}}{(gH)^{3/4}}\right)$
p = static pressure
Q = volume flow rate in m^2/s
r = radius
s = blade pitch at the exit
s_W^2 = variance of the on-axis velocity component
s_{VB}^2 = variance of the transverse (blue) velocity component
s_{VG}^2 = variance of the vertical (green) velocity component
s_{vp}^2 = variance of the inclined (purple) velocity component
U, V, W = transverse (blue), vertical (green) and on-axis velocity components
V = total velocity
V_B, V_G, V_P = transverse (blue), vertical (green) and inclined (purple) velocity components
V_{ex} = passage averaged exit velocity
V_r = resultant velocity of Fig. 5 on the horizontal plane
z = axial direction
β = flow angle with respect to circumferential direction on the blade-to-blade plane
γ = angle between the velocity vector and blade-to-blade plane
ΔU = measurement uncertainty of velocity component, U
ΔV = measurement uncertainty of velocity component, V
ΔW = measurement uncertainty of velocity component, W
λ = wavelength of LDV beams
Ω = rotor angular speed in radians/s
θ = angle between two optical trains of 3-D LDV system
ψ = loading coefficient $\left(\frac{H_g}{\Omega^2 r_1^2}\right)$
ϕ = flow coefficient $\left(\frac{Q}{A_1 \Omega r_1}\right)$

Subscripts

B, G, p = blue, green and purple colors
ex = exit
m = meridional direction
r = radial direction, resultant on horizontal plane
ϕ = circumferential direction
R = resultant on blade-to-blade plane
TE = trailing edge
1,2 = refer to inlet and exit conditions

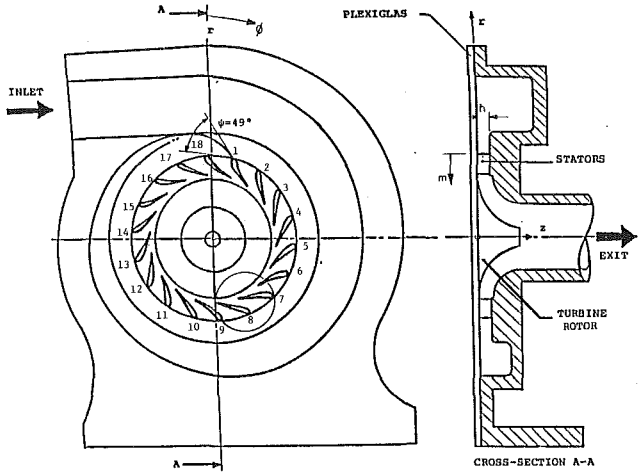

Fig. 2 Schematic showing the experimental turbine configuration

The geometric characteristics of the passage are summarized in Table 1. The rotor was not using during the tests, but instead, an aluminum body of revolution was installed to provide a smooth, continuous flow path downstream of the nozzle. The rotor will be included in the future measurement of this experimental program, and the effect of rotor on the nozzle flow field will be investigated by comparing the future results with the results of this paper.

The nondimensional specific speed (N_s), loading coefficient (ψ) and flow coefficient (ϕ) are estimated to be 0.069, 4.78, and 0.072, respectively for an assumed rotor rpm of 10,000, although the rotor was not installed during the experiments. These conditions correspond to a much lower flow rate, rpm and turbine inlet temperature as compared to those in practical applications. However, the present study focuses on the understanding of some of the fundamental flow mechanisms rather than a detailed loss and performance analysis at design conditions.

Flow Seeding. A TSI six-jet atomizer was used to seed the flow with two micrometers mean diameter propylene glycol particles at 10^5 Particles/cm^3. The atomizer was connected to the bottom of the settling chamber through a 31.75 mm (1.25 in.) flexible tube as shown in Fig. 1.

Laser and Optics. The three component LDV system used to measure the velocity of the flow through the nozzle vanes is shown in Fig. 1. A five Watt argon-ion Spectra Physics, model 164-09 laser was used as the light source. The laser beam leaving the tube is separated into components with different wavelengths in the dispersion prism. The first three beams with the highest intensity are used to measure the three velocity components. These beams have 0.5145, 0.488 and 0.4765 micrometer wavelengths and correspondingly, green, blue, and purple colors. The first two are sent through the optical train in the axial direction, while the third beam passes through a second train whose beam expander and focusing lens were inclined 30 degrees to the axial direction. Each beam is polarized through the polarization rotator and split into two equal intensity components at the beam splitter. The six beams cross at one common measuring volume, with three sets of fringes for the three different colors. The blue and the green colors are used to measure two orthogonal velocity components in the plane perpendicular to the optical axis. The purple color is used to obtain a nonorthogonal velocity component out of this plane. The scattered light from the particles in the measuring volume is collected in the off-axis backward scatter mode to decrease wall flare. Frequency shifters are placed between

Table 1 Passage geometry

Inlet radius	112 mm (4.41 in.)
Exit radius	85 mm (3.35 in.)
Chord length, c	50 mm (1.97 in.)
Radial chord length, c_r	27 mm (1.06 in.)
Blade height, h	12.7 mm (0.50 in.)
Pitch (in degrees)	20°
Solidity, c/s (based on exit pitch length)	1.685
Aspect ratio, h/c	0.254
Leading edge radius	2.59 mm (0.102 in.)
Trailing edge radius	0.813 mm (0.032 in.)
Number of blades, N	18
Inlet blade angle with tangential, β_1	80°
Exit blade angle with tangential, β_2	11°

Table 2 LDV characteristics

	Purple	Blue	Green
Wavelength, λ (μm)	0.4765	0.488	0.5145
Fringe Spacing (μm)	2.784	2.851	3.0
Diameter of measuring volume at e^{-2} intensity location (mm)	0.052	0.053	0.056
Length of measuring volume at e^{-2} intensity location (mm)	0.603	0.617	0.651
Number of stationary fringes	19	19	19

the beam splitters and the collecting optics to reduce fringe bias and to determine the flow direction. The beam expanders reduce the measuring volume diameter 3.75 times, and therefore considerably increase the spatial resolution. They improve the signal-to-noise ratio 50 times. The focal length of the transmitting lenses is 480 mm. The crossing angle for the 1.5 mm diameter beams if 9.82 degrees. The characteristics of the LDV optics are listed in Table 2. Further information on various components of the LDV system can be found in TSI manuals.

The laser and optical systems for the three component LDV were mounted on a milling machine table which can traverse 254 mm (10 in.) in the axial, 457.2 mm (18 in.) in the transverse and 558.8 mm (22 in.) in the vertical directions.

Data Acquisition System. The LDV photodetector signals are processed in three TSI 1990 counter type signal processors. The processed data is transferred to an IBM PC/AT compatible computer for further processing and data storage. In order to achieve the data transfer to the computer, a Metrabyte model CTM-05 counter-timer interface and three model PI012, 24 bit parallel digital I/O (Input/Output) interfaces were installed in the computer. The digital outputs of the three processors were connected to the PI012 I/O boards through 37 pin D type connectors and flat cables. To provide the control of the data transfer, and the coincidence of data coming from three different channels, an external circuit was designed, manufactured and incorporated into the data acquisition system. A data acquisition program was developed in the Pascal language. This program utilizes the subroutines of the Quinn Curtis software package. "Turbo Pascal Data Acquisition and Control Tools for Metrabyte."

Measuring Locations and Test Conditions. The LDV measurements were obtained mostly in the flow passage encircled in Fig. 2, where the blockage of the laser beam is minimum. Figure 3 shows the passage geometry at a larger scale where the limiting vanes have leading edges at 135 and 155 degrees, respectively, from the vertical in the clockwise direction. The five measurement stations are also shown in the same figure. They are located at 124 mm (4.88 in.), 110 mm (4.33 in.), 102 mm (4.01 in.), 90 mm (3.54 in.), and 83 mm (3.26 in.) radii from upstream to downstream. The first and fifth stations extend to the upstream and downstream of the

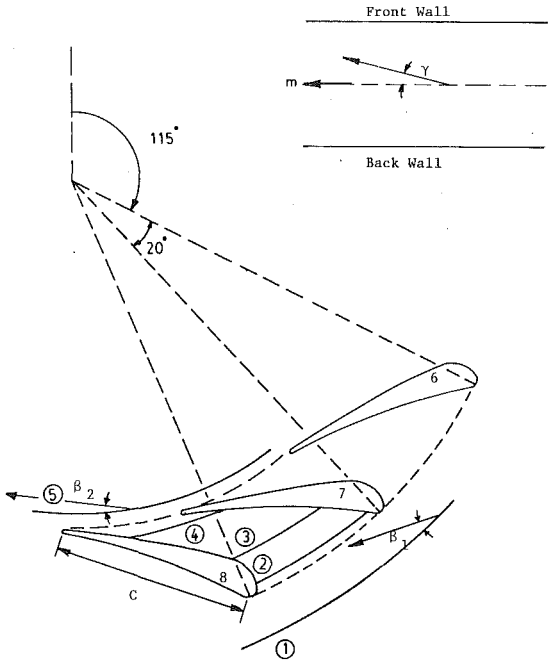

Fig. 3 Schematic showing the LDV measurement planes for mass flow rate (ṁ) = 0.0907 kg/s

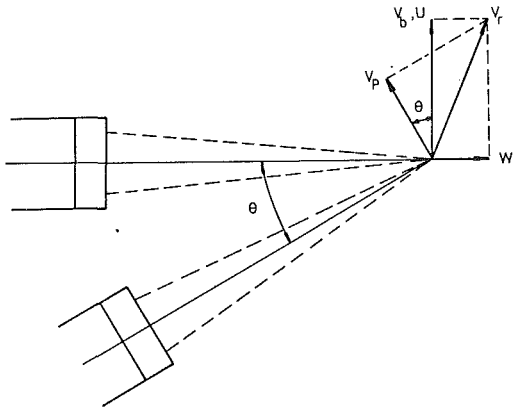

Fig. 4 Nonorthogonal arrangement of LDV third component

preceeding passage. Data were taken at five spanwise locations at each circumferential position of a measurement station. These spanwise positions are 1 mm (0.04 in.), 2.5 mm (0.1 in.), 4.5 mm (0.175 in.), 6.5 mm (0.25 in.), and 9 mm (0.35 in.) from the front end wall surface of the radial turbine test rig. The experiments were performed at an air mass flow rate of 0.0907 kg/s (0.2 lb/s). The measurements at the upstream (radius = 124 mm) and downstream (radius = 83 mm) stations were repeated at a mass flow rate of 0.1361 kg/s (0.3 lb/s). The measurement stations for the higher mass flow rate (0.1361 kg/s) experiments correspond to the stations 1 and 5 of Fig. 3. Data were obtained at 600 points in total including both low and high mass flow rate measurements.

Measuring Technique. The horizontal (blue) and vertical (green) components of velocity were measured directly by the LDV system. However, due to the inclined arrangement of the second train of the LDV optics (Fig. 4), the measured third component is nonorthogonal to the plane of the first two components. Then, the orthogonal on-axis component was calculated through a transformation relation. Referring to Fig. 4, this relation is

$$W = \frac{V_b \cos\theta - V_p}{\sin\theta} \tag{1}$$

where V_b and V_p are the horizontal (blue) and nonorthogonal (purple) components of velocity, and θ is the inclination angle between the two optical trains. The angle θ was limited to 30 deg by the geometry of the radial turbine test rig. Since the coincidence of the three velocity component measurements caused extremely long experiment times, the data were collected independently from the inclined LDV channel while the measurements from the other two orthogonal channels coincide. This resulted in inaccuracy of the computed variance of the on-axis velocity components through the transformation relation.

Since the variance of the on-axis velocity component cannot be determined accurately, the turbulence intensity is calculated only in the plane parallel to the end walls of the guidevanes using the variance of the two orthogonal velocity components. The relation used in the turbulence intensity calculations is

$$k = \frac{\sqrt{0.5\,(s_{VB}^2 + s_{VG}^2)}}{V_{ex}} \tag{2}$$

where s_{VB}^2 and s_{VG}^2 are the variances of the horizontal (blue) and vertical (green) velocity components, and V_{ex} is the passage averaged exit velocity.

When the measurements were conducted near the end wall surfaces, the reflection of the laser beams reduced the signal to noise ratio considerably, and the noise levels exceeded the signal amplitude at very close measurement locations to the end walls. Because of the end wall reflection problem, the closest measurement locations to the walls were determined as 1 mm (0.04 in.) from the plexiglass front end wall, and 3 mm (0.118 in.) from the back end wall, for the off-axis backward scatter technique. No wall reflection problems were encountered in the measurements near the blade surfaces. The minimum measurement distance from the blade surfaces was limited due to the blockage of the beams by the blades. It was possible to measure as close as 0.5 mm (0.0197 in.) from the blade surfaces when the measurement geometry was favorable.

Typical data rates were about 50 data/s, although this number changed considerably depending on the seeding droplet number density, reflections from the walls and the flow passage. Signal to noise ratio was in general more than 6 in most of the measurement locations. However, near the back end wall, the results were accepted down to a signal-to-noise ratio of 3.

Uncertainty Analysis. The uncertainty of the measured mean velocities were determined using the techniques described by Orloff et al. (1983) and Snyder et al. (1984). For 95 percent confidence level, these references related the measurement uncertainty interval to the sample size through the relation

$$\Delta U = \mp \frac{1.96 s_U}{\sqrt{N}} \tag{3}$$

where s_U is an estimator for the true standard deviation, N is the sample size, and the constant 1.96 corresponds to 95 percent confidence level. The uncertainties of the measured mean velocities increased with the flow turbulence in the downstream direction. The on-axis velocity component was calculated from the two independently measured velocity components using Eq. (1) as explained in the previous section. This equation has an amplifying effect on the standard deviation of the on-axis velocity component as demonstrated in references by Orloff et al. (1982) and Snyder et al. (1984). Therefore, the uncertainty of this component is significantly higher than the directly meas-

Table 3 Measurement uncertainties (∓)

Longitudinal, transverse, and vertical traverses	0.025 mm
Optical axis or plexiglass surface angular position	0.5°
Measuring location	0.3 mm
Inlet transverse velocity (Blue), $\Delta U/U_m$	0.57%
Inlet vertical velocity (Green), $\Delta V/V_m$	1.56%
Inlet on-axis velocity (Blue & Purple), $\Delta W/W_m$	14.3%
Exit transverse velocity (Blue), $\Delta U/U_m$	2.21%
Exit vertical velocity (Green), $\Delta V/V_m$	3.11%

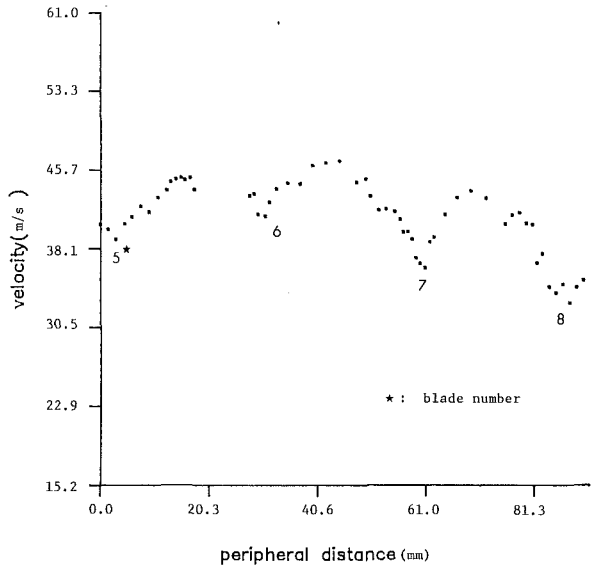

Fig. 5 Mean velocity survey at downstream (radius = 83 mm) midspan for ṁ = 0.0907 kg/s

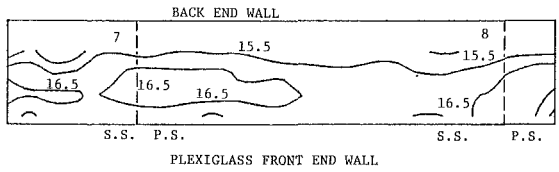

Fig. 6 Mean velocity contours for first (upstream) plane at radius = 124 mm, ṁ = 0.0907 kg/s (view against flow direction)

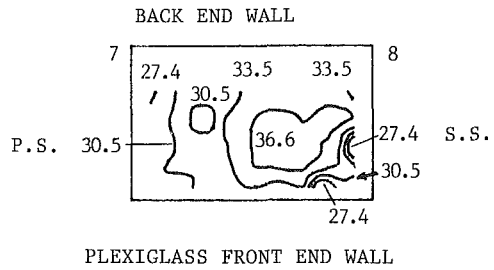

Fig. 7 Mean velocity contours for fourth plane at radius = 90 mm ṁ = 0.0907 kg/s (view against flow direction)

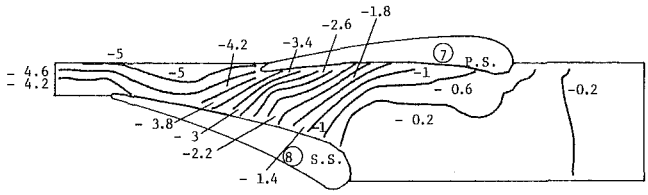

Fig. 8 Measured static pressure coefficient, c_p, contours at the plexiglass end wall for ṁ = 0.0907 kg/s

ured velocity components. A summary of the maximum uncertainties associated with the LDV system are given in Table 3.

Results and Discussion

The experimental measurements were taken at the mass flow rates 0.0907 kg/s and 0.1361 kg/s/ At these mass flow rates, the Reynolds numbers are 1.14×10^5 and 1.91×10^5, respectively, based on the passage averaged exit velocity, chord length and the cold air properties at the exit static temperature. The corresponding average exit Mach numbers are 0.109 and 0.182 respectively. The total pressure and temperature are 0.105×10^6 N/m^2 (15.2 psi) and 22°C (71.5°F), respectively, at the inlet to the guide vanes for 0.907 kg/s mass flow rate at which most of the measurements were obtained. The results of the LDV measurements include the mean velocity, flow angles, β and γ, and the turbulence intensities at the measurement stations shown in Fig. 3. Referring to Fig. 3, the angle β is defined with respect to the circumferential direction and is on the plane parallel to the end walls. The angle γ is the angle between the actual flow direction and the blade-to-blade plane parallel to the end walls. It is due to the spanwise velocity component. Some of the results are presented in this paper to describe the flow field through the guide vanes. The bulk of the measurements were obtained at a mass flow rate of 0.0907 kg/s. The mean flow results reported in Figs. 5 through 13 correspond to this mass flow rate.

Mean Velocity. An initial flow survey was carried out at midspan, downstream (radius = 83 mm) of the guide vanes across the exit of three flow passages to check the flow periodicity. The variation of the measured mean velocity with the circumferential direction is shown in Fig. 5. Measurements could not be obtained close to the sixth vane trailing edge, due to the blockage of the laser beams by the blades. The wakes of the fifth, sixth, seventh and eighth blades from the inlet can clearly be seen in the figure. The small differences in the velocities between the wakes and the free streams imply rapid mixing, which was also observed by Khalil et al. (1976). Possible reasons for such rapid mixing are the large flow acceleration, the high level of turbulence, and the predominant effect of swirling motion in the vaneless field. A comparison of the flow velocity levels in the different passages does not reveal exact flow periodicity, and indicates a difference in the mass flows through the channels. A two-dimensional computation of the flow through a radial inflow turbine scroll-nozzle assembly also predicted variation in the mass flow through the flow passages (Hamed et al., 1978).

Figures 6, 7, and 9 show the mean velocity contours at the first, fourth and fifth measurement stations of Fig. 3. The upstream mean velocities are quite uniform (Fig. 6), but not symmetrical between the two end walls. They are slightly lower near the back end wall due to flow separation after the 90 degree bend at the scroll exit (radius = 137 mm). The flow separation was confirmed by a flow visualization using laser sheet technique, however, a clear picture could not be taken. Figure 7 shows the velocity contours at station 4 slightly upstream (radius = 90 mm) of the throat. There are two lower velocity regions. First one is close to the front end wall near the suction surface, and the second one is in the same corner, but is a little away from the front end wall towards midspan. These lower velocity regions may indicate the existence of considerable amount of cross flows carrying the lower energy boundary layer fluid to the suction side corner, and furthermore towards the midspan location along the suction surface. Although, the radial pressure gradient has a force component

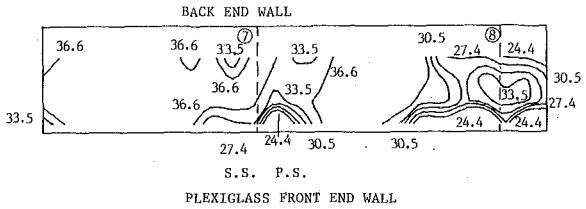

Fig. 9 Mean velocity contours for fifth (downstream) plane at radius = 83 mm, $\dot{m}$ = 0.0907 kg/s (view against flow direction)

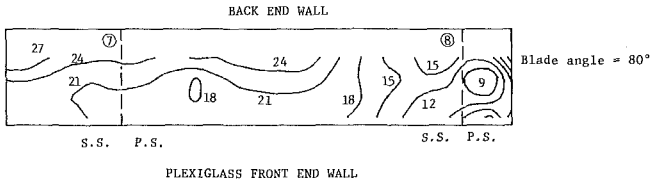

Fig. 10 β-flow angle contours for first (upstream) plane at radius = 124 mm, $\dot{m}$ = 0.0907 kg/s (view against flow direction)

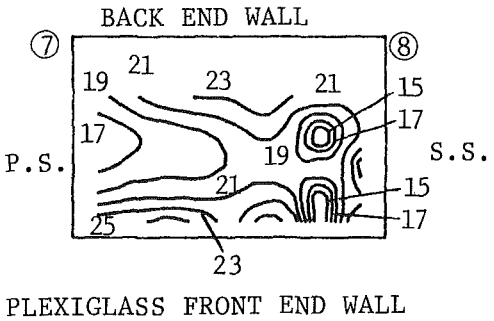

Fig. 11 β-flow angel contours for fourth plane at radius = 90 mm, $\dot{m}$ = 0.0907 kg/s (view against flow direction)

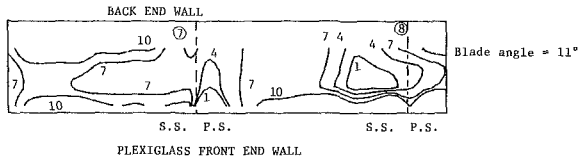

Fig. 12 β-flow angel contours for fifth plane at radius = 83 mm, $\dot{m}$ = 0.0907 kg/s (view against flow direction)

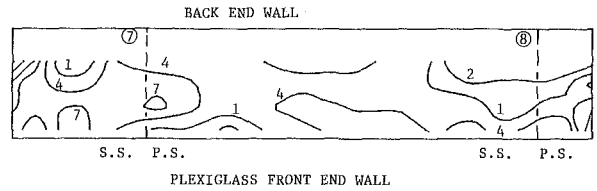

Fig. 13 γ-flow angle contours for first (upstream) plane at radius = 124 mm, $\dot{m}$ = 0.0907 kg/s (view against flow direction)

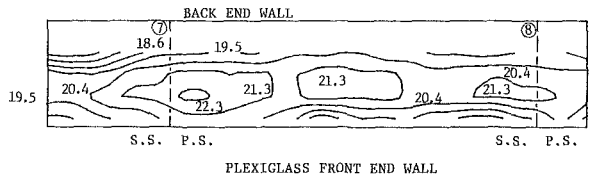

Fig. 14 Mean velocity contours for upstream plane at radius = 124 mm, $\dot{m}$ = 0.1361 kg/s (view against flow direction)

favoring a cross flow toward pressure side, the opposite pressure gradient due to blade geometry seems to be more dominant as illustrated in Fig. 8, which shows end wall static pressure coefficient, C_p, contours. These two counter affecting pressure fields weaken the strength of the secondary flows. The mean velocity contours at downstream station (radius = 83 mm) are given in Fig. 9. Due to the rapid mixing and very high turbulence fluctuations, it is very difficult to distinguish the free stream regions from the wakes for the two flow passages. At all the stations, the flow velocities are lower near the end walls due to the presence of boundary layers.

Flow Angles. Figures 10 through 12 show the contour plots for the flow angle, β, defined with respect to the circumferential direction. The plots are presented for three of the five measurement stations shown in Fig. 3. The flow angles, β, upstream of the passage (radius = 124 mm) as plotted in Fig. 10 are slightly higher towards the back end wall where the velocities are slightly lower after the 90 degree bend. The slower moving fluid near the back end wall is affected by the radial pressure gradient than in the rest of the cross-section and is directed closer to the radial direction. Figure 11 shows the flow angle, β, contours at station 4 (radius = 90 mm). There are high angle gradients near the suction surface extending from the corner of front end wall and the suction surface to the midspan. At the locations corresponding to lower velocities of Fig. 7, there is flow overturning. The flow overturning is because of the passage pressure gradient which is dominated by the pressure gradient from pressure to suction side due to blade shape. The contour plot of Fig. 12 gives the flow angle, β, distribution at the downstream station (radius = 83 mm). In general, the flow angles are smaller than the blade angle (11 degrees) which is defined as the trailing edge bisector angle measured from the circumferential direction at the center of the trailing edge circle. This overturning is mostly due to the passage cross flows from pressure to suction side occupying large flow areas because of the very low aspect ratio. Generally, the flow has a smaller angle in the regions affected by the wakes. This is probably due to the blockage caused by the vane thicknesses at the exit as explained by Risika (1964). Higher angles are observed near the end walls. The angle distributions between the two flow passages are not symmetric due to the differences of the flow through each blade channel as a result of the circumferential variation of the scroll cross-section which is described in the section "Test Rig."

Figure 13 shows the contour plots for the flow angle, γ, on the upstream station where the radius is 124 mm. A positive γ value shows a flow direction toward the plexiglass front wall. It is towards the front end wall almost everywhere at this station due to the 90 degree bend of the back wall at the inlet to the vaneless nozzle region. Its maximum value reaches to 7 degrees.

Effect of Mass Flow Rate. The measurements upstream and downstream of the passage were repeated for the mass flow of 0.1361 kg/s. Figures 14 through 17 illustrate the results of these higher mass flow rate measurements. Figure 14 shows the mean velocity contours at the upstream station (radius = 124 mm). Similar to the contour plot of Fig. 6, the velocities are quite uniform for 0.1361 kg/s, but the level of velocity is higher in accordance with the higher mass flow. The extent of the lower velocity regions close to the end walls seems to be more for the higher mass flow rate. The downstream station (83 mm radius) contour plot of Fig. 15 covers the full channel between the blades 7 and 8, but the passage between the blades 6 and 7 is only partially covered downstream. The wake behind the blade 7 of Fig. 15 at 0.1361 kg/s seems to be affecting a larger area suggesting that the fluctuations and the resulting mixing increased.

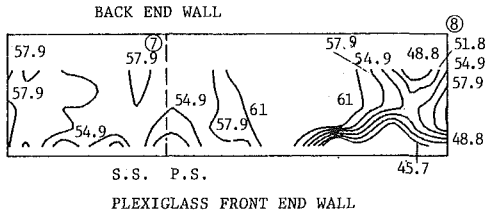

Fig. 15 Mean velocity contours for downstream plane at radius = 83 mm, $\dot{m}$ = 0.1361 kg/s (view against flow direction)

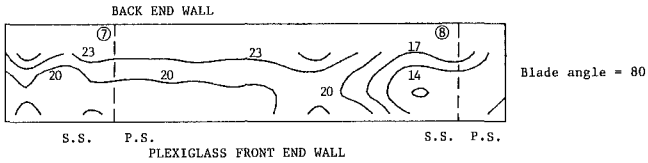

Fig. 16 β-flow angle contours for upstream plane at radius = 124 mm, $\dot{m}$ = 0.1361 kg/s (view against flow direction)

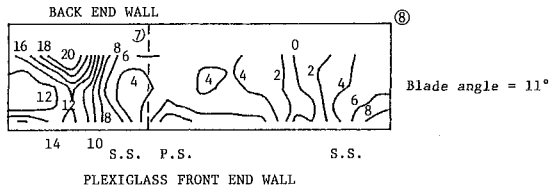

Fig. 17 β-flow angle contours for downstream plane at radius = 83 mm $\dot{m}$ = 0.1361 kg/s (view against flow direction)

Figure 16 for the flow angle, β, contours at a flow rate of 0.1361 kg/s and radius 124 mm (station 1) is very similar to Fig. 10. The angles, β, downstream of the passage (radius = 83 mm) are generally lower for the high mass flow rate (Fig. 17) as compared with those for the lower mass flow rate (Fig. 12). There are higher angle gradients and it is very difficult to separate the free stream from the wake.

Turbulence Intensities. Figures 18 and 19 show the turbulence intensity contours normalized with respect to passage average exit velocity on the blade-to-blade plane at 6.5 mm (midspan), and 1 mm, respectively, from the plexiglass front end wall. In both figures, a higher turbulence region appears near the pressure side after the leading edge, and the turbulence intensities increase in the downstream flow direction. These figures also depict the effect of end wall cross flow transporting higher turbulence fluid because of the passage pressure gradient. A comparison of Figs. 18 and 19 reveal that turbulence intensities are higher in Fig. 19 due to end wall proximity. Table 4 lists the passage averaged turbulence intensities at each measurement station for 0.0907 kg/s and 0.1361 kg/s mass flow rates. The average turbulence intensities increases with decreasing radius in the downstream flow direction. It increases with an increase in the mass flow rate at all stations. This decrease is from 23.81 percent to 17.23 percent at the downstream station (fifth) for the mass flow rate change from 0.0907 kg/s to 0.1361 kg/s.

Numerical Results. One of the primary goals of the experimental study was to provide a data base for the development, improvement and verification of turbomachinery computer programs. The flow field on the blade-to-blade midspan surface through the guide vanes of the radial turbine was computed using a "panel method". The results of these computations are presented in this section and compared with the experimental results.

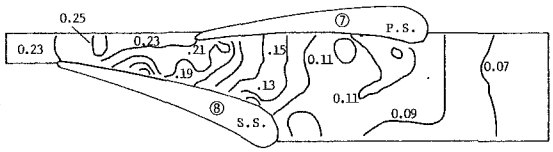

Fig. 18 Turbulence intensity, k, on blade-to-blade, midspan plane at $\dot{m}$ = 0.0907 kg/s

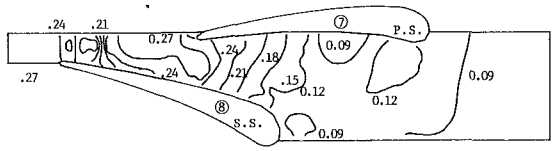

Fig. 19 Turbulence intensity, k, on blade-to-blade plane, 1 mm from the front end wall at $\dot{m}$ = 0.0907 kg/s

Table 4 Passage averaged turbulence intensities

Radius	124	110	102	90	83
Turbulence intensity at $\dot{m}$ = 0.0907 kg/s	9.04	10.11	11.03	21.0	21.81
Turbulence intensity at $\dot{m}$ = 0.1361 kg/s	8.08	—	—	—	17.23

The panel code was developed by McFarland (1982, 1984) to solve the inviscid, irrotational, compressible, blade-to-blade flow equations on a surface of revolution of variable stream sheet thickness. The compressibility effects are linearized in the governing equations and the solution is obtained using integral "panel method." The panel method used advanced surface singularity formulations adapted from those found in external flow analysis. The program is intended primarily for use in preliminary design studies, and it combines the advantages of rapid solution capability, robustness and versatility. Since a direct linear equation solver is used, a solution is always obtained even for extreme flow conditions, however, the accuracy decreases when the flow becomes transonic. The program primarily computes the flow on the blade surface, but can also be used to calculate the flow field inside the passage, though not as efficiently as on the blade surface. Further details of the solution method used in the "panel" code can be found in references by McFarland (1982, 1984).

The equations governing the flow through the guide vanes of the experimental turbine are simpler than the more general equations of McFarland (1984), because of the incompressible flow field and the constant flow channel height. These equations led to an exact solution of the flow field. The numerical solution was obtained at a velocity of 16.8 m/s and a flow angle, β, of 37.5° measured from circumferential at the inlet to the passage. These conditions match the passage averaged flow velocity and angle obtained by LDV measurements at the inlet for m = 0.0907 kg/s. The computed blade loading in terms of pressure coefficients, C_p, is shown in Fig. 20. The pressure gradient is from suction to pressure side near the leading edge due to the negative incidence. After the pressure coefficient curves cross each other at approximately 1/4 chord length downstream of the leading edge, the pressure gradient changes direction and acts from pressure to suction side. These results are consistent with the measured static pressure coefficient contours of Fig. 8. These opposite pressure gradient directions at upstream and downstream regions influence the end wall cross flow considerably. The computed velocity contours at midspan location through the guide vanes are plotted in Fig. 21. The flow acceleration around the pressure side of leading edge and flow deceleration further downstream are very clear. The figure also shows the stagnation region at the suction side

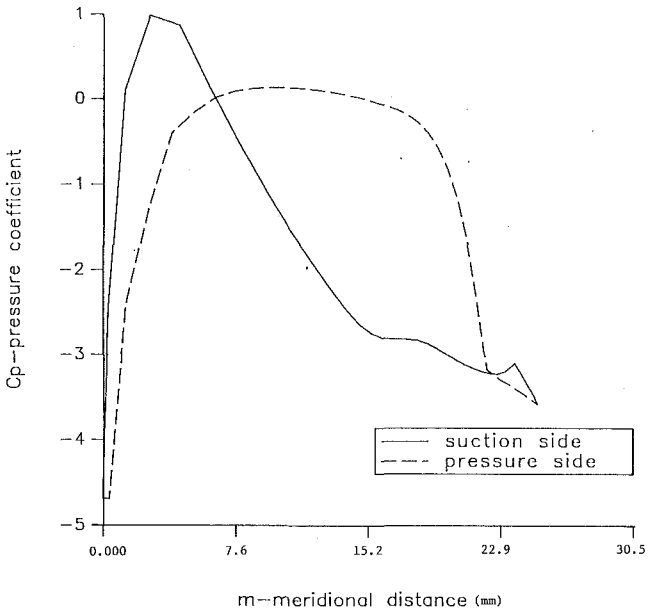

Fig. 20 Calculated blade surface pressure coefficient distribution for $V_1 = 16.8$ m/s, $B_1 = 37.5$ deg

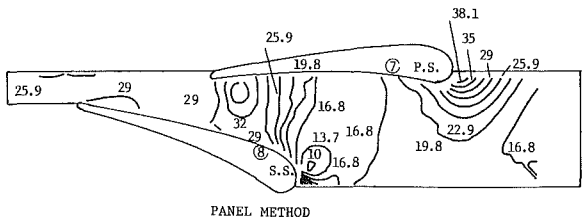

Fig. 21 Calculated velocity contours on blade-to-blade, midspan plane at $V_1 = 16.8$ m/s, $\beta_1 = 37.5$ deg

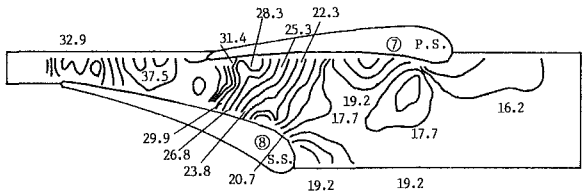

Fig. 22 LDV measured mean velocity contours on blade-to-blade, midspan plane at $\dot{m} = 0.0907$ kg/s

of theleading edge. This plot is in satisfactory agreement with the experimental results of Fig. 22 which were obtained by interpolating the mean velocity values at midspan location of the five measurement stations. The differences can be attributed to viscous and three dimensional effects.

Conclusion

The flow field through the blade passage was found to be influenced by the scroll geometry for the present experimental turbine test rig. The deviations from periodicity between flow channels and assymmetry with respect to the two end walls were attributed to this upstream influence. Significant end wall cross flows were observed inside the blade passages close to the trailing edge. Rapid mixing of the flow affected by the wakes and the free stream turbulence occurred downstream of the trailing edge. Average flow angle on downstream measuring plane was found to be lower than the exit blade angle. The flow turbulence increased in the downstream direction and this was considered to be one of the causes of rapid mixing at the exit from the blade passages. Mass flow rate increase did not change the inlet flow angle as expected, but it decreased the passage averaged exit flow angle. The normalized passage averaged turbulence intensity was reduced with the mass flow rate increase at both the inlet and exit measurement stations.

Results of an inviscid, panel method flow solution on the blade-to-blade surface through the nozzle blades agreed well with the experimental results. A few discrepancies were attributed to the viscous effects which were not taken into account in the numerical solution.

Acknowledgment

This work was partially supported by the U.S. Army Research Office-Durham, under equipment contract No. DAAL03-87-G-0017 and DAAL03-90-G-0129. We are grateful for this support and acknowledge our useful discussions with Dr. Thomas Doligalski, Chief Fluid Dynamic Branch.

References

Choo, Y. K., and Civinskas, K. C., 1985, "Three Dimensional Inviscid Analysis of Radial-Turbine Flow and a Limited Comparison with Experimental Data," *Proceedings of the ASME on Three Dimensional Flow Phenomena in Fluid Machinery*, Miami Beach, Florida, Nov.

Hamed, A., Baskharone, E., and Tabakoff, W., 1978, "A Flow Study in Radial Inflow Turbine Scroll-Nozzle Assembly," ASME JOURNAL OF FLUIDS ENGINEERING, Vol. 100, pp. 31–36, Mar.

Hashemi, S. G. R., Lemak, R. J., and Owczarek, J. A., 1984, "An Investigation of the Flow Characteristics and of Losses in Radial Nozzle Cascades," ASME *Journal of Engineering for Gas Turbines and Power*, Vol. 106, pp. 502–510, April.

Khalil, I. M., Tabakoff, W., and Hamed, A., 1976, "Losses in Radial Inflow Turbines," ASME JOURNAL OF FLUIDS ENGINEERING, Vol. 98, pp. 364–373, Sept.

Malak, M. F., Hamed, A., and Tabakoff, W., 1986, "3-D Flow Field Measurements in a Radial Inflow Turbine Scroll Using LDV," 32st International Gas Turbine Conference and Exhibit, Dusseldorf, Federal Republic of Germany, June, ASME Paper No. 86-GT-122.

McFarland, E. R., 1982, "Solution of Plane Cascade Flow Using Improved Surface Singularity Methods," ASME *Journal of Engineering for Power*, Vol. 104, July, pp. 668–674.

McFarland, E. R., 1984, "A Rapid Blade-to-Blade Solution for Use in Turbomachinery Design," ASME *Journal of Engineering for Gas Turbines and Power*, Vol. 106, April, pp. 376–382.

Orloff, K. L., and Snyder, P. K., 1982, "Laser Doppler Anemometer Measurements Using Nonorthogonal Velocity Components: Error Estimates," *Applied Optics*, Vol. 21, Jan., pp. 339–344.

Risika, J. W., 1964, "The Design and Performance Analysis of Radial Inflow Turbines," Northern Research and Engineering Corp., Cambridge, MA, Report No. 1067-1 and 1067-2.

Snyder, P. K., Orloff, K. L., and Reinath, M. S., 1984, "Reduction of Flow Measurement Uncertainties in Laser Velocimeters with Nonorthogonal Channels," *AIAA Journal*, Vol. 22, No. 8, Aug., pp. 1115–1123.

Tabakoff, W., Vittal, B. V. R., and Wood, B., 1983, "Three-Dimensional Flow Measurements in a Turbine Scroll," ASME Paper No. 83-GT-128.

Flow Measurements in a Model Burner—Part 1

D. F. G. Durão

M. V. Heitor

A. L. N. Moreira

Instituto Superior Técnico,
Technical University of Lisbon,
Department of Mechanical Engineering,
1096 Lisboa, Portugal

Laser-Doppler measurements of mean and turbulent velocity characteristics are reported in the developing region of the isothermal flow of a model of an industrial oxy-fuel burner. The burner consists of a central axisymmetric jet surrounded by sixteen circular jets, simulating the injection of oxygen in pratical burners. Errors incurred in the laser-Doppler measurements are estimated and bias effects due to unequal number density of seed particles in the various jet flows are investigated. The experiments have been carried out to investigate the mixing efficiency of the burner assembly without swirl motion and to assess the accuracy of calculation procedures in industrial burners. The results show that the present flow develops faster than related coaxial free jets with the same velocity ratio between central and peripheral air streams due to the comparatively high mixing rate peculiar to the present configuration. The existence of zones characterized by large turbulence anisotropy indicates the need to take account of the normal stresses in any proposed mathematical model to simulate the present flow field.

1 Introduction

Industrial burners operating with oxy-fuel conditions are commonly used in melting furnaces where both a high flame temperature and heat transfer rate are required to melt the charge, e.g., Booker (1982), Gibbs and Williams (1983), Schatz and Hueber (1984) and Bansal and McCombs (1986). However, their use in industrial furnaces is only economic if the benefits in fuel savings and productivity offset the cost of oxygen and this implies the use of optimized burner geometries. Nevertheless, the design of burners has relied almost exclusively on empirical methods, e.g., Gibbs and Williams (1983), and increased knowledge of the fluid flow in the vicinity of the burners is essential to further modifications in their geometry and to allow to predict their effects. This is the main objective of the work reported in this paper.

Safety requirements in oxy-fuel burner installations necessitate mixing of the fuel at, or just downstream of the burner face and, therefore, combustion efficiency is limited by the rates of mixing that can be achieved. In practice, multi-jet burner head configuration systems have been preferred to single and coaxial jets, since they improve the mixing efficiency considerably and produce lower sound pressure levels, although they increase the complexity of the burner. In addition, some designs of oxy-fuel burners incorporate means of hot gas recirculation, usually by swirl motion, to ensure flame stabilization. Measurements of mean and turbulent velocity characteristics in model burners are then required to evaluate particular geometrical configurations.

The present study reports laser-Doppler measurements of the isothermal flow in a model of an oxy-fuel burner in current development and use in industrial glass furnaces. This work follows those of Durão et al. (1987) and Carvalho et al. (1987) which present measurements and predictions of the flow and heat transfer characteristics of an oxy-fuel processing glass furnace. The burner consists of a central axisymmetric jet surrounded by sixteen circular jets inclined toward the centerline, simulating the oxygen jets used in practical burners.

Experiments in multi-jet configurations have not been reported in the literature, but related simplified flow geometries consisting of coaxial free jets have been studied by Champagne and Wygnanski (1971), Pratte and Keffer (1972), Durão and Whitelaw (1973) and Ribeiro and Whitelaw (1976–1980) with hot wire anemometry. Multi-jet flow configurations include additional complexities, such as comparatively high turbulence levels and recirculation zones, and their study is limited to the use of non-intrusive laser-Doppler velocimetry. However, accurate LDV-based measurements in turbulent multi-stream mixing flows require equal densities of seed particles in the various streams, as shown by Dibble et al. (1987).

The results presented in this paper include mean and turbulent velocity characteristics in the three spatial directions for a range of operating conditions of nonswirling flows. The effect of swirl on the flow field will be reported in Part 2 of this paper. The experiments are concerned with the developing region of the flow and provide a basis to improve our understanding of relevant transport processes in industrial burners, guide burner design and to assess the accuracy of calculation procedures in burners of practical interest. The main sources of imprecisions of the laser-Doppler measurements are identified and the related errors are estimated.

Section 2 describes the experimental method, gives details of the flow configuration, of the laser-Doppler velocimeter and of the errors incurred in the measurements. Section 3 presents and discusses the profiles of the mean and fluctuating

Contributed by the Fluids Engineering Division and presented at the Winter Annual Meeting, Boston, MA, December 13–18, 1987 of THE AMERICAN SOCIETY OF MECHANICAL ENGINEERS. Manuscript received by the Fluids Engineering Division August 5, 1987.

Table 1 Flow conditions

Run	Central jet					Peripheral jets			
	Axial air (l/s)	Tangential air (l/s)	Fuel-line (air) (l/s)	U_i (m/s)	Re ($\times 10^3$)	Flow rate (l/s)	U_0 (m/s)	Re ($\times 10^3$)	U_i/U_0
A1	4.0	—	—	20	17.6	9.0	20	6.0	1.0
A2	4.0	—	—	20	17.6	18.0	40	12.0	0.5
A3	3.3	—	0.7	20	17.6	9.0	20	6.0	1.0

velocity characteristics and the last section summarizes the main findings and conclusions.

2 Experimental

2.1 Flow Configuration and Flow Conditions. The burner arrangement consists of a central axisymmetric jet of 17mm diameter, D_i, surrounded by sixteen 6mm circular jets inclined at 4 deg towards the burner axis. The central jet includes the air flow to simulate the fuel-line and the atomization air. This can be fed separately through an axial entry to provide a non-swirling jet or through a swirl chamber which generates a tangential velocity by the injection of air through tangential slots. The fuel atomizer has the shape of a 30 deg truncated cone with four 1.5mm diameter holes disposed symmetrically along the inclined wall and one 2mm diameter hole at the center of the plane wall, aligned with the burner axis. The sixteen peripheral air jets simulate the injection of oxygen in practical burners and are located along a circle with 4mm in diameter, D_0.

The air flow rate is measured by three calibrated standard orifice meters for the central and the peripheral jets. The air flow rate to simulate the fuel is measured by a calibrated rotameter.

Table 1 summarizes the flow conditions analyzed in this paper. Each run is characterized by the ratio between the mean velocities in the central jet, U_i, and in the peripheral jets, U_0. The injection of fuel is studied in run A3, which is characterized by a centerline axial velocity at the exit of the burner, U_m, larger than U_i.

The origin of the axial axis, x, is taken at the exit plane of the jets and the tangential velocity is taken positive in the anticlockwise direction. The symmetry of the flow was verified in the vertical and in the horizontal plane, as discussed below.

2.2 Measurement Technique. Velocities were measured by a laser-Doppler velocimeter operated in the dual-beam, forward-scatter mode with sensitivity to the flow direction provided by light-frequency shifting from acousto-optic modulation (double Bragg cells). The resulting frequency shift varied between 0 and 10 MHz. The principal characteristics of the laser-Doppler velocimeter, and in particular those of the transmitting optics, are summarized in Table 2.

Table 2 Principal characteristics of the laser-doppler velocimeter

- 5W (nominal) Argon-Ion Laser: wavelength	514,5 nm
- focal length of focusing lens	300 mm
- beam diameter, at e^{-2} intensity	1,5 mm
- measured half-angle of beam intersection	4,92°
- fringe separation (line pair spacing)	3,00 μm
- calculated dimensions of measuring volume, at e^{-2} intensity (major and minor axis of the ellipsoid)	1.528; 0.132 mm
- velocimeter transfer constant	0.33 MHz/ms^{-1}

The central and the peripheral air jets were seeded with atomized silicone oil. The particles were supplied by several atomizers and injected in all the air ducts separately. The light scattered by the particles was collected by a lens (focal length of 200 mm) and focused into the pinhole aperture (0.300 mm) of a photomultiplier with a magnification of 0.74. The output of the photomultiplier was band-pass filtered and the resulting signal processed by the laboratory-built frequency counter described by Heitor et al. (1984).

The complete LDV system and the burner were mounted on two separate two-dimensional manual traversing units, allowing the positioning of the laser-velocimeter control volume within ± 0.5 mm.

The radial, V, and the tangential, W, velocity components were measured by traversing the control volume along the vertical and horizontal planes of symmetry, respectively. The axial velocity component, U, was measured along the two planes of symmetry and the discrepancies were found to be within the measuring accuracy. The distributions of Reynolds shear stresses, $\overline{u'v'}$ and $\overline{u'w'}$, were obtained respectively along the vertical and horizontal planes of symmetry, with the laser beams in the horizontal and vertical planes and at ± 45 deg, e.g., Durst et al. (1981) and Adrian (1983).

2.3 Accuracy of the Measurements. The tolerance on the output of the counter derives from the error in the clock count and from the resolution of the floating point data format and the maximum error is always less than 1 percent. Larger errors may, however, arise due to other sources and are discussed in the following paragraphs.

Nonturbulent Doppler broadening (systematic) errors due to gradients of mean velocity across the measuring volume, e.g., Kreid (1974), may affect the variance of the velocity fluctuations, but for the present experimental conditions are

Nomenclature

D = diameter
k = turbulent kinetic energy, $k=(\overline{u'^2}+\overline{v'^2}+\overline{w'^2})/2$
r = radial coordinate
R_{uv} = shear stress correlation coefficient, $R_{uv}=\overline{u'v'}/(\overline{u'^2}+\overline{v'^2})$
U = axial velocity, $U=\overline{U}+u'$
V = radial velocity, $V=\overline{V}+v'$
x = axial coordinate taken from the burner face
W = tangential velocity, $W=\overline{W}+w'$
ν_T = turbulent viscosity

Subscripts

CL = center line
CTR = seeding only the central jet
i = inner or central jet
m = maximum (at the exit of central jet)
0 = outer or peripheral jets
PER = seeding only the peripheral jets

sufficiently small for their effect to be neglected: the maximum error is of the order of $7\times10^{-4}U_i^2$ and occurs at the edge of the peripheral jets close to the burner face. Transit time broadening has been shown by Zang and Wu (1987) to be larger than shot noise, e.g., Adrain (1978), and to be the principal source of noise in laser-Doppler anemometry: for the present optical configuration the related signal-to-noise ratio is about 69 and the maximum error in the variance of the velocity fluctuations is of the order of $2\times10^{-3}U_i^2$.

In the experiments, the number of individual velocity values used to form the averages was always above 10,000. As a result, the largest statistical (random) errors were 1 percent and 4 percent, respectively for the mean and variance values, according to the analysis referred by Yanta and Smith (1978) for a 95 percent confidence interval.

No corrections were made for sampling bias, and the systematic errors that could have arisen were minimized by using high data rates in relation to the fundamental velocity fluctuation rate as suggested, for example, by Dimotakis (1978), Erdmann and Tropea (1981) and Edwards (1978): the data acquisition rate varied between 5 and 10 kHz, with the lower values at the edge of the jets. In addition, no correlations were found between Doppler frequencies and time interval between consecutive bursts, suggesting that bias effects are unimportant for the present flow conditions, e.g., Durão et al. (1985). Following the analysis of Glass and Bilger (1978) for coflowing streams, these errors are less than $+9$ and -10 percent for the mean and variance values, respectively.

"Fringe (angle)" bias is minimized by using large values of frequency shifting, e.g., Durst and Zaré (1974). For the present case, following the analysis of Whiffen (1975) and Lau et al. (1981), the acceptance angle was 360 deg for a fringe to particle velocity ratio larger than 1, which could be achieved with frequency shifting up to 10 MHz, even in the highly turbulent mixing region immediately downstream of the burner exit.

In order to minimize bias errors due to unequal particle densities in the central and peripheral jets, e.g., Dibble et al. (1987) and Birch and Dodson (1980), the two streams were seeded separately with rates of particles in proportion to the air flow rate in each one. In this way it is possible to obtain similar particle concentrations in all the jet flows, as discussed by Dibble et al. (1987). An overestimation of these bias effects have been quantified from measurements obtained by seeding only one of the air streams and found to be smaller than $0.2U_i$ and $4\times10^{-3}U_i^2$, respectively, for the mean and the variance values. These measurements will be presented and discussed in the next section.

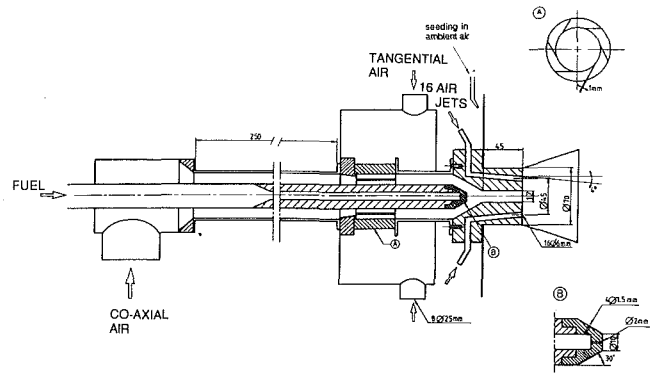

Fig. 1 Schematic diagram of burner assembly (model of an industrial oxy-fuel burner)

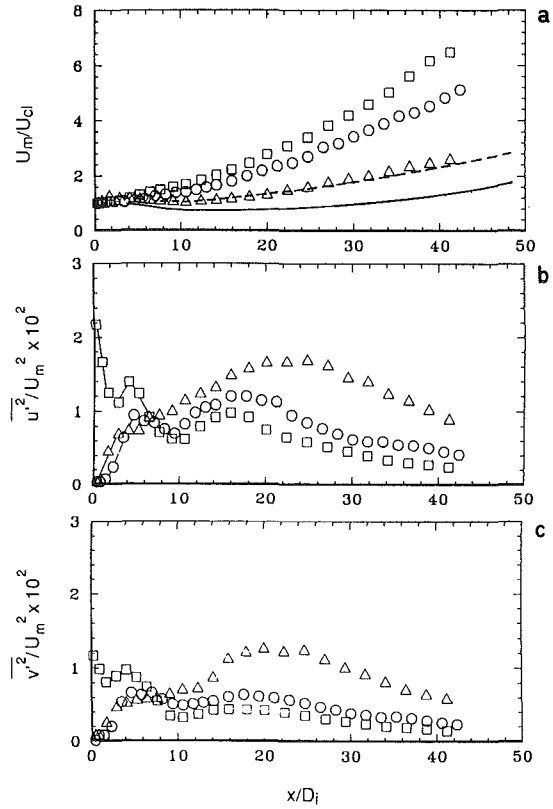

Fig. 2 Velocity distributions along the centerline; ○·Run A1; △·Run A2; □·Run A3; ____Ribeiro and Whitelaw (1980) $U_i/U_0=1.0$; ___Ribeiro and Whitelaw (1980) $U_i/U_0=0.65$. (*a*) Inverse of the mean axial velocity, $U_m/\overline{U}_{CL}$; (*b*) variance of axial velocity fluctuations, $u'^2/U_m^2\times10^2$; (*c*) variance of radial velocity fluctuations, $v'^2/U_m^2\times10^2$.

3 Results and Discussion

The results are presented and discussed under two headings. The first considers the mean and turbulent velocity characteristics of the flow for two velocity ratios U_i/U_0, and includes the influence of the injection of fuel on the flow field; the second discusses conditional measurements of mean and turbulent velocity characteristics by seeding only the central jet or the peripheral jets.

3.1 Mean and Turbulent Velocity Fields. Figure 2 presents the developing centerline distributions of the mean axial velocity and of the Reynolds normal stresses for runs A1, A2, and A3. The distributions of the mean axial velocity are plotted together with those obtained by Ribeiro and Whitelaw (1980) for coaxial air streams and include the regime of self-preservation. The results show that the decay of the centerline velocity is larger than that of free coaxial jets with similar velocity ratios between central and peripheral air streams. This is a consequence of the comparatively high mixing rates peculiar to the present multi-jet flow configuration, which is essential to improve the performance of oxy-fuel burners. The results also show that decreasing the value of U_i/U_0, by increasing the velocity of the peripheral jets, attenuates considerably the decay of the centerline velocity, giving rise to larger flames in practical burners. For a velocity ratio U_i/U_0 of unity the peripheral jets do not influence the mean velocity at the centerline up to $x/D_i=4$, but they do, however, affect the Reynolds stresses, particularly u'^2, which presents a local maximum at $x/D_i=4$ associated with the region where the mixing between the central and the peripheral jets has reached the centerline. The subsequent shape of the centerline distribution of u'^2 corresponds to the existence of a plateau in the mean velocity followed by its decay with tendency towards the self-preservation region. The values of u'^2 are larger than those of v'^2 due to the high production of u'^2 associated with the larger radial gradient (off center line) of the mean axial velocity,

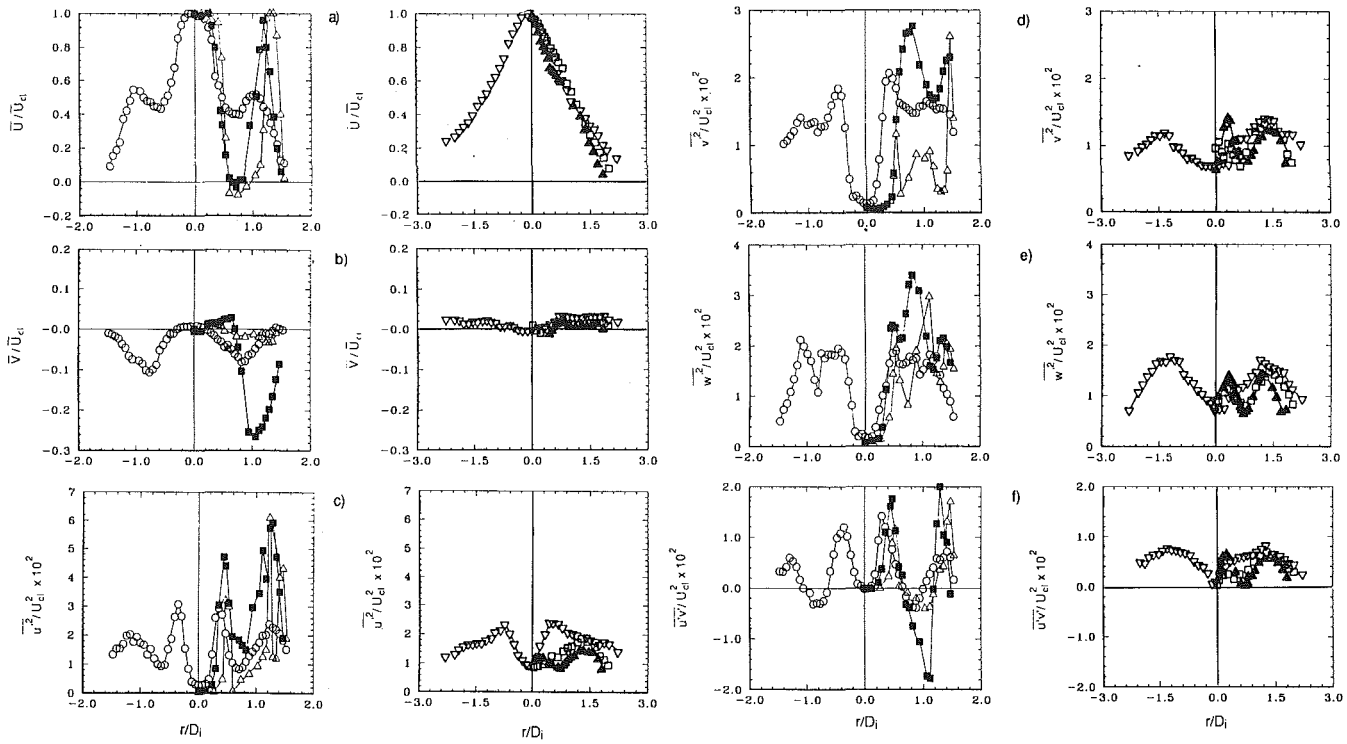

Fig. 3 Radial profiles of mean and turbulent velocity characteristics for run A1; △ -$x/D_i = 0.26$; ■ -$x/D_i = 1.0$; ○ -$x/D_i = 2.0$; ▲ -$x/D_i = 4.0$; □ -$x/D_i = 6.00$; ▽ -$x/D_i = 10.00$. (*a*) Mean axial velocity, $\bar{U}/U_{CL}$; (*b*) mean radial velocity, $\bar{V}/U_{CL}$; (*c*) variance of axial velocity fluctuations, $\overline{u'^2}/\bar{U}_{CL}^2 \times 10^2$; (*d*) variance of radial velocity fluctuations, $\overline{v'^2}/\bar{U}_{CL}^2 \times 10^2$; (*e*) variance of tangential velocity fluctuations, $\overline{w'^2}/\bar{U}_{CL}^2 \times 10^2$; (*f*) Reynolds shear stress, $\overline{u'v'}/\bar{U}_{CL}^2 \times 10^2$; (*g*) Reynolds shear stress $\overline{u'w'}/\bar{U}_{CL}^2 \times 10^2$; (*h*) correlation coefficient for Reynolds shear stress, R_{uv}; (*i*) ratio between shear stress and turbulent kinetic energy, $\overline{u'v'}/k$.

which stems from the dominance of the central jet for all the cases studied, as discussed below. The centerline distribution of v'^2 indicate values independent of the velocity ratio U_i/U_0 up to $x/D_i = 8$ and decreasing with this ratio far downstream. Since the production of v'^2 is negligible for the two velocity ratios studied (see below), it appears that the values of v'^2 are due mainly to redistributive effects and to turbulent diffusion as also discussed by Ribeiro and Whitelaw (1980).

The inclusion of air through the fuel injector (run A3) is shown to affect the distribution of Reynolds stresses up to $x/D_i = 6$ (note the value of the normalization velocity, U_m). Peak values of u'^2 are still higher than those of v'^2 due to the large production of u'^2 as a consequence of the large radial gradient of mean axial velocity in the central region imposed by the boundary conditions of this run.

Figure 3 shows the radial distributions of the mean velocity and Reynolds stresses for six consecutive axial stations between $x/D_i = 0.26$ and 10.0 and confirms the symmetry of the mean and turbulent flows at $x/D_i = 2$ and 10.0. The initial profiles of the mean velocity allow to identify a recirculation zone between the central and the peripheral jets extending up to $x/D_i = 1.0$ and show that the decrease of the central core is slower than the outer peripheral cores. The outer velocity peaks move towards the central part of the flow, which is associated with the maximum negative radial velocity of $-0.26U_i$ at one diameter downstream from the burner exit and away of the centerline.

The distribution of normal stresses exhibit three peaks in the near-burner region with u'^2 always higher than v'^2 and w'^2. This stems from the large production of u'^2 associated with the radial gradients of axial mean velocity, which are at least one order of magnitude larger than the gradients of radial and tangential velocities. The behaviour is consistent with the increase in the magnitude of the Reynolds shear stress, $\overline{u'v'}$, from $x/D_i = 0.26$ to $x/D_i = 1.0$, which shows a linear and symmetrical distribution at $x/D_i = 1.0$ with peak values of $\overline{u'v'}/U_{CL}^2 = 0.020$ and, therefore, considerably larger than those found in coaxial jets. The sign of the shear stress $\overline{u'v'}$ is consistent with the direction of the mean flow, with near-zero values coincident with the peak values of the mean axial velocity. The shear stress $\overline{u'v'}$ is positive along the edge of the central jet, suggesting that faster moving elements of central-jet fluid ($u' > 0$) tend to move outwards into the low-pressure

Fig. 3 (cont.)

region between jets (i.e., $v'>0$ and $\overline{u'v'}>0$). Similarly, the shear stress is negative along the inner edge of the peripheral jets, because the movement of jet-fluid particles towards the centerline ($v'<0$) are associated with positive axial velocity fluctuations (i.e. $u'>0$ and $\overline{u'v'}<0$) and is positive along the outer edge of the jets because the entrainment of external air ($v'<0$) results in negative axial velocity fluctuations (i.e., $u'<0$ and $\overline{u'v'}>0$). The results also show that the sign of $\overline{u'v'}$ is related to the sign of the shear strain $\partial\overline{U}/\partial r$ in accordance with a turbulent viscosity hypothesis ($\overline{u'v'}=-\nu_T\partial\overline{U}/\partial r$ where ν_T is a turbulent viscosity).

The radial distribution of the shear stress $\overline{u'w'}$ shows zero values along the central jet and at the centre of the peripheral jets and exhibits two peaks within a region one diameter downstream of the exit plane in the zone between the central and the peripheral jets. This is coincident with the inter-jets recirculation zone which terminates just downstream of $x/D_i=1$.

At two diameters downstream, the distribution of the mean axial velocity still exhibits a region of positive gradient located between two regions of opposite gradient and the Reynolds shear stresses $\overline{u'v'}$ still displays two changes in sign, but the magnitude of the normal stresses is comparatively low. The decrease in the negative peak of $\overline{u'v'}$ in the inner shear layer of the peripheral jets ($0.5<r/D_i<1.0$) is associated with the decrease in u'^2, which become smaller than v'^2 and w'^2. In addition, this anisotropic relation results from the interaction between normal stresses and normal strains, since $\partial\overline{U}/\partial x$ is positive and large and contributes as a sink of u'^2 and $\partial\overline{V}/\partial r$, although comparatively small, is negative and contributes as a source of v'^2. It must be noted that this behavior is not surprising because it occurs downstream the recirculation zone identified between the central and the peripheral jets and is similar to the turbulent structure near stagnation points in the wake of bluff bodies shown by Taylor and Whitelaw (1984) and Heitor et al. (1987).

The shear stress $\overline{u'w'}$ becomes negligibly small at $x/D_i=2.0$ and the normal stress w'^2 becomes of the order of v'^2.

The previous paragraphs indicate that the turbulent structure of the near-burner region is different from that reported by Durão and Whitelaw (1973) and Ribeiro and Whitelaw (1976, 1980) for coaxial jets with similar velocity ratios. The comparatively large wake between the jets in the present flow results in an unbalance between production and dissipation of turbulent kinetic energy, which increases turbulent diffusion and the rate of mixing between jets.

At four diameters downstream, the radial gradient of the mean axial velocity and the shear stress $\overline{u'v'}$ show near-zero values at $r/D_i=0.75$ and, in agreement with the centerline distributions of Fig. 2, suggest that the mixing between the central and the peripheral jets has reached the centerline.

Far downstream, the profiles of mean velocity of Fig. 3 display a monotonic behavior and the normal and shear stresses exhibit a trend similar to that of a fully-developed jet. The peaks for each normal stress distribution appear in the zone of maximum production of turbulent kinetic energy and, similarly to the results of Ribeiro and Whitelaw (1976 and 1980), still reveal strong anisotropy with u'^2 larger than v'^2 and w'^2. However, the shear stress normalized by the maximum velocity in each profile, $\overline{u'v'}/U_{CL}^2$, show maximum values around 0.008, which are still lower than the values given by Wygnanski and Fielder (1969) and Townsend (1976) for self-preserving jets (i.e. 0.020). This agrees with the centerline distributions of Fig. 2 and confirms the developing nature of the flow-region investigated.

Structure parameters, such as R_{uv} and $\overline{u'v'}/k$, have been calculated from the results and are plotted in Figs. 3(*h*) and 3(*i*). Their radial profiles show trends similar to those of $\overline{u'v'}$ shown in Fig. 3(*f*) and indicate two main types of behavior. Upstream of $x/D_i=4$, high and low values coexist with sharp gradients between them, indicating zones of eddy motion with

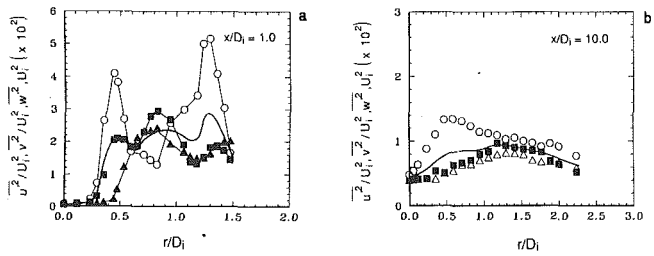

Fig. 4 Radial profiles of axial, radial and tangential normal stresses at: (*a*) $x/D_i=1.00$; (*b*) $x/D_i=10.00$; △ $-\overline{v'^2}/U_i^2$; ■ $-\overline{\omega'^2}/U_i^2$; ○ $-\overline{u'^2}/U_i^2$; ___ (2k/3)

strong directional preference e.g., Ribeiro and Whitelaw (1980). The correlation coefficient for shear stress, $\overline{u'v'}/k$ reaches values up to 0.50, which is significantly higher than the value of 0.30 reported by Bradshaw et al. (1967) and Harsha and Lee (1970) for turbulent shear flows. On the other hand, downstream $x/D_i=4.0$ the distributions of the structure parameters suggest that the zones of directional preference disappear as x increases and that the influence of extra source terms in the conservation equations for Reynolds stresses is minor: the values of R_{uv} and $\overline{u'v'}/k$ tend to 0.50 and 0.30, respectively.

The existence of zones characterized by large turbulence anisotropy in the present flow has important implications, because calculation methods based on scalar effective viscosities do not adequately represent the behavior of the normal stresses. Figure 4 complements the previous one and shows the radial distribution of 2/3 k at two axial locations, respectively $x/D_i=1.0$ and 10.0. The deviation from isotropy beyond the central zone is very clear, even at $x/D_i=10$ and, following the analysis of Ribeiro and Whitelaw (1980), suggests that turbulence is mainly transported in the axial direction through large scale eddies. On the other hand, the comparatively low magnitude of the normal stresses and their relative isotropy near the centerline suggest that the flow is dominated by dissipating small-scale eddies. Therefore, the present results imply that the calculation of the flow in industrial multi-jet burners should involve a turbulence model at the level of transport equations for the Reynolds stresses, rather than at the level of a turbulent viscosity closure.

3.2 Conditional Velocities on Central and Peripheral Jets Seed. In turbulent mixing flows, bias effects in LDV-based velocity measurements exist due to unequal seed density in the mixing streams, e.g., Birch and Dodson (1980), and in this subsection the limits of these bias are quantified by seeding only the central jet or the peripheral jets. The results are also used to analyse the mixing characteristics of the flow and to discuss the performance of the present burner geometry.

Figures 5 and 6 show, respectively, the centerline and radial distributions obtained at $x/D=4.0$ and 13.0, together with those obtained by seeding both streams.

The centerline distribution of the mean axial velocity conditioned on the central jet seed, U_{CTR}, is, as expected, larger than that conditioned on the peripheral jets seed, U_{PER}, with differences decreasing far downstream and outwards. On average, fluid originating from the peripheral jets has a smaller centerline velocity than fluid originating from the central jet. In addition, the radial profiles of the mean radial velocity show that the peripheral jets fluid are preferentially deflected towards the centerline ($V_{PER}<0$), while central jet fluid is, on average, deflected outwards, away from the centerline ($V_{CTR}>0$).

The differences between the conditioned turbulent velocities, with the exception of particular points in the profiles of u'^2, are small and within the errors incurred in the measurements and estimated in 2.3. Near the centerline at $x/D=4$, the axial variances of the conditioned velocity on the peripheral jets,

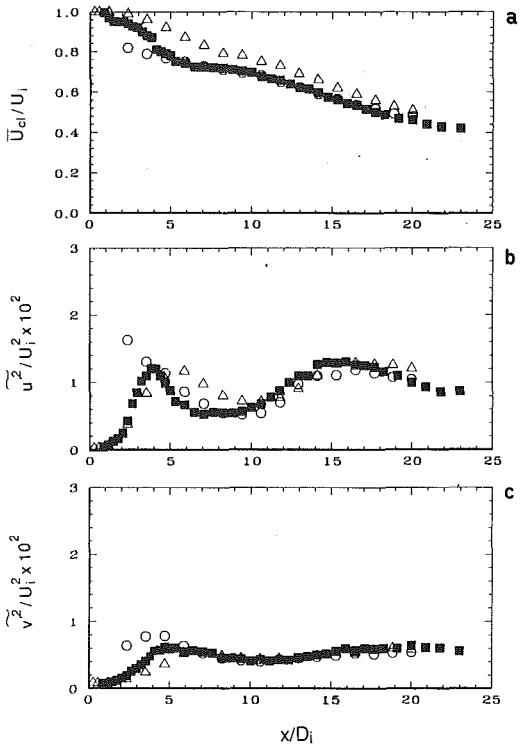

Fig. 5 Centerline distributions of conditional velocities on central and peripheral jets seed; △-seeding in the central jet; ○-seeding in the peripheral jets; ■-seeding in both streams. (*a*) Mean axial velocity, $\overline{U}/U_i$; (*b*) variance of axial velocity fluctuations, $\overline{u'^2}/U_i^2 \times 10^2$; (*c*) variance of radial velocity fluctuations, $\overline{v'^2}/U_i^2 \times 10^2$.

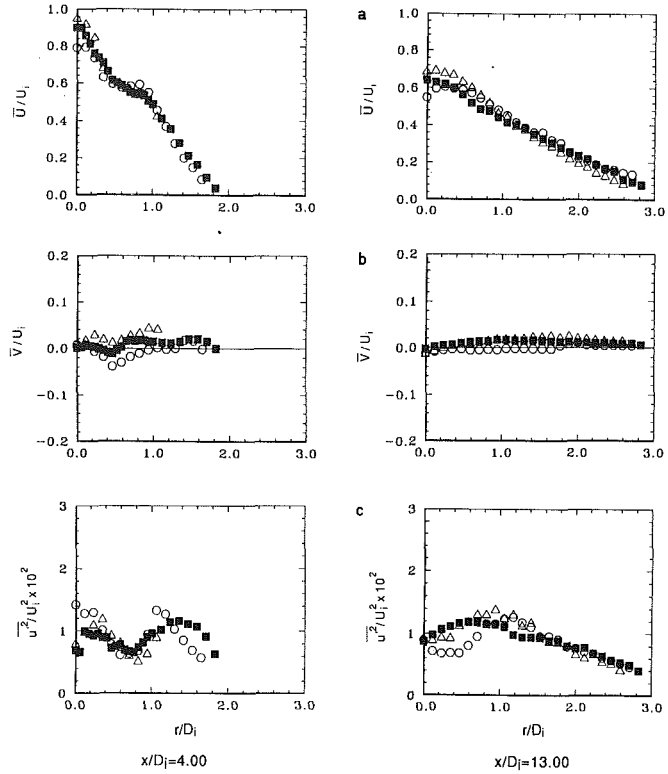

Fig. 6 Radial profiles of conditioned velocities on central and peripheral jets seed at $x/D_i = 4.00$ and $x/D_i = 13.00$; △-seeding in the central jet; ○-seeding in the peripheral jets; ■-seeding in both streams. (*a*) Mean axial velocity, $\overline{U}/U_i$; (*b*) mean radial velocity, $\overline{V}/U_i$; (*c*) variance of axial velocity fluctuations, $\overline{u'^2}/U_i^2 \times 10^2$; (*d*) variance of radial velocity fluctuations, $\overline{v'^2}/U_i^2 \times 10^2$; (*e*) Reynolds shear stress, $\overline{u'v'}/U_i^2 \times 10^2$.

$\overline{u^2}_{PER}$, tend to those of annular jets and, therefore, are higher than $\overline{u'^2}_{CTR}$, which are similar to the unconditioned values. Far downstream, at $x/D = 13$, the differences observed in the profiles of the conditioned axial variances are similar to those observed by Ribeiro and Whitelaw (1980) for different velocity ratios between central and peripheral coaxial air streams. Regardless of the physical interpretation, the conditioned results presented in Figs. 5 and 6 represent the limits of bias of velocity distributions due to unequal seeding in turbulent coaxial multi-jet flows.

4 Conclusions

Laser-Doppler measurements of the mean and turbulent velocity characteristics are reported in the developing region of the isothermal flow in the vicinity of an oxy-fuel model burner. The geometrical configuration is similar to that of coaxial jets where the annulus has been replaced by sixteen peripheral jets. The main sources of imprecision of the LDV measurements are identified and the related errors are estimated. The following is a summary of the more important findings and conclusions of this work.

- The principal source of imprecision of the LDV measurements results from bias effects due to unequal seed density in the central and peripheral jets. The limits of these bias are established by seeding only the peripheral jets.
- The present multi-jet assembly develops faster than related coaxial jets with similar velocity ratios between the central and the peripheral air streams, U_i/U_0, due to comparatively high mixing rates, which improve the performance of industrial burners. The decay of the centerline velocity is attenuated by decreasing the value of U_i/U_0 and may give rise to longer flames in practical burners.
- For $U_i/U_0 = 1$ the flow is characterized by considerably large values of the Reynolds shear stress and by zones of large turbulence anisotropy, which extend over all the length of the measurements. The normal stress in the axial direction is larger than those in the radial and tangential directions with the exception of a small region downstream the recirculating inter-jet zone. The turbulent structure is, therefore, different from that in related coaxial jets due to the comparatively large dominance of the central jet.
- In general, the experiments reported here provide evidence that the calculation of the aerodynamic field in multi-jet burner assemblies requires consideration of the individual stresses.

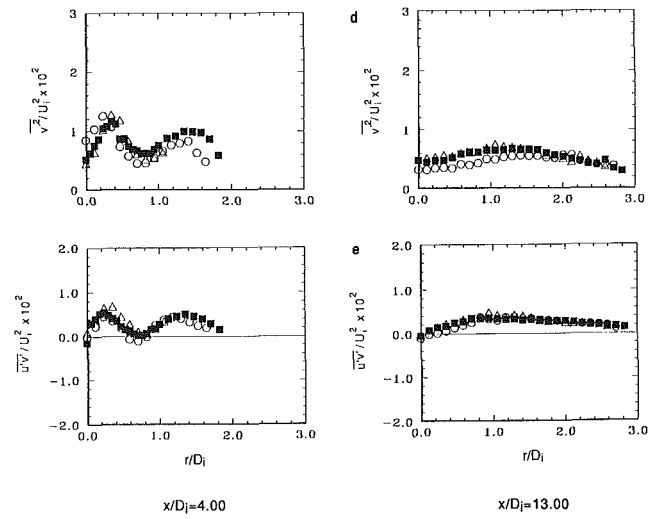

Fig. 6 (cont.)

Acknowledgments

The assistance of Mr. Jorge Coelho in plotting the results is gratefully acknowledged. Thanks are also due to Ms. Paula Marques for typing this report. The experiments were made at Centro de Termodinâmica Aplicada e Mecânica dos Fluídos da Universidade Técnica de Lisboa, CTAMFUTL-INIC.

References

Adrian, R. J., 1978, "Estimation of LDA Signal Strength and Signal-to-Noise Ratio," *TSI Quart.*, Vol. 14, pp. 3–8.

Adrian, R. J., 1983, "Laser Velocimetry," *Fluid Mechanics Measurements*, Hemisphere Pub. Corp., New York, pp. 155–244.

Bansal, R. K., and McCombs, N. R., 1986, "Low Cost Pressure Swing Absorption Oxygen Systems for Oxygen Enrichment of Glass Furnaces," *Proc. XIV Intl. Congress on Glass*, pp. 72–79.

Birch, A. D., and Dodson, M. G., 1980, "Some Aspects of Velocity Biasing in Turbulent Flows Resulting From Nonuniform Seeding," *Optical Acta*, Vol. 27, No. 1, pp. 3–8.

Booker, P. I., 1982, 'Developments in the Use of Oxygen in Glass Furnace Combustion Systems," *Glass*, May, pp. 172–178.

Bradshaw, P., Ferrins, D. H., and Atwell, N. P., 1967, "Calculation of Boundary-Layer Development Using the Turbulent Energy Equation," *J. Fluid Mechanics*, Vol. 28, pp. 593–616.

Carvalho, M. G., Durão, D. F. G., and Pereira, J. C. F., 1987, "Prediction of the Flow, Reaction and Heat Transfer in an Oxy-Fuel Glass Furnace," *Engineering Computations*, Vol. 4, No. 1, pp. 23–34.

Champagne, F. H., and Wygnanski, I. J., 1971, "An Experimental Investigation of Coaxial Turbulent Jets," *Int. J. Heat and Mass Transfer*, Vol. 14, pp. 1455–1464.

Dibble, R. W., Hartmann, V., Schefer, R. W., and Kollmann, W., 1987, "Conditional Sampling of Velocity and Scalars in Turbulent Flames Using Simultaneous LDV-Raman Scattering," *Experiments in Fluids*, Vol. 15, pp. 103–113.

Dimotakis, F., 1978, "Single Scattering Particle Laser-Doppler Measurements of Turbulence," AGARD CO 13, paper 10.7.

Durão, D. F. G., and Whitelaw, J. H., 1973, "Turbulent Mixing in the Developing Region of Coaxial Jets," ASME JOURNAL OF FLUID ENGINEERING, Vol. 95, pp. 467–473.

Durão, D. F. G., Heitor, M. V., and Moreira, A. L. N., 1987, "Temperature and Species Characteristics of the Flow in a Glass Smelting Kiln," Instituto Superior Técnico, Mech. Eng. Dept., Internal Report.

Durão, D. F. G., Laker, J. R., and Velho, A., 1985, "Velocity and Amplitude Bias and the Development of Laser Anemometry Counters," ASME Winter Annual Meeting, Miami Beach, Fla., Nov. 17–22.

Durst, F., and Zaré, M., 1974, "Removal of Pedestals and Directional Ambiguity of Optical Anemometer Signals," *J. Appl. Optics*, Vol. 13,(11), pp. 2562–2578.

Durst, F., Melling, A., and Whitelaw, J. H., 1981, *Principles and Practice of Laser-Doppler Anemometry*, 2nd ed., Academic Press.

Edwards, R. V. 1978, "How Real Are Particle Bias Errors?" Proc. 3rd Workshop on LV, Purdue University.

Erdmann, J. C., and Tropea, C. D., 1981, "Turbulence-Induced Statistical Bias in Laser Anemometry," *Proc. 7th Bienal Symp. on Turbulence*, Rolla, MO.

Gibbs, B. M., and Williams, A., 1983, "Fundamental Aspects on the Use of Oxygen in Combustion Process—A Review," *J. Institute of Fuel*, Vol. 56, pp. 74–83.

Glass, M., and Bilger, R. W., 1978, "The Turbulent Jet Diffusion Flame in a Coflowing Stream—Some Velocity Measurements," *Comb. Sci. and Tech.*, Vol. 18, pp. 165–177.

Harsha, P. T., and Lee, S. C., 1970, 'Correlation Between Turbulent Shear Stress and Turbulent Kinetic Energy," *AIAA Journal*, Vol. 8, No. 8, pp. 1508–1510.

Heitor, M. V., Laker, J. R., Taylor, A. M. K. P., and Vadifis, C., 1984, "Instruction Manual for the FS "Model 2" Doppler-Frequency Counter," Imperial College, Mech. Eng. Dept., Report FS/84/10.

Heitor, M. V., Taylor, A. M. K. P., and Whitelaw, J. H., 1987, "The Interaction of Turbulence and Pressure Gradients in Baffle-Stabilized Premixed Flame," *J. Fluid Mech.*, Vol. 181, pp. 387–413.

Kreid, D. K., 1974, "Laser-Doppler Velocimeter Measurements in Nonuniform Flow: Error Estimates," *Appl. Optics*, Vol. 13, No. 8, pp. 1872–1881.

Lau, J. C., Whiffen, M. C., Fisher, M. J., and Smith, D. M., 1981, "A Note on Turbulence Measurements With a Laser Velocimeter," *J. Fluid Mech.*, Vol. 102, pp. 353–366.

Pratte, B. D., and Keffer, J. F., 1972, "The Swirling Turbulent Jet," ASME *J. Basic Eng.*, pp. 739–748.

Ribeiro, M. M., and Whitelaw, J. H., 1976, "Turbulent Mixing of Coaxial Jets With Particular Reference to the Near Exit Region," ASME JOURNAL OF FLUIDS ENGINEERING, Vol. 98, pp. 284–292.

Ribeiro, M. M., and Whitelaw, J. H., 1980, "Coaxial Jets With and Without Swirl," *J. Fluid Mechanics*, Vol. 96, pp. 769–795.

Schatz, C., and Hueber, R. M., 1984, "Oxygen-Assisted Glass Melting Cuts Costs, Increased Pulls," *Ceramic Industry*, Mar., pp. 40–41.

Taylor, A. M. K. P., and Whitelaw, J. H., 1984, "Velocity Characteristics in the Turbulent Near Wake of Confined Axisymmetric Bluff Bodies," *J. Fluid Mech.*, Vol. 139, pp. 391–416.

Townsend, A. A., 1976, *The Structure of Turbulent Shear Flow*, Cambridge Univ. Press, 2nd ed.

Whiffen, M. C., 1975, "Polar Response of an LV Measurement Volume," *Proc. Minnesota Symp. on Laser Anemometry*, pp. 589–590.

Wygnanski, I., and Fielder, H., 1969, "Some Measurements in the Preserving Jet," *J. Fluid Mechanics*, Vol. 38, Part 5, pp. 577–612.

Yanta, W. J., and Smith, R. A., 1978, "Measurements of Turbulent-Transport Properties With a Laser-Doppler Velocimetry," AIAA Paper 73-169, 11th Aerospace Science Meeting, Washington.

Zhang, Z., and Wu, J., 1987, "On Principal Noise of Laser-Doppler Velocimetry," *Experiments in Fluids*, Vol. 5, pp. 193–196.

On the Mach Number Variation in Steady Flows of Dense Hydrocarbons

M. S. Cramer
Department of Engineering Science and Mechanics,
Virginia Polytechnic Institute and State University,
Blacksburg, VA 24061-0219

We consider the steady flow of five commonly encountered hydrocarbons in their dense gas regime. Isentropic flows are first examined and it is shown that dense gas effects lead to a non-monotone variation of the Mach number with density. It is also demonstrated that these effects may give rise to an increase, rather than the classical decrease, in the Mach number across oblique compression shocks. Significant increases in the shock detachment angle are also reported.

1 Introduction

The theory of perfect gases forms the basis for most of our intuition concerning the behavior of compressible fluids. However, dense gas effects may play a critical role in many applications. Examples include chemical transport and processing, two-phase flows, and Rankine power cycles. A new feature which arises for many fluids is an increase in the sound speed during isentropic expansion. This contrasts sharply with the perfect gas theory where the sound speed varies as

$$\rho^{\frac{\gamma-1}{2}} \text{ or } p^{\frac{\gamma-1}{2\gamma}},$$

where ρ, p, and $\gamma > 1$ are the fluid density, fluid pressure, and the ratio of specific heats. As a result, the isentropic expansion of a perfect gas always results in a decrease in the sound speed.

This nonclassical variation in the sound speed can lead to qualitative, in addition to quantitative, differences in the gasdynamic response. Recent surveys of these differences have been provided by Thompson (1971), Menikoff and Plohr (1989), Leidner (1990), and Cramer (1991). Of particular interest here is the fact that the decrease in the sound speed with increasing density may lead to a decrease in the Mach number during an isentropic expansion. A detailed description of this phenomenon can be found in the work of Leidner (1990), Cramer (1991), and Cramer and Best (1991). This nonclassical behavior is also implicit in Thompson's (1971) study as well as the more recent work on transonic nozzle flows by Warner (1990) and Chandrasekar and Prasad (1991), and Cramer and Crickenberger's (1992) analysis of the Prandtl-Meyer function.

Because the basic physics have already been described extensively in the previous investigations, here we simply note that the differential form of the Bernoulli equation for steady, isentropic flows of arbitrary single-phase gases can be written

$$\frac{d\mathrm{M}}{d\rho} = \frac{\mathrm{M}}{\rho} J, \tag{1.1}$$

where M is the local Mach number and

$$J \equiv 1 - \frac{\rho\Gamma}{a} - \frac{1}{M^2}. \tag{1.2}$$

Here the thermodynamic parameter

$$\Gamma \equiv \frac{a}{\rho} + \frac{\partial a}{\partial \rho}\bigg|_s \tag{1.3}$$

is frequently referred to as the fundamental derivative of gasdynamics. The quantities $a = a(\rho,s)$ and s are the thermodynamic sound speed and the fluid entropy, respectively. In the perfect gas theory,

$$\frac{\rho\Gamma}{a} = \frac{\gamma+1}{2} > 1, \tag{1.4}$$

and, as a result, $J < 0$ for all temperatures and pressures. It is easily verified that J is necessarily negative for any fluid, whether perfect or not, having $\rho\Gamma/a > 1$.

As a numerical example we consider normal heptane (C_7H_{16}). Reid et al. (1987) report a critical density, temperature and pressure of 0.233 gm/cm^3, 540°K and 27.04 atm. If we employ the Martin-Hou (1955) equation of state, we find that the minimum value of $\rho\Gamma/a$ on the critical isotherm is 0.474. At the same point, the pressure is computed to be 0.923 $p_c \approx 25$ atm and the sound speed is found to be approximately 105 m/s. It is clear from (1.3), and the value of $\rho\Gamma/a$, that the sound speed is a decreasing function of density or pressure at this point. This decrease becomes even more obvious when the above value of the sound speed is compared to the corresponding ideal gas, i.e., low pressure, value at the same temperature. This ideal gas value is given by the familiar formula $(\gamma RT)^{1/2}$, where R is the gas constant for heptane. At $T = 540$°K, $\gamma \approx 1.032$ and the sound speed is found to be 215 m/s, which is approximately twice as large as the dense gas value. At the point where $\rho\Gamma/a = 0.474$, $J < 0$, and the Mach number decreases with density, if $\mathrm{M} < 1.38$. If, on the other hand, the local Mach number is greater than 1.38, then $J > 0$ and the nonclassical increase in M with density is observed. One naturally expects that sufficiently large local Mach num-

Contributed by the Fluids Engineering Division for publication in the JOURNAL OF FLUIDS ENGINEERING. Manuscript received by the Fluids Engineering Division March 20, 1991.

bers can always be attained simply by increasing either the upstream Mach number or the stagnation pressure.

One objective of the present study is to verify this nonclassical behavior for a range of commonly encountered hydrocarbons. The well-known Martin-Hou (1955) equation will be employed to compute the variation of the Mach number with density along an isentrope. Our choice of the Martin-Hou equation is due to its proven accuracy over a wide range of fluids. It is generally regarded as more accurate than the well-known van der Waals or Redlich-Kwong equations of state. For example, we consider water at a temperature and density of 350°C and 0.0872 gm/cm^3. The Martin-Hou equation then yields a pressure of 148.88 atm. which differs by only about 0.6 percent with the accepted result of 148.02 atm recorded by Jones and Hawkins (1986). At the same temperature and density, the Redlich-Kwong and van der Waals equations yield a pressure of 157.25 atm and 163.93 atm, corresponding to errors of about 6 and 11 percent, respectively. The differences are even more dramatic at supercritical densities. For example at 400°C and 0.3584 gm/cm^3, the Martin-Hou equation yields an error of only about 4 percent whereas the Redlich-Kwong and van der Waals equations result in errors of 33 and 131 percent, respectively. It should be pointed out that the results presented in Section 2 have been predicted using rather general arguments and are expected to hold whenever $\rho\Gamma/a$ becomes less than one. In particular, such nonclassical behavior should be anticipated regardless of the equation of state employed, provided only that the predictions of this equation of state are qualitatively correct. Thus, computations involving both van der Waals and Redlich-Kwong equations of state are also expected to yield qualitatively similar results.

The work presented in the next section is seen to be closely related to that of Bober and Chow (1990) who examined the dense gas corrections required in the isentropic flow of methane. Our work demonstrates that striking qualitative differences must be accounted for, particularly when slightly heavier hydrocarbons are considered.

When it is recalled that the entropy rise across weak shock waves tends to be relatively small, it is at least reasonable to suggest that the Mach number change across oblique shocks might also differ qualitatively from that of the perfect gas theory. In the perfect gas theory, a compression corner generates an oblique compression shock across which the Mach number decreases. In Section 3 we demonstrate that this decreasing Mach number rule does not necessarily hold in the dense gas regime, particularly if $\rho\Gamma/a < 1$ at the pressures and temperatures of interest. Thus, not only is the isentropic theory of dense hydrocarbons qualitatively different but that involving oblique shocks is as well.

The fluids chosen for our study are hexane (C_6H_{14}), heptane (C_7H_{16}), octane (C_8H_{18}), nonane (C_9H_{20}), and decane ($C_{10}H_{22}$). Each is recognized to be of the alkane series of which methane is the lightest. Data required for the Martin-Hou equation are the critical properties and the standard boiling temperature. Computations involving entropy, internal energy, and the enthalpy require a knowledge of the ideal gas, i.e., low pressure, specific heats. In each case, the values of these parameters were taken from the data provided by Reid et al. (1987). Further details of the specific implementation are found in the articles by Cramer (1989) and Cramer and Best (1991).

In each case illustrated, the flow was found to be entirely in the single-phase regime. The saturation data was estimated through use of Riedel's (1954) vapor pressure formula. Earlier editions of the text by Reid et al. have compared Riedel's formula to other commonly used equations and have concluded it is one of the more accurate models in use.

As a numerical example, we consider octane and a point in the middle of the nonclassical regime depicted in Fig. 2.1. At a density of 0.4 ρ_c, the temperature and pressure were found to be approximately 555°K and 19.8 atmospheres, respectively.

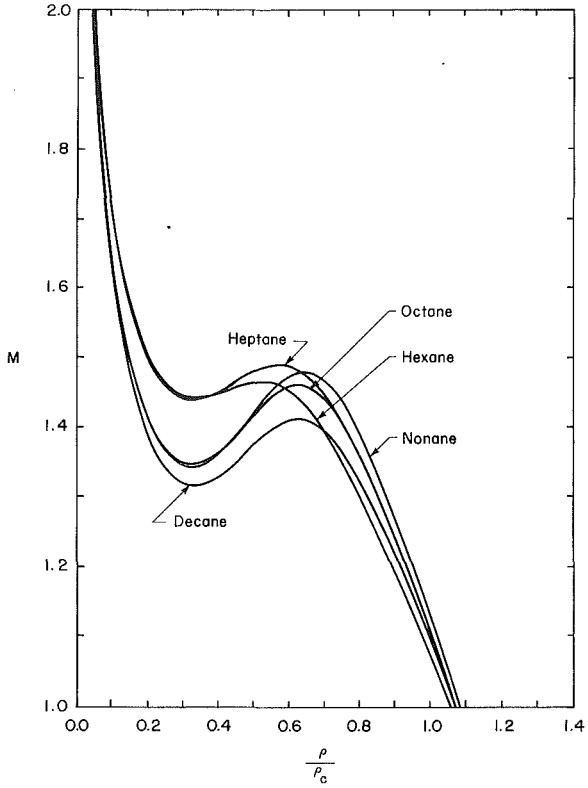

Fig. 2.1 Variation of Mach number with density along isentropes. The stagnation states for each isentrope are recorded in Table 2.1.

At this temperature, the saturation pressure was found to be approximately 20.4 atmospheres, which clearly demonstrates that the flow is in the single-phase regime, at least at this point. In our actual calculations, this comparison was automatically carried out for every point on the isentrope of interest.

It is important to emphasize that the nonclassical effects illustrated here are due to the decrease in sound speed rather than phase-change effects. On the other hand, metastable conditions frequently give rise to values of $\rho\Gamma/a < 1$. The work presented here clearly shows that nonclassical effects must be anticipated if such metastable states are encountered in experimental or numerical studies.

2 Isentropic Flows

The general scheme for the computation of isentropic flows is that developed by Cramer and Best (1991). Our approach is seen to be essentially the same as that outlined by Vinokur (1990). Stagnation properties, i.e., T_0, ρ_0, where T is the absolute temperature, are first specified. A density $\rho < \rho_0$ is then specified and the corresponding temperature is found by numerical iteration of the isentropic condition

$$s(\rho, T) = s_0, \tag{2.1}$$

where $s_0 \equiv s(\rho_0, T_0)$ is the stagnation entropy. Explicit expressions for the entropy, internal energy, and specific heat at constant volume have been given by Cramer and Best (1991). In order to save space we simply refer to this previous study. We note that the standard conditions of a stable thermodynamic equilibrium require that

$$c_v(\rho, T) \equiv T \left.\frac{\partial s}{\partial T}\right|_\rho > 0,$$

where c_v is the specific heat at constant volume. Thus, the iteration process is well-behaved and unique. Once T is determined, the pressure $p(\rho, T)$, sound speed $a(\rho, T)$, and enthalpy $h(\rho, T)$ are then computed through use of the equation

Table 2.1 Stagnation conditions for isentropes plotted in Fig. 2.1. The symbol V denotes the specific volume ($V = 1/\rho$), the subscripts o denote stagnation conditions and the subscripts c denote properties at the thermodynamic critical point. The quantity J_{max} is the computed maximum of J on the isentrope.

Fluid	$\frac{V_o}{V_c}$	$\frac{T_o}{T_c}$	$\frac{p_o}{p_c}$	J_{max}
Hexane (C_6H_{14})	0.7	1.06	1.77	0.05
Heptane (C_7H_{16})	0.7	1.06	1.85	0.10
Octane (C_8H_{18})	0.7	1.04	1.58	0.20
Nonane (C_9H_{20})	0.7	1.04	1.62	0.23
Decane ($C_{10}H_{22}$)	0.7	1.04	1.60	0.18

of state, the definition $h = e + p/\rho$, where e is the internal energy, and the explicit form of the sound speed

$$a = \left\{ \left.\frac{\partial p}{\partial \rho}\right|_T + \frac{T}{c_v \rho^2}\left(\left.\frac{\partial p}{\partial T}\right|_\rho\right)^2 \right\}^{1/2}.$$

The Mach number may be computed through use of the Bernoulli equation:

$$h(\rho, T) + \frac{M^2}{2} a^2(\rho, T) = h_0, \tag{2.2a}$$

where $h_0 \equiv h(\rho_0, T_0)$ is recognized as the stagnation enthalpy. Rearrangement of (2.2a) yields

$$M = \frac{\{2(h_0 - h)\}^{1/2}}{a}. \tag{2.2b}$$

Although it is not used explicitly in our computations, (1.1) is just the differential form of (2.2). That is, (1.1) is derived by combining the differential of (2.2) with Gibbs' relation

$$dh = Tds + \frac{1}{\rho} dp \tag{2.3}$$

and the condition of isentropic flow (2.1). Here we note that an alternate method for ensuring satisfaction of the isentropic condition (2.1) is to develop a set of differential equations in a manner similar to that of Leidner (1990), Bober and Chow (1991), or Cramer and Crickenberger (1992).

The results of sample calculations of the Mach number versus density variations are plotted in Fig. 2.1. The corresponding stagnation conditions are listed in Table 2.1. We have also employed (1.2) along with the computed values of M and $\rho\Gamma/a$ to compute and record the maximum values of J on each isentrope.

A comparison of the curves for hexane and heptane or those for octane and nonane suggests that the nonclassical phenomena tend to increase in strength with molecular weight. This is indeed consistent with the observation that increasing molecular complexity tends to increase the ideal gas specific heats. Increases in the specific heat tend to strengthen the sound speed decrease, resulting in smaller values of the scaled fundamental derivative $\rho\Gamma/a$. We may therefore conclude that, as the molecular complexity increases, the region where $J > 0$ tends to become larger and the maximum value of J tends to increase.

The results for decane would appear to contradict this conclusion. However, at fixed density, the value of $\rho\Gamma/a$ tends to decrease with temperature between the critical isotherm and the saturation line. Thus, the temperature drop associated with the isentropic expansion strengthens the nonclassical effect. Due to its relatively large specific heats, the temperature decrease in decane is weak compared to that of octane and nonane. Because the stagnation temperature used for decane is the same as that for octane and nonane, the corresponding temperatures along the isentrope for decane are somewhat larger than those of the two lighter fluids. Thus, the corresponding values of $\rho\Gamma/a$ remain somewhat larger leading to a weaker nonclassical effect. It is easily verified that the nonclassical effect in decane can be strengthened considerably by decreasing the stagnation temperature. For example, if we take $V = 0.7\ V_c$ and $T = 1.03\ T_c$, the maximum value of J on the isentrope is 0.26.

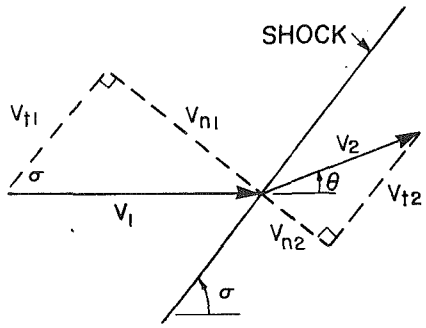

Fig. 3.1 Notation for oblique shock geometry.

Thus, the Mach number variation clearly differs from that of the perfect gas theory when dense gas effects result in values of the scaled fundamental derivative which are less than one. These differences are not only quantitative but qualitative. The practical significance of this result is seen when it is recalled that the classical treatment of isentropic flows employs the Mach number as a parameter for the computation of all other flow properties. However, the non-monotone character revealed here shows that this parameterization is no longer possible. Clearly, for a given choice of M, as many as three values of density, temperature or pressure may be obtained. It would appear that a better choice of parameters would either be the density or pressure.

Finally, we note that (1.1)–(1.2) may be combined with the standard differential forms of the isentropic condition (2.1), the quasi-one-dimensional mass equation and the Bernoulli equation to yield

$$\frac{1}{J}\frac{dM}{M} = \frac{d\rho}{\rho} = \frac{dp}{\rho a^2} = \frac{c_p}{\beta a^2}\frac{dT}{T} = -M^2\frac{dv}{v} = \frac{M^2}{1-M^2}\frac{dA}{A}, \tag{2.4}$$

where Gibbs' relation (2.3) and the definition of the coefficient of thermal expansion

$$\beta \equiv -\frac{1}{\rho}\left.\frac{\partial \rho}{\partial T}\right|_p \tag{2.5}$$

have been employed. Here v is the particle velocity and A is the streamtube area. In the usual way, it may be shown that (2.4) requires that the particle velocity increases and the pressure decreases during an isentropic expansion ($d\rho < 0$). If the thermal expansion coefficient (2.5) is positive, as it is for the majority of gases, the temperature will also decrease during the isentropic expansion. Furthermore, the last term in (2.4) may be used to show that the supersonic flows discussed in this section may be generated through use of a conventional converging-diverging nozzle. We may therefore conclude that the remainder of the flow properties behave qualitatively the same as in the perfect gas theory, even though the Mach number variation is nonclassical.

3 Oblique Shock Waves

For the present purposes, the most convenient form of the shock jump relations are given by

$$\rho_1 v_{n1} = \rho_2 v_{n2} = m, \tag{3.1}$$

$$\frac{p_2 - p_1}{V_2 - V_1} = -m^2, \tag{3.2}$$

$$v_{t1} = v_{t2}, \tag{3.3}$$

$$H(\rho_1, T_1, \rho_2, T_2) \equiv h_2 - h_1 - \frac{V_2 + V_1}{2}(p_2 - p_1) = 0, \tag{3.4}$$

where $V \equiv \rho^{-1}$ is the specific volume, v is the particle velocity and the subscripts n and t denote the components of $\mathbf{v}$ which

are normal and tangential to the shock surface. The geometry and notation are also depicted in Fig. 3.1. The quantity m is the mass flux through the oblique shock and Eq. (3.1) is recognized as the mass equation. Equations (3.2)–(3.3) represent the normal and tangential components of momentum. The last equation is the well-known Hugoniot relation, derived by combining jump conditions for the mass, momentum, and energy. The derivation of (3.1)–(3.4) may be found in any standard reference on gasdynamics, see, e.g., Thompson (1972) or Anderson (1990).

The input data for our computation are the upstream thermodynamic state (ρ_1, T_1), the upstream Mach number M_1, and the downstream density ρ_2. The latter condition is recognized as providing a measure of the shock strength. The analog in the perfect gas theory is the specification of either the flow deflection angle θ or the shock angle σ in addition to the freestream Mach number. In the present study, we restrict our attention to fluids having $\Gamma > 0$ everywhere. Thus, the shocks of interest will all be of the compression type and ρ_2 will be chosen to satisfy $\rho_2 \geq \rho_1$. Because the upstream thermodynamic state is known, all other thermodynamic properties, e.g., p_1, h_1, a_1, Γ_1, etc., may be computed in a manner similar to that employed in the previous section.

The downstream thermodynamic state is determined by solving the Hugoniot (3.4) iteratively for T_2. The general scheme is that already employed by Cramer and Crickenberger (1991) in their study of the dissipative structure of shock waves in dense gases. Once the downstream temperature is determined, all other thermodynamic properties may be computed. In particular, the pressure p_2 may be computed and (3.2) may be employed to determine the mass flux m. The normal components of the upstream and downstream Mach numbers are then determined by combining the mass Eq. (3.1) with the definition of the normal Mach numbers

$$M_{n1} \equiv \frac{v_{n1}}{a_1}, \quad M_{n2} \equiv \frac{v_{n2}}{a_2}. \tag{3.5}$$

In terms of the pressure jump, we find

$$M_{ni} = \frac{1}{\rho_i a_i}\left(-\frac{p_2 - p_1}{V_2 - V_1}\right)^{1/2}, \tag{3.6}$$

where $i = 1$ or 2. From the standard trigonometric manipulations, we find that the shock angle σ is given by

$$\sigma = \sin^{-1}\left(\frac{M_{n1}}{M_1}\right). \tag{3.7}$$

The flow deflection angle θ is found by combining trigonometry with the mass and tangential momentum equations to yield

$$\theta = \sigma - \tan^{-1}\left(\frac{\rho_1}{\rho_2}\tan\sigma\right). \tag{3.8}$$

For the purposes of comparison, we will also present results for perfect gases. The formulas employed are the standard ones found in any text on gasdynamics, see, e.g., Anderson (1990) or Thompson (1972).

To illustrate the differences between the dense gas behavior and that observed in the perfect gas regime, we have examined octane which is initially taken to be at its critical temperature of 568.8°K and a density equal to 0.4 $\rho_c \approx 0.093$ gm/cm^3. The corresponding pressure and nondimensional fundamental derivative are computed to be

$$p_1 \approx 0.8673 p_c \approx 21.3 \text{ atm and } \left.\frac{\rho\Gamma}{a}\right|_1 = 0.47.$$

For the fluids considered here the thermal expansion coefficient (2.4) is positive. As a result, the temperature will increase across each shock considered and $T_2 > T_1 = T_c$ for each case. Thus, all shocks reside in the single-phase region of the p-V diagram and checks with the saturation curve were not necessary.

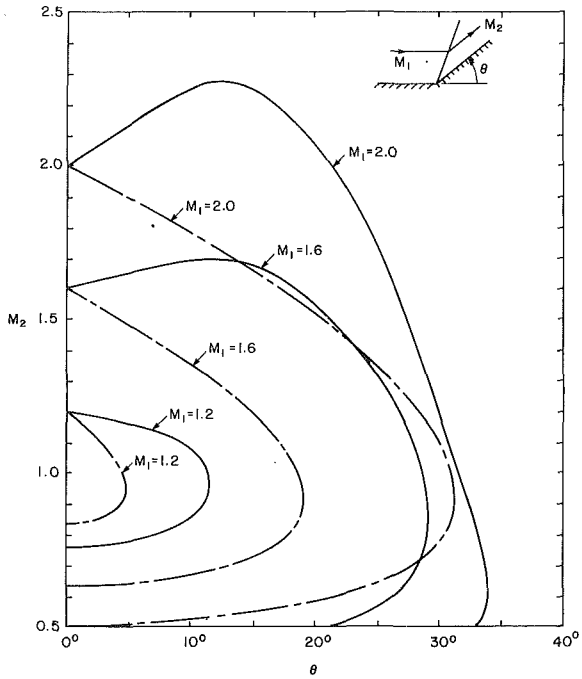

Fig. 3.2 Variation of downstream Mach number with downstream flow deflection angle. Fluid is octane at an upstream temperature and pressure of 568.8°K and 21.3 atm. The broken lines denote computations based on the classical perfect gas formulas with $\gamma = \gamma$ (568.8°K) $\approx$ 1.0273.

According to (1.2), $J_1 < 0$ if the Mach number is less than 1.37 and is positive if $M_1 > 1.37$. With these thermodynamic conditions as our upstream state we have computed the downstream Mach number variation with the downstream flow deflection angle for the cases $M_1 = 1.2$, 1.6, 2.0, where M_1 is the upstream Mach number. Plots are found in Fig. 3.2. As expected, both the $M_1 = 1.6$ and $M_1 = 2.0$ cases show an initial increase in the downstream Mach number M_2. Because $J_1 < 0$ for the case $M_1 = 1.2$, it is also not surprising that M_2 initially decreases. For the purposes of comparison we have also plotted the results of the perfect gas theory. The value of γ employed in the perfect gas theory was 1.0273 which corresponds to the value for octane at its critical temperature. Thus, the upstream states of both perfect and dense gas calculations are at exactly the same temperature. The perfect gas calculations are, of course, expected to be accurate at low, e.g., atmospheric, pressures whereas the dense gas results hold at the aforementioned pressure of 21.3 atm.

Significant quantitative differences include a large increase in the detachment angle, that is, the maximum flow deflection angle which can be attained for a fixed upstream state. In the case depicted, the increase in the detachment angle is largest when the upstream Mach number is small. For example, at a freestream Mach number of 1.2, a shock wave in a perfect, i.e., low pressure, gas will be detached for wedge half-angles of 5 deg and above. However, at the higher pressure indicated above, the shock will remain attached for wedge half-angles as large as 11 deg. That is, the detachment angle in the dense gas regime is seen to be over twice as large as that in the low pressure regime. If, on the other hand, we consider a fixed wedge having a half-angle of 5 deg, more detailed calculations reveal that the detachment Mach number is $M_{1d} \approx 1.20$ in the perfect gas limit and $M_{1d} \approx 1.11$ at the dense gas conditions employed in Fig. 3.2. If we take the onset of detachment as a crude indication of the onset of transonic flow effects, the results presented here strongly suggest that dense gas effects can narrow the transonic flow regime. Thus, the losses associated with transonic flows will be restricted to a smaller range of flow speeds.

A reasonable physical explanation for this narrowing of the transonic regime is related to the decrease of the intrinsic nonlinearity parameter (1.3). The appropriate form of the transonic similarity parameter for general, rather than perfect, gases is

$$K=\frac{M_1^2-1}{\left(\epsilon\frac{\rho\Gamma}{a}\right)^{2/3}},$$

where ϵ is a measure of the disturbance strength and we have employed M_1^2-1 rather than $1-M_1^2$ for this supersonic flow. For two flows with the same upstream Mach number, here we take $M_1 = 1.2$, the flow detachment angles are therefore expected to be related by

$$\epsilon_{PG}\frac{\rho\Gamma}{a}\bigg|_{PG}=\epsilon_{DG}\frac{\rho\Gamma}{a}\bigg|_{DG}, \tag{3.9}$$

where the subscripts *PG* and *DG* refer to the perfect gas and dense gas values, respectively. Thus, at the same freestream Mach number, the shock detachment angle is expected to be increased by the ratio of the fundamental derivatives. In the perfect gas case, we take

$$\epsilon_{PG}=5^\circ,\ \frac{\rho\Gamma}{a}\bigg|_{PG}=\frac{\gamma+1}{2}\approx 1.0137,$$

where (1.4) has been employed and the ideal gas ratio of specific heats for octane was taken to be $\gamma(568.8^\circ\text{K}) \approx 1.0273$. At the pressure and temperature employed in Fig. 3.2, $(\rho\Gamma/a)_{DG} \approx 0.47$. Substitution of these values in (3.9) then yields the estimate

$$\epsilon_{DG}\approx 10.8^\circ$$

which is within about 6 percent of the computed detachment angle. That is, the fundamental derivative in the dense gas region is roughly half that in the perfect gas region. As a result, the detachment angle is roughly doubled.

It should also be noted that the increase in detachment angle can also be observed at Mach numbers higher than those normally associated with transonic flow. For the thermodynamic state corresponding to that of Fig. 3.2, the dense gas detachment angle is greater than the perfect gas angle up to a freestream Mach number of approximately 2.1. Above this Mach number, the dense gas shock wave detaches at smaller angles than the low pressure gas. The explanation may again be related to the size of the fundamental derivative. As indicated by the computed value of Γ_1, the flow originates in a region of relatively small $\rho\Gamma/a$. Because Γ is a measure of the intrinsic nonlinearity of the fluid and detachment is caused by this nonlinearity, the detachment is delayed as long as the average value of $\rho\Gamma/a$ is small. Some justification for this claim is also seen by examination of the $M_1 = 1.2$ contours in Fig. 3.2. Because the shocks are relatively weak, both upstream and downstream conditions correspond to small values of $\rho\Gamma/a$. As a result, the differences between the perfect and dense gases are a maximum. On the other hand, the $M_1 = 2$ curves correspond to flows which have been shocked out of the small $\rho\Gamma/a$ region. Thus, less advantage is seen in these cases.

Because the fundamental derivative varies with density, it is of interest to determine the variation of the detachment angle with the upstream density. Here we have reconsidered octane at its critical temperature, i.e., $T_1 = T_c \approx 568.8^\circ$K, and a freestream Mach number $M_1 = 2$. Under these conditions, the perfect gas detachment angle is approximately 31.4°. For reference we also note that the detachment angle for a perfect diatomic gas ($\gamma = 1.4$) is approximately 23°, see, e.g., Thompson (1972) or Anderson (1990). The upstream density was varied and the detachment angle was computed. The results of these calculations are found in Table 3.1. Although the dense gas detachment angle is only about 8 percent larger than the perfect gas value when $\rho_1 = 0.4\,\rho_c$ ($V_1 = 2.5V_c$), this angle is approximately 46 percent larger than the perfect gas value when $\rho_1 = 0.2\rho_c$ ($V_1 = 5.0V_c$). Inspection of the values of the scaled fundamental derivative upstream of the shock reveals that the upstream value of $\rho\Gamma/a$ increases as V_1 increases. Clearly, as $V\to\infty$, $\rho\Gamma/a$ must approach the ideal gas value of 1.0137. The reason the detachment angle increases is that the compression shocks necessarily take the flow back into the small $\rho\Gamma/a$ region. It appears that the average value of $\rho\Gamma/a$ is sufficiently small to delay the detachment. We also note the dense gas detachment angle is actually less than the perfect gas value at $\rho_1 = 0.5\rho_c$. This turns out to be the approximate position of the local minimum in $\rho\Gamma/a$ on the critical isotherm. By the arguments just given, we might also expect to obtain a relatively low detachment angle. This is due to the fact the compression shock takes the flow into the large $\rho\Gamma/a$ region corresponding to liquid-like states. The typical downstream densities near the detachment state will be supercritical, i.e., $\rho > \rho_c$. Values of the fundamental derivative can take on values between 5 and 10 in this region. Thus, the average value of $\rho\Gamma/a$ is likely to be relatively large.

Table 3.1 Computed detachment angles θ_d for various upstream densities for octane. Here $V \equiv \rho^{-1}$ is the specific volume. The upstream temperature and Mach number were $T_c \approx 568.8^\circ$K and 2.0.

$\frac{V_1}{V_c}$	$\frac{p_1}{p_c}$	$\frac{\rho\Gamma}{a}\Big\vert_1$	θ_d
2.0	0.936	0.41	28.4°
2.5	0.867	0.47	34.0°
3.0	0.798	0.55	38.0°
3.5	0.733	0.62	40.9°
4.0	0.676	0.67	43.0°
4.5	0.626	0.71	44.7°
5.0	0.582	0.74	45.8°

Table 3.2 Detachment angles for various fluids. The subscripts *DG* and *PG* denote the results of dense and perfect gas calculations. Upstream states were taken to be $T_1 = T_c$, $\rho_1 = 0.25\,\rho_c$ and $M_1 = 1.5$.

Fluid	$\theta_d\vert_{DG}$	$\theta_d\vert_{PG}$
Hexane	25.9°	15.5°
Heptane	28.1°	15.6°
Octane	30.2°	15.7°
Nonane	31.9°	15.7°
Decane	33.9°	15.7°

As a final illustration of the increase in shock detachment angle we have computed this angle for each of the five hydrocarbons listed in Table 2.1. In each case, the upstream temperature was taken to be the critical value for the fluid of interest and the density was taken to be one-quarter of the fluid's critical density. The freestream Mach number was taken to be 1.5. These detachment angles have been recorded in Table 3.2 along with the corresponding perfect gas values. As with the calculations for octane, the ratio of specific heats employed in the perfect gas formulas is that evaluated at the upstream temperature. Under these conditions the dense gas effects increase the low pressure result by factors of 67–116 percent. As expected, the advantageous effects increase with molecular weight and specific heat.

For these fluids, the ratios of specific heats are fairly close to one. As a result, the changes in the ideal gas γ as each new fluid is considered is relatively small. Thus, at a fixed M_1, the changes in the perfect gas detachment angle are expected to be relatively small. This observation is borne out in the results recorded in Table 3.2.

4.1 Summary

The present study has given specific examples of nonclassical gasdynamic behavior in dense gases. The fluids discussed are

well-known hydrocarbons typically employed as fuels and encountered in chemical processing applications. The physical reason for the unusual behavior can be traced to the existence of a region of decreasing sound speed found in the dense gas regime of many fluids. The results of our calculations clearly illustrate the dramatic differences between dense and perfect gases.

Both the study of isentropic flows and that of oblique shock waves provide examples of qualitative differences with the perfect gas theory. An important consequence of the nonmonotone Mach number variation in isentropic flows is that the Mach number can no longer be used as the single parameter determining all other flow properties, at least when dense gases having moderately large specific heats are considered.

Quantitative differences include large increases in the detachment angles for oblique shocks. A doubling of this angle is easily obtained for a wide variety of upstream states and fluids. Because the stagnation pressure losses are likely to be lower for attached shock waves, the flow of dense hydrocarbons is expected to be more efficient than that at lower pressures or that predicted by the perfect gas theory.

The nonclassical behavior predicted here is also expected to be observed when other dense gas equations of state are employed. It is useful to note that the anti-intuitive behavior is a result of the natural dynamics of fluids of moderate complexity rather than numerical or experimental error.

Future work will report the extent to which smaller phenomena occurs in other fluids and the influence on Mach reflection and shock-induced boundary layer separation.

Acknowledgment

This research was supported by the National Science Foundation under Grant #CTS 891398. The author would also like to thank A. B. Crickenberger for his assistance in generating the results of Section 3.

References

Anderson, J. D., 1990, *Modern Compressible Flow with Historical Perspective*, 2nd Ed., McGraw-Hill.

Bober, W., and Chow, W. L., 1990 "Nonideal Isentropic Gas Flow Through Converging-Diverging Nozzles," ASME JOURNAL OF FLUIDS ENGINEERING, Vol. 112, pp. 455-460.

Chandrasekar, D., and Prasad, P., 1991, "Transonic Flow of a Fluid with Positive and Negative Nonlinearity through Nozzles," *Phys. Fluids A.*, Vol. 3, pp. 427-438.

Cramer, M. S., 1989, "Negative Nonlinearity in Selected Fluorocarbons," *Phys. Fluids A*, Vol. 1, pp. 1894-1897.

Cramer, M. S., 1991, "Nonclassical Dynamics of Classical Gases," Article in *Nonlinear Waves in Real Fluids*, ed. A. Kluwick, Springer-Verlag.

Cramer, M. S., and Best, L. M., 1991, "Steady Isentropic Flows of Dense Gases," *Phys. Fluids A*, Vol. 3, pp. 219-226.

Cramer, M. S., and Crickenberger, A. B., 1991, "The Dissipative Structure of Shock Waves in Dense Gases," *J. Fluid Mech*, Vol. 223, pp. 325-355.

Cramer, M. S., and Crickenberger, A. B., 1992, "The Prandtl-Meyer Function for Dense Gases," To appear in the *AIAA J.*

Jones, J. B., and Hawkins, G. A., 1986, *Engineering Thermodynamics*, 2nd Ed., Wiley.

Leidner, P., 1990, "Realgaseinflüsse in der Gasdynamik," Diplomarbeit, University of Karlsruhe, Karlsruhe, W. Germany.

Martin, J. J., and Hou, Y. C., 1955, "Development of an Equation of State for Gases," *AIChE J.*, Vol. 1, pp. 142-151.

Menikoff, R., and Plohr, B., 1989, "Riemann Problem for Fluid Flow of Real Materials," *Rev. Mod. Phys.*, Vol. 61, pp. 75-130.

Reid, R. C., Prausnitz, J. M., and Poling, B. E., 1987, *The Properties of Gases and Liquids*, 4th Edition, Wiley.

Riedel, L., 1954, "Eine neue Universelle Damfdruckformel-Untersuchungten über eine Erweiterung des Thereoms der übereinstimmenden Zustände. Teil 1," *Chem. Ing. Tech.*, Vol. 26, pg. 83.

Thompson, P. A., 1972, *Compressible-Fluid Dynamics*, McGraw-Hill, New York.

Thompson, P. A., 1971, "A Fundamental Derivative in Gasdynamics," *Phys. Fluids*, Vol. 14, pp. 1843-1849.

Warner, S. M., 1990, "Steady Non-Isentropic Flows in Dense Gases," Virginia Polytechnic Institute and State University Engineering Report, No. VPI-E-90-24.

Vinokur, M., 1990, Discussion of "Nonideal Isentropic Gas Flow Through Converging-Diverging Nozzles," ASME JOURNAL OF FLUIDS ENGINEERING, Vol. 112, pp. 460-461.

Aerodynamic Sensitivity Analysis Methods for the Compressible Euler Equations

Oktay Baysal
Associate Professor.

Mohamed E. Eleshaky
Graduate Research Assistant.

Mechanical Engineering and
Mechanics Department,
Old Dominion University,
Norfolk, VA 23529-0247

A mathematical formulation is developed for aerodynamic sensitivity coefficients based on a discretized form of the compressible, two-dimensional Euler equations. A brief motivating introduction to the aerodynamic sensitivity analysis and the reasons behind an integrated flow/sensitivity analysis for design algorithms are presented. Two approaches to determine the aerodynamic sensitivity coefficients, namely, the finite difference approach, and the quasi-analytical approach are discussed with regards to their relative accuracies and involved computational efforts. In the quasi-analytical approach, the direct and the adjoint variable methods are formulated and assessed. Also, several methods to solve the system of linear algebraic equations, that arises in the quasi-analytical approach, are investigated with regards to their accuracies, computational time and memory requirements. A new flow prediction concept, which is an outcome of the direct method in the quasi-analytical approach, is developed and illustrated with an example. Surface pressure coefficient distributions of a nozzle-afterbody configuration obtained from the predicted flowfield solution are compared successfully with their corresponding values obtained from a flowfield analysis code and the experimental data.

Introduction

Computational fluid dynamics (CFD) has recently evolved to a level of maturity to simulate complex flows with reasonable fidelity to the flow physics. Among many reasons responsible for this emergence of CFD, probably the most important one, is the increased accessibility and hence the wide spread use of the supercomputers with high computing speeds and large memories. The aerodynamic design now more than ever enjoys the results of CFD as an important part of its database. An illustration of the major reasons which push and pull CFD to design is given in Fig. 1.

Often the dilemma a designer is challenged with, however, is the conflicting targets derived from isolated CFD analyses for the individual components of an aircraft. An obvious remedy, whenever it is possible, is a combined analysis of the aerodynamics of an integrated structure. Examples for this include the airframe-propulsion integration (Murthy and Paynter, 1986) and the aircraft-stores integration (Baysal et al., 1991a). An important outcome of such an approach is the aerodynamic interference between the components. A drawback, however, is the prohibitively high cost of performing flow analyses for a large matrix of parameters associated with a complex, multicomponent configuration.

With this impetus, it is desirable to know the aerodynamic sensitivity of the instantaneous design to all the involved parameters and thereby reduce the analysis matrix to include only the parameters deemed most influencing. Also, a design optimization algorithm requires the first-order gradients of the objective and the constraint functions. Determination of these gradients necessitates the aerodynamic sensitivity coefficients, that is, the derivatives of the objective and the constraints with respect to the design variables. Since in most optimization

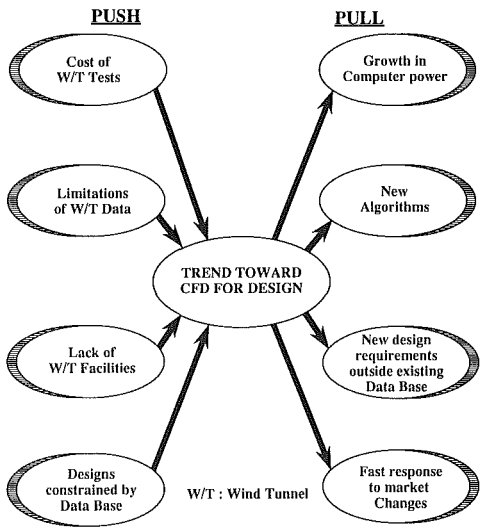

Fig. 1 The factors which push and pull the trend toward CFD for design (Murthy and Paynter, 1986)

Contributed by the Fluids Engineering Division and presented at the Winter Annual Meeting, Dallas, Texas, November 25-30, 1990 of THE AMERICAN SOCIETY OF MECHANICAL ENGINEERS. Manuscript received by the Fluids Engineering Division October 9, 1990.

procedures, a dominant contributor to the computational cost is the calculation of the sensitivity coefficients, it is desirable to develop efficient methods for this purpose. Generating the sensitivity coefficients by a finite difference approximation requires repeating the aerodynamic analysis with incremented values of the design variables. This simple approach has the disadvantage of being potentially computer intensive, particularly when a complex set of governing equations are being used for the flow analysis. A preferable approach is to obtain the sensitivity coefficients directly and analytically from an appropriate set of equations to eliminate the costly and repetitive flowfield analyses.

The primary objective of this study is to present several methods to determine the aerodynamic sensitivity coefficients based on a discretized form of the compressible, two-dimensional Euler equations. Besides obtaining accurate values of these coefficients, a major concern is the computational feasibility of each one of these methods. By far, the dominant consumer of the computation time is solving the set of linear algebraic equations resulting from the sensitivity equation. Therefore, several methods are incorporated and assessed from the computational resources point of view.

The sensitivity analysis has been widely used for structural designs in recent years (Adelman and Haftka, 1986), however, not for aerodynamic designs. Sobieski (1986) has made a plea to the CFD community for extending their present capability to include the sensitivity analysis. Elbanna and Carlson (1989) have presented a method to determine the sensitivity coefficients for the nonlinear, transonic, small perturbation equation in two dimensions. Yates (1987) has used a boundary-integral method to calculate aerodynamic sensitivities for small perturbation equations. In a survey paper by Dulikravich (1991), different aerodynamic shape design concepts have been presented and classified. Among these concepts is the control theory concept which has been first applied by Lions (1971) to systems governed by partial differential equations, then applied to aerodynamic design by Jameson (1988).

Conclusions that can be drawn from this literature survey are, first of all, there are very few investigations on aerodynamic sensitivity analysis, and they all are at their very early stages. The major contributors for such a phase lag in aerodynamic and structural sensitivity analyses are the nonlinear nature of the fluid dynamic equations, existence of discontinuities, such as shocks, and the difficulties associated with the aerodynamic surface and volume grid generation. Also, unlike most of the structural problems, the coefficient matrix of the sensitivity equation for aerodynamic is not symmetric. Only recently, due to the advent of the supercomputers with large memories, it has been possible to solve an aerodynamic sensitivity equation, since the size of a CFD grid is generally much larger than a structural grid.

Sensitivity Analysis

In order to demonstrate the determination of aerodynamic sensitivities, a design optimization problem has to be defined. That is, an objective function, its constraints, and pertinent design variables need to be identified. For this purpose, it is chosen to consider a nozzle-afterbody configuration, which is a nonaxisymmetric nozzle, with an internal and an external section (Fig. 2). A supersonic flow expands through the nozzle and mixes with the hypersonic external flow. The reasons for this particular problem can be itemized as follows: (i) Authors have produced two- and three-dimensional computational flow simulations for this configuration. Therefore, the computer program to solve the viscous or inviscid equations of single or multispecies gas flows is ready and benchmarked (Baysal et al., 1988, 1989, 1991b, 1991c). In the present paper, it will be referred to as the flowfield analysis code. (ii) Two and three-dimensional experimental data on the flowfield are available

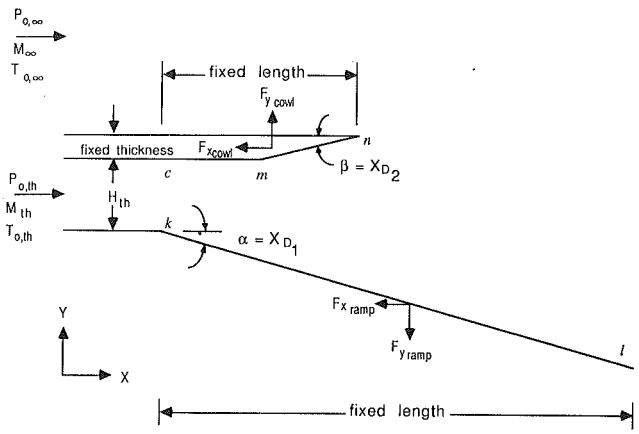

Fig. 2 A nozzle-afterbody configuration: nonaxisymmetric, internal-external nozzle expanding the supersonic flow to mix with the hypersonic freestream flow

(Cubbage and Monta, 1990). (iii) The constraints for this optimization process are relatively well established as a result of extensive high speed research on the National AeroSpace Plane (Doty et al., 1989). (iv) The configuration involves not only an external flow, but also an internal flow. Since the objective of the present paper is to demonstrate the derivation of the sensitivity coefficients and not the nozzle design, the problem is sufficiently simplified. The nozzle ramp and cowl contours are assumed to be straight lines and only their angles with the horizontal are varied.

Therefore, it is desired to determine the angles of the nozzle ramp, α, and of the cowl, β, that yield a maximum axial thrust force coefficient, F, subject to constraints, G_j. The angles α and β are the design variables, $\overline{X}_D$, for the present problem. Mathematically, it is required to get

$$\max[F(\overline{Q}(\overline{X}_D),\overline{X}_D)] \tag{1}$$

subject to

$$G_j(\overline{Q}(\overline{X}_D),\overline{X}_D)\le 0, \quad j=1,\text{NCON} \tag{2}$$

$$\overline{X}_{D_{\text{lower}}}\le \overline{X}_D \le \overline{X}_{D_{\text{upper}}} \tag{3}$$

where F is the objective function, NCON is the number of constraints, and $\overline{Q}$ is the vector of the conserved variables of the fluid flow. $\overline{X}_{D_{\text{lower}}}$ and $\overline{X}_{D_{\text{upper}}}$ are the lower and the upper bounds of the design variables.

The component of the axial thrust force due to nozzle wall shape, F_{axial}, is obtained by integrating numerically the pressure over the ramp and cowl surfaces.

$$F_{\text{axial}}=\int_k^l P_{\text{ramp}}\,dy+\int_m^n P_{\text{cowl}}\,dy \tag{4}$$

This force is normalized by the force associated with the inflow given by,

$$F_{\text{inflow}}=\int_k^c P_{th}(1+\gamma \text{M}_{th}^2)dy \tag{5}$$

In the case of an inflow parallel to the cowl with a constant Mach number, this force is centered at the mid-point of the line segment $\overline{kc}$, and its value is

$$F_{\text{inflow}}=P_{th}(1+\gamma \text{M}_{th}^2)H_{th} \tag{6}$$

where H_{th} is the throat height. By definition the axial thrust force coefficient is given by,

$$F=\frac{F_{\text{axial}}}{F_{\text{inflow}}} \tag{7}$$

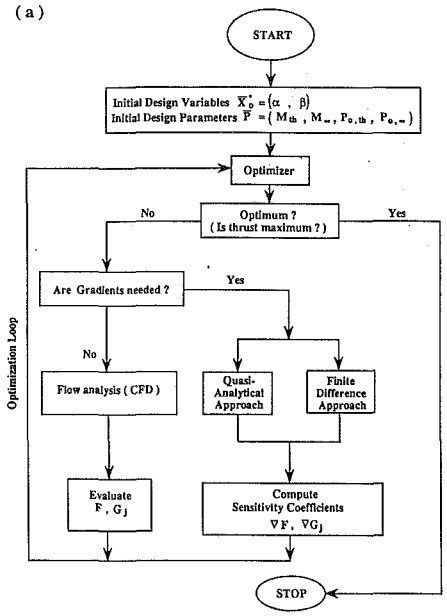

Fig. 3(*a*) Flow chart of an optimization procedure with sensitivity analysis

This axial thrust force coefficient is subject to three constraints. First, the static pressure at the ramp tip, P_l, is forced to reach a percentage C_1 of the free-stream static pressure, P_∞.

$$G_1(\bar{X}_D) = 1 - \frac{P_l}{C_1 P_\infty} \le 0 \tag{8}$$

The other two constraints are due to the static pressure at the cowl tip, P_n, being forced to fall within specified limits (C_2 and C_3) of the free stream static pressure, P_∞.

$$G_2(\bar{X}_D) = 1 - \frac{P_n}{C_2 P_\infty} \le 0 \tag{9}$$

$$G_3(\bar{X}_D) = \frac{P_n}{C_3 P_\infty} - 1 \le 0 \tag{10}$$

Although it is not done in the present paper, this nonlinear, constrained optimization problem can be solved using one of the well established optimization methods (Baysal and Eleshaky, 1991d). A flow analysis is performed every time the shape is perturbed by the optimization. The objective and the constraint functions are then recalculated using the new values of the flow properties. The direction and the magnitude of the next perturbation of the design variables are also determined using the flow properties. The objective function, constraints and their gradients are then used to determine the optimum design. The flowchart of this process is shown in Fig. 3(*a*).

The derivatives of the objective function, F, and constraints, G_j, with respect to the design variables, $\bar{X}_D$, are given by

$$\nabla F \equiv \frac{dF}{d\bar{X}_D} = \frac{\partial F}{\partial \bar{X}_D} + \left(\frac{\partial F}{\partial \bar{Q}}\right)^T \cdot \frac{\partial \bar{Q}}{\partial \bar{X}_D} \tag{11}$$

$$\nabla G_j \equiv \frac{dG_j}{d\bar{X}_D} = \frac{\partial G_j}{\partial \bar{X}_D} + \left(\frac{\partial G_j}{\partial \bar{Q}}\right)^T \cdot \frac{\partial \bar{Q}}{\partial \bar{X}_D} \quad j = 1, \text{NCON} \tag{12}$$

These derivatives are calculated using two approaches, namely, the finite difference approach and the quasi-analytical (or sensitivity analysis) approach.

Finite Difference Approach. A straightforward method to calculate the derivative of F and G_j is to use a finite difference approximation (Fig. 3(*b*)). For example,

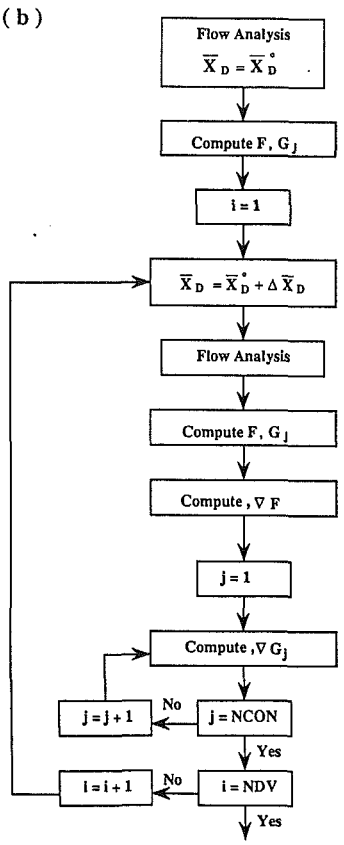

Fig. 3(*b*) Details of the finite difference approach

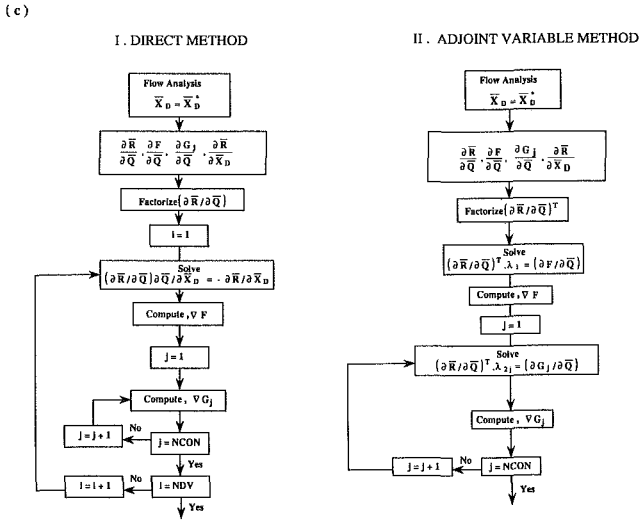

Fig. 3(*c*) Details of the quasi-analytical approaches

$$\frac{dF}{d\bar{X}_D} \approx \frac{F[\bar{Q}(\bar{X}_D + h), \bar{X}_D + h] - F[\bar{Q}(\bar{X}_D), \bar{X}_D]}{h} \tag{13}$$

A serious shortcoming of this method is the uncertainty in the choice of the perturbation step size, h (Haftka and Malkus, 1981). Also, this approach necessitates solving for the flowfield with the perturbed design variable ($\bar{X}_D + h$), which is particularly expensive, when the numbers of both flowfield governing equations and design variables are large.

Quasi-Analytical Approach. The governing equations for the two-dimensional, steady, compressible, inviscid flow of an

ideal gas with a constant specific heat ratio written in the residual vector form are

$$\overline{R}(\overline{Q}(\overline{X}_D),\overline{X}_D)=\frac{\partial \hat{f}}{\partial \xi}+\frac{\partial \hat{g}}{\partial \eta}=0 \tag{14}$$

where $\hat{f}$ and $\hat{g}$ are the fluxes in generalized coordinates (ξ, η) given by Baysal et al. (1988, 1989, 1991b, 1991c).

The quasi-analytical approach (Sobieski, 1986) begins with the differentiation of Eq. (14) with respect to the design variables to yield the sensitivity equation,

$$\left[\frac{\partial \overline{R}}{\partial \overline{Q}}\right]\left\{\frac{\partial \overline{Q}}{\partial \overline{X}_D}\right\}=-\left[\frac{\partial \overline{R}}{\partial \overline{X}_D}\right]\equiv R_v \tag{15}$$

Two different methods are used in this approach to obtain the sensitivity coefficients, namely, the direct method and the adjoint variable method.

Direct Method. With this method, Eq. (15) is solved for $\partial\overline{Q}/\partial\overline{X}_D$ and substituted into Eqs. (11) and (12). Equation (15) needs to be solved once for each design variable, X_D, so the direct method becomes costly when the number of design variables is large (Fig. 3(*c*)). However, one of the advantages of this method is its use in predicting the flowfield solution without actually solving the governing equations of the fluid flow (Eq. (14)). This concept is inspired by the reanalysis used in the structural design optimization (Noor and Whitworth, 1986). Writting the Taylor-series expansion for $\overline{Q}(\overline{X}^*_D+\Delta\overline{X}_D)$ about $\overline{Q}(\overline{X}^*_D)$ gives,

$$\overline{Q}(\overline{X}^*_D+\Delta\overline{X}_D)=\overline{Q}(\overline{X}^*_D)+\left(\frac{\partial \overline{Q}}{\partial \overline{X}_D}\right)_{X_D=X^*_D}\Delta\overline{X}_D+\text{h.o.t.} \tag{16}$$

Substitution of Eq. (15) into Eq. (16) results in,

$$\left[\frac{\partial \overline{R}(\overline{Q}(\overline{X}^*_D),\overline{X}^*_D)}{\partial \overline{Q}}\right]\Delta\overline{Q}=-\left[\frac{\partial \overline{R}(\overline{Q}(\overline{X}^*_D),\overline{X}^*_D)}{\partial \overline{X}_D}\right]\Delta\overline{X}_D \tag{17}$$

where $\Delta\overline{Q}=\overline{Q}(\overline{X}^*_D+\Delta\overline{X}_D)-\overline{Q}(\overline{X}^*_D)$. Equation (17) gives the changes in $\overline{Q}$ due to changes in $\Delta\overline{X}_D$. In other words, the flowfield solution, $\overline{Q}(\overline{X}^*_D+\Delta\overline{X}_D)$, associated with a configuration, $(\overline{X}^*_D+\Delta\overline{X}_D)$, is obtained via Eq. (17), when the flowfield solution, $\overline{Q}(\overline{X}^*_D)$, associated with the configuration, $\overline{X}^*_D$ is given. This feature is very important, especially, when solving the flowfield governing equations is computationally costly.

Prediction of the objective function, F, at a nearby configuration $(\overline{X}^*_D+\Delta\overline{X}_D)$ can be obtained in two ways. The first way is the use of a Taylor series expansion for F $[\overline{Q}(\overline{X}^*_D+\Delta\overline{X}_D),\overline{X}^*_D+\Delta\overline{X}_D]$ about F $[\overline{Q}(\overline{X}^*_D),\overline{X}^*_D]$ as follows:

$$F\Big|_{\substack{\bar{X}_D=\bar{X}^*_D+\Delta\bar{X}_D\\ \bar{Q}=\bar{Q}(\bar{X}^*_D+\Delta\bar{X}^*_D)}}=F\Big|_{\substack{\bar{X}_D=\bar{X}^*_D\\ \bar{Q}=\bar{Q}(\bar{X}^*_D)}}+(\partial F/\partial\overline{Q})^T\Big|_{\substack{\bar{X}_D=\bar{X}^*_D\\ \bar{Q}=\bar{Q}(\bar{X}^*_D)}}\cdot\Delta\overline{Q}+(\partial F/\partial\overline{X}_D)\Big|_{\substack{\bar{X}_D=\bar{X}^*_D\\ \bar{Q}=\bar{Q}(\bar{X}^*_D)}}\cdot\Delta\overline{X}_D+\text{h.o.t} \tag{18}$$

The second way to predict, F, value at a nearby configuration, $(\overline{X}^*_D+\Delta\overline{X}_D)$, is obtaining a predicted flowfield solution, $\overline{Q}(\overline{X}^*_D+\Delta\overline{X}_D)$, using Eq. (17) first, and then computing it analytically using Eq. (7).

Adjoint Variable Method. The adjoint variable method starts with substituting Eq. (15) into Eqs. (11) and (12) to yield,

$$\frac{dF}{d\overline{X}_D}=\frac{\partial F}{\partial \overline{X}_D}+\left(\frac{\partial F}{\partial \overline{Q}}\right)^T J^{-1}R_v \tag{19}$$

$$\frac{dG_j}{d\overline{X}_D}=\frac{\partial G_j}{\partial \overline{X}_D}+\left(\frac{\partial G_j}{\partial \overline{Q}}\right)^T J^{-1}R_v,\quad j=1,\text{NCON} \tag{20}$$

where $J^{-1}=[\partial\overline{R}/\partial\overline{Q}]^{-1}$. Then, defining vectors of adjoint variables $(\overline{\lambda}_1, \overline{\lambda}_{2j})$, that satisfy the following equations,

$$J^T\overline{\lambda}_1=\frac{\partial F}{\partial \overline{Q}} \tag{21}$$

$$J^T\overline{\lambda}_{2j}=\frac{\partial G_j}{\partial \overline{Q}},\quad j=1,\text{NCON} \tag{22}$$

Substitution of Eqs. (21) and (22) into Eqs. (19) and (20), respectively, yields

$$\frac{dF}{d\overline{X}_D}=\frac{\partial F}{\partial \overline{X}_D}+\overline{\lambda}_1^T R_v \tag{23}$$

$$\frac{dG_j}{d\overline{X}_D}=\frac{\partial G_j}{\partial \overline{X}_D}+\overline{\lambda}_{2j}^T R_v,\quad j=1,\text{NCON} \tag{24}$$

The adjoint variable method requires the solution of Eq. (21) and Eq. (22) once for each function G_j. Then, substitution in Eqs. (23) and (24) yields the derivatives of F and G_j. It should be noticed that the adjoint system of Eqs. (21) and (22) is independent of any differentiation with respect to $\overline{X}_D$; hence, the vectors $\overline{\lambda}_1$ and $\overline{\lambda}_{2j}$ in Eqs. (23) and (24) remain the same for all X_{Di}'s of the vector $\overline{X}_D$. Therefore, if the number of adjoint vectors (NCON + 1) is smaller than the number of design variables, the adjoint variable method is more efficient. Conversely, the direct method is more efficient when the number of design variables is smaller. The flow chart of this method is given in Fig. 3(*c*).

Both the direct and adjoint methods involve fewer computations than the finite difference approach, especially, when the number of design variables is large. One of the advantages of the sensitivity approach is that most of the elements of the jacobian matrix, $\partial\overline{R}/\partial\overline{Q}$, are already calculated in the flowfield solver; hence few computations are needed, as will be seen latter. Another advantage is that, when solving for either the adjoint vectors or for $(\partial\overline{Q}/\partial\overline{X}_D)$, the coefficient matrix needs to be factorized only once for a given configuration.

Solution Algorithms

In order to analyze numerically the flowfield for a given configuration during the optimization process, Eq. (14) is solved by the implicit, upwind, finite volume scheme reported by Baysal et al. (1988, 1989, 1991a, 1991b), to force the residual to zero at each point of the computational domain. Equation (14) can be written in an upwind discretized form at a general point (i,j) as follows:

$$\begin{aligned}\overline{R}_{i,j}=&[\hat{f}^+(M_{i+1/2,j})-\hat{f}^-(M_{i-1/2,j})\\&+\hat{g}^+(M_{i,j+1/2})-\hat{g}^-(M_{i,j-1/2})]_{i,j}\\&+\hat{f}^-_{i+1,j}(M_{i+1/2,j})-\hat{f}^+_{i-1,j}(M_{i+1/2,j})+\hat{g}^-_{i,j+1}(M_{i,j+1/2})\\&-\hat{g}^+_{i,j-1}(M_{i,j-1/2})\end{aligned} \tag{25}$$

where $\hat{f}^+$, $\hat{f}^-$, $\hat{g}^+$, and $\hat{g}^-$ are the operator-split inviscid fluxes, M represents the projected surface areas for these fluxes, and is associated with the coordinate transformation metrics. Consequently, $\overline{R}$ at point (i,j) can be viewed as a function of the $\overline{Q}$ values of the neighboring points. The differentiation of the residual expression to yield the jacobian matrix is then straightforward.

$$\frac{\partial[\overline{R}(\overline{Q}_{i\pm1,j\pm1},M_{i\pm1/2,j\pm1/2})]}{\partial[\overline{Q}_{i\pm1,j\pm1}]} \tag{26}$$

However, it is necessary to revise the residual expression (25) at the boundary points to include the boundary conditions. The advantage of using an implicit scheme over other possible techniques is that most of the elements in the jacobian matrix are usually available when forcing the residual to zero, except

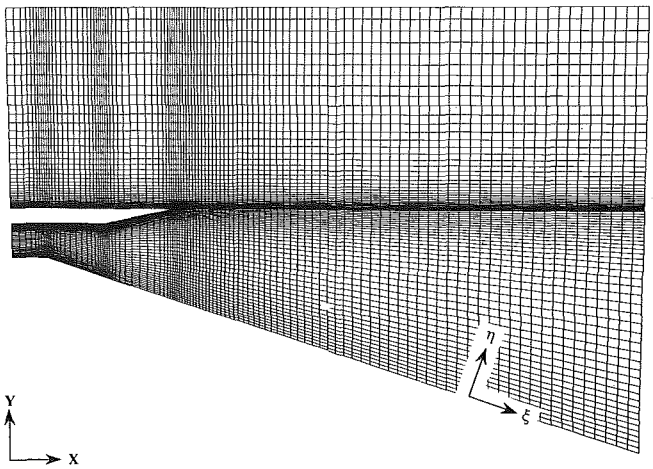

Fig. 4 A typical two dimensional grid used in the flowfield computations

those elements at the boundary points if an implicit treatment of the boundary conditions is not used during the flow analysis. An important advantage of using an upwind scheme over a central difference scheme is that, in the latter, zero elements may appear in the diagonal. This causes the failure of the solution to the system of linear algebraic Eqs. (15), (21), and (22) if no pivoting is employed.

Once the numerical values of all the elements in the jacobian matrix are obtained, the jacobian matrix can be assembled. The jacobian matrix has the dimension $(n \times n)$. In general, it is a banded block matrix with blocks of (4×4) for the two-dimensional flow. For a two-dimensional computational domain with I control volumes in the direction ξ and J control volumes in the direction η, the matrix dimension, n, is (4IJ). For the first-order upwind discretization of the governing equations, this yields a coefficient matrix with a half-bandwidth of $4(J+1)$. For instance, to analyze the flow for the example problem described in Fig. 2, a two-dimensional grid of (105×81) cells is used (Fig. 4). This results in a coefficient matrix which needs a computer memory of about 9.25 Gigabytes. Hence, to reduce this enormous memory requirement, two types of storage techniques can be used, namely, a sparse matrix storage or a diagonal storage of the banded matrices (Pissanetzky, 1984).

An important point is that ordering the unknowns of the linear systems (15), (21), and (22) influences the memory requirements. For example, when dealing with a supersonic flow in the streamwise direction and using an upwind scheme to solve the flow field, as it is the case herein, either the positive fluxes or the negative fluxes in the streamwise direction are zeros. Therefore, if the unknowns are ordered in the streamwise direction (ξ-direction), this results in a coefficient matrix with super- and sub-diagonal bandwidths $4(I+1)$ as shown in Fig. 5(a). Whereas, if the unknowns are ordered in the normal direction (η-direction), this results in a coefficient matrix with super-diagonal bandwidth $4(J+1)$ and sub-diagonal bandwidth of 7 as shown in Fig. 5(b). In the first type of ordering, it is required to store $((8I+9) \cdot 4IJ)$ elements, whereas in the second type of ordering, only $((4J+12) \cdot S4IJ)$ needs to be stored. For the grid shown in Fig. 4, the unknown ordering of Fig. 5(b) provides a 60 percent memory saving over the ordering of Fig. 5(a).

One difficulty which may arise, when solving for the adjoint vectors or $(\partial \overline{Q}/\partial \overline{X}_D)$, is that the coefficient matrix may be ill-conditioned in spite of the nonzero diagonal elements. This requires the preconditioning of the matrix, whether an iterative or a direct method is used to solve the system of the linear algebraic equation. In the present study, the solution of either

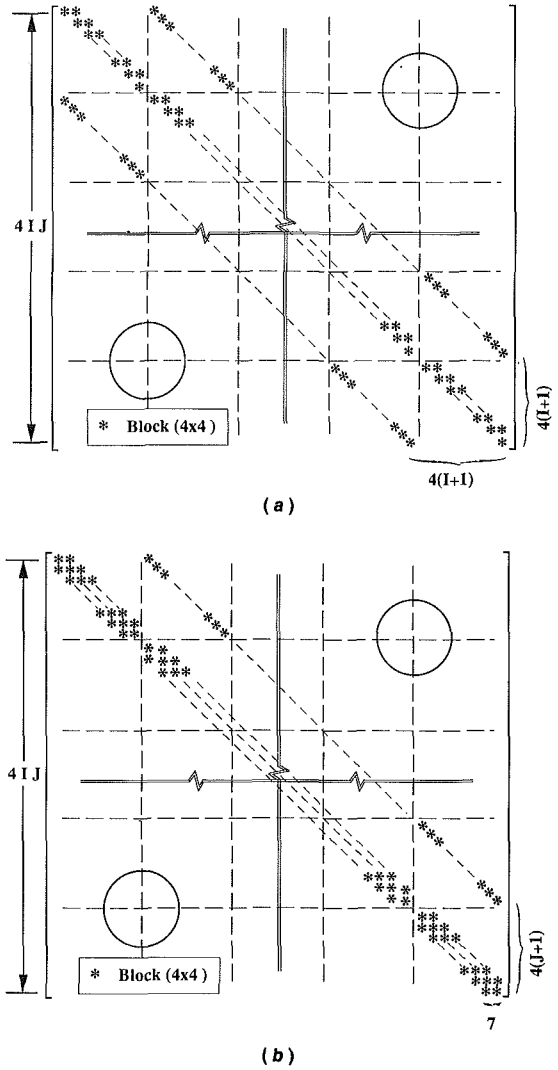

Fig. 5 The structure of the coefficient matrix $(\partial \overline{R}/\partial \overline{Q})$ with the unknowns ordered in: (a) streamwise direction; (b) normal direction

the adjoint vectors or $(\partial \overline{Q}/\partial \overline{X}_D)$, is achieved by using the standard Gauss elimination method after the off-diagonal zeros have been eliminated.

The right-hand side of Eq. (15) is evaluated by differentiating the upwind discretized form given by Eq. (25) for the general point (i,j) with respect to the design variables, $\overline{X}_D$ as follows,

$$\frac{\partial \overline{R}_{i,j}}{\partial \overline{X}_D} = \frac{\partial \hat{f}^+_{i,j}}{\partial (M_{i+1/2,j})} \cdot \frac{\partial (M_{i+1/2,j})}{\partial \overline{X}_D} - \frac{\partial \hat{f}^-_{i,j}}{\partial (M_{i-1/2,j})} \cdot \frac{\partial (M_{i-1/2,j})}{\partial \overline{X}_D}$$
$$+ \frac{\partial \hat{g}^+_{i,j}}{\partial (M_{i,j+1/2})} \cdot \frac{\partial (M_{i,j+1/2})}{\partial \overline{X}_D} - \frac{\partial \hat{g}^-_{i,j}}{\partial (M_{i,j-1/2})} \frac{\partial (M_{i,j-1/2})}{\partial \overline{X}_D}$$
$$- \frac{\partial \hat{f}^+_{i-1,j}}{\partial (M_{i-1/2,j})} \cdot \frac{\partial (M_{i-1/2,j})}{\partial \overline{X}_D} + \frac{\partial \hat{f}^-_{i+1,j}}{\partial (M_{i+1/2,j})} \cdot \frac{\partial (M_{i+1/2,j})}{\partial \overline{X}_D}$$
$$- \frac{\partial \hat{g}^+_{i,j-1}}{\partial (M_{i,j-1/2})} \cdot \frac{\partial (M_{i,j-1/2})}{\partial \overline{X}_D} + \frac{\partial \hat{g}^-_{i,j+1}}{\partial (M_{i,j+1/2})} \cdot \frac{\partial (M_{i,j+1/2})}{\partial \overline{X}_D} \quad (27)$$

As it is seen from Eq. (27), $\partial \overline{R}/\partial \overline{X}_D$ depends on the derivatives of the projected surface areas (M) with respect the design variables. If an analytical expression for $M = M(\overline{X}_D)$ exists, then this differention is straightforward. Otherwise, a finite difference approximation for $\partial M/\partial \overline{X}_D$ with a small step size $\Delta \overline{X}_D$ can be used.

Table 1 Upstream flow conditions for the nozzle-afterbody configuration

	Mach no.	T_0, R^0	P_0, psf
External Flow	6.000	885	51,984
Internal Flow	1.665	610	3,960

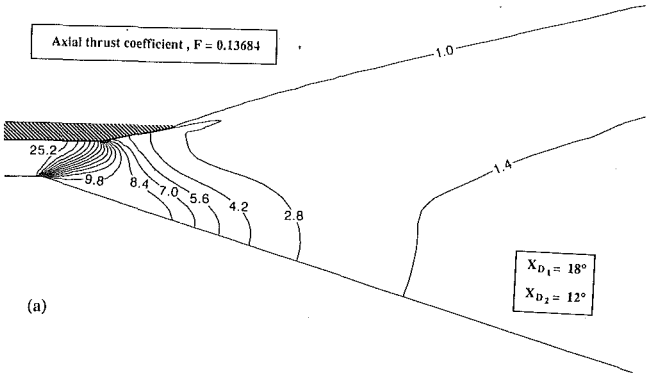

Fig. 6(*a*) Flow analysis for $X_{D1} = 18$ deg

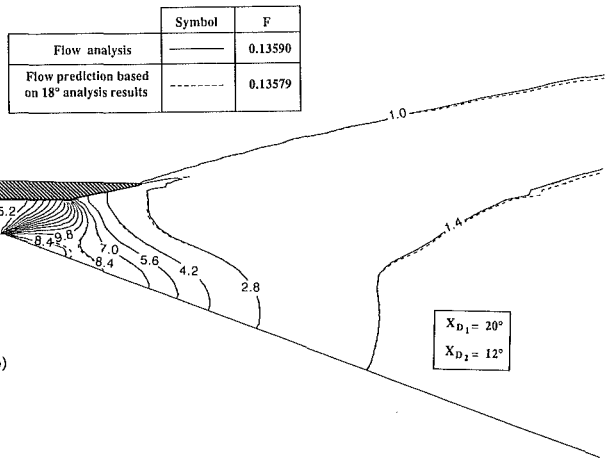

Fig. 6(*b*) Comparison of the flow analysis and the flow prediction for $X_{D1} = 20$ deg

Fig. 6 Normalized pressure contours, P/P_∞, of the nozzle flow

Finally, the right-hand sides of Eqs. (21) and (22) are obtained by differentiating the Eqs. (7), (8), (9), and (10) with respect to the vector of conserved variables of the flow, $\overline{Q}$.

Discussion of Results

An example case is chosen in order to investigate the methods used in calculating the aerodynamic sensitivity coefficients and to verify the accuracy and the feasibility of the flow prediction technique. The flow properties for this case are given in Table 1.

T_0 and P_0 are the total temperature and total pressure, respectively. The above upstream conditions are kept constant for all the results presented in this study. The experimental data for this test case is given by Cubbage and Monta (1990).

The first set of results helps studying the accuracy of the flow prediction technique. Hence, flowfield solutions for two configurations, where one is obtained by a small perturbation of the other, are obtained by solving Eq. (25). One of the configurations has $X_{D_1} = 20$ deg and $X_{D_2} = 12$ deg, while the other configuration has $X_{D_1} = 18$ deg and $X_{D_2} = 12$ deg. That is, changes in X_{D_1} and X_{D_2} are 2 and 0 deg, respectively. Equation (17) is solved for the changes in $\overline{Q}$ (i.e., $\Delta\overline{Q}$) due to the above changes in $\overline{X}_D$. The jacobian matrix and the right-hand side of Eq. (17) are evaluated using the flowfield solution (Fig. 6(*a*)) associated with the configuration ($X_{D_1} = 18$ deg, $X_{D_2} = 12$ deg). The predicted flowfield solution associated with the configuration ($X_{D_1} = 20$ deg, $X_{D_2} = 12$ deg) is then obtained by adding the computed changes in $\overline{Q}$ to the flowfield solution associated with the configuration ($X_{D_1} = 18$ deg, $X_{D_2} = 12$ deg).

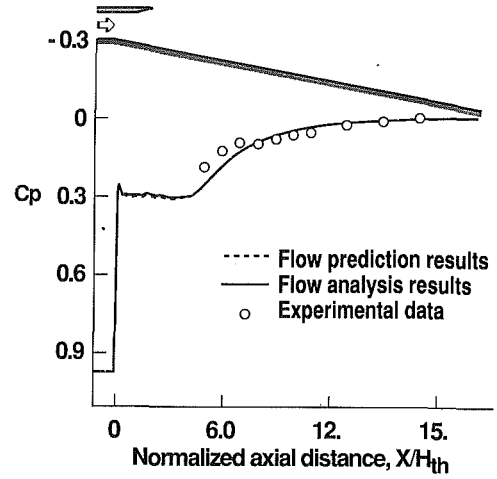

Fig. 7 Pressure coefficient distributions on the ramp surface obtained from different numerical approaches in comparisons with the experimental data (Cubbage and Monta, 1990)

The normalized pressure contours obtained via the flow prediction technique are successfully compared with their corresponding contours obtained by the flow analysis code (Fig. 6(*b*)). It is also seen from this figure that the axial thrust force coefficient, F, obtained using the flow prediction results differs only by 0.079 percent from that obtained using the flow analysis solution. However, when Eq. (18) is used to predict the axial thrust force for ($X_{D_1} = 20$ deg, $X_{D_2} = 12$ deg), it is found that its value (0.13273) differs by 2.33 percent from that obtained using the flow analysis solution. This increased error is due to the presence of two types of approximation errors that affect the value of F obtained via Eq. (18). These are the truncation error associated with Eq. (18), and the truncation error associated with Eq. (17), which enters Eq. (18) through $\Delta\overline{Q}$. On the other hand, when using the predicted flowfield solution, $\overline{Q}(\overline{X}_D^* + \Delta\overline{X}_D)$, only the second type of approximation error affects the predicted value of F. The surface pressure coefficient (C_p) distributions on the ramp obtained from the predicted flowfield solution are compared in Fig. 7 with their corresponding values obtained via the flow field analysis code and the experimental data. Examination of this figure indicates that the numerical results agree with each other as well as with the experimental data. The slight discrepancy with the data is attributed to the viscous effects that are not described in the governing equation of the flow (Eq. (14)). The results shown in Figs. 6 and 7 demonstrate the accuracy of predicting the flowfield solution when X_{D_1} is perturbed by 10 percent. Similarly, predictions of the axial thrust force coefficient, F, for the configuration ($X_{D_1} = 20$ deg, $X_{D_2} = 12$ deg) are given in Table 2 based on the perturbations of X_{D_1} by -25, -10, 5, and 25 percent.

Although the errors are relatively small for the indicated range of X_{D_1} perturbations, they grow with the increasing perturbation of X_{D_1}, as expected. With this table, it is verified that using Eqs. (7) and (17) yields smaller error than that obtained when using Eq. (18).

Table 2 Percent prediction errors in axial thrust force coefficient, F, using different methods

% Change in X_{D_1}	% Error in predicted F^a	% Error in predicted F^b
−25	5.461	−1.857
−10	−2.331	−0.079
5	0.197	−0.069
25	4.310	−1.767

All results are obtained for $\Delta X_{D_2} = 0$

% error in $F = \dfrac{F_p - F_a}{F_a} * 100$, where subscripts ($p$) and ($a$) refer to the predicted value and the value obtained by flow analysis code, respectively.

[a] F values are obtained using Eq. (18).

[b] F values are obtained using predicted flowfield solutions (Eqs. (7) and (17)).

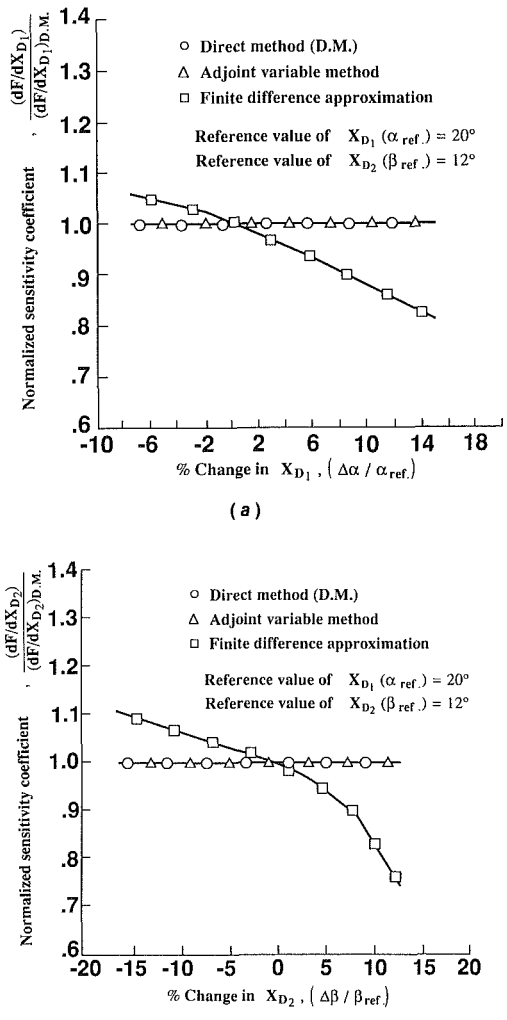

Fig. 8 Variation of the normalized sensitivity coefficient with the percent perturbation of the design variables for three methods. (*a*) Design variable is X_{D1}, (*b*) Design variable is X_{D2}

Next, the different methods used to calculate the sensitivity coefficients are compared for a configuration ($X_{D_1} = 20$ deg and $X_{D_2} = 12$ deg) and presented in Fig. 8. Only the derivatives of the objective function, F, with respect to design variables are considered. Obtaining these derivatives via the finite difference approximation Eq. (13) requires the perturbation of each design variable, X_D, by a step size ΔX_D. Then, the flowfield is computed for each new X_D using the flow analysis code. Since the best value for ΔX_D is not known a priori, different values of ΔX_D are attempted. The sensitivity coefficients obtained via all three methods are normalized by the sensitivity coefficients obtained by the direct method, where Eq. (17) is evaluated using the flowfield solution associated with ($X_{D_1} = 20$ deg, $X_{D_2} = 12$ deg). The results of the direct and the adjoint methods are identical. However, the results of the finite difference method deviate significantly from the quasi-analytical results. This reconfirms the findings of the previous investigations, (Haftka and Malkus, 1981), that the finite difference method results are dependent on the step size (Eq. (13)).

Table 3 Execution times to solve the system of linear algebraic equations in the quasi-analytical approaches

Technique	Execution time
Sparse matrix technique	22.5
Banded matrix solver (without pivoting)	1.0
Banded matrix solver (with pivoting)	1.4

All times are normalized by the time required for the banded matrix solver (without pivoting).
Grid size (105 × 81). Number of design variables = 2

Table 4 Execution times to compute the sensitivity coefficients of the objective function, ∇F

Approach	Time
Finite difference approximation (3 flowfield solutions)	2.872
Direct method (1 flowfield solution plus sensitivity coefficients via banded solver)	1.000
Adjoint variable method (1 flowfield solution plus sensitivity coefficients via banded solver)	0.970

All times are normalized by the time required for the direct method. Grid size (105 × 81). Number of design variables = 2. Number of adjoint vectors = 1.

Two different numerical techniques are used to solve the systems of linear algebraic equations that arise in the quasi-analytical approaches; namely, the sparse matrix technique and the banded matrix technique. Comparison of the two techniques as used in the present study, reveals that their memory requirements and the numerical accuracies are the same, whereas, their execution times are significantly different. Presented in Table 3 are the execution times required to solve the system of linear algebraic equations associated with a grid of size (105 × 81). This linear system has a square coefficient matrix with 33,280 rows. As can be seen in this table, the sparse matrix technique is less efficient, since it does not take advantage of the banded structure of the matrix.

The computational times to obtain the sensitivity coefficients of the objective function, F, by all three methods are given in Table 4 for two design variables. The system of linear equations arising from the quasi-analytical approach is solved using the banded matrix technique in which Gauss elimination without pivoting is used.

It is concluded from Table 4 that the adjoint variable method requires less time than the direct method. This is because there is only one adjoint vector (i.e., λ_1 for F) to be solved for when using the adjoint variable method. Whereas, in the direct method, there are two conserved variable derivatives, ($\partial \bar{Q}/\partial X_{D1}, \partial \bar{Q}/\partial X_{D2}$), to be solved for. In other words, the difference in the total execution time of the two methods is due to the extra time required for the forward and backward substitutions of the direct method. Also, the time required by the finite difference approximation is higher than that required by the direct method and the adjoint variable method. This is due to the repetitive flowfield analyses.

Conclusions

A mathematical development of the aerodynamic sensitivity coefficients, based on a discretized form of the compressible, two-dimensional Euler equations, are presented for a nozzle-afterbody configuration. Three methods are used to determine these sensitivity coefficients, namely, the finite difference method, the direct method, and the adjoint variable method. A comparison between these methods indicates that the finite difference approximation deviates from the quasi-analytical methods ± 5 percent for design variable changes, up to ± 5 percent. The direct and the adjoint variable methods yield identical results. Furthermore, both the direct and the adjoint variable methods are computationally more economical than the finite difference method in obtaining the aerodynamic sensitivity coefficients. However, the direct method is more economical than the adjoint variable method when the number of design variables is less than the number of adjoint vectors (the number of constraints plus one).

The systems of linear algebraic equations that arise in the direct and adjoint variable methods are solved using two techniques based on the standard Gauss elimination, namely, a sparse matrix technique and a banded matrix technique. A comparison between these techniques indicates that they give the same solution accuracy and require the same amount of computer memory. However, the sparse matrix technique is not economical for solving the above systems of equations.

A flow prediction and an objective function prediction concepts are developed for a nozzle-afterbody configuration. The predicted flowfield solution is successfully compared with the flowfield solution obtained via an analysis code. Also, the surface pressure coefficient distributions on the ramp of the nozzle-afterbody configuration obtained from the predicted flowfield solution are successfully compared with their corresponding values obtained from both the flow analysis code and the experimental data. Moreover, a parametric study is performed to determine the error in the predicted objective function as it varies with changes in a design variable. This study indicates that the error grows with the increasing change in the design variables; however, it is less that 2 percent for the nozzle-afterbody design variable change up to 25 percent.

Acknowledgment

This work is supported by NASA Langley Research Center under Grant No. NAG-1-1188. The technical monitor is David S. Miller.

References

Adelman, H. M., and Haftka, R. T. (eds), 1986, *Sensitivity Analysis in Engineering*, NASA Conference Publication 2457.

Adelman, H. M., and Haftka, R. T., 1986, "Sensitivity Analysis of Discrete Structural Systems," *AIAA Journal*, Vol. 24, No. 5, pp. 823–832.

Baysal, O., Engelund, W. C., and Tatum, K. E., 1988, "Navier-Stokes Calculations of Scramjet-Afterbody Flowfields," *Advances and Applications in Computational Fluid Dynamics* (ed., O. Baysal), FED-Vol. 66, ASME, New York, pp. 49–60.

Baysal, O., Eleshaky, M. E., and Engelund, W. C., 1989, "2-D and 3-D Mixing Flow Analyses of a Scramjet-Afterbody Configuration," *Proceedings of International Conference on Hypersonic Aerodynamics*, Paper No. 14, The Royal Aeronautical Society, London.

Baysal, O., Fouladi, K., Leung, R. W., and Sheftic, J. S., 1991a, "Interference Flows Past Cylinder-Fin-Sting-Cavity Assemblies," AIAA Paper No. 90-3095CP, AIAA 8th Applied Aerodynamics Conference, pp. 884–892. Also, *Journal of Aircraft*, Vol. 28, 1991.

Baysal, O., Hoffman, W. B., 1991b, "Simulation of 3-D Shear Flow Around a Nozzle-Afterbody at High Speeds," *Advances in Numerical Simulation of Turbulent Flows* (ed., I. Celik), FED-Vol. 110, ASME, New York, pp. 75–82. Also, to appear in *Journal of Fluids Engineering*, Vol. 1992.

Baysal, O., Eleshaky, M. E., and Engelund, W. C., 1991c, "Computations of Multispecies Mixing Between Scramjet Nozzle Flows and Hypersonic Freestream," AIAA Paper No. 89-0009. Also, *Journal of Propulsion and Power*, Vol. 7, 1991.

Baysal, O., and Eleshaky, M. E., 1991 d, "Aerodynamic Design Optimization Using Sensitivity Analysis and Computational Fluid Dynamics," AIAA Paper No. 91-0471. Also, to appear in *AIAA Journal*, Vol. 30, 1992.

Cubbage, J. M., and Monta, W. J., 1990, "Surface Pressure Data on a Scramjet External Nozzle Model at Mach 6 Using a Simulant Gas for the Engine Exhaust Flow," NASP CR-1058, NASA Langley Research Center, Hampton, VA.

Dulikravich, G. S., 1991, "Aerodynamic Shape Design and Optimization," AIAA Paper No. 91-0476.

Elbanna, H., and Carlson, L., 1989, "Determination of Aerodynamic Sensitivity Coefficients in the Transonic and Supersonic Regimes," AIAA Paper 89-0532.

Haftka, R. T., and Malkus, D. S., 1981, "Calculation of Sensitivity Derivatives in Thermal Problems by Finite Differences," *International Journal for Numerical Methods in Engineering*, Vol. 17, pp. 1811–1821.

Jameson, A., 1988, "Aerodynamic Design Via Control Theory," ICASE Report No. 88-150, NASA Langley Research Center, Hampton, VA.

Doty, J. H., Thompson, H. D., and Hoffman, J. D., 1989, "Optimum Thrust Two-Dimensional NASP Nozzle Study," NASP CR-1069, NASA Langley Research Center, Hampton, VA.

Lions, J. L., 1971, *Optimal Control of Systems Governed by Partial Differential Equations*, (translated by S. K. Mitter), Springer-Verlag, New York.

Murthy, S. N. B., and Paynter, G. C. (eds), 1986, *Numerical Methods for Engine-Airframe Integration*, Progress in Astronautics and Aeronautics Series, Vol. 102, AIAA Publications, New York.

Noor, A. K., and Whitworth, S. L., 1986, "Sensitivity Analysis for Large-Scale Problems," *Sensitivity Analysis in Engineering*, NASA Conference Publication 2457, pp. 357–374.

Pissanetzky, S., 1984, *Sparse Matrix Technology*, Academic Press, New York, pp. 13,14.

Sobieski, J. S., 1986, "The Case for Aerodynamic Sensitivity Analysis," *Sensitivity Analysis in Engineering*, NASA Conference Publication 2457, pp. 77–96.

Yates, E. C., Jr., 1987, "Aerodynamic Sensitivities from Subsonic, Sonic, and Supersonic Unsteady, Nonplanar Lifting Surface Theory," NASA Technical Memorandum 100502.

P. R. Souza Mendes
Assoc. Mem. ASME

M. F. Naccache

Department of Mechanical Engineering,
Pontifícia Universidade Católica-RJ,
Rio de Janeiro, RJ 22453, Brazil

Gravity-Driven Motion of a Layer of Viscoelastic Fluid Around a Horizontal Wire

A theoretical study of the free-surface flow of a viscoelastic fluid around a horizontal cylinder is reported in this paper. The fluid layer has initially a uniform thickness, and, at some instant of time, it starts to flow due to the presence of a gravity field. The result sought is the film thickness as a function of time and angular position. The mass- and momentum-conservation principles are employed in conjunction with the Maxwell constitutive equation. Using an integral method, a system of two nonlinear equations is obtained. The results are compared with the ones for a Newtonian fluid, and the elastic effects are shown to change dramatically the flow.

Introduction

The present paper is concerned with the flow of a thin layer of non-Newtonian fluid around a horizontal cylinder due to gravity. The analysis of such a motion is of industrial interest since, when horizontal wire coating is employed, the gravity effect causes the liquid coating material previously deposited to flow around the wire before solidification in the oven. This causes an eccentric coating layer, which is highly undesirable.

Therefore, prediction of the fluid motion around the wire is desirable to control the eccentricity of the deposited layer of electrical insulation. This flow has already been studied previously for a Newtonian fluid (Souza Mendes, 1989). However, the coating material employed in this application is generally a varnish, which consists of a solution of a synthetic resin in drying oil (Rodriguez, 1989). This polymeric solution displays a viscoelastic behavior, and the Newtonian model for the stress field is not applicable.

The present research is concerned with a qualitative analysis of viscoelastic effects on the flow of the fluid layer. In this connection, the Maxwell model (see for instance Bird et al., 1987) was selected as the constitutive relation for stress.

The Analysis

The motion under study is represented in Fig. 1. At time $t^* = 0$, a fluid layer of uniform thickness δ_0^* is deposited around a horizontal cylinder (or wire), and a gravity field g directed downward is switched on (Fig. 1(*a*)). At some layer time t^*, the fluid has moved downward due to gravity (Fig. 1(*b*)). In this configuration, surface tension effects are important, and, due to motion, viscoelastic forces also arise. For this sought-for application, the film thickness is typically very small, generally of the order of 1 or 2 percent of the wire radius.

The solution of the present problem is obtained by following the same path as the one described by Souza Mendes (1989), with the appropriate adaptations for the non-Newtonian behavior. For completeness, however, the whole analysis and procedure employed in the present paper is described in what follows.

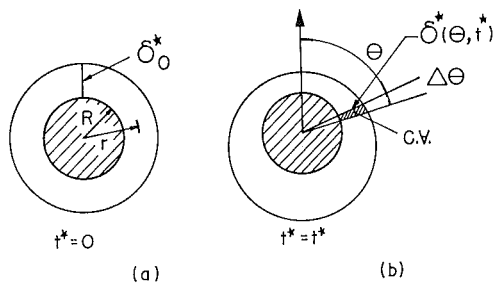

Fig. 1 Schematic of the problem

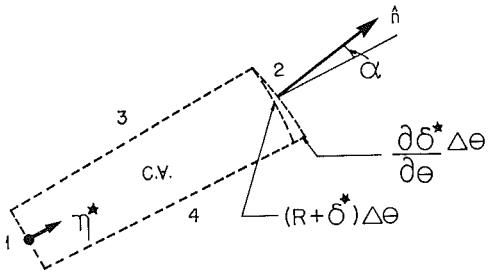

Fig. 2 The control volume $C\forall$

The principles of mass and θ-momentum conservation are evoked, and applied to the deformable control volume $C\forall$ shown at some instant t^* in Fig. 2.

In this two-dimensional analysis, the fluid density ρ is assumed to be invariant. The velocity field is given by $\mathbf{u} = u^*\hat{e}_r + v^*\hat{e}_\theta$. V^* stands for the velocity component v^* evaluated at the interface, i.e.,

$$V^*(\theta, t^*) \equiv v^*(R+\delta^*, \theta, t^*) \tag{1}$$

where $\delta^*(\theta, t^*)$ is the film thickness, measured in the radial direction, at some instant and θ location.

There exists a pressure difference Δp across the interface,

Contributed by the Fluids Engineering Division for publication in the JOURNAL OF FLUIDS ENGINEERING. Manuscript received by the Fluids Engineering Division August 16, 1990.

due to the surface tension. Since the present study is focused on very thin films ($\delta^* << R$), the curvature radius of the interface is nearly constant and close to $R + \delta_0^*$ (Markovitz et al., 1972, Krupiczka, 1985), where δ_0^* is the initial (and uniform along θ) film thickness. Therefore, if σ is the surface tension,

$$\Delta p = \frac{\sigma}{R + \delta_0^*} \tag{2}$$

Conservation of Mass. The continuity equation for the control volume $C\forall$ shown in Fig. 2 is ($\hat{n}$ is the unit vector normal to the control surface CS):

$$0 = \int_{CS} \mathbf{u} \cdot \hat{n} dA$$

$$= \int_1 \mathbf{u} \cdot \hat{n} dA + \int_2 \mathbf{u} \cdot \hat{n} dA + \int_3 \mathbf{u} \cdot \hat{n} dA + \int_4 \mathbf{u} \cdot \hat{n} dA \tag{3}$$

At surface 1, $\mathbf{u} = 0$, and hence $\int_1 \mathbf{u} \cdot \hat{n} dA = 0$. At surface 2,

$$\mathbf{u} = \frac{d\delta^*}{dt^*} \hat{e}_r + V^* \hat{e}_\theta \text{ and } \hat{n} = \cos\alpha \hat{e}_r - \sin\alpha \hat{e}_\theta. \tag{4}$$

Then, at surface 2,

$$\mathbf{u} \cdot \hat{n} = \left(\frac{d\delta^*}{dt^*} - V^* \tan\alpha \right) \cos\alpha. \tag{5}$$

Now it is observed that

$$\tan\alpha = \frac{1}{R + \delta^*} \frac{\partial \delta^*}{\partial \theta} \text{ and } \frac{d\delta^*}{dt^*} = \frac{\partial \delta^*}{\partial t^*} + \frac{V^*}{R + \delta^*} \frac{\partial \delta^*}{\partial \theta} \tag{6}$$

Substituting the above equations into Eq. (5), the dot product $\mathbf{u} \cdot \hat{n}$ becomes simply equal to $\partial\delta^*/\partial t^* \cos\alpha$, and

$$\int_2 \mathbf{u} \cdot \hat{n} dA = \frac{\partial \delta^*}{\partial t^*} (R + \delta^*) \Delta\theta, \tag{7}$$

where, assuming a unitary length along the third direction, dA was replaced by $(R + \delta^*) d\theta / \cos\alpha$.

It can be seen that

$$\int_3 \mathbf{u} \cdot \hat{n} dA + \int_4 \mathbf{u} \cdot \hat{n} dA = \frac{\partial}{\partial \theta} \left[\int_0^{\delta^*} v^* d\eta^* \right] \Delta\theta \tag{8}$$

where $\eta^* \equiv r - R$.

Now, Eqs. (7) and (8) are plugged into the continuity equation (Eq. (3)), yielding

$$0 = \left(1 + \frac{\delta^*}{R} \right) \frac{\partial \delta^*}{\partial t^*} + \frac{1}{R} \frac{\partial}{\partial \theta} \left[\delta^* V^* \int_0^1 v d\eta \right] \tag{9}$$

where $\eta \equiv \eta^*/\delta^*$ and $v \equiv v^*/V^*$.

The above equation is then made dimensionless, giving

$$0 = (1 + \delta) \frac{\partial \delta}{\partial t} + \frac{\partial}{\partial \theta} \left[V \delta \int_0^1 v d\eta \right] \tag{10}$$

where

$$\delta \equiv \frac{\delta^*}{R}, \; t \equiv t^* \sqrt{\frac{g}{R}}, \text{ and } V \equiv \frac{V^*}{\sqrt{gR}}, \tag{11}$$

g being the acceleration due to gravity.

Conservation of Linear Momentum. In the θ-direction, the principle of conservation of momentum gives, when applied to the control volume $C\forall$ shown in Fig. 2,

$$F_c + F_e = \int_{C\forall} \frac{\partial (\rho v^*)}{\partial t^*} d\forall + \int_{CS} v^* \rho \mathbf{u} \cdot \hat{n} dA. \tag{12}$$

The contact forces F_c are due to the shear stress ($T_{r\theta} \equiv \tau_{r\theta}^*$) at surface 1 and to the normal stress $T_{\theta\theta}$ acting on surfaces 3 and 4. The contribution of fluid motion to normal stresses is generally very small ($\tau_{\theta\theta}^* \simeq 0$, or $T_{\theta\theta} \simeq -\Delta p$), and it is common practice to neglect this effect in engineering analyses. For the present flow geometry and a Newtonian fluid, this hypothesis

Nomenclature

- $\mathbf{1}$ = unit tensor, dimensionless
- $\hat{e}_r$ = unit vector in r-direction, dimensionless
- $\hat{e}_\theta$ = unit vector in θ-direction, dimensionless
- F_c = contact forces in θ-direction, N
- F_e = external forces in θ-direction, N
- g = magnitude of $\mathbf{g}$, m/s^2
- $\mathbf{g}$ = acceleration due to gravity, m/s^2
- G = elastic modulus, N/m^2
- h = angular spacing between nodal points, dimensionless
- $\hat{n}$ = unit vector normal to and directed outward the control surface CS, dimensionless
- p = pressure, N/m^2
- r = radial coordinate, m
- R = wire radius, m
- Re = Reynolds number, $\equiv \rho R \sqrt{gR}/\mu$, dimensionless
- S = dimensionless parameter, $\equiv \rho g R^2/\sigma$
- t = dimensionless time, $\equiv t^* \sqrt{g/R}$
- t^* = time, s
- $\mathbf{T}$ = stress tensor field, N/m^2
- T_{ij} = ij-component of $\mathbf{T}$, N/m^2
- $\mathbf{u}$ = velocity field, m/s
- u^* = radial component of $\mathbf{u}$, m/s
- v = dimensionless tangential velocity, $\equiv v^*/V^*$
- v^* = tangential component of $\mathbf{u}$, m/s
- V = dimensionless tangential velocity at interface, $\equiv V^*/\sqrt{gR}$
- $V^*(\theta, t^*)$ = tangential velocity at interface (Eq. (1)), m/s
- α = angle between $\hat{n}$ and $\hat{e}_r$ (Fig. 2), dimensionless
- $\dot{\gamma}$ = first Rivlin-Ericksen tensor, $\equiv \text{grad}\mathbf{u} + (\text{grad}\mathbf{u})^T$, s^{-1}
- $\dot{\gamma}_{ij}$ = ij-component of $\dot{\gamma}$, s^{-1}
- δ = dimensionless layer thickness, $\equiv \delta^*/R$
- $\delta^*(\theta, t^*)$ = layer thickness (Fig. 1(b)), m
- δ_0 = dimensionless initial layer thickness
- δ_0^* = initial layer thickness (Fig. 1(a)), m
- Δp = pressure jump across interface due to surface tension, N/m^2
- Δt = time step, s
- $\Delta\theta$ = angular width of control volume $C\forall$ (Fig. 1(b)), dimensionless
- η = dimensionless radial coordinate, $\equiv \eta^*/\delta^*$
- η^* = radial coordinate (Fig. 2), $\equiv r - R$, m
- θ = angular coordinate, dimensionless
- λ = Deborah number, $\equiv \lambda^*/\sqrt{R/g}$, dimensionless
- λ^* = characteristic time of fluid, s
- μ = fluid viscosity, kg/ms
- ρ = fluid density, kg/m^3
- σ = surface tension, N/m
- τ = deviatoric stress tensor, $\equiv \mathbf{T} + p\mathbf{1}$, N/m^2
- τ_{ij} = ij-component of τ, N/m^2
- τ_w = dimensionless shear stress at cylinder surface, $\equiv \tau_w^*/\rho g R$
- τ_w^* = shear stress at cylinder surface, $\equiv \tau_{r\theta}(R, \theta, t^*)$, N/m^2

has been tested for a few cases. The results of these tests indicated that this simplifying assumption is also reasonable for the present flow. Therefore, the following expression has been used for the contact forces F_c:

$$F_c = -\tau_w^* R\Delta\theta - \Delta p \frac{\partial \delta^*}{\partial \theta}\Delta\theta, \tag{13}$$

where Δp is given by Eq. (2). It is observed from Eq. (13) that the surface tension effect depends directly on the thickness gradient along θ, the derivative $\partial\delta^*/\partial\theta$.

The shear stress at the wall τ_w^* is evaluated from the linear viscoelastic constitutive relation, in conjunction with the modulus of relaxation of the Maxwell fluid (see for instance Tanner, 1985):

$$\tau^* = \int_{-\infty}^{t^*} \frac{\mu}{\lambda^*} \exp\left(-\frac{t^* - t^{*\prime}}{\lambda^*}\right)\dot{\gamma} dt^{*\prime} \tag{14a}$$

where τ^* is the deviatoric stress tensor; μ is the fluid viscosity; λ^* is the relaxation time; and $\dot{\gamma}$ is the first Rivlin-Ericksen tensor. Observing that $\dot{\gamma}_{r\theta} = (V^*/\delta^*)\partial v/\partial\eta$ and that τ_w^* is the magnitude of the $r\theta$ component of τ^* evaluated at the wall, the following dimensionless expression may be written:

$$\tau_w(\theta, t) = \frac{1}{\lambda \mathrm{Re}}\int_0^t \exp\left(-\frac{t-t'}{\lambda}\right)\frac{V}{\delta}\frac{\partial v}{\partial \eta}\bigg]_{\eta=0} dt' \tag{14b}$$

where $\tau_w \equiv \tau_w^*/\rho g R$, $\mathrm{Re} \equiv \rho R\sqrt{gR}/\mu$ is the Reynolds number, and $\lambda \equiv \lambda^*/\sqrt{R/g}$ is the Deborah number.

The external forces F_e are due to gravity, and hence given by

$$F_e = \int_0^{\delta^*} \rho g \sin\theta (R + \eta^*) d\theta\, d\eta^* = \rho g \sin\theta \left(R\delta^* + \frac{\delta^{*2}}{2}\right)\Delta\theta. \tag{15}$$

The first term on the right-hand side of Eq. (12) may be written as

$$\int_{CV} \frac{\partial(\rho v^*)}{\partial t^*} d\forall = \rho\Delta\theta \int_0^{\delta^*} \frac{\partial v^*}{\partial t^*}(R + \eta^*) d\eta^* = \rho g R^2 \delta\Delta\theta \int_0^1 \frac{\partial (vV)}{\partial t}(1 + \delta\eta) d\eta \tag{16}$$

If the same reasoning employed to obtain the mass conservation equation (Eq. (10)) is followed while working on the right-most term of Eq. (12), the expression below is obtained with no particular difficulty:

$$\int_{CS} v^* \rho \mathbf{u} \cdot \hat{n} dA = \rho V^* \frac{\partial \delta^*}{\partial t^*} R(1+\delta)\Delta\theta + \frac{\partial}{\partial\theta}\left[\delta^* V^{*2}\int_0^1 v^2 d\eta\right]\rho\Delta\theta \tag{17}$$

Now Eqs. (2), (9), (12), (13), (15), (16), and (17) are combined, yielding, after some algebra, the following dimensionless equation:

$$-\delta\tau_w - \left(\frac{1}{S(1+\delta_0)}\delta\frac{\partial\delta}{\partial\theta} + \sin\theta\left(1 + \frac{\delta}{2}\right)\delta^2 = \delta^2\int_0^1 \frac{\partial(vV)}{\partial t}(1+\delta\eta)d\eta + \delta\frac{\partial}{\partial\theta}\left[\delta V^2\int_0^1 v^2 d\eta\right] - \delta V\frac{\partial}{\partial\theta}\left[\partial V\int_0^1 v d\eta\right] \tag{18}$$

where $S \equiv \rho g R^2/\sigma$.

Equations (10) and (18) are subjected to the following initial conditions:

$$V(\theta, 0) = 0; \text{ and } \delta(\theta, 0) = \delta_0 \tag{19}$$

The boundary conditions are:

$$V(0, t) = V(\pi, t) = 0; \text{ and } \frac{\partial\delta}{\partial\theta}(0, t) = \frac{\partial\delta}{\partial\theta}(\pi, t) = 0 \tag{20}$$

Evaluation of the Integral Terms. Further inspection upon Eqs. (10), (14*b*), and (18) shows that there are four terms where the tangential component $v \equiv v^*/V^*$ of the velocity appears, three of them involving integrals, and the fourth involving a derivative evaluated at the wall. The evaluation of these terms require the knowledge of the function $v^*(\eta, \theta, t)$.

In the present work, a sinusoidal profile of the form $v = \sin(\pi\eta/2)$ was adopted. This profile yields excellent results when used in conjunction with the integral momentum equation for the boundary layer flow past a flat plate. Moreover, results were also obtained with a linear profile ($v = \eta$), and comparisons showed that the thickness $\delta(\theta, t)$ is rather insensitive to the profile assumption. The assumed profile is used in the four terms mentioned above, the following results are obtained:

$$\int_0^1 v\, d\eta = \frac{2}{\pi};\quad \int_0^1 v^2 d\eta = \frac{1}{2};\quad \frac{\partial v}{\partial\eta}\bigg]_{\eta=0} = \frac{\pi}{2};$$

$$\int_0^1 \frac{\partial(vV)}{\partial t}(1+\delta\eta)d\eta = \frac{2}{\pi}\left(1 + \frac{2}{\pi}\delta\right)\frac{\partial V}{\partial t} - \left[\left(1 - \frac{2}{\pi}\right) + \left(1 - \frac{8}{\pi^2}\right)\delta\right]\frac{V}{\delta}\frac{\partial\delta}{\partial t} \tag{21}$$

With the above results, the final form of the governing equations can be obtained:

$$(1+\delta)\frac{\partial\delta}{\partial t} + \frac{2}{\pi}\frac{\partial(V\delta)}{\partial\theta} = 0 \tag{22}$$

and

$$\left[\left(1 - \frac{2}{\pi}\right) + \left(1 - \frac{8}{\pi^2}\right)\delta\right]V\delta\frac{\partial\delta}{\partial t} - \left\{\left(\frac{1}{S(1+\delta_0)}\right) + \left(\frac{1}{2} - \frac{2}{\pi}\right)V^2\right\}\delta\frac{\partial\delta}{\partial\theta} - \frac{2\delta^2}{\pi}\left(1 + \frac{2}{\pi}\delta\right)\frac{\partial V}{\partial t} - \left(1 - \frac{2}{\pi}\right)V\delta^2\frac{\partial V}{\partial\theta} = \delta\tau_w - \sin\theta\left(1 + \frac{\delta}{2}\right)\delta^2 \tag{23}$$

The problem under study is governed by the above partial differential equations for δ and V, together with the initial and boundary conditions given in Eqs. (19) and (20). The dimensionless shear stress τ_w that appears in Eq. (23) is given by Eq. (14*b*).

It can be seen that the parameters that influence this physical situation are S, Re, λ and the dimensionless initial film thickness δ_0. S is the ratio between gravity forces and forces due to surface tension; the modified Reynolds number Re compares gravity forces with viscous forces; and the Deborah number λ is the ratio between a characteristic time of the fluid and a characteristic time of the flow. The characteristic time of the fluid, i.e., the relaxation time, gives the order of magnitude of the time duration of the fluid's "memory."

Method of Solution

It can be observed that Eqs. (22) and (23) form a nonlinear system of partial differential equations. The Crank-Nicolson implicit scheme was employed to generate the algebraic discretization equations, which were solved with the aid of the Thomas algorithm together with an iterative scheme.

For a given instant of time, this iterative scheme consisted basically of (i) assuming initial guesses for δ and V; (ii) solving

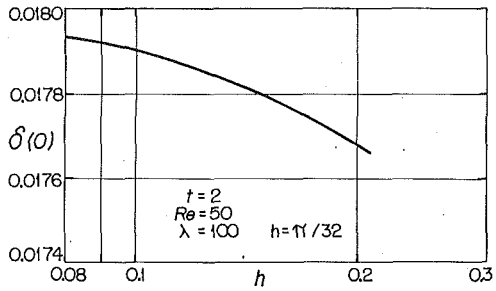

Fig. 3 Dependence of numerical solution on h

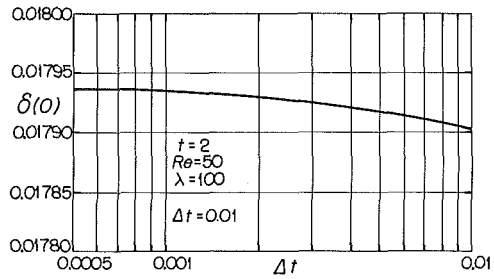

Fig. 4 Dependence of numerical solution on Δt

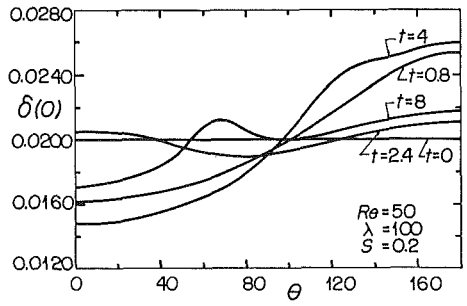

Fig. 5 Film thickness versus angle for various times

the set of algebraic equations generated from Eq. (22) using the Thomas algorithm and the initial guesses for δ; (iii) solving the set of algebraic equations generated from Eq. (23) using the Thomas algorithm and the present values of V; (iv) going back to step (ii), but now using the present values of δ; (v) proceeding in this manner until convergence is achieved. The initial guesses mentioned above were just the values at the previous time step. Convergence was typically achieved in three to four iterations.

The numerical evaluation of the hereditary integral that appears in the expression for τ_w (Eq. (14*b*)) is rather straightforward. At $t = 0$, $\tau_w = 0$. At $t + \Delta t$,

$$\tau_w(\theta, t+\Delta t) = \exp\left(-\frac{\Delta t}{\lambda}\right)\tau_w(\theta, t) + \frac{1}{\lambda \mathrm{Re}}\frac{\pi}{2}\int_t^{t+\Delta t}\exp\left(-\frac{t+\Delta t-t'}{\lambda}\right)\frac{V}{\delta}\,dt' \quad (24)$$

The integral in the above equation may be transformed at each time step, via the trapezoidal rule of numerical integration, into an algebraic expression involving V and δ evaluated at t and $t + \Delta t$. This expression is employed recursively to evaluate $\tau_w(\theta, t+\Delta t)$.

Due to symmetry, the solution domain in θ is from 0 to π. The grid employed was uniform, with 33 nodal points in θ and time steps varying from case to case in the range 0.01 to 0.1, depending upon the Reynolds number Re and on the Deborah number λ.

Numerical Uncertainty. A grid-independence test performed attested to the accuracy of the results obtained with the grid distribution utilized in the final runs. For a typical case (namely, $S = 0.2$, Re = 50, $\lambda = 100$, and $t = 2$), the dependence of the layer thickness δ at $\theta = 0$ deg on the angular spacing between nodal points h and on the time step Δt has been investigated. This is illustrated in Figs. 3 and 4.

The uncertainty of the numerical results was estimated as follows. An estimate of the exact value of $\delta(0)$, i.e., the solution for $h = 0$ and $\Delta t = 0$, was obtained with the aid of a two-variable (h and Δt) Taylor series expansion up to the second-order terms. The evaluation of the five partial derivatives involved was done via finite differences, which required extra computer runs to obtain solutions for eight other combinations of h and Δt in the vicinity of the result pertaining to $h = \pi/32$ and $\Delta t = 0.01$. Using this extrapolated result as a basis for comparison, it was found that the numerical uncertainty of the result for the typical case analyzed is below 1.0 percent.

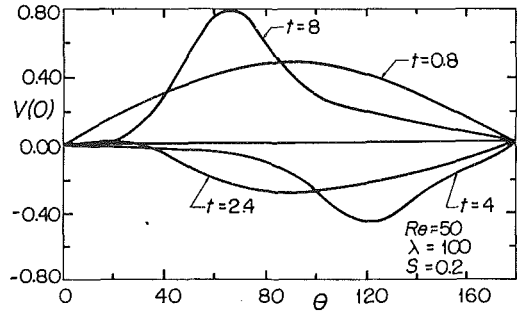

Fig. 6 Tangential velocity versus angle for various times

Results and Discussion

Attention will now be turned to the numerical results. All results reported in the present paper pertain to an initial thickness $\delta_0 = 0.02$ and to $S = 0.2$; the investigation was focused on the effects of the Deborah number λ and Reynolds number Re.

Figure 5 shows the variation of the film thickness δ with the angular position θ, for the case of Re = 50 and $\lambda = 100$. Comparing this figure with Fig. 3 of Souza Mendes (1989), it is seen that the viscoelastic behavior of the fluid plays an important role on the flow.

At instant $t = 0$, the film thickness is uniform and equal to its initial value δ_0. As time ellapses, the fluid falls around the cylinder due to gravity, and therefore the film thickness at the upper region diminishes, whereas at the lower region the thickness increases.

However, once a thickness gradient in the θ direction is established, a force due to surface tension appears, and acts to balance the gravity effect. Furthermore, the viscoelastic force is also present to influence the fluid motion. In contrast to what was observed for the Newtonian fluid in this Re range (Souza Mendes, 1989), the fluid acquires an oscillatory motion, which induces a wavy surface in the θ direction.

The behavior of the tangential velocity at the interface is illustrated in Fig. 6 for the same case shown in Fig. 5. It can be seen that the fluid accelerates very fast at the onset of the motion, when the only force acting on it is gravity. Soon surface tension and viscoelastic effects become important, and the velocity distribution $V(\theta, t)$ reaches high positive values at some early instant of time and then starts to oscillate with smaller magnitudes and changing sign periodically. Moreover, the velocity of maximum magnitude occurs at different θ locations for different times, and with different magnitudes.

Figure 7–11 show the variation of the film thickness at $\theta = 0$ deg with time, for different values of the modified Reynolds number Re. From its definition, it can be seen that low values of Re indicate high fluid viscosity, and vice-versa, for a given

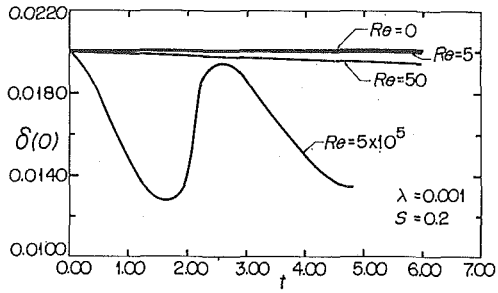

Fig. 7 Film thickness at $\theta = 0$ deg versus time for various Re's

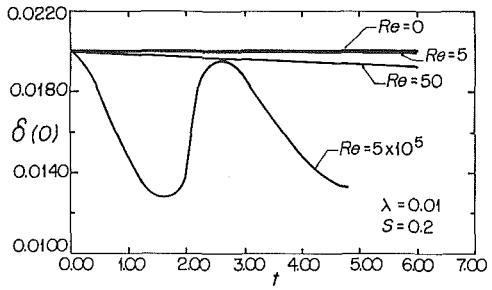

Fig. 8 Film thickness at $\theta = 0$ deg versus time for various Re's

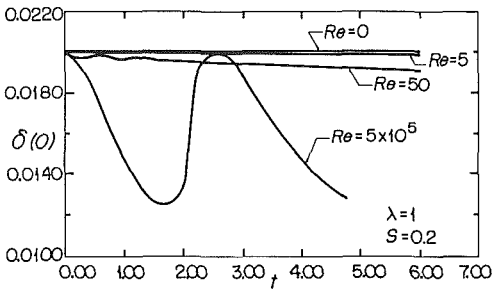

Fig. 9 Film thickness at $\theta = 0$ deg versus time for various Re's

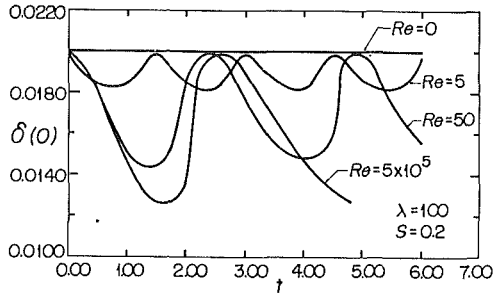

Fig. 10 Film thickness at $\theta = 0$ deg versus time for various Re's

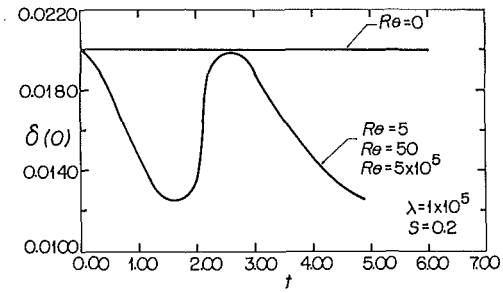

Fig. 11 Film thickness at $\theta = 0$ deg versus time for various Re's

cylinder radius and gravity field. Figures 7–11 differ in the values of the Deborah number, which is equal to 0.001, 0.01, 1.100 and 10^5, respectively.

As expected, it is observed in these figures that, independently of the value of the Deborah number, for infinite fluid viscosity (Re = 0), the fluid flows at infinitely small velocity, and no change in thickness is observed.

At the other extreme, when $\lambda\mathrm{Re} \to \infty$, there is also no dependence on λ. This is illustrated by comparing the curves for $\mathrm{Re} = 5 \times 10^5$ of Figs. 9, 10, and 11 with one another ($\lambda\mathrm{Re} = 5 \times 10^5$, 5×10^7, and 5×10^{10}, respectively). It is seen that these curves are identical. Moreover, the curve for Re = 5 and 50 in Fig. 11 ($\lambda\mathrm{Re} = 5 \times 10^5$ and 5×10^6, respectively) also coincides with these curves.

An inspection upon Eq. (14*b*) explains this trend. When the term $1/\lambda\mathrm{Re}$ in this equation is small enough to neutralize the effect of the memory term $\int_0^t \exp(-t-t'/\lambda)V/\delta\, dt'$, then the parameter λ alone becomes unimportant. This is true because this integral term is the only other term (besides $1/\lambda\mathrm{Re}$) where λ appears.

When $\lambda\mathrm{Re} \to \infty$, the shear stress τ_w tends to zero. This limiting case may be interpreted physically in two different ways. The first is the extreme case of a viscoelastic Maxwell fluid with very low fluid viscosity ($\mathrm{Re} \to \infty$), where no viscous damping for the fluid kinetic energy is available. This behavior was also observed for the Newtonian fluid (Souza Mendes, 1989), as expected. The other is the extreme case of a viscoelastic Maxwell fluid with very low elastic modulus ($G \to 0$, since $\lambda^* = \mu/G$).

The cases of Reynolds number values away from the two extremes mentioned above are now discussed. For $\lambda = 0.001$, 0.01 and 1 (Figs. 7, 8, and 9, respectively), the curve for Re = 5 shows that the film thickness at $\theta = 0°$ decreases very slowly with time, due to the high fluid viscosity. No oscillations are observed, and the viscoelastic fluid flows toward an equilibrium configuration, as does the Newtonian fluid. For Re = 50, the same trend is observed for $\lambda = 0.001$ and 0.01, except that the motion is somewhat faster due to the lower fluid viscosity. For $\lambda = 1$ (and Re = 50), tiny oscillations at early times are observed, which die away at $t \simeq 1.5$. These results for small to moderate Re values do not differ too much from the ones for $\lambda = 0$ (Newtonian fluid, Fig. 5 of Souza Mendes, 1989), showing that in this Re range the elastic effects are not very important for λ up to 1.

For $\mathrm{Re} = 5 \times 10^5$, however, departure from Newtonian behavior is clear, even for $\lambda = 0.001$. The higher the Deborah number, the lower the viscous damping observed, since the fluid elasticity (or memory) becomes more important than its viscous effects. For $\lambda = 1$ and higher (Figs. 9, 10, and 11), there is no more evidence of viscous effects for $\mathrm{Re} = 5 \times 10^5$.

For higher values of the Deborah number (Figs. 10 and 11), elastic effects dominate even for Re values as low as 5. No viscous effects are observed. For $\lambda = 100$ and Re = 5 (Fig. 10), a small-amplitude oscillatory motion with no damping occurs. As Re is increased, the amplitude increases and tends to its largest value (corresponding to $\tau_w = 0$). The amplitude increases with Re since, for a fixed value of λ, the lower the fluid viscosity, the lower is its elastic modulus G. For $\lambda = 10^5$ (Fig. 11), G is small enough to yield negligible wall shear stress even for Re as low as 5.

The effect of fluid elasticity on the present flow is further emphasized with the aid of Figs. 12 and 13. In Fig. 12, which pertains to a high fluid viscosity (Re = 50), it can be seen that the elasticity effect is dramatic. For $\lambda = 0$ (Newtonian fluid), 0.001, 0.01, and 1, the viscous effect dominates, and therefore there is a weak dependence on the Deborah number. As λ increases, however, the picture changes completely, with oscillations for $\lambda = 100$ and a maximum-amplitude oscillation for $\lambda = 10^5$. For a lower fluid viscosity ($\mathrm{Re} = 5 \times 10^5$, Fig. 13), elastic effects already dominant for λ as low as 0.001, and, for $\lambda = 1$ and higher, viscosity damping effects are already completely negligible.

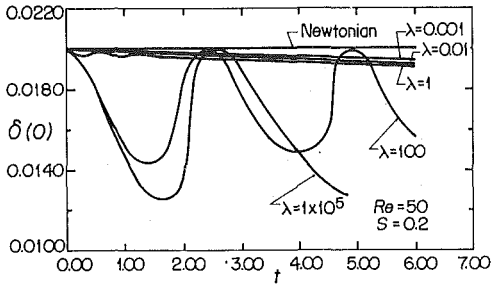

Fig. 12 Film thickness at θ = 0 deg versus time for various λ's

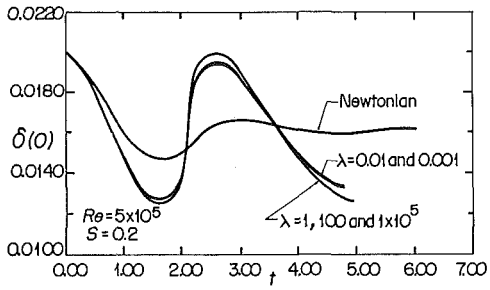

Fig. 13 Film thickness at θ = 0 deg versus time for various λ's

Conclusions

The purpose of the present paper is to report some progresses of the research presented in Souza Mendes (1989). Here the study was aimed at analyzing, the least qualitatively, the effects of a non-Newtonian fluid behavior on the flow of a thin film around a horizontal cylinder (wire).

Comparisons of the present results with results obtained for a Newtonian fluid showed that the viscoelastic behavior of the fluid plays an important role on the flow. The fluid acquires an oscillatory motion for much lower values of the Reynolds number, which makes the free surface to become wavy in the θ direction.

The tangential velocity $V(\theta, t)$ reaches high positive values at early instants of time and then starts to oscillate with smaller magnitudes, changing sign periodically. Moreover, the velocity of maximum magnitude occurs at different θ locations for different times, and with different magnitudes.

Independently of the value of the Deborah number, for infinite fluid viscosity (Re = 0), the fluid does not flow. At the other extreme, when λRe $\rightarrow \infty$, the wall shear stress becomes negligible and there is also no dependence on the Deborah number, and an undamped, large-amplitude oscillation is observed.

Inasmuch as as the Maxwell model has been chosen to describe the fluid behavior, some limitations were imposed to the analysis (Bird et al., 1987). No shear thinning effects are predicted with this model. Another nonlinear effect which cannot be predicted via the Maxwell model and which may be of importance in the present case is related to normal stress differences.

As discussed in Souza Mendes (1989), from what is experimentally observed in other geometries, instability phenomena might be expected for Re values larger than $\simeq$ 800. There are also other simplifying assumptions in the present analysis which may influence the results obtained. Therefore, before this approach is employed with confidence to predict real engineering situations, some comparisons with experimental results are needed for validation.

References

Bird, R. B., Armstrong, R. C., and Hassager, O., 1987, *Dynamics of Polymeric Liquids*, Wiley, New York, 2nd ed., Vol. 1.

Krupiczka, R., 1985, "Effect of Surface Tension on Laminar Film Condensation on a Horizontal Film," *Chem. Eng. Process.*, Vol. 19, pp. 199–203.

Markovitz, A., Mikic, B. B., and Bergles, A. E., 1972, "Condensation on a Downward-Facing Horizontal Rippled Surface," ASME *Journal of Heat Transfer*, Vol. 94, pp. 315–320.

Rodriguez, F., 1989, *Principles of Polymer Systems*, Hemisphere Publishing Co., New York, 3rd edition.

Souza Mendes, P. R., 1989, "Gravity-Driven Motion of a Fluid Layer Around a Cylinder," *Revista Brasileira de Ciências Mecânicas*, Vol. 11, No. 3, pp. 197–209.

Tanner, R. I., 1985, *Engineering Rheology*, Oxford Eng. Sci. Series, Oxford.

Separation and Surface Nuclei Effects in a Cavitation Susceptibility Meter

L. d'Agostino*

A. J. Acosta

California Institute of Technology,
Pasadena, Calif. 91125

This work is concerned with the effects of flow separation and surface nuclei on the operation of a fixed geometry Cavitation Susceptibility Meter (CSM) with laminar flow. Cavitation is induced under controlled conditions at the throat of a glass venturi tube for the measurement of the active nuclei concentration in water samples as a function of the applied tension. Both cavitation and flow velocity are monitored optically by a Laser Doppler Velocimeter. The throat pressure is determined indirectly from the upstream pressure and the local flow velocity. The results show that laminar flow separation and surface nuclei effects are the most stringent operational limitations. Separation in the diffuser increases the minimum attainable throat pressure above the susceptibility of most cavitation nuclei commonly found in technical waters. Surface nuclei can generate extensive sheet or spot cavitation at relatively high tensions even on optically finished glass surfaces. These phenomena are difficult to eliminate and bring therefore into question the practical utility of CSM's with laminar flow and fixed geometry for the measurement of the dependence of the cavitating nuclei concentration over wide ranges of the applied tension, as required for cavitation studies.

1 Introduction

The inception and extent of cavitation is determined by the concentration and susceptibility of nuclei, which locally trigger the onset of liquid rupture (Knapp et al., 1970). Knowledge of these properties of cavitation nuclei is essential for cavitation predictions and scaling. Among available methods for cavitation nuclei detection (Godefroy et al., 1981; Billet, 1985; Billet, 1986a), Cavitation Susceptibility Meters (CSM's) have long been proposed as standards cavitators in a variety of configurations (Shen et al., 1984; Gindroz et al., 1988) because of their unique feature of directly monitoring cavitating nuclei. Recently they also received significant attention in the attempt to extend their application to the measurement of the distribution of the active nuclei concentration on a wider range of applied tensions. In CSM's with fixed geometry cavitation is typically induced at the throat of a venturi tube, where cavitation nuclei contained in the liquid are, in principle, individually excited and can be detected either optically (Oldenziel, 1982a; Oldenziel, 1982b; d'Agostino and Acosta, 1991a; d'Agostino and Acosta 1991b) or acoustically (Lecoffre and Bonnin, 1979; Le Goff and Lecoffre, 1983; Shen et al., 1984). The throat pressure cannot be measured directly because of the extreme instability of the flow. It is therefore deduced from the upstream conditions and the energy equation using the measured local flow velocity or (less accurately) its estimate based on continuity, with or without corrections for viscous effects according to the specific situation. The dependence of the active nuclei concentration on the applied tension at the venturi throat is obtained by repeated measurements at different exhaust pressures.

Among the various phenomena interfering with proper operation of CSM's, flow separation and surface nuclei effects seem to impose the most serious limitations (Oldenziel, 1982a; d'Agostino and Acosta, 1991a; d'Agostino and Acosta, 1991b).

The present work is part of a systematic study on CSM's recently carried out at the California Institute of Technology and specifically focuses on the impact that these phenomena may have on the operation of CSM's with laminar flow and fixed geometry.

2 Experimental Apparatus and Procedure

The CSM used in this experiment has been described previously in detail (d'Agostino 1987; d'Agostino and Acosta, 1991a; d'Agostino and Acosta, 1991b), therefore only its most significant features are summarized here as required for clarity (see Fig. 1). By properly adjusting the exhaust pressure, cavitation nuclei are, in the average, individually excited at the throat section of a blown glass venturi tube, where they are monitored by a back-scattering Laser Doppler Velocimeter (LDV). In all operational conditions the noncavitating flow has a laminar potential core throughout the throat and the initial part of the diffuser. The amplitude and frequency of the filtered LDV signal are respectively used by the CSM Signal Processor to detect and measure the speed of up to 1024 cav-

*Now at the Dipartimento di Ingegneria Aerospaziale, Università degli Studi di Pisa, Italy.

Contributed by the Fluids Engineering Division for publication in the JOURNAL OF FLUIDS ENGINEERING. Manuscript received by the Fluids Engineering Division May 31, 1990.

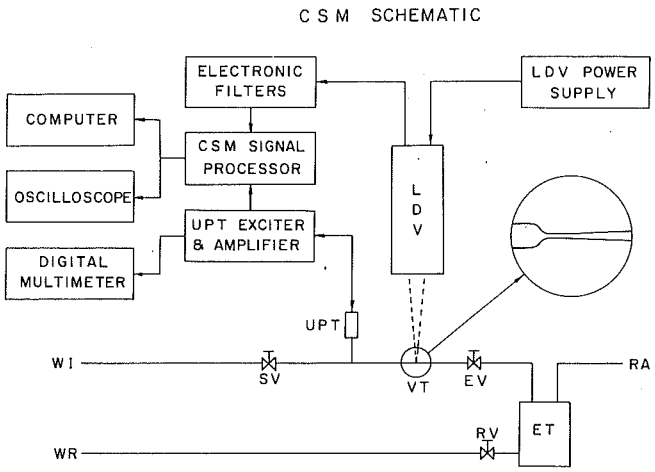

Fig. 1 Schematic of the various components of the CSM experimental apparatus: water inlet (WI), sampling valve (SV), upstream pressure transducer (UPT), venturi tube (VT), exhaust valve (EV), exhaust tank (ET), regulated air pressure line (RA), return valve (RT), water return (WR), laser Doppler velocimeter (LDV).

itation events, while the upstream pressure is simultaneously read by an absolute pressure transducer. A microcomputer is used for permanent data recording and reduction. The inception pressure at the throat is calculated from the upstream pressure and the throat velocity using Bernoulli's equation for ideal, incompressible, steady, fully wetted flow. The active nuclei concentration is determined by dividing the observed cavitation rate by the volume flux, and its dependence on the throat tension is obtained by repeating the measurements at different exhaust pressures.

Two venturi tubes of similar internal geometry (D_t = 1 mm, L_t = 7 mm, L_d = 10 mm, D_e = 1.2 mm ca.) but different length of their exit sections (only a few mm and about 3 cm) have been used in order to obtain different susceptibility to cavitation-separation. Both venturi tubes were made of blown glass, the most practical material with the necessary transparency for LDV operation, surface quality and regularity for flow stability, and mechanical resistance to cavitation damage. In the absence of a well defined inception criterion, the choice of the adjustable electro-optical sensitivity of the CSM is essentially arbitrary and therefore has been made by optimizing the CSM response with constant settings in all operational conditions. Velocity readings in the boundary layers and spurious noise-generated readings were eliminated by statistical filtering in the data reduction (d'Agostino and Acosta, 1991b). The inherent dispersion of the measured quantities, typically 400 Pa for the average throat pressure and 0.03 m/s for the average throat velocity, was always much larger than the measurement errors.

Three different forms of cavitation have been observed while testing tap water samples: travelling bubble cavitation, cavitation-separation and surface nuclei cavitation. Only the first one is the nominal operational regime of the CSM, where meaningful water quality measurements are possible (d'Agostino et al., 1989; d'Agostino and Green, 1989; d'Agostino and Acosta, 1991b). The others involve unwanted phenomena, which, as mentioned earlier, will be examined here because of the limitations they impose on the operation of CSM's.

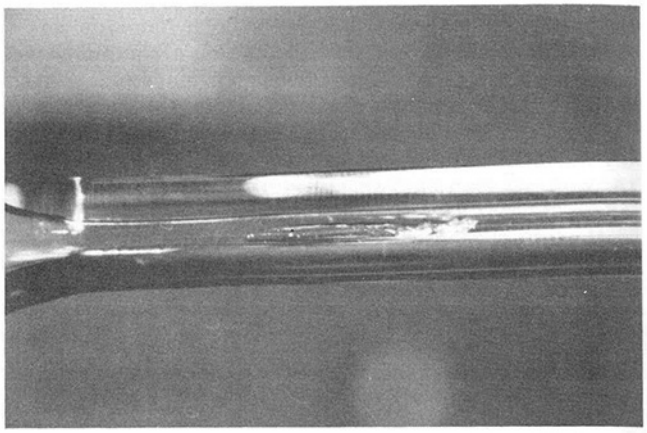

Fig. 2 Cavitation-separation of a tap water sample in the CSM venturi tube No. 2. The flow is from left to right, p_o = 1 atm., p_e = 5 kPa ± 2 percent and u_t = 13.5 m/s ± 0.2 percent. The cavitation-separation bubble originates in the diffuser and terminates in the exit section without reaching the exhaust.

3 Cavitation-Separation

Cavitation-separation has also been reported by previous investigators (Oldenziel, 1982a; Shen et al., 1986; Ito and Oba, 1980) and appears as an attached cavity in the upstream part of the diffuser (see Fig. 2). Most likely it is related to the well documented interaction of laminar separation with incoming free stream nuclei that get trapped in the low pressure recirculation region, where they may later develop into an attached cavity (Arakeri and Acosta, 1973). The cavitation-separation bubble is initially intermittent and tends to stabilize at lower pressures. When this cavity reaches the exhaust, as in the first venturi, the useful portion of the diffuser is drastically shortened and the throat pressure increases to a value only slightly lower than the exhaust pressure. In this case the cavitation-separation bubble is permanent, except for the exhaust pressures nearly equalling the water vapor pressure. Hence the presence of noncondensable gas seems to stabilize the cavitation-separation bubble by inhibiting its complete collapse. In the second venturi the cavitation-separation bubble reattaches in the longer exit section. The cavity is unsteady and has been observed only occasionally, mostly after the tube had been left dry and unused for some time. In general, cavitation-separation represents a serious problem because it causes an uncontrollable disruption of the venturi pressure field, inevitably compromising the operation of the CSM.

Laminar separation severely limits the allowable pressure recovery in the diffuser and consequently the minimum achievable throat pressure. This point is effectively illustrated by the application of Stratford's laminar separation criterion (Stratford, 1954):

$$(x+x_B)^2 C_p \left(\frac{dC_p}{dx}\right)^2 = 0.0104$$

Nomenclature

A = venturi cross-sectional area
C_p = pressure coefficient
D = venturi diameter
L = venturi section length
p = pressure
t = time
T = temperature
u = velocity
x = venturi axial coordinate

Subscripts

d = venturi tube diffuser
e = venturi tube exhaust
0 = water sample
t = venturi tube throat
u = upstream

Acronyms

CSM = Cavitation Susceptibility Meter
LDV = Laser Doppler Velocimeter

Here $C_p = (p-p_t)/(p_u-p_t)$ and x_B is the distance for the momentum thickness θ of a Blasius boundary layer (with zero pressure gradient) to reach the actual value of θ at the diffuser inlet, $x = 0$. Because of the steep inlet contraction in the venturi, θ essentially depends only on the throat length L_t and therefore $x_B \simeq L_t$. The above equation can be solved for the maximum pressure recovery $p_e - p_t$ as a function of the diffuser length $L_d = x$, thus defining the ideal nonseparating operational envelope of venturi-type CSM's with laminar flow. For any practical value of $L_d/x_B \simeq L_d/L_t$ the maximum laminar pressure recovery of the diffuser is comparable to the overall pressure drop across the venturi, and therefore relatively small. The available experimental data are in good agreement with the predictions of Stratford's laminar separation criterion.

Clearly, superior separation performance can be attained with developed turbulent flow in the diffuser, as documented by other investigators (Shen et al., 1984). However, this would prevent the accurate measurement of the throat pressure from the local velocity by introducing uncertain corrections for the viscous losses in addition to significant turbulent pressure fluctuations. In the present case the flow remains laminar (or very nearly so) throughout the upstream part of the diffuser because spontaneous transition would require tens of diameters and the use of transition promoting devices is clearly ruled out by the extreme instability of the flow.

These considerations also apply, at least qualitatively, to other types of CSM's with laminar pressure recovery. The maximum tensions compatible with laminar separation are generally lower than the critical tensions of free stream nuclei in technical waters at nearly atmospheric pressure, which are typically on the order of a few bars. It appears therefore that separation imposes very severe and elusive limitations on the performance of CSM's with laminar flow and fixed diffuser geometry.

4 Surface Nuclei Cavitation

Three forms of surface nuclei cavitation have been observed: sheet, spot and resonant cavitation. Sheet cavitation consists of relatively short and extremely thin attached cavities located at the throat and the upstream part of the diffuser (see Fig. 3). Since the optically smooth internal surface of the venturi does not provide any preferential inception points, sheet cavitation wanders rapidly and often intermittently all around the tube. Because of its small blockage effect, sheet cavitation does not heavily interfere with the operation of the CSM, but can introduce spurious cavitation counts due to bubbles originating from the disintegration of the trailing portion of the sheet cavities. These bubbles are released deep in the boundary layers and therefore generate abnormally low Doppler frequency readings, which often occur sequentially in small groups (see Fig. 4) and can easily be eliminated by statistical filtering in the data reduction.

Spot cavitation consists in the stable periodic release of cavities from localized points on the venturi throat surface. It has only been observed in the first venturi tube. Under stroboscopic light of commensurable frequency spot cavitation appears as a regular sequence of droplike shaped cavities, with their cusp facing upstream and tilted towards the venturi wall. The LDV measured cavity speed is lower than the fully wetted flow speed and decreases markedly in the upstream direction. These cavities appear to periodically originate from a microscopic surface nucleus and later be released in the flow as they grow large enough to be swept away by the incoming stream. The shearing action of the boundary layer on the cavities explains their peculiar shape and orientation. Spot cavitation disappeared after cleaning the venturi internal surface, unfortunately before photographic records could be taken. However, in no case it has been possible to detect any visible imperfection

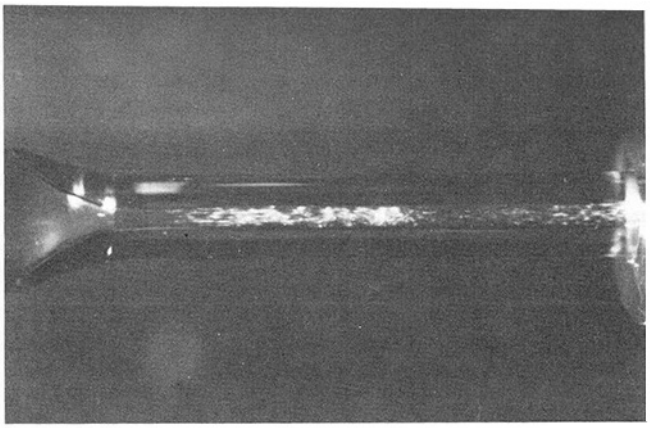

Fig. 3 Sheet cavitation of a tap water sample in the CSM venturi tube No. 2. The flow is from left to right, p_o = 1 atm, T_o = 21 ± 1°C, α_0 = 20.5 ± 1 ppm, p_t = −15.02 ± 0.390 kPa and u_t = 14.84 ± 0.026 m/s. Sheet cavitation occurs in small fuzzy streaks at the diffuser inlet.

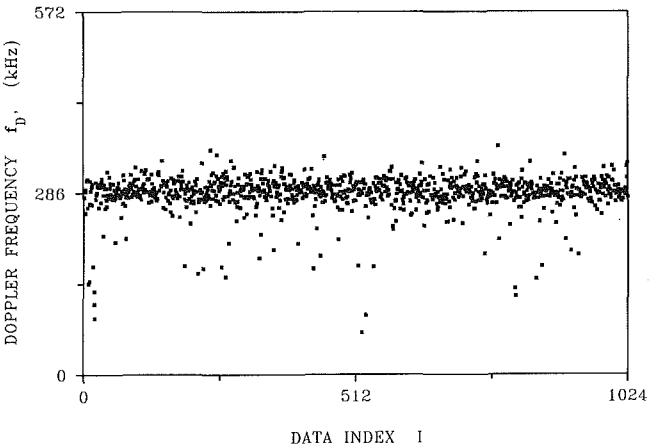

Fig. 4 Doppler frequency data f_D as a function of the data index I for a typical CSM run in the venturi tube No. 2. The data refer to the tap water sample of Fig. 3.

on the optically smooth internal surface of the venturi that could be safely identified as the nucleation agent.

Spot cavitation can also excite the venturi flow in stable self-sustained fluid dynamic oscillations at characteristic frequencies (resonant cavitation). The onset of these oscillations is likely due to the coupling between the periodic release of the cavities from the surface nucleus and the resulting perturbations of the venturi flow. Typical density distributions of the time intervals between cavitation events in resonant cavitation are shown for in Fig. 5, where the continuous line indicates the expected Poissonian distributions for uncorrelated cavitation events (d'Agostino and Acosta, 1991a). Note the striking deviation induced by resonant cavitation from the typical distribution in normal CSM operation, which closely follows the theoretical predictions (d'Agostino and Acosta, 1991b). The average separation between the cavities in Fig. 5 (1.2 cm) is about four times smaller than in normal operation at the highest cavitation rates, thus indicating that the effect of resonant cavitation can be quite substantial.

Spot, resonant and sheet cavitation do not produce immediately obvious indications of irregular operation and therefore are easily misinterpreted as free stream nuclei cavitation. As a consequence, optical cavitation monitoring, possibly with velocity measurement of individual cavities, is crucial for discriminating surface nuclei cavitation for CSM data validation. Furthermore, the occurrence of substantial cavitation even on optically smooth glass surfaces subject to relatively moderate tensions indicates that interfacial nuclei may be a serious source of errors in CSM's operating under less favorable conditions,

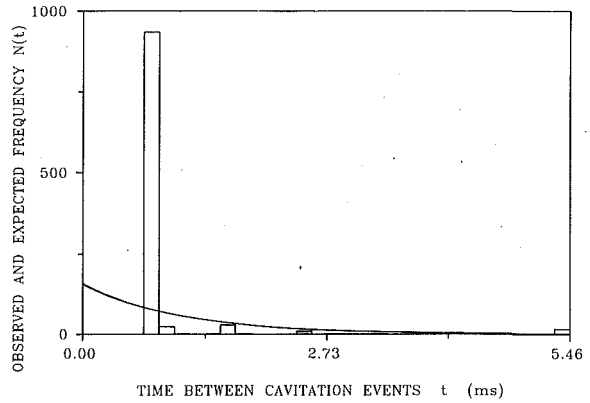

Fig. 5 Observed distribution of time intervals *t* between successive cavitation events in resonant cavitation conditions in the venturi tube No. 1 (histograms). The solid line indicates the expected Poissonian distribution for uncorrelated cavitation events.

commonly encountered in other applications. This may contribute to explain the large discrepancies consistently observed between the results of CSM's and alternative nuclei detection methods (Gowing et al., 1988; Godefroy et al., 1981).

5 Conclusions

The following conclusions can be drawn from the current experience on the CSM under investigation:

- the throat pressure limitations imposed by laminar separation are generally quite stringent and difficult to eliminate in fixed geometry diffusers;
- the maximum tension currently attainable with laminar flow (about -35 kPa for samples at atmospheric pressure) is often insufficient for cavitating the nuclei typically present in technical waters;
- surface nuclei effects may seriously interfere with CSM operation even at relatively moderate tensions on optically smooth blown glass surfaces;
- the discrimination of surface nuclei effects for CSM data validation requires direct optical observation and possibly velocity measurements of individual cavities;
- spot cavitation can develop into resonant cavitation in venturi tubes with short diffusers;
- the above difficulties may help explaining the observed discrepancies between the results of CSM's and alternative nuclei detection methods and, if not circumvented, bring into question the practical utility of CSM's with laminar flow and fixed geometry for the measurement of the active nuclei concentration distribution over realistic ranges of the applied tension, as required for cavitation studies.

Acknowledgments

This research has been funded by the Office of Naval Research and by the Naval Sea Systems Command General Hydromechanics Research Program administered by the David W. Taylor Naval ship Research and Development Center. The North Atlantic Treaty Organization - Consiglio Nazionale delle Ricerche, Italy, has also contributed to the support of this work through a 1982 and a 1983 Fellowship for Technological Research. Special thanks to Dr. T. T. Huang of DTNSRDC for his interest in this work, to Mr. Joe Fontana, Mr. Elton Daly, Mr. Rich Eastvedt, Mr. Leonard Montenegro, Mr. John Lee and to Miss Cecilia Lin of the Caltech staff for their assistance in the completion of the experiment and to Dr. Haskel Shapiro, Mr. Bob Kirkpatrick and their group for the design and implementation of the custom-made electronics.

References

Arakeri, V. H., and Acosta, A. J., 1973, "Viscous Effects in the Inception of Cavitation on Axisymmetric Bodies," ASME JOURNAL OF FLUIDS ENGINEERING, Vol. 95, pp. 519-527.

Billet, M., 1986a, "The Importance and Measurement of Cavitation Nuclei," *Advancements in Aerodynamics, Fluid Mechanics and Hydraulics*, Minneapolis, Minn, pp. 967-989.

Billet, M., 1986, b. Personal communication.

Billet, M., 1985, "Cavitation Nuclei Measurement—A Review," *ASME Cavitation and Multiphase Flow Forum*, Albuquerque, NM, pp. 31-38.

Chahine, G. L., and Shen, Y. T,. 1986, "Bubble Dynamics and Cavitation Inception in Cavitation Susceptibility Meters," ASME JOURNAL OF FLUIDS ENGINEERING, Vol. 108, pp. 444-452.

d'Agostino, L., and Acosta, A. J., 1983, "On the Design of Cavitation Susceptibility Meters," *American Towing Tank Conference*, Hoboken, NJ.

d'Agostino, L., 1987, "Experimental and Theoretical Study on Cavitation Inception and Bubbly Flow Dynamics," Ph.D. thesis, Report No. Eng. 183.16, California Institute of Technology, Pasadena, Calif.

d'Agostino, L., Thai Pham, and Green, S., 1989, "Comparison a of Cavitation Susceptibility Meter and Holographic Observation for Nuclei Detection in Liquids," ASME JOURNAL OF FLUIDS ENGINEERING, Vol. 111, No. 2, pp. 197-203.

d'Agostino, L., and Acosta, A. J., 1991a, "A Cavitation Susceptibility Meter with Optical Cavitation Monitoring—Part One: Design Concepts," ASME JOURNAL OF FLUIDS ENGINEERING, Vol. 113, pp. 261-269.

d'Agostino, L., and Acosta, A. J., 1991b, "A Cavitation Susceptibility Meter with Optical Cavitation Monitoring—Part Two: Experimental Apparatus and Results," ASME JOURNAL OF FLUIDS ENGINEERING, Vol. 113, pp. 270-277.

d'Agostino, L., and Green, S., 1989, "Simultaneous Cavitation Susceptibility Meter and Holographic Measurements of Nuclei in Liquids," *ASME Cavitation and Multiphase Flow Forum*, San Diego, Calif.

Gindroz, B., Avellan, F., and Henry, P., 1988, "Similarity Rules of Cavitation Tests: the Case of the Francis Turbine," *14th IARH Symposium on Progress within Large and High Specific Energy Units*, Trondheim, Norway.

Godefroy, H. W. H. E., Jansen, R. H. J., Keller, A. P., and van Renesse, R. L., 1981, "Comparison of Measuring and Control Methods of the Water Quality with Respect to Cavitation Behaviour," *Delft Hydraulics Laboratory Publication*.

Gowing, S., Vikram, C. S., and Burton, S., 1988, "Comparison of Holography, Light Scattering and Venturi Techniques for Bubble Measurements in a Water Tunnel," *ASME Cavitation and Multiphase Flow Forum*, FED Vol. 64, pp. 25-28.

Ito, Y., and Oba, R., 1980, "Cavitation Observations through a Fine Laser Beam Technique," *Report No. 337*, Institute of High Speed Mechanics, Tohoku University.

Knapp, R. T., Daily, J. W., and Hammitt, F. G., 1970, *Cavitation*, McGraw-Hill, New York.

Lecoffre, Y., and Bonnin, J., 1979, "Cavitation Tests and Nucleation Control," *International Symposium on Cavitation Inception*, New York, NY, pp. 141-145.

Le Goff, J. P., and Lecoffre, Y., 1983, "Nuclei and Cavitation," *14th Symposium on Naval Hydrodynamics*, National Academy Press, pp. 215-242.

Oldenziel, D. M., 1979, "New Instruments in Cavitation Research," *International Symposium on Cavitation Inception*, New York, NY, pp. 111-124.

Oldenziel, D. M., 1982a, "A New Instrument in Cavitation Research: the Cavitation Susceptibility Meter," ASME JOURNAL OF FLUIDS ENGINEERING, Vol. 104, pp. 136-142.

Oldenziel, D. M., 1982, "Utility of Available Instruments during Cavitation Tests," *Proceedings of Symposium on Operating Problems of Pump Stations and Power Plants*, IAHR, Amsterdam.

Oldenziel, D. M., Jansen, R. H. J., Keller, A. P., Lecoffre, Y., and van Renesse, R. L., 1982, "Comparison of Instruments for Detection of Particles and Bubbles in Water during Cavitation Studies," *Proceedings of Symposium on Operating Problems of Pump Stations and Power Plants*, IAHR, Amsterdam.

Shen, Y. T., Gowing, S., and Pierce, R., 1984, "Cavitation Susceptibility Meters by a Venturi," *International Symposium on Cavitation Inception*, ASME Winter Annual Meeting, pp. 9/18.

Shen, Y. T., and Gowing, S., 1985, "Scale Effects on Bubble Growth and Cavitation Inception in Cavitation Susceptibility Meters," *ASME Cavitation and Mutliphase Flow Forum*, Albuquerque, NM, pp. 14-16.

Shen, Y. T., Gowing, S., and Eckstein, B., 1986, "Cavitation Susceptibility Measurements of Ocean Lake and Laboratory Waters," *David W. Taylor Naval Ship Research and Development Center*, Report DTNSRDC-86/D19.

Stratford, B. S., 1954, "Flow in Laminar Boundary Layer near Separation," *Aeronautical Research Council*, R&M 3002.

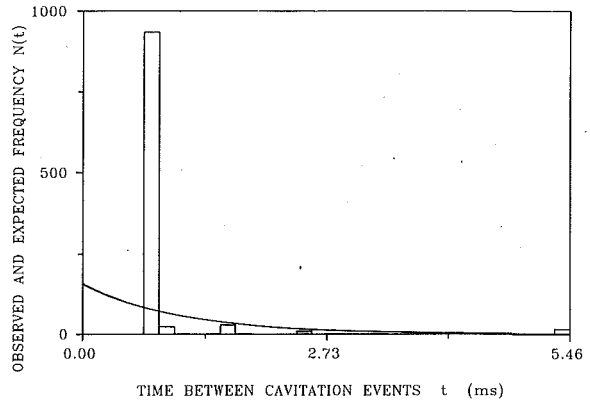

Fig. 5 Observed distribution of time intervals *t* between successive cavitation events in resonant cavitation conditions in the venturi tube No. 1 (histograms). The solid line indicates the expected Poissonian distribution for uncorrelated cavitation events.

commonly encountered in other applications. This may contribute to explain the large discrepancies consistently observed between the results of CSM's and alternative nuclei detection methods (Gowing et al., 1988; Godefroy et al., 1981).

5 Conclusions

The following conclusions can be drawn from the current experience on the CSM under investigation:

- the throat pressure limitations imposed by laminar separation are generally quite stringent and difficult to eliminate in fixed geometry diffusers;
- the maximum tension currently attainable with laminar flow (about -35 kPa for samples at atmospheric pressure) is often insufficient for cavitating the nuclei typically present in technical waters;
- surface nuclei effects may seriously interfere with CSM operation even at relatively moderate tensions on optically smooth blown glass surfaces;
- the discrimination of surface nuclei effects for CSM data validation requires direct optical observation and possibly velocity measurements of individual cavities;
- spot cavitation can develop into resonant cavitation in venturi tubes with short diffusers;
- the above difficulties may help explaining the observed discrepancies between the results of CSM's and alternative nuclei detection methods and, if not circumvented, bring into question the practical utility of CSM's with laminar flow and fixed geometry for the measurement of the active nuclei concentration distribution over realistic ranges of the applied tension, as required for cavitation studies.

Acknowledgments

This research has been funded by the Office of Naval Research and by the Naval Sea Systems Command General Hydromechanics Research Program administered by the David W. Taylor Naval ship Research and Development Center. The North Atlantic Treaty Organization - Consiglio Nazionale delle Ricerche, Italy, has also contributed to the support of this work through a 1982 and a 1983 Fellowship for Technological Research. Special thanks to Dr. T. T. Huang of DTNSRDC for his interest in this work, to Mr. Joe Fontana, Mr. Elton Daly, Mr. Rich Eastvedt, Mr. Leonard Montenegro, Mr. John Lee and to Miss Cecilia Lin of the Caltech staff for their assistance in the completion of the experiment and to Dr. Haskel Shapiro, Mr. Bob Kirkpatrick and their group for the design and implementation of the custom-made electronics.

References

Arakeri, V. H., and Acosta, A. J., 1973, "Viscous Effects in the Inception of Cavitation on Axisymmetric Bodies," ASME JOURNAL OF FLUIDS ENGINEERING, Vol. 95, pp. 519–527.

Billet, M., 1986a, "The Importance and Measurement of Cavitation Nuclei," *Advancements in Aerodynamics, Fluid Mechanics and Hydraulics*, Minneapolis, Minn, pp. 967–989.

Billet, M., 1986, b. Personal communication.

Billet, M., 1985, "Cavitation Nuclei Measurement—A Review," *ASME Cavitation and Multiphase Flow Forum*, Albuquerque, NM, pp. 31–38.

Chahine, G. L., and Shen, Y. T,. 1986, "Bubble Dynamics and Cavitation Inception in Cavitation Susceptibility Meters," ASME JOURNAL OF FLUIDS ENGINEERING, Vol. 108, pp. 444–452.

d'Agostino, L., and Acosta, A. J., 1983, "On the Design of Cavitation Susceptibility Meters," *American Towing Tank Conference*, Hoboken, NJ.

d'Agostino, L., 1987, "Experimental and Theoretical Study on Cavitation Inception and Bubbly Flow Dynamics," Ph.D. thesis, Report No. Eng. 183.16, California Institute of Technology, Pasadena, Calif.

d'Agostino, L., Thai Pham, and Green, S., 1989, "Comparison a of Cavitation Susceptibility Meter and Holographic Observation for Nuclei Detection in Liquids," ASME JOURNAL OF FLUIDS ENGINEERING, Vol. 111, No. 2, pp. 197–203.

d'Agostino, L., and Acosta, A. J., 1991a, "A Cavitation Susceptibility Meter with Optical Cavitation Monitoring—Part One: Design Concepts," ASME JOURNAL OF FLUIDS ENGINEERING, Vol. 113, pp. 261–269.

d'Agostino, L., and Acosta, A. J., 1991b, "A Cavitation Susceptibility Meter with Optical Cavitation Monitoring—Part Two: Experimental Apparatus and Results," ASME JOURNAL OF FLUIDS ENGINEERING, Vol. 113, pp. 270–277.

d'Agostino, L., and Green, S., 1989, "Simultaneous Cavitation Susceptibility Meter and Holographic Measurements of Nuclei in Liquids," *ASME Cavitation and Multiphase Flow Forum*, San Diego, Calif.

Gindroz, B., Avellan, F., and Henry, P., 1988, "Similarity Rules of Cavitation Tests: the Case of the Francis Turbine," *14th IARH Symposium on Progress within Large and High Specific Energy Units*, Trondheim, Norway.

Godefroy, H. W. H. E., Jansen, R. H. J., Keller, A. P., and van Renesse, R. L., 1981, "Comparison of Measuring and Control Methods of the Water Quality with Respect to Cavitation Behaviour," *Delft Hydraulics Laboratory Publication*.

Gowing, S., Vikram, C. S., and Burton, S., 1988, "Comparison of Holography, Light Scattering and Venturi Techniques for Bubble Measurements in a Water Tunnel," *ASME Cavitation and Multiphase Flow Forum*, FED Vol. 64, pp. 25–28.

Ito, Y., and Oba, R., 1980, "Cavitation Observations through a Fine Laser Beam Technique," *Report No. 337*, Institute of High Speed Mechanics, Tohoku University.

Knapp, R. T., Daily, J. W., and Hammitt, F. G., 1970, *Cavitation*, McGraw-Hill, New York.

Lecoffre, Y., and Bonnin, J., 1979, "Cavitation Tests and Nucleation Control," *International Symposium on Cavitation Inception*, New York, NY, pp. 141–145.

Le Goff, J. P., and Lecoffre, Y., 1983, "Nuclei and Cavitation," *14th Symposium on Naval Hydrodynamics*, National Academy Press, pp. 215–242.

Oldenziel, D. M., 1979, "New Instruments in Cavitation Research," *International Symposium on Cavitation Inception*, New York, NY, pp. 111–124.

Oldenziel, D. M., 1982a, "A New Instrument in Cavitation Research: the Cavitation Susceptibility Meter," ASME JOURNAL OF FLUIDS ENGINEERING, Vol. 104, pp. 136–142.

Oldenziel, D. M., 1982, "Utility of Available Instruments during Cavitation Tests," *Proceedings of Symposium on Operating Problems of Pump Stations and Power Plants*, IAHR, Amsterdam.

Oldenziel, D. M., Jansen, R. H. J., Keller, A. P., Lecoffre, Y., and van Renesse, R. L., 1982, "Comparison of Instruments for Detection of Particles and Bubbles in Water during Cavitation Studies," *Proceedings of Symposium on Operating Problems of Pump Stations and Power Plants*, IAHR, Amsterdam.

Shen, Y. T., Gowing, S., and Pierce, R., 1984, "Cavitation Susceptibility Meters by a Venturi," *International Symposium on Cavitation Inception*, ASME Winter Annual Meeting, pp. 9/18.

Shen, Y. T., and Gowing, S., 1985, "Scale Effects on Bubble Growth and Cavitation Inception in Cavitation Susceptibility Meters," *ASME Cavitation and Mutliphase Flow Forum*, Albuquerque, NM, pp. 14–16.

Shen, Y. T., Gowing, S., and Eckstein, B., 1986, "Cavitation Susceptibility Measurements of Ocean Lake and Laboratory Waters," *David W. Taylor Naval Ship Research and Development Center*, Report DTNSRDC-86/D19.

Stratford, B. S., 1954, "Flow in Laminar Boundary Layer near Separation," *Aeronautical Research Council*, R&M 3002.

DISCUSSION

Yves Lecoffre[2]

The authors should be congratulated for their detailed discussion on the physics of cavitation in venturi meters. The occurrence of sheet and spot cavitation is the main practical

[2]YLec Consultants, Saint Ismier, France.

problem in cavitation nuclei measurements and it is important to have a better understanding of their behavior.

When we used classical venturi design, despite the extreme caution in making the devices, we always had problems with the surface finish. We made more than 50 plexiglas venturi before making one of them work the right way. Then, we turned to high precision spark machining of stainless-steel venturi. Finally, the best solution was to make venturi by nickel electrodeposition. In all cases, extreme care had to be taken and a final hand polishing was often necessary to make the system work correctly. Among the acceptance tests, the venturi had to reach at least-2 bars when operated with tap water.

Finally, we turned to less classical designs and plexiglass venturi where a stainless-steel central body has been developed. They gave us less problems with unwanted cavitation types, like sheet or wall nuclei and made flow visualization quite easy.

Whatever the venturi type, we had Reynolds numbers in the same range as the authors had. The classical venturi had a throat diameter of 2 mm and the annular gap in the central body venturi was typically of 1 mm.

Despite these relatively low Reynolds numbers, it has always been possible to reach low tensions. The lower tension obtained has been -8 bars with the Grenoble tap water. In sea water, we have measured tensions of -5 bars in the Tahiti Lagoon. These two results have been obtained with water roughly saturated with air at atmospheric pressure.

When we use venturi in cavitation tunnels, for example GTH, the water susceptibility is generally below -1 bar when no nuclei are added. In this case, as well as in the case of natural waters, the venturi is the only method available to measure efficient nuclei.

When artificial nuclei are added in cavitation facilities, other methods can be used to measure nuclei, among whose the scattering, holography, phase method or a very recently developed hybrid method which uses simultaneously scattering, phase method and image processing with non-coherent light. In routine tests, the best fitted method may depend on the information required. For example, when it is necessary to know the diameter distribution of big bubbles, typically bigger than 50 μ, optical methods are much more precise than venturi.

We found good correlations between venturi and phase laser measurements in GTH. Venturi is considered as the reference, even though some problems still have to be solved, as for example complete automation of the system. Excellent correlations between bubble cavitation and venturi measurements have been found in Laurence Briançon Marjollet Thesis (1987).

In conclusion, it seems to me very important to remember that the development of venturi systems (Oldenziel, Lecoffre), has shown that the nuclei populations measured by optical methods, i.e., scattering or microscopy, were mainly containing nonefficient nuclei. This is the major reasons for the discrepancies found in the literature. Finally, the use of venturi to measure cavitation nuclei spectral over a wide range of critical pressures has been demonstrated by Marjollet (1987). This technique is used in routine tests in several European laboratories.

Additional References

Briançon Marjollet, L., 1987, "Couches Limites, Germes et Cavités en Interaction: Etude Physique," Thése Grenoble.

Lecoffre, Y., Menoret, L., Briançon Marjollet, L., Franc, J. P., and Michel, J. M., 1988, "Germes et Cavitation. Effets-Techniques De Contrôle-Résultats Récents," La Houille Blanche, No. 2.

Authors' Closure

First of all, I would like to thank Dr. Lecoffre for his kind words on our work. His comments deserve special consideration because of his long and well-known expertise in the field.

The determination of the inception pressure is crucial for the measurement of the active nuclei concentration distribution. Because of the extreme instability of the flow, the inception pressure can only be measured indirectly. This is invariably done using Bernoulli's equation for steady, incompressible, fully wetted flow, with or without corrections for viscous effects, depending on the specific situation. This method, however, only yields accurate results in flows where (as in our case) only sporadic cavitation occurs. It is clearly totally inadequate in the presence of extensive cavitation, when the flow is unsteady, nonhomogenous, nonbarotropic and heavily affected by the inertial effects due to the bubble response. In these conditions the application of Bernoulli's equation to flows with rapidly growing cavities invariably leads to gross overestimation of the cavitation tension.

Since the discharge pressure can never be negative, the inception tension is essentially limited by the pressure recovery in the diffuser. Turbulent flow, which is commonly encountered in CSM's reported in the literature, is clearly advantageous in this respect, by promoting boundary layer stability to separation. The maximum tensions (up to -800 kPa) reported by Dr. Lecoffre in CSM's of various configurations are much higher than those we have been able to obtain in fully wetted laminar flow, and clearly incompatible with laminar pressure recovery in the diffuser. At these tensions cavitation would be extensive (if not massive) in most technical waters. If my previous discussion is correct, at least part of the observed discrepancies is simply due to the underestimation of the cavitation pressure, the rest being due to the favorable effect of turbulence.

In view of our early negative experiences with plastic venturis of conventional design, I am rather surprised that Dr. Lecoffre and his collaborators have been able to successfully operate both conventional and central body venturis with plastic diffusers without significant surface nuclei cavitation, despite the erosive effects of imploding cavitation. As discussed in our paper, even optically smooth blown-glass venturi did not completely eliminate surface nuclei effects in our experiments at much lower tensions than reported by Dr. Lecoffre.

As indicated by Dr. Lecoffre, in general not all potential nuclei measured by indirect methods actually develop cavitation. However, in my opinion the observed discrepancies between the nuclei populations measured by CSM's and other indirect methods should only in part be attributed to this effect. Our comparisons of CSM and holographic results in water samples with a dominant population of air bubbles still showed that the CSM largely underestimated the active nuclei content (d'Agostino et al., 1989; d'Agostino and Green, 1989). This may be due to sensitivity limitations and, at higher cavitation rates, to interference effects among cavities. More importantly, the very same notion of cavitation inception is not clearly defined for nuclei exposed to unsteady pressure histories. I believe that any realistic comparison between results obtained by CSM's and other indirect methods should account for the dynamic nature of cavitation in the specific application.

As a final remark, it is important to note that surface nuclei, separation, bubble interference, turbulence, and other disturbing effects have quite a different impact on the operation of CSM's depending on their intended use. As long as CSM's are simply used as sophisticated standard cavitators, these effects are often irrelevant, if only relative information is required. In this case CSM's can be quite useful for direct water quality assessment. However, when CSM's are used to measure the distribution of the active nuclei concentration in the liquid over an extended range of tensions for comparison with other nuclei detection methods that yield similar spectral information, it is essential to precisely determine the source and inception conditions of cavitation, and disturbing effects can become quite important. In my opinion the effectiveness of CSM's in this latter role is still far from being conclusively demonstrated and deserves further investigation.

problem in cavitation nuclei measurements and it is important to have a better understanding of their behavior.

When we used classical venturi design, despite the extreme caution in making the devices, we always had problems with the surface finish. We made more than 50 plexiglas venturi before making one of them work the right way. Then, we turned to high precision spark machining of stainless-steel venturi. Finally, the best solution was to make venturi by nickel electrodeposition. In all cases, extreme care had to be taken and a final hand polishing was often necessary to make the system work correctly. Among the acceptance tests, the venturi had to reach at least-2 bars when operated with tap water.

Finally, we turned to less classical designs and plexiglass venturi where a stainless-steel central body has been developed. They gave us less problems with unwanted cavitation types, like sheet or wall nuclei and made flow visualization quite easy.

Whatever the venturi type, we had Reynolds numbers in the same range as the authors had. The classical venturi had a throat diameter of 2 mm and the annular gap in the central body venturi was typically of 1 mm.

Despite these relatively low Reynolds numbers, it has always been possible to reach low tensions. The lower tension obtained has been -8 bars with the Grenoble tap water. In sea water, we have measured tensions of -5 bars in the Tahiti Lagoon. These two results have been obtained with water roughly saturated with air at atmospheric pressure.

When we use venturi in cavitation tunnels, for example GTH, the water susceptibility is generally below -1 bar when no nuclei are added. In this case, as well as in the case of natural waters, the venturi is the only method available to measure efficient nuclei.

When artificial nuclei are added in cavitation facilities, other methods can be used to measure nuclei, among whose the scattering, holography, phase method or a very recently developed hybrid method which uses simultaneously scattering, phase method and image processing with non-coherent light. In routine tests, the best fitted method may depend on the information required. For example, when it is necessary to know the diameter distribution of big bubbles, typically bigger than 50 μ, optical methods are much more precise than venturi.

We found good correlations between venturi and phase laser measurements in GTH. Venturi is considered as the reference, even though some problems still have to be solved, as for example complete automation of the system. Excellent correlations between bubble cavitation and venturi measurements have been found in Laurence Briançon Marjollet Thesis (1987).

In conclusion, it seems to me very important to remember that the development of venturi systems (Oldenziel, Lecoffre), has shown that the nuclei populations measured by optical methods, i.e., scattering or microscopy, were mainly containing nonefficient nuclei. This is the major reasons for the discrepancies found in the literature. Finally, the use of venturi to measure cavitation nuclei spectral over a wide range of critical pressures has been demonstrated by Marjollet (1987). This technique is used in routine tests in several European laboratories.

Additional References

Briançon Marjollet, L., 1987, "Couches Limites, Germes et Cavités en Interaction: Etude Physique," Thése Grenoble.

Lecoffre, Y., Menoret, L., Briançon Marjollet, L., Franc, J. P., and Michel, J. M., 1988, "Germes et Cavitation. Effets-Techniques De Contrôle-Résultats Récents," La Houille Blanche, No. 2.

Authors' Closure

First of all, I would like to thank Dr. Lecoffre for his kind words on our work. His comments deserve special consideration because of his long and well-known expertise in the field.

The determination of the inception pressure is crucial for the measurement of the active nuclei concentration distribution. Because of the extreme instability of the flow, the inception pressure can only be measured indirectly. This is invariably done using Bernoulli's equation for steady, incompressible, fully wetted flow, with or without corrections for viscous effects, depending on the specific situation. This method, however, only yields accurate results in flows where (as in our case) only sporadic cavitation occurs. It is clearly totally inadequate in the presence of extensive cavitation, when the flow is unsteady, nonhomogenous, nonbarotropic and heavily affected by the inertial effects due to the bubble response. In these conditions the application of Bernoulli's equation to flows with rapidly growing cavities invariably leads to gross overestimation of the cavitation tension.

Since the discharge pressure can never be negative, the inception tension is essentially limited by the pressure recovery in the diffuser. Turbulent flow, which is commonly encountered in CSM's reported in the literature, is clearly advantageous in this respect, by promoting boundary layer stability to separation. The maximum tensions (up to -800 kPa) reported by Dr. Lecoffre in CSM's of various configurations are much higher than those we have been able to obtain in fully wetted laminar flow, and clearly incompatible with laminar pressure recovery in the diffuser. At these tensions cavitation would be extensive (if not massive) in most technical waters. If my previous discussion is correct, at least part of the observed discrepancies is simply due to the underestimation of the cavitation pressure, the rest being due to the favorable effect of turbulence.

In view of our early negative experiences with plastic venturis of conventional design, I am rather surprised that Dr. Lecoffre and his collaborators have been able to successfully operate both conventional and central body venturis with plastic diffusers without significant surface nuclei cavitation, despite the erosive effects of imploding cavitation. As discussed in our paper, even optically smooth blown-glass venturi did not completely eliminate surface nuclei effects in our experiments at much lower tensions than reported by Dr. Lecoffre.

As indicated by Dr. Lecoffre, in general not all potential nuclei measured by indirect methods actually develop cavitation. However, in my opinion the observed discrepancies between the nuclei populations measured by CSM's and other indirect methods should only in part be attributed to this effect. Our comparisons of CSM and holographic results in water samples with a dominant population of air bubbles still showed that the CSM largely underestimated the active nuclei content (d'Agostino et al., 1989; d'Agostino and Green, 1989). This may be due to sensitivity limitations and, at higher cavitation rates, to interference effects among cavities. More importantly, the very same notion of cavitation inception is not clearly defined for nuclei exposed to unsteady pressure histories. I believe that any realistic comparison between results obtained by CSM's and other indirect methods should account for the dynamic nature of cavitation in the specific application.

As a final remark, it is important to note that surface nuclei, separation, bubble interference, turbulence, and other disturbing effects have quite a different impact on the operation of CSM's depending on their intended use. As long as CSM's are simply used as sophisticated standard cavitators, these effects are often irrelevant, if only relative information is required. In this case CSM's can be quite useful for direct water quality assessment. However, when CSM's are used to measure the distribution of the active nuclei concentration in the liquid over an extended range of tensions for comparison with other nuclei detection methods that yield similar spectral information, it is essential to precisely determine the source and inception conditions of cavitation, and disturbing effects can become quite important. In my opinion the effectiveness of CSM's in this latter role is still far from being conclusively demonstrated and deserves further investigation.

A Statistical Analysis of Cavitation Erosion Pits

B. Belahadji

J. P. Franc

J. M. Michel

Institut de Mécanique de Grenoble,
Grenoble, France

An optical interferometric technique has been used to determine the 3-D shape of cavitation erosion pits. The method which is particularly suitable to the determination of pit diameter and pit depth is used for a statistical analysis of cavitation erosion pits. We analyzed numerous samples which were eroded at various velocities with two different fluids (mercury and water) on two geometrically similar venturi test sections of different length scales. General properties of histograms of pit size are pointed out. The influence of flow velocity on pitting rates corresponding to limited ranges of pit size is discussed. The contribution of each pit diameter to the total eroded surface is analyzed. Some results are given on pit depths and pit volumes.

1 Introduction

In cavitation erosion studies, several techniques may be used to quantify the damage on a material as pit counting (Stinebring, 1976), measurement of mean depth of deformation (Kato, 1975), or weight loss. Concerning the pit counting technique to which the present paper is devoted, the more studied parameter is pitting rate, i.e., the density of pits per unit surface area and per unit time of exposure, notwithstanding any pit size parameter. In the present analysis, we try to improve this technique in taking into account pit diameter and if possible pit depth. Then, damage is basically characterized by a histogram in size of pit density.

Such an approach describes more precisely the damage on a material as the contribution of small pits or large ones is obviously not equivalent. Even if only total pit density is of interest, discussion of results may be significantly complicated by the cut-off size which is characteristic of the counting technique used.[1] Pitting rate is actually strongly dependent upon this threshold size. In addition, pit size appears as an essential parameter in many studies. It is the case in cavitation erosion scaling which is the main motivation of the present research. In particular, for geometrically similar cavitating flows, an important point is to know how pit size is correlated to the general length scale and how the cut-off size has to be scaled to make relevant comparisons of total pitting rates. Taking into account pit size leads necessarily to a more complicated treatment. For the present research, a specific technique based upon an interference method has been developed. Its principle is described in section 2. It proved to be handy enough and quite suitable to the determination of histograms in size.

The present study is part of a program on cavitation erosion scaling which is in progress in France. Previous experiments (Lecoffre et al., 1985) allowed us to ascertain some scaling assumptions but a few points remained uncleared and required the determination of histograms in size. A large number of samples were eroded in this study under various conditions of flow velocity, fluid and geometric scale as presented in section 3. It is a storehouse of information that we tried to exploit. This paper is devoted to the presentation of the most reliable results we have obtained at the present time. A few points related to scaling rules are still under examination and require additional erosion tests.

2 Pit Analysis Technique

The pit analysis technique used in the present study was developed by G. Tribillon at the "Laboratoire d'Optique de Besançon" in France (Pierali and Tribillon, 1987; Pierali, 1989). It is based upon an interference method schematically presented in Fig. 1. A typical interferogram is given in Fig. 2.

The system is made of a metallographic microscope used with interferential objectives of Mirau type. The light source is a 100W mercury lamp equipped with a green filter centered on wavelength $\lambda = 0.546\mu m$. The light is divided into two

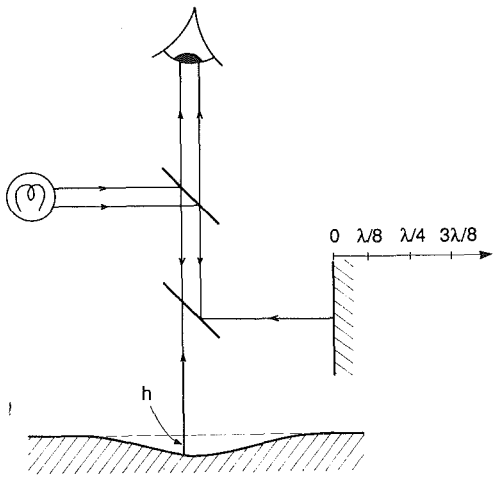

Fig. 1 Principle of the interference method

[1] And possibly of the degree of polish of the surface.

Contributed by the Fluids Engineering Division for publication in the JOURNAL OF FLUIDS ENGINEERING. Manuscript received by the Fluids Engineering Division September 24, 1990.

Fig. 2 Typical Interferogram (photograph)

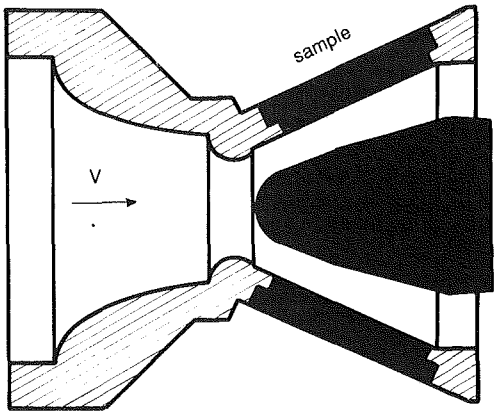

Fig. 3 Geometry of test sections

beams: a reference beam reflected by the mirror of the interferential objective and a second beam reflected by the deformed surface of the eroded sample.

At each point (x,y) of the observed surface, the light intensity I which results from the interference is given by:

$$I(x,y) = I_0 \left(1 + \gamma \cos 2\pi \frac{\delta(x,y)}{\lambda}\right) \quad (1)$$

where I_0 is the incident intensity, γ the fringe contrast, and δ the length difference between the two beams which depends upon pit depth h at location (x,y). In order to determine δ and consequently h and to get rid of constants I_0 and γ, the method developed by Tribillon consists in considering four different interferograms. They are obtained by successive translations of $\lambda/8$ of the reference mirror as shown on Fig. 1.

The four corresponding beam length differences and intensities are given by:

$$\delta_1 = -2h \qquad I_1 = I_0 \left(1 + \gamma \cos \frac{4\pi h}{\lambda}\right)$$

$$\delta_2 = \frac{\lambda}{4} - 2h \qquad I_2 = I_0 \left(1 + \gamma \sin \frac{4\pi h}{\lambda}\right)$$

$$\delta_3 = \frac{\lambda}{2} - 2h \qquad I_3 = I_0 \left(1 - \gamma \cos \frac{4\pi h}{\lambda}\right)$$

$$\delta_4 = \frac{3\lambda}{4} - 2h \qquad I_4 = I_0 \left(1 - \gamma \sin \frac{4\pi h}{\lambda}\right),$$

and from these formula, it can easily be shown that:

$$\frac{h}{\lambda/2} = \frac{1}{2\pi} \operatorname{Arctg} \frac{I_2 - I_4}{I_1 - I_3} \quad (2)$$

This expression proves that, at any point (x,y), the local depth h can be deduced from the four interferograms. Then it is possible to reconstruct the whole surface $h(x,y)$ of the sample under observation. In practice, the four interferograms are obtained by the displacement of the interferential objective by means of a piezoelectric transducer. The acquisition is made by a CCD camera and images of size 512×512 are stored and processed on a microcomputer. Three different magnifications have been used: $\times 10$, $\times 20$ and $\times 40$. With magnification $\times 40$, the size of the observed field is 0.142mm $\times$ 0.201mm.

From Eq. (1), it can be seen that the difference of altitude between two consecutive black fringes is $\lambda/2$. If grey levels are digitized on 8 bits, depth accuracy is of the order of only $\lambda/512$. Thus, the method is very sensitive to small differences in depth.

This high accuracy in depth is at the origin of a difficulty. If the local slope of a pit is too large, the CCD camera may not be able to distinguish two consecutive fringes. This leads to a loss of determination of function Arctg in Eq. (2) and then to the indefiniteness of pit depth. The limitation depends on magnification which determines space resolution. For magnification $\times 40$, the limit slope is approximately 34 deg whereas it is only 10 deg for magnification $\times 10$.

This problem can be limited by increasing computational tests to try to follow the determination of function Arctg. In a few cases, this difficulty is only partially overcome and computed surfaces present depth discontinuities. It is often the case for pits obtained with mercury as their depth is generally an order of magnitude greater than for water (see section 7).

As pits are generally circular, it is enough to restrict shape computation to a unique section going through its center. This procedure allows to reduce considerably computational times, what is essential when the method is implemented on a microcomputer. In the present work, pit diameter D is determined from a unique cross-section chosen visually. It is defined at 10 percent of pit depth.[2] The total surface which is analyzed is such that the number of pits lies between 150 and 200. Such a number proved to be enough to make relevant statistics and not too large to allow a rapid enough analysis. Several images close together are successively treated. Their number vary between 20 and 250 according to degree of erosion.

3 Characteristics of Eroded Samples

The samples which are analyzed in the present study were eroded on geometrically similar flows (Lecoffre et al., 1985). The basic geometry is a venturi shown in Fig. 3 with a central body. Cavitation appears in the form of a small cavity attached to the throat. It sheds vapour structures which collapse downstream and cause cavitation erosion. Samples are flush mounted on the diverging part. The table below presents the main test conditions.

[2]This choice is not purely conventional, as explained in section 4.

Nomenclature

D = pit diameter
h = pit depth
I = light intensity
V = flow velocity
δ = length difference between the two beams
λ = light wavelength
σ = cavitation parameter

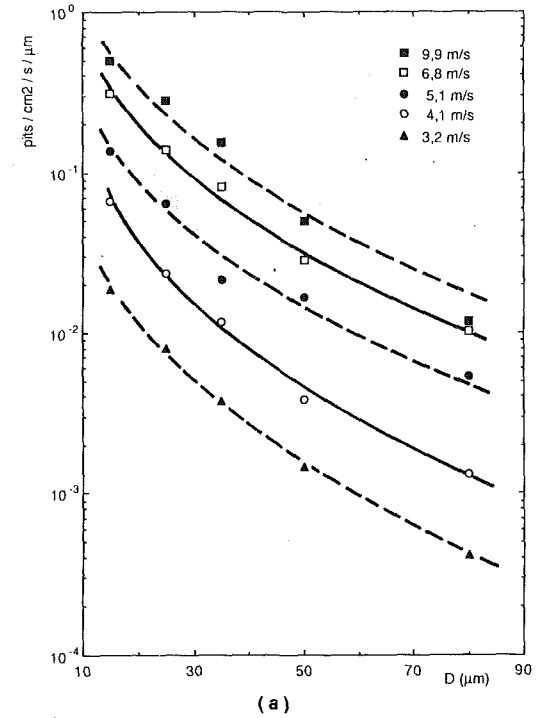

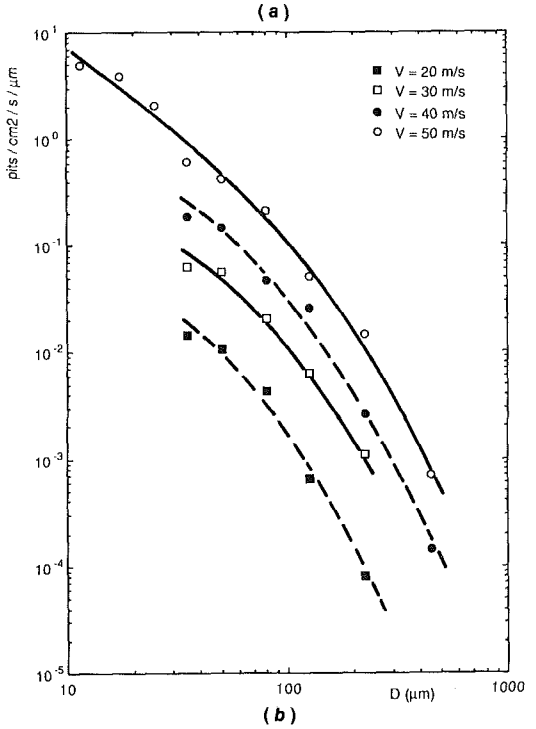

series N°	throat diameter (mm)	liquid	velocity (m/s)
1	Φ 40	mercury	1.9 to 9.9
2	Φ 40	water	20 to 57
3	Φ 120	water	20 to 57

Cavitation parameter (σ) defined by the ratio of downstream to upstream pressure was kept constant, which ensures a similar development of cavitation.

The tested material is stainless steel 316L. A few tests were carried out with aluminum for cavitation in water. In spite of a very short exposure to cavitation of the order of one minute, the surface was so much eroded that the present method, particularly suitable to isolated pits, could not be applied.

4 Histograms of Pit Diameter

Typical histograms of pit diameter are shown in Fig. 4. The

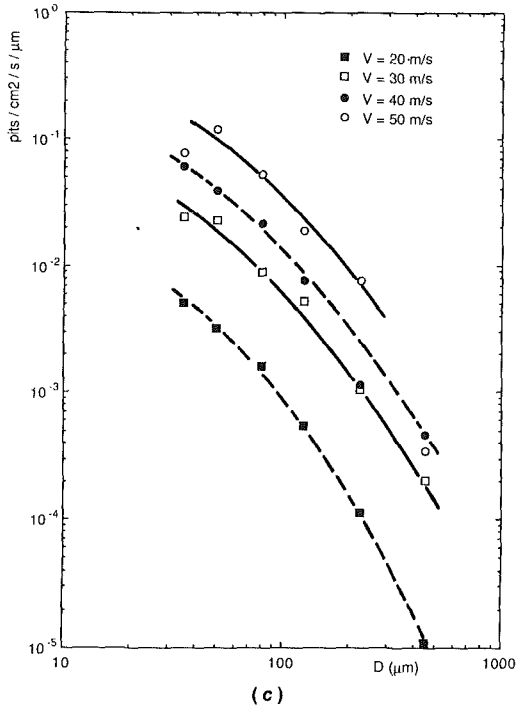

Fig. 4 *(a)* **Histogram of pit diameter—series No. 1**
(b) **Histogram of pit diameter—series No. 2**
(c) **Histogram of pit diameter—series No. 3**

ordinate is measured in pits/cm^2/s/μm; the μm dependency appears after dividing pitting rate in pits/cm^2/s by pit size bandwidth. Another type of representation named cumulative histogram is also used (Fig. 5 for instance); in that case the ordinate is measured in pits/cm^2/s and represents the density of pits of diameter greater than a given size plotted in abscissa.

Figure 4 shows, in all cases, that the smaller pits, the higher pitting rates. Contrary to Kato (1989), our histograms do not have a maximum for a given pit size.

For each series, histograms at different velocities have similar shapes. They can easily be superposed if a constant multiplying coefficient is applied to pitting rates. This is shown in Fig. 5 which presents reduced histograms. The coefficient depends only upon velocities and can be considered as independent of pit diameter.

In Fig. 5(*a*) we also plotted the total pitting rate corresponding to the limit $D = 0$ for the mercury tests. Total pit densities were obtained previously with a different counting technique (Lecoffre et al., 1985). The coefficients which were used to get the superposition of histograms in the range of diameter 10μm–90μm appear still valid for total pitting rates though they were determined by a quite different method. The present method allows to measure pits down to 10μm in diameter. The upper limit is given by the size of the image; it is of the order of a few hundreds of μm.

It is possible to measure pits smaller than 10μm; but, the smaller pits, the greater number we may overlook. This tends to make pitting rates decrease artificially for small diameters. In setting the cut-off size at 10μm, we are sure to have, for all diameters, a good determination of pit density.

To determine histograms in the whole range of diameter 10μm–500μm, it is necessary to use two different magnification rates. Magnification $\times 40$ allows to measure pits of diameter between 10μm and 100μm whereas magnification $\times 10$ is suitable to pits between 40μm and 500μm. Figure 6 shows the good comparison between histograms measured with different magnification rates. It was absolutely necessary to check this point in the case of mercury.

In contrast to the water case, the problem of slope limit often arises in mercury, preventing an exact determination of

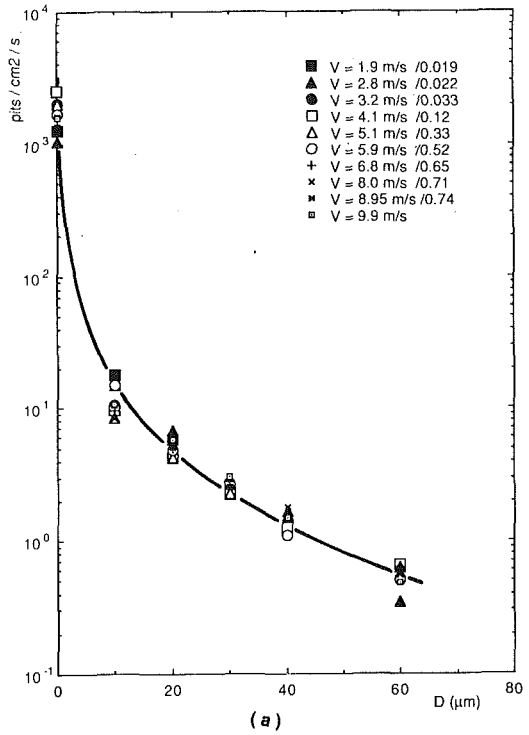

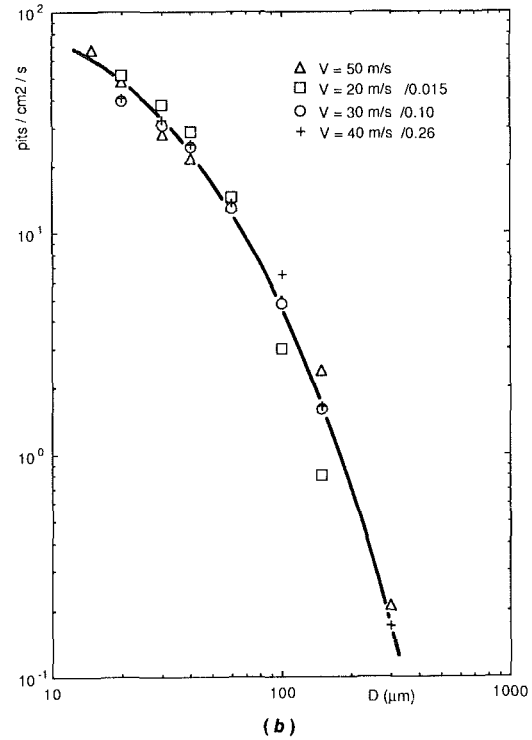

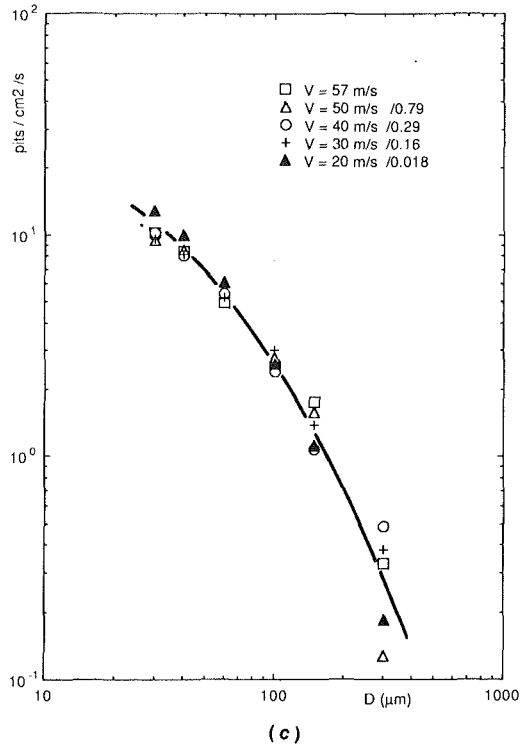

Fig. 5 (*a*) Cumulative reduced histograms—series No. 1 (*b*) Cumulative reduced histograms—series No. 2 (*c*) Cumulative reduced histograms—series No. 3

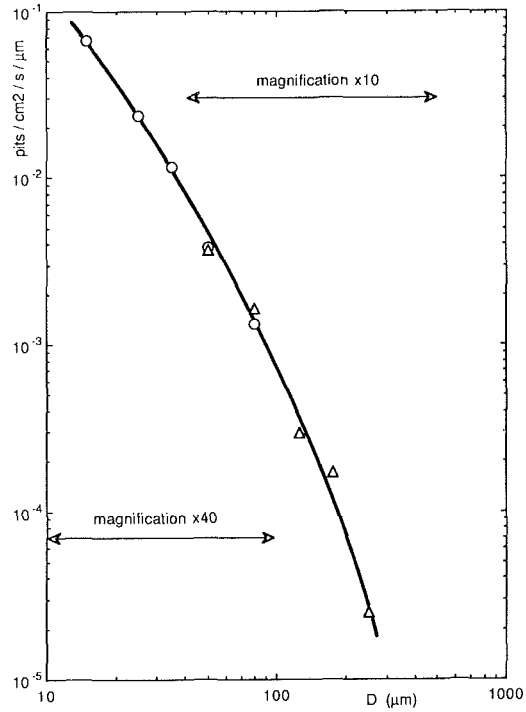

Fig. 6 Histograms measured with different magnifications—series No. 1—*V* = 4.1 m/s

pit depth. The calculated pit profile is regular and can be considered as exact in its outer part where the shape is weak, but becomes discontinuous and so unreliable in its inner part. The frontier between the two domains depends upon the slope limit which increases with magnification (see section 2). The estimated value of pit depth is generally wrong and paradoxically tends to increase with magnification.[3] This difficulty could alter the determination of pit size as pit diameter is defined at a given fraction (k) of pit depth.[4] In fact, the correct junction between histograms in Fig. 6 proves that, even if pit depth remains undetermined in mercury, estimations of pit diameter can be considered as reliable.

To obtain a good estimate of pit size, on the one hand, the value of k has to be low enough to be sure that pit diameter is calculated in the outer region where pit shape is correctly determined. On the other hand, it has to be large enough so that pit diameter is determined in a region of sufficiently high

[3]Even with the greatest magnification ×40 available, pit depth is underestimated in most cases for mercury.

[4]Here $k = 10$ percent.

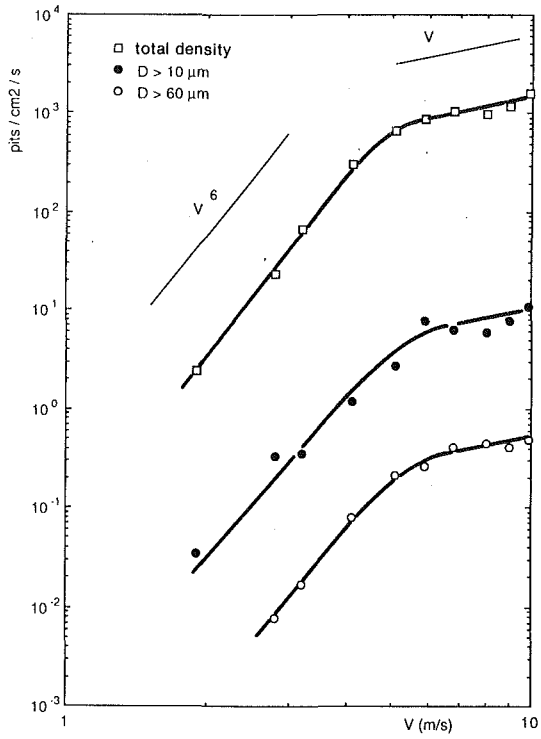

Fig. 7 Influence of velocity on pitting rates for different cut-off diameters—series No. 1

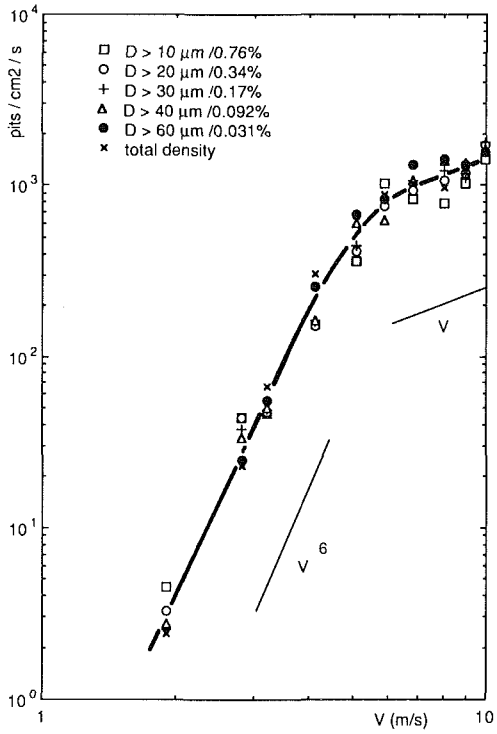

Fig. 8 Reduced pitting rates for different cut-off diameter—influence of velocity—series No. 1

slope where an error in depth generates a low enough error in diameter. In practice, the value $k = 10$ percent gives a good compromise.

5 Influence of Flow Velocity

In the present section, we examine the dependence of pitting rate with flow velocity. It is generally assumed that pitting rate increases as a high power V^n of the velocity which is of the order of 6 (see for instance Stinebring et al., 1980). This trend is valid in a limited range of velocity and the exponent (n) should tend to 1 at high enough velocity. It is the phenomenon of "saturation" presented below and discussed in more details by Lecoffre et al. (1985).

We do not want to discuss here in details the value of n. Our purpose is rather to know if the cut-off size has an influence on the velocity dependence and if partial pitting rates corresponding to limited ranges of pit have different behaviors with velocity or not.

Figure 7 presents the influence of velocity on pitting rates estimated for different cut-off sizes in the case of mercury erosion tests. It appears that the three curves have similar shapes and can be superposed by applying a constant multiplying coefficient independent of velocity (see Fig. 8). The same conclusion also applies to the two other series in water at two different length scales.[5] We now can conclude that a change in velocity affects equally all sizes. Density of small pits or large ones increases with velocity according to the same law.

The phenomenon of saturation in mercury at high enough velocity which was discussed elsewhere (Lecoffre et al., 1985) and which was initially established for total pitting rate appears valid independently for any size. If we consider only pits of a given size, their density increases proportionally to the flow velocity above a threshold of about 5m/s and this behavior applies to any size. Note that saturation was not seen for the data in water up to 57 m/s which is in agreement with the similarity laws developed by Lecoffre et al. (1985).

If we define $n_V(D)$ as the density of pits whose diameter is greater than D at velocity V, we can express mathematically the preceding results by the complete separation of variables D and V. In addition, if the influence on pitting rate of the velocity is known for a given reference size D_o, the histogram $n_V(D)$ at any velocity V can easily be deduced from a reference histogram $n_{V_0}(D)$ obtained for a given reference velocity V_o from the following equation:

$$n_V(D) = \frac{n_V(D_0)}{n_{V_0}(D_0)}\, n_{V_0}(D) \tag{3}$$

This point introduces a significant simplification for the determination of a family of histograms $n_V(D)$ corresponding to different velocities. This result is applied in this paper for cumulative histograms but also applies to spectra.

6 Eroded Surface

Histograms in size show a very rapid increase of pitting rate when pit size decreases. However, we can expect that small impacts cause smaller damage than larger ones, at least if damage is measured from eroded surfaces as it is the case in the present section. Then, the question is to compare the contributions of all sizes to total erosion and in particular to know if small pits which are very numerous contribute significantly or not to cavitation erosion.

Figure 9 presents, for the case of mercury, the eroded surface per class of diameter. All curves corresponding to different velocities show a maximum for a given pit size of the order of 30μm. This characteristic size is independent of flow velocity, which comes out of the existence of reduced histograms. The existence of this maximum means, on the one hand, that large pits are not numerous enough to erode the surface significantly, whereas, on the other hand, small pits concern a negligible surface although their density is very high.

In the case of water, similar results were obtained. For a throat diameter of 40mm (series 2), the characteristic diameter

[5]Corresponding diagrams are not presented here.

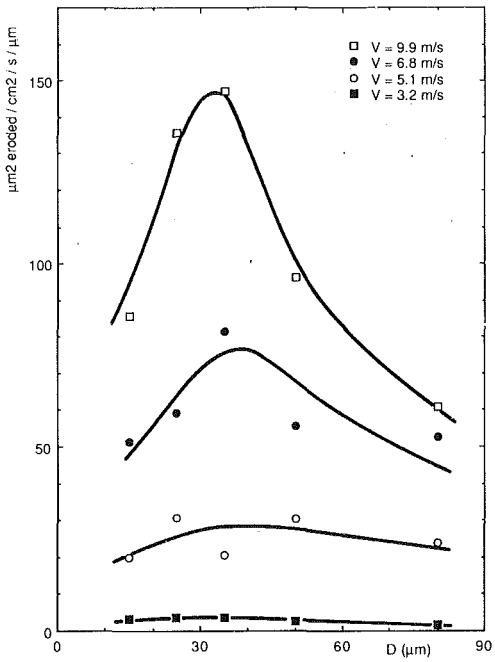

Fig. 9 Eroded surface per class of diameter—series No. 1

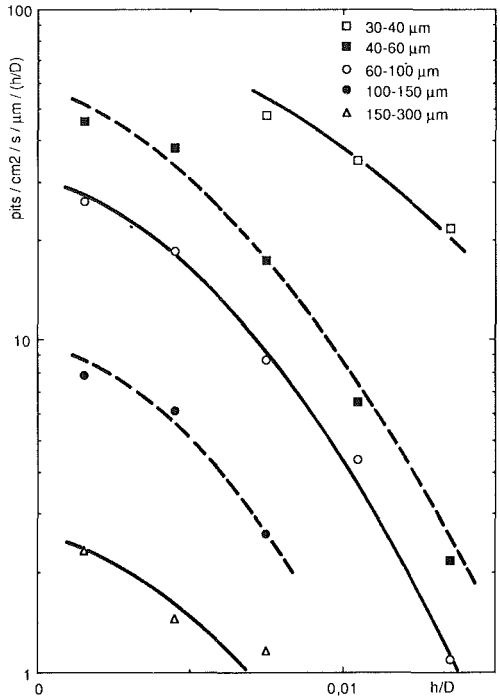

Fig. 10 Histograms of relative pit depth for various classes in diameter—series No. 2—V = 57 m/s

for which the eroded surface is maximum is of the order of 70μm. For a throat diameter of 120mm, this characteristic size is increased, but less than the global length scale; it is of the order of 100μm.

The estimation of the total eroded surface obtained in taking into account all sizes allows to determine the fraction of surface eroded per unit time of exposure. It gives a global estimate of the probability of overlapping of impacts according to the time of exposure. For example, from erosion tests of series 2 in water, and in considering all pits in the range 30μm-600μm, the ratio of the eroded surface to the exposed surface is 7.2 percent at 20m/s and 650 percent at 57m/s, per hour of exposure.

7 Pit Depth and Pit Volume

Pits are generally not very deep. Their reduced depth h/D is, in the case of water, generally smaller than 1 percent. It means that a pit of 0.1mm in diameter is less than 1μm deep. We could not determine pit depth owing to the problem of slope which was previously discussed for the case of mercury. However, we can roughly estimate that pits due to cavitation in mercury are deeper than for water. A value of reduced depth of a few percents seems most likely.

As a first approach, we calculated the mean values and rms values of reduced depth h/D for water. We did not notice any regular variation of reduced depth with pit diameter. On an average, large pits are not proportionally deeper than small ones; we can consider that mean shapes are similar. Yet, if we consider all pits of a given diameter, a great scattering in depth is observed. It shows that, even if pits can be statistically characterized by a mean shape independent of their size, there is a large variety of shapes around it.

The only systematic variation which could be pointed out is relative to flow velocity. In considering all pits of size between 30μm and 600μm, we obtained the following results:

	$V(m/s)$	20	30	40	50	57
h/D	series 2	0.26	0.35	0.33	0.42	0.51
(%)	series 3	0.32	0.38	0.37	0.43	0.50

The general trend is an increase of relative pit depth with velocity. Between 20m/s and 57m/s, h/D is multiplied by a coefficient of about 1.5 or 2.

As a second approach, we tried to introduce two-dimensional histograms, one dimension being pit size and the other dimension being pit depth. A typical two-dimensional histogram is given in Fig. 10. For all sizes, histograms of relative pit depth show the same trend. There is a continuously increasing number of pits which correspond to weaker and weaker deformations of the surface. This implies that there is no mean depth for pits of a given size. Mean values which were presented above are simply relative to a statistics on all pits which were taken into account i.e., which depth is greater than approximately $\lambda/4 \cong 0.1\mu$m.

The problem of the cut-off depth appears to be very similar to the one of the cut-off size discussed previously. Undoubtedly, two-dimensional histograms give a better description of cavitation damage, but the introduction of a second dimension brings new difficulties. In the case of water for which pit depth could be measured, it was also possible to determine pit volumes. They were calculated by rotating the pit profile and calculating the generated volume.

In the same way as we discussed the contribution of all sizes to the total eroded surface, we can easily estimate the contribution of all sizes to the "eroded volume." By eroded volume, we mean the cumulative volume of pits. As pits are only permanent deformations without material removal, such a data is not representative of mass loss.

Figure 11 presents, in the cases of erosion tests of series 2 in water, the distribution of eroded volumes with pit size. Results are quite similar to the ones obtained for eroded surfaces. In particular, there is a characteristic size for which the eroded volume shows a maximum. Larger pits give a smaller contribution due to their small density whereas smaller ones, although they are very numerous, have also a contribution of minor importance. The characteristic size for which the eroded volume is maximum is slightly greater than the one for which the eroded surface is maximum. For series 2 and 3, it is, respectively, of about 100μm and 200μm.

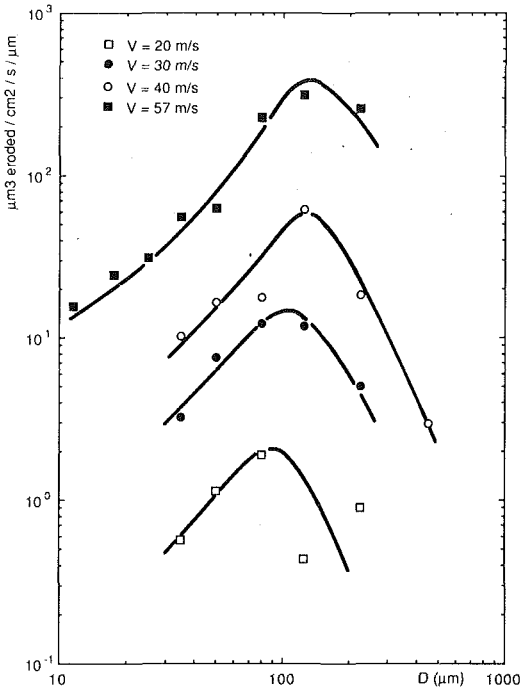

Fig. 11 Eroded volume per class of diameter—series No. 2

8 Uncertainty Estimates

For histograms (Figs. 4, 5, 6, 9, 10, 11) the uncertainties on abscissae D or h/D can be considered as negligible. Same conclusion for the abscissae of Figs. 7 and 8 which correspond to the velocity in the testing facility and which is known with a very good accuracy.

Uncertainty on pitting rates is estimated to ± 25 percent for $D \leq 200\mu$m. Large pits are less numerous and errors of statistical nature are greater; for $D > 200\mu$m, the uncertainty on pitting rate is estimated to ± 40 percent. Such uncertainties may appear quite large but represent in fact only a small fraction of full scale as pitting rate extends over several decades.

9 Conclusion

This paper presents an analysis of histograms in size of erosion pits. An interferometric method originally developed by Pierali and Tribillon (1987) was adapted to cavitation erosion in order to measure pit size. It is particularly suitable for pits of diameter in the range 10μm-500μm. Conclusions of this paper were focused on general properties of histograms. They were established for three conditions of erosion with two different fluids (mercury and water) on two similar test sections of different length scale. The following summarizes the important conclusions:

1. Histograms in size corresponding to different flow velocities can be reduced to a unique histogram by means of a multiplicative factor on pitting rates which is independent of diameter and depends only of flow velocity. Histograms have similar shapes whatever the flow velocity may be, i.e., pits are distributed among the different sizes in a similar way independent of flow velocity.

2. The influence of velocity on pitting rate is the same whatever the considered size may be. In particular, its influence is the same as for total pitting rate. In the case of erosion with mercury, it is shown that saturation, which was initially pointed out at high enough velocity for total pitting rate, applies individually to partial densities of pits of any given size.

3. Concerning eroded surface, all analyses have pointed out a characteristic size for which the contribution to the eroded surface is maximum. Smaller pits, although they are more numerous, have a minor contribution whereas larger ones have also a minor contribution but because of their small number. For stainless steel, this characteristic size is of the order of:

30μm for erosion in mercury on a venturi of 40mm in throat diameter

70μm for erosion in water on the same venturi of 40mm in throat diameter

100μm for erosion in water on the same venturi of 120mm in throat diameter.

4. Reduced pit depth h/D tends to increase with flow velocity. No correlation of pit depth with diameter was observed. On an average, pits have similar shapes, although there is a large scattering in shapes.

5. Eroded volumes as eroded surfaces present a maximum for a given pit size slightly greater than the one for eroded surfaces.

Further work, requiring complementary tests, is in progress to interpret such histograms in terms of scaling laws for cavitation erosion.

Acknowledgment

This research was supported by "Electricité de France" and C.E.R.G.

References

Kato, H., 1975, "A Consideration on Scaling Laws of Cavitation Erosion," *International Shipbuilding Progress*, Vol. 22, No. 253, pp. 305-327.

Kato, H., Ye, Y. P., and Maeda, M., 1989, "Cavitation Erosion and Noise Study on a Foil Section," *ASME Intern. Symp. on Cavitation Noise and Erosion in Fluid Systems*, San Francisco.

Lecoffre, Y., Marcoz, J., Franc, J. P., and Michel, J. M., 1985, "Tentative Procedure for Scaling Cavitation Damage," *ASME Intern. Symp. on Cavitation in Hydraulic Structure and Turbomachinery*, Albuquerque.

Pierali, C., 1989, "Traitement numérique d'interférogrammes et applications à la caractérisation tridimensionnelle des phénomènes d'érosion de cavitation," Thèse Université de Franche-Comté, Besançon.

Pierali, C., and Tribillon, G., 1987, "Traitement d'images 3D appliqué à la profilométrie optique pour l'étude du phénomène d'érosion de cavitation," *J. Optics* (Paris), Vol. 18, No. 1, pp. 9-18.

Stinebring, D. R., 1976, "Scaling of Cavitation Damage," MS thesis, The Pennsylvania State University.

Stinebring, D. R., Holl, J. W., and Arndt, R. E. A., 1980, "Two Aspects of Cavitation Damage in the Incubation Zone: Scaling by Energy Considerations and Leading Edge Damage," ASME JOURNAL OF FLUIDS ENGINEERING, Vol. 102, pp. 481-485.

Journal of Fluids Engineering

Technical Briefs

Local Anisotropy in Strained Turbulence at High Reynolds Numbers

P. A. Durbin[1] and C. G. Speziale[2]

It is shown that the hypothesis of local isotropy is implausible in the presence of significant mean rates of strain. In fact, it appears that in uniform shear flow near equilibrium, local isotropy can never constitute a systematic approximation, even in the limit of infinite Reynolds number. An estimate of the level of mean strain rate for which local isotropy is formally a good approximation is provided.

Introduction

It is frequently asserted that even in flows with significant mean rates of strain, the gradients of turbulent velocity are statistically isotropic if the Reynolds number is large (Tennekes and Lumley, 1972). This hypothesis of local isotropy has been debated for some time, but it has remained an *unproved* speculation. Experimental evidence gives grounds for suspicion: for instance, Townsend (1954), Uberoi (1957), and Marechal (1972) all found that when isotropic turbulence was subjected to homogeneous strain, the small scales became anisotropic; recent mixing layer experiments by Kuznetsov et al. (1990) provide evidence of local anisotropy at extremely high Reynolds numbers. Townsend concluded that the anisotropy was due to a *direct* effect of the mean strain on the small scale eddies. Anisotropy of passive scalar fluctuations in uniformly sheared turbulence was observed by Tavoularis and Corrsin (1981) and by Sreenivasan and Tavoularis (1980). In fact Sreenivasan (1991) recently argued that existing experiments suggest that local isotropy is not a natural property of scalars in shear flows, except perhaps at enormously high Reynolds numbers that are of no practical relevance. Numerical simulations, albeit at very low Reynolds numbers, also show rather large departures from local isotropy (Lee and Reynolds, 1985).

A criticism of some of these experiments is that the Reynolds numbers were too low for the spectral peaks of energy and dissipation to be well separated, this separation being necessary for the energy cascade to scramble the turbulence. Although one might expect that the anisotropy of the large scales would be reflected in the small scales unless a significant spectral separation of scales existed, the existence of a spectral gap does not rule out a direct effect of mean strain on the small scales. Indeed, Townsend inferred such a direct effect in his experiments. The observations which led to his inference were that when turbulence was strained the small scales became anisotropic, and that when the strain was released the small scales relaxed rapidly to isotropy even though the large scales remained anisotropic. Hence, sufficient nonlinear scrambling existed to prevent the large scale statistical structure from being imposed upon the small scales after removal of the strain. It might further be presumed that during the straining the large scales did not mediate the straining; it was felt directly at the small scales.

The reasoning that a large spectral separation implies independence of large and small scales was questioned on theoretical grounds by Brasseur (1990). In that case it was the existence of nonlocal interactions in wave number space which led Brasseur to question the traditional rationale for local isotropy. Here we will not work in spectral space, so there is no immediate connection between the present analysis and that of Brasseur.

It is sometimes argued that because the self-straining of small eddies is large compared to mean straining (their ratio is $O(v_\eta/\eta S) = O(\mathrm{Re}^{1/2})$ where η is the Kolmogoroff length scale, v_η is the Kolmogoroff velocity scale, S is the magnitude of mean strain and Re is the integral scale Reynolds number) the small scales should be uninfluenced by mean strain rates (Tennekes and Lumley, 1972). This reasoning does not recognize that the observed anisotropy can be due to a *relatively* small, but coherent bias superimposed upon the small-scale randomness.

In the present case, the dissipation rate tensor ($\epsilon_{ij} = 2\nu\overline{\partial_k u_i \partial_k u_j}$ with summation on repeated indices) is the small-scale statistic to be considered. An examination of the transport equation for ϵ_{ij} will show the direct effect of mean strain. This, not the experimental evidence, is the basis for the present suspicion that local isotropy is an implausible hypothesis. The dissipation rate tensor is of present interest because of its role in Reynolds stress dynamics and in second moment closure modelling.

Analysis

An evolution equation for ϵ_{ij} is obtained by differentiating the j-component of the fluctuating Navier-Stokes equations with respect to x_k, multiplying by $2\nu\partial_k u_i$, averaging, and then adding the result to itself with i and j transposed. For simplicity, attention is restricted to the case of incompressible, homogeneous turbulence, for which spatial derivatives of all turbulence statistics are zero. The transport equation for ϵ_{ij} can then be written as

$$\dot{\epsilon}_{ij} = -2\nu\overline{(\partial_i u_j + \partial_j u_i)\nabla^2 p} - \overline{\epsilon'_{ik}\partial_k u_j} - \overline{\epsilon'_{jk}\partial_k u_i} - 4\nu^2\overline{\partial^2_{km} u_i \partial^2_{km} u_j} - \epsilon_{ik}\partial_k U_j - \epsilon_{jk}\partial_k U_i - 2d_{klij}\partial_k U_l \quad (1)$$

where: u_i denotes the fluctuating velocity and U_i its mean; $\epsilon'_{ij} = 2\nu\partial_k u_i \partial_k u_j$ is the fluctuating dissipation tensor, $\epsilon_{ij} = \overline{\epsilon'_{ij}}$ is its mean; and

$$d_{ijkl} = 2\nu\overline{\partial_i u_k \partial_j u_l}. \quad (2)$$

We have used the fact that $d_{ijkl} = d_{jikl}$ in homogeneous turbulence. If the Poisson equation $\nabla^2 p = -\partial_k u_l \partial_l u_k - 2\partial_k u_l \partial_l U_k$ is

[1]Center for Turbulence Research, Stanford University, Stanford, CA 94035-3030.

[2]Institute for Computer Applications in Science and Engineering, NASA Langley Research Center, Hampton, VA 23665-5225.

Contributed by the Fluids Engineering Division of THE AMERICAN SOCIETY OF MECHANICAL ENGINEERS. Manuscript received by the Fluids Engineering Division February 8, 1991.

used to eliminate the pressure from (1),then

$$\dot{\epsilon}_{ij} = N_{ij} + 2(d_{ikjl} + d_{jkil})\partial_l U_k - \epsilon_{ik}\partial_k U_j - \epsilon_{jk}\partial_k U_i - 2d_{klij}\partial_k U_l \quad (3)$$

where

$$N_{ij} \equiv 2\nu\overline{(\partial_i u_j + \partial_j u_i)\partial_k u_l \partial_l u_k} - \overline{\epsilon'_{ik}\partial_k u_j} - \overline{\epsilon'_{jk}\partial_k u_i} - 4\nu^2\overline{\partial^2_{km}u_i\partial^2_{km}u_j} \quad (4)$$

contains the nonlinear and dissipative terms. Equation (3) is in a form which contains only derivatives of velocities.

Scale analysis shows (Tennekes and Lumley, 1972) that the individual terms in N_{ij} are $O(Re^{1/2})$ larger than the other terms in (3). If (3) is to be an equality, then these $O(Re^{1/2})$ terms must sum to zero and the combination of terms in (4) must make N_{ij} be comparable in magnitude to the other terms of (3). Only this combination of terms is relevant to the isotropy of ϵ_{ij}.

If the small scales are to be isotropic, then tensors composed by averaging products of gradients of the fluctuating velocity must have isotropic forms. Thus

$$\epsilon_{ij} = \frac{2}{3}\epsilon\delta_{ij}; \quad N_{ij} = \frac{2}{3}N\delta_{ij};$$

$$d_{ijkl} = \frac{4}{15}\epsilon\delta_{ij}\delta_{kl} - \frac{1}{15}\epsilon(\delta_{ik}\delta_{jl} + \delta_{jk}\delta_{il}) \quad (5)$$

in which $\epsilon_{ii} = 2\epsilon$ is twice the rate of kinetic energy dissipation, $N_{ii} = 2N$, and the identity $d_{kkij} = \epsilon_{ij}$ has been used. On substituting (5) into (3) one finds

$$\frac{2}{3}\dot{\epsilon}\delta_{ij} = \frac{2}{3}N\delta_{ij} - \frac{4}{15}\epsilon S_{ij} \quad (6)$$

where $S_{ij} = 1/2(\partial_i U_j + \partial_j U_i)$ is the mean rate of strain. Incompressibility requires that $S_{ii} = 0$. The contraction of (6) is

$$\dot{\epsilon} = N. \quad (7)$$

Hence (6) can only be satisfied if $S_{ij} \equiv 0$; conversely, local isotropy is formally inconsistent with the Navier-Stokes equations if $S_{ij} \neq 0$.

Discussion

In order to save the hypothesis that ϵ_{ij} is isotropic, one might be tempted to relax the constraint (5) that requires N_{ij} to be isotropic. To make ϵ_{ij} isotropic it would have to be assumed that N_{ij} has an anisotropic part exactly equal to $4/15\ \epsilon S_{ij}$:

$$N_{ij} - \frac{2}{3}N\delta_{ij} = \frac{4}{15}\epsilon S_{ij}. \quad (8)$$

If the equation for N_{ij} were written, it would be found that for N_{ij} to have exactly this anisotropy, a further condition must be satisfied, and so on ad infinitum. This is far more stringent than the original hypothesis of local isotropy, and we see no reason why the Navier-Stokes equations should enforce such conditions; since N_{ij} and ϵ_{ij} are of the same order in Reynolds number, there is no asymptotic rationale for asserting that N_{ij} should absorb all the anisotropy produced by mean straining. Indeed, we believe that (8) is inconsistent with the reasoning behind the assumption of local isotropy—the heuristic argument for local isotropy is that at high Reynolds numbers the nonlinear energy cascade makes small scales of fluid motion statistically independent of large scale and mean motions. To have a small scale correlation like N_{ij} depend directly and explicitly on S_{ij} is fundamentally inconsistent with this reasoning. Thus, to maintain the original hypothesis one must introduce contradictory lines of heuristic reasoning. This seems a convincing reason for dismissing (8); hence, while Eq. (6) is not a rigorous disproof of local isotropy, it does make the hypothesis rather implausible.

Under what conditions might local isotropy be a formally justifiable approximation? From Eq. (6), it is clear that local isotropy will not be a systematic approximation unless

$$N \gg \epsilon S^* \quad (9)$$

where $S^* = \|S_{ij}\|$ is a suitable norm. Estimation of the magnitude of N is a bit subtle, since it represents the net imbalance between vortex stretching and diffusion. The conventional estimate is (Reynolds, 1987)

$$N = O(\epsilon^2/k) \quad (10)$$

where k is the turbulent kinetic energy. The decay of ϵ is usually modeled by (10) after replacing the order of magnitude symbol by a constant of proportionality equal to about 2. It follows from (9) and (10) that

$$\frac{S^* k}{\epsilon} \ll 1 \quad (11)$$

is a necessary condition for local isotropy to constitute a formally justified approximation.

Another way to try and save local isotropy as a lowest order approximation would be to insist that N be $O(\epsilon/\tau_\eta)$ where τ_η is the Kolmogoroff time-scale. Then the mean rate of strain term in (6) would be $O(S^*\tau_\eta) = O(Re^{-1/2})$ smaller than the nonlinear term. But this scaling conflicts with incontrovertable evidence: in decaying grid turbulence $\epsilon \propto (t/\tau)^{-n}$ where τ is the integral time-scale (which has been estimated as k/ϵ in (11)) and $n \approx 2$. If N were $O(\epsilon/\tau_\eta)$ then n would have to be of order $Re^{1/2}$, which it certainly is not.

It will be shown that for certain basic shear flows, (11) is not satisfied and, hence that local isotropy is a questionable approximation—even in the limit of infinite Reynolds number. Homogeneous shear flow (where $S^* = 1/2\ S$, with S defined as the shear rate) is a basic turbulent flow that has been studied extensively by physical and numerical experiments (Tavoularis and Corrsin, 1981; Tavoularis and Karnik, 1989; Rogers et al., 1986). Experiments, numerical simulations and closure models indicate that in this flow k and ϵ grow exponentially in time, at the same rate. Therefore, at large times Sk/ϵ achieves an equilibrium value which is independent of both the shear rate S and the initial conditions. Physical and numerical experiments reach an equilibrium value of

$$\frac{Sk}{\epsilon} \approx 6 \quad (12)$$

which clearly is not consistent with (11). This seems to explain why the experiments of Tavoularis and Karnik (1989), which were at appreciable Reynolds numbers, yielded strongly anisotropic values for the turbulent dissipation rate. Since k and ϵ grow at the same exponential rate, so does the turbulence Reynolds number ($R_t = k^2/\epsilon\nu$). Hence (12) is the equilibrium value for homogeneous shear flow in the limit as $R_t \to \infty$—a state of affairs that precludes local isotropy from being a formally justifiable approximation. Even higher dimensionless shear rates can exist in wall bounded shear flows; Lee et al. (1990) found that Sk/ϵ can reach values larger than 16 near the walls of turbulent channel flow.

The approximate value in (12) was obtained from experiments for which R_t was not extremely high. However, in homogeneous shear flow Sk/ϵ can be written alternatively as

$$\frac{Sk}{\epsilon} = -\frac{1}{2b_{12}}\frac{\mathcal{P}}{\epsilon} \quad (13)$$

where $\mathcal{P} = -\overline{u_1 u_2}S$ is the turbulence production and $b_{12} = \overline{u_1 u_2}/2k$ is the shear component of the anisotropy tensor. The Schwartz inequality requires that $|b_{12}| \leq 1/2$. Furthermore, $\mathcal{P}/\epsilon \geq 1$ for an equilibrium shear flow; hence,

$$\frac{Sk}{\epsilon} \geq 1. \quad (14)$$

Thus it would appear that under no circumstance can local

isotropy represent a systematic approximation in homogeneous shear flow near equilibrium.

While the analysis presented here was carried out strictly for the case of homogeneous turbulence, it should carry over in an approximate sense to weakly inhomogeneous flows. The turbulence in the log region of a boundary layer is an example. Physical experiments at high Reynolds numbers (Rodi, 1982), as well as direct numerical simulations done at lower Reynolds numbers (Mansour et al., 1988), indicate that Sk/ϵ is in the range of 3 to 4 for $50 < y^+ < 100$ (were $y^+ = yu_*/\nu$ is the usual wall layer coordinate). This is not consistent with constraint (11); consequently, the commonly made assumption of local isotropy in the log layer of a high Reynolds number turbulent boundary layer appears to be questionable. The present considerations do not allow one to estimate the degree to which the small-scales are anisotropic, they only determine a condition when local isotropy is not a formally justified high Reynolds number approximation. However, some evidence exists that the dissipation tensor may be anisotropic in the log layer (Mansour et al., 1988).

Care must be taken in elevating a convenient hypothesis to a universally accepted principle. It was shown here that local isotropy is not a formally justifiable hypothesis if the nondimensional mean rate of strain (S^*k/ϵ) is not small: this is due to the direct influence of mean rate of strain upon the evolution of ϵ_{ij}. We have noted that this constraint on the rate of strain is not satisfied in many commonly encountered turbulent flows, for which local isotropy is often invoked in turbulence modeling studies. Future models should account for potentially significant anisotropies in the dissipation rate tensor.

Acknowledgments

We are grateful to Drs. R. Rogallo and M. J. Lee for discussing the subject of this paper with us. CGS acknowledges the support of the National Aeronautics and Space Administration under NASA contract No. NAS1-18605 while in residence at ICASE. Support provided by the CTR under its visitors program is also gratefully acknowledged by CGS.

References

Brasseur, J. G., 1991, "Comments on the Kolmogorov Hypothesis of Isotropy in the Small Scales," AIAA paper 91-0230.

Kuznetsov, V. R., Karyakin, M. Yu., and Praskovsky, A. A., 1990, "Anisotropy of Turbulence Fine-Scale Structure in High Reynolds Number Flows," Third European Turbulence Conference, Stokholm, Sweden.

Lee, M. J., and Reynolds, W. C., 1985, "Numerical Experiments on the Structure of Homogeneous Turbulence," *Turbulent Shear Flows*, Vol. 5, Springer-Verlag, New York, pp. 54–66.

Lee, M. J., Kim, J., and Moin, P, 1990, "Structure of Turbulence at High Shear Rate," *J. Fluid Mech.*, Vol. 216, pp. 561–583.

Mansour, N. N., Kim, J., and Moin, P., 1988, "Reynolds-stress and Dissipation Budgets in a Turbulent Channel Flow," *J. Fluid Mech.*, Vol. 194, pp. 15–44.

Maréchal, J., 1972, "Étude Expérimentale de la Déformation Plane d'une Turbulence Homogène," *J. de Mech.*, Vol. 11, pp. 263–294.

Reynolds, W. C., 1987, "Fundamentals of Turbulence for Turbulence Modeling and Simulation," in Lecture Notes for Von Kármán Institute, AGARD Lect. Ser. No. 86, pp. 1–66.

Rodi, W., 1982, "Examples of Turbulence Models for Incompressible Flows," *AIAA J.*, Vol. 20, pp. 872–879.

Rogers, M. M., Moin, P., and Reynolds, W. C., 1986, "The Structure and Modelling of the Hydrodynamic and Passive Scalar Fields in Homogeneous Turbulent Shear Flow," Stanford University Technical Report No. TF 19, Mechanical Engineering Department.

Sreenivasan, K. R., 1991, "On Local Isotropy of Passive Scalars in Turbulent Shear Flows," *Proc. Roy. Soc. London*, in press.

Sreenivasan, K. R., and Tavoularis, S., 1980, "On Skewness of Temperature Derivatives in Turbulent Flows," *J. Fluid Mech.*, Vol. 101, pp. 783–795.

Tavoularis, S., and Corrsin, S., 1981, "Experiments in Nearly Homogeneous Turbulent Shear Flow with a Uniform Mean Temperature Gradient," *J. Fluid Mech.*, Vol. 104, pp. 311–347.

Tavoularis, S., and Karnik, U., 1989, "Further Experiments on the Evolution of Turbulent Stresses and Scales in Uniformly Sheared Turbulence," *J. Fluid Mech.*, Vol. 204, pp. 457–478.

Tennekes, H., and Lumley, J. L., 1972, *A First Course in Turbulence*, MIT press, Cambridge, MA.

Townsend, A. A., 1954, "The Uniform Distortion of Homogeneous Turbulence," *Quart. J. Mech. Appl. Math.*, Vol. 7, pp. 104–127.

Uberoi, M. S., 1957, "Equipartition of Energy and Local Isotropy in Turbulent Flows," *J. Appl. Phys.*, Vol. 28, pp. 1165–1170.

Partial Acoustic Filtering Applied to the Equations of Compressible Flow

J. R. Torczynski[1]

Gas contained in a rectangular laser cell of large length and small width is subjected to large, transient, spatially nonuniform, volumetric heating when pumped. The heating time scale is much longer than the time required for an acoustic wave to traverse the width but can be comparable to the time required for an acoustic wave to traverse the length. Approximate equations describing the motion are derived by applying partial acoustic filtering to the equations of motion: pressure waves traversing the width are removed while pressure waves traversing the length are retained. For a simplified one-dimensional example, a significant density variation is found across the width of the laser cell; moreover, this density variation is in good agreement with a numerical solution of the unapproximated gas dynamic equations although the latter requires two orders of magnitude more computational time.

Nomenclature

A = heating amplitude scale
a = sound speed
L_x, L_z = domain extents in x, z
M_x, M_z = x and z Mach number scales
p = pressure
Q = volumetric heating
t = time
u, w = velocity x and z components
Δt = time step
$\Delta x, \Delta z$ = x and z grid spacings
γ = specific heat ratio
ρ = density
Υ = dissipation function
$\tilde{f}$ = nondimensional f
$\bar{f}$ = x-averaged f
$\hat{f}$ = difference $f - \bar{f}$
f_m = maximum of $|f|$
f_0 = initial or scale f

Introduction

The motion of gas in a laser cell is considered. Whereas many common lasers operate at low or near-vacuum pressures, the initial gas conditions considered herein are near room temperature and near or above atmospheric pressure, with the correspondingly higher densities, as discussed by Torczynski et al. (1989). As a result, density variations within the laser cell induced by gas motion produce significant refractive index

[1] Senior Member of the Technical Staff, Fluid and Thermal Sciences Department, Sandia National Laboratories, Albuquerque, NM 87185-5800.

Contributed by the Fluids Engineering Division of THE AMERICAN SOCIETY OF MECHANICAL ENGINEERS. Manuscript received by the Fluids Engineering Division June 29, 1990.

isotropy represent a systematic approximation in homogeneous shear flow near equilibrium.

While the analysis presented here was carried out strictly for the case of homogeneous turbulence, it should carry over in an approximate sense to weakly inhomogeneous flows. The turbulence in the log region of a boundary layer is an example. Physical experiments at high Reynolds numbers (Rodi, 1982), as well as direct numerical simulations done at lower Reynolds numbers (Mansour et al., 1988), indicate that Sk/ϵ is in the range of 3 to 4 for $50 < y^+ < 100$ (were $y^+ = yu_*/\nu$ is the usual wall layer coordinate). This is not consistent with constraint (11); consequently, the commonly made assumption of local isotropy in the log layer of a high Reynolds number turbulent boundary layer appears to be questionable. The present considerations do not allow one to estimate the degree to which the small-scales are anisotropic, they only determine a condition when local isotropy is not a formally justified high Reynolds number approximation. However, some evidence exists that the dissipation tensor may be anisotropic in the log layer (Mansour et al., 1988).

Care must be taken in elevating a convenient hypothesis to a universally accepted principle. It was shown here that local isotropy is not a formally justifiable hypothesis if the nondimensional mean rate of strain (S^*k/ϵ) is not small: this is due to the direct influence of mean rate of strain upon the evolution of ϵ_{ij}. We have noted that this constraint on the rate of strain is not satisfied in many commonly encountered turbulent flows, for which local isotropy is often invoked in turbulence modeling studies. Future models should account for potentially significant anisotropies in the dissipation rate tensor.

Acknowledgments

We are grateful to Drs. R. Rogallo and M. J. Lee for discussing the subject of this paper with us. CGS acknowledges the support of the National Aeronautics and Space Administration under NASA contract No. NAS1-18605 while in residence at ICASE. Support provided by the CTR under its visitors program is also gratefully acknowledged by CGS.

References

Brasseur, J. G., 1991, "Comments on the Kolmogorov Hypothesis of Isotropy in the Small Scales," AIAA paper 91-0230.

Kuznetsov, V. R., Karyakin, M. Yu., and Praskovsky, A. A., 1990, "Anisotropy of Turbulence Fine-Scale Structure in High Reynolds Number Flows," Third European Turbulence Conference, Stokholm, Sweden.

Lee, M. J., and Reynolds, W. C., 1985, "Numerical Experiments on the Structure of Homogeneous Turbulence," *Turbulent Shear Flows*, Vol. 5, Springer-Verlag, New York, pp. 54–66.

Lee, M. J., Kim, J., and Moin, P, 1990, "Structure of Turbulence at High Shear Rate," *J. Fluid Mech.*, Vol. 216, pp. 561–583.

Mansour, N. N., Kim, J., and Moin, P., 1988, "Reynolds-stress and Dissipation Budgets in a Turbulent Channel Flow," *J. Fluid Mech.*, Vol. 194, pp. 15–44.

Maréchal, J., 1972, "Étude Expérimentale de la Déformation Plane d'une Turbulence Homogène," *J. de Mech.*, Vol. 11, pp. 263–294.

Reynolds, W. C., 1987, "Fundamentals of Turbulence for Turbulence Modeling and Simulation," in Lecture Notes for Von Kármán Institute, AGARD Lect. Ser. No. 86, pp. 1–66.

Rodi, W., 1982, "Examples of Turbulence Models for Incompressible Flows," *AIAA J.*, Vol. 20, pp. 872–879.

Rogers, M. M., Moin, P., and Reynolds, W. C., 1986, "The Structure and Modelling of the Hydrodynamic and Passive Scalar Fields in Homogeneous Turbulent Shear Flow," Stanford University Technical Report No. TF 19, Mechanical Engineering Department.

Sreenivasan, K. R., 1991, "On Local Isotropy of Passive Scalars in Turbulent Shear Flows," *Proc. Roy. Soc. London*, in press.

Sreenivasan, K. R., and Tavoularis, S., 1980, "On Skewness of Temperature Derivatives in Turbulent Flows," *J. Fluid Mech.*, Vol. 101, pp. 783–795.

Tavoularis, S., and Corrsin, S., 1981, "Experiments in Nearly Homogeneous Turbulent Shear Flow with a Uniform Mean Temperature Gradient," *J. Fluid Mech.*, Vol. 104, pp. 311–347.

Tavoularis, S., and Karnik, U., 1989, "Further Experiments on the Evolution of Turbulent Stresses and Scales in Uniformly Sheared Turbulence," *J. Fluid Mech.*, Vol. 204, pp. 457–478.

Tennekes, H., and Lumley, J. L., 1972, *A First Course in Turbulence*, MIT press, Cambridge, MA.

Townsend, A. A., 1954, "The Uniform Distortion of Homogeneous Turbulence," *Quart. J. Mech. Appl. Math.*, Vol. 7, pp. 104–127.

Uberoi, M. S., 1957, "Equipartition of Energy and Local Isotropy in Turbulent Flows," *J. Appl. Phys.*, Vol. 28, pp. 1165–1170.

Partial Acoustic Filtering Applied to the Equations of Compressible Flow

J. R. Torczynski[1]

Gas contained in a rectangular laser cell of large length and small width is subjected to large, transient, spatially nonuniform, volumetric heating when pumped. The heating time scale is much longer than the time required for an acoustic wave to traverse the width but can be comparable to the time required for an acoustic wave to traverse the length. Approximate equations describing the motion are derived by applying partial acoustic filtering to the equations of motion: pressure waves traversing the width are removed while pressure waves traversing the length are retained. For a simplified one-dimensional example, a significant density variation is found across the width of the laser cell; moreover, this density variation is in good agreement with a numerical solution of the unapproximated gas dynamic equations although the latter requires two orders of magnitude more computational time.

Nomenclature

A = heating amplitude scale
a = sound speed
L_x, L_z = domain extents in x, z
M_x, M_z = x and z Mach number scales
p = pressure
Q = volumetric heating
t = time
u, w = velocity x and z components
Δt = time step
$\Delta x, \Delta z$ = x and z grid spacings
γ = specific heat ratio
ρ = density
Υ = dissipation function
$\tilde{f}$ = nondimensional f
$\bar{f}$ = x-averaged f
$\hat{f}$ = difference $f - \bar{f}$
f_m = maximum of $|f|$
f_0 = initial or scale f

Introduction

The motion of gas in a laser cell is considered. Whereas many common lasers operate at low or near-vacuum pressures, the initial gas conditions considered herein are near room temperature and near or above atmospheric pressure, with the correspondingly higher densities, as discussed by Torczynski et al. (1989). As a result, density variations within the laser cell induced by gas motion produce significant refractive index

[1] Senior Member of the Technical Staff, Fluid and Thermal Sciences Department, Sandia National Laboratories, Albuquerque, NM 87185-5800.

Contributed by the Fluids Engineering Division of THE AMERICAN SOCIETY OF MECHANICAL ENGINEERS. Manuscript received by the Fluids Engineering Division June 29, 1990.

variations and thereby significantly affect optical propagation through the gas, as noted by Neal et al. (1989). The laser cell is typically a rectangular enclosure, in which the gas motion is approximately two-dimensional. The cross-axis width of the laser cell (x direction) is usually much smaller than its length along the optical axis (z direction). The mechanism by which the laser is pumped heats the gas volumetrically. This heating can be large in the sense that the mean pressure rise thus produced can be comparable to or exceed the gas pressure prior to pumping. It is also spatially nonuniform, with 0(1) variations in both the x and z directions. Since the heating time scale is typically much longer than the time required for an acoustic wave to traverse the width of the enclosure, significant cross-axis gas motion occurs during the heating. The cross-axis refractive index gradients established in this manner act like a lens with a focal length that varies in time, and this lensing can be strong enough to cause changes in the optical stability of the laser resonator, as reported by Torczynski and Neal (1988). Thus, a quantitative understanding of the induced gas motion is essential to predicting the laser's optical characteristics, as observed by Neal et al. (1990).

If the heating does not vary in the z direction, no gas motion is induced in this direction, and the situation becomes one-dimensional. This situation has been studied analytically by Torczynski (1989) using the acoustic filtering method discussed by Rehm and Baum (1978) and Paolucci (1982). Numerical solutions have also been reported for two-dimensional Cartesian and axisymmetric geometries with heating that varied in both the x and z directions by Torczynski and Gross (1988) and Torczynski et al. (1989). These involved finite-difference representations of the mass, momentum, and energy equations for the compressible flow of a perfect gas, which were solved using an explicit scheme to advance time. For such a method, the maximum allowable time step is scaled by the ratio of the minimum spacing between grid points divided by the maximum "characteristic" speed, essentially the sum of the sound speed and the particle speed (see Book (1981) for discussions of time step limitations of explicit methods). Density variations are expected to be 0(1) in both the x and z directions, so roughly the same number of grid points are used in each direction. Since the width of the enclosure is usually much smaller than its length, the cross-axis grid spacing controls the time step selection. Thus, the time steps are very small relative to the heating time scale.

This small time step arises from the fact that the numerical method discussed above resolves cross-axis pressure waves, as indicated in Torczynski and Gross (1988). However, as has been demonstrated analytically in the one-dimensional case by Torczynski (1989), the wave aspect of the cross-axis pressure variation is not important to the physics of the motion. As a result, it is not necessary to solve the equation for the cross-axis pressure variation to determine the gas motion: it may be solved after the fact. If the two-dimensional situation is similar to the one-dimensional situation in this regard, then a large portion of the computational effort of the approach of Torczynski and Gross (1988) is spent resolving a phenomenon of minimal physical importance. Developing an approach which removes the wave aspect of the cross-axis pressure variation is thus a desirable objective, both computationally and physically. However, since the heating time scale can be of the same magnitude as the time required for an acoustic wave to traverse the length of the enclosure, significant waves can be produced that propagate in the z direction. In light of this consideration, it is not possible to use the two-dimensional version of the acoustically filtered equations developed by Rehm and Baum (1978) since all pressure waves have been eliminated from these equations. Rather, it is reasonable to develop a system of equations which reflects the fact that the pressure variation in the z direction behaves in a wavelike manner, whereas the pressure variation in the x direction does not. This partial acoustic filtering approach has the dual benefits of providing fundamental insight into the physics of such flows and of facilitating the development of more efficient computational methods by removing the stringent time step constraint caused by resolving cross-axis pressure waves.

Two-Dimensional Cartesian Geometry

Consider a perfect gas with zero shear viscosity, bulk viscosity, and thermal conductivity confined within a rectangular enclosure with side walls at $x=0$ and $x=L_x$ and end walls at $z=0$ and $z=L_z$, where $L_x \ll L_z$. The gas motion is governed by the solution of the mass, momentum, and energy conservation equations for a perfect gas, given by Torczynski (1989) in a convenient form:

$$\frac{\partial \rho}{\partial t}+\frac{\partial}{\partial x}\rho u+\frac{\partial}{\partial z}\rho w=0, \tag{1}$$

$$\frac{\partial}{\partial t}\rho u+\frac{\partial}{\partial x}\rho u^2+\frac{\partial}{\partial z}\rho uw+\frac{\partial p}{\partial x}=0, \tag{2}$$

$$\frac{\partial}{\partial t}\rho w+\frac{\partial}{\partial x}\rho uw+\frac{\partial}{\partial z}\rho w^2+\frac{\partial p}{\partial z}=0, \tag{3}$$

$$\frac{\partial p}{\partial t}+\gamma p\left(\frac{\partial u}{\partial x}+\frac{\partial w}{\partial z}\right)+u\frac{\partial p}{\partial x}+w\frac{\partial p}{\partial z}=(\gamma-1)Q. \tag{4}$$

Here, ρ is the density, p is the pressure, u is the velocity in the x direction, w the velocity in the z direction, γ the specific heat ratio, and Q the applied heating. The boundary conditions correspond to no flow through the boundaries: $u(0, z, t) = u(L_x, z, t) = 0$ and $w(x, 0, t) = w(x, L_z, t) = 0$. The gas is initially at rest with density ρ_0 and pressure p_0.

The heating has amplitude Q_0 and varies smoothly over a time scale t_0 in time and over length scales L_x and L_z in x and z, respectively. Significant density variations can be obtained in the x and z directions only if u is $O(L_x/t_0)$ and w is $O(L_z/t_0)$. Thus, the following dimensionless variables, denoted by tildes, are introduced:

$$\begin{aligned} u&=(L_x/t_0)\tilde{u}, & w&=(L_z/t_0)\tilde{w},\\ x&=L_x\tilde{x}, & z&=L_z\tilde{z},\\ t&=t_0\tilde{t}, & Q&=Q_0\tilde{Q},\\ \rho&=\rho_0\tilde{\rho}, & p&=p_0\tilde{p}. \end{aligned} \tag{5}$$

In the dimensionless variables, Eqs. (1) through (4) become the following:

$$\frac{\partial \tilde{\rho}}{\partial \tilde{t}}+\frac{\partial}{\partial \tilde{x}}\tilde{\rho}\tilde{u}+\frac{\partial}{\partial \tilde{z}}\tilde{\rho}\tilde{w}=0, \tag{6}$$

$$\frac{\partial}{\partial \tilde{t}}\tilde{\rho}\tilde{u}+\frac{\partial}{\partial \tilde{x}}\tilde{\rho}\tilde{u}^2+\frac{\partial}{\partial \tilde{z}}\tilde{\rho}\tilde{u}\tilde{w}+M_x^{-2}\frac{\partial \tilde{p}}{\partial \tilde{x}}=0, \tag{7}$$

$$\frac{\partial}{\partial \tilde{t}}\tilde{\rho}\tilde{w}+\frac{\partial}{\partial \tilde{x}}\tilde{\rho}\tilde{u}\tilde{w}+\frac{\partial}{\partial \tilde{z}}\tilde{\rho}\tilde{w}^2+M_z^{-2}\frac{\partial \tilde{p}}{\partial \tilde{z}}=0, \tag{8}$$

$$\frac{\partial \tilde{p}}{\partial \tilde{t}}+\gamma\tilde{p}\left(\frac{\partial \tilde{u}}{\partial \tilde{x}}+\frac{\partial \tilde{w}}{\partial \tilde{z}}\right)\tilde{u}\frac{\partial \tilde{p}}{\partial \tilde{x}}+\tilde{w}\frac{\partial \tilde{p}}{\partial \tilde{z}}=A\tilde{Q}, \tag{9}$$

where $A=(\gamma-1)Q_0t_0/p_0$ is the heating amplitude scale, and $M_x=(L_z/t_0)/\sqrt{p_0/\rho_0}$ and $M_z=(L_z/t_0)/\sqrt{p_0/\rho_0}$ are the Mach number scales, which are ratios of the transit times of acoustic waves traveling distances L_x and L_z to the heating time scale t_0.

Following Rehm and Baum (1978) and Paolucci (1982), the appearance of the large term M_x^{-2} in Eq. (7) indicates that the pressure takes the form

$$p(x, z, t)=\bar{p}(z, t)+\hat{p}(x, z, t), \tag{10}$$

$$\int_0^{L_x}\hat{p}(x, z, t)dx=0, \tag{11}$$

where $\hat{p}/\bar{p} = O(M_x^2)$. Note that $\bar{p}$ depends on z in partial acoustic filtering, whereas the analogous quantity in the acoustically filtered equations of Rehm and Baum (1978) has no spatial variation. Inserting this expansion into Eqs. (1) through (4), eliminating terms that are $O(L_x^2/L_z^2)$ or $O(M_x^2)$, integrating Eq. (4) over x from 0 to L_x, and subtracting the resultant average of Eq. (4) from Eq. (4), yields the following complete system of equations:

$$\frac{\partial \rho}{\partial t} + \frac{\partial}{\partial x}\rho u + \frac{\partial}{\partial z}\rho w = 0, \tag{12}$$

$$\frac{\partial}{\partial t}\rho u + \frac{\partial}{\partial x}\rho u^2 + \frac{\partial}{\partial z}\rho uw + \frac{\partial \hat{p}}{\partial x} = 0, \tag{13}$$

$$\frac{\partial}{\partial t}\rho w + \frac{\partial}{\partial x}\rho uw + \frac{\partial}{\partial z}\rho w^2 + \frac{\partial \bar{p}}{\partial z} = 0, \tag{14}$$

$$\frac{\partial \bar{p}}{\partial t} + \gamma \bar{p}\frac{\partial \bar{w}}{\partial z} + \bar{w}\frac{\partial \bar{p}}{\partial z} = (\gamma - 1)\bar{Q}, \tag{15}$$

$$\gamma \bar{p}\left(\frac{\partial u}{\partial x} + \frac{\partial \hat{w}}{\partial z}\right) + \hat{w}\frac{\partial \bar{p}}{\partial z} = (\gamma - 1)\hat{Q}, \tag{16}$$

$$\begin{aligned} \bar{f}(z, t) &= \frac{1}{L_x}\int_0^{L_x} f(x, z, t)\,dx, \\ \hat{f}(x, z, t) &= f(x, z, t) - \bar{f}(z, t), \end{aligned} \tag{17}$$

where $f \in \{p, Q, w\}$. In this notation, the bars denote averages in the x direction, and the hats denote deviations from the averages. Note that, by construction of Eq. (16) the integral of this equation from $x = 0$ to $x = L_x$ vanishes identically, so any velocity field u that satisfies Eq. (16) can simultaneously satisfy the required two boundary conditions, $u(0, z, t) = u(L_x, z, t) = 0$, even though Eq. (16) has only a first derivative for u. Equation (15) can be recast in conservation form (equivalent to entropy conservation):

$$\frac{\partial}{\partial t}\bar{p}^{1/\gamma} + \frac{\partial}{\partial z}\bar{w}\bar{p}^{1/\gamma} = \frac{(\gamma - 1)\bar{Q}\bar{p}^{1/\gamma}}{\gamma \bar{p}}. \tag{18}$$

Several observations can be made about Eqs. (12) through (16). Note that the cross-axis pressure variation $\hat{p}$ is decoupled from the gas motion since it appears only in Eq. (13). This equation for $\hat{p}$ doesn't need to be solved until after the other equations are solved to determine u, w, and ρ. Thus, although there is an extra equation in the new system (Eq. (13) for $\hat{p}$), it needs to be solved only for times at which knowledge of $\hat{p}$ is desired; moreover, it is solved simply by integrating with respect to x. In addition, Eq. (15) is a *one-dimensional* equation, and less computational work is required to solve it than would be required for a two-dimensional equation. Equation (16) can be written in another form for illustrative purposes:

$$\frac{\partial u}{\partial x} = \frac{\gamma - 1}{\gamma \bar{p}}\left[\hat{Q} - \bar{p}\frac{\partial \hat{w}}{\partial z} - \frac{\partial}{\partial z}\left(\frac{\bar{p}\hat{w}}{\gamma - 1}\right)\right]. \tag{19}$$

The three terms contained in the brackets on the right side of this equation represent the local deviation from the average rate of change of internal energy density due to entropy addition, work, and transport, respectively. If more energy is added at a point than is added on average, then $\partial u/\partial x$ is positive, so energy transport by the velocity field u is induced away from the point. Correspondingly, if too little energy is added compared with the average energy addition, then $\partial u/\partial x$ is negative, so energy transport by the velocity field u is induced toward the point. Thus, the induced velocity field u acts to level out cross-axis variations in the rate of change of internal energy density.

It is instructive to examine Eqs. (12) through (16) under several different limits. Suppose that no quantity varies with x. In this case, the situation becomes one-dimensional in the z direction, and Eqs. (12) through (16) reduce to the one-dimensional fully compressible equations of motion with heat addition for a perfect gas. Thus, the unapproximated equations are recovered in this limit. As another limit, suppose instead that no quantity varies with z. In this case, the situation becomes one-dimensional in the x direction, and Eqs. (12) through (16) reduce to the one-dimensional acoustically filtered equations discussed in Torczynski (1989). Thus, the acoustically filtered equations are recovered in this limit. A more interesting limit arises from applying acoustic filtering ideas in the z direction. In the limit that $M_z^2 \ll 1$ (recall both $M_x^2 \ll 1$ and $L_x^2/L_x^2 \ll 1$), Eqs. (12) through (16) reduce to the two-dimensional acoustically filtered equations of Rehm and Baum (1978) in the limit that $L_x^2/L_z^2 \ll 1$.

Explicit Solution Scheme

A generic explicit solution scheme is outlined below for Eqs. (12) through (16). This scheme is not purported to be the optimal method of solution for these equations; rather, it is intended to illustrate the differences between solving Eqs. (12) through (16) and solving Eqs. (1) through (4) along the lines of the method in Torczynski and Gross (1988). The u, w, $\bar{p}$, and ρ fields are presumed to be given at a specific time. Equations (12), (14), and (15) are then advanced explicitly in time to determine the new ρ, ρw, and $\bar{p}$ fields. The new $\hat{w}$ and $\hat{Q}$ fields are found from Eq. (17) and the specific model for Q, respectively. The new fields are then used in conjunction with Eq. (16) to determine the new u field. The u, w, $\bar{p}$, and ρ fields are now known at the new time, and the procedure can be repeated. Whenever the $\hat{p}$ field is desired, Eq. (13) is solved.

A formal stability analysis has not yet been completed for the solution method outlined above for Eqs. (12) through (16). However, it appears that the time step limitation discussed for the explicit solution of Eqs. (1) through (4) is replaced by a less stringent condition. Consider a finite-difference representation employing grid points with separations Δx and Δz in the x and z directions. Let u_m, w_m, and a_m be the maxima of $|u|$, $|w|$, and a (the sound speed), respectively, over the domain. The maximum allowable time step for the explicit solution of Eqs. (1) through (4) is scaled by the minimum of $\Delta z/(a_m + w_m)$ and $\Delta x/(a_m + u_m)$. Since $\Delta x \ll \Delta z$ by virtue of $L_x \ll L_z$, the latter term generally limits the time step. It is conjectured that the maximum allowable time step for the explicit solution of Eqs. (12) through (16) will be scaled by the minimum of $\Delta z/(a_m + w_m)$ and $\Delta x/u_m$ since the cross-axis pressure waves, which transport information at the sound speed, have been removed. If this idea is correct, then the time step will be larger than the time step for the method applied to Eqs. (1) through (4) by roughly a factor of $\Delta z/\Delta x$ or a_m/u_m, whichever is smaller. Since each of these factors is typically O(30–100), a substantial improvement in computational efficiency may be achieved.

As an example, consider a one-dimensional model of a nuclear-reactor-pumped laser, as in Torczynski et al. (1989), involving argon, initially at 300 K and 100 kPa, between two infinite planes separated by 2 cm. The gas is heated by fission fragments from 1-μm UO_2 coating on the side walls. The heating Q has the form $Q = Q_0 f(x/L_x)\exp[-(t/t_0)^2]$, where f is largest near the side walls and has a minimum at the centerplane, about which it is symmetric. (See Torczynski, 1989, for a detailed discussion of f.) In this example, $t_0 = 0.12$ ms and $Q_0 = 0.6$ kW/cm^3, which correspond to an energy deposition of 0.070 J/cm^3. Figure 1 shows the density and velocity fields at the peak of the heating, and Fig. 2 shows the pressure history. The open symbols result from an explicit solution of the full gas dynamic equations of the sort discussed above, and the solid curves are the solution of the one-dimensional version of Eqs. (12) through (16). In both cases, 100 points are used

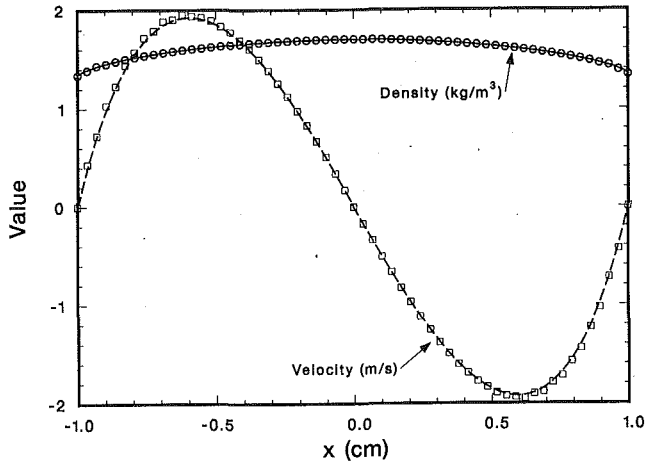

Fig. 1 Density and velocity versus position at $t = 0$ (peak heating): curves, partial acoustic filtering; symbols, full equations

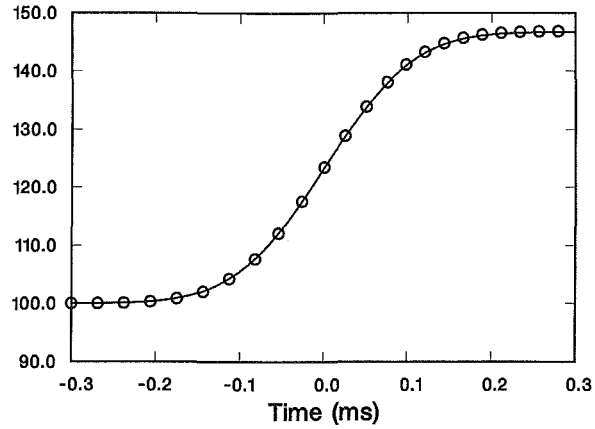

Fig. 2 Pressure versus time: solid curve, partial acoustic filtering; open symbols, full equations at $x = 0$ (only one point is shown for every 25 history points)

to discretize the domain. A mean time step of 0.12 μs (the time stepping is adaptive) is employed in the former based on the limitation discussed above, but a fixed time step of 12 μs is used in the latter, which represents a hundredfold reduction in computational effort. Since the sound speed in argon is 323 m/s (prior to heating) and flow velocities on the order of 2 m/s are observed, the ratio a_m/u_m is on the order of 100, which is comparable to the improvement seen. Note that the agreement between the two approaches is excellent, with no evidence of stability problems.

Conclusions

The motion of a perfect gas has been studied when the gas is subjected to large, transient, spatially nonuniform, volumetric heating while confined within a long rectangular enclosure of small width. The heating time scale is assumed to be long compared with the time required for an acoustic wave to travel across the width of the enclosure but may be short compared with the time required for an acoustic wave to travel along the length of the enclosure.

Partial acoustic filtering is developed and applied to the equations of motion for two-dimensional rectangular geometries. Approximate equations are derived which show that the pressure variation across the width is decoupled from the gas motion. Also, the velocity field across the width is seen to be driven by the deviation from the average in the rate of change of internal energy density and acts to level out cross-axis variations in this quantity. Arguments were presented indicating that the time step limitation imposed by the explicit solution of the approximate system may be much less stringent than the time step limitation imposed by the explicit solution of the original system.

In summary, partial acoustic filtering acts like an analytical filter by replacing an equation determining $\partial \rho u/\partial t$ (conservation of momentum in the x direction) with an equation determining $\partial u/\partial x$. This replacement removes pressure waves propagating across the width of the enclosure. It is possible that a computational method could be developed to solve the original system of equations which would act like a numerical filter to remove cross-axis pressure waves. Such a method would probably involve solving the x momentum equation in an implicit fashion.

Acknowledgments

This work was performed at Sandia National Laboratories, supported by the U.S. Department of Energy under contract number DE-AC04-76DP00789.

References

Book, D. L., 1981, *Finite-Difference Techniques for Vectorized Fluid Dynamics Calculations*, Springer-Verlag, New York, Chapter 4.

Neal, D. R., Sweatt, W. C., and Torczynski, J. R., 1989, "Resonator Design with an Intracavity Time-Varying Index Gradient," SPIE Paper 965-40, *Current Developments in Optical Engineering III*, R. E. Fischer and W. J. Smith, eds., *SPIE Proceedings*, Vol. 965, pp. 130–141.

Neal, D. R., Torczynski, J. R., and Sweatt, W. C., 1990, "Time-Resolved Wavefront Measurements and Analyses for a Pulsed, Nuclear-Reactor-Pumped Gain Region," *Optical Engineering*, Vol. 29, No. 11, pp. 1404–1412.

Paolucci, S., 1982, *On the Filtering of Sound from the Navier-Stokes Equations*, Sandia Report SAND82-8257, Sandia National Laboratories, Albuquerque, NM.

Rehm, R. G., and Baum, H. R., 1978, "The Equations of Motion for Thermally Driven Buoyant Flows," *Journal of Research of the National Bureau of Standards*, Vol. 83, pp. 297–308.

Torczynski, J. R., 1989, "On the Motion of a Gas Experiencing Range-Dependent Volumetric Heating," *Journal of Fluid Mechanics*, Vol. 201, pp. 167–188.

Torczynski, J. R., and Gross, R. J., 1988, "The Gasdynamics of Fission-Fragment Heating," *Proceedings of the 1st National Fluid Dynamics Congress*, C. Dalton, ed., AIAA, Washington, DC, pp. 1040–1047.

Torczynski, J. R., Gross, R. J., Hays, G. N., Harms, G. A., Neal, D. R., McArthur, D. A., and Alford, W. J., 1989, "Fission-Fragment Energy Deposition in Argon," *Nuclear Science and Engineering*, Vol. 101, No. 3, pp. 280–284.

Torczynski, J. R., and Neal, D. R., 1988, *Effect of Gasdynamics on Resonator Stability in Reactor-Pumped Lasers*, Sandia Report SAND88-1318, Sandia National Laboratories, Albuquerque, NM.

Reattachment Length Behind a Single Roughness Element in Turbulent Pipe Flow

J. Faramarzi[1] and E. Logan[2]

Introduction

As shear flow passes over an obstacle, it becomes separated on top of the obstacle. This separated shear layer curves sharply downstream in the reattachment region. Part of the shear layer

[1] Mechanical Engineer, Control Components, Inc., Rancho Santa Margarita, Calif.

[2] Professor, Mechanical and Aerospace Engineering Department, Arizona State University, Tempe, Ariz.

Contributed by the Fluids Engineering Division of THE AMERICAN SOCIETY OF MECHANICAL ENGINEERS. Manuscript received by the Fluids Engineering Division November 20, 1990.

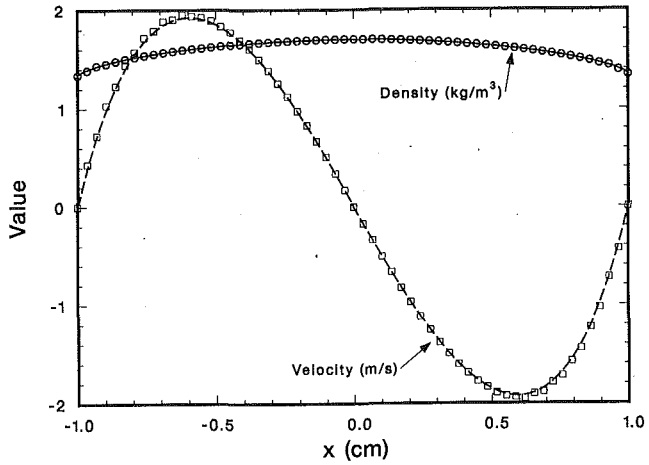

Fig. 1 Density and velocity versus position at $t = 0$ (peak heating): curves, partial acoustic filtering; symbols, full equations

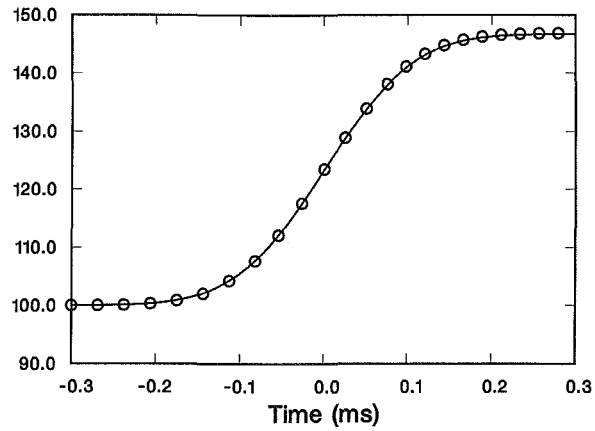

Fig. 2 Pressure versus time: solid curve, partial acoustic filtering; open symbols, full equations at $x = 0$ (only one point is shown for every 25 history points)

to discretize the domain. A mean time step of 0.12 μs (the time stepping is adaptive) is employed in the former based on the limitation discussed above, but a fixed time step of 12 μs is used in the latter, which represents a hundredfold reduction in computational effort. Since the sound speed in argon is 323 m/s (prior to heating) and flow velocities on the order of 2 m/s are observed, the ratio a_m/u_m is on the order of 100, which is comparable to the improvement seen. Note that the agreement between the two approaches is excellent, with no evidence of stability problems.

Conclusions

The motion of a perfect gas has been studied when the gas is subjected to large, transient, spatially nonuniform, volumetric heating while confined within a long rectangular enclosure of small width. The heating time scale is assumed to be long compared with the time required for an acoustic wave to travel across the width of the enclosure but may be short compared with the time required for an acoustic wave to travel along the length of the enclosure.

Partial acoustic filtering is developed and applied to the equations of motion for two-dimensional rectangular geometries. Approximate equations are derived which show that the pressure variation across the width is decoupled from the gas motion. Also, the velocity field across the width is seen to be driven by the deviation from the average in the rate of change of internal energy density and acts to level out cross-axis variations in this quantity. Arguments were presented indicating that the time step limitation imposed by the explicit solution of the approximate system may be much less stringent than the time step limitation imposed by the explicit solution of the original system.

In summary, partial acoustic filtering acts like an analytical filter by replacing an equation determining $\partial \rho u/\partial t$ (conservation of momentum in the x direction) with an equation determining $\partial u/\partial x$. This replacement removes pressure waves propagating across the width of the enclosure. It is possible that a computational method could be developed to solve the original system of equations which would act like a numerical filter to remove cross-axis pressure waves. Such a method would probably involve solving the x momentum equation in an implicit fashion.

Acknowledgments

This work was performed at Sandia National Laboratories, supported by the U.S. Department of Energy under contract number DE-AC04-76DP00789.

References

Book, D. L., 1981, *Finite-Difference Techniques for Vectorized Fluid Dynamics Calculations*, Springer-Verlag, New York, Chapter 4.

Neal, D. R., Sweatt, W. C., and Torczynski, J. R., 1989, "Resonator Design with an Intracavity Time-Varying Index Gradient," SPIE Paper 965-40, *Current Developments in Optical Engineering III*, R. E. Fischer and W. J. Smith, eds., *SPIE Proceedings*, Vol. 965, pp. 130–141.

Neal, D. R., Torczynski, J. R., and Sweatt, W. C., 1990, "Time-Resolved Wavefront Measurements and Analyses for a Pulsed, Nuclear-Reactor-Pumped Gain Region," *Optical Engineering*, Vol. 29, No. 11, pp. 1404–1412.

Paolucci, S., 1982, *On the Filtering of Sound from the Navier-Stokes Equations*, Sandia Report SAND82-8257, Sandia National Laboratories, Albuquerque, NM.

Rehm, R. G., and Baum, H. R., 1978, "The Equations of Motion for Thermally Driven Buoyant Flows," *Journal of Research of the National Bureau of Standards*, Vol. 83, pp. 297–308.

Torczynski, J. R., 1989, "On the Motion of a Gas Experiencing Range-Dependent Volumetric Heating," *Journal of Fluid Mechanics*, Vol. 201, pp. 167–188.

Torczynski, J. R., and Gross, R. J., 1988, "The Gasdynamics of Fission-Fragment Heating," *Proceedings of the 1st National Fluid Dynamics Congress*, C. Dalton, ed., AIAA, Washington, DC, pp. 1040–1047.

Torczynski, J. R., Gross, R. J., Hays, G. N., Harms, G. A., Neal, D. R., McArthur, D. A., and Alford, W. J., 1989, "Fission-Fragment Energy Deposition in Argon," *Nuclear Science and Engineering*, Vol. 101, No. 3, pp. 280–284.

Torczynski, J. R., and Neal, D. R., 1988, *Effect of Gasdynamics on Resonator Stability in Reactor-Pumped Lasers*, Sandia Report SAND88-1318, Sandia National Laboratories, Albuquerque, NM.

Reattachment Length Behind a Single Roughness Element in Turbulent Pipe Flow

J. Faramarzi[1] and E. Logan[2]

Introduction

As shear flow passes over an obstacle, it becomes separated on top of the obstacle. This separated shear layer curves sharply downstream in the reattachment region. Part of the shear layer

[1] Mechanical Engineer, Control Components, Inc., Rancho Santa Margarita, Calif.

[2] Professor, Mechanical and Aerospace Engineering Department, Arizona State University, Tempe, Ariz.

Contributed by the Fluids Engineering Division of THE AMERICAN SOCIETY OF MECHANICAL ENGINEERS. Manuscript received by the Fluids Engineering Division November 20, 1990.

fluid is deflected upstream into a highly turbulent recirculation zone by a strong adverse pressure gradient. Downstream shape of the obstacle has a strong effect on the size of the separated flow and limits the entrainment of this internal shear layer. Downstream of the reattachment a new sublayer starts to grow. The reattachment length for obstacles with a rectangular cross-sectional shape has been estimated by a number of investigators, e.g., Mueller and Robertson (1962), Bradshaw and Wong (1972), Bergeles and Athanassiadis (1983), and Logan and Phataraphruk (1989). The need to determine the reattachment length more precisely inspired the present investigation, the objective of which is to determine the dependence of reattachment length (L_R) on element height (H), element width (W), pipe radius (R), and Reynolds number (Re). Such results are helpful in evaluation of numerical schemes for predicting flow fields and heat transfer or mixing rates in the wakes of obstacles.

Apparatus and Test Method

Reattachment lengths were determined from pressure measurements and flow visualization techniques. Ring-shaped elements of square cross-section were fitted against the inside wall of 101.6 mm (4 in.) Plexiglas pipe shown in Fig. 1. Element heights of 0.10, 0.15, and 0.20 times the pipe radius were used in the tests. The width of elements were increased by combining square elements of the same height. A fully-developed air flow is produced upstream of the test section at Reynolds numbers of 64,000 and 113,600.

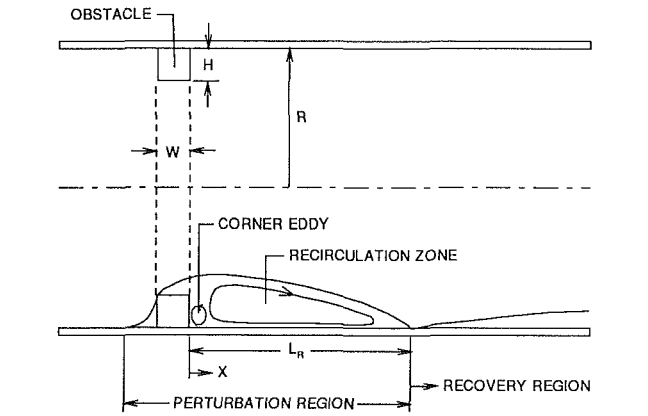

Fig. 1 Test configuration

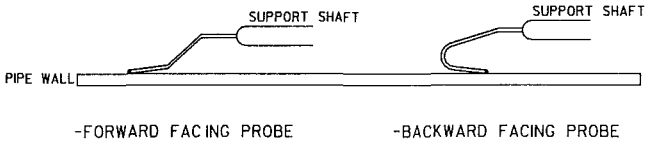

Fig. 2 Forward and backward-facing pressure probes

Pressure probes were made of 0.56-mm (0.0220-in.) hypodermic tubing and their form is depicted in Fig. 2. The probes were located in at the pipe wall and used to measure total pressure. They were connected to a Statham transducer, which was connected to a bridge amplifier and voltmeter. Static pressure was measured along the wall using 22 wall pressure taps on 5.1-mm (0.2-in.) centers and 11 taps on 10.2-mm (0.4-in.) centers. The probes were positioned by means of a micrometer-driven traversing device. The forward-facing probes were moved along the test section wall behind the element, and then the backward-facing probes were moved over the same path. Comparison of the resulting pressure readings led to precise determination of reattachment lengths. The accuracy of reattachment length was determined by examining its variation due to the uncertainty in measurements of pressure and length.

Flow visualization was used to locate the reattachment point as well. The wall pressure taps were used to inject a mixture of writing ink and rubbing alcohol. The mixture was forced

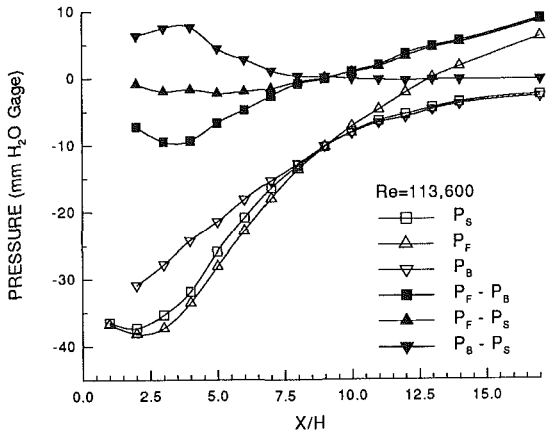

Fig. 3 Pressure versus *X/H* for *H/R* = 0.10, *W/H* = 1 (uncertainty in *X/H* = +/− 1 percent, in pressure = +/− 2 percent)

Table 1 Tabulated reattachment lengths

(*a*) Reattachment length results from pressure measurements

W/H	Re = 113000			Re = 64000		
	H/R = 0.1	*H/R* = 0.15	*H/R* = 0.2	*H/R* = 0.1	*H/R* = 0.15	*H/R* = 0.2
1	9.2	9.1	8.9	9.1	9.2	9.1
2	6.1	6.5	6.9	5.9	6.5	6.8
3	5.9	6.4	6.5	6.0	6.5	6.7
4	6.0	6.2	6.7	6.0	6.5	6.8
5	6.0	6.4	6.6	6.0	6.5	6.7
6	6.0	6.5	6.5	6.0	6.5	6.7
7	6.1	6.4	6.6	6.0	6.5	6.7
Accuracy (+/−)	0.3	0.25	0.2	0.3	0.25	0.2

(*b*) Reattachment length results from flow visualization

W/H	Re = 113000			Re = 64000		
	H/R = 0.1	*H/R* = 0.15	*H/R* = 0.2	*H/R* = 0.1	*H/R* = 0.15	*H/R* = 0.2
1	9.5	9	9	9.5	9	9
2	6	6.5	6.75	6	6.5	6.75
3	6	6.5	6.5	6	6.5	6.5
4	6	6.5	6.5	6	6.5	6.5
5	6	6.5	6.5	6	6.5	6.5
6	6	6.5	6.5	6	6.5	6.5
7	6	6.5	6.5	6	6.5	6.5
Accuracy (+/−)	0.5	0.33	0.25	0.5	0.33	0.25

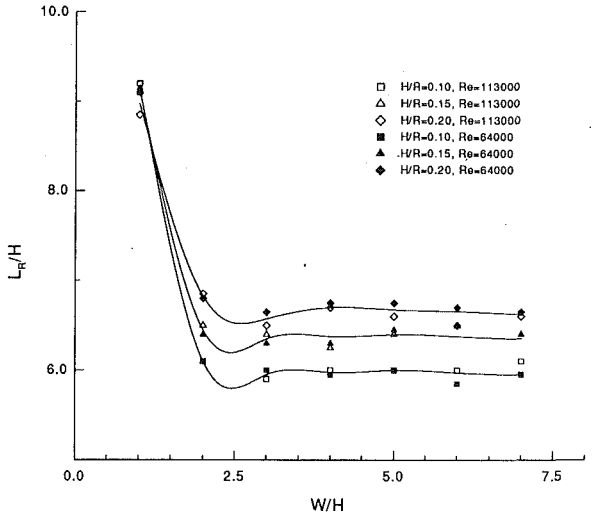

Fig. 4 Reattachment length versus element height (uncertainty in L_R/H = +/−0.25 for H/R = 0.20, +/−0.33 for H/R = 0.15, +/−0.5 for H/R = 0.10)

to move upstream or downstream from the point of injection by fluid stresses. When adjacent ports had outflows in opposite directions, the midpoint between the ports was assumed to be the reattachment point and its accuracy assumed to be one half the distance between the two adjacent ports.

Results

Figure 3 shows a typical result of the pressure measurements as a function of axial position X/H and height of the element H/R. In this figure, the symbols P_S, P_F, and P_B refer to the static pressure reading, the total pressure reading with the forward-facing tube, and the total pressure reading with backward-facing tube, respectively. In this and all other test cases, the curves representing the pressures as well as those representing the pressure differences intersect at the value of X/H corresponding to the reattachment point. The values of the non-dimensional reattachment length L_R/H are tabulated in Table 1 for values of H/R and W/H used in the tests. There was good agreement between the results from pressure measurements and flow visualization as seen from Table 1. The results also indicate that for highly turbulent flows (high Reynolds numbers) the reattachment length is independent of Reynolds number. Results of Table 1(*a*) are shown graphically in Fig. 4. As shown in this figure, as H/R increases, so does the entrainment of the internal shear layer and the reattachment length L_R/H.

Conclusions

The following conclusions are drawn regarding the flow reattachment length behind obstacles with rectangular cross-sectional shapes:

1) Reattachment length is independent of Reynolds number.

2) Reattachment length is a strong function of obstacle width for W/H less than some critical value. The critical value of W/H is between 1 and 2 for $H/R = 0.10$ and 0.15 and between 2 and 3 for $H/R = 0.20$.

3) The asymptotic value of reattachment length is a weak function of H/R. L_R/H reaches a minimum of 6.0 for $H/R = 0.10$ and 6.5 for $H/R = 0.15$ and 0.20.

References

Bergeles, G., and Athanassiadis, N., 1983, "The Flow Past a Surface Mounted Obstacle," ASME JOURNAL OF FLUIDS ENGINEERING, Vol. 105, pp. 461-463.

Bradshaw, P., and Wong, F. Y. F., 1972, "The Reattachment and Relaxation of a Turbulent Shear Layers," ASME *J. Fluid Mech.*, Vol. 46, pp. 113-135.

Logan, E., and Phataraphruk, P., 1989, "Mean Flow Downstream of Two-Dimensional Roughness Elements," ASME JOURNAL OF FLUIDS ENGINEERING, Vol. 111, pp. 149-153.

Mueller, T. J., and Robertson, J. M., 1962, "A Study of Mean Motion and Turbulence Downstream of Roughness Elements," *Proc. 1st Southeastern Conf. on Theoretical and Applied Mechanics*, pp. 326-340.